Design and Synthesis of Functionalised Polyethers and Polyesters

Yvonne Shuen Lann Choo

Doctor of Philosophy

School of Natural and Environmental Sciences

Newcastle University

November 2018

Abstract

Artificial photosynthesis, a game changer in the field of alternative energy, is believed to be able to provide greener hydrogen in near future for hydrogen powered vehicles via the photocatalytic splitting of water. The Nafion membrane that is currently being widely used in water splitting systems has a number of flaws including its selectivity, environmental inadaptability, the need to be moistened to conduct protons and swelling. With membranes playing an important role, the development of new membranes having improved properties would bring about change in efficiency of the water splitting device. This thesis covers two different approaches in membrane design and synthesis in an attempt to achieve an ideal polymer.

Chapter 1 gives an overview of the research area and objectives, starting from an introduction to the field of artificial photosynthesis with emphasis on photocatalytic water splitting and how the development of new membranes in place of Nafion could be beneficial for the field.

Chapter 2 starts off with the synthesis and characterisation of four pyrene-based polyethers (**AP Series**) and two clickable-pyrene-based polyethers (**YC Series**). Two different methods have been employed for the synthesis of these polymers with one being more favorable than the other. The two approaches and their pros and cons will be discussed.

Chapter 3 discusses the synthesis and characterisation of a successfully clicked pyrene derivative (**Pyr2COOMe**) and its potential polymerisation blueprint.

Chapter 4 begins with the synthesis and characterisation of six anthracene-based polyethers (**PA Series**) with varying degree of modifications and two tapered-anthracene-co-modified polyethers (**URV Series**). Membranes of **URV Series** were prepared via immersion precipitation and their surface morphologies were studied.

Chapter 5 highlights the synthesis, characterisation and coordination studies of a crown ether terephthalate derivative (**CM1**). The resemblance of its crystal XRD structure to an actual jellyfish will be shared.

Chapter 6 discusses the synthesis and characterisation of three terephthalate-based polyesters. One of the polyesters was synthesised from **CM1** monomer mentioned in **Chapter 5**.

Apart from **Chapter 1**, every other chapter has been written in the format of a paper with their respective introduction and conclusion.

Lastly, **Chapter 7** includes a summary of each chapter in addition to a list of possible future work.

Publications

Results collected in Chapter 2 are used in the preparation of the following article:

Y.S.L. Choo, A.C. Benniston, P. Waddell, Synthesis and Characterisation of Pyrene-based Polyethers.

Results collected in Chapter 3 are used in the preparation of the following article:

Y.S.L. Choo, P. Waddell, A.C. Benniston, Synchronised “Click” and Templated Synthesis of a Fluorescent Pyrene Crown Ether.

Results collected in Chapter 4 are used in the preparation of the following article:

Y.S.L. Choo, A.C. Benniston, M. Giamberini, J.A. Reina, Light Driven Irreversible Organogelation of Anthracene-containing Polyethers: Fluorescent Redox Switched Memory Materials.

Results collected in Chapter 5 and 6 are used in the preparation of the following article:

Y.S.L. Choo, A.C. Benniston, P. Waddell, Synthesis of Crown Ether Containing Highly Substituted Terephthalate Monomers and their Attempted Polyester Formation.

Dedication

This thesis is dedicated to my family for their unconditional love and support through the ups and the downs of my PhD journey.

Thank you for having faith in me. I love you.

Acknowledgements

As unconventional as it can get, I would like to start this section off by giving myself a pat on the back for getting this far, thank you for persevering through tough times and for being kinder to yourself. If I were to describe what my PhD was like, I would say that it has been a growth process, like a metamorphosis. I have learned a lot from my journey and I would like to believe it has transformed me for the better.

Getting this far would not have been possible without the people that I have met throughout my PhD. Since there are so many people whom I have crossed paths with, I'd like to take this opportunity to highlight individuals whom I am exceptionally grateful to. However, to those I might have missed out, do know that our personal encounters will always be cherished in my heart and that I am forever thankful to have been given the opportunity to get to know you.

To start off, I would like to thank my supervisor, Prof. Andrew Benniston for giving me the chance to pursue a PhD under his supervision. Since first year, Andy has given me a lot of freedom to take control of my research project. He has been guiding me through the process and has always been there during the hard times. He is very supportive and has always believed in my abilities even when I am in doubt. For that, I am truly grateful. To Jane, who has always assisted me in admin related tasks, I would like to thank you for all your help. Appreciate it!

Next, I would like to thank my current colleagues, Lily and Dima for keeping me company at all times, for having knowledgeable discussions and for cracking jokes at times of need. The lab would have been lonely without the both of you, thanks for being such good friends. To Tom who has been colleagues with me during the first two years of my PhD, thank you for being a good listener and for helping me cope with my first year abroad. To Pau and Maria, whom I've missed, thank you for all the good times together! I would like to thank all the members of the MPL/Photon cluster for your presence and for the willingness to share (knowledge, skills, lab equipment/chemicals, etc).

I would also like to express my gratitude towards Dr Corinne Wills and Dr Paul Waddell for their help in the acquisition of NMR spectra and crystal XRD structures, respectively.

I would like to then take the chance to thank Dr Marta Giamberini and Dr Jose Antonio Reina for giving me the opportunity to work in your research laboratory for 4.5 months. I have learned a whole lot from the both of you throughout my research/collaborative visit in Tarragona and have met a lot of good friends along the way whom I am still in touch with 2 years after my visit. Some of which are (in no specific order): Jie, Cristina, Xavier, Krzysztof, Alberto, Ruben, Issac, Lorena, Adrian, Rita, Gianmarco, Mario, Mimmo, Pepa, Dailyn, etc… and many many more! Thank you for being friends with me and for sharing your expertise in polymer science ☺ Thank you Prof. Angels Serra Albet for your teaching me lots of Catalan words/phrases along the way.

Thank you Pn Azura Ishak for being a part of my journey since my secondary school years. Thank you for inspiring me to pursue Chemistry and for being the best Chemistry teacher in my life!

Last but not least, none of this would have been possible without the continuous and unconditional love and support from my family. They have been financially, psychologically and physically supporting me to pursue Chemistry. They have always encouraged me to chase my dreams and be the ones to tell me not to worry about anything else besides my studies/research because they've got it all covered. For all that, I am forever grateful. I hope you will all be proud and happy of my achievements! Thank you dad (Choo Wing Keong), mom (Nancy Lim) and Dann (Daniel Choo), I love you.

The Highlights of My PhD

http://yvonnechoo.tumblr.com/

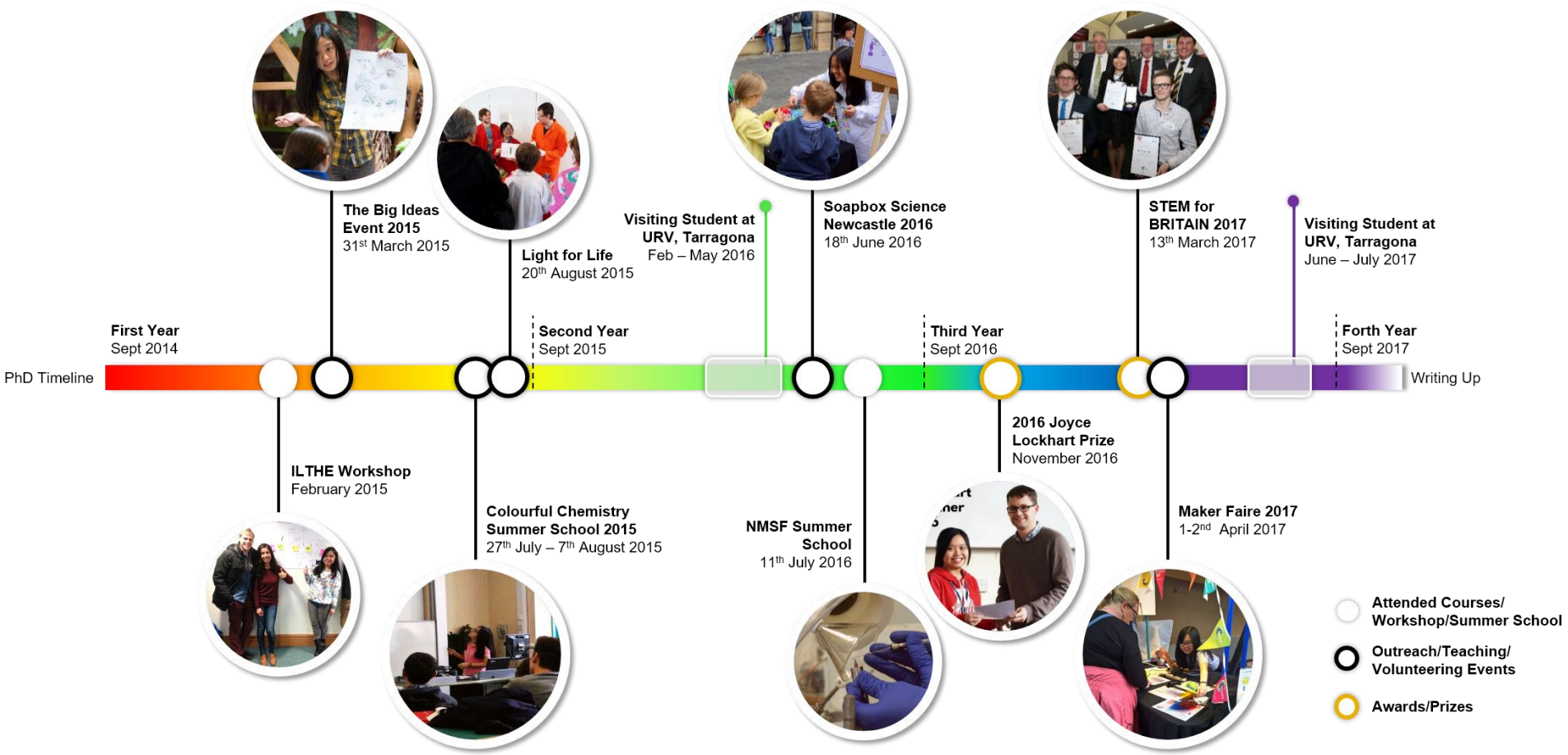

Abbreviations

% w/w	Weight-weight percentage
^{13}C	Carbon
18C6	18-crown-6
^{1}H	Proton
3D	Three-dimensional
9-ACA	Anthracene-9-carboxylic acid
AFM	Atomic force microscopy
AIQ	Aggregation-induced quenching
$AlCl_3$	Aluminium chloride
approx.	Approximately
AQ	Anthraquinone
BD	1,4-butandiol
BHT	Butylated hydrotoluene
br	Broad peak
Br_2	Bromine
BZALD	Benzaldehyde
calcd.	Calculated
cat.	Catalyst
CB	Conduction Band
CD_3CN	Deuterated acetonitrile
$CDCl_3$	Chloroform
CGC	Critical gelation concentration
COSY	Homonuclear correlation spectroscopy
Cu(0)	Copper
CuAAC	Copper-catalysed azide-alkyne cycloaddition
$CuSO_4$	Copper sulphate
D_2O	Deuterium oxide
DCM	Dichloromethane
DFT	Density functional theory
DME	1,2-dimethoxyethane
DMF	Dimethylformamide
DMSO	Dimethyl sulfoxide
DOSY	Diffusion ordered spectroscopy

DSC	Differential scanning calorimetry
e/m	Excimer/monomer ratio
EA	Ethyl acetate
EC	Electrochemical
ECH	Epichlorohydrin
EG	Ethylene glycol
EO	Ethylene oxide
EPO	Endoperoxide
Et_2O	Diethyl ether
EtOH	Ethanol
FEP	Fluorinated ethylene propylene
FT-IR	Fourier-transform infrared spectroscopy
FTMS	Fourier-transform based mass spectrometry
FW	Formula weight
GC	Gas chromatography
GPC	Gel permeation chromatography
H_2	Hydrogen gas
H_2O	Distilled water
h-h	Head to head
HMBC	Heteronuclear multiple bond correlation
HNO_3	Nitric acid
HSQC	Heteronuclear single quantum correlation
h-t	Head to tail
K_2CO_3	Potassium carbonate
K_a	Binding constant
KF	Potassium fluoride
KOH	Potassium hydroxide
KPF_6	Potassium hexafluorophosphate
LC	Liquid crystalline
$LiPF_6$	Lithium hexafluorophosphate
LMWG	Low-molecular-weight gelator
m/z	Mass charge ratio
MeCN	Acetonitrile
MeOH	Methanol

$MgSO_4$	Magnesium sulphate
Milli-Q water	Millipore ultrapure water
min	Minute
MM+	Molecular dynamics simulation
Mn	Number average molecular weight
mod.	Modified/modification
M_w	Weight average molecular weight
N_2	Nitrogen gas
Na_2CO_3	Sodium carbonate
NaAsc	Sodium L-ascorbate
$NaBH_4$	Sodium borohydride
NaH	Sodium hydride
$NaHSO_3$	Sodium bisulfite
NaI	Sodium iodide
NaN_3	Sodium azide
nanoESI	Nano-Electrospray Ionisation
$NaPF_6$	Sodium hexafluorophosphate
NH_4Cl	Ammonium chloride
NH_4OAc	Ammonium acetate
NH_4PF_6	Ammonium hexafluorophosphate
NMR	Nuclear magnetic resonance
OLED	Organic light-emitting-diode
oligo-THF	Oligotetrahydrofuran
P(ECH-co-EO)	Poly(epichlorohydrin-co-ethylene oxide)
PAZE	Poly[2(aziridin-1-yl)-ethanol]
PCl_5	Phosphorus pentachloride
PDI	Polydispersity index
PEC	Photoelectrochemical cell
PECH	Polyepichlorohydrin
PEM	Proton exchange membrane
PET	Polyethylene terephthalate
PFA	Paraformaldehyde
PFSA	Perfluorosulfonic acid
POG	Polymeric organogelator

POM	Polarised optical microscopy
prep-TLC	Preparative thin layer chromatography
PS	Polystyrene
Pt	Platinum
PtAn	Phthalic anhydride
PTC	Phase-transfer catalyst
PTFE	Poly(tetrafluoroethylene)
p-TsCl	4-toluenesulfonyl chloride
PV	Photovoltaic
Py1	Pyrene
RH	Relative humidity
RMS	Root mean square
RNA	Ribonucleic acid
RT	Room temperature
S_0	Ground state
S_1	Excited state
sat.	Saturated
SCLCP	Side-chain liquid crystal polymers
SEC	Size-exclusion chromatography
SFE	Solar-energy to fuel-energy conversion efficiency
sh	Shoulder peak
SI	Supporting information
S_N2	Nucleophilic substitution
SPP^N	Solvent dipolarity-polarisability scale
STH	Solar-to-hydrogen efficiency
$T_{50\%}$	Temperature corresponding to 50% weight loss
TAP	Potassium 3,4,5-tris[4-(n-dodecan-1-yloxy)benzyloxy]benzoate
TBAB	Tetrabutylammonium bromide
TBTA	tris[(1-benzyl-1H-1,2,3-triazol-4-yl)methyl]amine
T_c	Clearing temperature
TCE	1,1,2,2-tetrachloroethane
TCL	Terephthaloyl chloride
TEA	Triethylamine

T_{endset}	Endset decomposition temperature
TetraEG	Tetraethylene glycol
TFA	Trifluoroacetic acid
T_g	Glass transition temperature
TGA	Thermogravimetric analysis
THF	Tetrahydrofuran
TIPS	Triisopropylsilyl ether
TLC	Thin layer chromatography
T_{max}	Peak mass loss rate temperature
TMS-N_3	Trimethylsilyl azide
TMV	Tobacco Mosaic Virus
TNBT	Titanium (IV) n-butoxide
T_{onset}	Onset decomposition temperature
TriEG	Triethylene glycol
TriEGdiNH_2	Triethylene glycol diamine
TS	Transition state
t-t	Tail to tail
unmod.	Unmodified
UV-Vis	Ultraviolet-visible
VB	Valence band
w/v	Weight volume ratio
XRD	X-ray diffraction
Zn	Zinc powder
$Zn(OAc)_2$	Zinc acetate
λ_{Abs}	Absorption wavelengths
λ_{Em}	Emission wavelengths
λ_{Exc}	Excitation wavelengths
Φ_{Flo}	Quantum yield

Table of Contents

List of Schemes, Figures and Tables

Schemes

Chapter 2

Chapter 3

Chapter 4

Chapter 5

Chapter 6

Figures

Chapter 1

Chapter 2

Chapter 3

Chapter 4

Chapter 5

Chapter 6

Chapter 2 (SI)

Chapter 3 (SI)

Chapter 4 (SI)

Chapter 5 (SI)

Chapter 6 (SI)

Tables

Chapter 2

Chapter 3

Chapter 4

Chapter 5

Chapter 6

Chapter 2 (SI)

Chapter 3 (SI)

Chapter 4 (SI)

Chapter 5 (SI)

Chapter 6 (SI)

Chapter 1

General Introduction and Research Objectives

1. General Introduction

To ensure a better reading experience, this thesis comes with a detachable A3-size map containing a compilation of chemical structures of the synthesised compounds, the chemical reactions involved and their corresponding chapter location to allow readers to navigate easily across chapters. The map can be found at the inner back cover of this thesis.

1.1 Overview

Since the industrial revolution, there has been an increase in human population and global energy demand. Most of the energy required for sustaining development has been supplied by the combustion of fossil fuels. This has led to a rise in carbon dioxide emission, thereby effectuating environmental problems such as global warming and climate change. In addition, the continual dependence on the finite fossil resources has eventually caused it to deplete. Since then, there has been a resurgence of interest in the development of renewable energy resources.

Among many of the existing renewable energy resources (e.g. solar, wind, tidal, hydroelectric, etc.), artificial photosynthesis appeared to be most viable and promising[1]. It mimics the process of natural photosynthesis which directly converts sunlight into high-value, energy-rich solar fuels (e.g. H_2, methanol, etc.) via the use of photoactive materials in an integrated device setup (photoelectrochemical cell, PEC)[2,3]. For the system to be considered economically viable, its solar-energy to fuel-energy conversion efficiency (SFE) needs to reach the threshold of 10 %[1,4]. To date, the reported solar-to-hydrogen (STH) efficiencies for photocatalytic water splitting are around < 1-18 % with some as high as > 20 % but the latter usually require the use of concentrated light and precious/expensive materials[4,5]. Although this technology has been receiving increasing attention over the years, it still remains at the level of laboratory curiosity due to many unaddressed practical development aspects of the device and its lack of cost competitiveness compared to fossil-fuel derived hydrogen

(from steam methane reforming, coal gasification, etc.)[3,6,7]. Thus, any research that focuses on the optimisation or alteration on the components of the device such as its photocatalyst, proton exchange membrane or even its cell design would be very beneficial to the future of the system.

1.2 Photoelectrochemical cell (PEC)

There are three main types of PEC used in photocatalytic water splitting mainly: a) fully integrated/wireless PEC, b) partially integrated/wired PEC and c) non-integrated/modular PEC as shown in Figure 1.

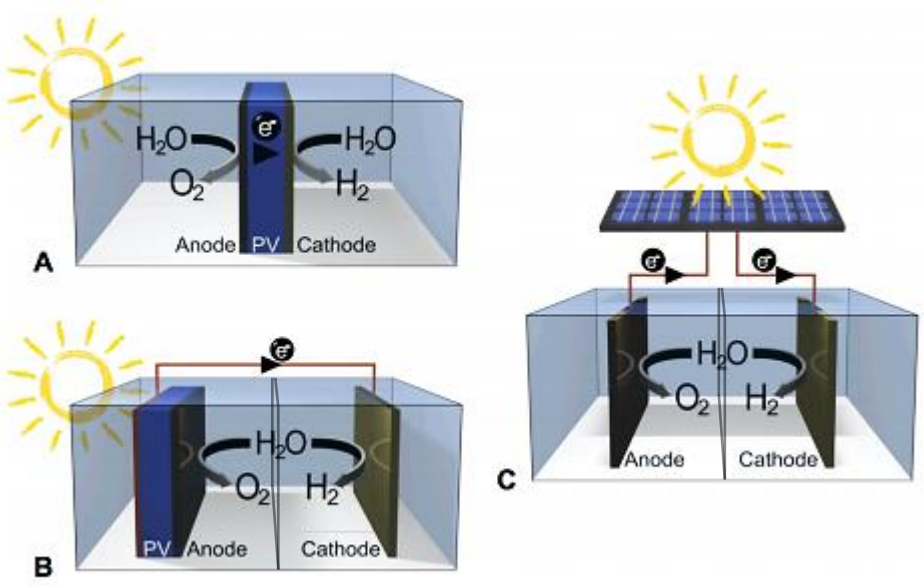

Figure 1: *Schematic representation of the types of photoelectrochemical (PEC) cell used in photocatalytic water splitting:* ***a)*** *fully integrated/wireless PEC,* ***b)*** *partially integrated/wired PEC and* ***c)*** *non-integrated/modular PEC. Image courtesy of Bonke et al.*[4]

The wireless PEC in Figure 1a, also known as the “absorber-in-membrane” design contains catalyst-covered semiconductors arranged in tandem while embedded in a single proton exchange membrane, PEM[8,9]. A much clearer representation of a wireless cell can be seen in Figure 2. In such a system where the external wire is absent, the membrane not only provides a path for protons conduction, it also provides mechanical support for the components of the cell. As a result of not having an external wire, electron transport occurs through the electrically conductive materials within the PEM.

The wired PEC in Figure 1b contains two separated electrodes: a catalyst-covered photoabsorber and a counter electrode, both immersed in liquid electrolyte. In this cell, the two electrodes are usually separated by a PEM into two compartments. The photoanode will be exposed to direct sunlight whereas the counter electrode/cathode can be kept in the dark[4,8,9].

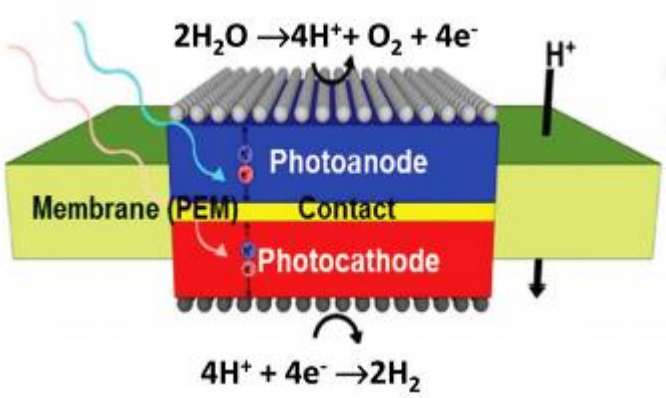

Figure 2: *1D representation of an integrated membrane-based system for artificial photosynthesis. The image shows the nature of light absorption, carrier transport, catalysis and ion transport through the membrane. Image courtesy of Fountaine et al.[10,11]*

The third type of PEC shown in Figure 1c is a modular system with its photovoltaic, PV and electrochemical, EC elements separated by external wiring. Like the wired system, the anode and cathode are compartmented by a PEM into two separate cells connected to an external PV[4].

1.2.1 Basic Principles of Photoelectrochemical Water Splitting

Water splitting is an uphill reaction, so in order to drive the reaction, the photoanode needs to absorb light to make its electrode potential higher than 1.23 V[12]. As shown in Figure 3, when the irradiated light has energy greater than the bandgap (E_{BG}) of the photoanode, electrons from its valence band, VB gets excited into the conduction band, CB, leaving holes in the VB[13,14]. The holes can then move to the surface of the electrode, where water is oxidised to produce O_2 while the photo-generated electrons get transferred across to the cathode to react with protons to produce H_2.

$$Anode: 2H_2O_{(l)} \rightarrow O_{2(g)} + 4H^+ + 4e^-$$

$$Cathode: 4H^+ + 4e^- \rightarrow 2H_{2(g)}$$

$$Overall: 2H_2O_{(l)} \rightarrow O_{2(g)} + 2H_{2(g)}$$

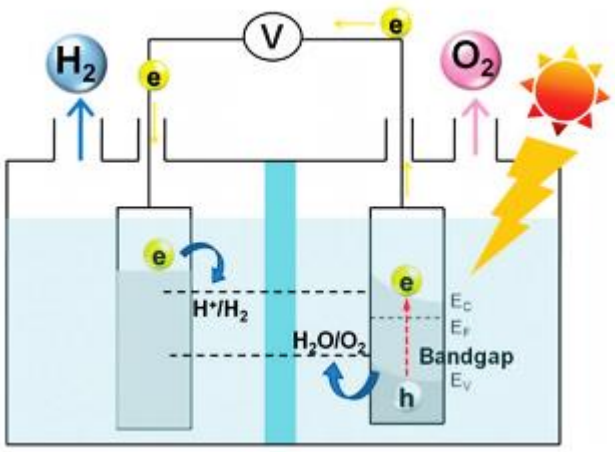

Figure 3: *Schematic diagram of the basic principles of water splitting for a photoelectrochemical cell with an n-type semiconductor photoanode. Oxygen is evolved at the photoanode while hydrogen is evolved at the photocathode (Pt Sheet). Image courtesy of Chen et al.*[13]

1.2.2 Proton Exchange Membrane (PEM)

PEM are usually based on polymer electrolytes. They are polymers which have negatively charged groups attached to its backbone.

In a wired PEC, PEM plays an exceptionally important role as a separator (illustrated in Figure 4) to prevent the recombination of H_2 and O_2 (the mixture of both gasses would constitute to an explosive mixture) and to allow the transportation of proton from anode to cathode with low resistance so as to balance the flow of electrons in the external circuit[6,10,15]. The ultimate goal towards an efficient artificial photosynthetic system would be to have minimal product crossover because efficiency can be loss to the recombination of H_2 and O_2. If O_2 from the anode crosses over to the cathodic side, it can lead to the reduction of oxygen to water at the cathode which causes a loss of current and efficiency[10].

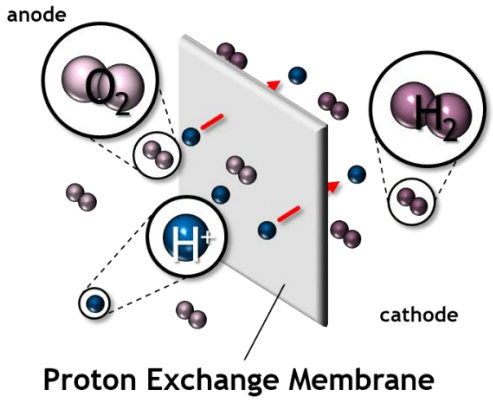

Figure 4: *Cartoon representation of the proton exchange membrane, PEM in a photoelectrocatalytic cell, PEC.*

Pioneering work in the development of PEM began with Grubb in 1959. He started off with materials such as polystyrene divinylbenzene sulfonic acid (Nepton type) and sulfonated phenol formaldehyde (Amberplex type) membranes with conductivities between 0.008 – 0.03 S/cm (very low conductivities compared to Nafion – 0.1 S/cm). The membranes required complete hydration to function and have been used on board the Gemini Spacecraft in 1965. The membranes were later found to have poor stability as it degraded while being used in the Gemini polyelectrolyte fuel cells (PEFCs), thereby limiting the devices' performances and lifetimes[16,17].

Between the 1970s and 1990s, perfluorosulfonic acid (PFSA)-based membranes such as Nafion (by DuPont), Dow membranes (by Dow Chemical Company), Flemion and Aciplex membranes (by Asahi Glass Company), Neosepta-F (by Tokuyama) and Gore-Select (by W. L. Gore and Associates, Inc.) were developed. These membranes were developed for the chlor-alkali electrolysis and were found to have good conductivities (0.01 – 0.1 S/cm) at 100 % relative humidity (RH). The chemical structures of the PFSA-based membranes were shown in Figure 5[17].

Later in the 1990s, hydrocarbon based PEMs have made a comeback due to a renewed interest as being economically favourable. Since then, research focused on improving its thermal and structural stability have yielded better batches of polymers having stable protonic conductivity over a wide temperature and RH range. In addition, composite membranes, blends and diverse systems were also studied with focus on applicability in high temperature and low RH conditions[17].

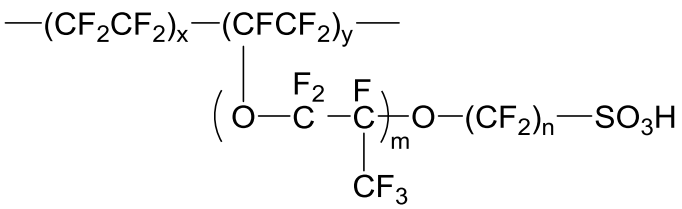

Nafion® 117	m > 1; n = 2; x = 5-13.5; y = 1000
Flemion®	m = 0, 1; n= 1-5
Aciplex®	m = 0, 3; n = 2-5; x = 1.5-14
Dow membrane	m = 0; n = 2; x = 3.6-10

Figure 5: *Chemical structure of Nafion 117, Flemion, Aciplex and Dow membrane.*

The chemical structures of some of the sulfonated aromatic hydrocarbon based polymers used as PEM were shown in Figure 6.

Poly(styrene sulfonic acid), PSSA

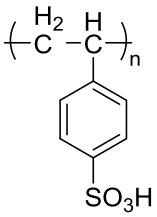

Sulfonated PEEK

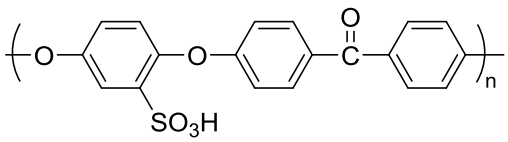

Sulfonated PPBP

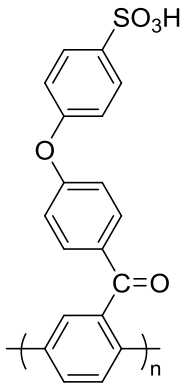

PBI-AS

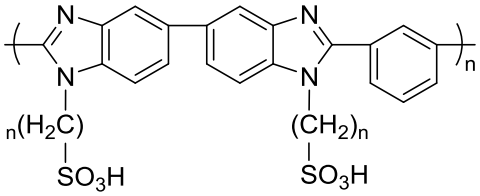

Sulfoarylated PBI

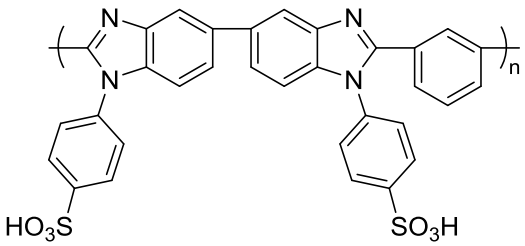

Sulfonated Poly(phenylene sulfide)

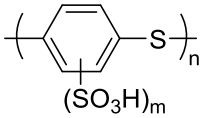

Figure 6: *Chemical structure of hydrocarbon based PEMs.*

Various optimisation approaches have been employed to improve the hydrocarbon based PEMs. Some of which involved fine tuning the extent of

sulfonation, the duration of sulfonation, modification of polymer backbone and the use of different strong acid polymer combinations.

Composite membranes such as grafted membranes and organic/inorganic nanocomposites have been developed over the years. Grafted membranes were prepared by radiation grafting with styrene followed by sulfonation. Some typical systems are PVDF/PSSA (polystyrene sulfonic acid), PVDF-co-HFP/PSSA, FEP/PSSA and ETFE/PSSA. They are typically inexpensive with conductivities comparable to Nafion at 100 % RH[18].

Organic/inorganic nanocomposite membranes consisting of SiO_2 / Polyethylene oxide (PEO) were prepared by hydrolysis and condensation reaction. The membranes were doped with acidic surfactant molecules such as monodeodecylphosphate (MDP) and phosphotunstic acid (PWA). The membranes were found to be thermally stable at high temperatures above 100 ^oC and have conductivities 10^{-4} S/cm at 160 ^oC [19].

1.3 Nafion

Nafion, a PFSA polymer has been the benchmark material and the most extensively used membrane to date for artificial photosynthesis[10]. It was developed by Dr Walther Grot at DuPont in the late 1960s as a result of modifying Teflon. It is also known as one of the most promising PEMs among PSFAs[15]. Figure 7 shows the chemical structure of Nafion which consists of a hydrophobic poly(tetrafluoroethylene) (PTFE) backbone and perfluoroether side chains that ends with a hydrophilic sulfonate group. The PTFE backbone provides mechanical support whilst the sulfonate group provides proton conduction. The mechanical and electrochemical properties of Nafion could be tuned by changing the length of the side chain and the ratio of the two phases[10,20].

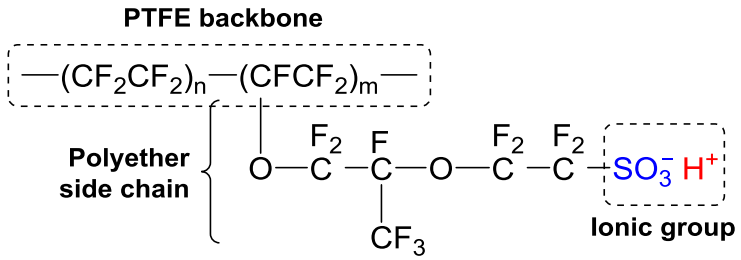

Figure 7: *Chemical structure of Nafion.*

Despite its advantageous properties (e.g. mechanical robustness, high proton conductivity, etc), Nafion's poor selectivity (high gas permeation/crossover leading to chemical degradation)[8], poor environmental recyclability, its reduced proton conductivity at elevated temperatures (> 80 ^{o}C) and its need to be moist to conduct protons have been several shortcomings that are limiting its utility, applicability and performance[10]. The hydration of Nafion eventually leads to the impairment of its mechanical properties due to swelling[21].

It is important to understand the transport mechanisms at the molecular level in hydrated Nafion membranes to better understand the reasons for its low selectivity against protons. The following are the two types of proton-conducting mechanisms known to occur through the hydrophilic domains of Nafion[15,22] (Figure 8):

a) **Grotthuss mechanism (also known as structure diffusion):**
   This mechanism involves the hopping of proton from one hydrolysed ionic site (SO_3^- H_3O^+) to another through an infinite network of hydrogen bonds.
b) **Vehicle mechanism:**
   This mechanism involves the formation of an ion adduct ($H^+(H_2O)$) that is composed of a proton and a diffusible carrier molecule (e.g. H_2O). The adduct will then be dragged across the membrane by its water molecule.

Figure 8: *Model of proton conduction.* ***Top:*** *Grotthuss Mechanism where protons are passed along the hydrogen bonds;* ***Bottom:*** *Vehicle Mechanism where the movement takes place with the aid of a moving "vehicle", e.g.* H_2O *or as complex ion* H_3O^+*. Image courtesy of Kreuer et al.*[22]

At high RH environment or low temperature, there is high water uptake into the polymer membrane. Protons are transported through Nafion via the Grotthuss mechanism. The hydrophilic clusters are at its largest (4 nm diameters) with large interconnecting pores (1 nm). This provides good diffusional transport rapid exchange between the hydrated proton sites which leads to high conductivity. Grotthuss mechanism has a lower activation energy and transport distance than the vehicle mechanism[10,23–25].

At low RH or high temperature, there is low water uptake into the polymer membrane causing the hydrophilic clusters to shrink (2.4 nm). This makes Grotthuss mechanism difficult so protons are transported through Nafion via the vehicle mechanism. As water is drawn by proton in the vehicle transport across the membrane, it leads to pore narrowing and poor diffusional transport which decreases conductivity. The membrane is less selective because water-ion adducts carrying protons are diffusing through the continuous hydrophilic pathways in Nafion[10,23–25].

The PEC used in artificial photosynthetic systems operate at very low current densities. A crossover current density of 0.5 mA cm^{-2} would lead to a 2.5 % loss of a 20 mA cm^{-2} photocurrent density. Thus, for every few mA cm^{-2} loss of current due to crossover of gases would result in a substantial loss of products[10].

The rate of crossover of gasses is governed by the water content in the polymer membrane, the thickness of the membrane as well as the RH, pressure and temperature of the cell. The use of a thin hydrated polymer membrane, high RH, pressure and temperature would result in a high rate of crossover. This is because at high temperature, gas shows greater molecular movement. The increase in hydrogen partial pressure during water splitting increases the hydrogen crossover rate from cathode to anode. High RH condition and high water uptake in the membrane lead to an increase in gas solubility in the membrane and an increase in diffusion coefficient, respectively. A thin membrane would facilitate diffusivity of gases which would lead to an increase in the rate of crossover[26]. The H_2 and O_2 permeabilities for Nafion 117 are 3.8 x 10^{12} mol cm^{-1} s^{-1} and 2.0 mol cm^{-1} s^{-1}, respectively. These values are relatively high compared to that of a bipolar (BP) membrane (1.1 x 10^{12} mol cm^{-1} s^{-1} for H_2 and 0.45 mol cm^{-1} s^{-1} for O_2)[10,27].

As a result of its poor selectivity and high crossover, Nafion membrane no longer appears to be the most appropriate candidate for use in artificial photosynthesis. Two approaches can be taken to solve the problem:

a) by building on the existing polymers via the synthesis of composites/blends or
b) by the development of new PEM materials as alternatives to Nafion.

This thesis is driven by the latter approach.

1.4 Ion-Transporting Membranes

1.4.1 Polyether-Containing Ion Channels

Polyethers such as crown ethers have been extensively studied in the area of molecular recognition of cations. The following are three different approaches/designs of ion channels based on polyethers.

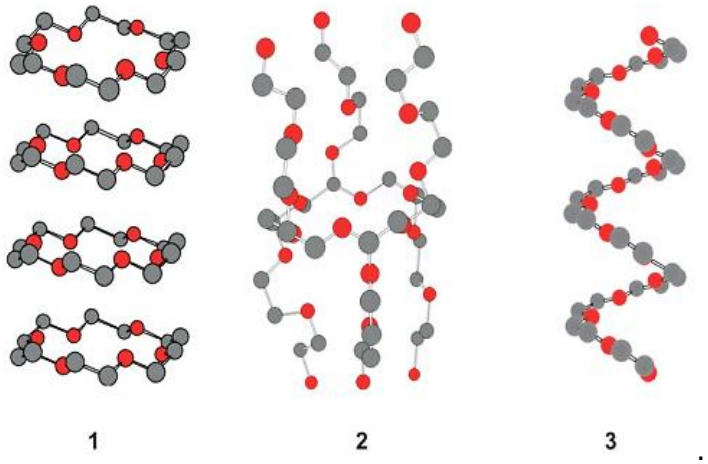

Figure 9: *Ion channel models based on polyethers:* ***1)*** *cylindrical stacking of crown ethers,* ***2)*** *polyether strands and* ***3)*** *polyether helix. Image courtesy of Koert et al.*[28]

Among the three model structures shown, the cylindrical stacking of crown ethers (Figure 9.1) is the worst model because of its strong cation binding sites. The crown ether binding sites tend to cause protons/cations transport intermittency as a high energy is required for protons to “jump” from one crown ether molecule to another[28]. An example of such systems can be found in Figure 10a and 10b where crown ether bearing peptides are aligned into an ion channel[29,30].

In contrast, the helix motif shown in Figure 9.3 is the best among the three due to its continual arrangements of weak cation binding sites. An example of a polyether helix can be observed in Figure 10c – oligotetrahydrofuran, oligo-THF[28]. Unfortunately, the only drawback of oligo-THF is its lengthy synthetic procedures involving a number of complex steps.

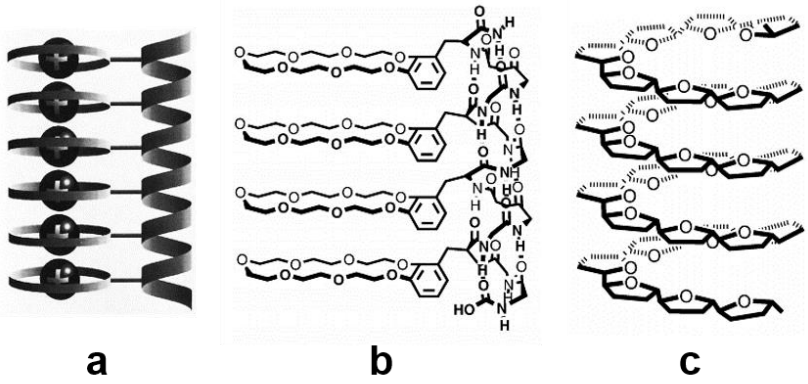

Figure 10: a) *A simplified schematic illustration of compound* ***b****,* ***b)*** *schematic illustration of aligned crown rings forming a transmembrane channel and* ***c)*** *schematic illustration of a polyether helix (oligo-THF helix). Image courtesy of Voyer et al.*[29,30]

Various complications were observed for the synthesis of all three model structures of polyether (Figure 9) relating to the intermittency of proton transport (high energy barrier of discontinuous transport between aligned crown ethers), main chain random-coil transformation of polyether and the very challenging synthesis of oligo-THF[31].

The only way to obtain polyether-lined helical structure (similar to Figure 9c) without having to go through the conventional ring opening polymerization is via the use of supramolecular chemistry, also known as “chemistry beyond the molecule”[32]. It involves the study of molecular recognition and high-order assemblies formed by non-covalent intermolecular interactions[32,33] (e.g. van der Waals forces, hydrogen bonding, etc) which eventually guides the macromolecule towards self-assembly/self-organisation.

Tobacco Mosaic Virus (TMV), a simple virus consisting of 2130 proteins and viral RNA, is one of the best understood complex biological supramolecular systems[34,35]. As shown in Figure 11, TMV exhibits a sophisticated self-assembly

mechanism – the proteins in TMV are in the shape of a taper group and act like an exo-receptor that drives the exo-recognition process, bringing along its viral RNA chain which constitutes the self-assembled molecular architecture of TMV seen on the top right[36].

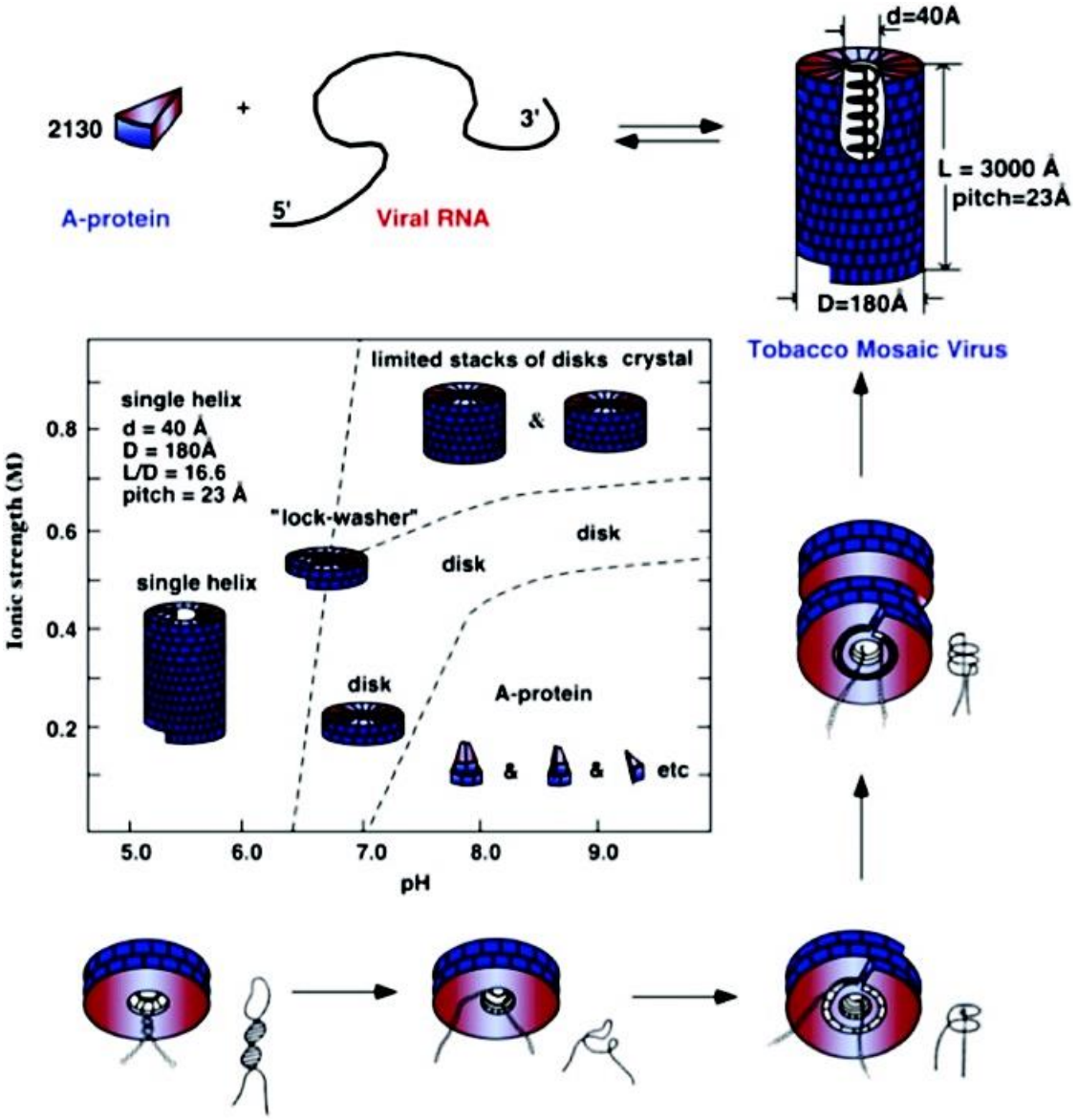

Figure 11: *Self-assembly mechanism of TMV. Image courtesy of Percec et al.*[36]

This eventually became the molecular inspiration for Percec and his group to synthesise polymers that mimics TMV with self-assembling tapered minidendritic side groups in the 1980s[37]. Therefore, it would be expected that if a tapered shape unit is attached to a polymer chain, it will probably result in cylindrical supramolecular structures similar to that of TMV.

1.4.2 Liquid-Crystalline Self-Assembling Polymer Membranes

Anisotropic functional materials for use as ion transport materials can be prepared from self-organised structures (e.g. liquid crystals). Various intermolecular interactions such as hydrogen bonding, ionic interactions, π-π interactions, etc can be utilised for the construction of supramolecular structures[38].

As mentioned in section 1.4.1, the combination of tapered shape liquid crystal mesogens with a polymeric chain could result in cylindrical supramolecular structures. The structures would have a localised permeation path lined with the polymer backbone in helical arrangements surrounded by the tapered groups as portrayed in Figure 12[39].

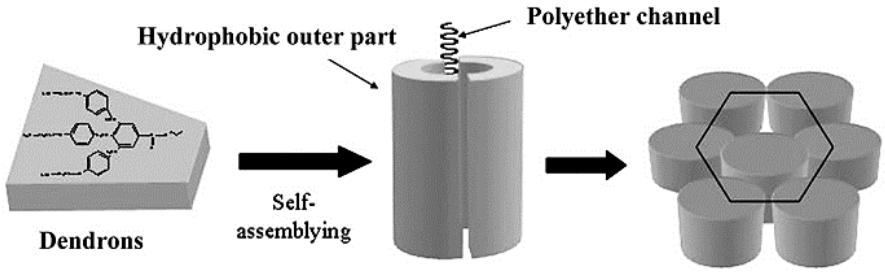

Figure 12: *Self-assembly of Polymer A into columnar structures. Image courtesy of Tylkowski et al.*[39]

In the last decade, researchers from URV who are also our collaborators have pioneered in the preparation and characterisation of side chain liquid-crystalline polyamines (poly[2(aziridin-1-yl)-ethanol], **PAZE**)[40,41] and polyethers[31,39,42] (poly(epichlorohydrin), **PECH** and poly(epichlorohydrin-co-ethylene oxide), **P(ECH-co-EO)**) via chemical modification with potassium 3,4,5-tris[4-(n-dodecan-1-yloxy)benzyloxy]benzoate, **TAP**. The types of columnar mesophase obtained are dependent on the degree of modification of the polymers. The majority of the reported polymers, in particular the **PECH** and **P(ECH-co-EO)**-based exhibited desired liquid crystalline behaviour, could self-assemble into columnar structures and the resulting polymer membranes are homeotropically oriented[31,39,42]. Most importantly, the polymers were found to have conductivities (8.8 mS/cm at 30 ºC in 5 % RH and 14 mS/cm at 50 ºC in 5 % RH) comparable

to that of Nafion (13.2 mS/cm at 30 ^{o}C in 100 % RH) and do not require moisture for proton conduction. This makes them promising alternatives to Nafion[31].

Earlier this year, Bogdanowicz *et al*.[43] carried out the first insight study on the permeaselective cation transport in one of their oriented **P(ECH-co-EO) TAP**-modified membranes (36 %). The results showed that proton conduction in the membrane happens via hopping along the polyether backbone as well as the lateral ester group interactions as shown in Figure 13a[43]. As water uptake test revealed low water absorption of the polymer over time, it is hopeful to say based on its exceptional properties that this series of polymer has the potential to be alternatives to Nafion.

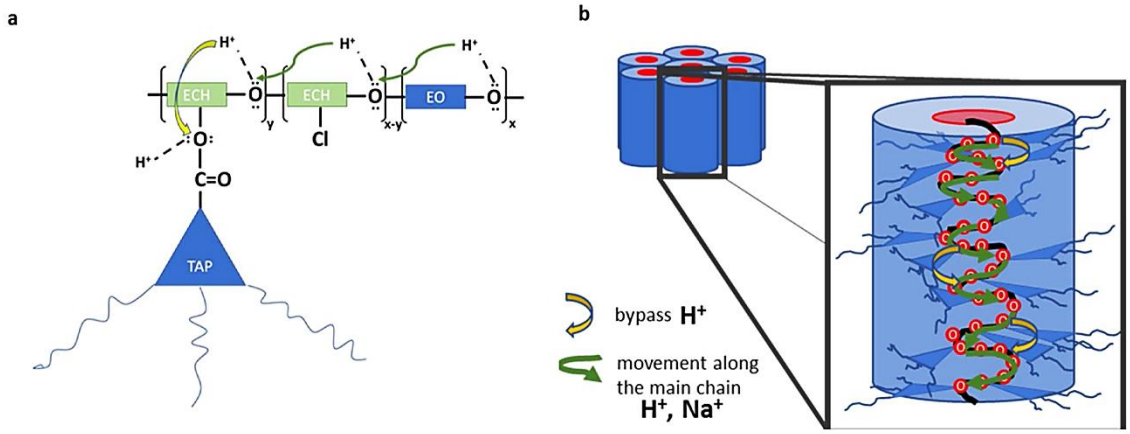

Figure 13: *Schematic representation of proton movement inside the ionic channel:* ***a)*** *hopping proton along polymeric chain (****ECH****: epichlohydrin and* ***EO****: ethylene oxide) and* ***b)*** *ion movement through single column. Image courtesy of Bogdanowicz et al.*[43]

1.5 Literature-Inspired Membranes

In a book section, Percec[44] mentioned that it would be a good starting point to begin the development of a building block by mimicking at least, at the most basic level the primary structure of a macromolecule that determines a particular function. In short, he meant structure determines function and so it would be good to start by mimicking the structure of a compound carrying a particular function of choice. The statements he made in that book chapter ended up influencing the two proposed approaches that have been attempted in this thesis.

In this thesis, two different family of polymers have been synthesised with the aim of discovering new/better polymer alternatives to Nafion. The synthesis, characterisation and testing of these polymers are discussed over five chapters with the first three allocated for **PECH**-based polymers whilst the remaining two for terephthalate-based polyesters.

PECH-based polymers in Chapter 2, 3 and 4 are inspired by literature examples of liquid-crystalline polymer membranes as mentioned in Section 1.4.2. Various planar aromatic moieties (pyrene and anthracene) are used instead of the hydrophobic liquid crystalline moieties (**TAP**).

In chapter 2, two series of polymers are prepared as follows:

1. **AP Series:** Chemical modification of **PECH** with **PCOOK** (4 polymers in total with degree of modification between 23 – 35 %)
2. **YC Series:** Chemical modification of **PECH** with **uPPCOOK** (2 polymers in total with degree of modification of around 34 %)

The incorporation of symmetrical (**PCOOK**) and clickable (**uPPCOOK**) pyrene derivatives into the backbone of **PECH** have yielded polymers with solubility issues due to the presence of “pseudo” crosslinks. Thus, the synthesis and characterisation of new pyrene derivatives are discussed in Chapter 3.

Chapter 3 involves the synthesis and characterisation of clicked pyrene derivatives (**Pyr2COOMe** and **Pyr3COOMe**). The new pyrene derivatives were prepared by copper-catalysed azide-alkyne cycloaddition (CuAAC) between clickable pyrene (**uPPCOOMe**) and azide-terminated tetraethylene glycol (**TetraEGdiN$_3$**) or azocrown ether (**AC-N$_3$**).

In Chapter 4, a totally different planar aromatic group (9- substituted anthracene, **9-ACAK**) is incorporated into **PECH** via chemical modification to produce a total of six **PA polymers** with degree of modification between 20 – 93 %). The unexpected gelation of **PA polymers** have been studied and has led to the synthesis of **URV polymers** (chemical modification of **PA polymers** with **TAP**).

Terephthalate-based polyesters in Chapter 5 and 6 are inspired by the literature examples of crown-ether ion channels as aforementioned in Section 1.4.1. In Chapter 5, the synthesis, characterisation and coordination studies of crown

ether monomer, **CM1** are discussed in-depth, followed by the synthesis of its pre-polymer and copolymers (Chapter 6).

Each chapter in this thesis is structured in the format of a standalone paper each containing a separate introduction in their respective research areas.

1.5.1 General Design Ideas/Hypothesis

The generalised design idea for the synthesis of **P**unnels – **PECH**-based "tunnel" polymers (Chapter 2 – 4) can be easily described with the use of metaphors as shown in Figure 14.

Imagine **PECH**-based polymer as a long strand of Christmas lights where the wire represents the **PECH** polymer backbone while each light bulb represents a pyrene/anthracene unit. The combination of different coloured light bulbs and the total number of light bulbs used would affect the overall appearance of the Christmas decoration. Similarly, by chemically modifying **PECH**-based polymers with different planar aromatic groups and at different degree of modification, there will be much higher probability of finding the best conditions/combinations where the resulting polymer would self-assemble into proton transportable tunnels upon being thermally treated.

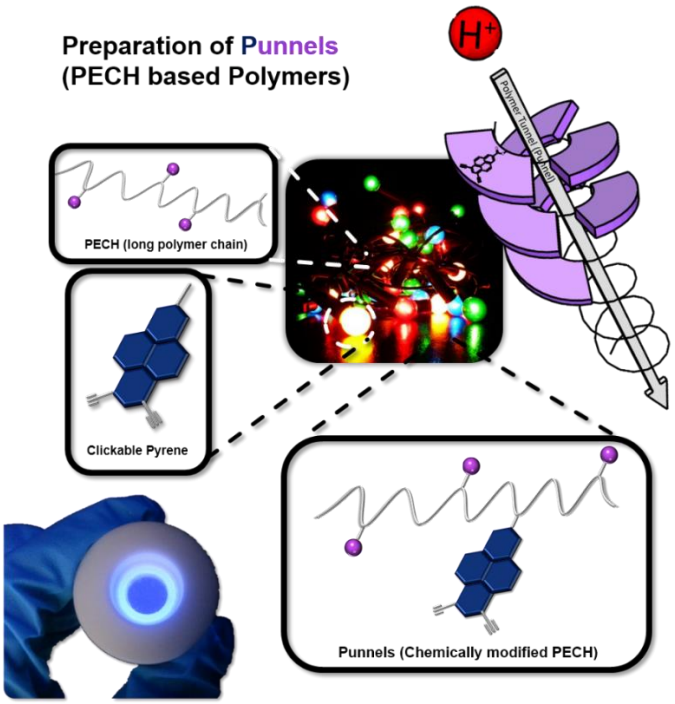

Figure 14: *Cartoon representation of the design idea of* **P**unnels*.*

As for the generalised design idea of terephthalate-based polyesters (Figure 15), with the strained core of the crown ether monomer, **CM1** and its low affinity to protons, it is envisaged that proton would be transported smoothly across the hypothetically aligned crown ether cavities of the polyester.

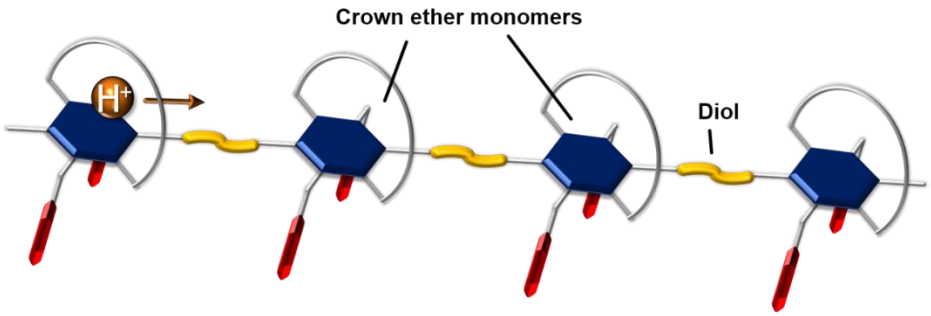

Figure 15: *Cartoon representation of a proton moving through the hypothetically orientated cavity of crown ether polyesters.*

2. Research Objectives

The objectives of this thesis are as follows:

- Synthesis and characterisation of pyrene-based polyethers via the chemical modification of **PECH** with various clickable (Chapter 2) and clicked pyrene derivatives (Chapter 3).
- Synthesis and characterisation of anthracene-containing polyethers via the chemical modification of **PECH** with potassium 9-anthracenecarboxylate, **9-ACAK** (Chapter 4).
- Synthesis and characterisation of **TAP**-anthracene-containing polyethers via chemical modification of **PA polymers** with **TAP** (Chapter 4).
- Preparation of **URV** membranes via immersion precipitation and thermal treatment (Chapter 4).
- Synthesis, characterisation and binding studies of crown ether terephthalates (Chapter 5).
- Synthesis and characterisation of terephthalate-based polyesters (Chapter 6).

References

1 D. Kim, K. K. Sakimoto, D. Hong and P. Yang, *Angew. Chemie - Int. Ed.*, 2015, **54**, 3259–3266.

2 S. Chu, X. Kong, S. Vanka, H. Guo, Z. Mi and Z. Mi, in *Semiconductors and Semimetals*, Elsevier, 2017, vol. **97**, pp. 223–255.

3 R. Detz, J. N. H. Reek and B. van der Zwaan, *Energy Environ. Sci.*, 2018, **11**, 0–18.

4 S. A. Bonke, M. Wiechen, D. R. MacFarlane and L. Spiccia, *Energy Environ. Sci.*, 2015, **8**, 2791–2796.

5 N. Chouhan, R.-S. Liu and J. Zhang, *Photochemical Water Splitting*, 2017.

6 A. Aricò, M. Girolamo, S. Siracusano, D. Sebastian, V. Baglio and M. Schuster, *Membranes (Basel).*, 2017, **7**, 25.

7 M. R. Shaner, H. A. Atwater, N. S. Lewis and E. W. McFarland, *Energy Environ. Sci.*, 2016, **9**, 2354–2371.

8 F. Nandjou and S. Haussener, *J. Phys. D. Appl. Phys.*, 2017, **50**, 124002.

9 A. D. Berger, *Integrated Modeling and Design of Photoelectrochemical Water-Splitting Cells*, University of California, Berkeley, 2014.

10 S. Chabi, K. M. Papadantonakis, N. S. Lewis and M. S. Freund, *Energy Environ. Sci.*, 2017, **10**, 1320–1338.

11 K. T. Fountaine and H. A. Atwater, *Opt. Express*, 2014, **22**, A1453.

12 S. L. McFarlane, B. A. Day, K. McEleney, M. S. Freund and N. S. Lewis, *Energy Environ. Sci.*, 2011, **4**, 1700–1703.

13 H. M. Chen, C. K. Chen, R. S. Liu, L. Zhang, J. Zhang and D. P. Wilkinson, *Chem. Soc. Rev.*, 2012, **41**, 5654–5671.

14 M. G. Lee, J. S. Park and H. W. Jang, *J. Korean Ceram. Soc.*, 2018, **55**, 185–202.

15 N. Li and M. D. Guiver, *Macromolecules*, 2014, **47**, 2175–2198.

16 W. T. Grubb, *J. Electrochem. Soc.*, 1959, **106**, 275.

17 M. Rikukawa and K. Sanui, *Prog. Polym. Sci.*, 2000, **25**, 1463–1502.

18 T. Kallio, M. Lundström, G. Sundholm, N. Walsby and F. Sundholm, *J. Appl.*

Electrochem., 2002, **32**, 11–18.

19 I. Honma, Y. Takeda and J. M. Bae, *Solid State Ionics*, 1999, **120**, 255–264.

20 C. Korzeneewski, E. Adams and D. Liu, *Appl. Spectrosc.*, 2008, **62**, 634–639.

21 G. Gebel and J. Lambard, *Macromolecules*, 1997, **30**, 7914–7920.

22 K. - D Kreuer, A. Rabenau and W. Weppner, *Angew. Chemie (Int. Ed. English)*, 1982, **21**, 208–209.

23 W. Y. Hsu, T. D. Gierke and T. D. Gierke, *Macromolecules*, 1982, **15**, 101–105.

24 S. Gottesfeld and T. A. Zawodzinski, *Polymer Electrolyte Fuel Cells*, Wiley-Blackwell, 2008, pp. 195–301.

25 P. Colomban, *Proton Conductors : Solids, Membranes and Gels - Materials and Devices*, Cambridge University Press, 1992.

26 K. D. Baik, B. K. Hong and M. S. Kim, *Renew. Energy*, 2013, **57**, 234–239.

27 K. Sun, R. Liu, Y. Chen, E. Verlage, N. S. Lewis and C. Xiang, *Adv. Energy Mater.*, 2016, **6**, 1600379.

28 U. Koert, L. Al-Momani and J. R. Pfeifer, *Synthesis (Stuttg).*, 2004, **2004**, 1129–1146.

29 N. Voyer and M. Robitaille, *J. Am. Chem. Soc.*, 1995, **117**, 6599–6600.

30 J. C. Meillon and N. Voyer, *Angew. Chemie (International Ed. English)*, 1997, **36**, 967–969.

31 K. A. Bogdanowicz, S. V. Bhosale, Y. Li, I. F. J. Vankelecom, R. Garcia-Valls, J. A. Reina and M. Giamberini, *J. Memb. Sci.*, 2016, **509**, 10–18.

32 F. Huang and E. V. Anslyn, *Chem. Rev.*, 2015, **115**, 6999–7000.

33 F. M. Menger, *Proc. Natl. Acad. Sci.*, 2002, **99**, 4818–4822.

34 A. Klug, *Angew. Chemie Int. Ed. English*, 1983, **22**, 565–582.

35 V. Percec, A. Kornyshev, A. Kornyshev, C. F. J. Faul and C. R. Safinya, *Philos. Trans. R. Soc. A Math. Phys. Eng. Sci.*, 2006, **364**, 2709–2719.

36 B. M. Rosen, C. J. Wilson, D. A. Wilson, M. Peterca, M. R. Imam and V.

Percec, *Chem. Rev.*, 2009, **109**, 6275–6540.

37 H. J. Sun, S. Zhang and V. Percec, *Chem. Soc. Rev.*, 2015, **44**, 3900–3923.

38 M. Yoshio, T. Kagata, K. Hoshino, T. Mukai, H. Ohno and T. Kato, *J. Am. Chem. Soc.*, 2006, **128**, 5570–5577.

39 B. Tylkowski, N. Castelao, M. Giamberini, R. Garcia-Valls, J. A. Reina and T. Gumí, *Mater. Sci. Eng. C*, 2012, **32**, 105–111.

40 X. Montané, K. A. Bogdanowicz, G. Colace, J. A. Reina, P. Cerruti, A. Lederer and M. Giamberini, *Polym. (United Kingdom)*, 2016, **105**, 298–309.

41 X. Montané, K. A. Bogdanowicz, J. Prats-Reig, G. Colace, J. A. Reina and M. Giamberini, *Polym. (United Kingdom)*, 2016, **105**, 234–242.

42 S. V. Bhosale, M. A. Rasool, J. A. Reina and M. Giamberini, *Polym. Eng. Sci.*, 2013, **53**, 159–167.

43 K. A. Bogdanowicz, D. Pirone, J. Prats-Reig, V. Ambrogi, J. A. Reina and M. Giamberini, *Polymers (Basel).*, 2018, **10**, 416.

44 V. Percec, *From Synthetic Macromolecules to Biological-Like Complex Systems,* Springer, Cham, 2013, pp. 173–197.

Chapter 2

Synthesis and Characterisation of Pyrene-based Polyethers

1. Introduction

Side-chain liquid-crystal polymers (SCLCP) have been of interest for decades due to their compelling optical, mechanical and rheological properties[1] as well as applicability in the field of optical data storage[2], electro-optical display[3], gate insulators for organic field effect transistors[4], etc. The ability for the resulting SCLCP to self-assemble[5,6] and their relatively good processibility[7,8] are sought after properties in the field of ion-transporting membranes. Several SCLCP based on polyepichlorohydrin, **PECH** and its co-polymer, **P(ECH-co-EO)** synthesised by Bogdanowicz *et al.* were able to self-assemble into ionic channels. The resulting ion-transporting membranes have properties comparable to Nafion[9].

PECH has been used as the main chain for many polyether-based SCLCP as it is a flexible backbone that does not require long spacer between the polymer main chain and mesogen to allow liquid crystallinity[10,11]. In addition, it has labile chlorines that would be useful for nucleophilic side-chain substitution[12]. Although many reported **PECH**-based SCLCP required the use of flexible spacer, a handful of researches still managed to synthesise **PECH**-based SCLCP that were liquid crystalline (LC) without a spacer[13,14]. Some others were even able to obtain LC **PECH**-based SCLCP using non-mesogenic moieties[15,16].

Since LC self-assembly was known to be governed solely by properties of the mesogenic groups with no influence from the polymer backbone[17,18], this gave rise to the idea of directly incorporating non-mesogenic polyaromatic moieties that were capable of π-π stacking onto **PECH** without an additional spacer. Hypothetically, the π-π interactions would then be the driving force of self-assembly in this new series of polymer.

Among many polyaromatic moieties shortlisted, pyrene turned out to be most interesting as it is well-known for possessing high fluorescence quantum yield[19], chemical stability, tunable emission behaviours in micro-environments, strong tendency to form an excimer and most importantly, has a large planar surface that can effectively π-stack between molecules[20,21]. This meant that the

introduction of pyrene into **PECH** would eventually make the resulting polymer fluorescent. Its π-π stacking interactions (in the form of an excimer peak) can then be monitored via fluorescence spectroscopy. What kind of properties does such a polymer possess? Will this result in a polymer with dual functionality? Will the π-π stacking between pyrene moieties bring about the ability to self-assemble like the SCLCP (containing LC mesogens) reported in literature? To answer these questions, this research needed to be carried out.

In this chapter, not only will the synthesis and characterisation of pyrene monomers (**PCOOK** and **uPPCOOK**) be discussed, the pros and cons of two different methods used in the chemical modification of **PECH** as well as the effect of "pseudo-crosslinks" will also be explored. During the characterisation of **AP** and **YC polymers**, swelling was observed in both polymer series when dissolved in various organic solvents which prompted the study of its partial solubility. UV-Vis and fluorescence spectroscopy were employed to explain the relative proximity of pyrene moieties within each polymers.

2. Experimental

2.1 Materials

Reagents and solvents were bought from commercial suppliers at the highest purity possible and were used without further purification unless otherwise specified. Pyrene, **Py1** (98 %), phthalic anhydride, **PtAn** (99 %), $AlCl_3$ (99 %), PCl_5 (≥ 98 %), potassium tert-butoxide (95 %), 1,2-dimethoxyethane, **DME** (anhydrous, 99.5 %), polyepichlorohydrin, **PECH** (average M_w ~700,000 by GPC), KF (≥ 99 %), DMF (anhydrous, 99 %) and 18-crown-6, **18C6** (≥ 99.5 %) were supplied by Sigma Aldrich while tetrabutylammonium bromide, **TBAB** (99+ %) was supplied by Acros Organics. 6,8-di(isopropylsilylprop-1-ynyl)pyrene-2-carboxylic acid methyl ester, **PPCOOMe** was synthesised by past researchers from the Benniston group using previously reported procedures[22] and has been repeated to obtain more products. THF stabilized with BHT (ACROS Organics) was dried over activated 4 Å molecular sieves under nitrogen atmosphere for several days before use.

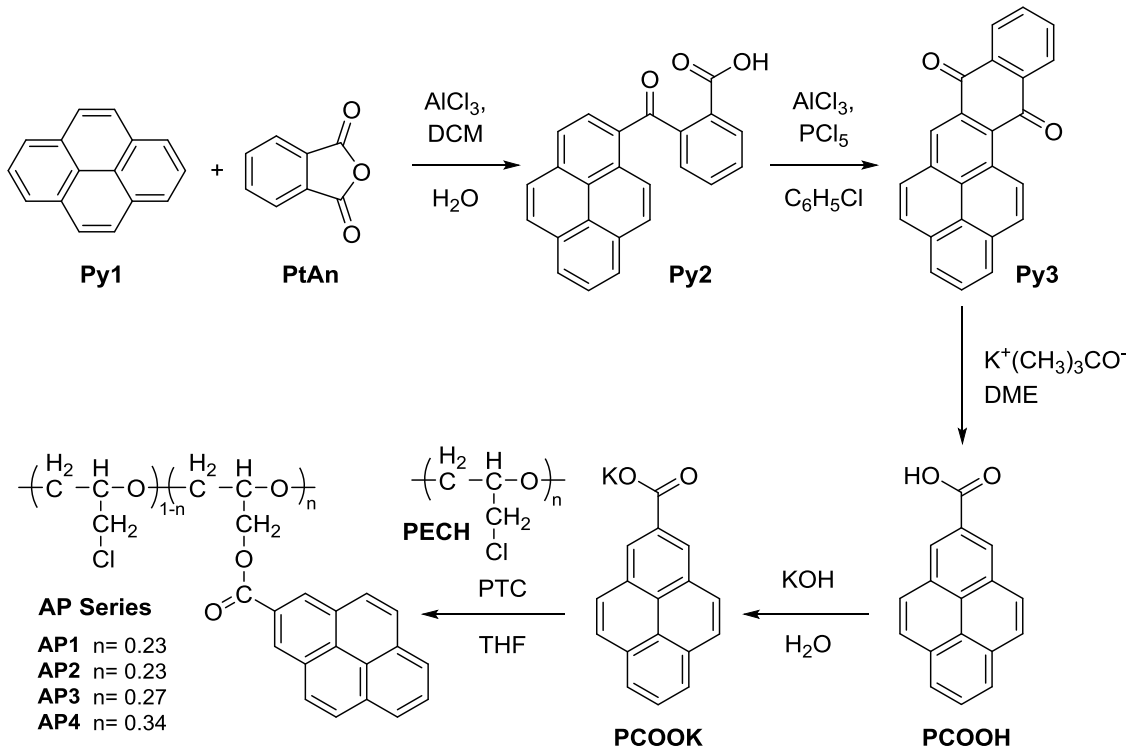

Scheme 1: *Preparation of the* **AP Series***.*

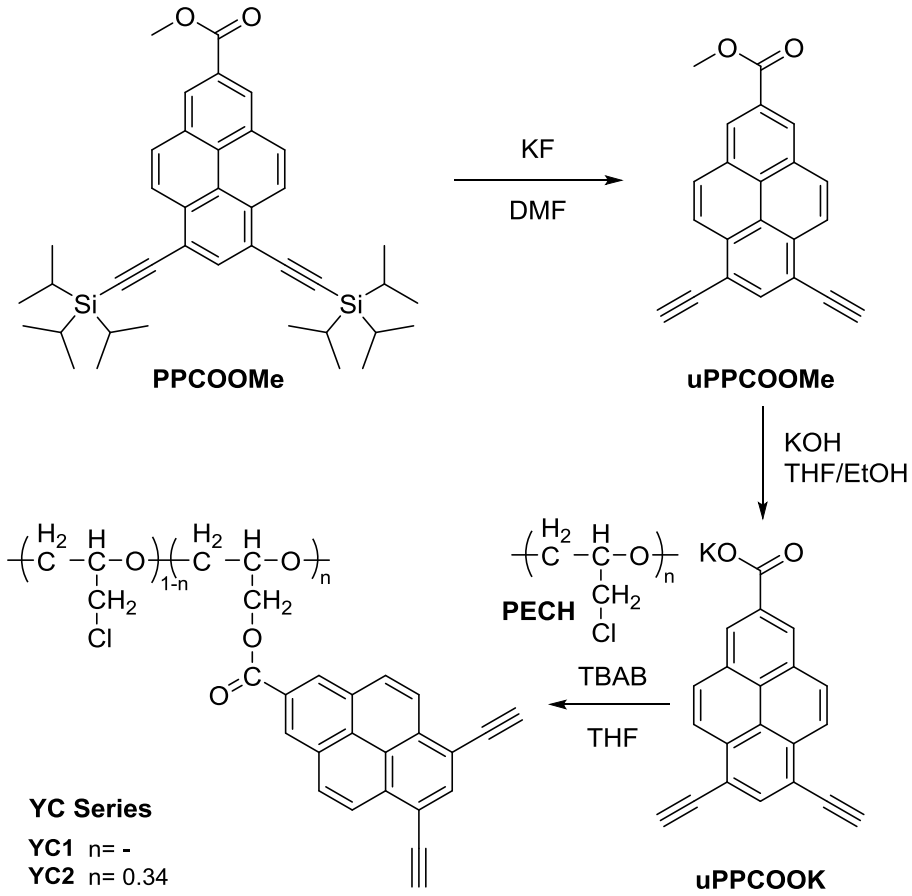

Scheme 2: *Preparation of the* **YC Series***.*

2.2 Synthesis of Potassium Pyrene-2-carboxylate, **PCOOK**

2.2.1 Synthesis of Intermediate, **Py2**

$AlCl_3$ (15.4 g, 115.5 mmol) was added portion wise to a suspension of pyrene, **Py1** (9.4 g, 46.5 mmol) and phthalic anhydride, **PtAn** (6.9 g, 46.5 mmol) in 280 mL of anhydrous DCM under N_2. The reaction mixture was refluxed at 41 ^oC for 3 hours, monitored with TLC. Solvent was evaporated till dryness. The residue was cooled to 0 ^oC and was suspended in 500 mL of distilled water. The pH of the suspension was adjusted to 0-1 by addition of concentrated hydrochloric acid. The resulting solid was suction filtered, rinsed with 300 mL of ice water and dried under high vacuum. The solid was later suspended in 500 mL of glacial acetic acid at 130 ^oC for 5 minutes. The solid was filtered hot with additional rinsing with 150 mL of hot glacial acetic acid. The filtrate was poured into 1 L of ice water. The resulting solid was suction filtered, washed with 200 mL of ice water and dried under high vacuum to yield **Py2** (15.46 g, 43.8 mmol, 94%) as a bright yellow powder.

^{1}H NMR (300 MHz, DMSO-d_6) δ 13.02 (s, 1H, H17), 9.15 (d, J = 9.4 Hz, 1H, H10), 8.43 (dd, J = 8.6, 3.6 Hz, 3H, H9, H6, H8), 8.35 (d, J = 9.0 Hz, 1H, H5), 8.27 – 8.17 (m, 3H, H3, H4, H7), 7.97 (dd, J = 7.5, 1.5 Hz, 1H, H16), 7.83 (d, J = 8.1 Hz, 1H, H2), 7.81 – 7.69 (m, 2H, H14, H15), 7.63 (dd, J = 7.1, 1.6 Hz, 1H, H13).

The ^{1}H NMR spectrum of the purified product was consistent with the literature data[23].

2.2.2 Synthesis of Intermediate, **Py3**

To a suspension of **Py2** (15.4 g, 43.7 mmol) in chlorobenzene (290 mL) was added PCl_5 (13.7 g, 65.8 mmol) and $AlCl_3$ (9.36g, 70.5 mmol). The reaction mixture was heated to reflux at 132 ^oC for 2.5 hours under N_2 and with TLC monitoring. The reaction mixture was rotary evaporated to dryness. The residue was cooled to 0 ^oC and was suspended in 450 mL of distilled water. The solid was suction filtered, washed with 400 mL of water and dried under high vacuum to yield **Py3** (14.12 g, 42.2 mmol, 97 %) as a dark maroon powder.

^{1}H NMR (300 MHz, Chloroform-d) δ 9.99 (d, J = 9.6 Hz, 1H, H10), 9.06 (s, 1H, H3), 8.43 – 8.38 (m, 1H, H13), 8.38 – 8.34 (m, 1H, H9), 8.32 (dd, J = 2.3, 0.8 Hz,

1H, H16), 8.31 – 8.26 (m, 2H, H8, H6), 8.22 (d, *J* = 2.3 Hz, 2H, H4, H5), 8.10 (t, *J* = 7.6 Hz, 1H, H7), 7.88 – 7.75 (m, 2H, H14, H15).

The ^{1}H NMR spectrum of the product was consistent with the literature data[23].

X-ray crystal structure (Figure 13) and refinement data (Table 2) available in SI.

2.2.3 Synthesis of Pyrene-2-carboxylic acid, PCOOH

Distilled water (4.8 mL, 266.4 mmol) was added to a suspension of **Py3** (14.1 g, 42.2 mmol) in 1,2-dimethoxyethane (210 mL). Potassium tert-butoxide (95.2 g, 848.4 mmol) was then added portion-wise to the reaction mixture that was vigorously stirred. The reaction mixture was heated to reflux at 95 ^{o}C for 17 hours under N_2 and with TLC monitoring. The reaction mixture was rotary evaporated to dryness. The residue was cooled to 0 ^{o}C and was suspended in 1 L of distilled water. The suspension was acidified to pH 1-2 with concentrated hydrochloric acid. The resulting solid was suction filtered and suspended in 1.5 L of distilled water. The suspension was left to stir overnight. The solid was collected by suction filtration and was dried under high vacuum to yield crude of **PCOOH**. The material was dry packed into a silica column with DCM:Hexane (1:1) and was eluted with DCM, slowly increased to 10 % MeOH in DCM and finally to DCM:MeOH: 30 % NH_3 (90:9:1) to yield pure **PCOOH** (6.54 g, 26.6 mmol, 63 %) as dark maroon/black powder.

^{1}H NMR (300 MHz, DMSO-d_6) δ 13.27 (br s, H11), 8.87 (s, 2H, H1, H3), 8.39 – 8.31 (m, 4H, H6, H8, H4, H10), 8.27 (d, *J* = 9.0 Hz, 2H, H5, H9), 8.16 (dd, *J* = 8.2, 7.2 Hz, 1H, H7).

The ^{1}H NMR spectrum of the purified product was consistent with the literature data[23].

2.2.4 Synthesis of Potassium Pyrene-2-carboxylic acid, PCOOK

2.0 mL of 6 M KOH (0.7 g, 12.5 mmol) was added dropwise to a suspension of **PCOOH** (3.0 g, 12.2 mmol) in distilled water (34 mL). The reaction mixture was allowed to stir at RT overnight, covered in foil. The following day, the dark brown suspension was rotary evaporated till dryness. Chloroform was added to the residue before sonicating for 10 minutes. The suspension was filtered and left to

dry under high vacuum to yield **PCOOK** as a dark brown powder (3.38 g, 11.9 mmol, 98 %).

^{1}H NMR (400 MHz, DMSO-d_6) δ 8.79 (s, 2H, H1, H3), 8.23 (d, *J* = 7.6 Hz, 2H, H6, H8), 8.19 (d, *J* = 8.9 Hz, 2H, H4, H10), 8.11 (d, *J* = 9.0 Hz, 2H, H5, H9), 8.06 – 8.00 (m, 1H, H7).

^{13}C NMR (101 MHz, DMSO-d_6) δ 168.79 (C17), 139.58 (C2), 130.84 (C13,C14), 129.73 (C11,C12), 128.14 (C4,C10), 126.63 (C5,C9), 126.19 (C1,C3), 125.94 (C7), 124.51 (C6,C8), 124.05, 123.99 (C15,C16).

FT-IR (ν_{max}, cm^{-1}) 1600, 1547 (asymmetric COO^- stretching vibration), 1379 (symmetric COO- stretching vibration), 1256 (aromatic =C-H in plane deformation vibration), 822, 780, 746, 730, 705 (aromatic C-H out of plane deformation vibrations).

(-)nanoESI-FTMS (m/z): found $[M-K]^-$ 245.0610, calcd. for $C_{17}H_9O_2$: 245.0608.

2.3 Synthesis of Potassium 6,8-bisethynylpyrene-2-carboxylate, **uPPCOOK**

2.3.1 Synthesis of 6,8-bisethynylpyrene-2-carboxylic acid methyl ester, **uPPCOOMe**

PPCOOMe (1.1 g, 1.8 mmol) was dissolved in anhydrous DMF (60 mL) and refluxed at 120 ^{o}C under Ar. To pre-dried KF (1.1 g, 18.9 mmol) was added anhydrous DMF (35 mL). When all KF solubilised, the solution was added dropwise to the reaction mixture. The reaction mixture was left to reflux overnight and monitored with TLC. Upon completion, H_2O (55 mL) was added to the reaction mixture at RT. The resulting solid was suction filtered to yield **uPPCOOMe** (0.40 g, 1.3 mmol, 72 %) as a brown powder.

^{1}H NMR (300 MHz, Chloroform-*d*) δ 8.88 (s, 2H, H1, H3), 8.58 (d, *J* = 9.1 Hz, 2H, H5, H9), 8.37 (s, 1H, H7), 8.23 (d, *J* = 9.1 Hz, 2H, H4, H10), 4.10 (s, 3H, H11), 3.63 (s, 2H, H21, H22).

^{13}C NMR (75 MHz, Chloroform-*d*) δ 167.39 (C12), 135.28 (C7), 133.35 (C15,C16), 131.02 (C13,C14), 129.88 (C4,C10), 128.18 (C2), 127.14 (C1, C3), 126.10 (C5,C9), 124.05 (C17), 121.62 (C18), 117.13 (C6,C8), 83.59 (C21,C22), 81.55 (C19,C20), 52.73 (C11).

FT-IR (ν_{max}, cm^{-1}) 3288, 3247 (≡C-H stretching vibrations), 1711 (aromatic ester C=O stretching vibration), 1310, 1232 (aromatic ester C-O stretching vibrations), 899, 815, 766 (aromatic C-H out of plane bending vibrations).

(+)nanoESI-FTMS (m/z): found $[M+H]^+$ 309.0912, calcd. for $C_{22}H_{13}O_2$: 309.0910.

X-ray crystal structure (Figure 12) and refinement data (Table 1) available in SI of Chapter 3.

2.3.2 Synthesis of Potassium 6,8-bisethynylpyrene-2-carboxylate, **uPPCOOK**

35 mL of 7 M KOH in EtOH (in excess) was added dropwise to a refluxing solution of **uPPCOOMe** (0.5 g, 1.6 mmol) in 105 mL of THF/EtOH (90:15). The reaction mixture was monitored with TLC. Upon completion, the reaction mixture was cooled to RT and suction filtered. The resulting solid was stirred in EtOH (50 mL) to remove excess KOH. The suspension was suction filtered to yield **uPPCOOK** (0.46 g, 1.4 mmol, 88 %) as a dark brown powder.

^{1}H NMR (300 MHz, DMSO-d_6) δ 8.88 (s, 2H, H1, H3), 8.43 (s, 4H, H4, H10, H5, H9), 8.26 (s, 1H, H7), 4.83 (s, 2H, H20, H21).

^{13}C NMR (75 MHz, DMSO-d_6) δ 167.74 (C11), 140.99 (C2), 133.00 (C7), 131.98 (C14,C15), 130.88 (C4,C10), 129.71 (C12,C13), 127.96 (C1,C3), 123.72 (C5,C9), 123.67 (C17), 122.97 (C16), 115.55 (C6,C8), 86.82 (C20,C21), 81.31 (C18,C19).

FT-IR (ν_{max}, cm^{-1}) 3273 (≡C-H stretching vibration), 1600, 1546 (asymmetric COO^- stretching vibrations), 1390 (symmetric COO- stretching vibration), 824 (aromatic C-H out of plane bending vibration).

(-)nanoESI-FTMS (m/z): found $[M-K]^-$ 293.0604, calcd. for $C_{21}H_9O_2$: 293.0608.

2.4 Polymers

2.4.1 Modification of **PECH** *with* **PCOOK, AP Series**

A solution of PECH pre-dissolved in dry THF at RT overnight was heated to 60 ^oC. To it was added PTC followed by **PCOOK**. The reaction mixture was left to stir at 65^oC for 4 days covered in aluminium foil. The resulting mixture was left to

cool to RT and was precipitated out with H_2O. The precipitated polymer was filtered and dried before being re-dissolved in THF. The polymer solution was re-precipitated by addition of the THF solution to water. The purification process was repeated twice or trice (depending on its purity). The resulting polymer was dried under high vacuum with heating over 3 days to yield **AP polymers**. The reaction conditions are specified in Table 1 (Section 3.3).

2.4.2 Modification of PECH *with* uPPCOOK, YC Series

A solution of PECH pre-dissolved in dry THF at RT overnight was heated to 60^{o}C. To it was added TBAB followed by **uPPCOOK**. The reaction mixture was left to stir at 65^{o}C for 4-6 days covered in aluminium foil. The resulting mixture was left to cool to RT and was precipitated out with H_2O. The precipitated polymer was filtered and dried before being re-dissolved in THF. The polymer solution was re-precipitated by addition of the THF solution to water. The purification process was repeated twice or trice (depending on its purity). The resulting polymer was dried under high vacuum with heating over 3 days to yield **YC polymers**. The reaction conditions are specified in Table 5 (Section 3.4).

2.5 Characterisation

2.5.1 Nuclear Magnetic Resonance (NMR) Spectroscopy

^{1}H NMR spectra of **Py2** (in DMSO-d_6), **Py3** (in $CDCl_3$) and **PCOOH** (in DMSO-d_6) were recorded on Bruker Avance III 300 MHz; ^{1}H and ^{13}C NMR spectra of **PCOOK** (in DMSO-d_6) was recorded on Jeol ECS 400 MHz whilst **uPPCOOMe** (in $CDCl_3$) and **uPPCOOK** (in DMSO-d_6) were recorded on Bruker Avance III 300 MHz. ^{1}H and ^{13}C NMR spectra of **AP** and **YC polymers** in deuterated tetrachloroethane (TCE-d_2) were recorded on Bruker Avance III 700 MHz. 2D NMR such as ^{1}H-^{1}H correlation (COSY), ^{1}H-^{13}C heteronuclear single quantum correlation (HSQC), ^{1}H-^{13}C heteronuclear multiple bond correlation (HMBC) were used to substantiate ^{1}H and ^{13}C NMR assignments of the synthesised compounds. For polymer samples, quantitative ^{1}H and ^{13}C NMR were both recorded with a 5 seconds pulse delay and 20,000-40,000 number of scans. Polymer samples were prepared in the dark as 10-20 % (w/v) solutions.

2.5.2 FT-IR Spectroscopy

FT-IR spectra were obtained using Spectrum Two FT-IR Spectrometer fitted with a diamond crystal plate ATR unit (PerkinElmer).

2.5.3 Mass Spectrometry

Mass spectrometry analyses of the newly synthesised products were performed on a Thermo Scientific LTQ Orbitrap XL spectrometer equipped with an Advion NanoMate inlet in positive and negative ionisation modes by the team at EPSRC UK National Mass Spectrometry Facility, Swansea University.

2.5.4 X-ray Crystallography

Crystal structure data for **Py3** were collected at 100 K on beamline I19 at Diamond Light Source using Synchrotron radiation (λ = 0.6889 Å). Cell refinement and data reduction were undertaken using the software APEX3 (Bruker, 2015). Using Olex2 (Dolomanov, 2009), the structure was solved using XS (Sheldrick, 2008) and refined by XL (Sheldrick, 2008). All non-hydrogen atoms were refined anisotropically. Hydrogen atoms were placed with idealised geometry with atomic displacement parameters constrained to be an appropriate multiple of the U_{eq} of the parent atom.

2.5.5 Thermogravimetric analysis (TGA)

TGA were carried out in a Mettler TGA SDTA 851e thermobalance. Approximately 8 mg of samples were heated from 30 to 650 ^{o}C at 10 ^{o}C/min in a nitrogen atmosphere (100 mL/min).

2.5.6 Differential Scanning Calorimetry (DSC)

Calorimetric studies were carried out in a Mettler DSC822e Differential Scanning Calorimeter. Approximately 5 mg of samples were weighed into 40 µL aluminium crucibles covered with a pierced lid. The analyses were performed in dynamic mode at a heating and cooling rate of 10 ^{o}C/min using nitrogen as a purge gas (100 mL/min).

2.5.7 Gel Permeation Chromatography (GPC)

The number average (M_n) and weight average (M_w) molecular weight of polymers were determined by the use of an Agilent 1200 Series GPC-SEC system consisting of three columns in series (PLgel 20 µm MIXED-A, PLgel 5 µm MIXED-D and PLgel 3 µm MIXED-E) and a refractive index detector. Monodispersed polystyrene (PS) standards were used for calibration and the mobile phase (THF with toluene as internal standard) was eluted at a flow rate of 1.0 mL/min. The sample concentrations used were 5-10 mg/mL.

2.5.8 Spectroscopy

All solvents used for UV-Vis and fluorescence experiments were bought at the highest available grade and their purity were checked before the experiments.

UV-Vis Experiments

Absorption spectra were recorded using UV-1800 UV-Vis Spectrophotometer. Samples were dissolved in spectroscopic grade solvent in a 1 cm by 1 cm quartz cuvette. Baseline was corrected prior to measurements.

Fluorescence Experiments

Fluorescence emission and excitation spectra were recorded using a Shimadzu RF-6000 Spectrofluorophotometer. Measurements were repeated several times at varying concentrations and excitation wavelengths.

3. Results and discussion

3.1 Synthesis of Potassium Pyrene-2-carboxylate, **PCOOK**

Potassium pyrene-2-carboxylate, **PCOOK** was synthesised via deprotonation of pyrene-2-carboxylic acid, **PCOOH** with potassium hydroxide as shown in Scheme 1. The large-scale, full synthesis of **PCOOH** have previously been reported[23].

A distinctive feature to note in the ^{13}C NMR spectrum of **PCOOK** in Figure 4 (SI) is the shift in the carbonyl carbon peak from 167.8 ppm (in ^{13}C NMR spectrum of

reported **PCOOH**[23]) to 168.8 ppm in deuterated DMSO. This confirms the successful synthesis of a carboxylate salt.

The negative nanoESI of **PCOOK** (Figure 9 – SI) showed the presence of $[M-K]^-$ species at m/z = 245.0610 (in MeOH) which matched its corresponding theoretical isotope model within a mass error of 1 ppm.

The two strong peaks at 1547 and 1379 cm^{-1} in the FT-IR spectrum of **PCOOK** in Figure 1 correspond to the characteristic asymmetric and symmetric stretching of the carboxylate carbonyl C=O bond, respectively. The clear shift in the C=O stretching vibrations from 1685 cm^{-1} in **PCOOH** to 1547 cm^{-1} in **PCOOK** once again supported the successful synthesis of the new compound.

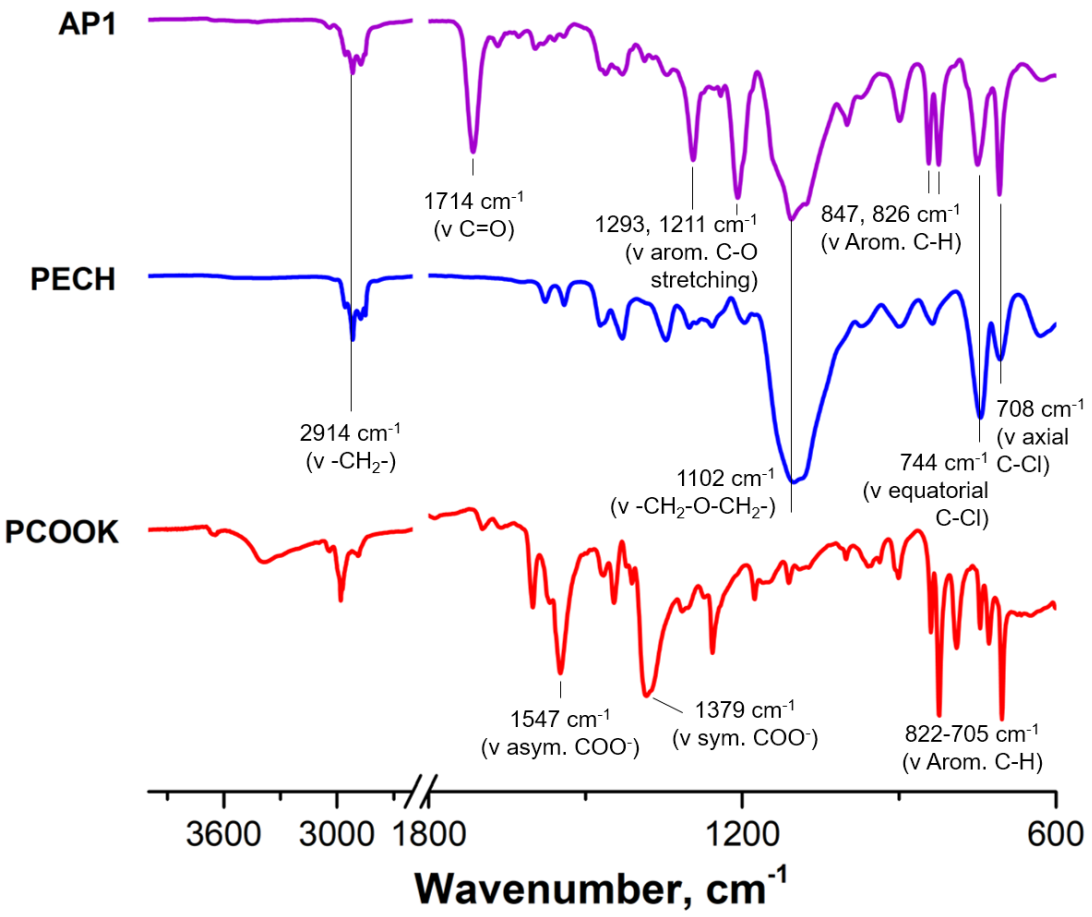

Figure 1: *FT-IR spectra of* **PCOOK**, **PECH** *and* **AP1**.

3.2 Synthesis of Potassium 6,8-bisethynylpyrene-2-carboxylate, **uPPCOOK**

6,8-bisethynylpyrene-2-carboxylic acid methyl ester, **uPPCOOMe** was synthesised by deprotecting 6,8-di(isopropylsilylprop-1-ynyl)pyrene-2-carboxylic acid methyl ester, **PPCOOMe** with the use of KF in DMF at 120 ºC as shown in Scheme 2. **PPCOOMe** was synthesised by past researchers from the Benniston group using previously reported procedures[22] and was repeated to obtain more products. A combined source of **PPCOOMe** was used for the synthesis of **uPPCOOMe** and was found to have a 72 % yield.

The successful deprotection of the triisopropylsilyl ethers, TIPS, in **PPCOOMe** was confirmed by the appearance of a singlet at 3.63 ppm integrating to 2 protons (terminal acetylene protons – H21,22) in the ^{1}H NMR spectrum of **uPPCOOMe** (Figure 2).

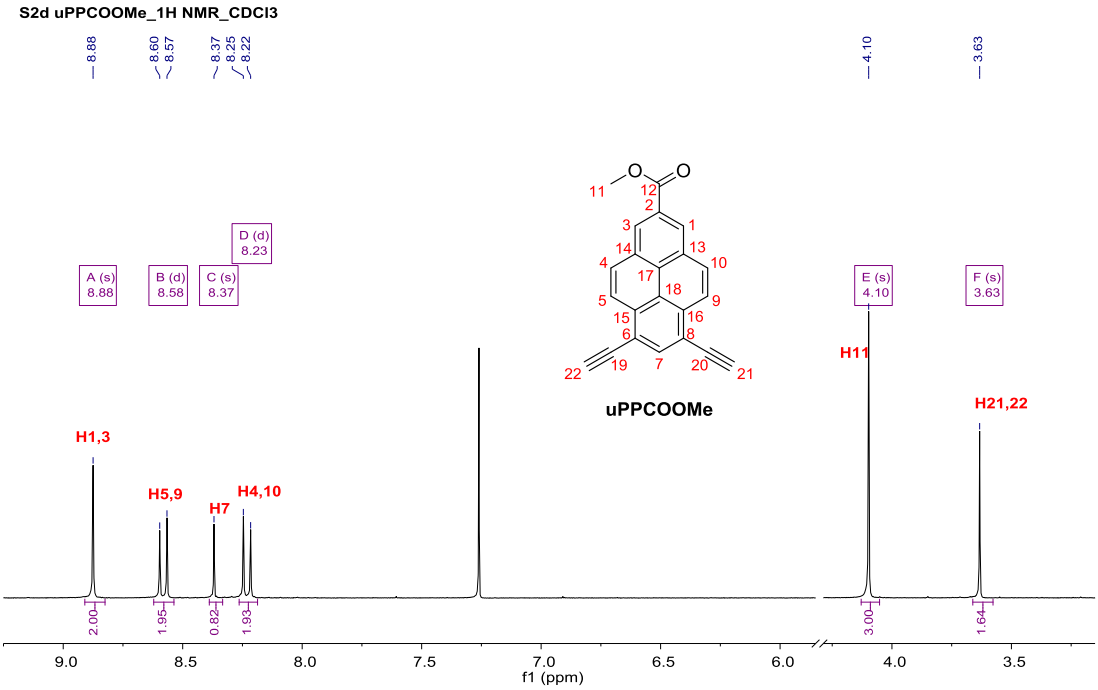

^{1}H NMR (300 MHz, Chloroform- *d*) δ 8.88 (s, 2H, H1, H3), 8.58 (d, *J* = 9.1 Hz, 2H, H5, H9), 8.37 (s, 1H, H7), 8.23 (d, *J* = 9.1 Hz, 2H, H4, H10), 4.10 (s, 3H, H11), 3.63 (s, 2H, H21, H22).

Figure 2: *^{1}H NMR spectrum (300 MHz, $CDCl_3$) of* **uPPCOOMe***.*

The positive nanoESI of **uPPCOOMe** (Figure 10 – SI) showed the presence of $[M+H]^+$ species at m/z = 309.0912 (in DCM/MeOH + NH_4OAc) which matched its corresponding theoretical isotope model within a mass error of 1 ppm.

The peaks at 3288 and 3247 cm^{-1} observed in the FT-IR spectrum of **uPPCOOMe** in Figure 3 correspond to the ≡C-H stretching vibrations of terminal alkynes. This reaffirms the successful synthesis of **uPPCOOMe**.

With the use of vapour diffusion, crystals of **uPPCOOMe** were able to be grown in the fridge from DCM/MeCN. Its X-ray crystal structure and corresponding refinement data are shown in Figure 12 and Table 1 (Chapter 3 – SI), respectively.

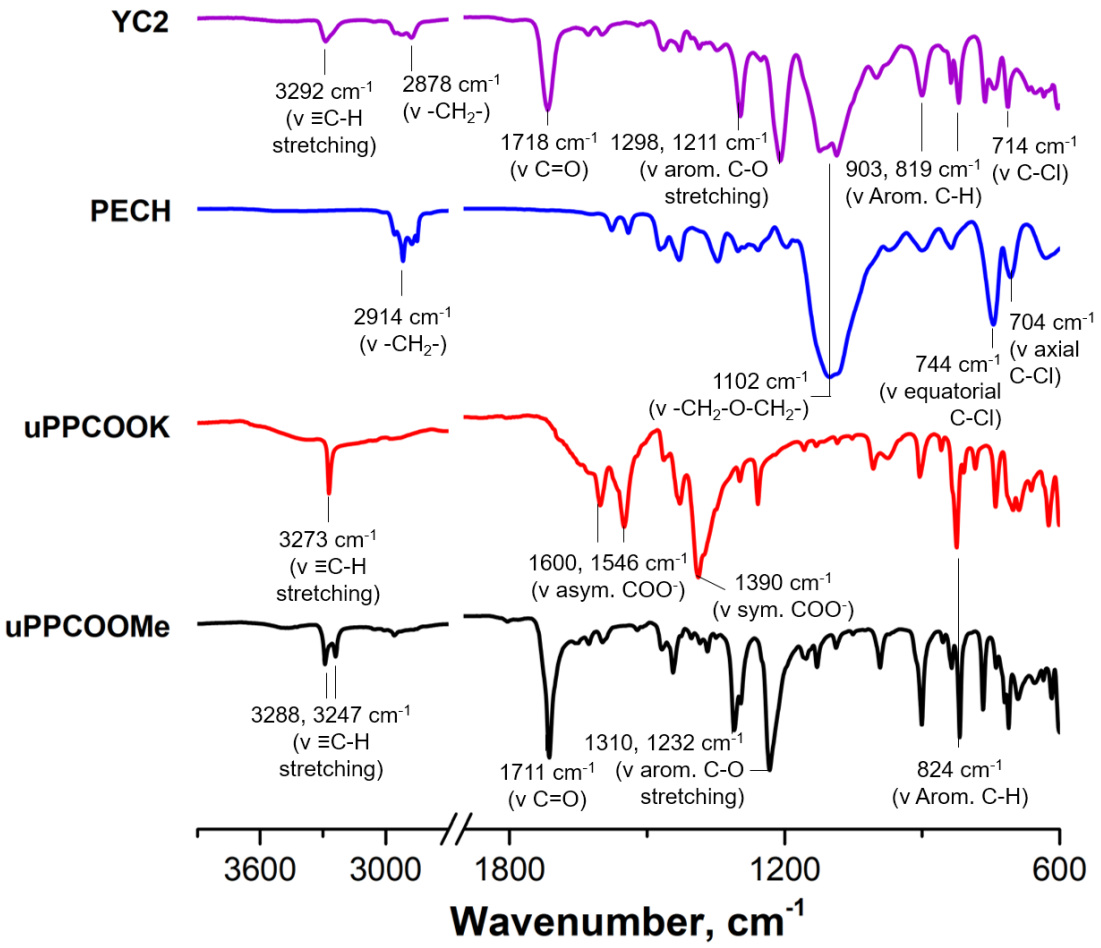

Figure 3: *FT-IR spectra of* **uPPCOOMe***,* **uPPCOOK***,* **PECH** *and* **YC2***.*

Potassium 6,8-bisethynylpyrene-2-carboxylate, **uPPCOOK** was synthesised via deprotonation of **uPPCOOMe** with potassium hydroxide as shown in Scheme 2.

The first noticeable change upon isolation of the new compound is that the potassium salt **uPPCOOK** is no longer soluble in $CDCl_3$, hence, the carbonyl carbon peak could not be used for comparison as both NMR spectra were recorded in different solvents.

The protons of the pyrene core were observed as three singlets at 8.88 ppm (H1,3), 8.43 ppm (H4,10,5,9) and 8.26 ppm (H7) from the ^{1}H NMR spectrum of **uPPCOOK** (Figure 4). Since two of the proton peaks overlapped into one at 8.43 ppm no splitting pattern can be observed. The absence of a singlet attributed to protons on a methyl ester is a sign of successful synthesis of **uPPCOOK**.

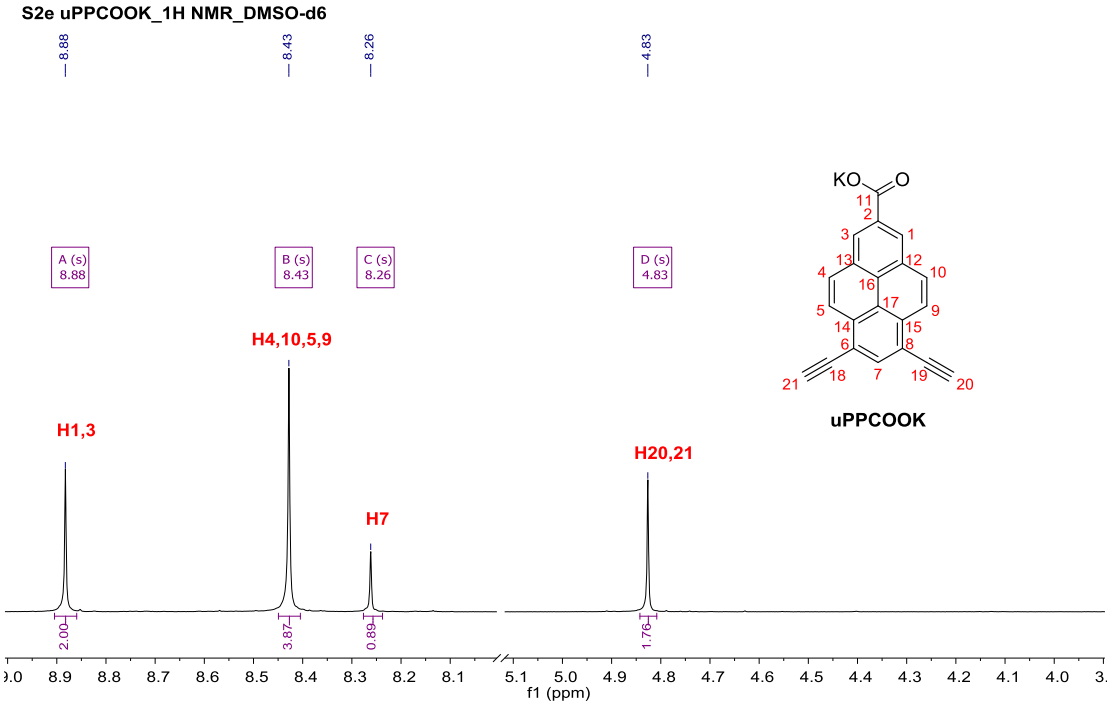

Figure 4: *^{1}H NMR spectrum (300 MHz, DMSO-d_6) of* **uPPCOOK**.

The negative nanoESI of **uPPCOOK** (Figure 11 – SI) showed the presence of $[M-K]^-$ species at m/z = 293.0604 (in MeOH) which matched its corresponding theoretical isotope model within a mass error of 1 ppm.

From the FT-IR spectrum of **uPPCOOK** in Figure 3, the peak at 3273 cm^{-1} corresponds to the ≡C-H stretching vibrations of terminal alkynes, whilst the peaks at 1600 and 1546 cm^{-1} (asymmetric) as well as at 1390 cm^{-1} (symmetric) correspond to the characteristic stretching of carboxylate carbonyl C=O bond. When comparing to the FT-IR spectrum of **uPPCOOMe**, a shift in C=O stretching vibrations of **uPPCOOK** from 1711 cm^{-1} (ester C=O stretching) to 1600 cm^{-1} (carboxylate C=O stretching) can be observed which substantiates the successful synthesis of the potassium salt.

3.3 Modification of PECH *with* PCOOK, AP Series

AP Series polymers were synthesised via S_N2 substitution with the use of carboxylate anion (**PCOOK**) as nucleophile as shown in Scheme 1. The chemical modification conditions and product yields of **AP polymers** are reported in Table 1.

AP Series (PECH: PCOOK)	PECH	PCOOK	PTC	THF (mL)	Yield (%)[1]
AP1 (1:0.4)	0.45 g, 4.9 mmol	0.55 g, 1.9 mmol	18C6 0.51 g, 1.9 mmol	42	92
AP2 (1:0.6)	0.50 g, 5.4 mmol	0.92 g, 3.2 mmol	18C6 0.86 g, 3.2 mmol	53	93
AP3 (1:0.8)	0.50 g, 5.4 mmol	1.23 g, 4.3 mmol	18C6 1.14 g, 4.3 mmol	53	98
AP4 (1:0.4)	0.50 g, 5.4 mmol	0.62 g, 2.2 mmol	TBAB 0.70 g, 2.2 mmol	53	92

[1]Percentage yield was calculated from the degree of modification of PECH.

Table 1: *Chemical modification conditions and product yields of* **AP Polymers***.*

Since all four polymers of this series exhibited similar trend in their NMR and IR spectra, only the spectra of **AP1** will be used in this discussion. The assignments were made based on their 2D-NMR spectra. The ^{1}H and ^{13}C NMR data of **AP1** and their corresponding assignments are shown in Table 1 (SI).

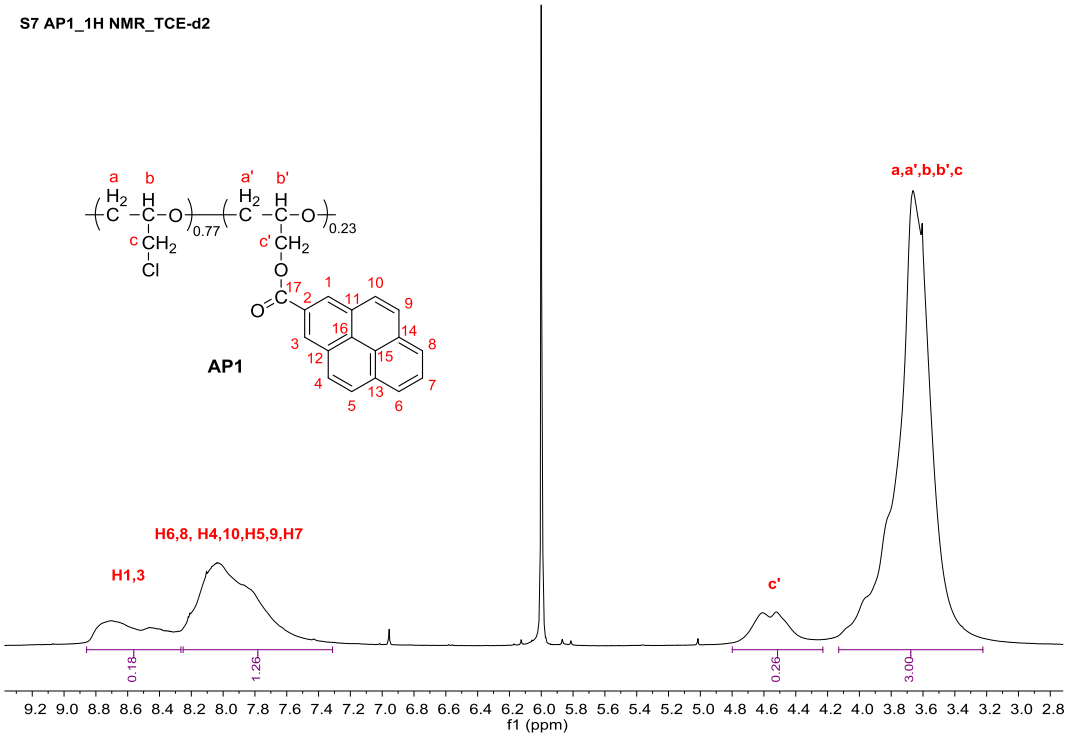

Figure 5: *^{1}H NMR spectrum (700 MHz, TCE-d_2) of* **AP1**.

Since the polymer contains many repeating units, slight deviation of each units would give rise to slightly different NMR signals which overlap with one another giving rise to broad signals as shown in the ^{1}H and ^{13}C NMR spectra of the **AP Polymers**.

From the ^{1}H NMR spectrum of **AP1** as shown in Figure 5, the aromatic region shows two broad, irregularly shaped and overlapped peaks between 8.86 and 7.32 ppm which corresponded to protons from the pyrene moieties. The “camel humps” peak around 4.80-4.23 ppm can be attributed to the two methylenic **c’** protons in the modified repeating unit, while the broad peak around 4.14-3.22 ppm are the main chain methylenic and methynic protons **a**, **a’**, **b**, **b’** and **c** of the modified and unmodified repeating units.

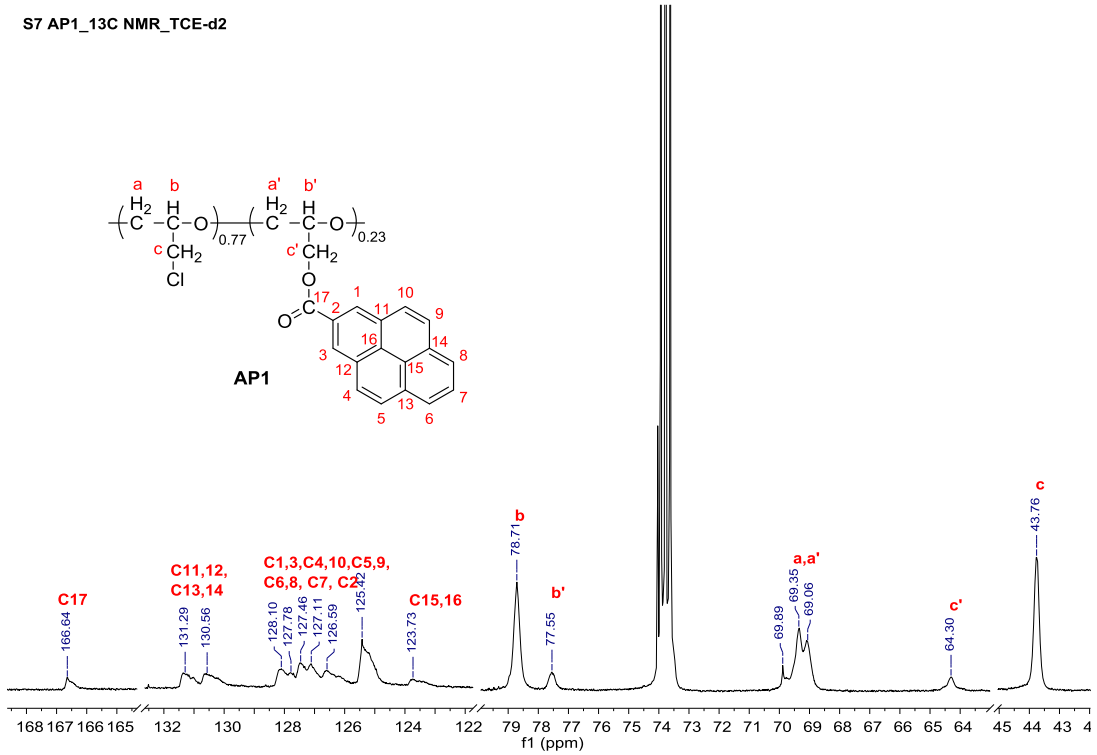

Figure 6: *^{13}C NMR spectrum (176 MHz, TCE-d_2) of* **AP1**.

From the ^{13}C NMR spectrum of **AP1** in Figure 6, the broad peak located most downfield at 166.6 ppm corresponds to the carbonyl carbon of pyrene which falls in the chemical shift region of an ester. The main chain carbons **a** and **a'** appeared as a broad overlapped peak at 69.4 ppm with two shoulders at 69.9 and 69.1 ppm, whereas carbon **b** and **b'** appeared as two well separated peaks at 78.1 and 77.6 ppm, respectively. The methylenic carbons **c** and **c'** of the unmodified and modified unit also appeared very well resolved, with the modified carbon **c'** being more deshielded (64.3 ppm) than carbon **c** (43.8 ppm). This can be explained by the close proximity of carbon **c'** to the carbonyl group.

Since ^{1}H NMR spectra were recorded with a pulse delay time of 5 seconds and with sufficient number of scans, integration values obtained from the spectra could be used for the quantitative determination of the degree of modification of the **AP Series** polymers. The degree of modification of **AP1** from ^{1}H NMR spectra was calculated as follows (using integration values from Figure 5):

$$\text{Degree of Mod. of } \mathbf{AP1} = \frac{Quotient_{mod.protons}}{Quotient_{mod.+unmod.protons}} \times 100\ \%$$

$$= \frac{100 \times \left(\frac{Integral_{aromatic\ peaks} + Integral_{proton\ c'}}{n_{protons\ integrated}}\right)}{Quotient_{mod.protons} + \frac{Integral_{protons\ a,a'\ b,b'\ and\ c} - n_{mod.protons}(Quotient_{mod.protons})}{n_{protons\ integrated}}}$$

$$= \frac{\frac{(0.18 + 1.26) + 0.26}{(9 + 2)}}{0.15 + \frac{3.00 - 3(0.15)}{5}} \times 100\ \%$$

$$= 23\ \%$$

The calculated degree of modifications of **AP polymers** are shown in Table 2.

Polymer (PECH:PCOOK)	Modification (%)	T_g (°C)
PECH (1:0.0)	0	-23
AP1 (1:0.4)	23	23
AP2 (1:0.6)	23	25
AP3 (1:0.8)	27	36
AP4 (1:0.4)	35	47

Table 2: *Calculated degree of modification and glass transition temperature, T_g of* **PECH** *and* **AP polymers**.

The degree of modification of **AP polymers** appeared to have reached a plateau at around 25 % despite increasing amounts of **PCOOK** being introduced to the PECH backbone (**AP1** – **AP3**). However, when the same amount of **PCOOK** (40 %) was used for the modification of PECH in **AP1** and **AP4**, a change in the phase transfer catalyst (PTC) from 18C6 to TBAB seemed to have improved the modification degree from 23 % to 35 %. Although both PTC are efficient PTC commonly used in the chemical modification of **PECH**[24], TBAB appeared to be more suited for **PCOOK** than 18C6.

In the FT-IR spectrum (Figure 1) of **AP1**, the presence of a strong peak at 1714 cm^{-1} attributed to the characteristic ester carbonyl group and the absence of strong peaks attributed to COO^- from the starting material, **PCOOK**, implied successful chemical modification of **PCOOK** onto the **PECH** backbone.

Upon chemical modification, the resulting **AP polymers** appeared as hard, dark brown solids. The polymers were also found to be partially soluble and swollen (gelatinous) in the organic solvents tested (THF, $CHCl_3$, DCM, TCE, toluene, etc).

This phenomena may be a result of “pseudo-crosslinks” from π-π interactions between the pyrene moieties which will be further discussed in Section 3.6. All of the **AP polymers** were fluorescent in solution (Figure 10d).

In addition to structural characterisation, the polymers were characterised with DSC, TGA and GPC. Glass transition temperature, T_g of the polymers were determined from the second heating curve in their respective DSC thermograms and are shown in Table 2. As the degree of modification increases across the series, the value of T_g also increases as expected due to the increasing number of side bulky aromatic groups.

The thermal stability of **AP polymers** was studied by TGA and the results are reported in Table 3. **AP polymers** in general were more thermally stable than **PECH** with values of char yield within the range of 20-25 % (which approx. 15 % more than that of **PECH**). The rate of degradation of **AP polymers** were almost similar to that of **PECH** (around 370 ^oC) based on the temperature at which 50 % of weight has been lost, $T_{50\%}$. Although **AP4** (35 % modified) is the highest modified polymer in the series, it did not exhibit a much higher or lower degradation rate than its counterparts which are approximately 25 % modified. The peak mass loss rate temperature, T_{max} of **AP polymers** were also found to be very similar to **PECH**, appearing only slightly lower (around 360 ^oC).

Polymer	$T_{50\%}$ (^oC)[a]	Char Yield, %	T_{onset} (^oC)[b]	T_{endset} (^oC)[c]	T_{max} (^oC)[d]
PECH	362	7.1	349	373	363
AP1	371	20.4	343	385	362
AP2	367	21.3	343	378	360
AP3	373	22.4	337	384	354
AP4	370	23.6	338	381	354

[a] Temperature corresponding to 50 % weight loss; [b] Onset decomposition temperature; [c] Endset decomposition temperature; [d] Peak mass loss rate temperature.

Table 3: *TGA data of* **AP Polymers***.*

The average molecular weight (M_w), number average molecular weight (M_n) and polydispersity index of **AP Series** were determined via GPC and are reported in Table 4.

Polymer	Modification (%)	M_n[a]	M_w[a]	PDI (M_w/M_n)
PECH	0	122800	582700	4.75
AP1	23	26100	157600	6.03
AP2	23	45000	430700	9.58
AP3	27	55100	288000	5.22
AP4	35	27700	188400	6.81

[a] Average molecular weights relative to PS standard by GPC, using THF/Toluene as the eluent.

Table 4: *GPC Data of* **AP Series***.*

It was expected that with the slight increasing degree of modification across the series, there should be a noticeable increase in the trend of molecular weight. However, this was not what was observed. Keeping in mind that GPC operates with the assumption that the polymer introduced in the system behaves like that of PS in THF/toluene, the introduction of pyrene moiety into the backbone of **PECH** could greatly alter the hydrodynamic volume of the system, making it very different to the starting **PECH** polymer. Another possibility regarding the absence of a trend could be due to the method used in the preparation of GPC samples. Since **AP polymers** exhibited partial solubility in the THF/toluene, all samples were filtered and only the filtrates were used in the measurements. The filtration may have removed a portion of polymer with larger molecular weight leaving behind smaller molecular weight fractions. Hence, in this case, there will not be a predictable trend between the molecular weight of **AP polymers** and the degree of modification. The GPC molecular weight distribution curves of **AP Series** (Figure 14 – SI) showed evidence of bimodality. This justifies the large PDI values observed in Table 4.

It is important to note that **PECH** was purchased from Sigma Aldrich and was reported to have an average molecular weight (M_w) of around 700,000 by GPC. This data is significantly higher than the actual experimental data obtained (122,800) which may be due to the solvent system and the calibrant range used as well as the partial solubility of the **AP polymers**.

3.4 Modification of **PECH** *with* **uPPCOOK, YC Series**

YC Series polymers were synthesised via S_N2 substitution with the use of carboxylate anion (**uPPCOOK**) as nucleophile as shown in Scheme 2. The

chemical modification conditions and product yields of **YC polymers** are reported in Table 5.

YC Series (PECH: uPPCOOK)	PECH	uPPCOOK	TBAB	THF (mL)	Yield (%)[1]
YC1 (1:0.5) (6 days)	0.22 g, 2.4 mmol	0.40 g, 1.2 mmol	0.38 g, 1.2 mmol	24	-*
YC2 (1:0.4) (4 days)	0.28 g, 3.0 mmol	0.41 g, 1.2 mmol	0.39 g, 1.2 mmol	30	46

[1]Percentage yield was calculated from the degree of modification of PECH; *Too little product left due to repeated purification.

Table 5: *Chemical modification conditions and product yields of* **YC Polymers**.

As a result of repeated purifications, very little **YC1** polymer was left to be able to run a quantitative NMR analysis. Thus, only the ^{1}H and ^{13}C NMR spectra of **YC2** will be used in this discussion.

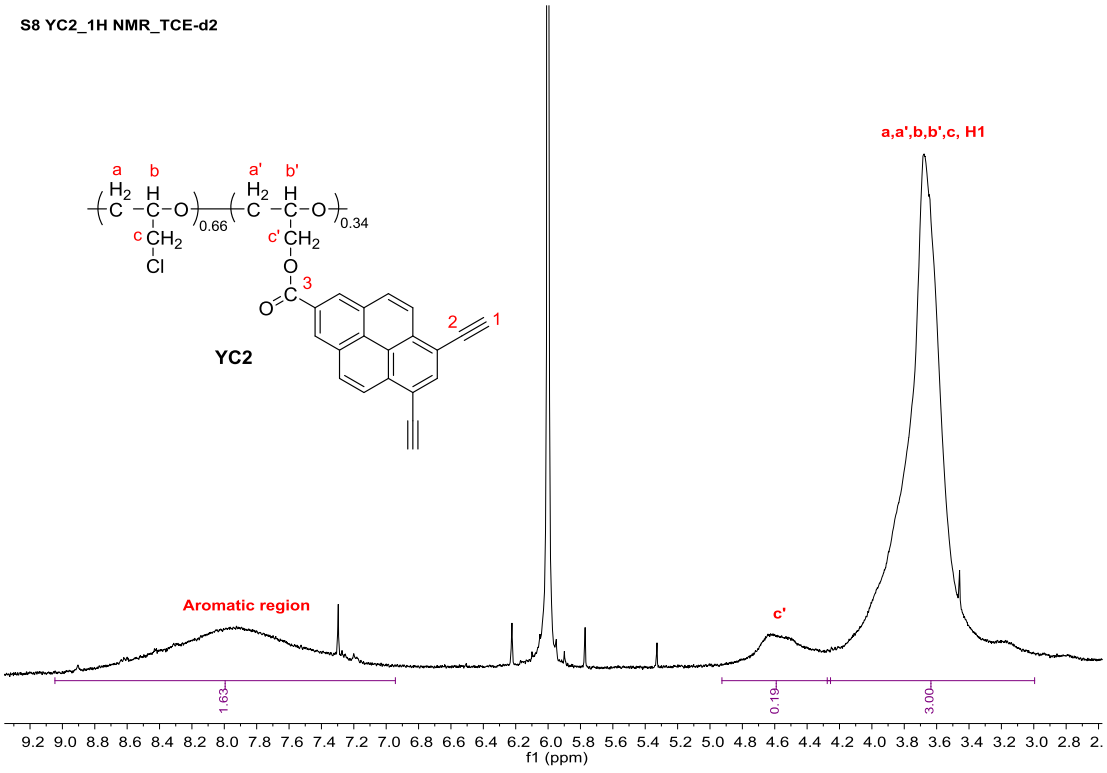

Figure 7: *^{1}H NMR spectrum (400 MHz, TCE-d_2) of* **YC2**.

From the ^{1}H NMR spectrum of **YC2** in Figure 7, three regions can be observed: a very broad peak at 7.90 ppm corresponding to the aromatic protons of pyrene, a small bump at 4.60 ppm attributed to the methylenic **c'** protons in the modified

repeating unit and a huge peak around 4.20-3.19 ppm belonging to the main chain methylenic and methynic protons **a**, **a'**, **b**, **b'** and **c** of the modified and unmodified repeating units.

Unlike the ^{13}C NMR spectrum of **AP1** in Figure 6, the ^{13}C NMR spectrum of **YC2** (Figure 7) was noisier and the region corresponding to the aromatic carbons of pyrene were much less visible/distinguishable. This could be due to partial solubility of **YC2** in organic solvents similar to that experienced by **AP series** as mentioned in Section 3.3. However, the carbonyl carbon peak at 168.5 ppm is still visible and located in the chemical shift region of an ester, suggesting successful modification of **uPPCOOK** onto the **PECH** main chain. The main chain carbons **a** and **a'** appeared as a broad overlapped peak at 69.3 ppm whilst carbon **b** and **b'** appeared as two separated peaks at 78.7 and 77.2 ppm, respectively. The methylenic carbons **c** and **c'** of the unmodified and modified unit appeared very well resolved, with the modified carbon **c'** being more deshielded (59.3 ppm) than carbon **c** (43.8 ppm). This can be explained by the close proximity of carbon **c'** to the carbonyl group.

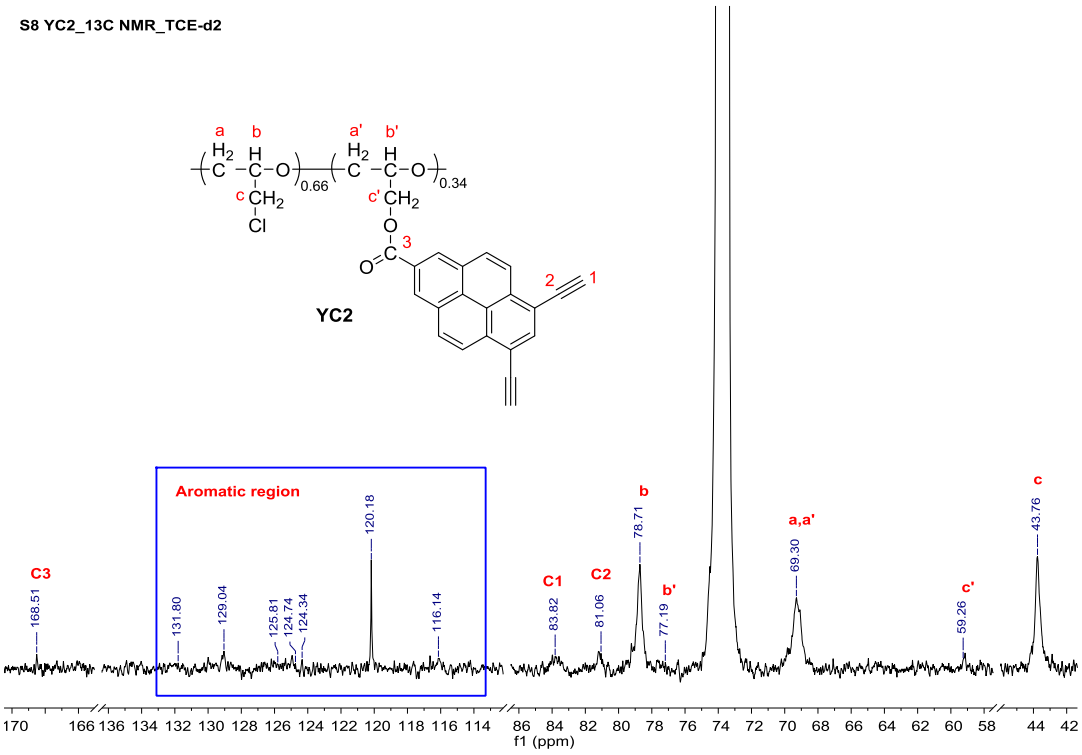

Figure 8: *^{13}C NMR spectrum (101 MHz, TCE-d_2) of **YC2**.*

As ^{1}H NMR spectra were recorded with a pulse delay time of 5 seconds and with sufficient number of scans, integration values obtained from the spectra could be

used for the quantitative determination of the degree of modification of **YC2**. The degree of modification of **YC2** from ^{1}H NMR spectra was calculated as follows (using integration values from Figure 7):

$$\text{Degree of Mod. of } \mathbf{YC2} = \frac{Quotient_{mod.protons}}{Quotient_{mod.+unmod.protons}} \times 100\ \%$$

$$= \frac{100 \times \left(\frac{Integral_{aromatic\ peaks} + Integral_{proton\ c'}}{n_{protons\ integrated}}\right)}{Quotient_{mod.protons} + \frac{Integral_{protons\ a,a'\ b,b'\ and\ c} - n_{mod.protons}(Quotient_{mod.protons})}{n_{protons\ integrated}}}$$

$$= \frac{\frac{(1.63) + 0.19}{(7+2)}}{0.20 + \frac{3.00 - 5(0.20)}{5}} \times 100\ \%$$

$$= 34\ \%$$

The calculated degree of modifications of **YC polymers** are shown in Table 6.

Polymer (PECH:uPPCOOK)	Modification (%)	T_g (°C)
PECH (1:0.0)	0	-23
YC1 (1:0.5)*	-	-
YC2 (1:0.4)	34	42

*Too little product left due to repeated purification.

Table 6: *Calculated degree of modification and glass transition temperature, T_g of **PECH** and **YC polymers**.*

The calculated degree of modification of **YC2** was found to be 34 % which is relatively high since only 40 % of **uPPCOOK** was introduced in the reaction.

In the FT-IR spectrum (Figure 3) of **YC2**, the presence of a strong peak at 1718 cm^{-1} corresponding to the characteristic ester carbonyl group, and the absence of strong peaks attributing to COO$^-$ from the starting material, **uPPCOOK**, implied successful chemical modification of **uPPCOOK** onto the **PECH** backbone.

Both **YC polymers** appeared as brown flakes upon purification. Similar to **AP polymers**, this series of polymer also swell in various organic solvents which can be attributed to “pseudo-crosslinks” from π-π interactions between the pyrene moieties (Section 3.6). **YC polymers** were fluorescent in solution and in solid state (Figure 10d).

DSC, TGA and GPC were used as additional structural characterisation of **YC2**. Glass transition temperature, T_g of **YC2** determined from the second heating curve in its DSC thermogram and is shown in Table 6. The T_g of **YC2** (42 ^oC) is much higher than **PECH**'s (-23 ^oC) due to the present of side bulky aromatic groups (pyrene moieties).

The thermal stability of **YC2** was studied by TGA and the results are reported in Table 7. **YC2** with 45 % was found to be far more thermally stable than **PECH** with 7 % char yield. The rate of degradation can be deduced from the temperature at which 50 % of weight has been lost, $T_{50\%}$. **PECH** having the lower $T_{50\%}$ (362 ^oC) degraded faster than **YC2** (34 % modified) at 495 ^oC. The peak mass loss rate temperature, T_{max} was higher in **PECH** (363 ^oC) than **YC2** (355 ^oC).

Polymer	$T_{50\%}$ (^oC)[a]	Char Yield, %	T_{onset} (^oC)[b]	T_{endset} (^oC)[c]	T_{max} (^oC)[d]
PECH	362	7.1	349	373	363
YC1*	-	-	-	-	-
YC2	495	44.9	331	404	355

[a] Temperature corresponding to 50 % weight loss; [b] Onset decomposition temperature; [c] Endset decomposition temperature; [d] Peak mass loss rate temperature; *Too little product left due to repeated purification.

Table 7: *TGA data of* **YC Polymers***.*

The average molecular weight (M_w), number average molecular weight (M_n) and polydispersity index of **YC2** was determined via GPC and are reported in Table 8.

Polymer	Modification (%)	M_n[a]	M_w[a]	PDI (M_w/M_n)
PECH	0	122800	582700	4.75
YC1*	-	-	-	-
YC2	34	16300	65200	4.00

[a] Average molecular weights relative to PS standard by GPC, using THF/Toluene as the eluent; *Too little product left due to repeated purification.

Table 8: *GPC Data of* **YC Series***.*

It was expected that upon chemical modification, there should be an increase in molecular weight since new side groups were introduced into the polymer backbone. However, upon chemical modification, **YC2** has a much smaller M_n and M_w than **PECH**. Keeping in mind that GPC operates with the assumption that the polymer introduced in the system behaves like that of PS in THF/toluene, the

introduction of pyrene moiety into the backbone of **PECH** could greatly alter the hydrodynamic volume of the system, making it very different to the starting **PECH** polymer. Another possibility could be due to the method used in the preparation of **YC2** GPC sample. Since **YC2** exhibited partial solubility in the THF/toluene, the sample was filtered and only the filtrate was used in the measurement. The filtration may have removed a portion of polymer with larger molecular weight leaving behind smaller molecular weight fractions. Hence, in this case, there will not be a predictable trend between the molecular weight of **YC polymers** and the degree of modification. The GPC molecular weight distribution curves of **YC2** and **PECH** (Figure 15 – SI) showed evidence of bimodality. This justifies the large PDI values observed in Table 8.

It is important to note that **PECH** was purchased from Sigma Aldrich and was reported to have an average molecular weight (M_w) of around 700,000 by GPC. This data is significantly higher than the actual experimental data obtained (122,800) which may be due to the solvent system and the calibrant range used as well as the partial solubility of the **YC polymers**.

3.5 The Design Idea of AP *and* YC Series

The synthesis of **AP** and **YC series** were driven by the idea of concurrently incorporating liquid crystallinity and fluorescent properties in a single polymer via chemical modification of pyrene derivatives into **PECH** to get the best of both worlds. Although pyrene derivatives, **PCOOK** and **uPPCOOK** by themselves were not liquid crystals, several research groups in the past have shown that it is possible to obtain liquid crystalline polymers from non-liquid crystalline/mesogenic groups[15,16]. Hence, to try out this hypothesis, **AP series** was synthesised by chemical modification of **PECH** with **PCOOK** whereas **YC series** was synthesised by chemical modification of **PECH** with **uPPCOOK**.

Prior to the successful synthetic procedures described in Section 2.4, two methods as shown in Scheme 3 were initially attempted for the chemical modification of pyrene moieties (**Pyr1** and **uPPCOOK**) onto **PECH** backbone. Method 1 involved S_N2 substitution via the use of alkoxide (hydroxyl group on **Pyr1** was converted to an alkoxide with NaH) as the nucleophile. This method gave rise to more side reactions (dehydrochlorination) than chemical modification

which led to the formation of unsaturated vinylether units accompanied by chain scission. Similar dehydrochlorination issues were reported by Perez *et al.* when they attempted chemical modification of **PECH** with phenolate (which was generated in situ from dry phenol and NaH)[25,26]. The unsaturated vinylether units were identified by the presence of two singlets at 4.1 ppm (-O-CH_2-C=CH_2) and 4.3 ppm (C=CH_2 protons) in its ^{1}H NMR spectrum (in $CDCl_3$) which matched to those found in literature[27].

On the other hand, method 2 involved S_N2 substitution via the use of carboxylate anion (**uPPCOOK**) as the nucleophile. This method turned out to be most ideal as the reaction conditions yielded polymers which showed no sign of dehydrochlorination. Unfortunately, the introduction of pyrene moieties onto **PECH** backbone brought in solubility/swelling problems for the polymers when dissolved in organic solvents.

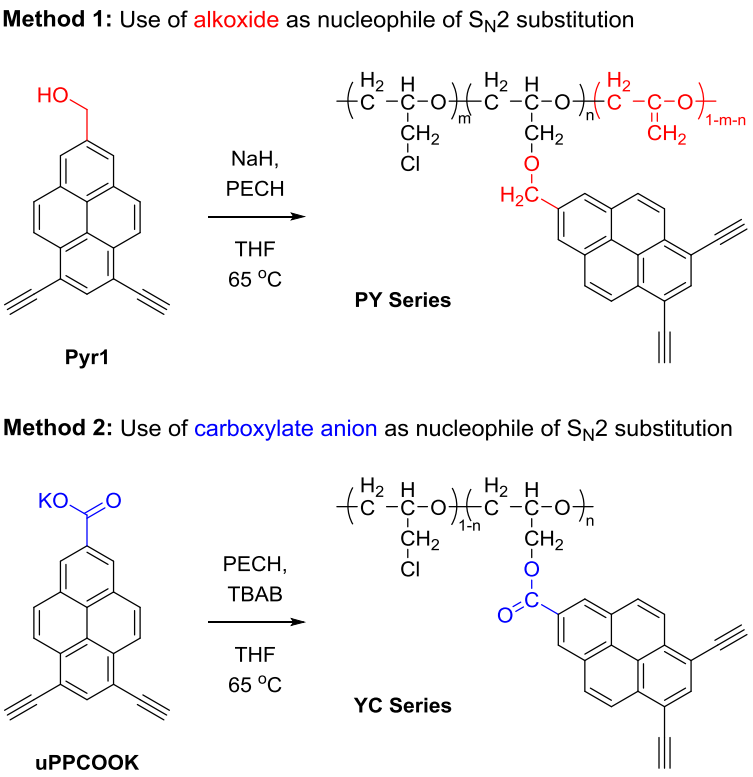

Scheme 3: *Methods used for the preparation of polyethers,* ***PY*** *and* ***AP Series****.*

With decreasing amounts of starting material (**uPPCOOK)**, more of it needed to be synthesised (in bulk) from scratch. However, in the process of repeated synthesis, the scaled-up procedures were found to be far more challenging and much less efficient, leading to very low yields of **uPPCOOMe** to work with. As a

result, the ester derivative (**uPPCOOMe**) obtained from the bulk synthesis was used for the synthesis of more interesting pyrene derivatives such as the ones with added “pseudo crown ether cavity” as discussed in Chapter 3 whilst **YC polymers** were put on hold.

AP polymers were then prepared as an alternative to **YC polymers** which involved the chemical modification **PECH** with a much simpler pyrene core, **PCOOK** that was significantly easier to prepare in bulk. This alternate series would still enable the concept (of whether the incorporation of a planar moiety like pyrene would offer any form of liquid crystallinity to the resulting polymer) to be tested out. Unfortunately, like **YC series**, **AP series** also have problems with their solubility and modification quantity. Therefore, in Chapter 4, the synthesis and characterisation of a new planar photoactive group (anthracene) via chemical modification with **PECH** will be discussed.

3.6 Proposed Explanation for the Partial Solubility of Pyrene Polymers

Since both **AP** and **YC polymers** were synthesised and purified in the dark, photo-initiated side reactions / crosslinking can be ruled out as being the cause of its partial solubility in solvents. The other possible cause would be the close proximity of pyrene moieties in the polymer backbone. To proove this, UV-Vis absorption and emission spectra of the monomers (**PCOOK** and **uPPCOOK**) and the polymers (**AP1** and **YC2**) were recorded in THF. All four samples were diluted accordingly prior to measurement so as the absorbance value at the wavelength of excitation was below 0.04 and the absorbance value at λ_{max} did not exceed 0.10. The recorded spectral data were shown in Table 9 whilst the spectra were compared in Figure 10.

Compound (THF)	λ_{Abs} (nm)	λ_{Em} (nm)	e/m ratio[1]	λ_{Exc} (nm)
PCOOK	253, 268[sh], 280, 308, 322, 337	384, 397, 417, 444[sh]	-	310
AP1	265, 308, 322, 337, 395[sh], 471[br]	400, 419[sh], 486[sh], 544[br]	0.56	310
uPPCOOK	264, 274, 277, 285, 299, 343, 361, 378, 381	390[sh], 406[sh], 412, 426	-	370
YC2	270, 342, 359, 378, 412[sh]	393, 416, 440, 527[br]	2.17	350

[1]Excimer/Monomer (e/m) ratio was calculated by comparing the fluorescence intensity of the excimer band to that of its monomer peak; [br] = broad peak; [sh] = shoulder peak.

Table 9: *UV-Vis absorption and emission spectral data of* ***PCOOK, AP1, uPPCOOK*** *and* ***YC2*** *in THF.*

According to a paper by Bains *et al.*, the approximated distance between two pyrenes can be estimated from its excimer/monomer (e/m) ratio[28]. The e/m ratios of both **AP1** and **YC2** polymers were calculated by comparing the respective fluorescence intensity of the excimer band (in bold **red**) as shown in Table 9 with its monomer peak (in bold **blue**). **YC2** with an e/m value of 2.17 contains pyrene moieties that are in closer proximity with one another than those in **AP1** (0.56). These e/m values were comparable to the ones observed in literature[28]: 2.62 and 0.68 with estimated distances of approximately 5.4 Å and 21.6 Å, respectively. With neighbouring pyrene moieties so close-by, it is unsuprising that there will be π-π interactions involved which would lead to a decrease in their solubility in organic solvents[29].

Pyrene has been abundantly used in the field of graphene chemistry to graft/anchor/immobilise a variety of moieties onto the graphenic surfaces by putting the stable π-π interactions to good use[30,31]. With that said, it is therefore possible that the relatively strong π-π interactions between closely located pyrene units in **AP1** and **YC2** formed intra- and inter-molecular "pseudo-crosslinks" within themselves as shown in Figure 9.

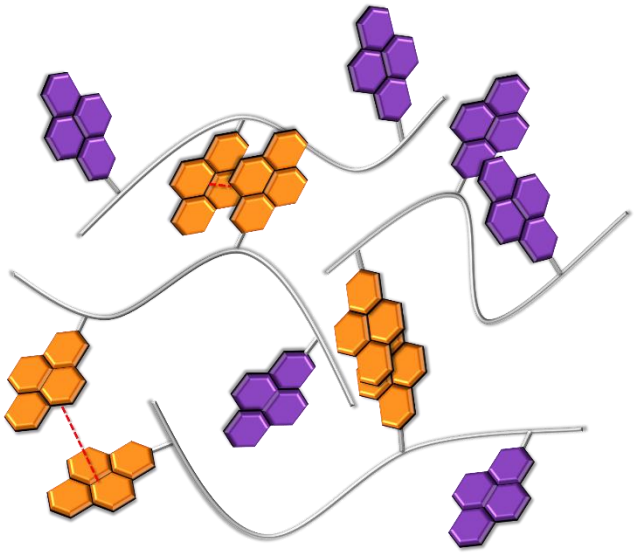

Figure 9: *Cartoon representation of "pseudo-crosslinks" in* ***AP1*** *with red dashed lines representing π-π interactions between two neighbouring pyrenes (orange).*

Polymers with "pseudo-crosslinks" would resemble polymers with covalent crosslinks bringing about a decrease in solubility as well as swelling in organic solvents[32] which coincided with what was observed for both the **AP** and **YC series**.

To ease comparison, all of the absorption and emission spectra were normalised, compiled and individually compared (Figure 10). The spectra were also colour coded according to their observed colours when irradiated under 365 nm as shown in Figure 10d. Since all of the compounds had pyrene in them, a series of vibrational spaced absorption bands characteristic of the $S_0 \rightarrow S_2$ transition of pyrene can be observed between 300 – 380 nm.

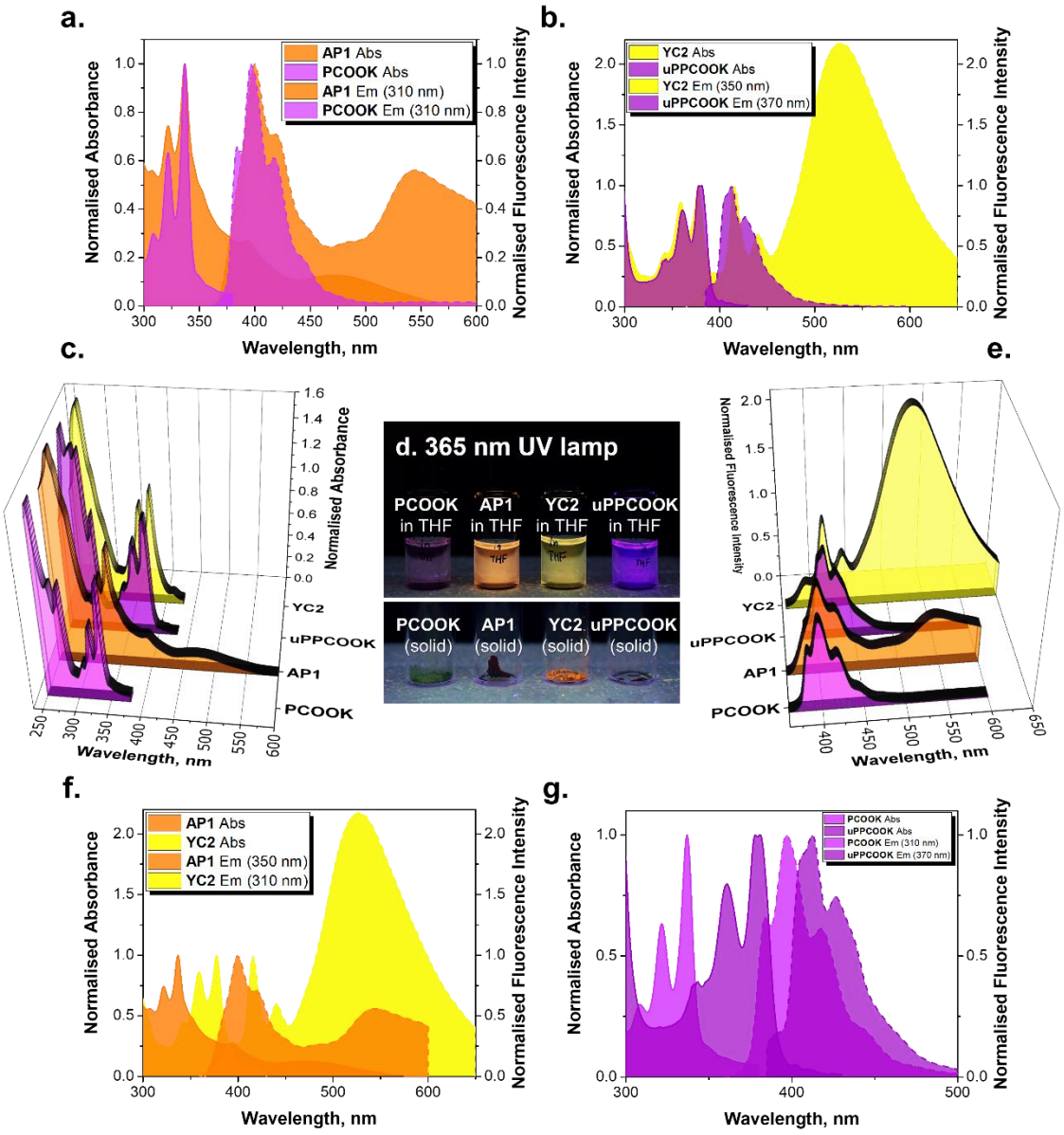

Figure 10: *Comparison of normalised absorption and emission spectra of* ***a) PCOOK*** *and* ***AP1****,* ***b) uPPCOOK*** *and* ***YC2****,* ***c)*** *comparison of all normalised absorption spectra,* ***d)*** *comparison of all samples in THF and in solid state under 365 nm UV lamp,* ***e)*** *comparison of all normalised emission spectra, comparison of normalised absorption and emission spectra of* ***f) AP1*** *and* ***YC2*** *and* ***g) PCOOK*** *and* ***uPPCOOK****.*

In Figure 10a, the characteristic pyrene vibrational absorption bands of both **PCOOK** and **AP1** are seen well overlapped at 308, 322 and 337 nm. However, the absorption spectrum of **AP1** appeared very broad with two new peaks at 395 and 471 nm. On the other hand, the emission spectrum of **AP1** appeared red shifted from that of **PCOOK** with “monomer” emissions at 400, 419 and 486 nm

followed by a broad excimer band at 544 nm. The broad peaks observed in both the absorption and emission spectra of **AP1** can be attributed to intramolecular pyrene-pyrene interactions in the polymer[33].

From Figure 10b, the absorption spectrum of the polymer (**YC2**) is slightly blue shifted from its monomer (**uPPCOOK**), with characteristic pyrene vibrational bands at 342, 359 and 378 nm. Interestingly, the lowest energy band out of the three $S_0 \rightarrow S_2$ transitions in the absorption spectrum of **uPPCOOK** is split into two (at 378 and 381 nm – more visible from Figure 10g). Similar to that of **AP1**, the emission spectrum of **YC2** also appeared red shifted from **uPPCOOK** with "monomer" emissions at 393, 416 and 440 nm and an intense broad excimer band at 527 nm.

The absorption spectra of **YC2** and **uPPCOOK** are red shifted by around 40 nm from **AP1** and **PCOOK**, respectively, whilst similar but less drastic red shifts (around 20 nm) was observed in the emission spectra in Figure 10f and 10g. The red shift in absorption and emission spectra can be ascribed to the increase in conjugation from an ordinary 2- substituted pyrene (**PCOOK**) to 2- substituted pyrene with terminal acetylenes on the 6,8- positions (**uPPCOOK**).

4. Conclusions

In this chapter, two series of pyrene-based **PECH** polymers (**AP** and **YC Series**) have been successfully synthesised via chemical modification with pyrene derivatives **PCOOK** and **uPPCOOK**, respectively. All of the synthetic procedures and structural characterisation of the monomers and polymers were discussed. Alkoxide was used as a nucleophile in previous attempts to modify of **PECH** but was found to have caused dehydrochlorination in the resulting polymer. Hence, the carboxylate anion was used instead (as nucleophile in the S_N2 substitutions). Both **AP** and **YC polymers** had problems with solubility and were found to swell when dissolved in organic solvents. With the use of UV-Vis and fluorescence spectroscopy the relative proximity of pyrene in the polymers were studied. The emission spectra of both polymers showed the presence of a broad excimer band at 544 nm (**AP1**) and 527 nm (**YC2**) indicating the presence of intramolecular pyrene-pyrene interactions in the polymers. The absorption and emission spectra of **uPPCOOK** and **YC2** were significantly red shifted from that of **PCOOK** and

AP1 due the presence of terminal acetylenes on the 6,8- positions which greatly increased their conjugation. **YC2** (e/m ratio of 2.17) contained pyrene moieties that are in much closer proximity that those in **AP1** (0.56). Pyrene moieties in close proximity encouraged π-π interactions leading to the formation of “pseudo-crosslinks”. These crosslinks resembled covalent crosslinks found in polymers and likewise, led to partial solubility (swelling) in organic solvents. Due to solubility issues in the current series of polymers, a new series of polymer were synthesised as discussed in Chapter 4, using anthracene in place of pyrene to test out the concept of dual properties (liquid crystallinity and fluorescence) in a single polymer.

Appendix. Supplementary Information, SI

Supplementary information, SI related to this chapter can be found at the end of this thesis.

References

1 G. Trimmel, S. Riegler, G. Fuchs, C. Slugovc and F. Stelzer, *Adv. Polym. Sci.*, 2005, **176**, 43–87.

2 Y. H. Gursel, B. F. Senkal, M. Kandaz and F. Yakuphanoglu, *Polym. Adv. Technol.*, 2011, **22**, 90–93.

3 P. Kandasamy, R. Keerthiga, S. Vijayalakshmi and T. Kaliyappan, *Mol. Cryst. Liq. Cryst.*, 2015, **606**, 1–11.

4 E. Doganci, C. Cakirlar, S. Bayir, F. Yilmaz and M. Yasin, *J. Appl. Polym. Sci.*, 2017, **134**, 45207.

5 S. Ma, Y. Cai, Y. Tu, Y. Guan and X. Chen, *Polym. Chem.*, 2016, **7**, 3520–3529.

6 L. Chen, Y. Yuan, J. Li and H. Zhang, *Polym. Adv. Technol.*, 2018, **29**, 1039–1047.

7 D. Roudini and P. J. S. Foot, *Sci. Prog.*, 2016, **99**, 262–277.

8 A. J. J. Kragt, D. J. Broer and A. P. H. J. Schenning, *Adv. Funct. Mater.*, 2018, **28**, 1704756.

9 K. A. Bogdanowicz, S. V. Bhosale, Y. Li, I. F. J. Vankelecom, R. Garcia-Valls, J. A. Reina and M. Giamberini, *J. Memb. Sci.*, 2016, **509**, 10–18.

10 C. Pugh and V. Percec, *Effect of the Polymer Backbone on the Thermotropic Behavior of Side-Chain Liquid Crystalline Polymers,* 1988, pp. 97–118.

11 L. Callau, J. A. Reina, A. Mantecón, M. Tessier and N. Spassky, *Macromolecules*, 1999, **32**, 7790–7797.

12 X. Han, R. A. Shanks and D. Pavel, *Macromol. Chem. Phys.*, 2004, **205**, 743–751.

13 Q. F. Zhou, X. Zhu and Z. Wen, *Macromolecules*, 1989, **22**, 491–493.

14 X. Han, R. A. Shanks and D. Pavel, *Eur. Polym. J.*, 2005, **41**, 984–991.

15 C. Imrie, F. E. Karasz and G. S. Attard, *Die Makromol. Chemie, Rapid Commun.*, 1993, **357**, 351–357.

16 S. Malik, P. K. Dhal and R. A. Mashelkar, *Macromolecules*, 1995, **28**, 2159–2164.

17 H. Kawakami, Y. Mori, H. Abe and S. Nagaoka, *J. Memb. Sci.*, 1997, **133**, 245–253.

18 A. Rapp, I. Schnell, D. Sebastiani, S. P. Brown, V. Percec and H. W. Spiess, *J. Am. Chem. Soc.*, 2003, **125**, 13284–13297.

19 G. He, N. Yan, J. Yang, H. Wang, L. Ding, S. Yin and Y. Fang, *Macromolecules*, 2011, **44**, 4759–4766.

20 G. Wang, X. Chang, J. Peng, K. Liu, K. Zhao, C. Yu and Y. Fang, *Phys. Chem. Chem. Phys.*, 2015, **17**, 5441–5449.

21 M. Shyamal, S. Maity, P. Mazumdar, G. P. Sahoo, R. Maity and A. Misra, *J. Photochem. Photobiol. A Chem.*, 2017, **342**, 1–14.

22 A. C. Benniston, A. Harriman, S. L. Howell, C. A. Sams and Y.-G. Zhi, *Chem. - A Eur. J.*, 2007, **13**, 4665–4674.

23 J. Casas-Solvas, T. Mooibroek, S. Sandramurthy, J. Howgego and A. Davis, *Synlett*, 2014, **25**, 2591–2594.

24 J. A. Reina, V. Cádiz, A. Mantecón and A. Serra, *Die Angew. Makromol. Chemie*, 1993, **209**, 95–109.

25 M. Pérez, J. A. Reina, A. Serra and J. C. Ronda, *Polymer (Guildf).*, 2000, **41**, 7331–7337.

26 M. Perez, J. A. Reina, A. Serra and J. C. Ronda, *Acta Polym.*, 1998, **49**, 312–318.

27 T. Iizawa, T. Nishikubo, M. Ichikawa, Y. Sugawara and M. Okawara, *J. Polym. Sci. Polym. Chem. Ed.*, 1985, **23**, 1893–1906.

28 G. K. Bains, S. H. Kim, E. J. Sorin and V. Narayanaswami, *Biochemistry*, 2012, **51**, 6207–6219.

29 Y. Shao, G. Z. Yin, X. Ren, X. Zhang, J. Wang, K. Guo, X. Li, C. Wesdemiotis, W. Bin Zhang, S. Yang, M. Zhu and B. Sun, *RSC Adv.*, 2017, **7**, 6530–6537.

30 V. Georgakilas, J. N. Tiwari, K. C. Kemp, J. A. Perman, A. B. Bourlinos, K. S. Kim and R. Zboril, *Chem. Rev.*, 2016, **116**, 5464–5519.

31 Y. Zhang, C. Liu, W. Shi, Z. Wang, L. Dai and X. Zhang, *Langmuir*, 2007, **23**, 7911–7915.

32 S. Nandi and H. H. Winter, *Macromolecules*, 2005, **38**, 4447–4455.

33 B. X. Valderrama-García, E. Rodríguez-Alba, E. G. Morales-Espinoza, K. M. Chane-Ching, E. Rivera, S. Reed and M. Resendiz, *Molecules*, 2016, **21**, 172.

Chapter 3

Synthesis and Characterisation of Clicked Pyrene Derivatives

1. Introduction

Copper-catalysed azide-alkyne cycloaddition (CuAAC) also known as click reaction is described as "a set of near-perfect" reaction[1] because it is straight-forward, has high tolerance to reaction conditions, substrate structures and functional groups, provides robust binding of versatile molecules and most importantly it is regioselective in the generation of 1,4-disubstituted-1,2-3-triazole molecules[1–4]. Click chemistry has been utilised in various fields ranging from organic synthesis, polymer/material chemistry to medicinal/life science applications[4,5].

Macrocyclic structures on the other hand, are interesting and useful for its diverse utility in catalysis, molecular recognition, host-guest chemistry[6], etc. Unfortunately, due to continual synthetic challenges[7,8] (e.g. many synthetic steps, low yield, the use of high dilution method), the synthesis of macrocycles tend to be uneconomical. A viable solution would be via the use of click chemistry. To date, many papers have been published reporting successful synthesis of a number of click macrocycles carrying intriguing properties like in anion-binding, chemical sensing[6,7,9,10], etc. Some even reported the involvement of the 1,2,3-triazole rings from the click macrocycles in metal ion binding[6,9].

From Chapter 2, it was found that all of the pyrene-based **PECH** polymers synthesised via chemical modification encountered solubility issues. The cause of the partial solubility and swelling of those polymers was the presence of "pseudo-crosslinks" induced by the close proximity of adjacent pyrene moieties. One way to suppress the formation of pseudo-crosslinks would be to synthesise bulkier pyrene derivatives before attaching them onto **PECH**.

Since the ultimate goal of synthesising pyrene-based **PECH** polymers was to utilise them as proton/cation transporting membranes (as mentioned in Chapter 2), it will be worth attempting click reactions on the terminal acetylene ends of **uPPCOOMe** (pyrene derivative from Chapter 2) with crown ether bulky groups. This would not only provide the new pyrene derivatives with additional functionality (cation binding ability) resembling to click macrocycles, it should also

be bulky enough to prevent “pseudo-crosslinks” when being chemically modified onto **PECH** at a later stage.

Therefore, in this chapter, the synthesis and characterisation of clicked pyrene derivatives (**Pyr2COOMe** and **Pyr3COOMe**) via CuAAC will be discussed in addition to the design ideas, foresights and future work.

2. Experimental

2.1 Materials

Reagents and solvents were bought from various commercial suppliers at the highest purity possible and were used without further purification unless otherwise specified. 6,8-bisethynylpyrene-2-carboxylic acid methyl ester, **uPPCOOMe** was synthesised by procedures reported in Chapter 2. THF stabilized with BHT (ACROS Organics) was dried over activated 4 Å molecular sieves under nitrogen atmosphere for several days before use.

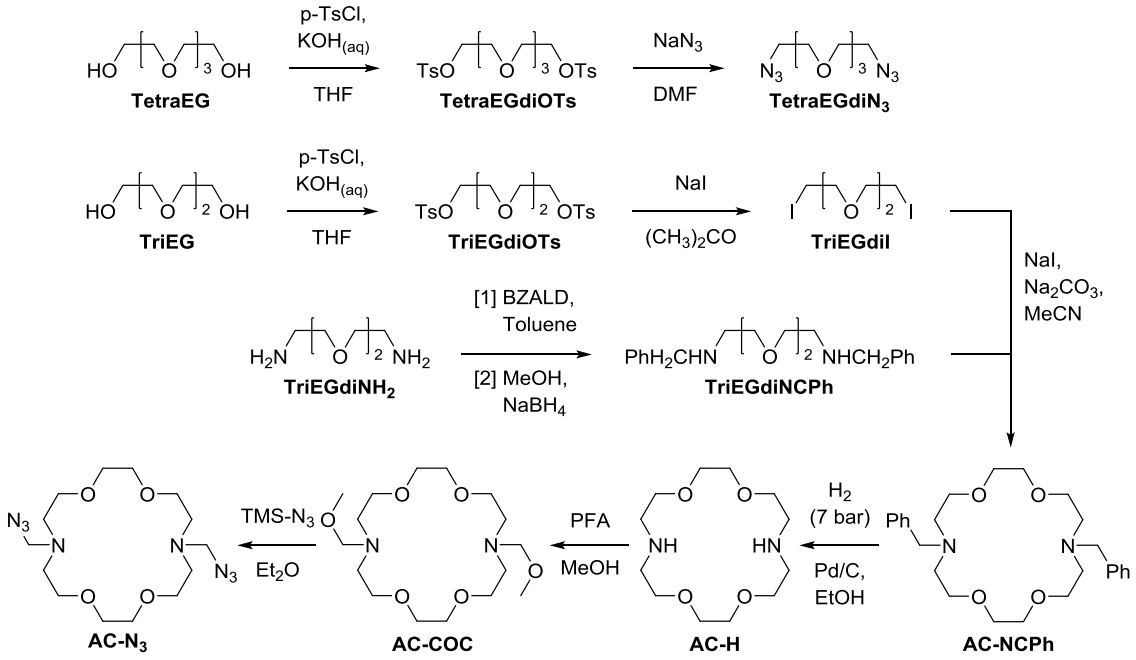

Scheme 1: *Preparation of* **TetraEGdiN$_3$** *and* **AC-N$_3$***.*

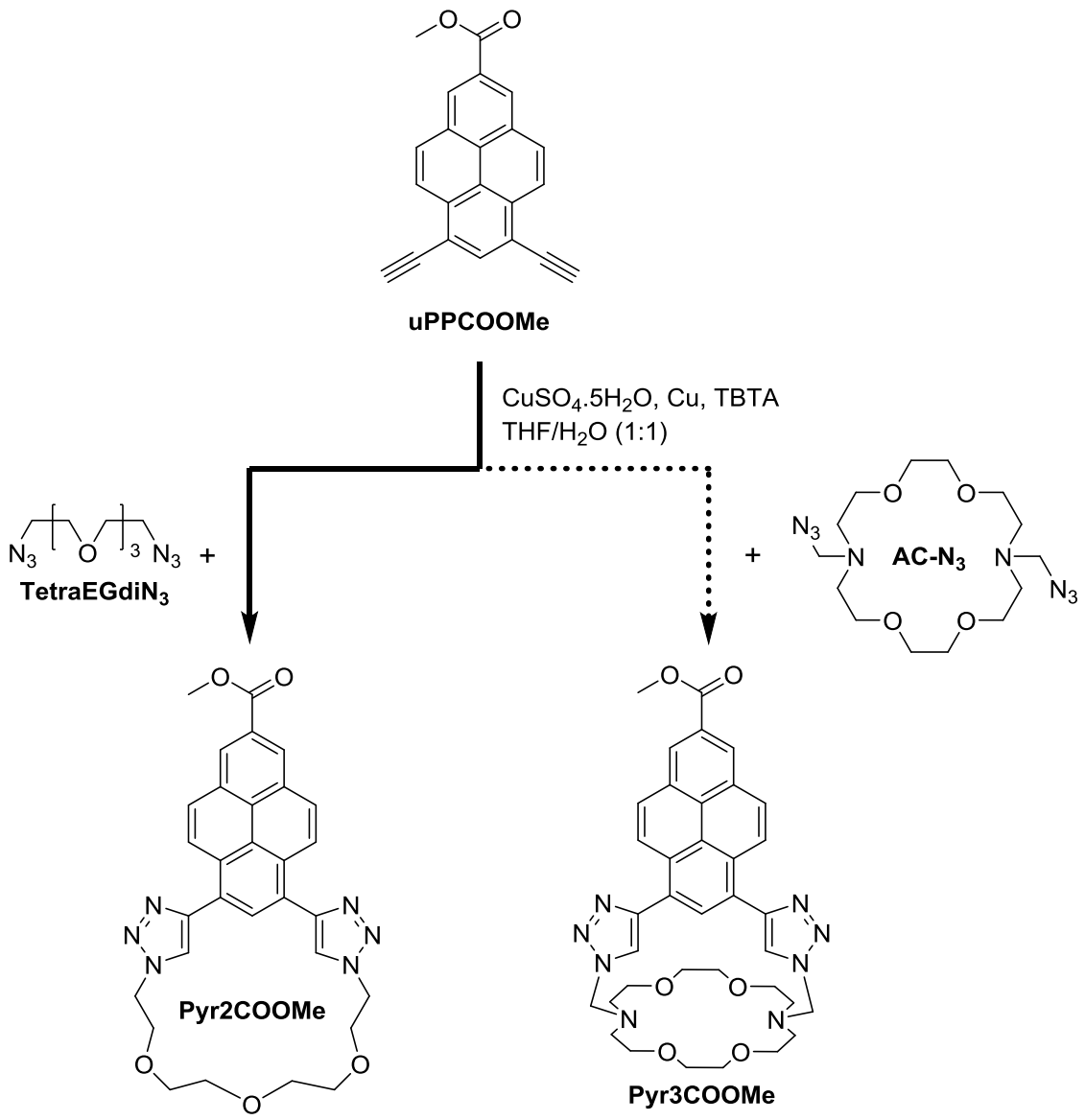

Scheme 2: *Preparation of* **Pyr2COOMe** *and* **Pyr3COOMe***.*

2.2 Synthesis of Tetraethylene glycol bisazides, TetraEGdiN$_3$

2.2.1 Synthesis of Tetraethylene glycol ditosylate, TetraEGdiOTs

50 mL of THF was added to a flask containing **TetraEG** (2.2 mL, 12.7 mmol) and p-TsCl (7.1 g, 37.2 mmol). The flask was cooled to 0 ^{o}C in an ice bath. With a syringe pump, 12 mL of 7 M KOH (4.7 g, 83.8 mmol) was added dropwise into the reaction mixture over 1 hour. The reaction mixture was allowed to stir for another 2 hours, monitored with TLC. Upon completion, the mixture was extracted with H_2O/Et_2O (25 mL/75 mL). The aqueous layer was re-extracted with Et_2O (3 x 15 mL). The combined organic layer was washed with sat. NH_4Cl and dried over $MgSO_4$. The solvent was removed under reduced pressure. The

resulting oil was dried under high vacuum using freeze-thaw cycles to yield a viscous pale yellow oil (6.19 g, 12.3 mmol, 97 %).

^{1}H NMR (300 MHz, Chloroform-*d*) δ 7.81 – 7.75 (m, 4H, H2), 7.39 – 7.28 (m, 4H, H1), 4.17 – 4.12 (m, 4H, H3), 3.70 – 3.64 (m, 4H, H4), 3.60 – 3.51 (m, 8H, H5, H6), 2.44 (s, 6H, H7).

The ^{1}H NMR spectrum of the purified product was consistent with the literature data[11].

2.2.2 Synthesis of Tetraethylene glycol bisazides, **TetraEGdiN$_3$**

NaN_3 (1.2 g, 18.5 mmol) was added little by little to **TetraEGdiOTs** (1.9 mL, 4.7 mmol) pre-dissolved in 15 mL of anhydrous DMF under N_2 at RT. The reaction mixture was left to reflux for 20 hours at 80 ^{o}C, with TLC monitoring. Upon completion, the reaction was cooled to 0 ^{o}C and the solvent was removed via vacuum distillation. Et_2O (20 mL) was added to the residue and the suspension was suction filtered. The residue was thoroughly washed with additional Et_2O. The filtrate was dried in vacuo to yield a yellow orangey liquid (1.09g, 4.5 mmol, 96 %). The liquid was kept in the freezer and thawed before use.

^{1}H NMR (300 MHz, Chloroform-*d*) δ 3.66 (d, *J* = 4.4 Hz, 12H, H2, H3, H4), 3.39 (t, *J* = 5.0 Hz, 4H, H1).

The ^{1}H NMR spectrum of the purified product was consistent with the literature data[12].

2.3 Synthesis of Diazo-18-crown-6 derivative, **AC-N$_3$**

2.3.1 Synthesis of Triethylene glycol ditosylate, **TriEGdiOTs**

THF (51 mL) was added to a flask containing **TriEG** (2.0 g, 13.3 mmol) and p-TsCl (7.5 g, 39.3 mmol). The flask was cooled to 0 ^{o}C in an ice bath. With a syringe pump, 13 mL of 7 M KOH (5.1 g, 90.9 mmol) was added dropwise into the reaction mixture over 1 hour. The reaction mixture was allowed to stir for another 2 hours, monitored with TLC. Upon completion, the mixture was extracted with H_2O/EA (25 mL/75 mL). The aqueous layer was re-extracted with EA (3 x 15 mL). The combined organic layer was washed with sat. NH_4Cl and dried over $MgSO_4$. The solvent was removed under reduced pressure. The

resulting oil was dried under high vacuum using freeze-thaw cycles to yield a white solid (6.00 g, 13.1 mmol, 98 %).

^{1}H NMR (300 MHz, Chloroform-*d*) δ 7.85 – 7.73 (m, 4H, H2), 7.37 – 7.29 (m, 4H, H1), 4.16 – 4.08 (m, 4H, H3), 3.70 – 3.61 (m, 4H, H4), 3.52 (s, 4H, H5, H6), 2.44 (s, 6H, H7).

The ^{1}H NMR spectrum of the purified product was consistent with the literature data[13].

2.3.2 Synthesis of Triethylene glycol bisiodide, TriEGdiI

Acetone (25 mL) was added to a flask containing **TriEGdiOTs** (2.5 g, 5.5 mmol) and NaI (2.5 g, 16.8 mmol). The reaction mixture was refluxed at 60 ^{o}C for 16 hours with TLC monitoring. Upon completion, the mixture was suction filtered. The filtrate was rotary evaporated to dryness. The residue was then extracted with $CHCl_3$ (30 mL) and water (3 x 15 mL), followed by of brine (15 mL). The combined organic layer was dried under $MgSO_4$. The solvent was removed to yield reddish brown oil (1.94 g, 5.2 mmol, 95 %).

^{1}H NMR (300 MHz, Chloroform-*d*) δ 3.81 – 3.74 (m, 4H), 3.68 (s, 4H), 3.27 (dd, *J* = 7.3, 6.5 Hz, 4H).

The ^{1}H NMR spectrum of the purified product was consistent with the literature data[14].

2.3.3 Synthesis of Triethylene glycol bisbenzylamine, TriEGdiNCPh

TriEGdiNH$_2$ (1.5 g, 10.1 mmol) and **BZALD** (2.2 g, 20.7 mmol) were dissolved in dry toluene (86 mL). With a Dean-Stark setup, the reaction mixture was refluxed at 110 ^{o}C for 5 hours with TLC monitoring. Upon completion, the reaction mixture was allowed to cool to RT, the solvent was removed under reduced pressure. The residue was suspended in MeOH (21 mL) and cooled to 0 ^{o}C in an ice bath. $NaBH_4$ (4.6 g, 121.6 mmol) was added portion-wise into the stirring suspension at RT under N_2. The reaction mixture was removed from the ice bath and allowed to go back to RT. The reaction mixture was left to react for another 3.5 hours with TLC monitoring. Once completed, the solvent was rotary evaporated to dryness. The residue was re-dissolved in water (45 mL) and extracted with $CHCl_3$ (3 x 15 mL). The combined organic layer was dried over $MgSO_4$ and solvent removed to yield a pale yellow oil (2.99 g, 9.1 mmol, 90%).

^{1}H NMR (300 MHz, Chloroform-*d*) δ 7.42 – 7.20 (m, 10H, H1, H2, H3), 3.82 (s, 4H, H4), 3.69 – 3.56 (m, 8H, H6, H7, H8), 2.87 – 2.77 (m, 4H, H5), 1.75 (s, 2H, H9).

The ^{1}H NMR spectrum of the purified product was consistent with the literature data[15].

2.3.4 Synthesis of Diazo-18-crown-6 derivative, AC-NCPh

TriEGdiNCPh (2.0 g, 6.1 mmol) in dry MeCN (30 mL) was slowly added to a flask containing **TriEGdiI** (1.9 g, 5.1 mmol) pre-dissolved in dry MeCN (76 mL). NaI (0.4 g, 2.7 mmol) in dry MeCN (15 mL) was then added, followed by the addition of Na_2CO_3 (2.6 g, 24.5 mmol). The reaction mixture was refluxed at 90 ^{o}C for 21 hours with vigorous stirring and TLC monitoring. Upon completion, the reaction mixture was cooled to RT and suction filtered. The filtrate was rotary evaporated till dryness and kept under high vacuum. The residue was re-dissolved in dioxane:acetone (26 mL, 1:1) mixture and refluxed at 90 ^{o}C. The solution was allowed to cool gradually to RT, transferred to fridge then to a freezer to be kept overnight. The crystals were filtered off and re-dissolved in water (36 mL) and $CHCl_3$ (30 mL). The aqueous layer was extracted with $CHCl_3$ (3 x 6 mL). The combined organic layer was dried over $MgSO_4$ and solvent was removed. The crude was recrystallised in hexane/ethanol mixture (36 mL:8.1 mL) to yield white feather-like crystals (1.19 g, 2.7 mmol, 53%)

^{1}H NMR (400 MHz, Chloroform-*d*) δ 7.37 – 7.17 (m, 10H, H1, H2, H3), 3.68 (s, 4H, H4), 3.66 – 3.58 (m, 16H, H6, H7), 2.82 (t, *J* = 5.9 Hz, 8H, H5).

The ^{1}H NMR spectrum of the purified product was consistent with the literature data[16].

2.3.5 Synthesis of Diazo-18-crown-6, AC-H

AC-NCPh (1.2 g, 2.7 mmol) was re-crystallised in hot EtOH (10 mL). Once crystals formed, the crystals and the supernatant liquid were transferred into a reaction vessel, the flasks were rinsed with fresh EtOH (5 mL). The reaction vessel was degassed and pressurised with 7 bar of H_2. The setup was left to react at RT for 22 hours, with TLC monitoring. Upon completion, the vessel content was poured through a pad of Celite and the filtrate was concentrated under

reduced pressure. The white residue was recrystallized from hot hexane (25 mL) to yield white crystals (0.25 g, 1.0 mmol, 37 %)

^{1}H NMR (300 MHz, Chloroform-*d*) δ 3.64 – 3.56 (m, 16H, H2, H3), 2.84 – 2.75 (m, 8H, H1).

The ^{1}H NMR spectrum of the purified product was consistent with the literature data[17,18].

2.3.6 Synthesis of Diazo-18-crown-6 derivative, **AC-N$_3$**

Dry MeOH (10 mL) was added to a flask containing **AC-H** (0.3 g, 1.1 mmol) and PFA (58.0 mg, 1.9 mmol) pre-flushed with N_2. The reaction mixture was stirred at RT for 20 hours with TLC monitoring. The solvent was rotary evaporated to dryness and dry diethyl ether (2 mL) was added to the residue (crude **AC-COC**) under N_2 at 20 ^{o}C. TMS-N_3 (0.3 mL, 2.3 mmol) was slowly added to the stirring solution and the setup was left to stir overnight with TLC monitoring. The precipitate were separated via centrifugation and was rinsed with additional diethyl ether before drying it under high vacuum. The resulting solid (0.26 g, 0.7 mmol, 64 %) was kept in the freezer and was thawed before use.

AC-COC

^{1}H NMR (300 MHz, Chloroform-*d*) δ 4.16 (s, 4H, H4), 3.65 – 3.58 (m, 16H, H3, H2), 3.25 (s, 6H, H5), 3.00 (t, *J* = 5.9 Hz, 8H, H1).

AC-N$_3$

^{1}H NMR (400 MHz, Chloroform-*d*) δ 4.54 (s, 4H, H4), 3.63 (s, 8H, H3), 3.62 (t, *J* = 5.5 Hz, 8H, H2), 2.95 (t, *J* = 5.5 Hz, 8H, H1).

The ^{1}H NMR spectrum of the purified final product was consistent with the literature data[19].

2.4 Synthesis of Clicked Pyrene Derivative, **Pyr2COOMe**

TBTA (18.4 mg, 34.7 µmol) and copper powder (22.0 mg, 0.3 mmol) were added to N_2 purged solution of **TetraEGdiN$_3$** (85.0 mg, 0.3 mmol) in dry THF (40 mL) at RT. 80 mL of $CuSO_4$ (9.1 mg, 36.4 µmol) solution was added dropwise into the reaction mixture over 20 minutes. This was then followed by dropwise addition of **uPPCOOMe** (107.0 mg, 0.3 mmol) pre-dissolved in dry THF)40 mL) (purged with

N_2) over 20 minutes. The reaction mixture was allowed to react at 40 ^oC for 1 hour with TLC monitoring. The reaction mixture was allowed to cool to RT before suction filtered to remove unreacted copper powder. The filtrate was extracted with DCM (120 mL) and the combined organic layer was dried over $MgSO_4$. Upon drying with rotary evaporator, the residue was purified with silica preparative TLC. Crude pre-dissolved in DCM/MeOH (5 mL, 7:3) was spotted onto the baseline of the prep-TLC plate and was then eluted with EA:Pet (100 mL, 7:3). The purification resulted in yellow crystals (76.00 mg, 137.5 µmol, 46 %).

^1H NMR (400 MHz, Chloroform-*d*) δ 9.34 (d, *J* = 9.3 Hz, 2H, H5, H9), 8.88 (s, 2H, H1, H3), 8.30 (s, 2H, H21, H22), 8.26 (d, *J* = 9.3 Hz, 2H, H4, H10), 8.20 (s, 1H, H7), 4.78 – 4.72 (m, 4H, H23, H24), 4.09 (s, 3H, H11), 3.96 – 3.91 (m, 4H, H25, H26), 3.80 – 3.74 (m, 4H, H27, H28), 3.69 – 3.64 (m, 4H, H29, H30).

^{13}C NMR (101 MHz, Chloroform-*d*) δ 167.75 (C12), 148.72 (C19,C20), 131.35 (C13,C14), 129.42 (C7), 129.36 (C17,C18,C6,C8), 128.99 (C4,C10), 127.70 (C2), 126.76 (C5,C9), 126.20 (C1,C3), 125.42 (C15,C16), 124.65 (C21,C22), 71.61 (C27,C28), 71.43 (C29,C30), 70.26 (C25,C26), 52.61 (C11), 50.80 (C23,24).

FT-IR (v_{max}, cm^{-1}) 3143, 3068 (C-H stretching in triazole), 2872 (N_3 asymmetric stretching vibration), 1716 (aromatic ester C=O stretching vibration), 1299, 1215 (aromatic ester C-O stretching vibrations), 831, 768 (aromatic C-H out of plane bending vibrations).

(+)nanoESI-FTMS (m/z): found $[M+H]^+$ 553.2183, calcd. for $C_{30}H_{29}O_5N_6$: 553.2194.

X-ray crystal structure (Figure 13) and refinement data (Table 2) available in SI.

2.5 Synthesis of Clicked Pyrene Derivative, **Pyr3COOMe**

TBTA (11.3 mg, 21.0 µmol) and copper powder (13.8 mg, 0.2 mmol) were added to N_2 purged solution of **AC-N_3** (79.7 mg, 0.2 mmol) in dry THF (12 mL) at RT. $CuSO_4$ (49 mL, 5.3 mg, 21.0 µmol) solution was added dropwise into the reaction mixture over 20 minutes. This was then followed by dropwise addition of **uPPCOOMe** (65.9 mg, 0.2 mmol) pre-dissolved in dry THF (25 mL) (purged with N_2) over 20 minutes. The reaction mixture was allowed to react at 40 ^oC for 18

hours with TLC monitoring. The reaction mixture was allowed to cool to RT and was extracted with DCM (60 mL) and the combined organic layer was dried over $MgSO_4$. Upon drying with rotary evaporator, the residue was purified with silica plug packed with DCM. Crude pre-dissolved in DCM (2.5 mL) was wet-packed onto the silica plug and was then eluted with more DCM. One fraction from the purification process showed potential to be the desired compound, however, as there was only 26 mg of that impure fraction, further purification was not proceeded.

2.6 Characterisation

2.6.1 Nuclear Magnetic Resonance (NMR) Spectroscopy

^{1}H and ^{13}C NMR spectra of **Pyr2COOMe** in deuterated chloroform ($CDCl_3$) were recorded on Jeol ECS 400 MHz. 2D NMR such as ^{1}H-^{1}H correlation (COSY), ^{1}H-^{13}C heteronuclear single quantum correlation (HSQC), ^{1}H-^{13}C heteronuclear multiple bond correlation (HMBC) were used to substantiate ^{1}H and ^{13}C NMR assignments of the synthesised compounds.

2.6.2 FT-IR Spectroscopy

FT-IR spectra were obtained using Spectrum Two FT-IR Spectrometer fitted with a diamond crystal plate ATR unit (PerkinElmer).

2.6.3 Mass Spectrometry

Mass spectrometry analyses of the newly synthesised products were performed on a Thermo Scientific LTQ Orbitrap XL spectrometer equipped with an Advion NanoMate inlet in positive and negative ionisation modes by the team at EPSRC UK National Mass Spectrometry Facility, Swansea University.

2.6.4 X-ray Crystallography

Crystal structure data for **uPPCOOMe** was collected on a Xcalibur, Atlas, Gemini ultra diffractometer equipped with an Enhance Ultra (Cu) X-ray Source ($\lambda_{CuK\alpha}$ = 1.54184 Å) and an Oxford Cryosystems CryostreamPlus open-flow N_2 cooling device. Cell refinement, data collection and data reduction were undertaken via software CrysAlisPro, Agilent Technologies, Version 1.171.36.32 (release 02-08-2013 CrysAlis171 .NET) (compiled Aug 2 2013,16:46:58). Intensities were

corrected for absorption using CrysAlisPro, Agilent Technologies, Version 1.171.36.32 (release 02-08-2013 CrysAlis171 .NET) (compiled Aug 2 2013,16:46:58) Analytical numeric absorption correction using a multifaceted crystal model based on expressions derived by R.C. Clark & J.S. Reid. (Clark, R. C. & Reid, J. S. (1995). Acta Cryst. A51, 887-897).

Crystal structure data for **Pyr2COOMe** was collected on a DLS_I19_upgrade diffractometer equipped with an Synchrotron ($\lambda_{MoK\alpha}$ = 0.71073 Å) and an Oxford Cryosystems CryostreamPlus open-flow N_2 cooling device. Cell refinement, data collection and data reduction were undertaken via software SAINT v8.37A (Bruker, 2015). Intensities were corrected for absorption using SADABS-2014/5 (Bruker,2014) was used for absorption correction. wR2(int) was 0.1114 before and 0.0627 after correction. The Ratio of minimum to maximum transmission is 0.7028. The \l/2 correction factor is 0.00150.

Using Olex2 (Dolomanov, 2009), the structures were solved using XT (Sheldrick, 2015) and refined by XL (Sheldrick, 2008).

2.6.5 Spectroscopy

All solvents used for UV-Vis and fluorescence experiments were bought at the highest available grade and their purity were checked before the experiments.

UV-Vis Experiments

Absorption spectra were recorded using UV-1800 UV-Vis Spectrophotometer. Samples were dissolved in spectroscopic grade solvent in a 1 cm by 1 cm quartz cuvette. Baseline was corrected prior to measurements.

Fluorescence Experiments

Fluorescence emission and excitation spectra were recorded using a Shimadzu RF-6000 Spectrofluorophotometer. Measurements were repeated several times at varying concentrations and excitation wavelengths.

3. Results and discussion

3.1 Synthesis of Tetraethylene glycol bisazides, **TetraEGdiN$_3$**

The tetraethylene glycol bisazides, **TetraEGdiN$_3$,** was synthesised by S_N2 substitution of the tosylate groups in **TetraEGdiOTs** by sodium azide as shown in Scheme 1. The synthesis of **TetraEGdiOTs** and **TetraEGdiN$_3$** have previously been reported[20,21]. Their respective ^{1}H NMR spectra were found to be consistent with the literature. From the FT-IR spectrum in Figure 3, the presence of a peak at 2100 cm^{-1} corresponding to the characteristic asymmetric stretching vibration of an azide once again supported the successful synthesis of **TetraEGdiN$_3$**.

3.2 Synthesis of Diazo-18-crown-6 derivative, **AC-N$_3$**

The synthesis of diazo-18-crown-6 derivative, **AC-N$_3$,** was more complexed and required a total of seven steps as shown in Scheme 1. The total synthetic procedure described in Section 2.3 was derived from a combination of reported sources as follows: the synthesis of **TriEGdiI**[22], **AC-H**[23], **AC-COC**[24] and **AC-N$_3$**[19]. The respective ^{1}H NMR spectra of the intermediates involved were consistent to those found in the literature. From the FT-IR spectrum in Figure 3, the presence of a peaks at 2090 and 2020 cm^{-1} corresponding to the characteristic asymmetric stretching vibrations of an azide once again made evident of the successful synthesis of **AC-N$_3$**.

3.3 Synthesis of Clicked Pyrene Derivative, **Pyr2COOMe**

The clicked pyrene derivative, **Pyr2COOMe**, was synthesised via a click reaction between **TetraEGdiN$_3$** and 6,8-bisethynylpyrene-2-carboxylic acid methyl ester, **uPPCOOMe** as shown in Scheme 2. The full synthesis of **uPPCOOMe** was described in Section 2.3.1 of Chapter 2.

Table 1 shows a list of reaction conditions attempted for the synthesis of **Pyr2COOMe**. It was found that the reaction which utilised Cu(0) as the copper source, $CuSO_4.5H_2O$ as the oxidising agent and tris[(1-benzyl-1H-1,2,3-triazol-4-yl)methyl]amine, TBTA as the ligand was the only workable reaction condition among the four. Hence, only the details of the reaction condition successfully yielded **Pyr2COOMe** are reported in Section 2.4.

Cu source (equiv)	Oxi. agent (equiv)	Red. agent (equiv)	Solvent (ratio)	Ligand (equiv)	T, °C (h)	Reaction
$CuSO_4$ (0.4)	-	NaAsc (0.6)	THF/H_2O (1:1) air	-	60 (1)	x
$CuSO_4$ (0.4)	-	NaAsc (0.6)	THF/H_2O (1:1) N_2	-	60 (18)	x
CuI (0.07)	-	-	THF/H_2O (3:1) N_2	-	50 (16)	x
Cu(0) (1.0)	$CuSO_4$ (0.1)	-	THF/H_2O (1:1) N_2	TBTA (0.1)	40 (1)	√

Table 1: *Reaction conditions attempted for the synthesis of* ***Pyr2COOMe****.*

Successful synthesis of **Pyr2COOMe** was confirmed from its ^{1}H NMR spectrum (Figure 1) by the appearance of a singlet at 8.30 ppm attributed to the H21 and H22 protons from the 1,2,3-triazoles and the absence of a singlet corresponding to the terminal acetylene protons previously seen in the starting material, **uPPCOOMe**. Prominent multiplet signals around 4.75 ppm and 3.93-3.57 ppm can be attributed to the OCH_2 protons (H23 – H30) on the newly enclosed "crown-ether-like cavity".

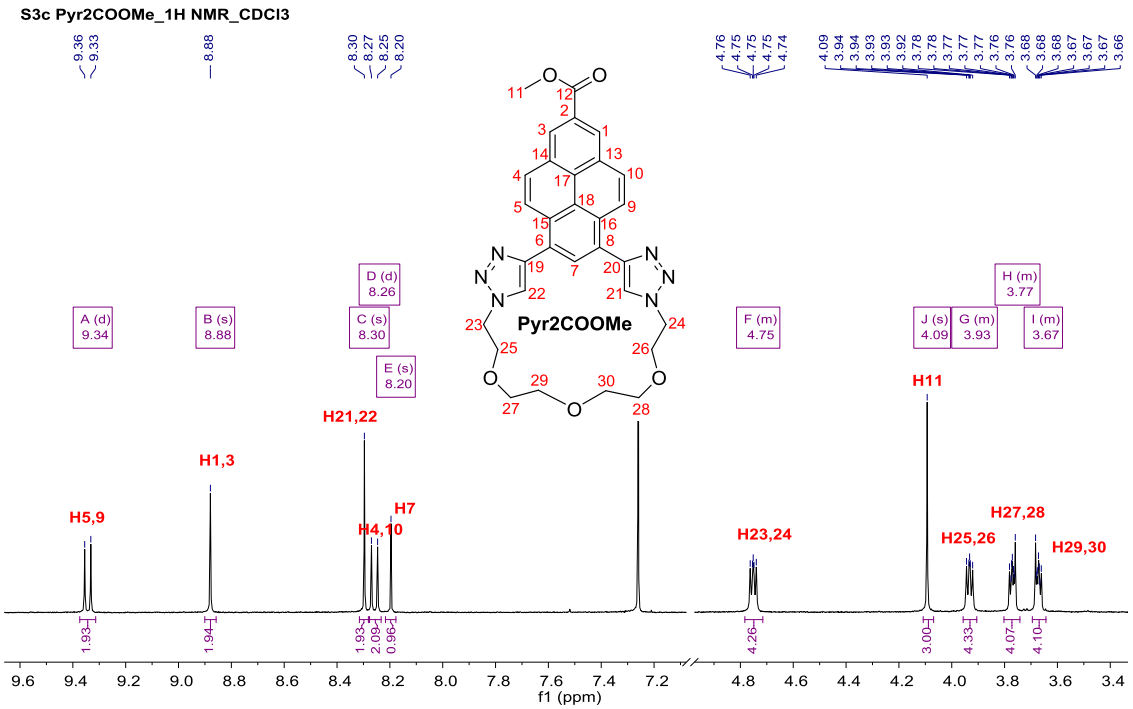

^{1}H NMR (400 MHz, Chloroform- *d*) δ 9.34 (d, *J* = 9.3 Hz, 2H, H5, H9), 8.88 (s, 2H, H1, H3), 8.30 (s, 2H, H21, H22), 8.26 (d, *J* = 9.3 Hz, 2H, H4, H10), 8.20 (s, 1H, H7), 4.78 – 4.72 (m, 4H, H23, H24), 4.09 (s, 3H, H11), 3.96 – 3.91 (m, 4H, H25, H26), 3.80 – 3.74 (m, 4H, H27, H28), 3.69 – 3.64 (m, 4H, H29, H30).

Figure 1: *^{1}H NMR spectrum (400 MHz, $CDCl_3$) of* ***Pyr2COOMe****.*

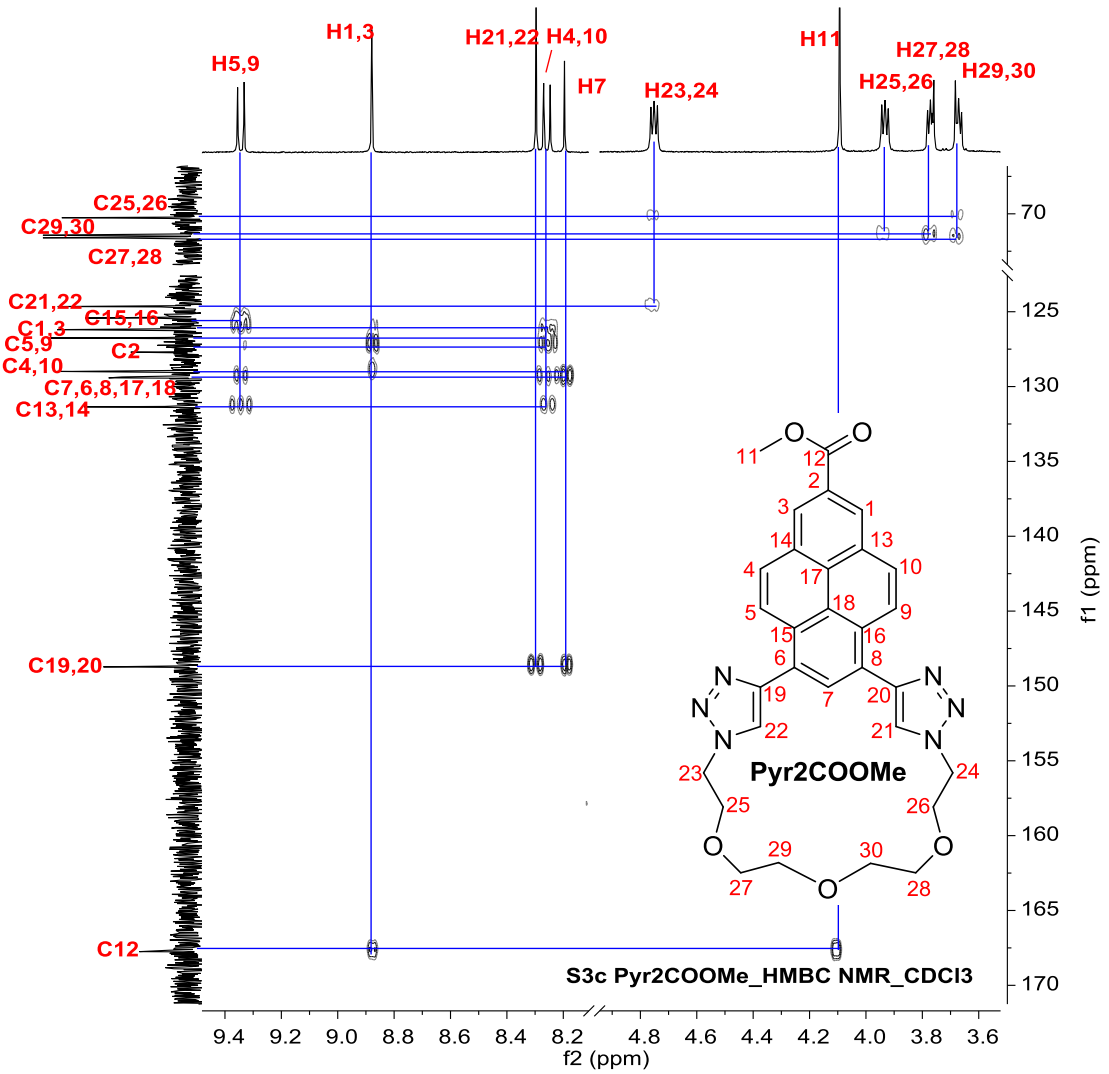

Figure 2: *HMBC NMR spectrum (400 MHz, $CDCl_3$) of* ***Pyr2COOMe****.*

From the HMBC NMR spectrum in Figure 2, a correlation between the two protons on the 1,2,3-triazoles (H21, H22) and their neighbouring triazole carbons (C19, C20) and pyrene's carbon (C7) were observed, thereby suggesting that the 'clicks' were made on the 6,8-ends of the pyrene.

In order to rule out the possibility of dimer formation, mass spectrometry was employed. The positive nanoESI of **Pyr2COOMe** (Figure 11 – SI) showed the presence of a $[M+H]^+$ species at m/z = 553.2183 (in DCM/MeOH + NH_4OAc) which matched its corresponding theoretical isotope model within a mass error of 2 ppm.

From the FT-IR spectrum of **Pyr2COOMe** (Figure 3), the absence of terminal alkynes ≡C-H stretching vibrations at 3288 and 3247 cm^{-1}, the absence of asymmetrical stretching vibration of azide at 2100 cm^{-1} and the presence of a C-

H stretching vibration of 1,2,3-triazole at 3143 cm^{-1} reaffirm the successful synthesis of **Pyr2COOMe**.

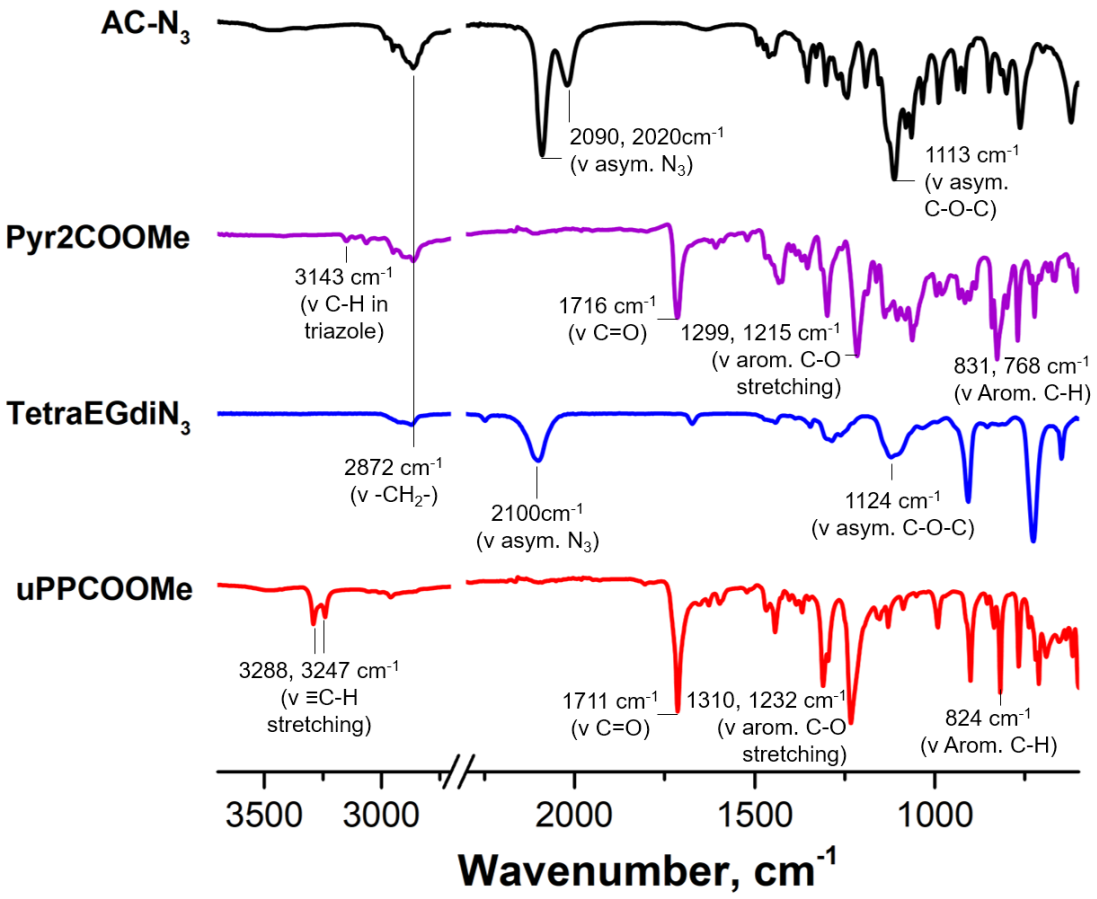

Figure 3: *FT-IR spectra of* **uPPCOOMe**, **TetraEGdiN3**, **Pyr2COOMe** *and* **AC-N3**.

The unequivocal identification of **Pyr2COOMe** was made via X-ray crystallography where the crystals grown from DCM were used. The X-ray crystal structure contains two crystallographically-independent molecules in the asymmetric unit of this structure. Parts of both of these molecules were modelled as disordered over two positions.

With the use of vapour diffusion, crystals of **uPPCOOMe** were grown in the fridge from DCM/MeCN. Its X-ray crystal structure and corresponding data are shown in Figure 12 and Table 1 (SI). A similar method was employed for the growth of the crystals of **Pyr2COOMe** as shown in Figure 13 and Table 2 (SI).

As shown in Figure 4, **uPPCOOMe** appeared to have a slightly curved core structure which contributed to the observed waviness of its side and angled views. The neighbouring pyrene moieties are arranged in head-to-head stacking

and slightly displaced, with a calculated co-facial π-π stacking distance of 3.54 Å. The pyrene moieties in **uPPCOOMe** adopted an overall herringbone packing motif[25,26] as shown in Figure 4c with a centroid-to-centroid distance of 3.807 Å.

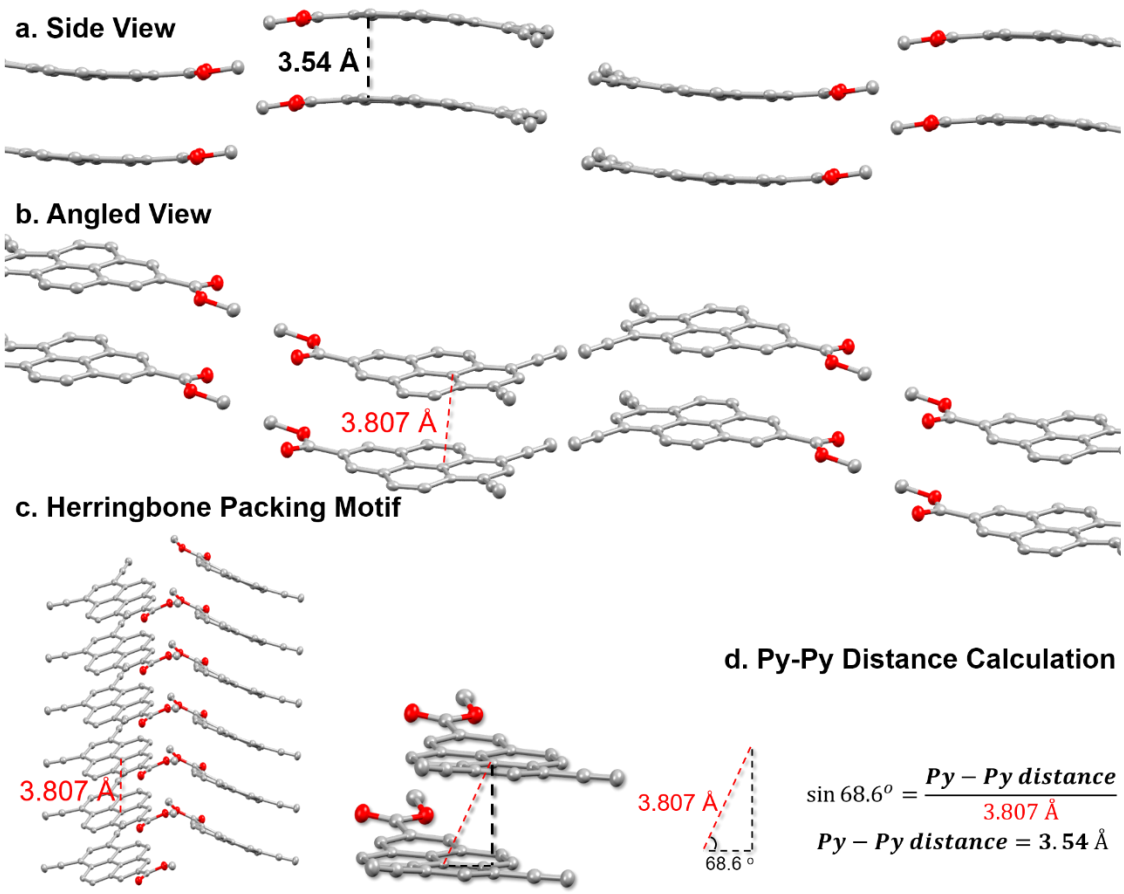

Figure 4: a) *Side view,* ***b)*** *angled view and* ***c)*** *herringbone crystal packing motif of* **uPPCOOMe** *including* ***d)*** *Py-Py distance calculation.*

In contrast, the crystal packing of **Pyr2COOMe** shown in Figure 5c suggested that the pyrene moieties adopted a brickstone packing motif[27] with alternating pitch angles from within the column. The pitch angle between Py_1 rows and Py_2 rows (53.3 °) was greater than the pitch angle between Py_2 rows and Py_1 rows (25.7 °). The two adjacent pyrene moieties between the Py_1 and Py_2 rows adopted a slipped face-to-face motif with an off-set head-to-head stacking. The ideal π-stack distance between the pyrene moieties of Py_1 and Py_2 was calculated with the use of Pythagoras' theorem from its centroid-to-centroid distance of 4.474 Å and pitch angle of 53.3 °. Interestingly, no significant π-π stacking interaction was observed between the pyrene moieties of Py_2 and Py_1 since the pyrene in Py_2 was positioned above the crown ether cavity of a

neighbouring pyrene in Py_1. The stacking of the Py_2 to Py_1 rows may be driven by non-covalent interactions between the 1,2,3-triazole rings of a pyrene from Py_1 and the adjacent pyrene core from Py_2 resulting in a calculated intermolecular distance of 3.72 Å.

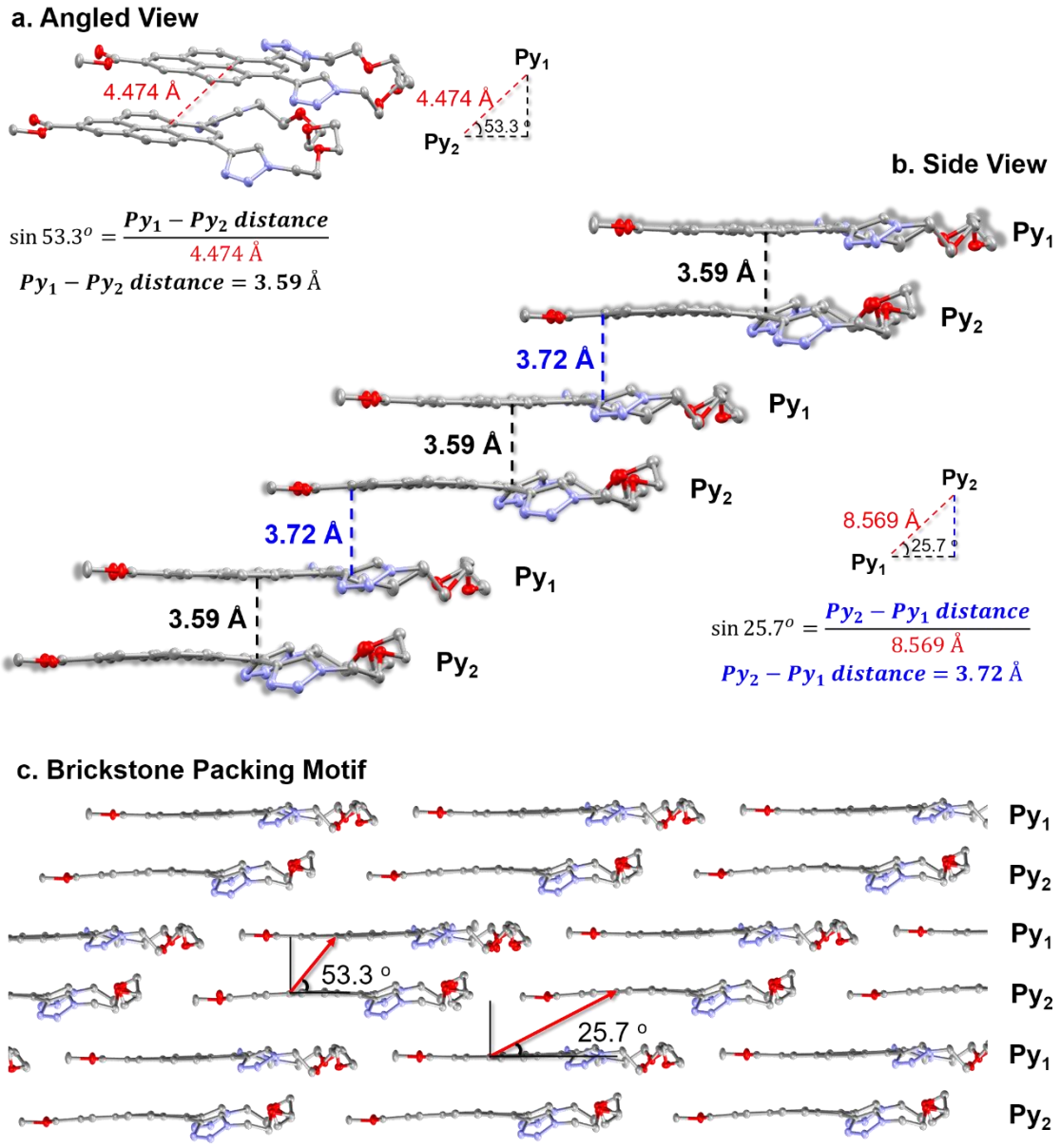

Figure 5: a) *Angled view,* ***b)*** *side view crystal packing of* **Pyr2COOMe** *including calculation of Py-Py distances and* ***c)*** *brickstone crystal packing motif of* **Pyr2COOMe** *with labelled pitch angles.*

As predicted, the incorporation of the tetraethylene glycol chains via CuAAC in the synthesis of **Pyr2COOMe** did successfully lengthen the distance of π-π stacking between the pyrene moieties by 5 – 18 Å.

3.3.1 Proposed Mechanisms for Click Reaction

Intriguingly, despite the use of a relatively short azide terminated tetraethylene glycol chain, as compared to the length between the two terminal acetylene ends in **uPPCOOMe**, the synthesis of **Pyr2COOMe** yielded primarily the main compound and not its dimer/polymer. In fact, no other distinguishable side products were isolated. Since this click macrocyclic reaction was not performed under high dilution conditions or in the presence of a templating agent, there must have been some conducive interactions in the click reaction that encouraged the formation of **Pyr2COOMe**. As a result, the following mechanism (shown in Scheme 3) was proposed based on a proposed catalytic model by Fokin *et al.* involving the presence of a dinuclear copper intermediate during the CuAAC reaction[28,29].

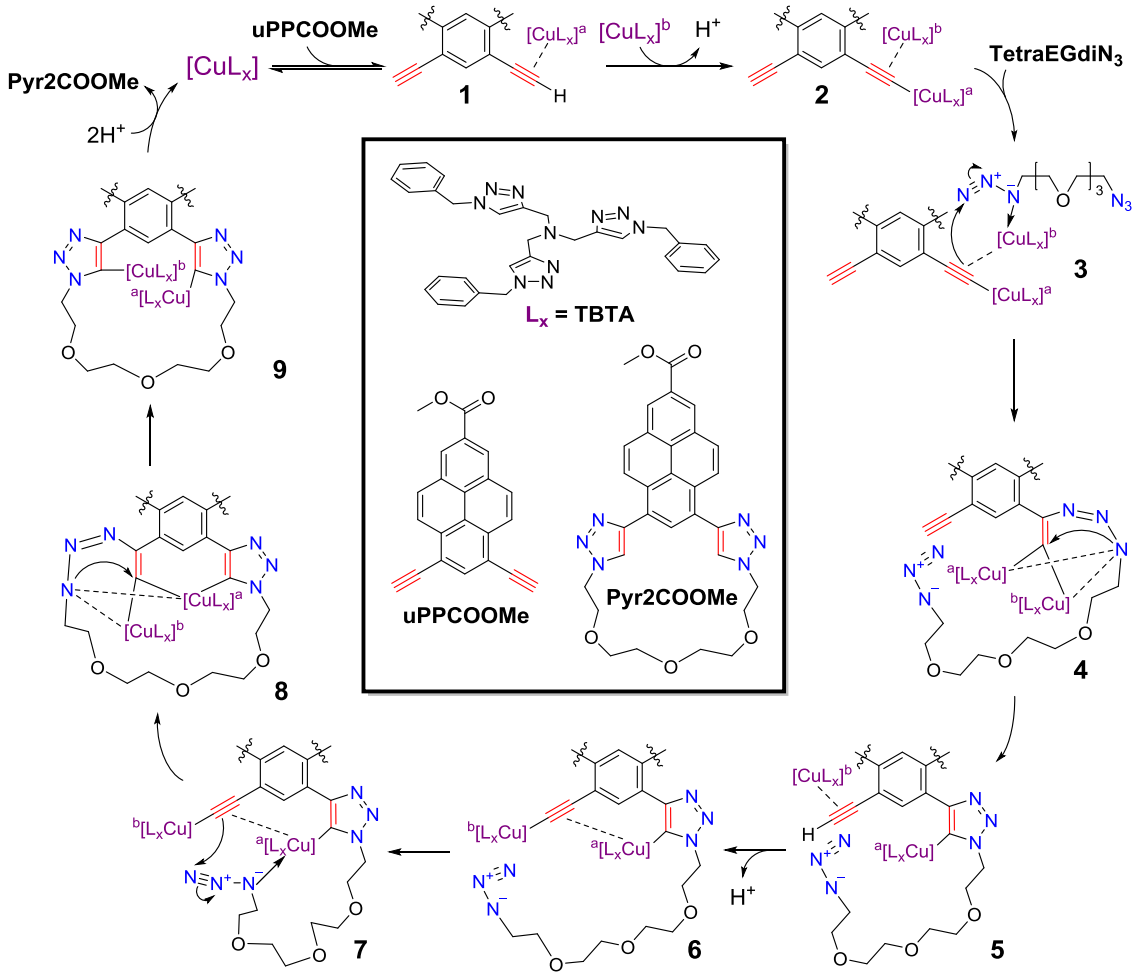

Scheme 3: *Proposed mechanism for the copper-catalysed azide-alkyne cycloaddition (CuAAC) reaction involved in the synthesis of* ***Pyr2COOMe*** *(parts of the chemical structure of pyrene has been abbreviated for clarity).*

In this scheme, TBTA was used as a ligand to accelerate/promote the CuAAC reaction rate and to protect Cu(I) ions from aerobic aqueous condition. For clarity, TBTA has been abbreviated as L_x whereas parts of the chemical structure of pyrene have been omitted in the proposed mechanism.

The mechanism begins at one of the terminal acetylene ends of **uPPCOOMe** where a copper species $[CuL_x]^a$ is pi-bounded to an alkyne group forming intermediate **1**. The same copper species $[CuL_x]^a$ is then sigma-bounded to the terminal end of the alkyne group following the removal of a proton. A second copper species $[CuL_x]^b$ then interacts with the alkyne group bearing a sigma bound $[CuL_x]^a$ forming intermediate **2**. The σ-bound copper acetylide bearing the π-bound enriched copper atom reversibly coordinates one of the azide ends of **TetraEGdiN$_3$** forming complex **3**. Next, the β-carbon of the acetylide nucleophilically attack the N-3 of the azide to form the first C-N covalent bond (intermediate **4**). This is then followed by fast ligand exchange which resulted in ring closure to form intermediate **5**. With the $[CuL_x]^a$ still attached at the 5- position of the newly formed 1,2,3-triazole ring, the free $[CuL_x]^b$ is π-bounded to the remaining terminal acetylene end of **uPPCOOMe**. Similar to what was described for the formation of intermediate **1**, the copper species $[CuL_x]^b$ is then sigma bounded to the terminal end of the alkyne group following the removal of a proton. Due to close proximity, the copper species $[CuL_x]^a$ at the 5- position of the 1,2,3-triazole ring then interacts with the alkyne group with a σ-bound $[CuL_x]^b$ to form intermediate **6**. It then intramolecularly coordinates with the free azide on the other end of the same molecule to form complex **7**. Similar to what has been mentioned for the formation of intermediate **5**, intermediate **9** containing two $[CuL_x]$ at the 5- positions and two 1,2,3-triazole rings is formed. Upon protonation, **Pyr2COOMe** is obtained, rendering both $[CuL_x]$ free to be used in another cycle of the mechanism. Therefore, the proposed mechanism justifies why the formation of **Pyr2COOMe** is favoured in the CuAAC reaction described in Section 2.4.

3.4 Synthesis of Clicked Pyrene Derivative, Pyr3COOMe

The synthesis of clicked pyrene derivative, **Pyr3COOMe** as seen in Scheme 2 was attempted using two different reaction conditions shown in Table 2. Unlike the synthesis of **Pyr2COOMe**, the use of Cu(0) as the copper source, $CuSO_4$ as

the oxidising agent and TBTA as the ligand did not successfully yield **Pyr3COOMe**. The closest to success in this case was the second attempt which yielded 26mg of an impure fraction containing aromatic and aliphatic peaks which may be indicative of **Pyr3COOMe**. Unfortunately, due to minute amounts containing mostly impurities, no further purification was attempted to isolate the potential product.

One could speculate that the length of the CH_2 arms holding the azocrown and the azides were too short to favour 'click' on both terminal acetylene ends on the pyrene. It could also be that the reaction condition was not the most ideal for this combination of reactants. Further reactions needed to be carried out before any conclusions can be made regarding the probability of synthesising such species.

Cu source (equiv)	**Oxi. agent (equiv)**	**Solvent (ratio)**	**Ligand (equiv)**	**T, ^oC (duration)**	**High Dilution Method[1]**	**Reaction**
Cu(0) (1.0)	$CuSO_4$ (0.1)	THF/H_2O (1:1) N_2	TBTA (0.1)	40 (10 days)	Yes	x
Cu(0) (1.0)	$CuSO_4$ (0.1)	THF/H_2O (1:1) N_2	TBTA (0.1)	40 (28 hours)	No	Maybe[2]

[1]High dilution method involves the addition of dilute solutions of **uPPCOOMe** and **AC-N_3** via syringe pumps over 10 days into a flask containing Cu source, oxidising agent and ligand; [2]One fraction from the purification process showed potential to be the desired compound, however, as there was only 26 mg of that impure fraction, further purification was not proceeded.

Table 2: *Reaction conditions attempted for the synthesis of* ***Pyr3COOMe****.*

3.5 The Design Idea of Clicked Pyrene Derivatives

The synthesis of clicked pyrene derivatives **Pyr2COOMe** and **Pyr3COOMe** were attempted in order to create more interesting pyrene species with added functionalities to be chemically modified onto **PECH** at a later stage.

As previously mentioned in Chapter 2, the incorporation of a pyrene derivative onto a flexible polyether backbone (**PECH**) would not only be a compelling addition in terms of its added fluorescent properties, the π-π interactions between neighbouring pyrene moieties could be the driving force of self-assembly in this new series of polymer. However, the two series of pyrene-**PECH** polymers attempted (**AP** and **YC Series**) had solubility issues due to "pseudo-crosslinks" driven by the close proximity of pyrene moieties. It was envisaged that by performing CuAAC reactions on the terminal acetylene ends of **uPPCOOMe** (at the 6,8- positions), the distance between two pyrene moieties could be

lengthened depending on the size of protruded areas of the groups attached (perpendicular to pyrene plane) as visualised in Figure 6. The extended length between pyrene moieties will then prevent the formation of “pseudo-crosslinks” which could hamper the solubility of the polymer.

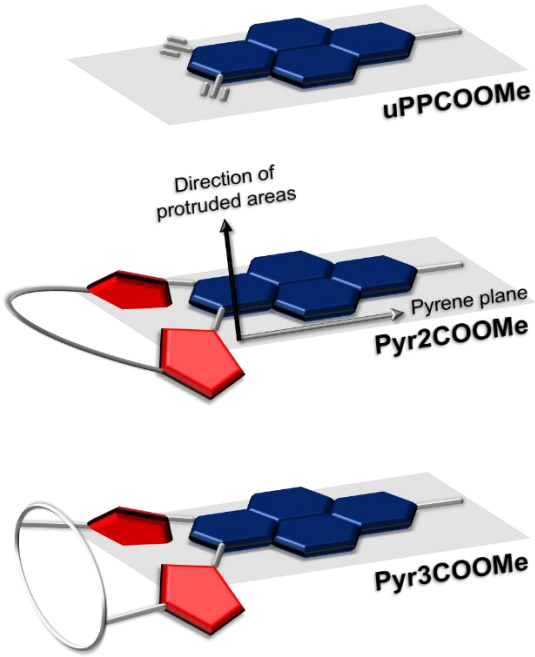

Figure 6: *Cartoon representation of* **uPPCOOMe***,* **Pyr2COOMe** *and* **Pyr3COOMe** *(with emphasis on protruded areas perpendicular to its plane).*

In the synthesis of **Pyr2COOMe**, an azide terminated tetraethylene glycol chain was introduced to the terminal acetylene ends of **uPPCOOMe** at the 6,8-positions to make a pyrene clicked macrocycle with a cavity between the size of a 15-crown-5 and a 18-crown-6. Together with the O atoms from the tetraethylene glycol chain, the resulting 1,2,3-triazole units might even be able to participate/enhance/stabilise the interaction of its cavity with alkaline metal cations, just like the ones mentioned in the literature[8,30]. Hypothetically speaking, if **PECH** was chemically modified with **Pyr2COOMe**, the new series of polymers (**CP polymers**) would be trifunctional, whereby it could: (1) self-assemble into a polyether tunnel (**T1**) via the π-π stacking of the pyrene core, (2) be fluorescent in nature and (3) carry a second polyether tunnel (**T2**) by the alignment of its “clicked” crown ether chain as shown in Figure 7b. This could bring about new possibilities of having polymers that have both protons and cations transportable tunnels.

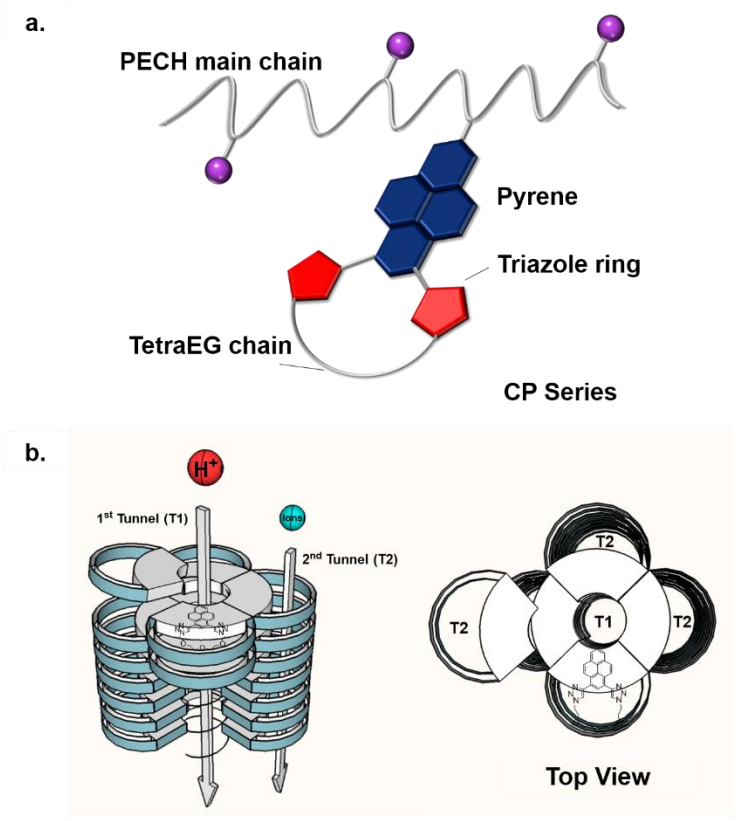

Cartoon representation of hypothetical stacking of CP Polymers

Figure 7: *Cartoon representation of* ***a)*** **CP Series** *and* ***b)*** *the hypothetical stacking of* **CP Polymers**.

An azide terminated diazo-18-crown-6 derivative was used in the synthesis of **Pyr3COOMe** in place of an azide terminated tetraethylene glycol chain. This pyrene derivative was designed with the aspiration of obtaining a slanted crown cavity that could possibly bring about interesting morphology/interior architectural change of the resulting polymer. The structure of **Pyr3COOMe** after MM+ energy-minimisation (Figure 8c) appeared to be slanted at an angle. Thus, if **PECH** was chemically modified with **Pyr3COOMe**, the resulting polymer may contain polyether tunnels nonparallel to one another. The tunnel that is formed via π-π stacking of pyrene moieties would remained parallel to the surface of the polymer, whilst the second tunnel formed via alignment of its "clicked" azocrown ether may be tilted at an angle (with assumptions that the pyrene moieties followed the MM+ energy-minimised structure).

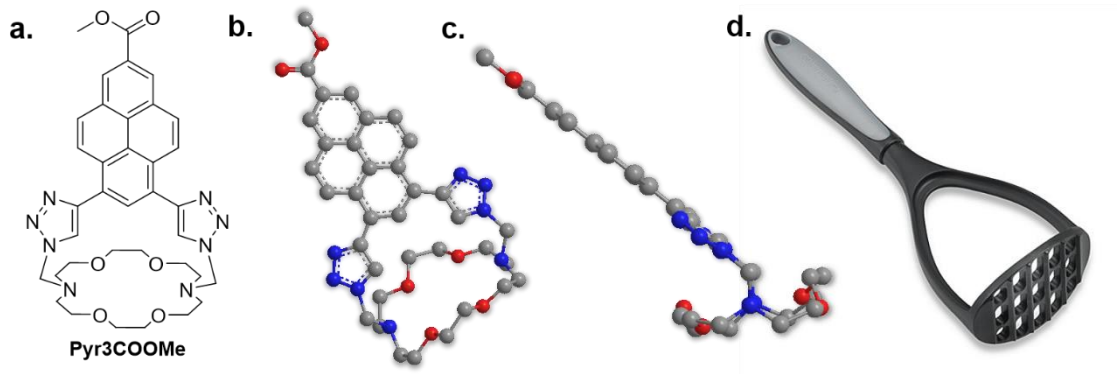

Figure 8: *Chemical structure of* ***a)*** **Pyr3COOMe**, ***b)*** *front view,* ***c)*** *side view of MM+ energy-minimised structure of* **Pyr3COOMe** *and* ***d)*** *potato masher as an analogue of* **Pyr3COOMe**.

Pyr3COOMe can be easily visualised as a potato masher (Figure 8d) whereby pyrene is the handle of the masher, the two side arms that hold the base of the masher are the 1,2,3-triazole rings and methylene spacers while the base of the masher is the azocrown ether. Regrettably, all of the attempts to synthesise **Pyr3COOMe** (as discussed in Section 3.4) were unsuccessful. No further attempts could be made due to time limitations.

3.6 Coordination Experiments of Pyr2COOMe

Since **Pyr2COOMe** has a cavity resembling to that of a crown ether, it would be interesting to see what cations would fit/interact with its cavity. Thus, a series preliminary studies involving the use of ^{1}H NMR, UV-Vis and fluorescence spectroscopy and a series of cations were carried out, to ascertain the best spectroscopic technique for the determination of cation binding constants for **Pyr2COOMe**. Note that acetonitrile was used based on the mutual solubility of **Pyr2COOMe** and the hexafluorophosphate salts.

For the ^{1}H NMR experiment, a stock solution of **Pyr2COOMe** in acetonitrile was prepared by dissolving 10 mg of **Pyr2COOMe** in 2.5 mL of CD_3CN. The solution was then divided into 5 NMR tubes and the initial ^{1}H NMR spectra were recorded. In each NMR tube, one hexafluorophosphate salt (~1 mg) was added. TFA was pre-diluted in CD_3CN (10 µL in 0.5 mL CD_3CN) before 5 µL of it was added into the last NMR tube. Final ^{1}H NMR spectra of the 5 samples were recorded and compared as shown in Figure 9.

A similar stock solution of **Pyr2COOMe** as mentioned above was prepared for the UV-Vis and fluorescence measurements, however, the acetonitrile used was of spectroscopic grade and non-deuterated. The initial absorption, emission and excitation spectra were recorded before tiny amounts of $LiPF_6$ and $NaPF_6$ were added to the cuvette. The final absorption, emission and excitation spectra were also recorded after the addition of the hexafluorophosphate salt.

From the stacked ^1H NMR spectra shown in Figure 9, several peaks were seen shifted upon addition of $LiPF_6$ and $NaPF_6$ whilst no/negligible changes were observed in samples containing KPF_6, NH_4PF_6 and TFA. This suggested that only the Li^+ and Na^+ cations were interacting with **Pyr2COOMe**. In the case of Li^+, the presence of cation seemed to reduce the solubility of **Pyr2COOMe** in CD_3CN leading to very weak ^1H NMR signals as shown in red. Apart from the decreased intensity in proton signals, H11, H23,24 and H25,26, peaks appeared deshielded whilst H27,28 and H29,30 coalesced into a single peak. The insoluble nature of **Pyr2COOMe**-Li^+ complex formed in CD_3CN eventually caused it to precipitate out of solution.

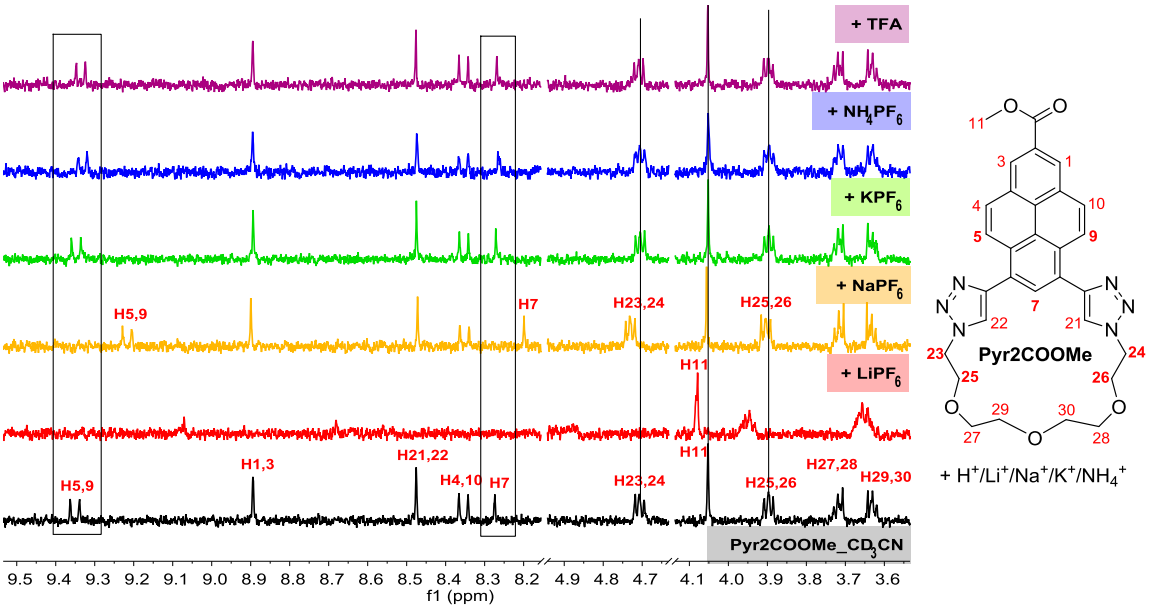

Figure 9: *Stacked ^1H NMR spectra of* **Pyr2COOMe** *in CD_3CN before and after the addition of $LiPF_6$, $NaPF_6$, KPF_6, NH_4PF_6 and TFA. The chemical structure of* **Pyr2COOMe** *shown on the right is labelled the same way as its 2D NMR in $CDCl_3$ (Figure 10 - SI), however, only protons are shown and those showing chemical shifts/interactions are emphasised in* ***bold****.*

In the case of Na^+, peaks attributed to the CH_2 protons in the crown-ether-like chain (H23,24 and H25,26) were shifted downfield, whereas those corresponding to the C-H aromatic protons of pyrene (H7 and H5,9) were shifted upfield. Whilst no other CH_2 protons in the chain experienced noticeable chemical shifts, the downfield shifts of H23,24 (+0.03 ppm) and H25,26 (+0.01 ppm) were an indication of Na^+ ion interaction[31,32]. The Na^+ ion in this case did not appear to be interacting with all O atoms from within the crown-ether-like cavity due to the absence of chemical shifts from the other two CH_2 protons (H27,28 and H29,30). Instead, it appeared to hover closer towards the pyrene-end of the cavity which can then explain the agostic interactions[33,34] observed between C-H7-Na^+ and C-H5,9-Na^+ reflected by upfield shifts of H7 (-0.07 ppm) and H5,9 (-0.13 ppm), respectively.

Finally, in the case of K^+, NH_4^+ and H^+, no significant change in chemical shift was observed in all of the ^{1}H NMR spectra, thereby suggesting that the cavity of **Pyr2COOMe** may be too large for any cation interaction to take place. Hence, the subsequent UV-Vis and fluorescence measurements were only carried out in the presence of Li^+ and Na^+ ions.

The normalised absorption, emission and excitation spectra of **Pyr2COOMe** in spectroscopic grade CH_3CN are shown in Figure 10. Unlike the absorption spectra of typical pyrene derivatives, the vibronic band structures attributed to the π-π* transitions of **Pyr2COOMe** were much less pronounced/broadened and resembled more of a substituted pyrene[35–37] due to the interaction between pyrene and the diethylene glycol chain (cyclised via CuAAC at 6,8- positions).

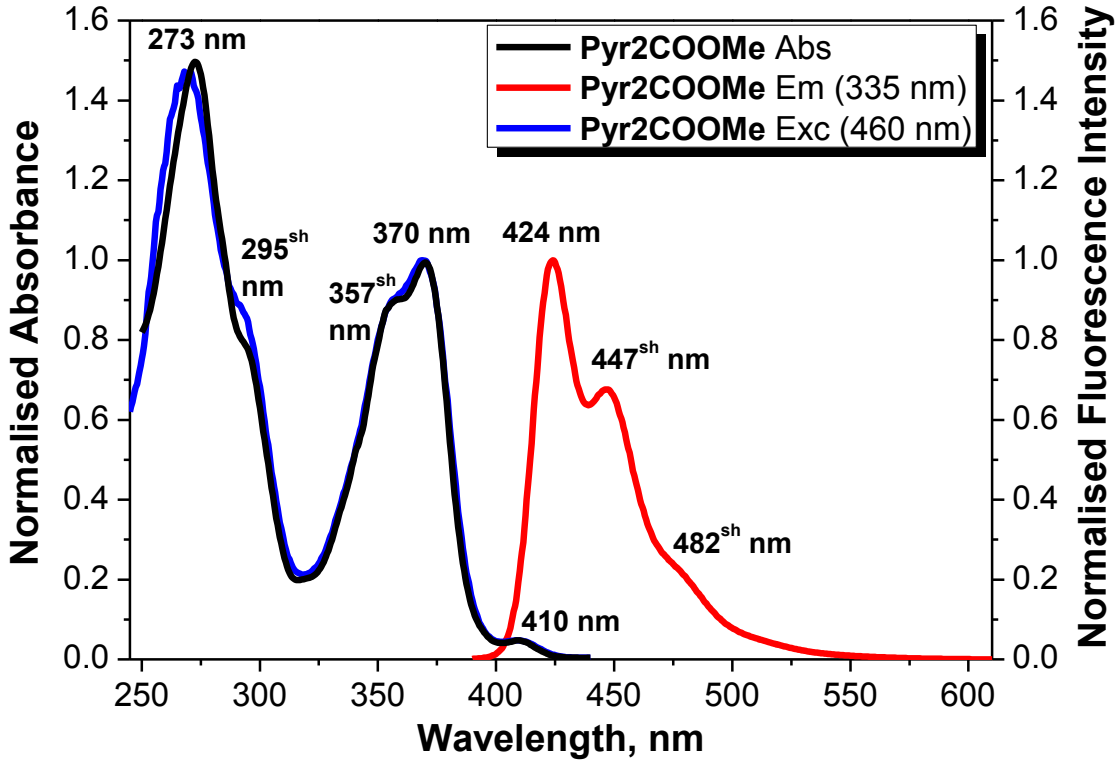

Figure 10: *Normalised absorption, emission and excitation spectra of* **Pyr2COOMe** *in acetonitrile.*

Due to insignificant changes in the absorption and emission spectra of **Pyr2COOMe** upon addition of cations, the final spectra are omitted from Figure 10 and the spectral observations are described below.

The addition of $LiPF_6$ into **Pyr2COOMe** in CH_3CN did not induce a change in its absorption spectrum, however, a decrease in the intensity of its emission spectrum was observed. This can be attributed to the precipitation of the insoluble **Pyr2COOMe**-Li^+ complex. Since fluorescence spectroscopy was much more sensitive than UV-Vis spectroscopy, the tiny changes in **Pyr2COOMe** concentration upon addition of Li^+ were only observable in its emission spectra.

Likewise, the addition of $NaPF_6$ did not yield any obvious changes in the absorption spectrum of **Pyr2COOMe** in CH_3CN. Despite its apparent ^1H NMR chemical shifts mentioned earlier on, the presence of Na^+ did not reciprocate a change in its emission spectra. Therefore, the best method of determining the binding constant of **Pyr2COOMe** is ^1H NMR titrations with $NaPF_6$ in CD_3CN. Due to a time limitation, the NMR titration experiment was not carried out.

4. Conclusions

In this chapter, two types of azides (**TetraEGdiN$_3$** and **AC-N$_3$**) were synthesised and characterised as starting materials for the CuAAC reaction with a pyrene derivative from Chapter 2, **uPPCOOMe**. The reaction conditions used for the synthesis of clicked pyrene derivatives (**Pyr2COOMe** and **Pyr3COOMe**) were discussed with emphasis on the successful reaction condition for the synthesis of **Pyr2COOMe** and why the same reaction condition did not work for the synthesis of **Pyr3COOMe**. A proposed scheme was used to explain why CuAAC of **Pyr2COOMe** favoured cyclisation over dimerization/polymerisation. Apart from adding functionalities to **uPPCOOMe**, the clicked pyrene derivatives were initially synthesised with hope to tackle solubility issues of pyrene-**PECH** polymers previously mentioned in Chapter 2. The incorporation of tetraethylene glycol chains to **uPPCOOMe** to form **Pyr2COOMe** did lengthen the π-π stacking distance by 5-18 Å. This meant that it could potentially alleviate the issue of "pseudo-crosslinks" if it was chemically modified onto **PECH**. Preliminary cation coordination experiments were carried out on **Pyr2COOMe** via the use of ^{1}H NMR, UV-Vis and fluorescence spectroscopy. Changes in ^{1}H NMR chemical shifts of **Pyr2COOMe** were observed in the presence of $NaPF_6$, suggested the possibility of binding. Therefore for future work, thorough titration experiments with $NaPF_6$ should be carried out on **Pyr2COOMe** in CD_3CN for the determination of the binding constant. The synthesis of **Pyr3COOMe** should also be reattempted using cation-coordinated **AC-N$_3$** instead of uncoordinated ones.

Appendix. Supplementary Information, SI

Supplementary information, SI related to this chapter can be found at the end of this thesis.

References

1 M. Tireli, S. Maračić, S. Lukin, M. J. Kulcsár, D. Žilić, M. Cetina, I. Halasz, S. Raić-Malić and K. Užarević, *Beilstein J. Org. Chem.*, 2017, **13**, 2352–2363.

2 L. Zhu, C. J. Brassard, X. Zhang, P. M. Guha and R. J. Clark, *Chem. Rec.*, 2016, **16**, 1501–1517.

3 J. E. Hein and V. V. Fokin, *Chem. Soc. Rev.*, 2010, **39**, 1302–1315.

4 L. Jin, D. R. Tolentino, M. Melaimi and G. Bertrand, *Sci. Adv.*, 2015, **1**, e1500304–e1500304.

5 L. Liang and D. Astruc, *Coord. Chem. Rev.*, 2011, **255**, 2933–2945.

6 V. Haridas, K. Lal, Y. K. Sharma and S. Upreti, *Org. Lett.*, 2008, **10**, 1645–1647.

7 S. Binauld, C. J. Hawker, E. Fleury and E. Drockenmuller, *Angew. Chemie - Int. Ed.*, 2009, **48**, 6654–6658.

8 A. A. Salman, M. Tabandeh, T. Heidelberg and R. S. Duali Hussen, *Carbohydr. Res.*, 2015, **406**, 41–45.

9 S. H. Kim, H. S. Choi, J. Kim, S. J. Lee, D. T. Quango and J. S. Kim, *Org. Lett.*, 2010, **12**, 560–563.

10 M. Tyagi, N. Taxak, P. V. Bharatam and K. P. R. Kartha, *RSC Adv.*, 2012, **2**, 11366–11371.

11 X. Jiang, X. Yang, C. Zhao and L. Sun, *J. Phys. Org. Chem.*, 2009, **22**, 1–8.

12 C. Wang, D. Abegg, D. G. Hoch and A. Adibekian, *Angew. Chemie Int. Ed.*, 2016, **55**, 2911–2915.

13 A. Y. Ji, Q. M. Jin, D. J. Zhang, H. Zhu, C. Su, X. H. Duan, L. Bian, Z. P. Sun, Y. C. Ni, J. Zhang, Z. Yang and Z. Q. Yin, *ACS Med. Chem. Lett.*, 2017, **8**, 191–195.

14 D. F. Caffrey and T. Gunnlaugsson, *Dalt. Trans.*, 2014, **43**, 17964–17970.

15 M.-L. Teyssot, M. Fayolle, C. Philouze and C. Dupuy, *European J. Org. Chem.*, **2003**, 54–62.

16 R. Crossley, Z. Goolamali, J. J. Gosper and P. G. Sammes, *J. Chem. Soc. Perkin Trans. 2*, 1994, **0**, 513.

17 F. Li, J. Xie and F. Feng, *New J. Chem.*, 2015, **39**, 5654–5660.

18 P. A. Mosier-Boss, *Spectrochim. Acta Part A Mol. Biomol. Spectrosc.*, 2005, **61**, 527–534.

19 R. G. Kostyanovsky, K. A. Lyssenko, O. G. Nabiev, G. K. Kadorkina and I. I. Chervin, *Russ. Chem. Bull.*, 2014, **63**, 772–774.

20 F. Schmidt, I. C. Rosnizeck, M. Spoerner, H. R. Kalbitzer and B. König, *Inorganica Chim. Acta*, 2011, **365**, 38–48.

21 F. Tran, A. Odell, G. Ward and N. Westwood, *Molecules*, 2013, **18**, 11639–11657.

22 Y.-N. Zhao, Z.-Z. Yang, S.-H. Luo and L.-N. He, *Catal. Today*, 2013, **200**, 2–8.

23 C. P. C. Prabhakaran, J. D. White and A. Publication, *Org. Synth.*, 1990, **68**, 227.

24 W. J. Gee and S. R. Batten, *Eur. J. Inorg. Chem.*, 2013, **2013**, 3240–3248.

25 X. Feng, N. Seto, C. Z. Wang, T. Matsumoto, J. Tanaka, X. F. Wei, M. R. J. Elsegood, L. Horsburgh, C. Redshaw and T. Yamato, *ChemistrySelect*, 2016, **1**, 1926–1932.

26 Z. F. Yao, J. Y. Wang and J. Pei, *Cryst. Growth Des.*, 2018, **18**, 7–15.

27 J. Gierschner and S. Y. Park, *J. Mater. Chem. C*, 2013, **1**, 5818–5832.

28 B. T. Worrell, J. A. Malik and V. V Fokin, *Science.*, 2013, **340**, 457–460.

29 M. Yang, J. Li and P. R. Chen, *Chem. Soc. Rev.*, 2014, **43**, 6511–6526.

30 Y. H. Lau, P. J. Rutledge, M. Watkinson and M. H. Todd, *Chem. Soc. Rev.*, 2011, **40**, 2848–2866.

31 Z. Chen, P. J. Moehs and R. A. Sachleben, *J. Chem. Soc. Perkin Trans. 2*, 1996, **0**, 2549.

32 K. Torizuka and T. Sato, *Org. Magn. Reson.*, 1979, **12**, 190–195.

33 Y. Zhang, J. C. Lewis, R. G. Bergman, J. A. Ellman and E. Oldfield, *Organometallics*, 2006, **25**, 3515–3519.

34 M. Brookhart, M. L. H. Green and G. Parkin, *Proc. Natl. Acad. Sci. U. S. A.*, 2007, **104**, 6908–14.

35 A. D'Aléo, E. Cecchetto, L. de Cola and R. M. Williams, *Sensors*, 2009, **9**, 3604–3626.

36 A. Wiessner, G. Hüttmann, W. Kühnle and H. Staerk, *J. Phys. Chem.*, 1995, **99**, 14923–14930.

37 T. Soujanya, A. Philippen, S. Leroy, M. Vallier and F. Fages, *J. Phys. Chem. A*, 2000, **104**, 9408–9414.

Chapter 4

"Vampire POGs" – Light Driven Irreversible Organogelation of Anthracene-containing Polyethers

1. Introduction

Polyepichlorohydrin (**PECH**) has been an interesting class of polyethers since the early 80s. It was widely used due to its commercial availability, side-chain chlorine sites abundancy and elasticity in the preparation of thermosets[1], photosensitive polymers[2] and side-chain liquid-crystal polymers (SCLCP)[3] via chemical modifications in the presence of various phase transfer catalysts[1]. In this alternative energy era where the search is ongoing for new and improved proton conducting materials, chemically modified **PECH** and its co-polymer, **P(ECH-co-EO)** are beginning to find their way into being some of the promising alternatives to Nafion[4]. The prepared **PECH** and **P(ECH-co-EO)**-based membranes were reported to have conductivities comparable to that of Nafion, and importantly do not need to be moistened to conduct protons[4].

Anthracene on the other hand, has been well known for its photophysical properties for centuries. When introduced into different chemical systems, anthracene give rise to a new range of materials with very fascinating properties and applications[5–8]. This triggered the idea of incorporating fluorescent, planar anthracene moieties in the form of potassium 9-anthracenecarboxylate, **9-ACAK**, in increasing ratios onto **PECH** to see if any of the resulting **PA polymers** would exhibit liquid crystallinity that could drive the self-assembly of its polyether backbone into columnar structures. This would not only create polymers with "proton-transportable tunnels", but would also give fluorescent monitoring properties as an added bonus. To test the idea out, a series of **PA polymers** were prepared.

During the synthesis and purification of **PA polymers**, irreversible formation of gel-like substances were observed which prompted the study of **9-ACAK**, **PA polymers** and their relationship with light. Uncanny resemblance of **PA polymers'** response to light (irreversible sol to gel transformation) and a vampire's response to light (irreversible life to death transformation) has led to

the term “Vampire POGs” being coined. POGs (Polymeric organogelators) are high molecular weight gelators with good ability to gelate[9].

It is important to highlight that the idea of incorporating anthracene into a polymer is not new, in fact, a variety of anthracene derivatives have been included into main-chain polymers[10], side-chain polystyrene[11,12] as well as being attached to the ends of a polystyrene chain[13]. The novelty comes from the fact that all of the published examples of organogelators that involve photodimerisation of anthracene (such as **PECH**-based supramolecular organogelators[14], anthracene-containing binary gelators[15] and anthracene-containing low-molecular-weight-gelators[16], to name a few) required the use of heating and cooling for gels to form which was not the case for “Vampire POGs” as it gelates irreversibly upon light irradiation at room temperature.

Although “Vampire POGs” are somewhat interesting, a new series of polymers needed to be made to give us a better view of the effects of anthracene in **PECH**. Therefore, a tapered liquid crystal (LC) mesogen, **TAP** (potassium 3,4,5-tris[4-(n-dodecan-1-yloxy)benzyloxy]benzoate) was introduced into the main chain of **PA4** and **PA6** to produce an enhanced series of **URV polymers**. This series of polymer is envisaged to have improved LC properties than its **PA** counterparts and would not form gels upon irradiation. The **URV polymers** were then fabricated into membranes and their surface morphologies were studied with AFM, XRD and contact angle analysis.

In this chapter, the synthesis, characterisations of **PA** and **URV polymers** will be discussed in addition to the analyses conducted for the demystification of the “Vampire POGs” phenomenon.

2. Experimental

2.1 Materials

Reagents and solvents were bought from Fisher Scientific at the highest purity possible and were used without further purification unless otherwise specified. Anthracene-9-carboxylic acid, **9-ACA** (98+ %) was supplied by Alfa Aesar while polyepichlorohydrin, **PECH** (average M_w ~700,000 by GPC) was supplied by Sigma Aldrich. Potassium 3,4,5-tris[4-(n-dodecan-1-yloxy)benzyloxy]benzoate,

TAP was synthesised by our collaborators in Spain using previously reported procedures[17]. THF stabilized with BHT (ACROS Organics) was dried over activated 4 Å molecular sieves under nitrogen atmosphere for several days before use.

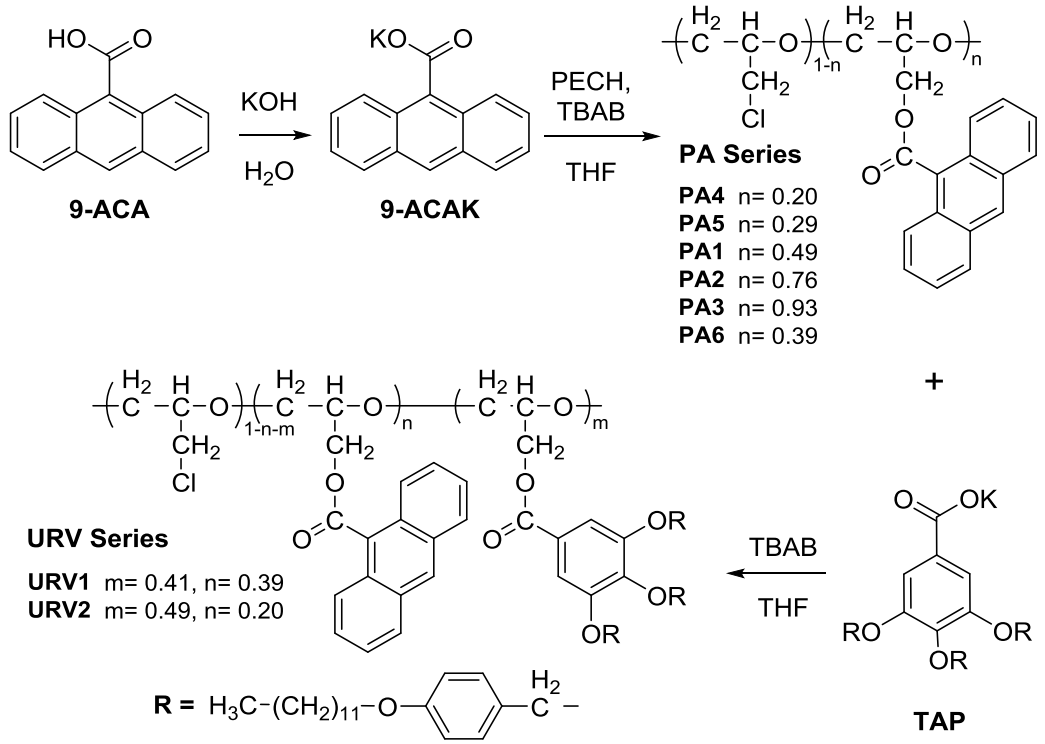

Scheme 1: *Preparation of* **PA** *and* **URV Series***.*

2.2 Synthesis of Potassium 9-anthracene carboxylate, 9-ACAK

H_2O (156 mL) was added to a flask containing **9-ACA** (7.0 g, 31.5 mmol) and KOH (1.9 g, 33.9 mmol). The reaction mixture was left to stir at RT overnight (in the dark) with TLC monitoring. Upon completion, the solvent was rotary evaporated to dryness. The residue was suspended in $CHCl_3$ (30 mL) and the suspension was sonicated for 30 minutes. The solid was isolated via suction filtration and was dried under high vacuum to yield a light yellow powder (8.15 g, 31.3 mmol, 99 %).

^{1}H NMR (400 MHz, DMSO-d_6) δ 8.28 (s, 1H, H10), 8.25 – 8.20 (m, 2H, H1, H8), 7.97 (ddd, J = 8.2, 1.5, 0.7 Hz, 2H, H4, H5), 7.45 – 7.34 (m, 4H, H3, H6, H2, H7).

^{13}C NMR (101 MHz, DMSO-d_6) δ 171.55 (C15), 143.53 (C9), 131.25 (C13,C14), 128.19 (C1,C8), 127.68 (C4,C5), 125.82 (C11,C12), 124.90 (C3,C6), 123.84 (C2,C7), 122.34 (C10).

The ^{1}H NMR spectrum of the purified product was consistent with the literature data[18].

FT-IR (ν_{max}, cm^{-1}) 1546, 1318 (asymmetric COO^- stretching vibration), 1427, 1389 (symmetric COO- stretching vibration), 737 (aromatic C-H out of plane bend)

(-)nanoESI-FTMS (m/z): found $[M-K]^-$ 221.0611, calcd. for $C_{15}H_9O_2$: 221.0608.

2.3 Polymers

2.3.1 Modification of PECH *with* 9-ACAK*,* PA Series

A solution of **PECH** pre-dissolved in dry THF at RT overnight was heated to 60 ^{o}C. To it was added TBAB followed by **9-ACAK**. The reaction mixture was left to stir at 65 ^{o}C for 4 days covered in aluminium foil. The resulting mixture was left to cool to RT and was precipitated out with H_2O. The precipitated polymer was filtered and dried before being re-dissolved in THF. The polymer solution was re-precipitated by addition of the THF solution to water. The purification process was repeated twice or trice (depending on its purity). The resulting polymer was dried under high vacuum with heating over 3 days to yield **PA polymers**. The reaction conditions are specified in Table 1 (Section 3.2).

2.3.2 Modification of PA Polymers *with* TAP*,* URV Series

A solution of **PA polymer** pre-dissolved in dry THF at RT overnight was heated to 60 ^{o}C. To it was added TBAB followed by **TAP**. The reaction mixture was left to stir at 65 ^{o}C for 8 days covered in foil. The resulting mixture was left to cool to RT and was precipitated out of hot H_2O (70 ^{o}C, 800 mL). The precipitated polymer was filtered and dried in a heated (45 ^{o}C) desiccator overnight before being re-dissolved in THF (5-15 mL, with slight heating). The polymer solution was re-precipitated in boiling EtOH (96 %, 800 mL). The purification process was repeated twice or trice (depending on its purity). The resulting polymer was dried under high vacuum with heating over 3 days to yield **URV polymers**. The reaction conditions are specified in Table 7 (Section 3.3).

TAP

^{1}H NMR (700 MHz, Chloroform-*d*) δ 7.23 (s, 2H, H2), 7.01 – 6.93 (m, 4H, H7), 6.90 (s, 2H, H7'), 6.56 – 6.48 (m, 4H, H8), 6.47 (s, 2H,H8'), 4.60 (s, 4H, H5), 4.51 (s, 2H, H5'), 3.79 – 3.52 (m, 12H, H10', H11', H10, H11), 1.69 (p, *J* = 6.9 Hz, 2H, H12'), 1.58 (t, *J* = 7.4 Hz, 4H, H12), 1.39 (p, *J* = 7.2 Hz, 2H, H13'), 1.35 – 1.11 (m, 46H, H13-H20, H14'-H20'), 0.88 (t, *J* = 7.0 Hz, 9H, H21, H21').

^{13}C NMR (176 MHz, Chloroform-*d*) δ 173.19 (C22), 158.65, 158.61 (C9,C9'), 152.05 (C3), 139.93 (C4), 132.78 (C1), 130.09 (C7'), 129.54 (C7), 129.07 (C6), 114.00, 113.87 (C8,C8'), 108.10 (C2), 74.75 (C5'), 70.48 (C5), 67.95 (C10'), 67.90 (C10), 32.13 (C19,C19'), 32.10, 30.02, 29.98, 29.93, 29.92, 29.87, 29.82, 29.68, 29.66, 29.60, 29.55 (C11-C18,C11'-C18'), 26.35 (C13,C13'), 22.87 (C20,C20'), 14.27 (C21,C21').

FT-IR (ν_{max}, cm^{-1}) 2916 (-CH_2-, -CH_3), 2848 (-OCH_2-, symmetric CH_2 stretching vibration), 1557 (asymmetric COO^- stretching vibration), 1515 (aromatic C=C stretching), 1365 (symmetric COO^- stretching vibration), 1247 (aromatic ether C-O stretching band), 1173, 1123 (aromatic in-plane C-H bending), 815, 793, 718 (aromatic C-H out of plane bend)

(-)nanoESI-FTMS (m/z): found $[M-K]^-$ 991.7003, calcd. for $C_{64}H_{95}O_8$: 991.7032.

2.4 Membrane Preparation

2.4.1 FEP Support

A fluorinated ethylene propylene (FEP) sheet support from Saint-Gobain Performance Plastic, with a thickness of 5 mil (127 µm) was used. The support was cleaned with acetone and was left to dry before use.

2.4.2 Immersion Precipitation

All membranes of the **URV Series** were prepared by immersion precipitation. A homogeneous polymer solution in THF (10 % w/w) was casted as a 2 cm diameter circle on a FEP sheet support. The wet film and its support was immersed in a Milli-Q bath. Diffusion of both solvent into bath and water into the cast film were observed. The film was left in the bath till no further streaks/clouds of diffusion can be observed to ensure complete exchange of solvents, thereby

yielding an opaque solid polymer membrane. The membranes were left to dry at RT overnight and were baked the next day.

2.4.3 Thermal Treatment

For small scale thermal treatment: A polymer membrane on its FEP support was mounted on a hot stage (Linkam TP92) and was heated at 10 ^{o}C/min to a temperature above its clearing temperature. It was then left to cool slowly at 0.5 ^{o}C/min to its designated temperature characteristic of each polymer and was kept isothermal for 24 hours before gradually cooling back to RT. The temperature program was set up based on POM observations. In order for the mesophases to grow slowly, an isothermal temperature slightly lower than the polymer's clearing temperature was used[19].

For larger scale thermal treatment: Polymer membranes on their FEP supports were thermally treated with the same temperature program in a Carbolite Gero Laboratory Oven – AX60.

The membranes were kept at RT in petri dishes containing moisture absorbing silica gel beads and can be easily separated from its support to yield transparent membranes with uniform thickness of 100-120 µm (measured with a Mitutoya QuantuMike Digital Micrometer – IP65 with 1 µm sensitivity). The average of 4 measurements were taken for each membranes and were shown to be uniform.

2.5 Characterisation

2.5.1 Nuclear Magnetic Resonance (NMR) Spectroscopy

^{1}H and ^{13}C NMR spectra of **9-ACAK** in deuterated dimethylsulphoxide (DMSO-d_6) were recorded on Jeol ECS 400 MHz whilst those of **TAP** and the polymers in deuterated chloroform ($CDCl_3$) and deuterated tetrachloroethane (TCE-d_2), respectively were recorded on Bruker Avance III 700 MHz. 2D NMR such as ^{1}H-^{1}H correlation (COSY), ^{1}H-^{13}C heteronuclear single quantum correlation (HSQC), ^{1}H-^{13}C heteronuclear multiple bond correlation (HMBC) were used to substantiate ^{1}H and ^{13}C NMR assignments of the synthesised compounds. For polymer samples, quantitative ^{1}H and ^{13}C NMR were both recorded with a 5 seconds pulse delay and 20,000-40,000 number of scans. Polymer samples were prepared in the dark as 10-20 % (w/v) solutions.

2.5.2 FT-IR Spectroscopy

FT-IR spectra were obtained using Spectrum Two FT-IR Spectrometer fitted with a diamond crystal plate ATR unit (PerkinElmer).

2.5.3 Thermogravimetric analysis (TGA)

TGA were carried out in a Mettler TGA SDTA 851e thermobalance. Approximately 8 mg of samples were heated from 30 to 650 ^{o}C at 10 ^{o}C/min in a nitrogen atmosphere (100 mL/min).

2.5.4 Differential Scanning Calorimetry (DSC)

Calorimetric studies were carried out in a Mettler DSC822e Differential Scanning Calorimeter. Approximately 5 mg of samples were weighed into 40 µL aluminium crucibles covered with a pierced lid. The analyses were performed in dynamic mode at a heating and cooling rate of 10 ^{o}C/min using nitrogen as a purge gas (100 mL/min).

2.5.5 Polarised Optical Microscopy (POM)

The liquid crystalline mesophases, their textures and respective clearing temperatures were observed and characterised using an Axiolab Zeiss Polarised Optical Microscope fitted with a Linkam TP92 Hot Stage.

2.5.6 Gel Permeation Chromatography (GPC)

The number average (M_n) and weight average (M_w) molecular weight of polymers were determined by the use of an Agilent 1200 Series GPC-SEC system consisting of three columns in series (PLgel 20 µm MIXED-A, PLgel 5 µm MIXED-D and PLgel 3 µm MIXED-E) and a refractive index detector. Monodispersed polystyrene (PS) standards were used for calibration and the mobile phase (THF with toluene as internal standard) was eluted at a flow rate of 1.0 mL/min. The sample concentrations used were 5-10 mg/mL.

2.5.7 X-ray Diffraction (XRD)

A Bruker-AXS D8-Discover diffractometer equipped with parallel incident beam (Göbel mirror), vertical θ-θ goniometer, XYZ motorized stage and with a General

Area Diffraction System, GADDS was used for XRD measurements. Polymer samples were either placed directly on the sample holder for reflection mode or with a membrane support intact for transmission analysis. An X-ray collimator system close-to-the-sample allowed an area of 500 μm to be analysed. The X-ray diffractometer parameters were set to 40 kV and 40 mA to generate $Cu_{k\alpha}$ radiation. HI-STAR GADDS detector equipped with a multiwire proportional counter of 30 x 30 cm with a 1024 x 1024 pixel was placed at 30cm from the sample. The collected *frame* (2D XRD pattern) was adjusted to allow distance coverage between the ranges of 2θ from 0.9 up to 9.2 º. Slight modifications were made: i) SAXS attachment added (He beam path) to allow diffracted X-ray beam to pass through, reducing low angle air scattering; and ii) a beam stop added directly on the detector face to stop direct X-ray beam. The exposition time was set to 120s per *frame* and was first chi-integrated to generate the chi vs. intensity diffractograms. Each small lines separation corresponds to ≈100 μm.

2.5.8 Atomic Force Microscopy (AFM)

AFM images were recorded with an Agilent 5500 (Agilent Technologies) in tapping mode at a scan rate of 0.7-2 Hz. An extra-thin cantilever tip (HiRes-C19/Cr-Au, MikroMasch) with a spring constant of 0.5 N/m, resonance frequency of 65 kHz and tip radius of 1 nm was used to record phase images of 1x1 μm^2 at room temperature in unfiltered air. The microscope was located in an active vibration isolation chamber (Agilent Technologies) on a sturdy table to eliminate external vibration noise. The AFM images were analysed with Nanotec WSxM 5.0 and their respective RMS values were calculated.

2.5.9 Contact Angle Measurements

Static contact angle measurements were carried out using sessile drop method at room temperature with a Rame-Hart (Mountain Lakes, NJ) NRL model 100-00 contact angle goniometer. A micropipette was used to dispense 2 μL of probe droplets of high purity water to the sample surface. The static contact angles of the ultrapure water drops were measured on five different spots. The contact angles were determined using a tangent 2 or circle fitting models and the average of five readings were recorded.

2.5.10 Spectroscopy

All solvents used for UV-Vis and fluorescence experiments were bought at the highest available grade and their purity were checked before the experiments.

UV-Vis Experiments

Absorption spectra were recorded using Shimadzu UV-1800 UV-Vis Spectrophotometer. Samples were dissolved in spectroscopic grade solvent in a 1 cm by 1 cm quartz cuvette. Baseline was corrected prior to measurements.

Fluorescence Experiments

Fluorescence emission and excitation spectra were recorded using a Shimadzu RF-6000 Spectrofluorophotometer. Measurements were repeated several times at varying concentrations and excitation wavelengths. Fluorescence quantum yields were estimated using perylene in EtOH (Φ_{Flo} = 0.92) as standard[20]. The absorbance at the λ_{exc} of the sample solutions were strictly kept below 0.04 while the absorbance at the λ_{max} below 0.10.

3. Results and discussion

3.1 Synthesis of Potassium 9-anthracene carboxylate, **9-ACAK**

Potassium 9-anthracene carboxylate, **9-ACAK** was synthesised via deprotonation of 9-anthracene carboxylic acid, **9-ACA** with potassium hydroxide as shown in Scheme 1.

The characteristic carbon peak of carbonyl carbon of **9-ACAK** in deuterated DMSO was observed at chemical shift of 171.6 ppm which was more downfield than the reported carbonyl carbon peak of 9-anthracene carboxylic acid, **9-ACA** (170.3 ppm)[21], suggesting successful synthesis of carboxylate salt. The ^{1}H and ^{13}C NMR spectra of **9-ACAK** were assigned based on its 2D NMR spectra shown in Figure 1 (Supporting Information (SI)).

Based on the FT-IR spectrum of **9-ACAK** in Figure 3, the strong peaks at 1546, 1318; 1427 and 1389 cm^{-1} corresponded to the characteristic asymmetric and symmetric stretching of carboxylate carbonyl C=O bond, respectively. The shift in the C=O stretching from 1683 cm^{-1} in **9-ACA** to 1546 cm^{-1} in **9-ACAK** once

again substantiated the conformation of its structure and supported the NMR spectroscopy result described earlier.

3.2 Modification of PECH *with* 9-ACAK*,* PA Series

PA Series polymers were synthesised via S_N2 substitution with the use of carboxylate anion (**9-ACAK**) as nucleophile as shown in Scheme 1. The chemical modification conditions and product yields of **PA polymers** are reported in Table 1.

PA Series (PECH: 9-ACAK)	PECH	9-ACAK	TBAB	THF (mL)	Yield (%)[1]
PA4 (1:0.2)	1.20 g, 13.0 mmol	0.68 g, 2.6 mmol	0.84 g, 2.6 mmol	115	93
PA5 (1:0.3)	1.20 g, 13.0 mmol	1.01 g, 3.9 mmol	1.26 g, 3.9 mmol	115	92
PA6 (1:0.4)	3.00 g, 32.4 mmol	3.38 g, 13.0 mmol	4.18 g, 13.0 mmol	280	96
PA1 (1:0.5)	1.60 g, 17.3 mmol	2.25 g, 8.7 mmol	2.79 g, 8.7 mmol	150	81
PA2 (1:0.8)	1.20 g, 13.0 mmol	2.69 g, 10.3 mmol	3.34 g, 10.4 mmol	115	78
PA3 (1:1.0)	1.20 g, 13.0 mmol	3.35 g, 12.9 mmol	4.18 g, 13.0 mmol	115	67

[1]Percentage yield was calculated from the degree of modification of **PA Series**.

Table 1: *Chemical modification conditions and product yields of* ***PA Polymers****.*

Since all six polymers of this series exhibited similar trend in their NMR and IR spectra, only the spectra of **PA6** will be used in this discussion. The assignments were made based on their 2D-NMR spectra. The ^{1}H and ^{13}C NMR data of **PA6** and their corresponding assignments are shown in Table 1 (SI).

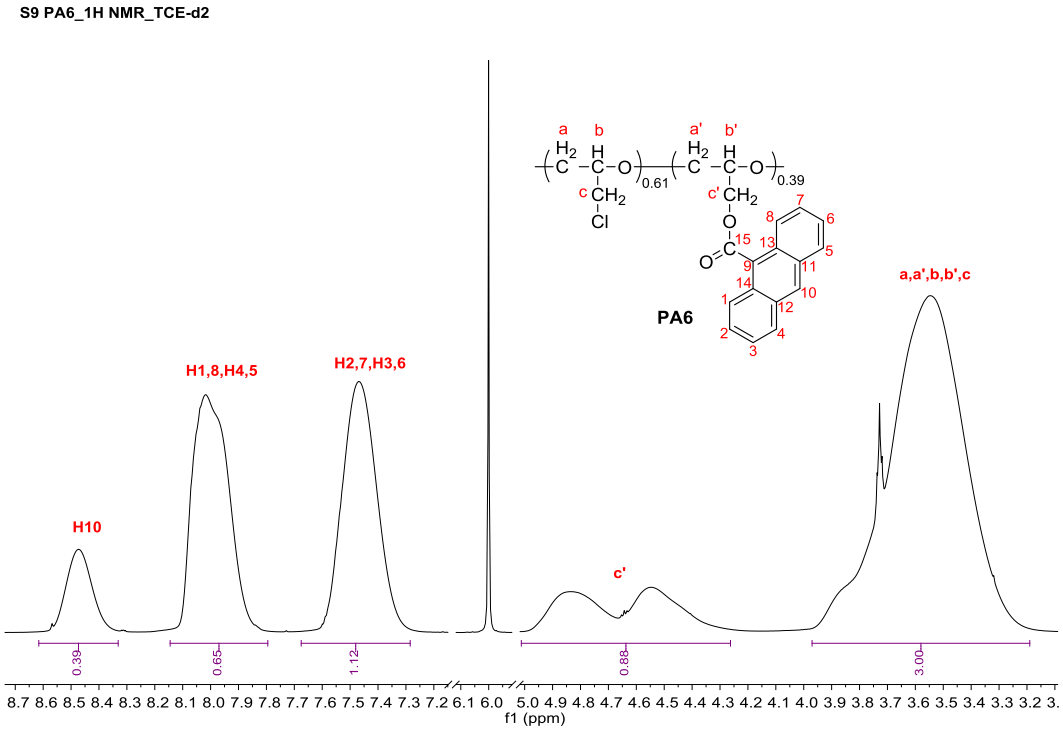

Figure 1: ^{1}H NMR spectrum (700 MHz, TCE-d_2) of **PA6**.

Broad signals in two regions are distinctive features to note when looking at ^{1}H and ^{13}C NMR spectra of **PA polymers**. From the ^{1}H NMR spectrum of **PA6** as shown in Figure 1, the aromatic region shows three broad, partially overlapped signals at 8.47, 8.02 and 7.47 ppm which corresponded to protons from the anthracene moieties. The two “camel hump” peaks around 5.01-4.26 ppm can be attributed to the two methylenic **c’** protons in the modified repeating unit while the broad peak around 3.97-3.19 ppm are the main chain methylenic and methynic protons **a**, **a’**, **b**, **b’** and **c** of the modified and unmodified repeating units.

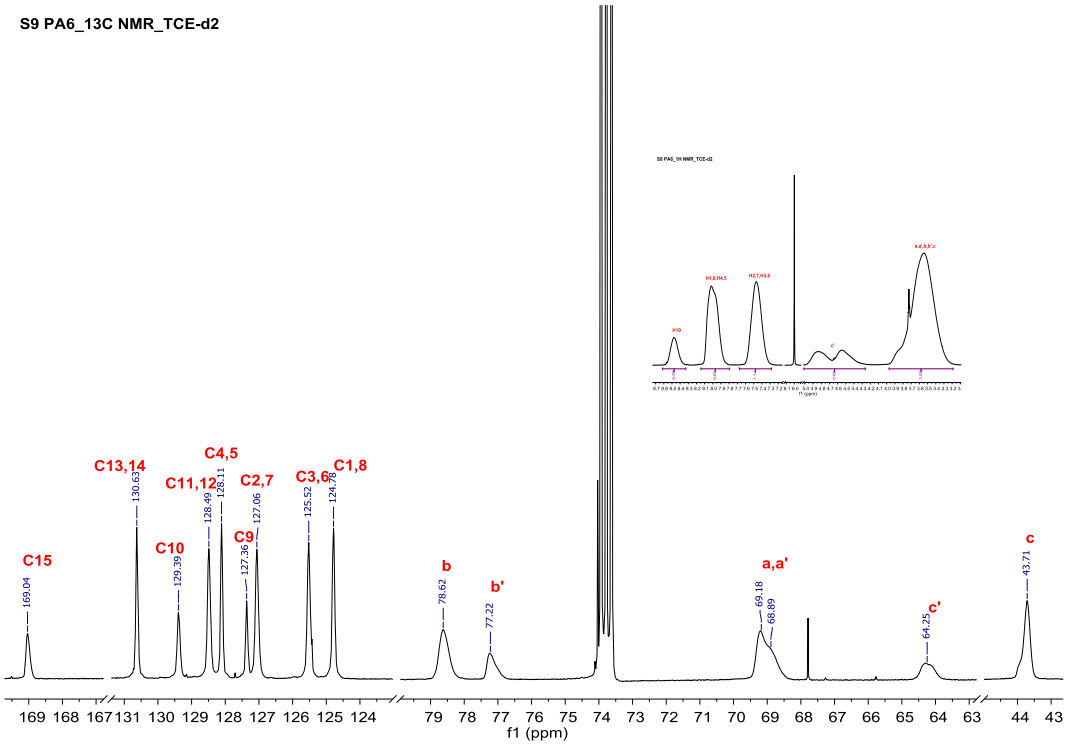

Figure 2: *^{13}C NMR spectrum (176 MHz, TCE-d_2) of* **PA6***.*

The carbonyl carbon of anthracene appeared as a broad peak at 169.0 ppm as shown in Figure 2 which is in the chemical shift region for an ester. The main chain carbons **a** and **a'** appeared as a broad overlapped peak at 69.2 ppm with a shoulder at 68.9 ppm, while carbon **b** and **b'** appeared as two well separated peaks at 78.6 and 77.2 ppm, respectively. The methylenic carbons **c** and **c'** of the unmodified and modified unit also appeared very well resolved, with the modified carbon **c'** being more deshielded (64.3 ppm) than carbon **c** (43.7 ppm). This can be explained by the close proximity of carbon **c'** to the carbonyl group.

As ^{1}H NMR spectra were recorded with a pulse delay time of 5 seconds and with sufficient number of scans, integration values obtained from the spectra could be used for the quantitative determination of the degree of modification of the **PA Series** polymers. The degree of modification of **PA6** from ^{1}H NMR spectra was calculated as follows (using integration values from Figure 1):

$$\text{Degree of Mod. of } \mathbf{PA6} = \frac{Quotient_{mod.protons}}{Quotient_{mod.+unmod.protons}} \times 100\ \%$$

$$= \frac{100 \times \left(\frac{Integral_{aromatic\ peaks} + Integral_{proton\ c'}}{n_{protons\ integrated}}\right)}{Quotient_{mod.protons} + \frac{Integral_{protons\ a,a'\ b,b'\ and\ c} - n_{mod.protons}(Quotient_{mod.protons})}{n_{protons\ integrated}}}$$

$$= \frac{\frac{(0.39 + 0.65 + 1.12) + 0.88}{(9 + 2)}}{0.28 + \frac{3.00 - 3(0.28)}{5}} \times 100\ \%$$

$$= 39\ \%$$

The calculated degree of modifications of **PA polymers** are shown in Table 2.

Polymer (PECH:9-ACAK)	Modification (%)	T_g (ºC)
PECH (1:0.0)	0	-23
PA4 (1:0.2)	20	13
PA5 (1:0.3)	30	32
PA6 (1:0.4)	39	45
PA1 (1:0.5)	49	59
PA2 (1:0.8)	76	84
PA3 (1:1.0)	93	98

Table 2: *Calculated degree of modification and glass transition temperature, T_g of* **PECH** *and* **PA polymers**.

The degree of modification of **PA polymers** appeared to be quantitative up to about 50 %. Any modifications attempted above this appeared to be slightly lower than the amount of **9-ACAK** introduced, which may be explained by the decrease in the percentage of accessible reactive sites[17].

In the FT-IR spectrum (Figure 3) of **PA6**, the presence of a strong peak at 1715 cm^{-1} corresponding to the characteristic ester carbonyl group and the disappearance of strong peaks attributing to COO^- from the starting material, **9-ACAK**, implied successful chemical modification of **9-ACAK** onto the **PECH** main chain.

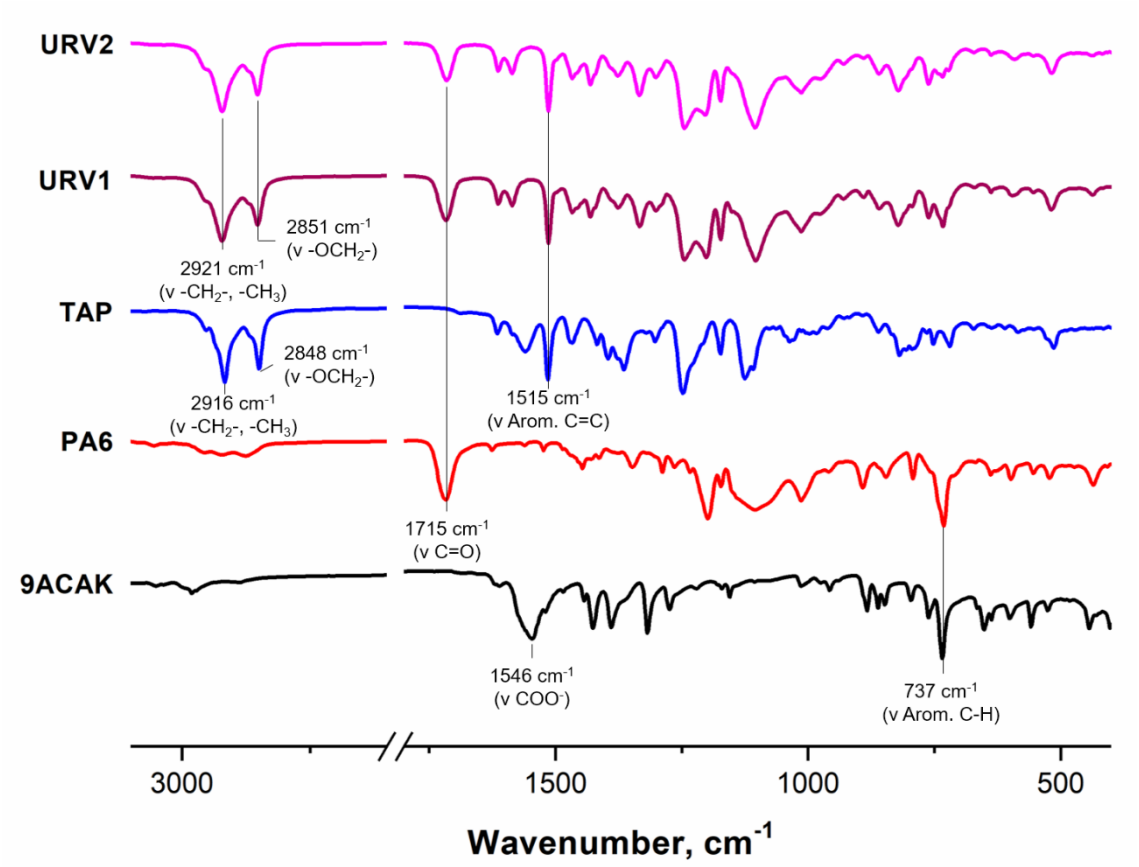

Figure 3: *FT-IR spectra of* **9-ACAK**, **PA6**, **TAP** *and* **URV polymers**.

Significant change in physical properties of the polymers across the series can be observed in Figure 4a. Polymer **PA4** (20 %) being the least modified in the series appeared to be darker in colour and flexible at RT, whereas **PA3** (93 %) being the most modified in the series appeared to be brittle, flaky and yellow in colour. Polymer **PA6** (not shown in picture), at 39 % modification has physical properties in between **PA5** and **PA1**, it appeared to be hard at RT with a beige brown hue. All of the **PA polymers** were fluorescent in solid state as seen in Figure 4b.

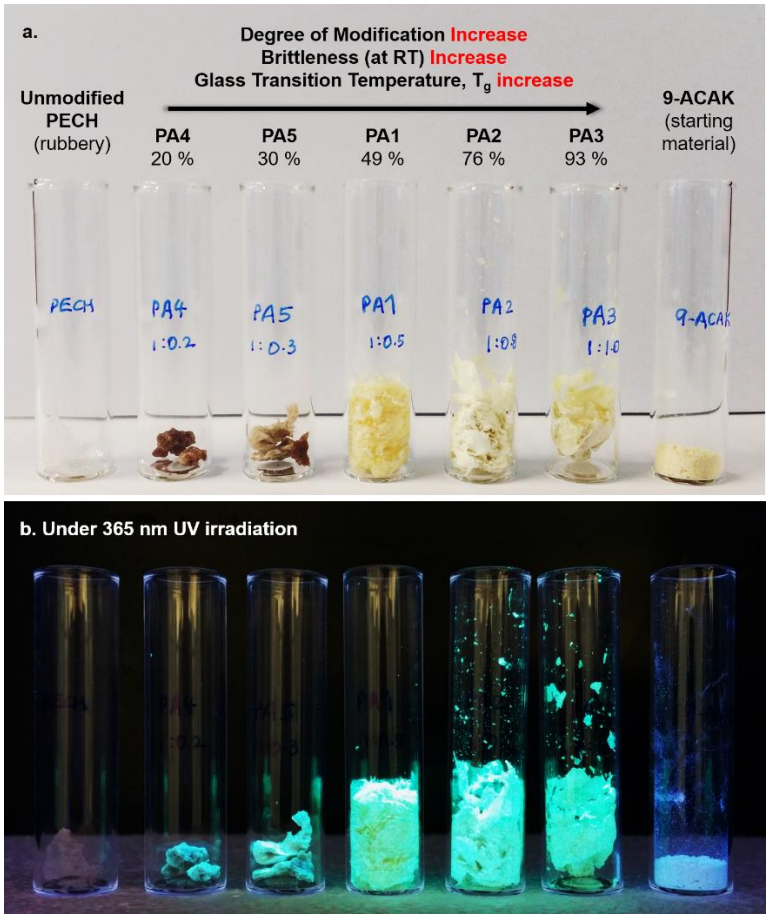

***Figure 4: a)* PA Series** *in order of increasing degree of modification and* ***b)* PA Series** *under 365 nm UV irradiation.*

In addition to structural characterisation, the polymers were characterised with DSC, TGA and GPC. Glass transition temperature, T_g of the polymers were determined from the second heating curve in their respective DSC thermograms and are shown in Table 2. As the degree of modification increases across the series, the value of T_g also increases as expected due to the increasing number of side bulky aromatic groups.

The thermal stability of **PA polymers** was studied by TGA and the results are reported in Table 3. **PA polymers** in general appeared to be more thermally stable than **PECH** with values within the range of 9-10 % char yield, which is 3 % more than that of **PECH**. The rate of degradation decreases with increasing degree of modification which can be deduced from the temperature at which 50 % of weight has been lost, $T_{50\%}$. **PECH** having the lowest $T_{50\%}$ (362 ^{o}C) degraded the fastest as compared to **PA3** (93 % modified) at 390 ^{o}C. The peak mass loss

rate temperature, T_{max} increases with increasing degree of modification of **PA polymers**.

Polymer	$T_{50\%}$ (°C)[a]	Char Yield, %	T_{onset} (°C)[b]	T_{endset} (°C)[c]	T_{max} (°C)[d]
PECH	362	7.1	349	373	363
PA4	370	10.1	351	384	369
PA5	372	10.2	353	388	371
PA1	376	10.2	355	393	375
PA2	383	9.9	354	405	376
PA3	390	9.3	367	408	389
PA6*	366	11.4	345	382	331

[a] Temperature corresponding to 50 % weight loss; [b] Onset decomposition temperature; [c] Endset decomposition temperature; [d] Peak mass loss rate temperature; ***PA6** was synthesised in bulk, thus its values would not be comparable with the rest of the **PA Series**.

Table 3: *TGA data of* **PA Polymers***.*

The average molecular weight (M_w), number average molecular weight (M_n) and polydispersity index of **PA Series** were determined via GPC and are reported in Table 4.

Polymer	Modification (%)	M_n[a]	M_w[a]	PDI (M_w/M_n)
PECH	0	122800	582700	4.75
PA4	20	105000	459900	4.38
PA5	30	102400	467600	4.56
PA1	49	100600	647900	6.44
PA2	76	66400	316100	4.76
PA3	93	43200	246500	5.70
PA6*	39	173700	894300	5.15

[a] Average molecular weights relative to PS standard by GPC, using THF/Toluene as the eluent; ***PA6** was synthesised in bulk, thus its values would not be comparable with the rest of the **PA Series**.

Table 4: *GPC Data of* **PA Series***.*

It was expected that with the increasing degree of modification across the series, there should be an increased trend of molecular weight. However, this was not what was observed. Keeping in mind that GPC operates with the assumption that the polymer introduced in the system behaves like that of PS in THF/toluene, the introduction of anthracene moiety into the backbone of **PECH** could greatly alter the hydrodynamic volume of the system, making it very different to the starting **PECH** polymer. Another possibility regarding the absence of a trend could be due to the method used in the preparation of GPC samples. To ensure only fully

solubilised fractions were introduced into GPC, all samples were filtered and only the filtrates were used in the measurements. However, due to the viscosity of polymer solution, the filtration may have removed a portion of polymer with larger molecular weight leaving behind smaller molecular weight fractions. Hence, in this case, there will not be a predictable trend between the molecular weight of **PA polymers** and the degree of modification. The GPC molecular weight distribution curves of **PA Series** (Figure 10 – SI) showed evidence of bimodality. This justifies the large PDI values observed in Table 4.

It is important to note that **PECH** was purchased from Sigma Aldrich and was reported to have an average molecular weight (M_w) of around 700,000 by GPC. This data is significantly higher than the actual experimental data obtained (122,800) which may be due to the solvent system and the calibrant range used.

3.2.1 Photocatalytic Decomposition and Photodimerisation of Anthracene

In order to explain the photo-driven organogelation (Section 3.2.2) observed in **PA series** containing dangling anthracene moieties, it is necessary to firstly understand the possible photo-driven reactions on **9-ACAK**. In literature, anthracene derivatives were found to be able to photodimerise in anaerobic conditions upon irradiation by > 300 nm UV light source and the process is reversible upon irradiation by < 270 nm UV light or by heat[22]. This phenomena was found to occur in **9-ACA** in THF under N_2 upon irradiation through a 300 nm cut-off filter for 40 hours[23]. The photodimerisation of such species usually occur as head-to-tail (h-t) dimers, because they form less sterically hindered and thermodynamically stable species as compared to their head-to-head (h-h) or tail-to-tail (t-t) counterparts which easily revert back to the monomeric form at RT[24–26].

In aerobic conditions upon irradiation by > 300 nm UV light, anthracene derivatives form endoperoxides which were found to be reversible upon irradiation by ≤ 320 nm UV light[27] or by heat[28,29]. Instead of reverting back to anthracene, the heating of certain anthracene endoperoxides leads to the formation of anthraquinone (**AQ**) as the major product[30]. The irreversible decomposition of anthracene endoperoxide to **AQ** was also seen in the presence of catalytic amounts of base, such as NaOH, KOH, etc[30].

To study the photocatalytic decomposition and photodimerisation of **9-ACAK**, NMR, XRD, FT-IR, UV and fluorescence spectroscopy were employed while a variety of solvents were also used.

9-ACAK (5 mg, 20.0 µmol) was dissolved in various deuterated solvents (0.5-0.7 mL) as shown in Table 5 and was purged with nitrogen gas before being sealed in an NMR tube. The entire preparation process was done in the dark. The initial ^{1}H and COSY NMR spectra were recorded. The NMR tubes were then irradiated under 365 nm UV for a total of 21.5 hours over 4 days. The reactions were monitored before the start of each irradiation and at the end of each day, after approximately 4-6 hours of irradiation.

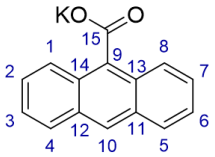

9-ACAK

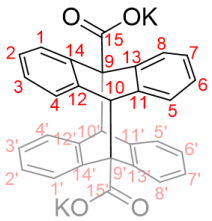

di-9ACAK

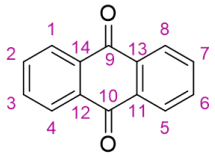

AQ

^{1}H NMR assignments, ppm	H10	H1,8	H4,5	H2,3,6,7	H1,1',8,8'	H4,4',5,5'	H2,2',3,3',6,6',7,7'	H10,10'	H1,4,5,8	H2,3,6,7
a. THF-d_8	8.23 (s)	8.54-8.51 (m)	7.91-7.88 (m)	7.34-7.23 (m)	-	-	-	-	-	-
b. TCE-d_2	-	-	-	-	-	-	-	-	8.33-8.26 (m)	7.87-7.79 (m)
c. CD_3OD	8.38 (s)	8.28-8.19 (m)	8.04-7.95 (m)	7.52-7.39 (m)	7.06-6.99 (m)	6.99-6.92 (m)	6.76-6.64 (m)	5.95 (s)	8.33-8.28 (m)	7.90-7.85 (m)
d. DMSO-d_6	8.28 (s)	8.25-8.20 (m)	7.98-7.95 (m)	7.45-734 (m)	6.96-6.93 (m)	6.71-6.68 (m)	6.54-6.51 (m)	5.98 (s)	8.28-8.16 (m)	7.98-7.93 (m)
e. D_2O	8.57 (s)	8.16-8.12 (m)	8.10-8.05 (m)	7.65-7.55 (m)	7.07-7.03 (m)	6.93-6.90 (m)	6.87-6.83 (m)	5.80 (s)	-	-

Table 5: *^{1}H NMR assignments of* **9-ACAK**, **di-9ACAK** *and* **AQ** *in a range of solvents* ***a)*** *THF-d_8,* ***b)*** *TCE-d_2,* ***c)*** *CD_3OD,* ***d)*** *DMSO-d_6 and* ***e)*** *D_2O (arranged in order of increasing dielectric constant).*

Based on Table 5, D_2O appeared to be the most ideal deuterated solvent to monitor the photodimerisation of **9-ACAK** via NMR spectroscopy mainly because of the solubility of the species involved.

From the ^{1}H and ^{13}C NMR spectra (Figure 5 and 6) of the 21.5 hours 365 nm photo-irradiated **9-ACAK** in D_2O, a new compound attributing to a photodimer of **9-ACAK**, **di-9ACAK** can be observed concurrently with the unconverted **9-ACAK**. The integration value of H10 protons of both compounds show that

approximately 80 % of **9-ACAK** has been successfully converted into **di-9ACAK**. With the same irradiation duration, however, only approximately 30 % of **di-9ACAK** was produced in CD_3OD. When irradiated in THF-d_8, the formation of **di-9ACAK** was untraceable in real-time as a result of partial solubility of **9-ACAK** and complete insolubility of **di-9ACAK**. The ^1H NMR spectrum of its residue in DMSO-d_6 showed the presence of approximately 22 % of **di-9ACAK**.

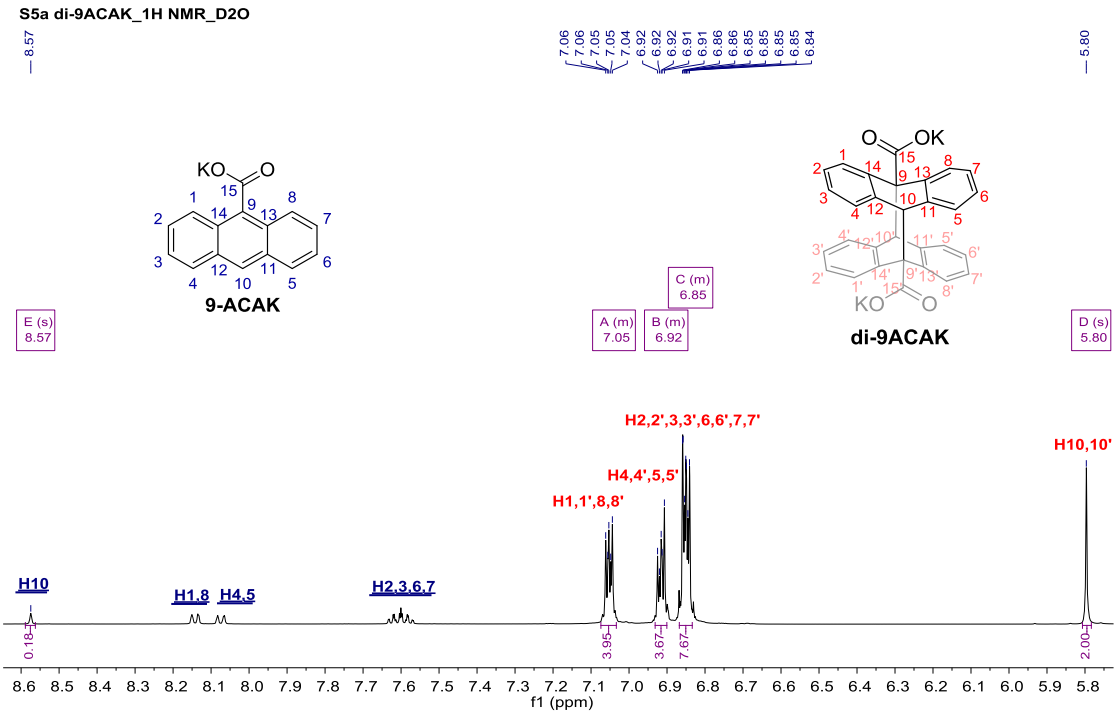

^1H NMR (500 MHz, Deuterium Oxide) δ 7.07 – 7.03 (m, 4H, H1, H1', H8, H8'), 6.93 – 6.90 (m, 4H, H4, H4', H5, H5'), 6.87 – 6.83 (m, 8H, H2, H2', H3 H3', H6, H6', H7, H7'), 5.80 (s, 2H, H10, H10').

Figure 5: *^1H NMR spectrum (500 MHz, D_2O) of* **di-9ACAK** *with minute amounts of unreacted* **9-ACAK**.

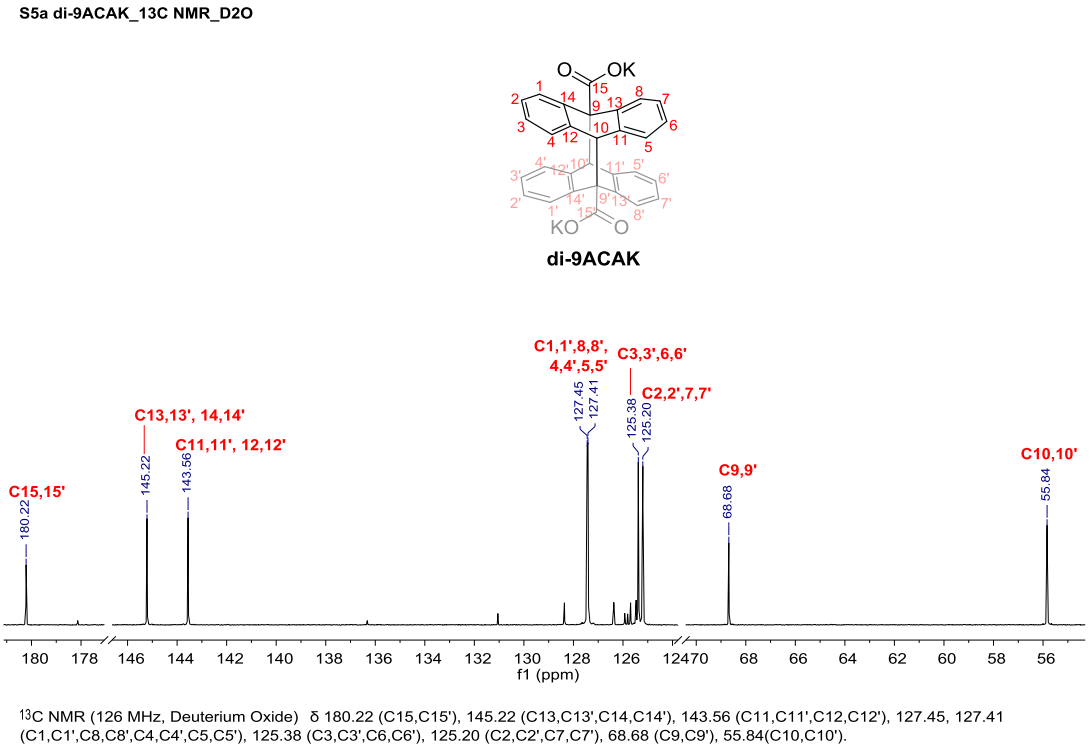

^{13}C NMR (126 MHz, Deuterium Oxide) δ 180.22 (C15,C15'), 145.22 (C13,C13',C14,C14'), 143.56 (C11,C11',C12,C12'), 127.45, 127.41 (C1,C1',C8,C8',C4,C4',C5,C5'), 125.38 (C3,C3',C6,C6'), 125.20 (C2,C2',C7,C7'), 68.68 (C9,C9'), 55.84(C10,C10').

Figure 6: *^{13}C NMR spectrum (126 MHz, D_2O) of* **di-9ACAK** *with minute amounts of unreacted* **9-ACAK**.

In all three cases, the medial bridgehead protons, H10,10' were seen as a singlet at 5.80 ppm (D_2O), 5.95 ppm (CD_3OD) and 5.98 ppm (DMSO-d_6) which are in range with that seen of the h,t photodimer **9-ACA**, **di-9ACA** (5.60 ppm in DMSO-d_6)[23].

The characteristic carbonyl carbon peak of **di-9ACAK** in D_2O was observed at 180.2 ppm (Figure 6), at a region more downfield than its monomer, **9-ACAK** (178.1 ppm in D_2O). A similar trend was also observed in the carbonyl carbon peaks of **9-ACA** (170.3 ppm in DMSO-d_6) and **di-9ACA** (174.3 ppm in DMSO-d_6)[23], elucidating the successful synthesis of photodimer, **di-9ACAK**. The bridgehead carbons C9, 9' (68.7 ppm) and C10, 10' (55.8 ppm) were also seen at similar regions to that of the h,t **di-9ACA** (64.3 ppm and 54.3ppm, respectively)[23]. In the HMBC spectrum of **di-9ACAK** (Figure 5 – SI), the absence of correlation from H10 (5.80 ppm) to C10' (55.8 ppm) or that from H10' (5.80 ppm) to C10 (55.8 ppm) indicated that the bridgehead carbons C9, 9' were attached to C10', 10, respectively, attributing to a h,t (9,10'; 9',10) photodimer, **di-9ACAK**. The h,t **di-9ACAK** was found to revert back to its monomer, **9-ACAK** when irradiated under 254 nm UV light in H_2O solution as shown Scheme 2.

Besides the formation of **di-9ACAK**, small amounts of pale yellowish precipitate (**AQ**) could be observed when **9-ACAK** was irradiated in N_2-purged D_2O, although theoretically under anaerobic conditions the photodimerisation process should be clean. This may be due to poor degassing procedure, without the use of glove box, leading to the formation of anthracene endoperoxide (**9ACAK-EPO**). In the presence of catalytic amounts of KOH (carried on from the synthesis of **9-ACAK**), **9ACAK-EPO** further decomposes into **AQ** as shown in Scheme 2. Similar observations were seen when CD_3OD was used. Instead of precipitating out of solution, the **AQ** formed in CD_3OD crystallised out of solution due to its partial solubility in CD_3OD and complete insolubility in D_2O.

The proposed mechanism of the base catalysed decomposition of **9ACAK-EPO (Scheme 2a)** has been structured based on a scheme proposed for unsubstituted anthracene[30] which starts from a Kornblum-DeLaMare rearrangement. Hydroxide ion from KOH takes away a proton from **9ACAK-EPO** to form intermediate **I1** through transition state **TS1**. **I1** then goes through a second transition state, **TS2** where it takes away a proton from another **9ACAK-EPO** to form intermediate **I2**. In the presence of O_2, **I2** will be converted to **AQ** through a process resembling to that of the industrial anthraquinone process.

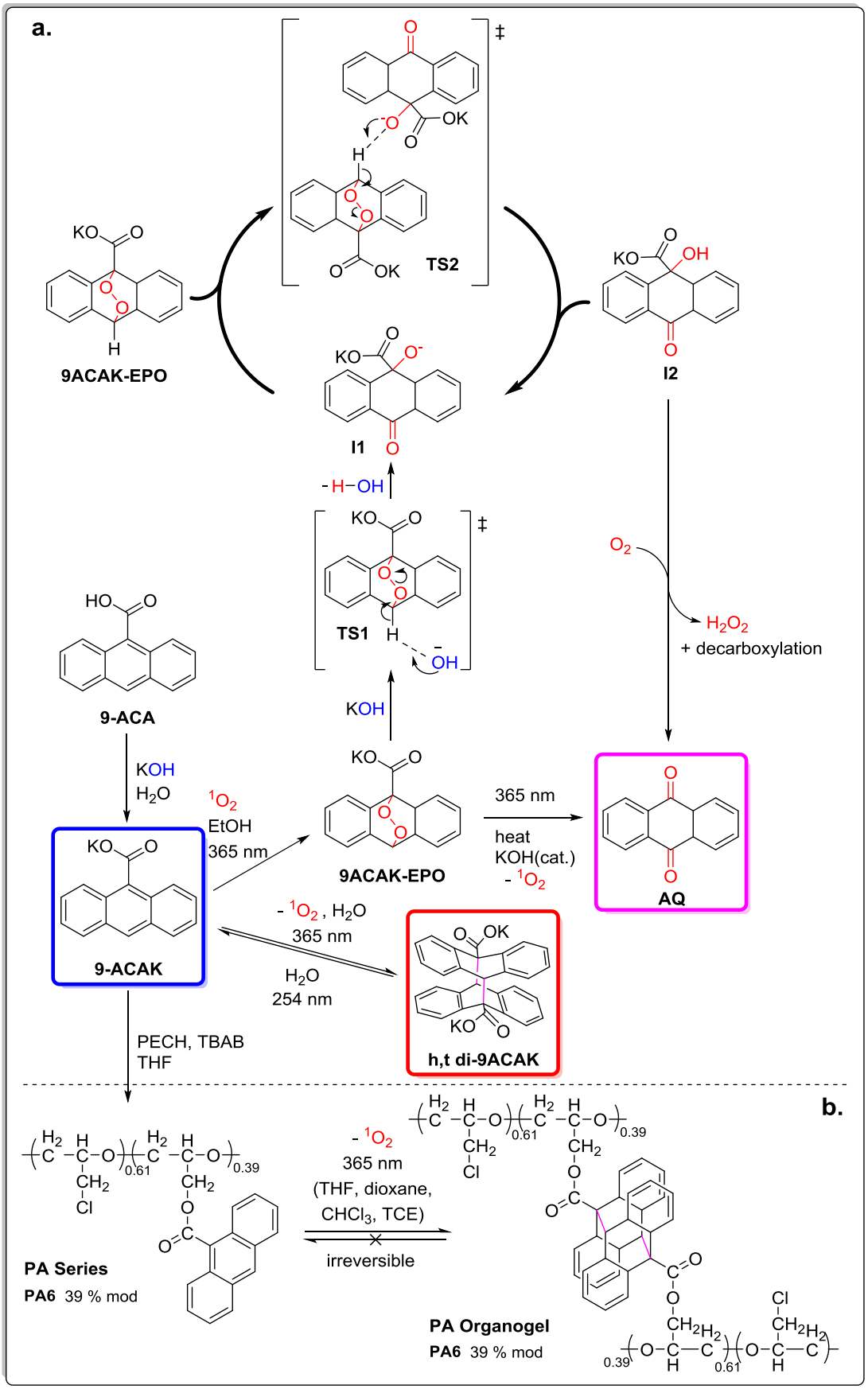

Scheme 2: a) *Photodimerisation of* **9-ACAK** *and the proposed mechanism for the base catalysed decomposition of* **9ACAK-EPO** *and* ***b)*** *Photo-driven organogelation of* **PA Series**.

AQ also crystallises out of solution when **9-ACAK** was irradiated in N_2-purged ethanol. The crystals (**AQ**) were confirmed via NMR spectroscopy (in DMSO-d_6) and X-ray crystallography.

Interestingly, the formation of **AQ** was not observed in N_2-purged THF-d_8 although the solution was also prepared the same way as D_2O and CD_3OD. This may be due to the insolubility of KOH in THF which prevented the base-catalysed irreversible decomposition of **9ACAK-EPO** to **AQ**.

Based on the comparison FT-IR spectra of **9-ACAK** and **di-9ACAK** in Figure 7, the shift in peaks attributing to the asymmetric stretching of carboxylate carbonyl C=O bond from 1546 cm^{-1} (in **9-ACAK**) to 1582 cm^{-1} (in **di-9ACAK**) indicated that C=O was bonded to something less conjugated, which supported the formation of photodimer. In addition, the appearance of two peaks at 1472 and 1450 cm^{-1} (splitting of C-H bending)[31], the disappearance of the characteristic medial (9,10-) C-H out-of-plane bend at 884 cm^{-1} of anthracene and the appearance of a new peak at 780 cm^{-1} (characteristic of dianthracenes)[32,33] further substantiates the formation of **di-9ACAK**.

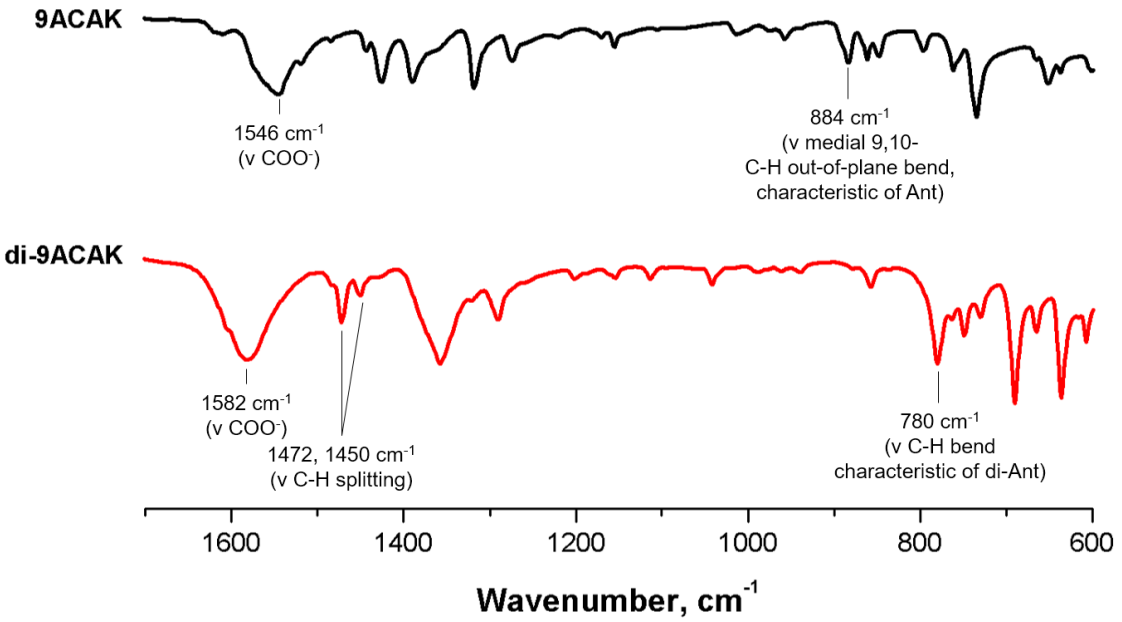

Figure 7: *FT-IR spectra of* **9-ACAK** *and* **di-9ACAK**.

3.2.2 Photo-driven Organogelation of PA Series

As **PA polymers** were prepared via the modification of **PECH** with **9-ACAK**, any 'microscopic' level responses deriving from the attached anthracene moieties would result in the possible formation of stimuli responsive materials. With previously discussed formation of h,t **di-9ACAK** from **9-ACAK** in anaerobic conditions in the presence of 365 nm UV light source, the hypothesis was tested out as follows.

An inverted vial test was firstly carried out to determine the critical gelation concentration (**CGC**) of **PA6** in N_2-purged THF as shown in Figure 8. **CGC** is the lowest concentration (% w/w) of the gelator (**PA6**) that leads to the formation of a stable gel[34].

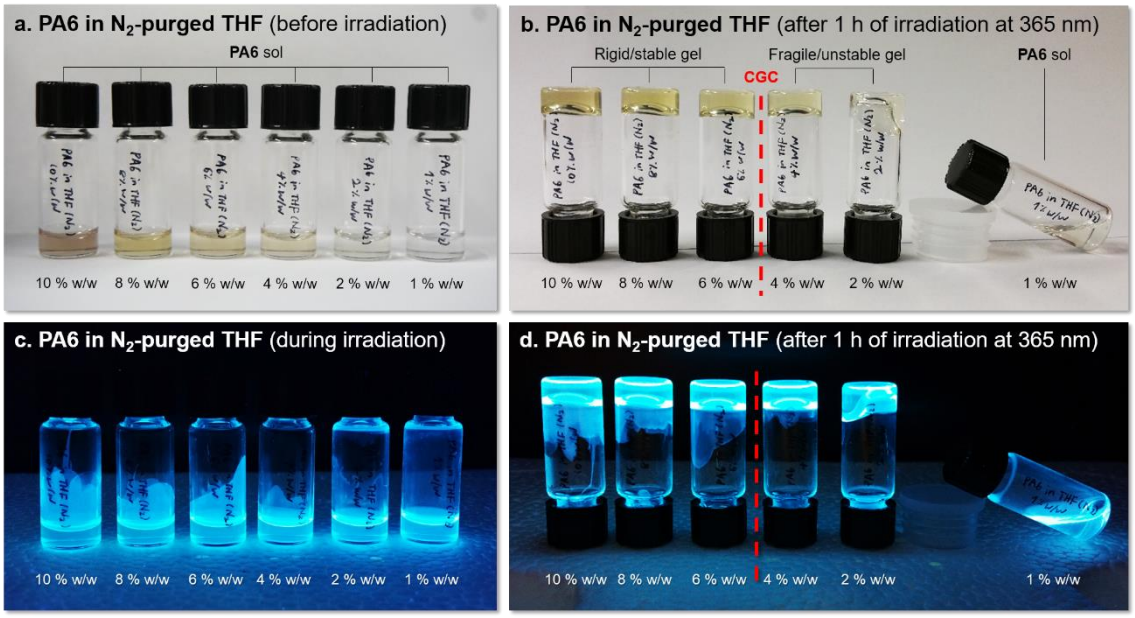

Figure 8: *Inverted vial test of a series of concentration (% w/w) of* **PA6** *in N_2-purged THF* ***a)*** *before irradiation,* ***b)*** *after 1 hour of irradiation at 365 nm (UV off),* ***c)*** *during irradiation at 365 nm and* ***d)*** *after 1 hour of irradiation at 365 nm (UV on).*

Based on the results, the **CGC** of **PA6** in N_2-purged THF was found to be approximately 6 % w/w. The gels formed from **PA6** sol of 2 % w/w and 4 % w/w were fragile and would crumble upon vigorous shaking whilst with increasing % w/w above the **CGC**, the gels were found to be increasingly robust. Hence, 10% w/w was the most preferred concentration and will be used as a standardised concentration for all of the inverted vial tests carried out in this section.

A homogeneous polymer solution (10 % w/w) was prepared by dissolving a polymer in an N_2-purged solvent overnight in a sealed vial covered in aluminium foil. Two of each polymer solution combinations were prepared where one was kept in the dark and another was left to irradiate under 365 nm UV lamp for 1 hour. After irradiation, the polymers were subjected to an inverted vial test.

In the inverted vial test as shown in Figure 9, the unmodified backbone polymer, **PECH** and the enhanced **URV1** polymer showed no changes after irradiation, whereas both **PA polymers** (**PA4** and **PA6**) formed rigid gels after irradiation. This shows that only in the presence of anthracene moieties as seen in **PA polymers** will gels form upon irradiation. With as little as 20 % of modification of **9-ACAK** on **PECH**, organogelation could still occur suggesting how powerful 'microscopic' level changes were that result in the apparent physical changes. However, **URV1** with added **TAP** group in the polymer backbone containing anthracene moieties did not gelate. This could be attributed to the physical separation of adjacent anthracene moieties by **TAP** which in turn disturbs the aggregation of the molecules, thereby preventing photodimerisation of anthracene (crosslinking points).

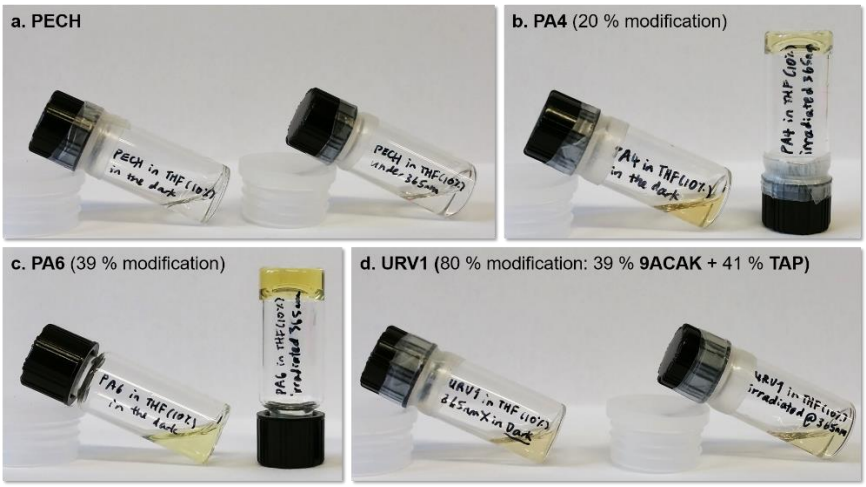

Figure 9: *Inverted vial test (before and after comparisons) of 10 % w/w of* ***a)*** **PECH***,* ***b)*** **PA4***,* ***c)*** **PA6** *and* ***d)*** **URV1** *in N_2-purged THF.*

In order to check if it was a solvent dependent organogelation, various N_2-purged solvents were used in the inverted vial test as shown in Figure 10. Among many solvents tested, **PA6** were only soluble in four solvents (Table 3 – SI). It turns out the organogelation of 10 % w/w **PA6** was observable in all four solvents regardless of the polarity (reflected by its corresponding solvent dipolarity-

polarisability scale, SPP^N values[35]) and nature of the solvents as long as **PA6** was fully solubilised before irradiation.

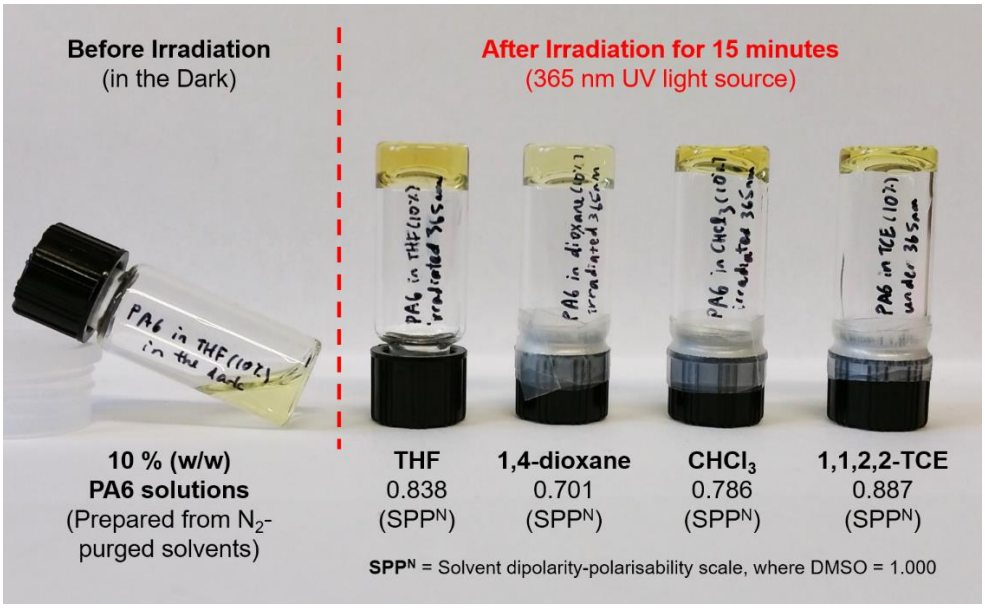

Figure 10: *Inverted vial test (before and after comparisons) of 10 % w/w of* **PA6** *in various N_2-purged solvents.*

Further elucidation of the organogelation phenomenon was carried out with NMR spectroscopy as well as UV-Vis and fluorescence spectroscopy (Section 3.2.3). Two homogeneous 10 % w/w deuterated polymer solutions were prepared by dissolving **PA6** in N_2-purged THF-d_8 and N_2-purged TCE-d_2, respectively. Both solutions were prepared in the dark and the initial NMR spectra were recorded. The solutions were then irradiated under 365 nm UV lamp for > 20 hours before the final NMR spectra were recorded (THF-d_8 in Figure 11, TCE-d_2 in Figure 6 – SI).

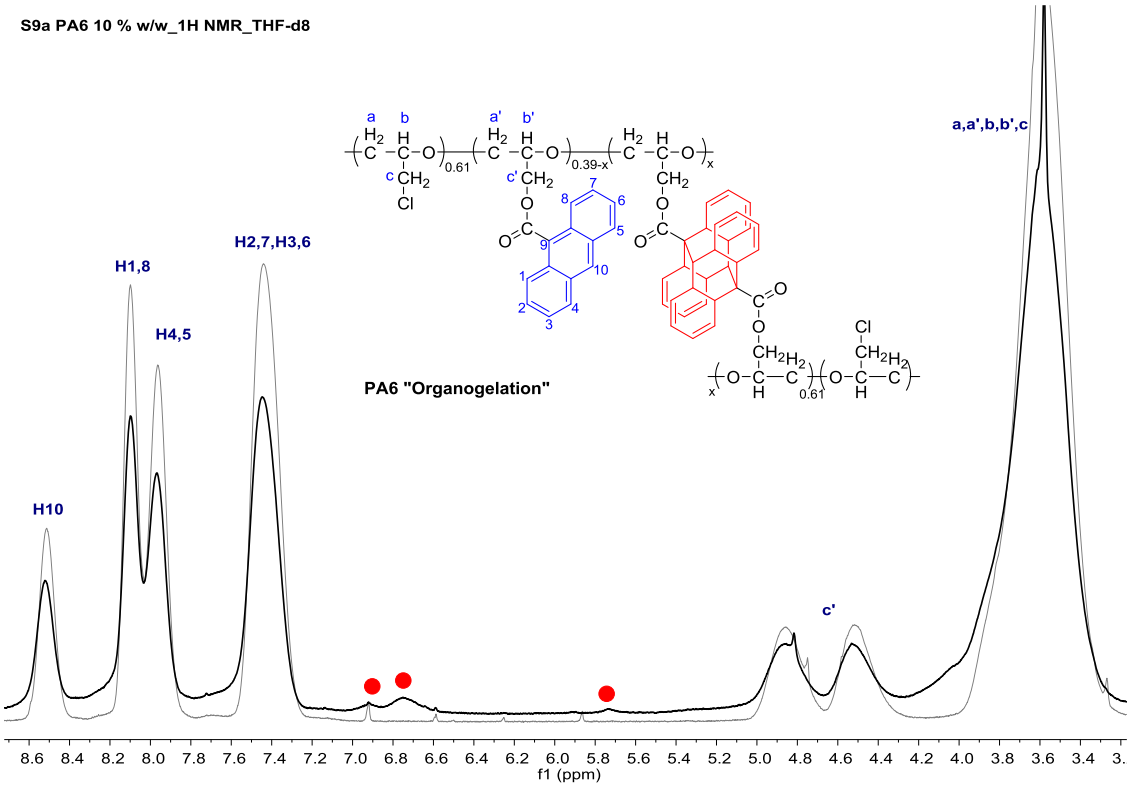

Figure 11: *^{1}H NMR spectra (300 MHz, THF-d_8) of* **PA6** *(before and after).*

The initial ^{1}H NMR spectrum of **PA6** in N_2-purged THF-d_8 (grey line in Figure 11) shows the presence of aromatic peaks belonging to that of the anthracene moiety in **PA6**. However, upon irradiation under 365 nm (**bold** line in Figure 11), the spectrum appeared broader with notable decrease in the aromatic peaks intensity and the appearance of three new peaks (6.90, 6.75 and 5.73 ppm) that are all in the chemical shift range seen in **di-9ACAK** (Table 5). This suggests that photodimerisation of anthracene moieties within the polymer (crosslinked points) could be the cause of the organogelation of **PA6** in THF.

It is important to note that the peaks attributing to that of the possible crosslinked points resembling to a photodimer, **di-9ACAK** did not show any incremental change after longer hours of irradiation. This shows that minute amounts of crosslinking in **PA6** can already result in a drastic physical change leading to the formation of a gel. Due to low concentration of crosslinked species, 2D NMR could not be employed for the confirmation of peaks resembling **di-9ACAK** in the gel of **PA6**.

Interestingly, in addition to the formation of peaks similar to **di-9ACAK**, peaks deriving from **AQ** are also observed in the ^{1}H NMR spectrum of 365 nm irradiated

PA6 in TCE-d_2 (Figure 6 – SI). This was not the case for **PA6** in THF-d_8 even though both NMR solutions were prepared in a similar way. A few postulations can be made regarding the solubility of oxygen (more soluble in TCE than in THF), poor degassing procedure (without the use of glove box) as well as the solubility of KOH (more soluble in TCE than in THF). As previously mentioned in Section 3.2.1, the poor degassing procedure could lead to the formation of **9ACAK-EPO** which could end up as **AQ** in the presence of catalytic amounts of KOH.

Infrared spectra of the sol and gel of **PA6** in THF were recorded but could not be used because the peaks characteristic to the crosslinked species in the gel were too weak to be considered genuine in comparison to the overpowering THF solvent peaks.

Since **di-9ACAK** (in H_2O) exhibited some degree of reversibility back to the anthracene monomer (**9-ACAK**) when irradiated at 254 nm, an instinctual hypothesis would be that the gel of **PA6** should also be reversible back to its sol state. By exposing the **PA6** gels (10 % w/w in THF) to various conditions such as the 254 nm UV irradiation (for > 5 hours) and heat, it remained unchanged as a yellowish transparent gel. Thus, it can be concluded that the organogelation of **PA6** in THF is irreversible. Similar irreversibility/stability was observed in polyethylene terephthalate (PET) polymers containing anthracene[36] and anthracene based low-molecular-weight gelator (LMWG)[16]. In the case of PET-anthracene polymers, Jones *et al.* ascribed the cause to the formation of anthracene-9,10-endoperoxide as a competing side reaction to the [4+4] photodimerisation, that underwent irreversible thermal and photochemical decomposition which resulted in crosslinked polymer chains and some unidentified oxidised products[36]. LMWG on the other hand emphasised the stability of the photodimer based gel as it showed negligible transformation of gel phase into solution even after long hours of UV irradiation[16].

In the current case of **PA6**, one could argue that 10 % w/w **PA6** in THF was too high of a concentration used as it forms a rigid gel with tight molecular packing but at the same time loses its photoirradiation efficiency[37]. The inner filter effect and turbidity of the gel causes UV light to scatter, thus preventing photocleavage of crosslinked points inside the organogel and hindering reversibility[38]. Another reason could be that the temperature required for cleavage of the photodimer is

much higher than the temperature reachable by the gel before the solvent evaporates off **PA6** (THF boiling point 65 ^{o}C).

3.2.3 UV-Vis and Fluorescence Studies of 9-ACAK and PA6

Since the NMR spectroscopy method as discussed in Section 3.2.2 could not conclusively show the presence of crosslinked points (photodimers) within the gel, UV-Vis and fluorescence studies were carried out to further substantiate the organogelation of **PA6**.

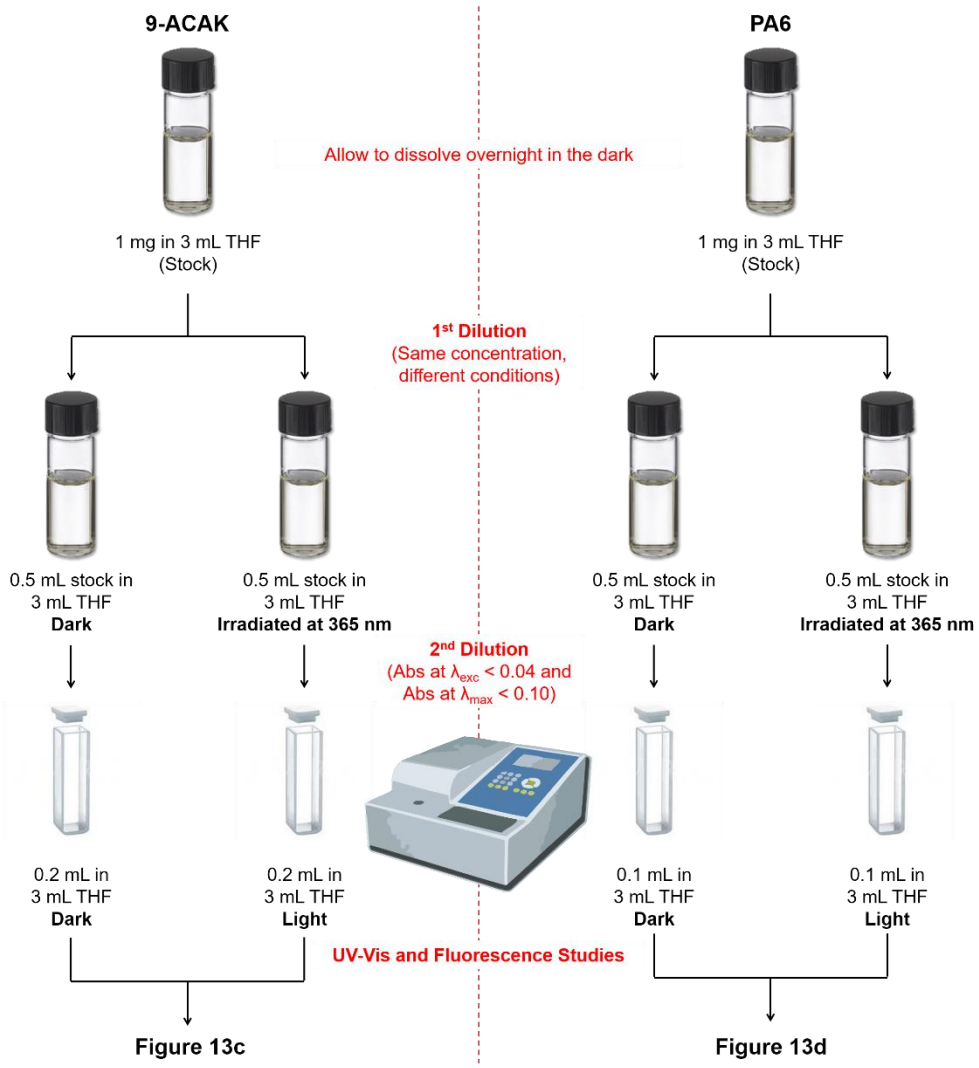

Figure 12: *Preparation of homogeneous solutions of* **9-ACAK** *and* **PA6** *for UV-Vis and fluorescence measurements.*

To begin with, homogeneous solutions of **9-ACAK** and **PA6** (~1 mg in 3 mL solvent) were prepared by dissolving the respective solids in N_2-purged spectroscopic grade THF overnight in a sealed vial covered in aluminium foil as shown in Figure 12. The stock solutions were then diluted into two separate vials

(0.5 mL stock solution in 3 mL solvent), giving rise to a total of four vials. Two vials (**9-ACAK** and **PA6**) were kept in the dark while the other two were irradiated under 365 nm UV lamp for 4 hours. All four solutions were diluted accordingly prior to measurements so as the absorbance value at the wavelength of excitation did not exceed 0.04 and the absorbance value at λ_{max} did not exceed 0.10. The recorded spectra are shown in Figure 13.

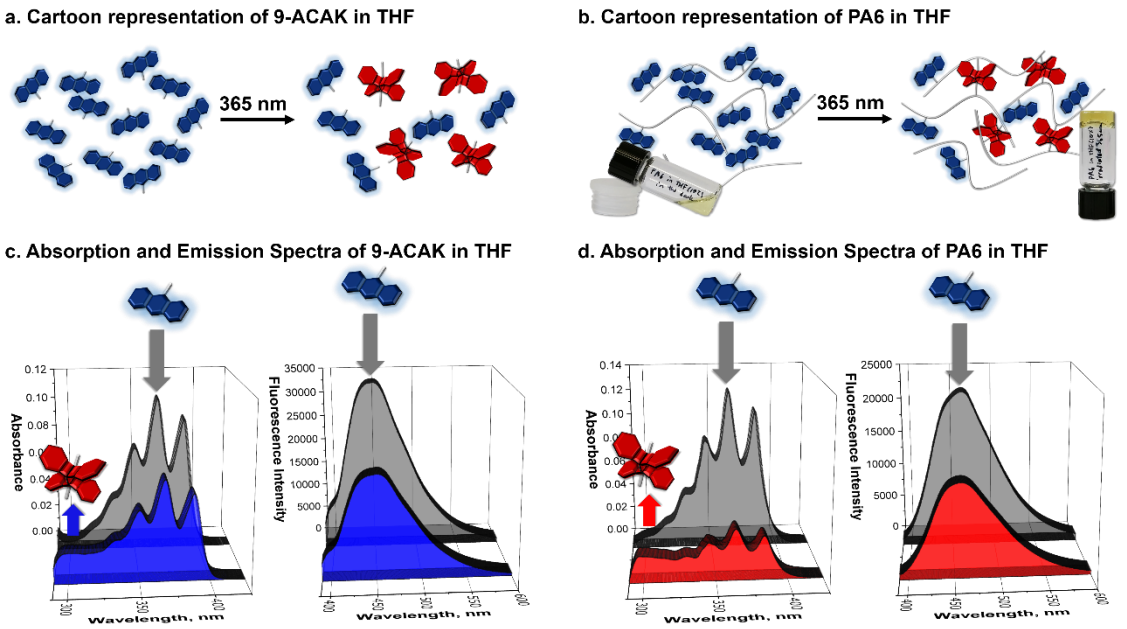

Figure 13: a) *Cartoon representation of* **9-ACAK** *in THF,* ***b)*** *Cartoon representation of* **PA6** *in THF,* ***c)*** *Absorption and Emission Spectra of* **9-ACAK** *in THF (Dark – Grey, Light – Blue) and* ***d)*** *Absorption and Emission Spectra of* **PA6** *in THF (Dark – Grey, Light – Red).*

A series of vibrationally spaced absorption bands at 334, 351, 368 and 389 nm characteristic of the π-π* transition of anthracene can be observed from the absorption spectra of **9-ACAK** kept in the dark (Figure 13c – grey). After 4 hours of irradiation under 365 nm UV lamp, the absorption band at 300-400 nm decreased while a structureless broad absorption band appeared at 297 nm (Figure 13c – blue). The concurrent occurrence of both bands suggests incomplete photoconversion, and that two different species were present in the irradiated solution. The former belonged to unreacted **9-ACAK** and the latter was the photodimer **di-9ACAK**. As the number of **9-ACAK** molecules in solution decreased due to photodimerisation the emission decreased. The emission peak

and its shoulder decreased in intensity and were slightly red-shifted from 450 nm to 453 nm and 396 nm to 397 nm, respectively.

Polymer **PA6** as seen in Figure 13d has as a similar evolution trend as **9-ACAK** upon irradiation, however, the finger-like absorption bands correlating to the anthracene core were blue shifted by approximately 5 nm to 330, 346, 364 and 384 nm. Since anthracene is highly sensitive to steric hindrances in its neighbourhood[39], the hypsochromic shift can be attributed to the change in fluorophore environment when **9-ACAK** was chemically modified onto the **PECH** backbone. Unlike **9-ACAK**, no shoulder band was observed in the emission spectra of **PA6** (λ_{max} = 462 nm), but upon irradiation the emission band experienced a slight blue-shift to 459 nm (grey).

Compound (Solvent)	**Conditions**	**λ_{Abs} (nm)**	**λ_{Em}[1] (nm)**	**Φ_{Flo}[2]**
9-ACAK (THF)	**Dark**	334, 351, 368, 389	396^{sh}, 450	0.39
	Light	297^{br}, 334, 351, 368, 389	397^{sh}, 453	0.32
PA6 (THF)	**Dark**	330, 346, 364, 384	462	0.12
	Light	297^{br}, 330, 346, 364, 384	459	0.29
9-ACAK (H_2O)	**Dark**	314^{sh}, 330, 346, 364, 384	389, 410, 434, 462^{sh}	-
di-9ACAK[3] (H_2O)	**-**	283^{sh}, 314^{sh}, 330, 346, 364, 384	389, 410, 434, 462^{sh}	-

[1]Excitation wavelength, λ_{Exc} = 380 nm; [2]Quantum yields of **9-ACAK** and **PA6** in N_2-purged THF were estimated with respect to perylene in EtOH (Φ_{Flo} = 0.92) as the standard at room temperature; [3]**di-9ACAK** isolated from the NMR experiment in Figure 5 - Section 3.2.1, ^{br} = broad peak; ^{sh} = shoulder peak.

Table 6: *UV/Vis absorption, emission and quantum yield data of* **9-ACAK** *and* **PA6** *in THF (in dark and light conditions) and* **9-ACAK** *and* **di-9ACAK** *in H_2O.*

In contrast to the absorption spectra, a comparison of the emission spectra of **9-ACAK** and **PA6** in dark and light conditions revealed a notable red shift (approximately 12 nm and 6nm, respectively) which could be ascribed to: i) the closer proximity of anthracene moieties in **PA6** than in **9-ACAK**, which could bring about π-π stacking of the polyaromatic units[40] as well as ii) an interaction between the **PECH** polymer backbone and the respective anthracene moieties in **PA6**.

The quantum yield of **9-ACAK** after irradiation (Table 6) was found to be slightly lowered from 0.39 to 0.32. A significant increase by 2.5 fold in the quantum yield

of **PA6** is observed, which is attributed to an aggregation-induced quenching (AIQ) phenomenon[41]. Before irradiation the anthracene moieties dangling off the main chain polymer in the dilute solution of **PA6** are aggregated, giving rise to a system with a high local fluorophore concentration similar to that of a concentrated solution. As a result quenching occurred as reflected by the low (0.12) quantum yield. Photodimerisation of the anthracene moieties in **PA6** helped reduce the number of anthracene moieties. With a lowered local fluorophore concentration the quantum yield is restored to a higher value (0.29). In addition, the photodimerisation of anthracene moieties in **PA6** induced organogel formation through the formation of intra- and inter-molecular entanglements.

To ease comparison all of the absorption and emission spectra were normalised and compiled as shown in Figure 14. Absorption spectra of dark and light **PA6** in THF are blue shifted, while the corresponding emission spectra are red shifted in comparison to **9-ACAK** (dark and light in THF). A consistent shoulder peak was found in both the emission spectra of **9-ACAK** but it was not present in **PA6**.The 297 nm peak attributed to the photodimer **di-9ACAK** was seen as a more intense peak in **PA6** than in **9-ACAK**.

When **9-ACAK** was dissolved in a polar solvent (H_2O), its emission spectrum appeared sharper, structured with finger-like peaks mirroring and overlapping with its absorption spectrum. This is because water molecules are expected to solvate and hydrogen bond to the COO^- and possibly COOH groups in **9-ACAK**. This would in turn inhibit free rotation of the functional groups in both the ground and excited states, resulting in more resolved emission spectra[42]. As for the absorption spectrum of the isolated **di-9ACAK** in H_2O from Section 3.2.1, perfect overlap can be observed with the exception of a strong shoulder peak at 283 nm (dimer). Since **di-9ACAK** is nonfluorescent, the minute amount of residual **9-ACAK** is the only one contributing to the emission spectrum (Figure 14c).

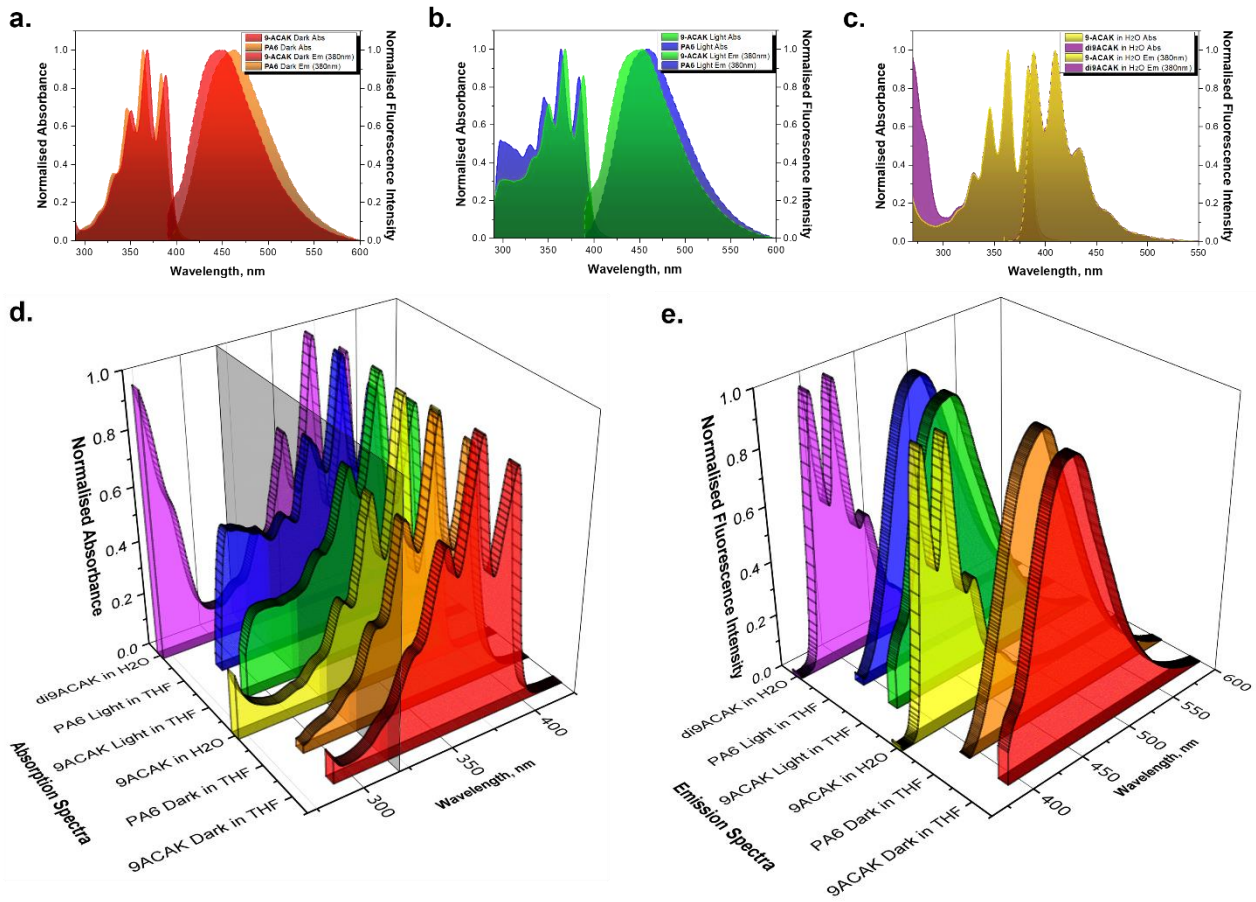

Figure 14: *Comparison of normalised absorption and emission spectra of* ***a)*** **9-ACAK** *and* **PA6** *in THF (Dark),* ***b)*** **9-ACAK** *and* **PA6** *in THF (Light),* ***c)*** **9-ACAK** *and* **di-9ACAK** *in H_2O,* ***d)*** *comparison of all normalised absorption spectra and* ***e)*** *comparison of all normalised emission spectra.*

3.3 Modification of PA Polymers *with* TAP, URV Series

URV Series were prepared as shown in Scheme 1 by introducing **TAP** (synthesised by our collaborators) into partially modified **PA polymers** (**PA6** and **PA4**) via S_N2 substitution, similar to the first chemical modification. The chemical modification conditions and product yields of **URV polymers** are reported in Table 7.

URV Series (9-ACAK:TAP)	PA (mod %)	TAP	TBAB	THF (mL)	Yield (%)[1]
URV1 (1:0.6)	**PA6** (39 %), 0.50 g, 3.0 mmol	1.96 g, 1.9 mmol	0.61 g, 1.9 mmol	60	91
URV2 (1:0.8)	**PA4** (20 %), 0.20 g, 1.5 mmol	1.27 g, 1.2 mmol	0.40 g, 1.2 mmol	24	57

[1]Percentage yield was calculated from the degree of modification of the **URV Polymers**.

Table 7: *Chemical modification conditions and product yields of* **URV Polymers***.*

With reference to the ^1H, ^{13}C and 2D NMR spectra of both starting materials (**TAP** and **PA polymers** - SI), the NMR spectra of **URV1** have been appropriately assigned as shown in Figures 15 and 16. The breakdown of the ^1H and ^{13}C NMR assignments are recorded in Table 2 (SI).

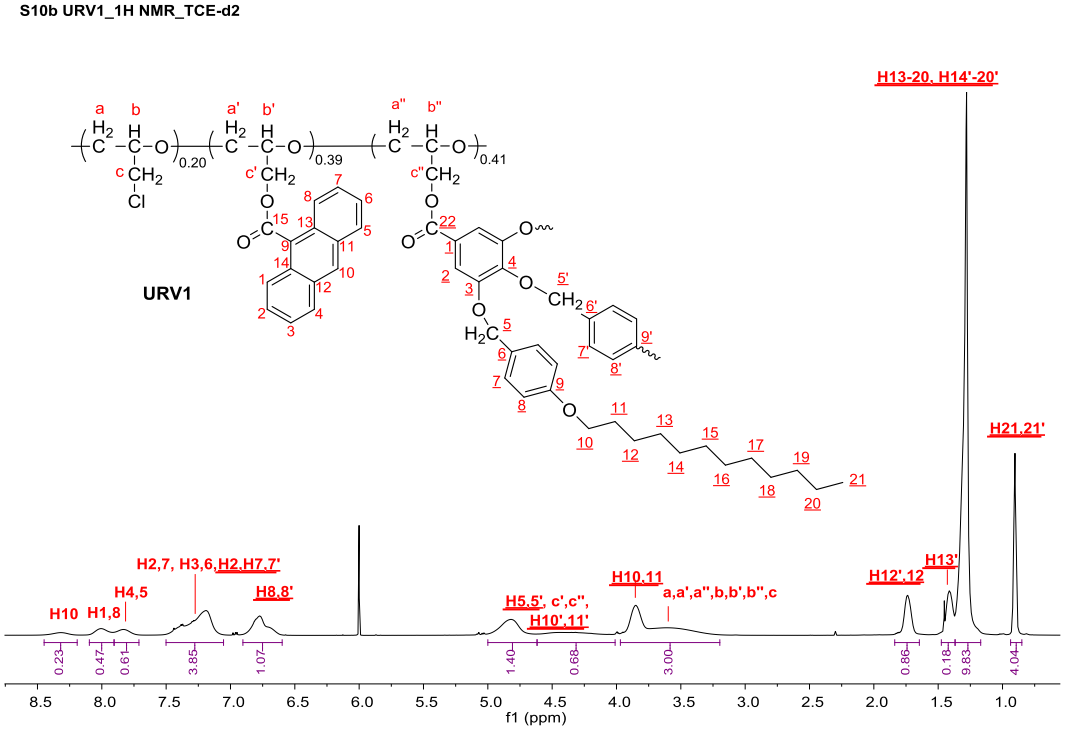

Figure 15: *^1H NMR spectrum (700 MHz, TCE-d_2) of* **URV1***.*

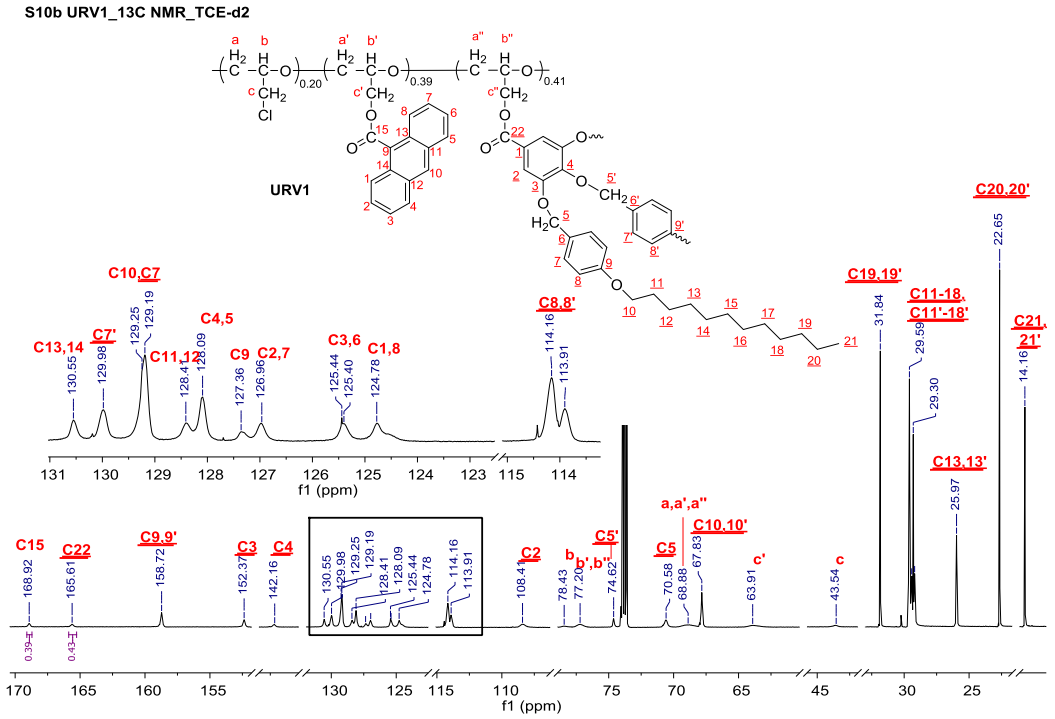

Figure 16: *^{13}C NMR spectrum (176 MHz, TCE-d$_2$) of* **URV1**.

From the ^{1}H NMR spectrum of **URV1** (Figure 15) the aromatic region shows five broad overlapping signals within 8.45 ppm to 6.60 ppm, attributed to protons from anthracene (9H) and **TAP** (14H). The mid region, consisting of four broadly overlapped peaks between 5.00 ppm to 3.19 ppm, correspond to the protons from the methoxy groups sandwiched between the two aromatic rings (H5,5'), protons of the dodecyloxy alkyl chains nearest to the aromatic ring (H10,10',11,11'), four methylenic protons **c'** (anthracene) and **c"** (**TAP**) protons as well as main chain methylenic and methynic protons **a**, **a'**, **a"**,**b**, **b'**,**b"** and **c** of the modified and unmodified repeating units. Four broad partially overlapped peaks in the aliphatic region belonged to protons from the dodecyloxy alkyl chains of **TAP** (63H).

The ^{13}C NMR spectrum of **URV1** (Figure 16) appeared much more complex and crowded. Two very well resolved broad peaks at the downfield end of the spectrum correspond to the carbonyl carbon of anthracene (168.9 ppm) and **TAP** (165.6 ppm). The carbonyl carbon peak of **URV1** attributed to anthracene was slightly shifted upfield as compared to that in **PA6** (169.0 ppm). The main chain carbons **a**, **a'** and **a"** were seen as a very broad peak at 68.9 ppm, whilst carbon **b** (78.4 ppm) were distinguishable from carbon **b'** and **b"** (77.2 ppm) which appeared to overlap. Similarly, the methylenic carbons **c** of the unmodified unit

(43.5 ppm) were located apart, more deshielded than the methylenic carbons **c'** and **c''** of the modified unit (63.9 ppm).

Since both ^{1}H and ^{13}C NMR spectra of **URV Series** were recorded with a pulse delay time of 5 seconds and with a sufficient number of scans (20,000-40,000 for ^{13}C NMR), integration values obtained from both spectra could be used quantitatively for the determination of the degree of modification of the **URV Series** polymers. Both methods and their calculations are shown as follows:

$$\text{Degree of Mod. of } \mathbf{TAP} \text{ in } \mathbf{URV1} \text{ (Quantitative } ^{1}\text{H NMR)} = \frac{Quotient_{mod.TAP}}{Quotient_{mod.Anthracene}} \times Degree\ of\ Mod._{\boldsymbol{PA6}}$$

$$= \frac{\frac{Integral_{aliphatic\,(H12-21)} + Integral_{aliphatic\,(H12'-21')}}{n_{aliphatic\ protons}}}{\frac{Integral_{aromatic\,H10}}{n_{aromatic\ proton}}} \times 39\ \%$$

$$= \frac{\frac{(0.86 + 0.18 + 9.83 + 4.04)}{(63)}}{\frac{0.23}{1}} \times 39\ \%$$

$$= \frac{0.24}{0.23} \times 39\ \%$$

$$= 41\ \%$$

$$\text{Degree of Mod. of } \mathbf{TAP} \text{ in } \mathbf{URV1} \text{ (Quantitative } ^{13}\text{C NMR)} = \frac{\delta_{C=O\ TAP}}{\delta_{C=O\ Ant}} \times Degree\ of\ Mod._{\boldsymbol{PA6}}$$

$$= \frac{0.43}{0.39} \times 39\ \%$$

$$= 43\ \%$$

The degree of modification **TAP** in **URV1** was calculated based on the degree of modification of **PA6** (39 %) while **URV2** was based on **PA4** (20 %). Both methods of calculation as shown above gave a degree of modification that tally (± 2 %), hence, for standardisation purposes and for comparison with **PA Series**, only the degree of modification calculated from the ^{1}H NMR spectra were used. The calculated degree of modifications of **URV polymers** are shown in Table 8.

Polymer (9ACAK:TAP)	Modification (%)	T_g (°C)
PECH	0[a]	-23
PA6	39[a]	45
URV1 (1:0.6)	41[a], 43[b]	38
PA4	20[a]	13
URV2 (1:0.8)	49[a], 47[b]	30

[a] Calculation based on ^{1}H NMR; [b] Calculation based on ^{13}C NMR.

Table 8: *Calculated degree of modification and glass transition temperature, T_g of* **PECH***,* **PA** *and* **URV polymers***.*

The degree of modification of **TAP** in **URV1** was not quantitative as only 41 % out of the 60 % of **TAP** was modified onto the already anthracene populated **PECH** backbone. To counter the problem, **PA4** with a slightly lower degree of modification was used. Unfortunately, the resulting **URV2** was yet again found to be not quantitative with only a tiny bit more of **TAP** incorporated, giving rise to 49 % modification out of the 80 % introduced. This may be explained by the conformational inaccessibility[43] of the remaining chloride groups making it more difficult for bulky **TAP** to gain access to the free spots.

In the FT-IR spectrum (Figure 3) of **URV1** and **URV2**, the appearance of new peaks at 2921 cm^{-1} (v -CH_2-, -CH_3) and 2851 cm^{-1} (v -OCH_2-, symmetric CH_2 stretching vibration) similar to that in **TAP**, the disappearance of the 1557 cm^{-1} (v asymmetric COO^- stretching vibration) previously seen in the FT-IR of **TAP**, as well as the presence of a strong peak at 1715 cm^{-1} (v C=O of ester) similar to the one in **PA6**, were signs that chemical modification of **TAP** on **PA6** main chain was successful.

Glass transition temperatures (T_g) of the **URV Series** were determined from the second heating curve (third scan) in their respective DSC thermograms and are shown in Table 8. The T_g for **URV1** (38 °C) is slightly higher than **URV2** (30 °C). With T_g values of around RT, **URV polymers** appeared flexible and slightly more stretchable than its starting **PA polymer**.

A second heating DSC thermogram of **URV1** also revealed the presence of two endothermic phases with one being the glass transition step (T_g = 38 °C) and the other being the clearing temperature, T_c (around 90 °C). Similar observations to that of **URV1** were also seen in the DSC thermogram of **URV2** with T_g (at 30 °C)

and T_c (around 85 ^oC). These data were then confirmed by POM observations. As both **URV polymers** contained around the same amount of **TAP** groups (between 40-50% modified), their clearing temperatures were not too far off.

The thermal stability of **URV polymers** was studied by TGA and the results are reported in Table 9.

In general, **URV polymers** have similar, if not higher thermal stability than their **PA** counterparts, with char yield values of 10.6 % (**URV1**) and 13.0 % (**URV2**). Their rates of degradation were lower than their starting **PA polymers**; the observed $T_{50\%}$ of **URV1** (391 ^oC) is thermally much more stable but degrades around the same rate as **URV2 (**393 ^oC). The T_{max} was found to be higher in **URV polymers** as compared to their starting **PA polymers.**

Polymer	$T_{50\%}$ (^oC)[a]	Char Yield, %	T_{onset} (^oC)[b]	T_{endset} (^oC)[c]	T_{max} (^oC)[d]
PECH	362	7.1	349	373	363
PA6*	366	11.4	345	382	331
URV1	391	10.6	344	389	389
PA4	370	10.1	351	384	369
URV2	393	13.0	357	430	385

[a] Temperature corresponding to 50 % weight loss; [b] Onset decomposition temperature; [c] Endset decomposition temperature; [d] Peak mass loss rate temperature; *__PA6__ was synthesised in bulk, thus its values may not be comparable with the rest of the **PA Series**.

Table 9: *TGA data of* **PA** *and* **URV Polymers***.*

The average molecular weight (M_w), number average molecular weight (M_n) and polydispersity index of **PA** and **URV series** were determined via GPC and are reported in Table 10.

Polymer	Modification (%)	M_n[a]	M_w[a]	PDI (M_w/M_n)
PECH	0	122800	582700	4.75
PA6*	39	173700	894300	5.15
URV1	39 | 41	300100	1440700	4.77
PA4	20	105000	459900	4.38
URV2	20 | 49	188600	521300	2.76

[a] Average molecular weights relative to PS standard by GPC, using THF/Toluene as the eluent; *__PA6__ was synthesised in bulk, thus its values may not be comparable with the rest of the **PA Series**.

Table 10: *GPC Data of* **PA** *and* **URV Series***.*

Once again, with similar expectations as the **PA series**, there should be an increase in molecular weight for the **URV series** as bulky **TAP** groups were introduced. Polymers **URV1** and **URV2** both have higher M_n and M_w compared to their starting polymer **PA6** and **PA4**, respectively. In theory, **URV2** with a higher degree of modification of **TAP**, but a slightly lower degree of modification of anthracene, should still give higher M_n and M_w values than **URV1**. However, this was not the case. As previously mentioned in Section 3.2, the hydrodynamic volume of the system changes with different degree of modifications. Thus, ruling out a predictable trend between the molecular weight of **URV** and **PA polymers** and their degree of modifications.

3.3.1 Membrane Preparation and Characterisation

URV membranes were prepared via immersion precipitation (Section 2.4.2) and were thermally treated (Section 2.4.3) before its surface morphologies were analysed.

In order to determine the right baking temperature, DSC was firstly recorded from reaction purified polymers. DSC of the polymers were performed in three scans: (1) heated from -100 ^oC to 170 ^oC at 10 ^oC/min, (2) cooled from 170 ^oC back to -100 ^oC at 10 ^oC/min, (3) re-heated from -100 ^oC to 170 ^oC at 10 ^oC/min. The polymers were observed under POM for the verification of the phase transitions in their respective DSC thermograms.

The first DSC scan of both **URV polymers** showed the presence of glass transition, T_g of around 30-38 ^oC and two endotherms (at 60 and 85-90 ^oC). The first endotherm at 60 ^oC is believed to have been caused by local melting of crystallised areas within the polymer. However, upon cooling and re-heating, the endotherm was not seen in the third scan due increased difficulty for the system to be ordered in the molten state. The second endotherm at 85-90 ^oC was observable in both the first and third DSC scans which can be attributed to the clearing temperature, T_c.

From the POM images (**URV1** in Figure 7 of SI and **URV2** in Figure 8 of SI), one distinctive feature to note would be the vibrant colours of both the initial polymers. This is due to the presence of some lyotropic LC structures. When the polymers were purified by re-precipitation (Section 2.3.2), the formation of ordered phases

is favoured by the presence of the previous solution. The presence of the solvent influences local mobility which can also favour interactions between different parts of the polymer leading to possible formations of lyotropic LC. This is not surprising because previous PAZE polymers have been reported to be more ordered when they were freshly precipitated than after undergone thermal treatments[44]. When the polymers were heated above 60 ^{o}C, its colours began to fade away. Even upon cooling, the polymers' colourful textures were not recovered. This is because molecular organisations were much more difficult to achieve from its molten state than from solution precipitation.

With the results obtained from DSC and POM, the immersion precipitated polymer membranes were baked at 35 ^{o}C (for 3 hours), a temperature slightly below their T_c and above their T_g to allow slow growth of mesophases[19].

Upon thermal treatment both treated **URV membranes** appeared transparent as compared to their opaque untreated counterparts as shown in Figure 17c, with an average thickness of 100 µm. The visual appearances of treated and untreated **URV1** membranes indicated that something may have happened to the orientation of the mesogens in the polymer. Under cross polarised light (Figure 17a), the untreated **URV1** membrane appeared bright white whereas the treated **URV1** membrane appeared dark/black. This may be due to random orientation of the mesogenic groups in the untreated membrane diffracting cross polarised light in various directions giving rise to liquid crystalline appearance. Once it is thermally treated, the mesogenic groups aligned homeotropically resulting in a black membrane[45]. However, a black membrane under cross polarised light may also be an indication that the membrane contains overly small domains which do not scatter light.

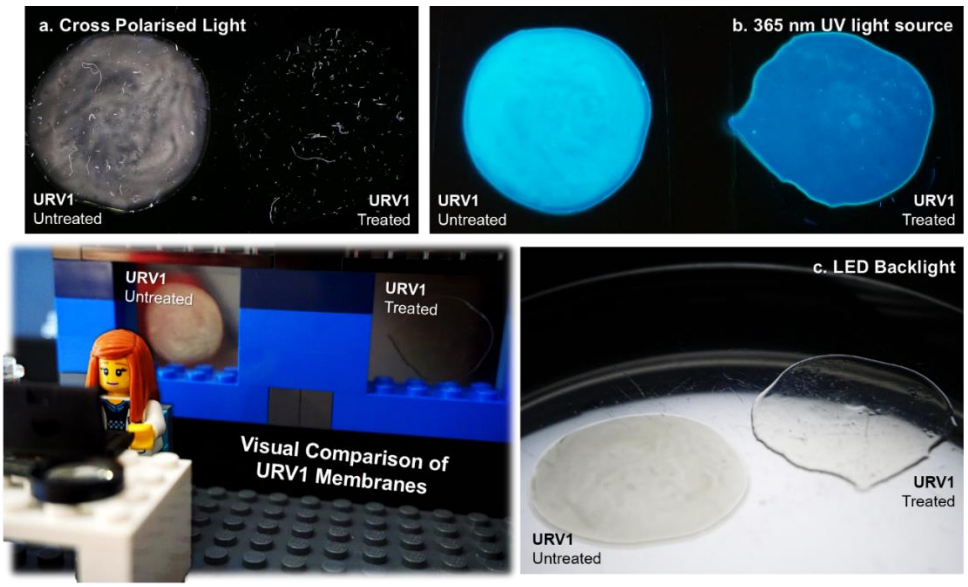

Figure 17: *Visual comparison of* **URV1** *membranes under* ***a)*** *cross polarised light,* ***b)*** *365 nm UV light source and* ***c)*** *LED backlight.*

In order to verify the existence of orientation in the treated membranes, XRD and AFM were carried out. From the XRD analysis of both **URV polymers**, only one broad reflection was observed in all of the diffractograms with peak maxima at 2θ = 1.9 º, d_{100} = 46.5 Å for **URV1** membranes (Figure 18a and 18b) and 2θ = 2.1 º, d_{100} = 42.0 Å for **URV2** membranes (Figure 18c and 18d). If one assumes the limits of the peak to be 2θ = 1.5-3.5 º, the intercolumnar distance would be approximately between 58.8 and 25.2 Å. This means that the columnar domains were poorly defined and very widely distributed which could be an indication that the system is on the way of forming a LC columnar phase. Since it is not yet well defined, it is considerably amorphous. Thus, the membrane appeared transparent upon thermal treatment and black under cross polarised light because the domains are so small and do not scatter light.

With hopes of obtaining a better oriented membrane, a different thermal treatment cycle was attempted on a new piece of **URV1** membrane where it was baked at a much higher temperature (60 ºC) than before (35 ºC). Unfortunately, similar XRD diffractograms with were a broad reflection (2θ = 1.9 º, d_{100} = 46.5 Å) was observed.

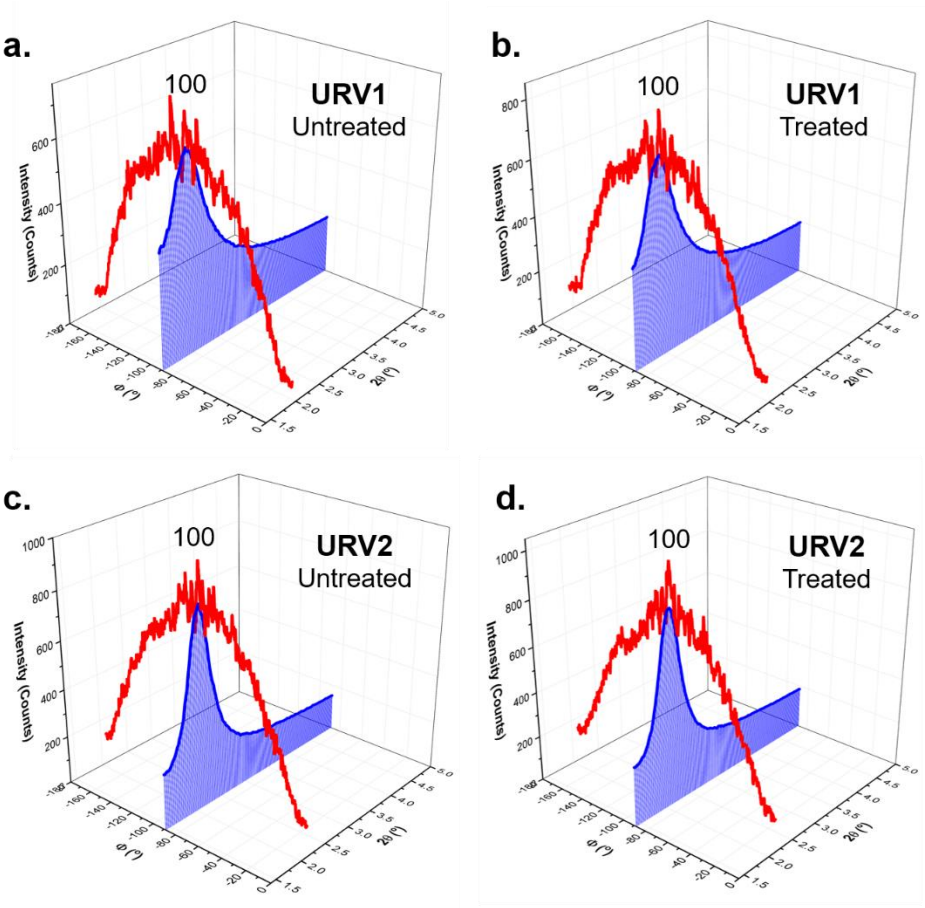

Figure 18: *Comparison of XRD diffractograms (Blue) and azimuthal scan (Red) on the* d_{100} *reflection for thermally treated and untreated* **URV membranes**.

Tapping-mode atomic force microscopy (AFM) was employed for the visualization of surface morphology of the untreated and thermally treated **URV membranes**. From the AFM 3D topography images in Figure 19, the surface morphology of thermally treated **URV membranes** were drastically changed from being bumpy and filled with "voids" (resembling to that of the surface of Mars) to exhibiting closely-packed / clusters of island-like structures. The apparent changes in surface morphology suggested possible orientation of the aromatic / tapered moieties in the polymer backbone. However, unlike homeotropically oriented **HP1** (63 % **TAP** modified **PECH** polymer) membranes reported by Bogdanowicz *et al.*[4], no fingerprint-like pattern was visible from the phase images of thermally treated **URV1** and **URV2** membranes (with 41 % and 49 % **TAP** modification, respectively) thereby ruling out the possibility of homeotropic orientation. The distorted-wave pattern as seen from the topography images of thermally treated **URV membranes** showed non-homogeneity.

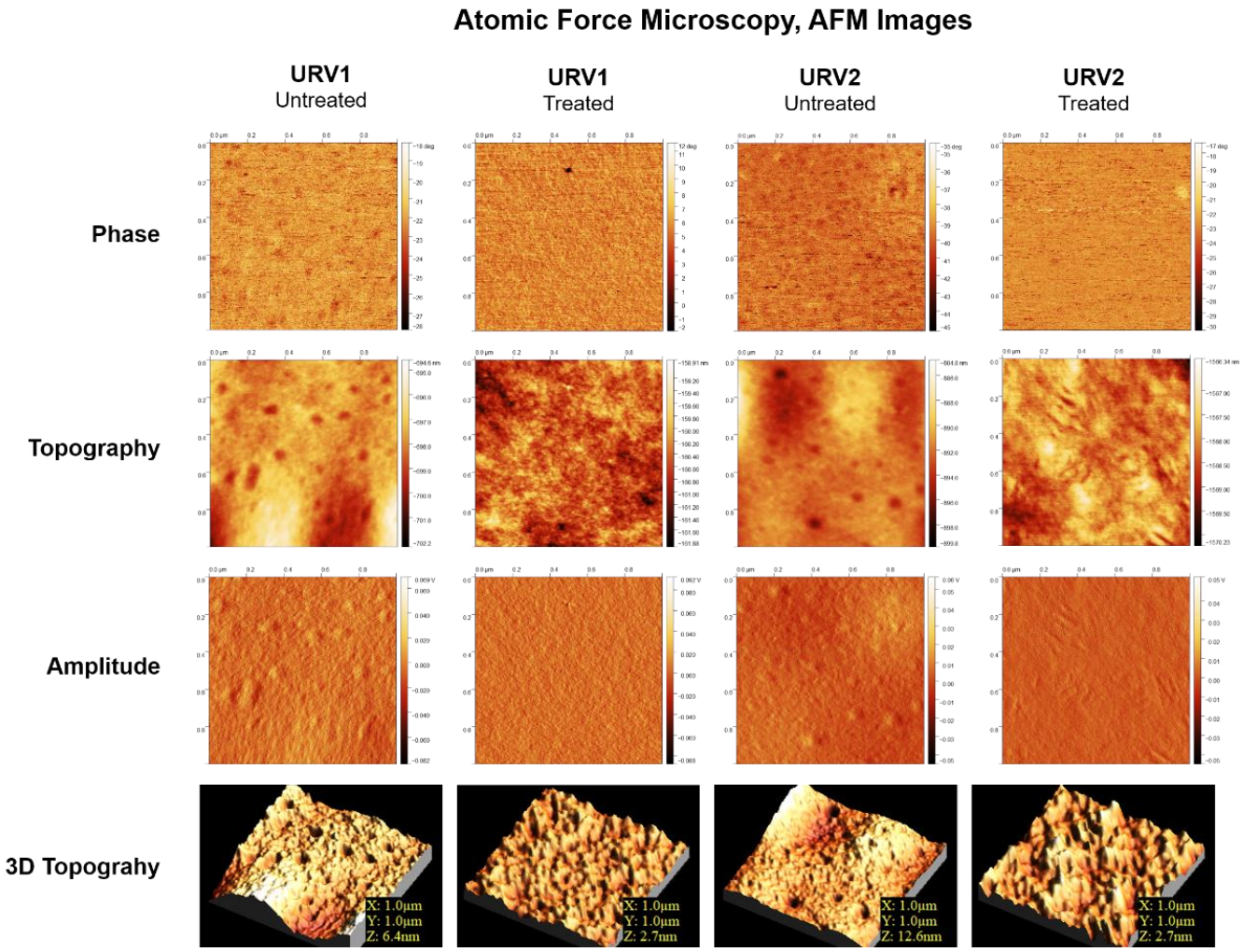

Figure 19: *AFM phase, topography, amplitude and 3D topography images of thermally treated and untreated* **URV membranes***.*

Root-Mean-Squared (RMS) surface roughness on the air side of untreated and thermally treated **URV membranes** were calculated from the topography images as shown in Figure 20a. The RMS values were generally low with similar trend observed between untreated and treated membranes. Untreated **URV1** membrane is slightly smoother (RMS = 0.9 nm) than **URV2** (RMS = 1.3 nm) but upon thermal treatment, both of the treated membranes were smoothened to an RMS value of 0.3 nm.

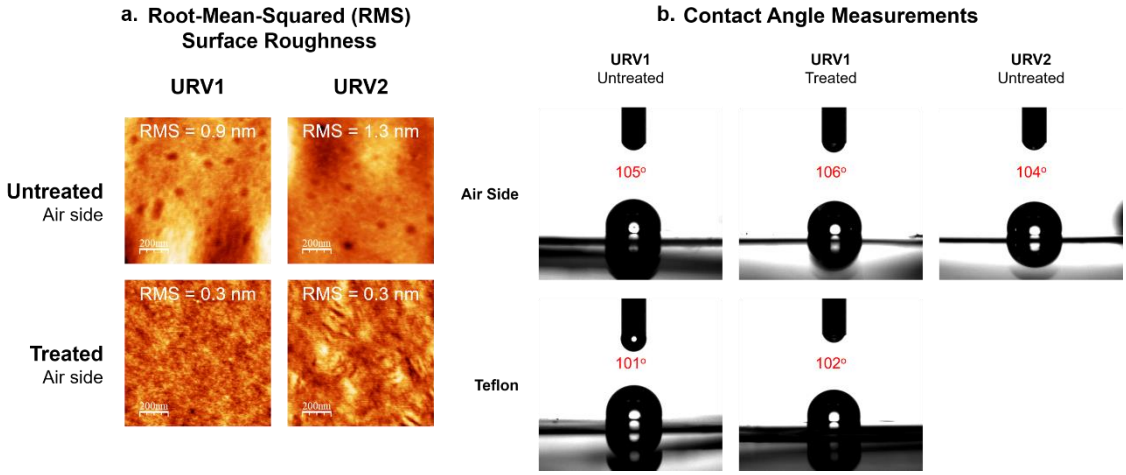

Figure 20: a) *Root-Mean-Squared (RMS) surface roughness and* ***b)*** *contact angle measurements of untreated and thermally treated* **URV membranes** *on its air and Teflon sides.*

Water contact angle measurements were carried out on both air and Teflon sides of untreated and treated **URV1** membranes (Figure 20b). Results show that there were slight discrepancies between the air and Teflon sides which in theory should be consistent as the membranes were thermally treated in a homogeneously heated system. The discrepancies and negligible hydrophobicity changes could also be substantiating factors for the claim of homeotropic orientation being absent in thermally treated **URV** membranes. Thus, although there was a change in local organisation in the thermally treated **URV** membranes, which resulted in a change in surface morphology, RMS and physical appearance under cross polarised light (complete darkness as seen in Figure 17a of the thermally treated **URV1** membrane) is a result of no orientation but is on its way forming a LC columnar phase.

4. Conclusions

In this chapter, six anthracene-bearing **PECH** polymers (**PA Series**) and two others containing **TAP** (**URV Series**) have been successfully synthesised and characterised. The accidental discovery of “Vampire POGs” led to more in-depth organogelation studies via the use of NMR, UV-Vis and fluorescence spectroscopy. It was found that the organogelation phenomenon originated from the photodimerisation of anthracene moieties on the side chain of **PECH**. Upon irradiation under 365 nm UV lamp, photodimers formation acted as crosslinking points, leading to polymer chain entanglement in the form of irreversible gel formation. Thankfully with the incorporation of **TAP**, the anthracene moieties in **URV polymers** were obstructed to an extent where organogelation was prevented. This allowed **URV membranes** to be fabricated via immersion precipitation followed by thermal treatment at a temperature slightly below its T_c. The surface morphology studies (XRD, AFM and contact angle analysis) carried out on **URV membranes** revealed a change in local organisation but not to be mistaken for a change in orientation. This could mean one of two things: i) the thermal treatment conditions used were unsuitable, or ii) the presence of anthracene moieties in **TAP**-containing **PECH** distort the polymer’s ability to exhibit liquid crystallinity. Therefore, for future work, more **URV membranes** with lowered anthracene ratios needed to be synthesised and the thermal treatment conditions of the membranes needed to be optimised before any conclusive statements can be made.

Appendix. Supplementary Information, SI

Supplementary information, SI related to this chapter can be found at the end of this thesis.

References

1 M. Pérez, J. A. Reina, A. Serra and J. C. Ronda, *Acta Polym.*, 1998, **49**, 312–318.

2 T. Nishikubo, T. Shimokawa, T. Fujii, T. Iizawa, Y. Harita and M. Koshiba, *J. Polym. Sci. Part A Polym. Chem.*, 1988, **26**, 2881–2898.

3 X. Han, R. A. Shanks and D. Pavel, *Macromol. Chem. Phys.*, 2004, **205**, 743–751.

4 K. A. Bogdanowicz, S. V. Bhosale, Y. Li, I. F. J. Vankelecom, R. Garcia-Valls, J. A. Reina and M. Giamberini, *J. Memb. Sci.*, 2016, **509**, 10–18.

5 S. MN and C. PR, *Res. Rev. J. Chem.*, **5**, 45–52.

6 M. J. Kory, M. Wörle, T. Weber, P. Payamyar, S. W. van de Poll, J. Dshemuchadse, N. Trapp and A. D. Schlüter, *Nat. Chem.*, 2014, **6**, 779–784.

7 P. Kissel, D. J. Murray, W. J. Wulftange, V. J. Catalano and B. T. King, *Nat. Chem.*, 2014, **6**, 774–778.

8 G. A. Bullen, J. H. R. Tucker and A. F. A. Peacock, *Chem. Commun.*, 2015, **51**, 8130–8133.

9 C. L. Esposito, P. Kirilov and V. G. Roullin, *J. Control. Release*, 2018, **271**, 1–20.

10 T. Ishii, Y. Tezuka, S. Kawamoto and T. Uno, *J. Photochem. Photobiol. A Chem.*, 1994, **83**, 55–62.

11 T. Torii, H. Ushiki and K. Horie, *Polym. J.*, 1992, **24**, 1057–1067.

12 T. Torii, H. Ushiki and K. Horie, *Polym. J.*, 1993, **25**, 173–183.

13 M. Coursan, J. P. Desvergne and A. Deffieux, *Macromol. Chem. Phys.*, 1996, **197**, 1599–1608.

14 D. Liu, D. Wang, M. Wang, Y. Zheng, K. Koynov, G. K. Auernhammer, H.-J. Butt and T. Ikeda, *Macromolecules*, 2013, **46**, 4617–4625.

15 M. Ayabe, T. Kishida, N. Fujita, K. Sada and S. Shinkai, *Org. Biomol. Chem.*, 2003, **1**, 2744.

16 C. Wang, D. Zhang, J. Xiang and D. Zhu, *Langmuir*, 2007, **23**, 9195–9200.

17 S. V. Bhosale, M. A. Rasool, J. A. Reina and M. Giamberini, *Polym. Eng. Sci.*, 2013, **53**, 159–167.

18 V. V. Utochnikova, A. S. Kalyakina, I. S. Bushmarinov, A. A. Vashchenko, L. Marciniak, A. M. Kaczmarek, R. Van Deun, S. Bräse and N. P. Kuzmina, *J. Mater. Chem. C*, 2016, **4**, 9848–9855.

19 X. Montané, K. A. Bogdanowicz, G. Colace, J. A. Reina, P. Cerruti, A. Lederer and M. Giamberini, *Polym. (United Kingdom)*, 2016, **105**, 298–309.

20 A. M. Brouwer, *Pure Appl. Chem.*, 2011, **83**, 2213–2228.

21 R. Zheng, Q. Zhou, H. Gu, H. Jiang, J. Wu, Z. Jin, D. Han, G. Dai and R. Chen, *Tetrahedron Lett.*, 2014, **55**, 5671–5675.

22 S. Méry, D. Haristoy, J.-F. Nicoud, D. Guillon, H. Monobe and Y. Shimizu, *J. Mater. Chem.*, 2003, **13**, 1622–1630.

23 Y.-K. Song, K.-H. Lee, W.-S. Hong, S.-Y. Cho, H.-C. Yu and C.-M. Chung, *J. Mater. Chem.*, 2012, **22**, 1380–1386.

24 S. Karthikeyan and V. Ramamurthy, *Tetrahedron Lett.*, 2005, **46**, 4495–4498.

25 T. Salzillo, E. Venuti, C. Femoni, R. G. Della Valle, R. Tarroni and A. Brillante, *Cryst. Growth Des.*, 2017, **17**, 3361–3370.

26 H. Ihmels, *European J. Org. Chem.*, 1999, **1999**, 1595–1600.

27 H. Fidder, A. Lauer, W. Freyer, B. Koeppe and K. Heyne, *J. Phys. Chem. A*, 2009, **113**, 6289–6296.

28 M. A. Filatov and M. O. Senge, *Mol. Syst. Des. Eng.*, 2016, **1**, 258–272.

29 J. Tanabe, D. Taura, N. Ousaka and E. Yashima, *Org. Biomol. Chem.*, 2016, **14**, 10822–10832.

30 M. Klaper, P. Wessig and T. Linker, *Chem. Commun.*, 2016, **52**, 1210–1213.

31 H. Bouas-Laurent, J.-P. Desvergne, A. Castellan and R. Lapouyade, *Chem. Soc. Rev.*, 2000, **29**, 43–55.

32 R. Bhola, P. Payamyar, D. J. Murray, B. Kumar, A. J. Teator, M. U. Schmidt, S. M. Hammer, A. Saha, J. Sakamoto, A. D. Schlüter and B. T. King, *J. Am. Chem. Soc.*, 2013, **135**, 14134–14141.

33 S. Singh and C. Sandorfy, *Can. J. Chem.*, 1969, **47**, 257–263.

34 Z. Qi, N. L. Traulsen, P. Malo de Molina, C. Schlaich, M. Gradzielski and C. A. Schalley, *Org. Biomol. Chem.*, 2014, **12**, 503–510.

35 J. Catalán, V. López, P. Pérez, R. Martin-Villamil and J.-G. Rodríguez, *Liebigs Ann.*, 1995, **1995**, 241–252.

36 J. R. Jones, C. L. Liotta, D. M. Collard and D. A. Schiraldi, *Macromolecules*, 2000, **33**, 1640–1645.

37 A. Dawn, N. Fujita, S. Haraguchi, K. Sada and S. Shinkai, *Chem. Commun.*, 2009, **0**, 2100.

38 M. Takizawa, A. Kimoto and J. Abe, *Dye. Pigment.*, 2011, **89**, 254–259.

39 D. A. M. Egbe, S. Türk, S. Rathgeber, F. Kühnlenz, R. Jadhav, A. Wild, E. Birckner, G. Adam, A. Pivrikas, V. Cimrova, G. Knör, N. S. Sariciftci and H. Hoppe, *Macromolecules*, 2010, **43**, 1261–1269.

40 T. Hinoue, Y. Shigenoi, M. Sugino, Y. Mizobe, I. Hisaki, M. Miyata and N. Tohnai, *Chem. - A Eur. J.*, 2012, **18**, 4634–4643.

41 Y. Hong, J. W. Y. Lam and B. Z. Tang, *Chem. Commun.*, 2009, **0**, 4332.

42 M. S. A. Abdel-Mottaleb, H. R. Galal, A. F. M. Dessouky, M. El-Naggar, D. Mekkawi, S. S. Ali and G. M. Attya, *Int. J. Photoenergy*, 2000, **2**, 47–53.

43 X. Montané, K. A. Bogdanowicz, J. Prats-Reig, G. Colace, J. A. Reina and M. Giamberini, *Polym. (United Kingdom)*, 2016, **105**, 234–242.

44 A. Sakalyte, *Proton Transport Membranes based on Liquid Crystalline Polymers having Columnar Mesophases,* Universitat Rovira I Virgili, 2013.

45 Y. Xia, F. Serra, R. D. Kamien, K. J. Stebe and S. Yang, *Proc. Natl. Acad. Sci. U. S. A.*, 2015, **112**, 15291–6.

Chapter 5

Synthesis, Characterisation and Binding Studies of Crown Ether Terephthalates

1. Introduction

Terephthalate derivatives are the building blocks that make up the most important polyester to date, polyethylene terephthalate (PET). PET has been known for its robustness, high transparency/flexibility and superior barrier properties[1]. These positive features not only have enabled it to be widely used in commercial applications (e.g. bottles, packaging, thermal insulating materials, etc) but also in research-biased areas such as in rechargeable polymer batteries[2], OLED, solar cells[3], etc. Regardless of the blending of additional agents, the terephthalate core still maintains its structure; making it an ideal core to modify on. Hence, there is no doubt that the actual terephthalate could support other substituents (such as a crown ether) which would bring about additional special properties to the final polymer. Features could include the ability to transport ions and fluorescence-based remote sensing which would be of interest for potential applications in proton transporting membranes. The questions of interest would be could crown ether channels form within a polymer? Would the bulky aryl groups control any polymer morphology? What fluorescent properties might the polymer possess?

To answer these questions a novel crown ether monomer, **CM1** and its dimer, **CM1a** were firstly synthesised from a moderately intense fluorescent terephthalate core[4], **I3**. **CM1** displayed fluorescence both in solution and in the solid state. Much to our surprise, not only did the crystal structure of **CM1** resembled the shape of a jellyfish, so does its bluish fluorescence when it's dissolved in $CHCl_3$. Better still, its asymmetric unit is exactly half the molecule!

By employing several analytical techniques such as NMR, UV and fluorescence spectroscopy, cation and proton binding studies of **CM1** have been carried out. Selective cation interaction of **CM1** with K^+ ions were observed. A relatively low binding constant, K_a of **CM1** towards protons suggests that any interaction is weak which may be an advantage when being incorporated into a polymer.

In this chapter, the synthesis and characterisations of **CM1** and **CM1a** will be discussed in addition to the computational modelling and binding studies of **CM1**.

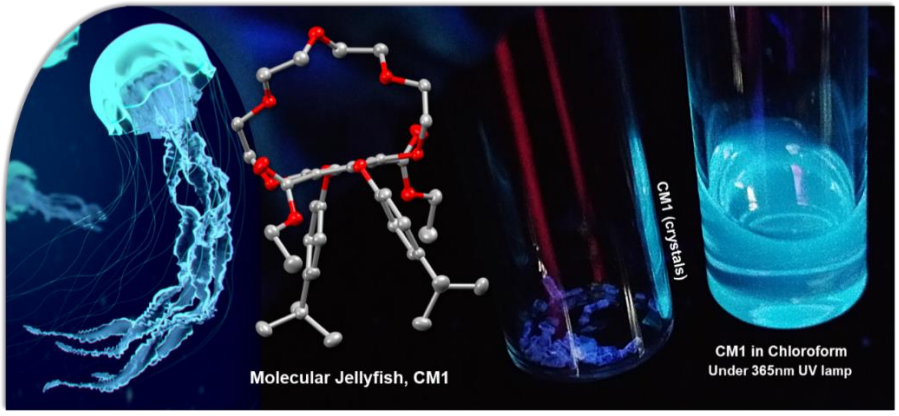

2. Experimental

2.1 Materials

Reagents and solvents were bought from commercial suppliers at the highest purity possible and were used without further purification unless otherwise specified. Diethyl-2,5-dihydroxyterephthalate (97 %), bromine (≥ 99.5 %), 4-tertbutylphenol (99+ %), pyridine (99.8 %) and zinc (purum, powder) were supplied by Sigma Aldrich. **TetraEGdiOTs** was synthesised by procedures reported in Chapter 3. Anhydrous DCM and MeCN were both dried under calcium hydride in respective solvent stills and were distilled before use.

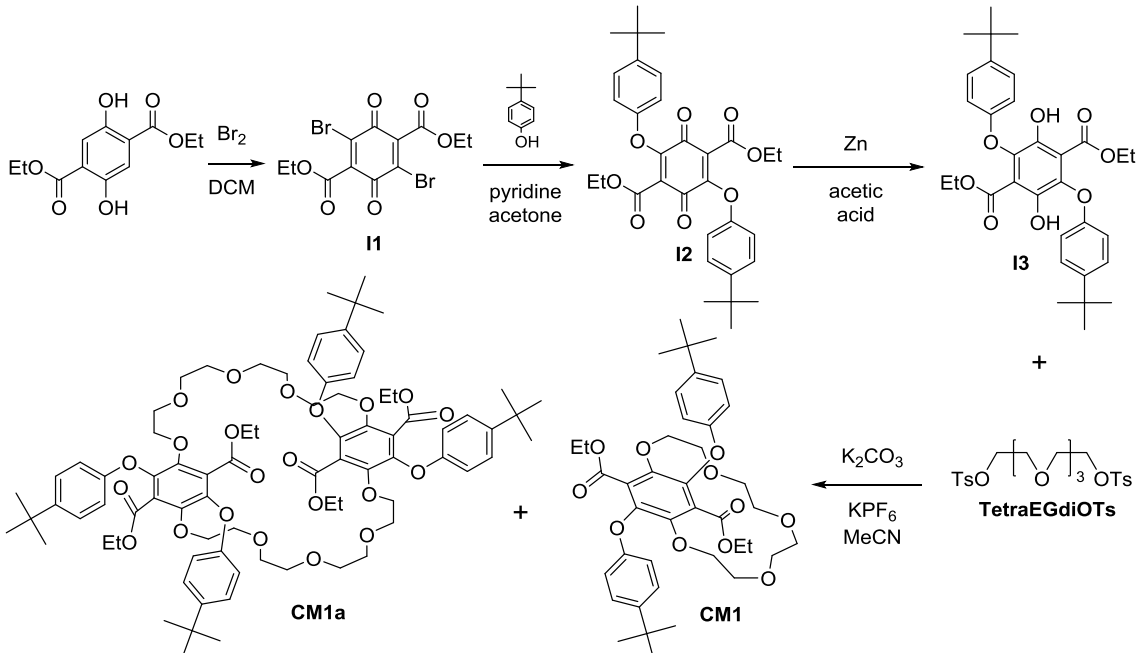

Scheme 1: *Preparation of* **CM1** *and* **CM1a***.*

2.2 Synthesis of Crown Ether, **CM1**

2.2.1 Synthesis of Intermediate, **I1**

Br_2 (5.5 mL, 107.3 mmol, excess) was added dropwise to diethyl-2,5-dihydroxyterephthalate (8.6 g, 33.8 mmol) pre-dissolved in DCM (200 mL). The reaction mixture was left to stir at RT for 30 hours with TLC monitoring. Upon completion, the reaction mixture was washed with sat. $NaHSO_3$ solution followed by H_2O until the aqueous layer changed colour from reddish brown to colourless. The combined organic layer was dried over $MgSO_4$ and the solvent was removed under reduced pressure. The yellow crude was recrystallized from hot EtOH (100 mL) and HNO_3 (1.8 mL) to yield fine yellow needle-like crystals (9.26 g, 22.6 mmol, 67 %).

^{1}H NMR (300 MHz, Chloroform-*d*) δ 4.45 (q, *J* = 7.1 Hz, 4H, H1), 1.39 (t, *J* = 7.1 Hz, 6H, H2).

The ^{1}H NMR spectrum of the purified product was consistent with the literature data[4].

2.2.2 Synthesis of Intermediate, **I2**

I1 (6.4 g, 15.6 mmol), 4-tert-butylphenol (4.7 g, 31.2 mmol) and pyridine (6.3 mL, 77.9 mmol) were dissolved in acetone (170 mL). The reaction mixture was refluxed for 3 hours with TLC monitoring. The reaction mixture was then washed with 15% $CuSO_4$ solution until the blue colour of the solution no longer changed to a darker blue colour as a result of formation of the $CuSO_4$ – pyridine complex. The combined organic layer was washed with H_2O and was dried over $MgSO_4$. The solvent was removed under reduced pressure. The reddish orange crude was recrystallized with hot EtOH to yield orangey yellow needle-like crystals (8.07 g, 14.7 mmol, 94 %).

^{1}H NMR (300 MHz, Chloroform-*d*) δ 7.34 (d, *J* = 8.9 Hz, 4H, H4), 6.99 (d, *J* = 8.9 Hz, 4H, H3), 3.91 (q, *J* = 7.2 Hz, 4H, H1), 1.30 (s, 18H, H5), 1.15 (t, *J* = 7.2 Hz, 6H, H2).

The ^{1}H NMR spectrum of the purified product was consistent with the literature data[4].

2.2.3 Synthesis of Intermediate, **I3**

Acetic acid (125 mL) was added to a flask containing **I2** (8.0 g, 14.6 mmol) and Zn powder (1.9 g, 29.1 mmol, excess). The reaction mixture was sonicated for 1 hour before it was left to stir at RT overnight with TLC monitoring. The reaction mixture was filtered to remove Zn powder. The reaction mixture was diluted with DCM before it was washed with sat. $NaHCO_3$ solution. The neutralisation was stopped when no effervescence was observed during washing. The combined organic layer was dried over $MgSO_4$ and the solvent was removed under reduced pressure. The crude was recrystallized in from EtOH to yield yellow needle-like crystals (7.88 g, 14.3 mmol, 98 %).

^{1}H NMR (300 MHz, Chloroform-*d*) δ 10.21 (s, 2H, H6), 7.32 – 7.27 (m, 4H, H4), 6.81 – 6.74 (m, 4H, H3), 4.22 (q, *J* = 7.1 Hz, 4H, H1), 1.29 (s, 18H, H5), 0.99 (t, *J* = 7.1 Hz, 6H, H2).

The ^{1}H NMR spectrum of the purified product was consistent with the literature data[4].

2.2.4 Synthesis of Crown Ether, **CM1**

Anhydrous DCM (150 mL) was added to a flask (F1) containing **I3** (6.2 g, 11.3 mmol) and **TetraEGdiOTs** (5.7 g, 11.3 mmol) under N_2. In a separate flask (F2), anhydrous MeCN (50 mL) was added to K_2CO_3 (4.7 g, 34.0 mmol) and KPF_6 (3.1 g, 16.8 mmol). F2 was heated to reflux and was kept under N_2. The solution in F1 was then added dropwise to F2 via a syringe pump over 3 days. The reaction mixture was vigorously stirred for another 6 days under N_2 and reflux conditions. The flasks were both covered in aluminium foil throughout the 9-days-long reaction with TLC monitoring. At day 9, the reaction mixture was cooled to RT and the suspension was filtered and washed with DCM. The filtrate was dried under reduced pressure. The resulting residue was re-dissolved with DCM and washed with H_2O. The combined organic layer was rapidly flushed through a silica plug with DCM as eluent and gradually switched to EA. All of the flushes were combined and dried under reduce pressure to yield a viscous oil. The crude

material was then dry packed into a silica column with DCM and was eluted with petroleum ether : EA (5 : 1), slowly increasing the ratio to 4 : 1. From the viscous oil, several products (**CM1** and **CM1a**) were isolated and identified. The isolated **CM1** was recrystallized from hot MeOH (1 mg **CM1** in 0.4 mL hot MeOH) to yield pure **CM1** (0.80 g, 1.1 mmol, 10 %) in the form of sugar-like rectangular crystals while **CM1a** (1.60 g, 1.1 mmol, 19 %) was isolated as a viscous oil.

CM1

^{1}H NMR (700 MHz, Chloroform-*d*) δ 7.29 – 7.26 (m, 4H, H8), 6.86 – 6.83 (m, 4H, H7), 4.73 (ddd, *J* = 13.0, 9.0, 1.3 Hz, 2H, H1, H1'), 4.17 (dq, *J* = 10.9, 7.1 Hz, 2H, H5), 4.05 (dq, *J* = 10.9, 7.1 Hz, 2H, H5), 3.93 (ddd, *J* = 13.1, 3.5, 1.5 Hz, 2H, H1, H1'), 3.76 (ddd, *J* = 10.7, 9.1, 1.5 Hz, 2H, H2, H2'), 3.67 – 3.63 (m, 4H, H4, H4', H2, H2'), 3.61 (ddd, *J* = 10.0, 5.7, 2.2 Hz, 2H, H3, H3'), 3.51 (ddd, *J* = 11.8, 5.8, 2.2 Hz, 2H, H4, H4'), 3.47 (ddd, *J* = 9.3, 6.7, 2.2 Hz, 2H, H3, H3'), 1.28 (s, 18H, H9), 0.99 (t, *J* = 7.1 Hz, 6H, H6).

^{13}C NMR (176 MHz, $CDCl_3$) δ 164.50 (C16), 155.33 (C12), 145.08 (C11,C15), 140.79 (C13), 126.28 (C8), 125.93 (C14), 115.13 (C7), 72.13 (C2,C2'), 71.98 (C3,C3'), 71.60 (C1,C1'), 70.90 (C4,C4'), 61.58 (C5), 34.32 (C10), 31.66 (C9), 13.88 (C6).

FT-IR (ν_{max}, cm^{-1}) 2956 (asymmetric C-H stretching vibration from -CH_2-, -CH_3), 1737 (aromatic ester C=O stretching vibration), 1507 (aromatic C=C stretching vibration), 1212, 1179 (aromatic ester C-O stretching vibrations), 838, 811 (aromatic C-H out of plane bending vibrations).

(+)nanoESI-FTMS (m/z): found $[M+K]^+$ 747.3126, calcd. for $C_{40}H_{52}O_{11}K$: 221.0608 and $[M+NH_4]^+$ 726.3834, calcd. for $C_{40}H_{56}O_{11}N$: 726.3848.

X-ray crystal structure (Figure 9) and refinement data (Table 1) available in SI.

CM1a

^{1}H NMR (700 MHz, Chloroform-*d*) δ 7.28 – 7.24 (m, 8H, H8), 6.85 – 6.81 (m, 8H, H7), 4.19 (t, *J* = 5.4 Hz, 8H, H1), 4.12 (q, *J* = 7.1 Hz, 8H, H5), 3.57 (t, *J* = 5.3 Hz, 8H, H2), 3.51 – 3.46 (m, 16H, H3, H4), 1.28 (s, 36H, H9), 1.03 (t, *J* = 7.1 Hz, 12H, H6).

^{13}C NMR (176 MHz, $CDCl_3$) δ 163.85 (C16), 155.51 (C12), 145.41 (C15), 145.23 (C11), 141.69 (C13), 126.66 (C14), 126.31 (C8), 115.22 (C7), 73.07 (C1), 70.73, 70.61 (C3,C4), 69.99 (C2), 61.78 (C5), 34.33 (C10), 31.66 (C9), 13.92 (C6).

FT-IR (ν_{max}, cm^{-1}) 2960 (asymmetric C-H stretching vibration from -CH_2-, -CH_3), 1733 (aromatic ester C=O stretching vibration), 1507 (aromatic C=C stretching vibration), 1212, 1177 (aromatic ester C-O stretching vibrations), 836, 815 (aromatic C-H out of plane bending vibrations).

(+)nanoESI-FTMS (m/z): found $[M+NH_4]^+$ 1434.7349, calcd. for $C_{80}H_{108}O_{22}N$: 1434.7358.

2.3 Characterisation

2.3.1 Nuclear Magnetic Resonance (NMR) Spectroscopy

^{1}H NMR spectra of intermediates **I1**, **I2** and **I3** in deuterated chloroform ($CDCl_3$) were recorded on Bruker Avance III 300 MHz whilst ^{1}H and ^{13}C NMR spectra of **CM1** and **CM1a** in deuterated chloroform ($CDCl_3$) were recorded on Bruker Avance III 700 MHz. 2D NMR such as ^{1}H-^{1}H correlation (COSY), ^{1}H-^{13}C heteronuclear single quantum correlation (HSQC), ^{1}H-^{13}C heteronuclear multiple bond correlation (HMBC) were used to substantiate ^{1}H and ^{13}C NMR assignments of the synthesised compounds.

2.3.2 FT-IR Spectroscopy

FT-IR spectra were obtained using Spectrum Two FT-IR Spectrometer fitted with a diamond crystal plate ATR unit (PerkinElmer).

2.3.3 Mass Spectrometry

Mass spectrometry analyses of the newly synthesised products were performed on a Thermo Scientific LTQ Orbitrap XL spectrometer equipped with an Advion NanoMate inlet in positive ionisation mode by the team at EPSRC UK National Mass Spectrometry Facility, Swansea University.

2.3.4 X-ray Crystallography

Crystal structure data for **CM1** was collected on a Xcalibur, Atlas, Gemini ultra diffractometer equipped with an fine-focus sealed X-ray tube ($\lambda_{CuK\alpha}$ = 1.54184 Å)

and an Oxford Cryosystems CryostreamPlus open-flow N_2 cooling device. Cell refinement, data collection and data reduction were undertaken via software CrysAlisPro 1.171.38.42b (Rigaku OD, 2015). Intensities were corrected for absorption using CrysAlisPro 1.171.38.42b (Rigaku Oxford Diffraction, 2015) Empirical absorption correction using spherical harmonics, implemented in SCALE3 ABSPACK scaling algorithm.

The structure was solved using XT (Sheldrick, 2015) and refined by XL (Sheldrick, 2008) through the Olex2 interface (Dolomanov, 2009),

2.3.5 Spectroscopy

All solvents used for UV-Vis and fluorescence experiments were bought at the highest available grade and their purity were checked before the experiments.

UV-Vis Experiments

Absorption spectra were recorded using Shimadzu UV-1800 UV-Vis Spectrophotometer. Samples were dissolved in spectroscopic grade solvent in a 1 cm by 1 cm quartz cuvette. Baseline was corrected prior to measurements.

Fluorescence Experiments

Fluorescence emission and excitation spectra were recorded using a Shimadzu RF-6000 Spectrofluorophotometer. Measurements were repeated several times at varying concentrations and excitation wavelengths.

3. Results and discussion

3.1 Synthesis of Crown Ether, **CM1** *and its Dimer,* **CM1a**

The high dilution method, often employed for the preparation of macrocycles, was used in the synthesis of crown ether, **CM1** to promote cyclisation over polymer chain formation. As shown in Scheme 1, **CM1** was synthesised via cyclisation of **I3** and **TetraEGdiOTs** with the use of K_2CO_3 as a base and KPF_6 as a templating agent. Although **I3** has previously been reported[4], slightly improved reaction conditions and work-up procedures have been used (Section 2.2). The two main products **CM1** and its dimer, **CM1a** were isolated and characterised via 2D NMR spectroscopy, FT-IR, mass spectrometry and where possible, X-ray

crystallography. With the help of 2D NMR spectra (SI), all of the ^{1}H and ^{13}C peaks of **CM1** and **CM1a** were successfully assigned.

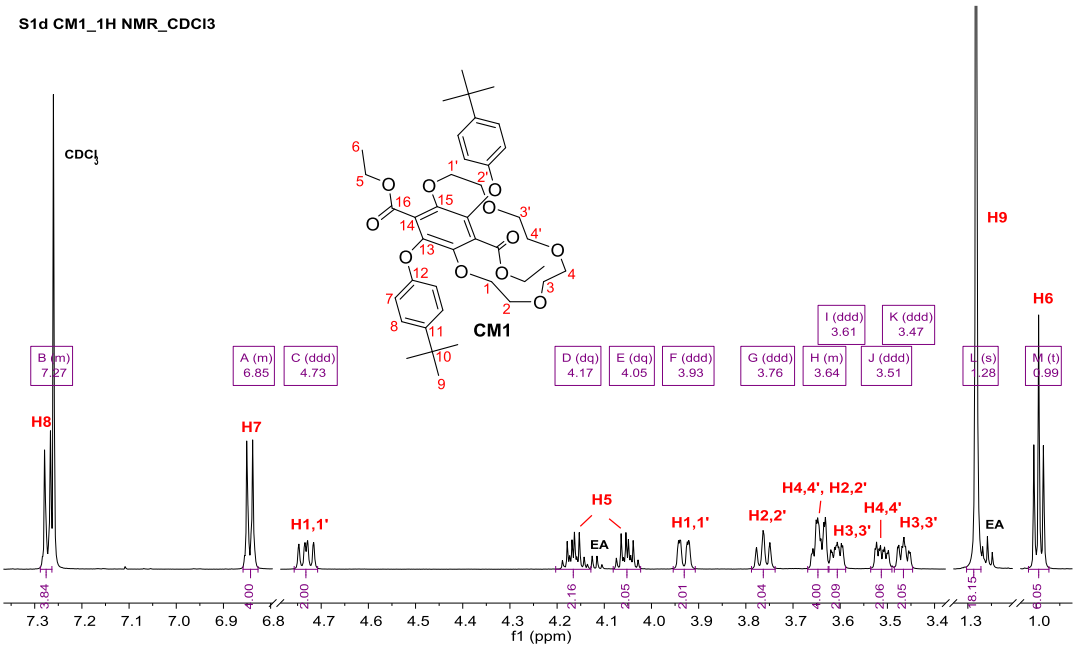

^{1}H NMR (700 MHz, Chloroform - *d*) δ 7.29 – 7.26 (m, 4H, H8), 6.86 – 6.83 (m, 4H, H7), 4.73 (ddd, *J* = 13.0, 9.0, 1.3 Hz, 2H, H1, H1'), 4.17 (dq, *J* = 10.9, 7.1 Hz, 2H, H5), 4.05 (dq, *J* = 10.9, 7.1 Hz, 2H, H5), 3.93 (ddd, *J* = 13.1, 3.5, 1.5 Hz, 2H, H1, H1'), 3.76 (ddd, *J* = 10.7, 9.1, 1.5 Hz, 2H, H2, H2'), 3.67 – 3.63 (m, 4H, H4, H4', H2, H2'), 3.61 (ddd, *J* = 10.0, 5.7, 2.2 Hz, 2H, H3, H3'), 3.51 (ddd, *J* = 11.8, 5.8, 2.2 Hz, 2H, H4, H4'), 3.47 (ddd, *J* = 9.3, 6.7, 2.2 Hz, 2H, H3, H3'), 1.28 (s, 18H, H9), 0.99 (t, *J* = 7.1 Hz, 6H, H6).

Figure 1: *^{1}H NMR spectrum (700 MHz, $CDCl_3$) of* **CM1**.

The ^{1}H NMR spectrum of **CM1** as shown in Figure 1 is more complicated than a reported structure with a similar strained crown core[5], with prominent multiplet signals around 3.94-3.45 ppm and 4.73 ppm attributed to the OCH_2 protons of the crown ether. By careful inspection of the proton correlations in the COSY NMR spectrum of **CM1** (Figure 2), the two H1 protons and two of that of H1' appeared diastereotropic with one of each protons corresponding to that of a doublet of a doublet of a doublet at 4.73 ppm, more downfield than the other at 3.93 ppm. Similarly, one proton each from H2 and H2' appeared slightly downfield (3.76 ppm) than the other at 3.64 ppm which happened to overlap with a pair of protons from H4 and H4'. The remaining pair of protons from H4 and H4' appeared at 3.51 ppm. Protons from H3 and H3' also appeared at two separate peaks (3.61 ppm and 3.47 ppm) which correlate with peaks of H4 and H4'.

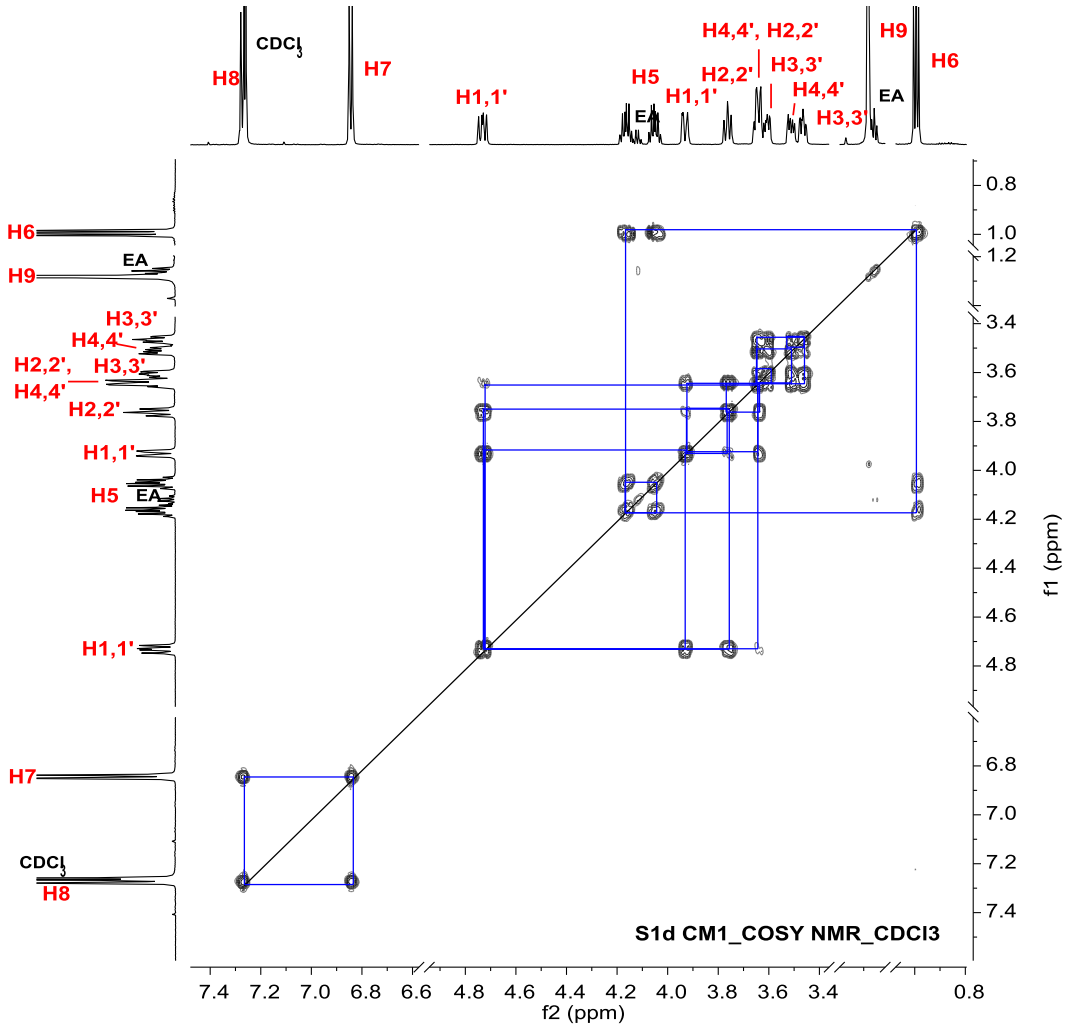

Figure 2: *COSY NMR spectrum (700 MHz, $CDCl_3$) of* **CM1**.

Interestingly, two sets of complex mirroring multiplets (4.17 and 4.05 ppm – H5) were seen correlated to the triplet (H6) at 0.99 ppm. This was due to slowly interconverting conformers of **CM1** which imparted inequivalence to the CH_2 protons on the ethyl ester groups. Similar observation has been reported[4] which has given the inspiration to some possible conformations shown in Figure 4.

To make it easier for the visualisation of conformers, both the wedge-dash diagram and its corresponding crystal XRD structure of **CM1** were displayed side by side as shown in Figure 3, with the inequivalent CH_2 protons (H_a and H_b) colour coded. If you imagine a piece of paper lying parallel on top of the central benzene ring, any structures appearing above it like the crown ether chain would be represented by a wedge whilst any structures appearing below it would be represented by a dash. One thing to note would be that the crown ether chain in all of the proposed conformers in Figure 4 will be 'locked' at the wedged position.

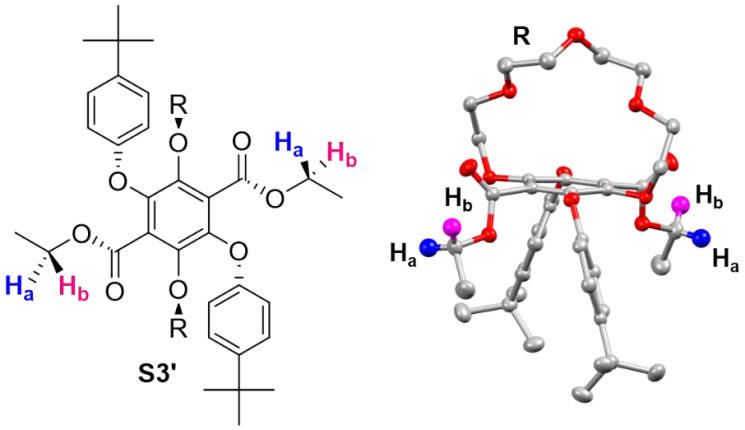

Figure 3: *Crystal XRD structure of* **CM1** *(Hydrogen H_a and H_b were labelled with colours to ease comparison) and its corresponding wedge-dash diagram.*

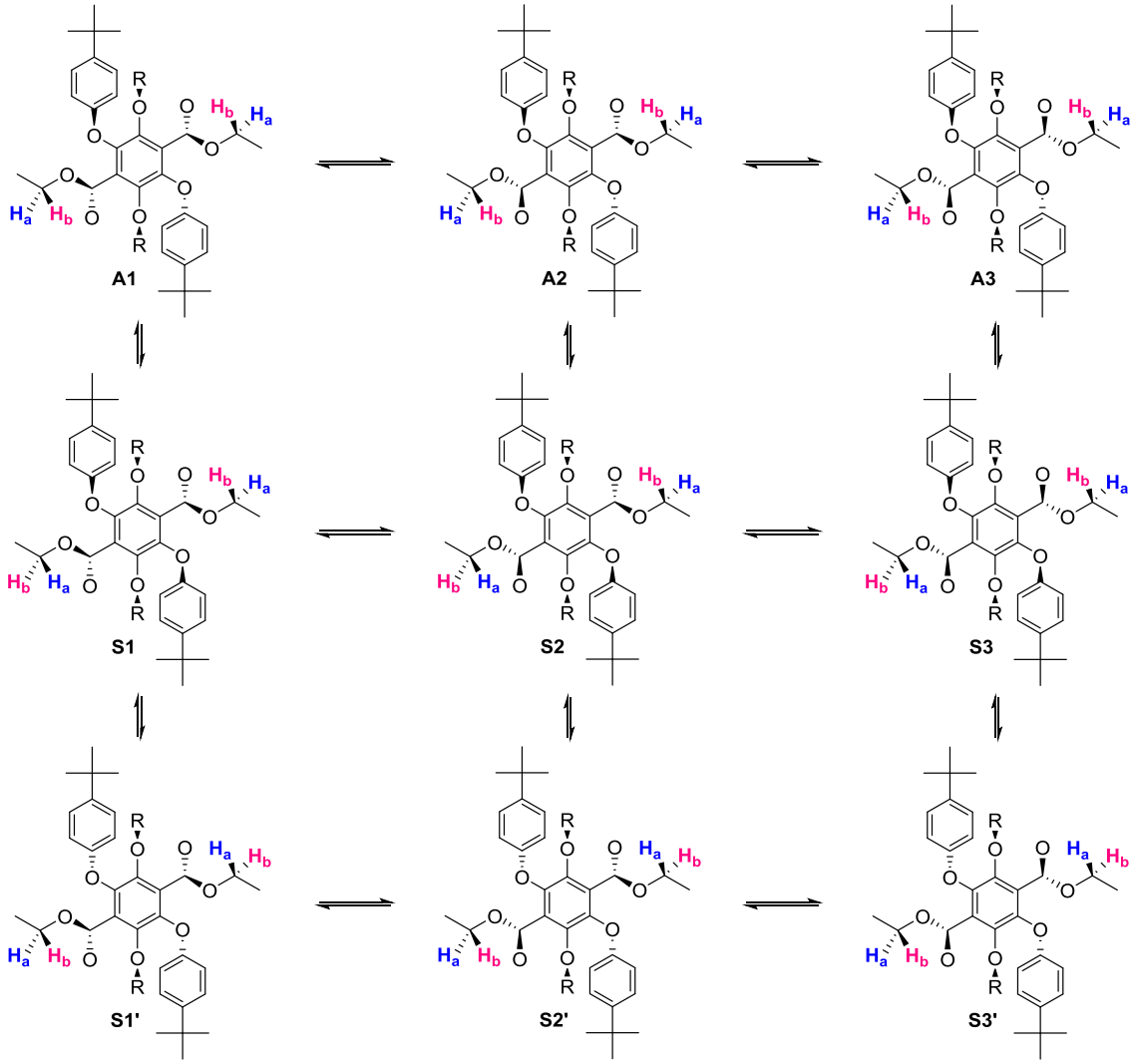

Figure 4: *Possible conformations for* **CM1** *depending on the 'Up-Up' (Syn) and 'Up-Down' (Anti) arrangements of the two aryl groups and the two ester groups*

(the ester C=O bond was replaced with wedge-dash to reflect a twist at the carbonyl carbon; the crown ether alkyl chain was replaced with **R** *for clarity).*

In Figure 4, the three conformers from the first row contain 'anti' arrangements of the two aryl groups while the six conformers from the second and third rows were all 'syn' with wedges for the former three and dash for the latter three. Viewing by columns, the first and third column consist of conformers with 'syn' arrangements of the two ester groups (wedges for the former, dash for the latter) whereas the second column consist of conformers with 'anti' arrangements of the two ester groups. All these variations gave a total of 9 interconvertible conformers which are possible for **CM1** depending on its relative orientation of the aryl groups and ester groups.

The presence of bulky crown ether chain (labelled R) spanning on top of the central core has restricted the rotation of the aryl and ester groups. This locks the groups on one or the other side of the plane causing H_a and H_b to lie in different environments, resulting in inequivalence as shown by the two doublets of quartets in the ^{1}H NMR of **CM1** (Figure 1).

Variable temperature ^{1}H NMR spectra and their corresponding COSY correlations, were highly informative of changes to the conformation of **CM1** in deuterated toluene. Hence, a selection of spectra focusing on the crown ether chain region ranging from 183 K to 373 K are shown in Figure 5. As the temperature increased, most of peaks were shifted upfield except for both the H2,2' peaks which shifted downfield. Apart from the shift in peaks, no coalescence of the two methylene multiplets or the diastereotropic CH_2 protons were observed when the temperature was increased. However, there is a loss in resolution when the temperature was lowered to 183 K.

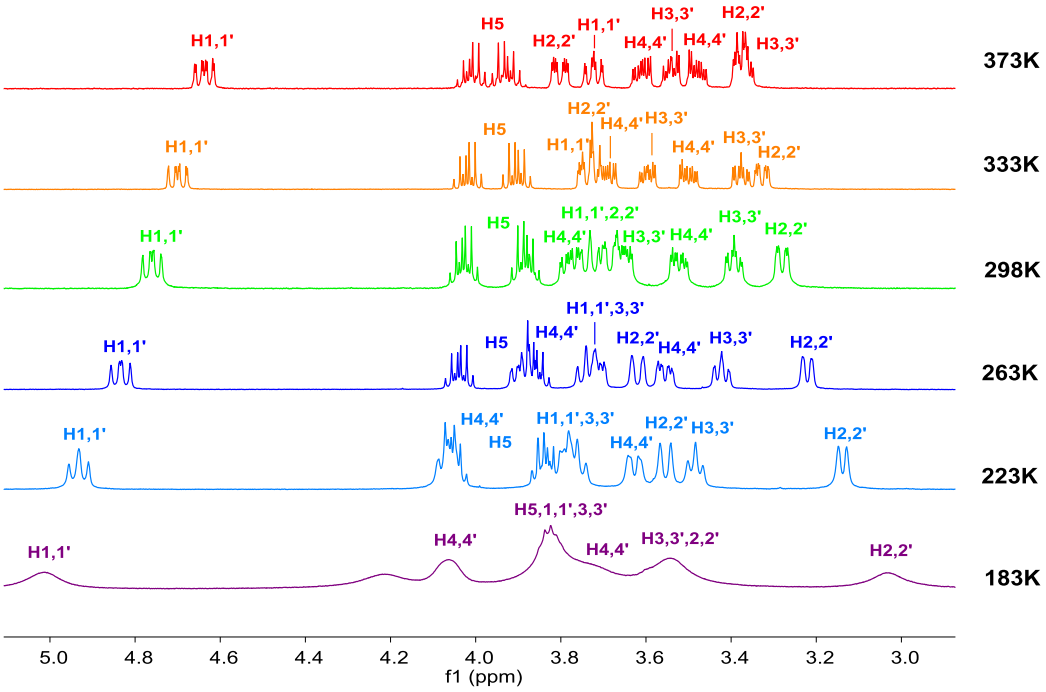

Figure 5: *Selected variable temperature ^{1}H NMR spectra (500 MHz, Toluene-d_8) of* **CM1** *between 183 K and 373 K highlighting the methylene proton region.*

Unlike **CM1**, its dimer, **CM1a** has a very straightforward ^{1}H NMR spectrum (Figure 6) which tallies with a reported structure with a similar crown ether dimer core and ethyl ester groups[6]

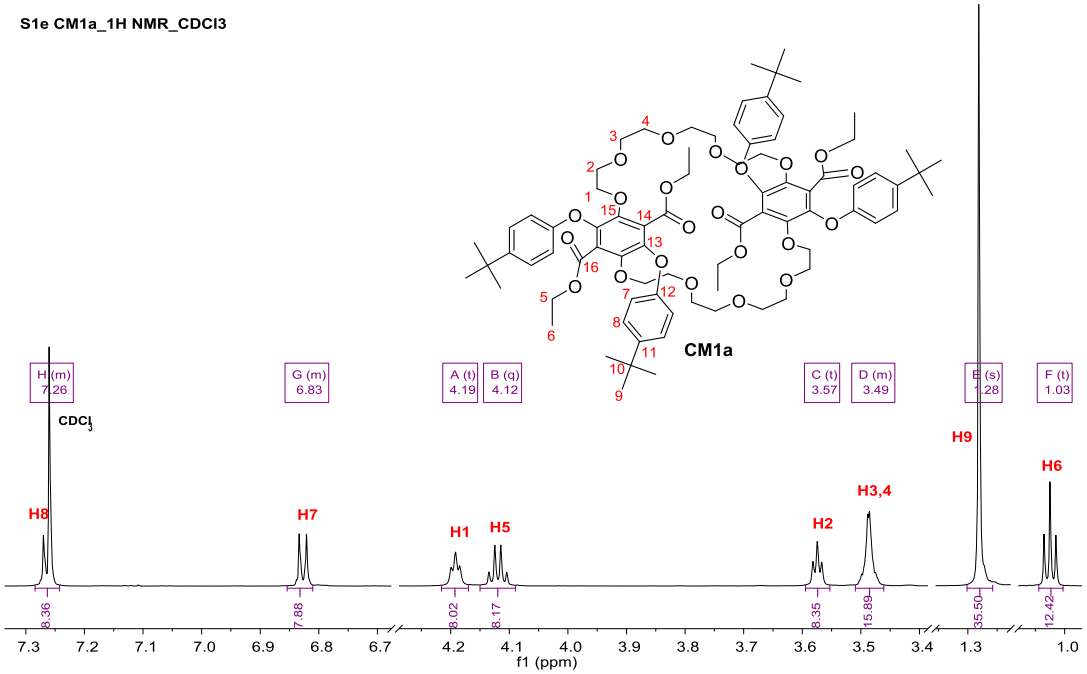

^{1}H NMR (700 MHz, Chloroform - *d*) δ 7.28 – 7.24 (m, 8H, H8), 6.85 – 6.81 (m, 8H, H7), 4.19 (t, *J* = 5.4 Hz, 8H, H1), 4.12 (q,*J* = 7.1 Hz, 8H, H5), 3.57 (t, *J* = 5.3 Hz, 8H, H2), 3.51 – 3.46 (m, 16H, H3, H4), 1.28 (s, 36H, H9), 1.03 (t, *J* = 7.1 Hz, 12H, H6).

Figure 6: *^{1}H NMR spectrum (700 MHz, $CDCl_3$) of* **CM1a**.

The H1, H2, H3 and H4 protons belonging to the OCH_2 protons of **CM1a** appeared at 4.19, 3.57 and 3.49 ppm, respectively. The CH_2 protons of the ethyl ester groups appeared as a quartet at 4.12 ppm whilst its CH_3 protons appeared as a triplet at 1.03 ppm.

Mass spectrometry was employed for the further corroboration of **CM1** and **CM1a**. The positive nanoESI of **CM1** (Figure 6 – SI) showed the presence of $[M+K]^+$ species at m/z = 747.3126 (in DCM/MeOH + KOAc) and $[M+NH_4]^+$ species at m/z = 726.3848 (in DCM/MeOH + NH_4OAc). As for CM1a (Figure 7 – SI), the positive nanoESI showed the presence of $[M+NH_4]^+$ species at m/z = 1434.7349 (in DCM/MeOH + NH_4OAc). All three mass spectra matched their corresponding theoretical isotope model within a mass error of 2 ppm.

When comparing the FT-IR spectra (Figure 8 – SI) of **I3**, **CM1** and **CM1a**, a distinct shift from 1661 cm^{-1} (**I3**) to 1737 cm^{-1} (**CM1**) and 1733 cm^{-1} (**CM1a**) can be observed in the peak corresponding to the characteristic ester carbonyl group C=O stretching vibration. This can be attributed to the successful cyclisation on the 2, 5 positions of the terephthalate core (**CM1** and **CM1a**) which used to be two hydroxyl groups (**I3**) that were capable of forming intramolecular hydrogen bonds with the carbonyl oxygen.

As a result of their drastically different physical properties where **CM1** is a crystalline solid while **CM1a** is an oil, X-ray crystallography was used for the unequivocal identification of **CM1**. The crystal structure of **CM1** as shown in Figure 7 has an asymmetric unit that is half of its molecule. Selected bond lengths and angles from the X-ray crystal structure of **CM1** were reported in Table 1.

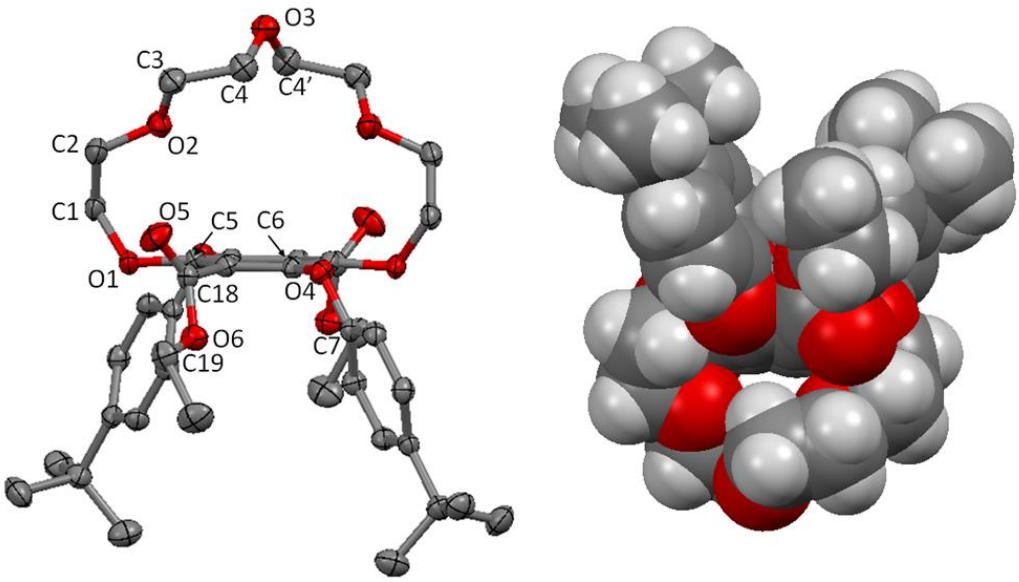

Figure 7: *X-ray crystal structure of* **CM1** *with selected atom labelling (left) and a space-filling model (right).*

Atoms	Bond Length / Å	Atoms	Angle / º
O1-C1	1.4459(18)	**C5-O1-C1**	116.84(10)
O1-C5	1.3760(16)	**C3-O2-C2**	113.70(11)
O2-C2	1.4211(18)	**C4-O3-C4**	115.93(17)
O2-C3	1.421(2)	**C6-O4-C7**	117.64(10)
O3-C4	1.4240(18)	**C18-O6-C19**	117.35(11)
O4-C6	1.3892(17)	**O1-C1-C2**	112.25(13)
O4-C7	1.3932(17)	**O2-C2-C1**	107.81(12)
O5-C18	1.1982(18)	**O2-C3-C4**	109.09(12)
O6-C18	1.3349(18)	**O3-C4-C3**	113.32(13)
O6-C19	1.4553(17)	**O5-C18-O6**	124.87(13)

Table 1: *Selected bond length and angles for X-ray crystal structure of* **CM1***.*

3.1.1 Cation Binding Studies of CM1

Based on **CM1**'s crystal structure (Figure 7 – left), the crown ether moiety appeared unobstructed as the two bulky tert-butyl aryl groups pointed away from its cavity and are located syn to one another. However, when viewed as the space-filling model (Figure 7 – right), the alkoxy chain spanning across the aromatic ring appeared to be blocked up. This gave rise to the question of whether the cavity would be big enough for any cation fit in it. Upon performing a

structural database search on ConQuest, no other x-ray crystal structure of compounds with similar features to **CM1** could be found, let alone ones with a bound cation in its cavity.

To our surprise, the ^{1}H NMR spectra of **CM1** recorded in CD_3OD in the absence and presence of K^+ ions (KPF_6) did show subtle differences as shown in Figure 8. Small downfield shifts and changes in splitting patterns were observed from the OCH_2 protons on the alkoxy chain but the aromatic protons (H7 and H8) and the CH_3 protons of the ethyl ester groups (H6) remained unchanged. This may potentially be attributed to some cation-crown interaction whereby the K^+ ion does not necessarily bind within the cavity but may reside at the periphery of the crown and interact with the oxygen atoms on the alkoxy chain. This would explain the positive nanoESI mass spectrometry results of **CM1** for the presence of $[M+K]^+$ species. The unique interaction of a K^+ ion with **CM1** in CD_3OD was later found to be selective as all the other cation salts ($LiPF_6$, $NaPF_6$ and NH_4PF_6) revealed no changes or shifts in the ^{1}H NMR signals. Since all the salts used were hexafluorophosphate salts, any anion interaction with the crown ether can be ruled out.

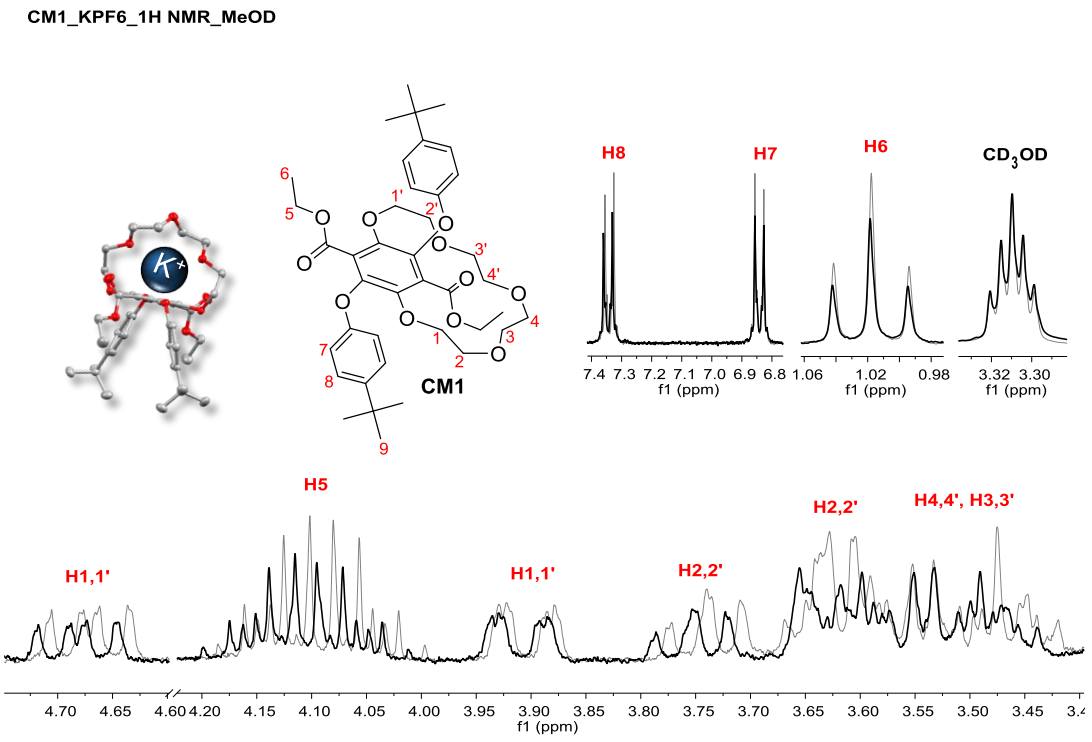

Figure 8: *^{1}H NMR spectra (300 MHz, CD_3OD) of* **CM1** *before (grey) and after (**bold**) addition of K^+ ions.*

Absorption and emission spectra of **CM1** in MeOH were also recorded in the absence and presence of cation salts. Unfortunately, no significant change was observed. As for the crown-ether-cation complex crystallisations attempted with sodium, potassium and ammonium hexafluorophosphate salts, only free **CM1** (uncomplexed) was crystallised in all of the cases. As it appears, this phenomenon is not uncommon[7].

Noting the fluxional nature of the compound in solution, and that the jellyfish-like structure in the crystal was conceivably not the lowest energy conformation, molecular modelling calculations were in addition performed. Using the X-ray determined molecular structure as the starting point an energy minimisation calculation using DFT (B3LYP) and a 6-311G basis set was performed. There was only a minor structural alteration which suggested the solid state structure actually represented the lowest energy conformation. Basic molecular dynamics simulations (MM+) were far more informative and several conformations and their respective energies are illustrated in Figure 9. In full agreement with the solid state structure and the DFT calculation, the syn *tert*-butyl aryl arrangement would appear to be the lowest energy conformation; the trans structure is slightly higher in energy by *ca.* 5 kcal mol^{-1}. Two other higher energy conformations sampled are associated with alteration in the crown ether structure.

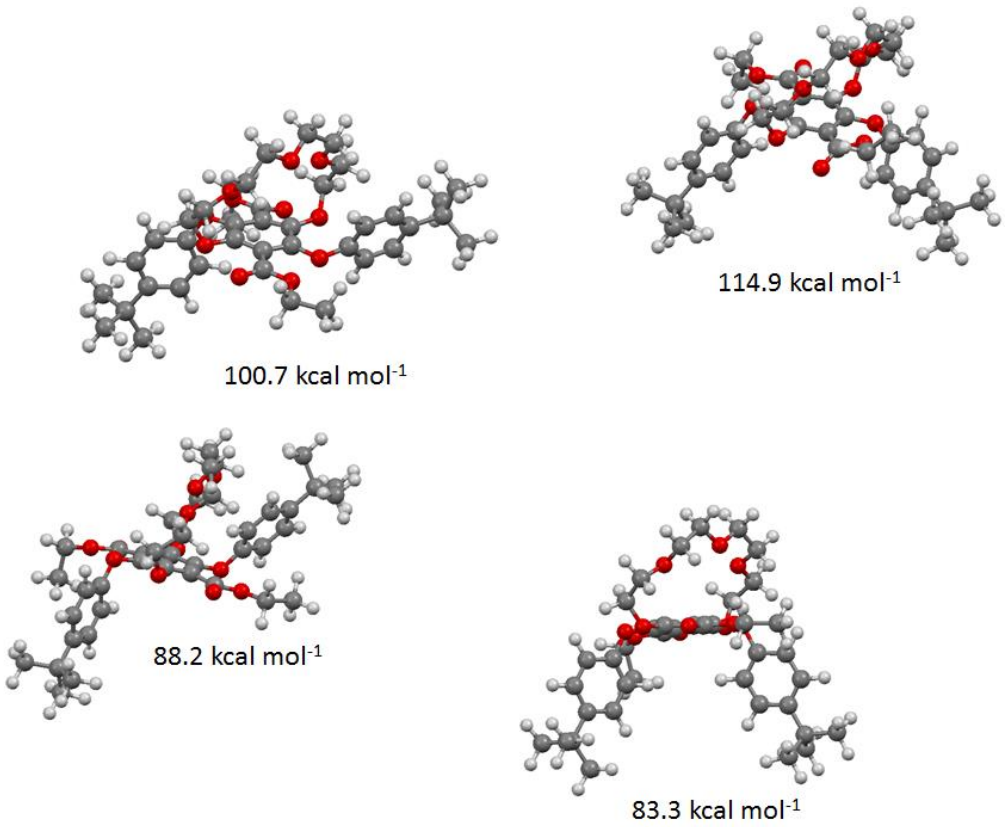

Figure 9: *A sample of calculated gas phase conformations and their energies of* **CM1** *using molecular dynamics simulations at the MM+ level.*

Since all attempts to grow crystals of the K^+ adduct with **CM1** failed we turned our attention to DFT calculations to try and ascertain a probable structure. Starting from the solid state structure a K^+ ion was placed in several positions within bonding distances to disparate oxygen atoms of the crown and the structures were energy minimised in Gaussian using B3LYP and a 6-311G basis set. From several calculations two structures, as shown in Figure 10, emerged as conceivable adducts of **CM1** with a K^+ ion; differing only slightly in energy because of small structural variations. Several key points stand out from examination of the structures. The first to note is the use of only three oxygen atoms of the crown ether with the two aryl oxygen atoms playing no part in binding to the potassium ion. This latter observation is perhaps not too surprising considering the severe structural distortion that would be required to accommodate the potassium ion. The K-O bond distances to the crown ether oxygens are in good agreement with those found in several X-ray structures of relevant macrocyclic complexes. E.g. the K-O bond distances of 17-hydroxy-15<O_5-(1,2)benzene-2_4-coronand-5>[8] falls within the range of 2.76-3.09 Å.

Additional oxygen donor interactions to the K^+ appear to be via the ethyl ester, using the ethyl oxygen in structure A and the carbonyl oxygen for structure B; the latter structure being *ca*. 4 kcal mol^{-1} more stable. For both structures there is the possibility of a K-O5 interaction although the actual distances are rather long. The K-C1 and K-C2 distances are potentially just within the crystallographically determined range (2.990-3.117Å) to be considered an η^2 interaction to the aryl ring. It is worth noting that the analogue structures calculated for **CM1** with the smaller Li^+ ion (Figure 10 – SI) showed that only two oxygen atoms of the crown bind to the metal ion but with the ester still able to participate in ion binding. The Li-O5 distance is also far too long to be considered significant. The combination of weaker interactions is likely one reason for the observed lack of binding of **CM1** with Li^+. The structure of **CM1** with Na^+ (Figure 11 – SI) is more akin to the K^+ structure shown.

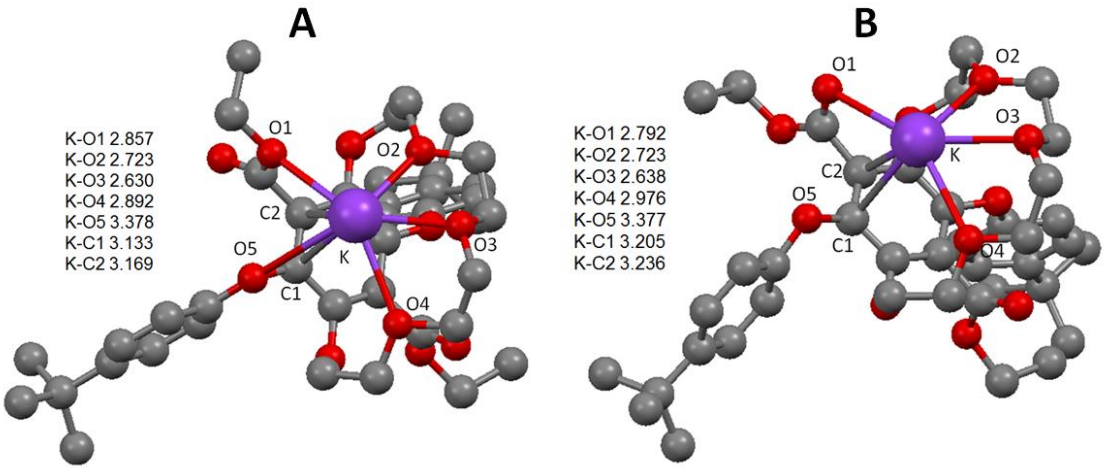

Figure 10: *Gaussian calculated energy-minimised gas phase structures for a K^+ adduct of* **CM1** *using B3LYP and a 6-311G basis set. Distances shown as the insert are in Å and hydrogens are omitted for clarity.*

3.1.2 Proton Binding Studies of CM1

Since **CM1** was designed with the vision of being polymerised into a polymer containing long proton transportable tunnels, it would be interesting to first test out its ability to coordinate with protons. In order to do that, several NMR titration experiments were conducted in $CDCl_3$ using trifluoroacetic acid, TFA as the proton source. Fresh solutions were prepared for each of the titration experiments.

A 2 – 5 mM solution of **CM1** was prepared by dissolving a known amount of **CM1** in 1 mL of $CDCl_3$ in an enclosed GC vial. The solution was then divided into two parts with one weighed directly into an NMR tube while the other part was used to prepare the guest solution (TFA). This ensured that the concentration of host stayed constant throughout the titration. Upon recording the initial ^1H and COSY NMR spectrum of the host solution, the guest solution was added with a microliter syringe in increments of 1 µL. With each addition, a ^1H and COSY NMR spectra were recorded. Upon reaching 20 µL, the guest solution was added with an increment of 20 µL until a total of 100 µL was reached. The recorded COSY NMR spectra were very useful in the identification of complex diastereotropic proton peaks from its respective ^1H NMR spectra. Titration experimental details along with their fitted data plots are shown in SI.

Interestingly, no chemical shifts were observed throughout the titration experiment for most of the proton peaks of **CM1** aside from H3,3' and H4,4' (protons from the crown ether chain) and H5 (protons from the ester side groups). This may be due to selective interactions of H^+ with the oxygen atoms in certain parts of **CM1**'s structure. By focusing on the region between 3.90-3.40 ppm in the stacked ^1H NMR spectra of selected mol % as shown in Figure 11a, the chemical shift data obtained from peaks corresponding to H3,3', H3,3' and H4,4' were non-linearly fitted using Micromath Scientist and Bindfit as shown in Figure 11b.

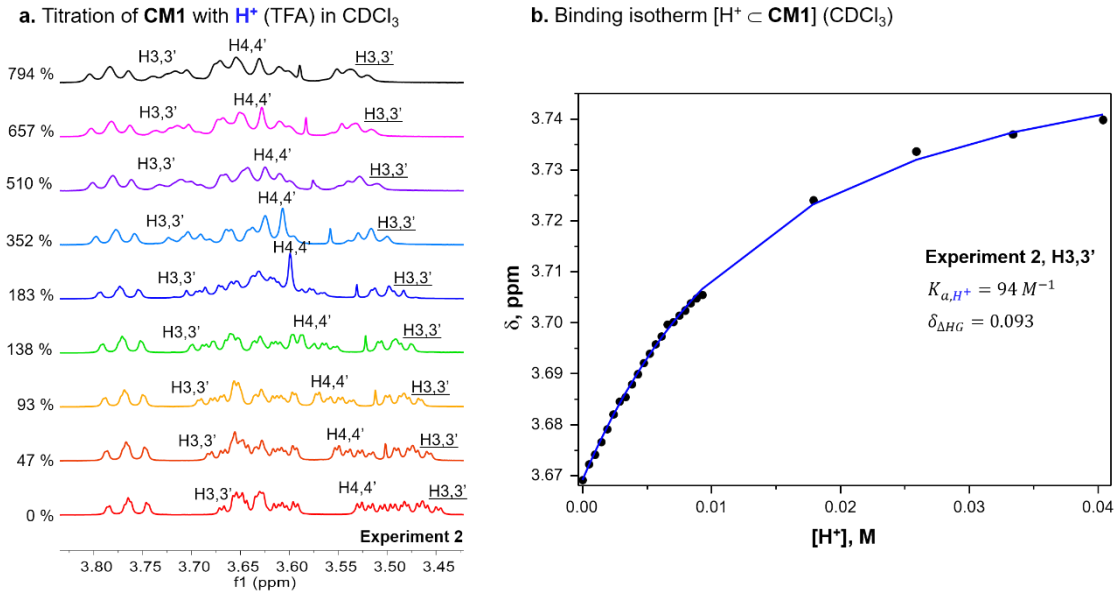

Figure 11: a) *Partial ^{1}H NMR spectra (500 MHz, 298 K, $CDCl_3$) stack plot of* **CM1** *(5 mM) titration with TFA from 0 to 794 mol % and* ***b)*** *Non-linear fit of binding isotherm [$H^+ \subset$* **CM1***] based on H3,3' (Titration Experiment 2).*

By using both of the following equations, Micromath Scientist software was programmed to fit data from the titration of **CM1** and H^+ to a simple 1:1 binding model to obtain K_a.

$$[HG] = \frac{1}{2}\left([G]_0 + [H]_0 + \frac{1}{K_a}\right) - \sqrt{\left([G]_0 + [H]_0 + \frac{1}{K_a}\right)^2 - 4[H]_0[G]_0} \qquad (1)$$

$$\Delta\delta = \delta_{\Delta HG}\left(\frac{[HG]}{[H]_0}\right) \qquad (2)$$

$$where\ [HG] = concentration\ of\ 1{:}1\ host-guest\ complex$$
$$[H]_0 = initial\ concentration\ of\ host$$
$$[G]_0 = initial\ concentration\ of\ guest$$
$$K_a = binding\ constant\ (1{:}1)$$
$$\Delta\delta = observed\ changes\ in\ chemical\ shift$$
$$\delta_{\Delta HG} = chemical\ shift\ of\ host-guest\ complex$$

Bindfit, on the other hand, is an open access website that has a built in fitting algorithm that is based upon this paper[9]. By uploading the data obtained in the form of an excel file, the website intelligently fits the data plots and provides reliable K_a estimated values. The binding constant, log K_a values and the binding free energy, ΔG values of **CM1** with H^+ obtained by both methods for all three experiments are summarised in Table 2.

Experiment	Proton	Scientist®[1]		Bindfit[2]	
		log K_a, M^{-1}	ΔG, kJmol^{-1}	log K_a, M^{-1}	ΔG, kJmol^{-1}
1	**H3,3'**	2.21	-12.6	2.05	-11.7
	H3,3'	1.89	-10.8		
2	**H3,3'**	1.97	-11.3	2.00	-11.4
	H3,3'	1.80	-10.3		
	H4,4'	2.06	-11.8		
3	**H3,3'**	2.21	-12.6	1.94	-11.1
	H3,3'	1.73	-9.9		
	H4,4'	1.99	-11.3		

[1]Micromath Scientist® and [2]Bindfit (http://app.supramolecular.org/bindfit/) are non-linear fitting software used to calculate the binding constant. Micromath Scientist calculations were done by Prof Andrew Benniston.

Table 2: *Summary of binding constants K_a of* **CM1** *determined by ^1H NMR titration experiments in $CDCl_3$ using appropriate non-linear fitting software.*

The average log K_a values estimated using Micromath Scientist were found to be closed to the values obtained from Bindfit, giving rise to an overall log K_a value of around 2 M^{-1}. As the proton log K_a value of **CM1** (2.2 M^{-1}) is relatively small compared to the other cation binding constants, one could argue that because the value is low, it resembles more of the association constant log K_a of the protonation of an ester instead of the binding constant log K_a as shown in Scheme 2.

Based on literature, the association constant of the protonation of ester was found to be very small (log K_a = between -15 and -1 M^{-1}) [10–12]. The binding constants of crown ethers with weak cation bindings were found in the range of 10-120 M^{-1} (log K_a = 1.0-2.1 M^{-1})[13–16] while the binding constants of crown ethers with protons (H^+) were found to have log K_a of around 2.9 M^{-1} and ΔG (300 K) of -15.9 kJ/mol (15-crown-5)[17,18]. Therefore, we can confidently say that the values obtained from the titration experiments of **CM1** with H^+ was indeed the binding constant since the log K_a (2.2 M^{-1}) and ΔG (-13 kJ/mol) values were comparable to the reported values of 15-crown-5 with H^+.

Several attempts made to crystallise the protonated complex with TFA were to no avail. Likewise, no $[M+H]^+$ species were detected in the positive nanoESI spectrum of **CM1**. Similar to what was observed with cations in Section 3.1.1, the absorption and emission spectra of **CM1** in $CHCl_3$ recorded in the absence and presence of H^+ ions (TFA) also showed no significant change.

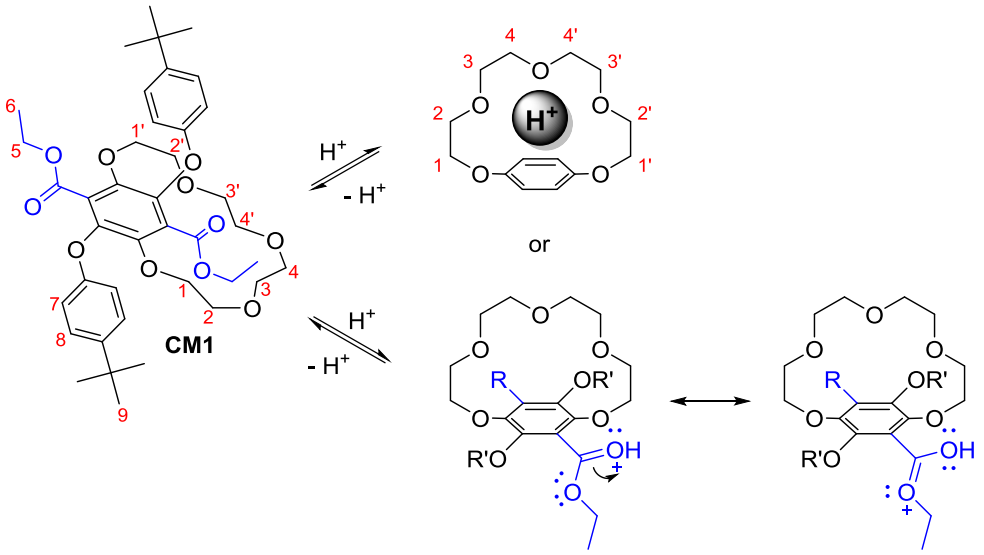

Scheme 2: *Possible interactions of* **CM1** *with* H^+ *(within the crown ether cavity or externally protonating the ester groups).*

With the K_a value of **CM1** with H^+ being low thereby reflecting weak interactions, it could be used to our advantage. Since **CM1** will eventually be polymerised into a polymer with aligned crown ether rings in the form of a tunnel, the low binding affinity to H^+ would mean that there will not be any concerns regarding intermittency of transport due to proton being stuck in its cavities. Details of the polymerisation of **CM1** with 1,4-butanediol, **BD** will be reported and discussed in Chapter 6.

4. Conclusions

In this chapter, the successful synthesis and characterisation of crown ether **CM1** and its dimer **CM1a** were discussed. The coincidental resemblance of its crystal structure and bluish fluorescence (in $CHCl_3$) of a real life jellyfish has made it an interesting molecule to study. The ^1H NMR spectrum of **CM1** was unexpectedly complex due to the presence of diastereotropic crown ether chain protons and inequivalent CH_2 protons on its ester groups. With reference to a structure in literature[4] with similar inequivalent CH_2 protons, a total of nine conformers were proposed. Being one of the only two strained cores of its kind[5], more in-depth binding studies were carried out via the use of NMR spectroscopy. **CM1** was found to be selectively interacting with K^+. The crown ether cation interaction was reflected in its ^1H NMR and positive nanoESI spectra but not in its absorption and emission spectra. Unfortunately, no crown ether cation complex has been

successfully crystallised. Computational modelling studies showed that [**CM1** K^+] complex is probable with K-O bond distances within agreeable range, however, the structure was found to be more stable when additional oxygen donor interactions with the carbonyl oxygen was involved. Three host-guest titration experiments (**CM1** and H^+ in $CDCl_3$) were carried out and data of the three most obviously shifted protons H3,3', H3,3' and H4,4' were non-linearly fitted using Micromath Scientist and Bindfit for the determination of binding constant, K_a. With a low log K_a value (2.2 M^{-1}), **CM1**'s weak interaction with H^+ can be used to our advantage via polymerisation. Hence, the polymerisation of **CM1** was proceeded with its synthetic procedures and characterisation discussed in the next chapter.

Appendix. Supplementary Information, SI

Supplementary information, SI related to this chapter can be found at the end of this thesis.

References

1 V. B. Gupta and Z. Bashir, in *Handbook of Thermoplastic Polyesters*, Wiley-VCH Verlag GmbH & Co. KGaA, Weinheim, FRG, 2005, pp. 317–361.

2 Z. Tehrani, T. Korochkina, S. Govindarajan, D. J. Thomas, J. O'Mahony, J. Kettle, T. C. Claypole and D. T. Gethin, *Org. Electron. physics, Mater. Appl.*, 2015, **26**, 386–394.

3 T. Kuwabara, T. Nakashima, T. Yamaguchi and K. Takahashi, *Org. Electron. physics, Mater. Appl.*, 2012, **13**, 1136–1140.

4 A. C. Benniston, T. P. L. Winstanley, H. Lemmetyinen, N. V. Tkachenko, R. W. Harrington and C. Wills, *Org. Lett.*, 2012, **14**, 1374–1377.

5 J. Yao, W. Wu, W. Liang, Y. Feng, D. Zhou, J. J. Chruma, G. Fukuhara, T. Mori, Y. Inoue and C. Yang, *Angew. Chemie - Int. Ed.*, 2017, **56**, 6869–6873.

6 M. Pérez-Alvarez, F. M. Raymo, S. J. Rowan, D. Schiraldi, J. F. Stoddart, Z. H. Wang, A. J. . White and D. J. Williams, in *Tetrahedron*, Pergamon, 2001, vol. **57**, pp. 3799–3808.

7 K. M. Doxsee, D. S. Keegan, H. R. Wierman, J. R. Hagadorn and M. Arimura, *Pure Appl. Chem.*, 1993, **65**, 429–434.

8 E. Weber and M. Czugler, *Inorganica Chim. Acta*, 1982, **61**, 33–38.

9 D. Brynn Hibbert and P. Thordarson, *Chem. Commun.*, 2016, **52**, 12792–12805.

10 J. Andraos, Y. Chiang, A. J. Kresge, I. G. Pojarlieff, N. P. Schepp and J. Wirz, *J. Am. Chem. Soc.*, 1994, **116**, 73–81.

11 Y. Chiang, A. J. Kresge and J. Jones, *J. Am. Chem. Soc.*, 1994, **116**, 8358–8359.

12 R. Gómez-Bombarelli, M. González-Pérez, M. T. Pérez-Prior, E. Calle and J. Casado, *J. Org. Chem.*, 2009, **74**, 4943–4948.

13 J. M. A. Spiteri, C. J. Mallia, G. J. Scerri and D. C. Magri, *Org. Biomol. Chem.*, 2017, **15**, 10116–10121.

14 T. Terashima, M. Kawabe, Y. Miyabara, H. Yoda and M. Sawamoto, *Nat. Commun.*, 2013, **4**, 2321.

15 J. B. Smith, S. H. Kerr, P. S. White and A. J. M. Miller, *Organometallics*, 2017, **36**, 3094–3103.

16 F. Arnaud-Neu, R. Delgado and S. Chaves, *Pure Appl. Chem.*, 2003, **75**, 71–102.

17 R. B. Sharma, P. Kebarle and A. T. Blades, *J. Am. Chem. Soc.*, 1984, **106**, 510–516.

18 J. C. Chambron and M. Meyer, *Chem. Soc. Rev.*, 2009, **38**, 1663–1673.

Chapter 6

Synthesis and Characterisation of Terephthalate-based Pre-polymers and their Polymerisation

1. Introduction

Based on the aforementioned positive features of polyethylene terephthalate (PET)[1] and the robustness of the terephthalate core in Chapter 5, terephthalate-based pre-polymers and its copolymers needed to be synthesised and characterised in order to answer the main question of interest: would the incorporation of crown ether based terephthalate (**CM1**) encourage the formation of proton/cation transportable channels within a polymer?

The resulting polymer is envisaged to have proton transportable channels as shown in the picture. Since **CM1** was found to have relatively weak interactions with a proton, (Chapter 5), the channels formed by the parallel alignment of crown ether rings should have no issues regarding the intermittency of transport.

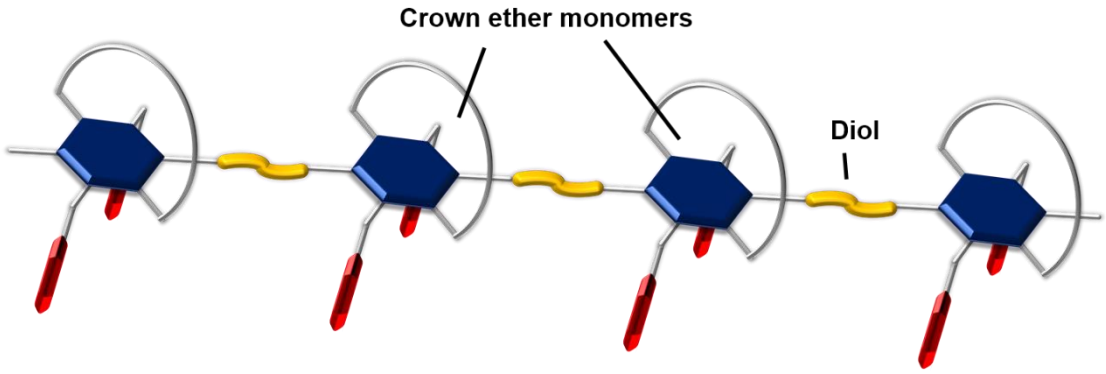

Cartoon representation of oriented crown ether polyesters (hypothetical)

In this chapter, the synthesis and characterisation of intermediate (**I4**), symmetrical pre-polymers (**EG-I3-EG**, **BD-I4-BD**, **BD-CM1-BD**), asymmetrical counterparts (**BD-I4** and **BD-CM1**) and copolymers (**Poly(EGI3EG-TCL)**, **Poly(BDI4BD-TCL)** and **Poly(BDCM1BD-TCL)**) will be discussed. Furthermore, the number average, weight average molecular weights (M_n, M_w) and polydispersity index, PDI, of the copolymers will be acquired by two different methods (NMR and GPC) and the results will be compared.

2. Experimental

2.1 Materials

Reagents and solvents were bought from commercial suppliers at the highest purity possible and were used without further purification unless otherwise specified. Titanium (IV) n-butoxide (99+ %) and terephthaloyl chloride, **TCL** (99 %) were supplied by Alfa Aesar while iodomethane (99 %), ethylene glycol, **EG** (99.8 %), 1,4-butandiol, **BD** (99 %) and zinc acetate dehydrate (≥ 98 %) were supplied by Sigma Aldrich. Intermediates **I3** and **CM1** were synthesised by procedures reported in Chapter 5. THF stabilized with BHT (ACROS Organics) was dried over activated 4 Å molecular sieves under nitrogen atmosphere for several days before use.

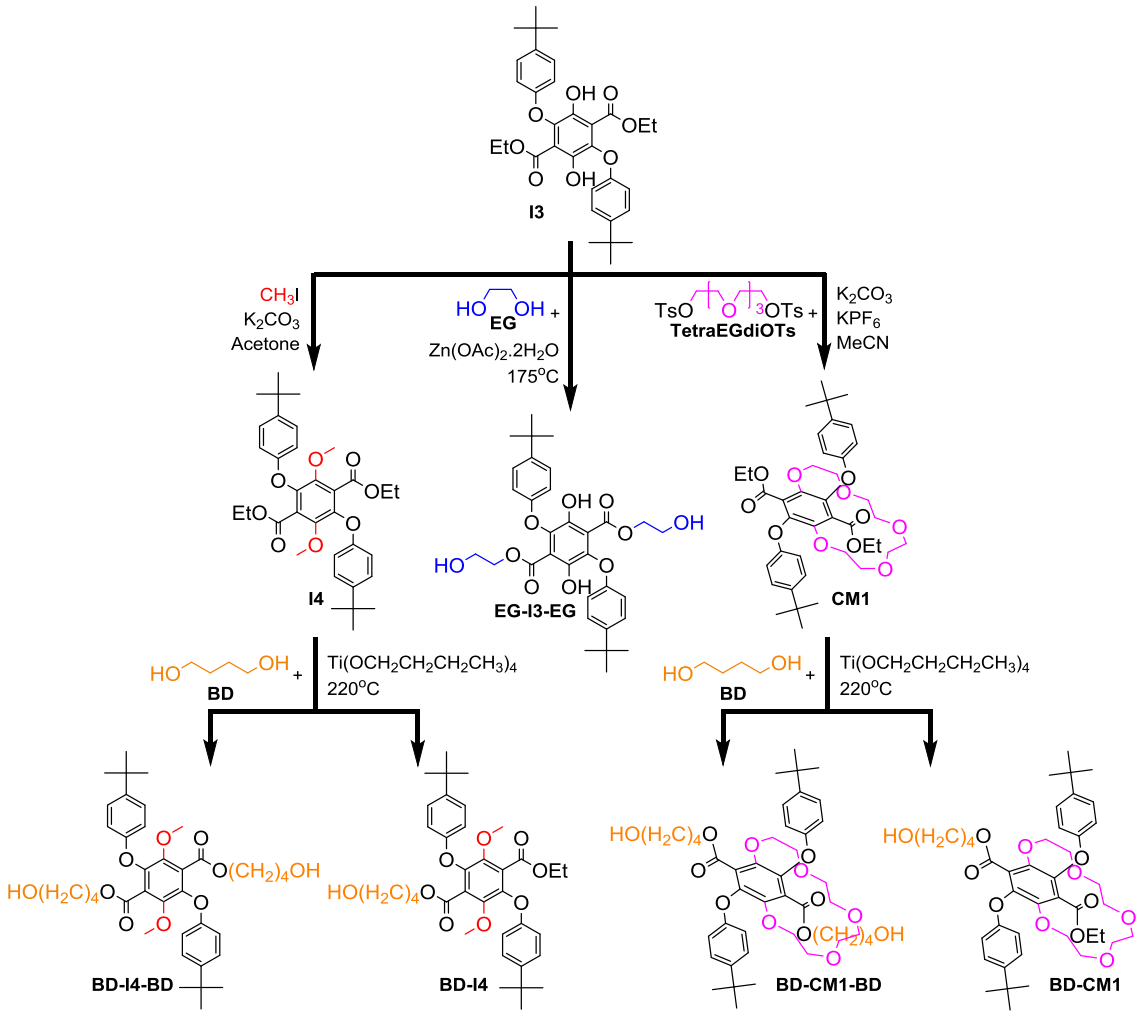

Scheme 1: *Preparation of pre-polymers* **EG-I3-EG**, **BD-I4-BD** *and* **BD-CM1-BD**.

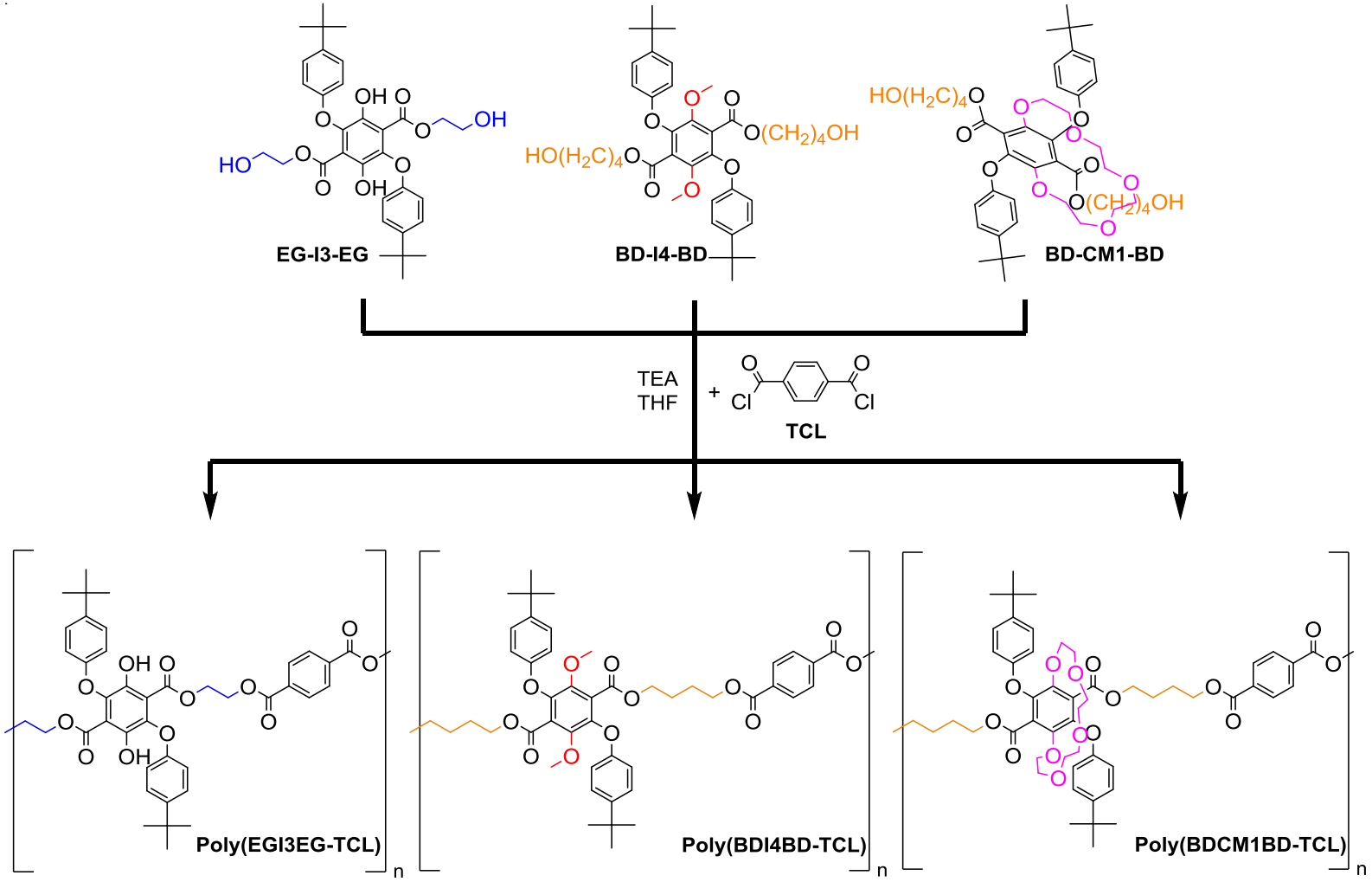

Scheme 2: *Preparation of polyesters* **Poly(EGI3EG-TCL)**, **Poly(BDI4BD-TCL)** *and* **Poly(BDCM1BD-TCL)**.

2.2 Synthesis of Pre-polymer, **EG-I3-EG**

EG (26 mL, 0.5 mol, excess) was added to a flask containing **I3** (1.0 g, 1.8 mmol) and $Zn(OAc)_2.2H_2O$ (50.0 mg, 0.2 mmol). The distillation set-up was covered in aluminium foil and was heated to 175 ^oC with a sand bath for 17 hours with TLC monitoring. The reaction mixture was cooled to RT. The suspension was suction filtered, the resulting solid was rinsed with H_2O and left to dry. The solid was dissolved in DCM and quickly flushed through a silica plug with DCM / EA. The flushes were collected and dried under reduced pressure. The resulting solid was dry packed into a silica column with DCM : petroleum ether (1 : 1) and was eluted with the same solvent gradually increasing to DCM and finally DCM with 5 % MeOH. Note that this column chromatography had to be done quickly as the compound seemed to decompose on silica. Alternative purification attempts with alumina column and recrystallisation were both unsuccessful. The purification yielded greenish yellow crystals (0.25 g, 0.4 mmol, 24 %).

^1H NMR (400 MHz, Chloroform-*d*) δ 10.27 (s, 2H, H6), 7.41 – 7.34 (m, 4H, H4), 6.88 – 6.81 (m, 4H, H3), 4.30 – 4.25 (m, 4H, H1), 3.55 – 3.49 (m, 4H, H2), 1.31 (s, 18H, H5).

^{13}C NMR (101 MHz, $CDCl_3$) δ 168.59 (C8), 155.96 (C12), 147.41 (C11), 145.46 (C13), 138.69 (C10), 126.88 (C4), 114.79 (C9), 113.68 (C3), 68.53 (C1), 60.45 (C2), 34.40 (C14), 31.59 (C5).

FT-IR (ν_{max}, cm^{-1}) 3574 (alcohol O-H stretching vibration), 2960 (asymmetric C-H stretching vibration from $-CH_2-$, $-CH_3$), 1676 (aromatic ester C=O stretching vibration), 1507 (aromatic C=C stretching vibration), 1227, 1174 (aromatic ester C-O stretching vibrations), 826, 721 (aromatic C-H out of plane bending vibrations).

(+)nanoESI-FTMS (m/z): found $[M+H]^+$ 583.2538, calcd. for $C_{32}H_{39}O_{10}$: 583.2538 and $[M+NH_4]^+$ 600.2798, calcd. for $C_{32}H_{42}O_{10}N$: 600.2803.

X-ray crystal structure (Figure 15) and refinement data (Table 2) available in SI.

2.3 Synthesis of Pre-polymer, **BD-I4-BD**

2.3.1 Synthesis of Intermediate, **I4**

CH_3I (0.8 mL, 12.9 mmol) was added dropwise into a flask containing **I3** (1.5 g, 2.7 mmol) and K_2CO_3 (1.9 g, 13.7 mmol) pre-dissolved in acetone (106 mL) at reflux. The reaction mixture was left to stir for 1 hour with TLC monitoring. It was then cooled to RT. The suspension was filtered and the filtrate was dried under reduced pressure. The crude was recrystallized with hot hexane to form colourless sugar-like tiny cube crystals (1.03 g, 1.8 mmol, 67 %).

^{1}H NMR (300 MHz, Chloroform-*d*) δ 7.34 – 7.22 (m, 4H, H4), 6.86 – 6.80 (m, 4H, H3), 4.16 (q, *J* = 7.1 Hz, 4H, H1), 3.81 (s, 6H, H6), 1.29 (s, 18H, H5), 1.08 (t, *J* = 7.1 Hz, 6H, H2).

^{13}C NMR (75 MHz, $CDCl_3$) δ 164.00 (C10), 155.58 (C11), 146.48 (C7), 145.40 (C12), 142.04 (C8), 126.84 (C9), 126.34 (C4), 115.11 (C3), 62.08 (C6), 61.89 (C1), 34.34 (C13), 31.63 (C5), 13.96 (C2).

FT-IR (v_{max}, cm^{-1}) 2959 (asymmetric C-H stretching vibration from -CH_2-, -CH_3), 1736 (aromatic ester C=O stretching vibration), 1507 (aromatic C=C stretching vibration), 1205, 1170 (aromatic ester C-O stretching vibrations), 821 (aromatic C-H out of plane bending vibration).

(+)nanoESI-FTMS (m/z): found $[M+H]^+$ 579.2946, calcd. for $C_{34}H_{43}O_8$: 579.2952.

X-ray crystal structure (Figure 14) and refinement data (Table 1) available in SI.

2.3.2 Synthesis of Pre-polymer, **BD-I4-BD**

BD (35 mL, 0.4 mol, excess) was added to a flask containing **I4** (1.8 g, 3.1 mmol) and $Ti(OCH_2CH_2CH_2CH_3)_4$ (0.3 mL, 0.9 mmol). The distillation set-up was covered in aluminium foil and was heated to 220 ^oC with a sand bath for 76 hours with TLC monitoring. The reaction mixture was cooled to RT. H_2O was added to the reaction mixture until a suspension formed before it was suction filtered. The residue was allowed to dry and was dissolved in DCM. The solution was quickly flushed through silica plug with DCM / EA. The first flush containing unreacted **I4** was discarded while the subsequent flushes were combined and dried under reduced pressure. The resulting viscous oil was wet packed into a silica column

with minimum amount of DCM and was eluted with DCM : EA (19 : 1) gradually increasing the polarity to 4 : 1. The fractions were collected in vials and were combined based on TLC. From the crude, several products were isolated and identified as follows: **BD-I4-BD** (0.21 g, 0.3 mmol, 10 %) and its asymmetric form **BD-I4** (0.35 g, 0.6 mmol, 19 %). Both products were isolated in the form of a brown oil. Note that **BD-I4** was eluted first followed by **BD-I4-BD**.

BD-I4-BD

^{1}H NMR (400 MHz, Chloroform-*d*) δ 7.31 – 7.25 (m, 4H, H4), 6.85 – 6.80 (m, 4H, H3), 4.15 (t, *J* = 6.4 Hz, 4H, H1), 3.78 (s, 6H, H6), 3.46 (t, *J* = 6.3 Hz, 4H, H15), 2.61 (s, 2H, H16), 1.59 – 1.50 (m, 4H, H2), 1.44 – 1.35 (m, 4H, H14), 1.28 (s, 18H, H5).

^{13}C NMR (101 MHz, $CDCl_3$) δ 164.02 (C10), 155.46 (C11), 146.29 (C7), 145.45 (C12), 141.82 (C8), 126.79 (C9), 126.34 (C4), 114.96 (C3), 65.65 (C1), 62.19 (C15), 62.01 (C6), 34.29 (C13), 31.59 (C5), 28.84 (C14), 24.89 (C2).

FT-IR (v_{max}, cm^{-1}) 3596 (alcohol O-H stretching vibration), 2959 (asymmetric C-H stretching vibration from -CH_2-, -CH_3), 1732 (aromatic ester C=O stretching vibration), 1507 (aromatic C=C stretching vibration), 1213, 1170 (aromatic ester C-O stretching vibrations), 830 (aromatic C-H out of plane bending vibration), 733 (C-C skeletal rocking vibration of -$(CH_2)_2$- and -$(CH_2)_3$-).

(+)nanoESI-FTMS (m/z): found $[M+Na]^+$ 689.3285, calcd. for $C_{38}H_{50}O_{10}Na$: 689.3296 and $[M+NH_4]^+$ 684.3737, calcd. for $C_{38}H_{54}O_{10}N$: 684.3742.

BD-I4

^{1}H NMR (400 MHz, Chloroform-*d*) δ 7.31 – 7.27 (m, 4H, H4, H4'), 6.86 – 6.81 (m, 4H, H3', H3), 4.21 – 4.12 (m, 4H, H1, H1'), 3.81 (s, 3H, H6'), 3.78 (s, 3H, H6), 3.49 (t, *J* = 6.3 Hz, 2H, H15), 1.62 – 1.52 (m, 2H, H2), 1.47 – 1.37 (m, 2H, H14), 1.30 – 1.28 (m, 18H, H5', H5), 1.07 (t, *J* = 7.1 Hz, 3H, H2').

^{13}C NMR (101 MHz, $CDCl_3$) δ 164.10 (C10), 163.93 (C10'), 155.56 (C11, C11'), 146.47 (C7'), 146.37 (C7), 145.47, 145.44 (C12, C12'), 142.07 (C8'), 141.85 (C8), 126.93 (C9'), 126.77 (C9), 126.37, 126.35 (C4', C4), 115.13 (C3'), 115.01 (C3),

65.67 (C1), 62.34 (C15), 62.12 (C6'), 62.02 (C6), 61.89 (C1'), 34.35, 34.34 (C13', C13), 31.64 (C5, C5'), 29.03 (C14), 24.99 (C2), 13.94 (C2').

FT-IR (ν_{max}, cm^{-1}) 3596 (alcohol O-H stretching vibration), 2959 (asymmetric C-H stretching vibration from -CH_2-, -CH_3), 1736 (aromatic ester C=O stretching vibration), 1507 (aromatic C=C stretching vibration), 1213, 1170 (aromatic ester C-O stretching vibrations), 830 (aromatic C-H out of plane bending vibration), 733 (C-C skeletal rocking vibration of -$(CH_2)_2$- and -$(CH_2)_3$-).

(+)nanoESI-FTMS (m/z): found $[M+H]^+$ 623.3206, calcd. for $C_{36}H_{47}O_9$: 623.3215.

2.4 Synthesis of Pre-polymer, BD-CM1-BD

BD (7.3 mL, 0.1 mol, excess) was added to a flask containing **CM1** (0.4 g, 0.6 mmol) and $Ti(OCH_2CH_2CH_2CH_3)_4$ (80 µL, 0.2 mmol). The distillation set-up was covered in aluminium foil and was heated to 220 ^oC with a sand bath for 18 hours with TLC monitoring. The reaction mixture was cooled to RT. H_2O was added to the reaction mixture until a suspension formed before it was suction filtered. The residue was allowed to dry and was wet packed into a silica column with a minimum amount of DCM and was eluted with DCM with 0.5 % MeOH gradually increasing polarity to DCM with 3.5 % MeOH. The fractions were collected in vials and were combined based on TLC. From the crude, several products were isolated and identified as follows: **BD-CM1-BD** (0.20 g, 0.3 mmol, 43 %) and its asymmetric form **BD-CM1** (0.13 g, 0.2 mmol, 31 %). Note that **BD-CM1** (white crystalline flakes) was eluted first followed by **BD-CM1-BD** (white flakes).

BD-CM1-BD

^1H NMR (500 MHz, Chloroform-*d*) δ 7.33 – 7.26 (m, 4H, H8), 6.86 – 6.82 (m, 4H, H7), 4.69 (ddd, *J* = 13.0, 8.9, 1.3 Hz, 2H, H1, H1'), 4.20 (ddd, *J* = 10.9, 6.8, 5.9 Hz, 2H, H5), 4.07 (ddd, *J* = 10.9, 6.7, 5.9 Hz, 2H, H5), 3.91 (ddd, *J* = 13.0, 3.6, 1.5 Hz, 2H, H1, H1'), 3.80 – 3.71 (m, 2H, H2, H2'), 3.66 – 3.55 (m, 6H, H2, H2', H4, H4', H3, H3'), 3.54 – 3.41 (m, 8H, H4, H4', H3, H3', H18), 1.59 (s, 2H, H19), 1.55 – 1.43 (m, 4H, H6), 1.41 – 1.31 (m, 4H, H17), 1.29 (s, 18H, H9).

^{13}C NMR (126 MHz, $CDCl_3$) δ 164.47 (C16), 155.29 (C12), 145.24 (C11), 144.95 (C15), 140.59 (C13), 126.37 (C8), 125.98 (C14), 115.01 (C7), 72.00 (C2, C2'),

71.94 (C3, C3'), 71.58 (C1, C1'), 70.85 (C4, C4'), 65.43 (C5), 62.35 (C18), 34.35 (C10), 31.67 (C9), 29.09 (C17), 24.90 (C6).

FT-IR (ν_{max}, cm^{-1}) 3337 (alcohol O-H stretching vibration), 2953 (asymmetric C-H stretching vibration from -CH_2-, -CH_3), 1733 (aromatic ester C=O stretching vibration), 1507 (aromatic C=C stretching vibration), 1212, 1179 (aromatic ester C-O stretching vibrations), 837, 811 (aromatic C-H out of plane bending vibrations).

(+)nanoESI-FTMS (m/z): found $[M+NH_4]^+$ 814.4367, calcd. for $C_{44}H_{64}O_{13}N$: 814.4372.

BD-CM1

^{1}H NMR (500 MHz, Chloroform-*d*) δ 7.30 – 7.26 (m, 4H, H8, H8'), 6.87 – 6.81 (m, 4H, H7, H7'), 4.71 (dddd, *J* = 18.8, 13.0, 9.0, 1.3 Hz, 2H, H1, H1'), 4.24 – 4.12 (m, 2H, H5, H5'), 4.11 – 4.00 (m, 2H, H5, H5'), 3.92 (dddd, *J* = 17.5, 13.0, 3.5, 1.5 Hz, 2H, H1, H1'), 3.76 (dddd, *J* = 10.5, 8.8, 4.8, 1.4 Hz, 2H, H2, H2'), 3.68 – 3.57 (m, 6H, H2, H2', H4, H4', H3, H3'), 3.55 – 3.41 (m, 6H, H4, H4', H3, H3', H18), 1.54 – 1.44 (m, 2H, H6), 1.42 – 1.32 (m, 2H, H17), 1.29 (s, 18H, H9, H9'), 1.11 (s, 1H, H19), 0.99 (t, *J* = 7.1 Hz, 3H, H6').

^{13}C NMR (126 MHz, $CDCl_3$) δ 164.55 (C16'), 164.41 (C16), 155.32 (C12, C12'), 145.18, 145.13 (C11, C11'), 144.92 (C15, C15'), 140.87 (C13'), 140.53 (C13), 126.35, 126.30 (C8, C8'), 126.02 (C14), 125.91 (C14'), 115.16 (C7'), 115.01 (C7), 72.06 (C2, C2'), 72.01 (C3, C3'), 71.61, 71.59 (C1, C1'), 70.93, 70.85 (C4, C4'), 65.39 (C5), 62.36 (C18), 61.59 (C5'), 34.34 (C10, C10'), 31.67 (C9, C9'), 29.10 (C17), 24.91 (C6), 13.88 (C6').

FT-IR (ν_{max}, cm^{-1}) 3337 (alcohol O-H stretching vibration), 2956 (asymmetric C-H stretching vibration from -CH_2-, -CH_3), 1737 (aromatic ester C=O stretching vibration), 1507 (aromatic C=C stretching vibration), 1212, 1179 (aromatic ester C-O stretching vibrations), 837, 811 (aromatic C-H out of plane bending vibrations).

(+)nanoESI-FTMS (m/z): found $[M+NH_4]^+$ 770.4103, calcd. for $C_{42}H_{60}O_{12}N$: 770.4110.

2.5 Polymers

2.5.1 Synthesis of **Poly(EGI3EG-TCL)**

EG-I3-EG (250.0 mg, 0.4 mmol) was dissolved in anhydrous THF (5 mL) at RT. Upon complete solubilisation, the solution was cooled to 0 ^{o}C in an ice bath. TEA (180 µL, 1.3 mmol) was added. In a separate flask, **TCL** (87.0 mg, 0.4 mmol) was dissolved in anhydrous THF (5 mL). The **TCL** solution was then added dropwise into the reaction mixture via a syringe pump over the course of 1 hour. The reaction mixture was allowed to react at RT over 3 days covered in aluminium foil. The reaction mixture was then suction filtered and the filtrate was dried under reduced pressure. The residue was purified by re-dissolving in $CHCl_3$ and added to Et_2O. The precipitate was dissolved in small amounts of $CHCl_3$ and allowed to dry to yield a semi-opaque pale yellow film (61.00 mg, 7.2 µmol, 2 %).

2.5.2 Synthesis of **Poly(BDI4BD-TCL)**

BD-I4-BD (250.0 mg, 0.4 mmol) was dissolved in anhydrous THF (5 mL) at RT. Upon complete solubilisation, the solution was cooled to 0 ^{o}C in an ice bath. TEA (160 µL, 1.1 mmol) was added. In a separate flask, **TCL** (76.0 mg, 0.4 mmol) was dissolved in anhydrous THF (4 mL). The **TCL** solution was then added dropwise into the reaction mixture via a syringe pump over the course of 1 hour. The reaction mixture was allowed to react at RT over 4 days covered in aluminium foil. The reaction mixture was then suction filtered and the filtrate was dried under reduced pressure. The residue was purified by re-dissolving in $CHCl_3$ and added to Et_2O. The precipitate was dissolved in small amounts of $CHCl_3$ and allowed to dry to yield **Poly(BDI4BD-TCL)_1** as an off-white opaque brittle film (28.00 mg). The filtrate from the purification was dried under reduced pressure, re-dissolved in $CHCl_3$ and re-precipitated in hexane twice to yield **Poly(BDI4BD-TCL)_3**, similarly being off-white, opaque and brittle (263.00 mg, 33.6 µmol, 8 %).

Poly(BDI4BD-TCL)_1 was later found to be a mixture of polymer and starting material, **BD-I4-BD**. Thus, its percentage yield could not be calculated without its estimated molecular weight, M_n from its ^{1}H NMR spectrum.

2.5.3 Synthesis of Poly(BDCM1BD-TCL)

BD-CM1-BD (115.0 mg, 0.1 mmol) was dissolved in anhydrous THF (2 mL) at RT. Upon complete solubilisation, the solution was cooled to 0 ^{o}C in an ice bath. TEA (60 µL, 0.4 mmol) pre-dissolved in anhydrous THF (0.8 mL) was added. In a separate flask, **TCL** (29.0 mg, 0.1 mmol) was dissolved in anhydrous THF (1 mL). The **TCL** solution was then added dropwise into the reaction mixture via a syringe over the course of 1 hour. The reaction mixture was allowed to react at RT over 6 days covered in aluminium foil. The reaction mixture was then filtered through a pipette cotton plug and the filtrate was dried under reduced pressure. The residue was purified by dissolving in THF and added to $CHCl_3$. The filtrate was dried under reduced pressure to yield **Poly(BDCM1BD-TCL)** as an off-white opaque polymer film (95.80 mg). The percentage yield of **Poly(BDCM1BD-TCL)** could not be calculated without its estimated molecular weight, M_n from its ^{1}H NMR spectrum.

2.6 Characterisation

2.6.1 Nuclear Magnetic Resonance (NMR) Spectroscopy

^{1}H and ^{13}C NMR spectra of **I4** in deuterated chloroform ($CDCl_3$) were recorded on Bruker Avance III 300 MHz, those of **EG-I3-EG**, **BD-I4-BD** and **BD-I4** in deuterated chloroform ($CDCl_3$) were recorded on Jeol ECS 400 MHz and those of **BD-CM1-BD** and **BD-CM1** were recorded on Bruker Avance III HD 500 MHz. 2D NMR such as ^{1}H-^{1}H correlation (COSY), ^{1}H-^{13}C heteronuclear single quantum correlation (HSQC), ^{1}H-^{13}C heteronuclear multiple bond correlation (HMBC) were used to substantiate ^{1}H and ^{13}C NMR assignments of the synthesised compounds. For polymer samples, ^{1}H NMR spectra were recorded using Jeol ECS 400 MHz and Bruker Avance III 700 MHz in deuterated chloroform ($CDCl_3$). Diffusion ordered NMR spectroscopy (DOSY) was used to determine the diffusion coefficient and relative size estimation as well as for verification of NMR peaks belonging to the different polymer chain combinations present in each polymer.

2.6.2 FT-IR Spectroscopy

FT-IR spectra were obtained using Spectrum Two FT-IR Spectrometer fitted with a diamond crystal plate ATR unit (PerkinElmer).

2.6.3 Mass Spectrometry

Mass spectrometry analyses of the newly synthesised products were performed on a Thermo Scientific LTQ Orbitrap XL spectrometer equipped with an Advion NanoMate inlet in positive ionisation mode by the team at EPSRC UK National Mass Spectrometry Facility, Swansea University.

2.6.4 X-ray Crystallography

Crystal structure data for **EG-I3-EG** was collected on a Xcalibur, Atlas, Gemini ultra diffractometer equipped with an fine-focus sealed X-ray tube ($\lambda_{CuK\alpha}$ = 1.54184 Å) and an Oxford Cryosystems CryostreamPlus open-flow N_2 cooling device. Cell refinement, data collection and data reduction were undertaken via software CrysAlisPro 1.171.38.42b (Rigaku OD, 2015). Intensities were corrected for absorption using CrysAlisPro 1.171.38.42b (Rigaku Oxford Diffraction, 2015) Analytical numeric absorption correction using a multifaceted crystal model based on expressions derived by R.C. Clark & J.S. Reid. (Clark, R. C. & Reid, J. S. (1995). Acta Cryst. A51, 887-897) Empirical absorption correction using spherical harmonics, implemented in SCALE3 ABSPACK scaling algorithm.

Crystal structure data for **I4** was collected on a Xcalibur, Atlas, Gemini ultra diffractometer equipped with an fine-focus sealed X-ray tube ($\lambda_{CuK\alpha}$ = 1.54184 Å) and an Oxford Cryosystems CryostreamPlus open-flow N_2 cooling device. Cell refinement, data collection and data reduction were undertaken via software CrysAlisPro 1.171.38.42b (Rigaku OD, 2015). Intensities were corrected for absorption using CrysAlisPro 1.171.38.42b (Rigaku Oxford Diffraction, 2015) Empirical absorption correction using spherical harmonics, implemented in SCALE3 ABSPACK scaling algorithm.

Using Olex2 (Dolomanov, 2009), the structures were solved using ShelXT (Sheldrick, 2015) and refined by XL (Sheldrick, 2008).

2.6.5 Differential Scanning Calorimetry (DSC)

Calorimetric studies were carried out in a Mettler DSC822e Differential Scanning Calorimeter. Approximately 5 mg of samples were weighed into 40 µL aluminium crucibles covered with a pierced lid. The analyses were performed in dynamic

mode at a heating and cooling rate of 10 ^{o}C/min using nitrogen as a purge gas (100 mL/min).

2.6.6 Gel Permeation Chromatography (GPC)

The number average (M_n) and weight average (M_w) molecular weight of polymers were determined by the use of an Agilent 1200 Series GPC-SEC system consisting of three columns in series (PLgel 20 µm MIXED-A, PLgel 5 µm MIXED-D and PLgel 3 µm MIXED-E) and a refractive index detector. Monodispersed polystyrene (PS) standards were used for calibration and the mobile phase (THF with toluene as internal standard) was eluted at a flow rate of 1.0 mL/min. The sample concentrations used were 5-10 mg/mL.

3. Results and discussion

3.1 Synthesis of Pre-polymer, **EG-I3-EG**

Pre-polymer, **EG-I3-EG** was synthesised via transesterification[2] of **I3** and ethylene glycol, **EG**, in the presence of a catalyst, zinc acetate as shown in Scheme 1. Upon successful purification, **EG-I3-EG** was isolated and characterised by 2D NMR spectroscopy, FT-IR, mass spectrometry and X-ray crystallography.

A distinctive feature suggesting successful synthesis of **EG-I3-EG** can be observed from the ^{1}H NMR spectrum in Figure 1, whereby methylene protons H1 and H2 no longer appeared as quartet and triplet (^{1}H NMR spectrum of **I3** – Chapter 5 - Figure 3 SI) but as multiplets at 4.27 ppm and 3.52 ppm, respectively.

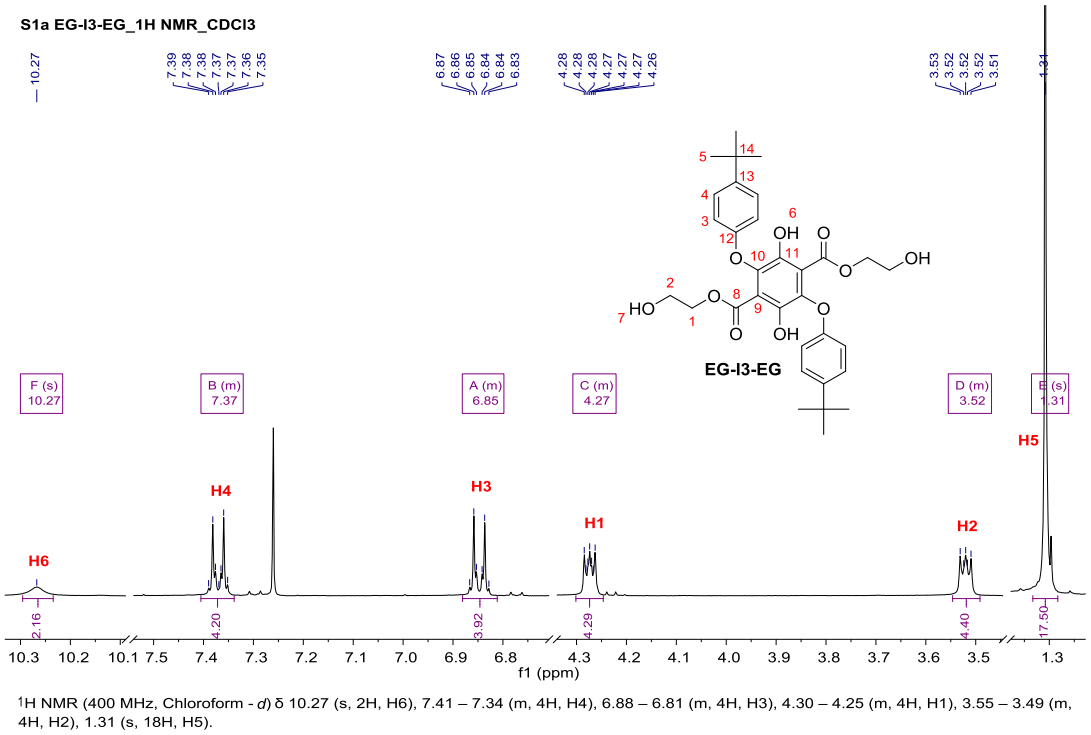

^{1}H NMR (400 MHz, Chloroform - *d*) δ 10.27 (s, 2H, H6), 7.41 – 7.34 (m, 4H, H4), 6.88 – 6.81 (m, 4H, H3), 4.30 – 4.25 (m, 4H, H1), 3.55 – 3.49 (m, 4H, H2), 1.31 (s, 18H, H5).

Figure 1: *^{1}H NMR spectrum (400 MHz, $CDCl_3$) of* **EG-I3-EG**.

The positive nanoESI of **EG-I3-EG** (Figure 7 – SI) showed the presence of $[M+H]^+$ species at m/z = 583.2538 and $[M+NH_4]^+$ species at m/z = 600.2798 (in DCM/MeOH + NH_4OAc). Both mass spectra matched their corresponding theoretical isotope model within a mass error of 1 ppm.

The appearance of a new peak at 3574 cm^{-1} in the FT-IR spectrum of **EG-I3-EG** in Figure 13 (SI) corresponding to the O-H stretching vibration of an alkyl alcohol, once again substantiated the successful synthesis of the pre-polymer. The shift corresponding to the characteristic C=O stretching vibration of an aromatic ester of **EG-I3-EG** was observed at a higher wavenumber (1676 cm^{-1}) than that of **I3** (1661 cm^{-1}).

With the use of vapour diffusion, crystals of **EG-I3-EG** were able to be grown in the fridge from chloroform/hexane. Its X-ray crystal structure and corresponding data are shown in Figure 15 (SI).

3.2 Synthesis of Pre-polymer, BD-I4-BD

Intermediate **I4** was synthesised as the “stunt double” of **CM1** with hopes to find the best polymerisation conditions for **CM1** without having to sacrifice precious **CM1** in the process. By substituting the hydroxyl groups on the terephthalate core

of **I3** with methyl groups from iodomethane in the presence of K_2CO_3 as a base, **I4** was successfully synthesised with a 67 % yield and was characterised as follows.

From the ^{1}H NMR spectrum of **I4** in Figure 2 (SI), the disappearance of the singlet corresponding to the hydroxyl protons and the appearance of a new singlet at 3.81 ppm (H6) integrating to 6 protons confirmed the successful synthesis of **I4**.

The positive nanoESI of **I4** in Figure 8 (SI) showed the presence of $[M+H]^+$ species at m/z = 579.2946 (in DCM/MeOH + NH_4OAc) matching its corresponding theoretical isotope model within a mass error of 1 ppm.

In the FT-IR spectrum of **I4** in Figure 5, a very obvious shift in the peak corresponding to the characteristic C=O stretching vibration of an aromatic ester can be observed from 1661 cm^{-1} (**I3** – Figure 13, SI) to 1736 cm^{-1}. This is due to the successful substitution at the 2, 5 positions where the hydroxyl groups were previously located. With no intramolecular H-bonding present weakening the C=O stretching as seen in **I3**, the C=O stretching vibration of **I4** was restored to its commonly known region at a higher wavenumber.

The X-ray crystal structure in Figure 14 (SI) of sugar-like crystals grown from acetone was found to match with **I4**.

The crystals of **I4** was then used in the synthesis of its pre-polymer, **BD-I4-BD** via transesterification[3] with 1,4-butandiol, **BD** in the presence of a catalyst, titanium (IV) butoxide, TNBT, as shown in Scheme 1. Upon successful purification by column chromatography, **BD-I4-BD** and its asymmetrical sibling **BD-I4** were isolated and characterised by 2D NMR spectroscopy, FT-IR, mass spectrometry and X-ray crystallography.

Due to the difference in symmetry between the two compounds, respective 2D NMR spectra of **BD-I4-BD** and **BD-I4** could be assigned. From the ^{1}H NMR spectrum of **BD-I4-BD** in Figure 2, peaks attributed to the CH_2 protons on the newly attached butyl chains were seen as triplets at 4.15 ppm (H1) and 3.46 ppm (H15) as well as at 1.54 ppm (H2) and 1.40 ppm (H14) as multiplets. The two protons from the terminal OH groups could also be seen as a broad peak at 2.61 ppm.

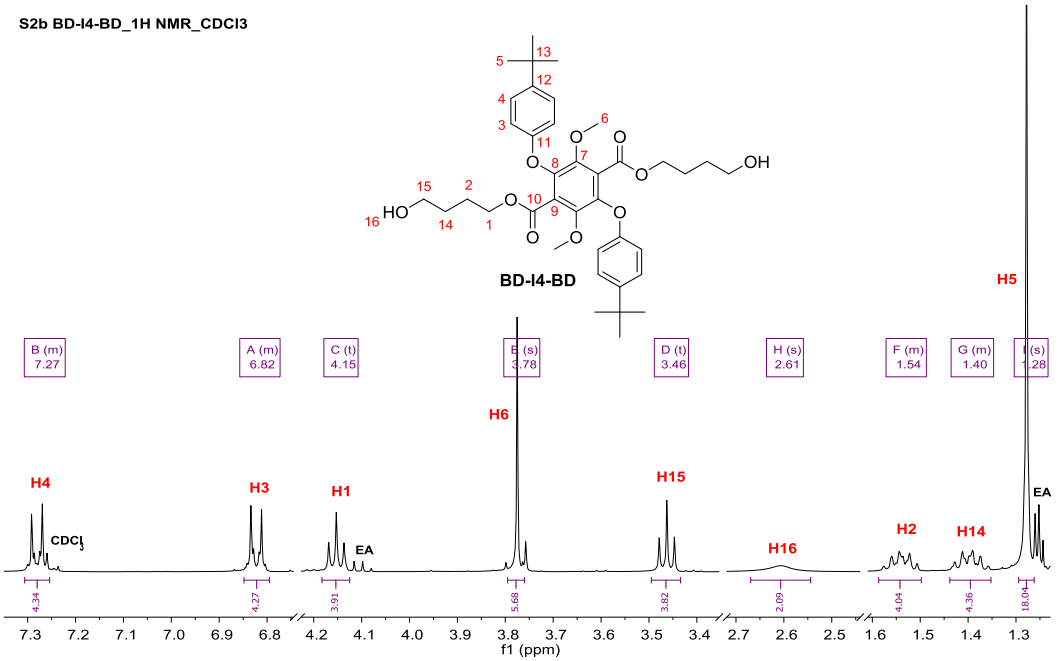

^{1}H NMR (400 MHz, Chloroform - *d*) δ 7.31 – 7.25 (m, 4H, H4), 6.85 – 6.80 (m, 4H, H3), 4.15 (t, *J* = 6.4 Hz, 4H, H1), 3.78 (s, 6H, H6), 3.46 (t, *J* = 6.3 Hz, 4H, H15), 2.61 (s, 2H, H16), 1.59 – 1.50 (m, 4H, H2), 1.44 – 1.35 (m, 4H, H14), 1.28 (s, 18H, H5).

Figure 2: *^{1}H NMR spectrum (400 MHz, $CDCl_3$) of* **BD-I4-BD**.

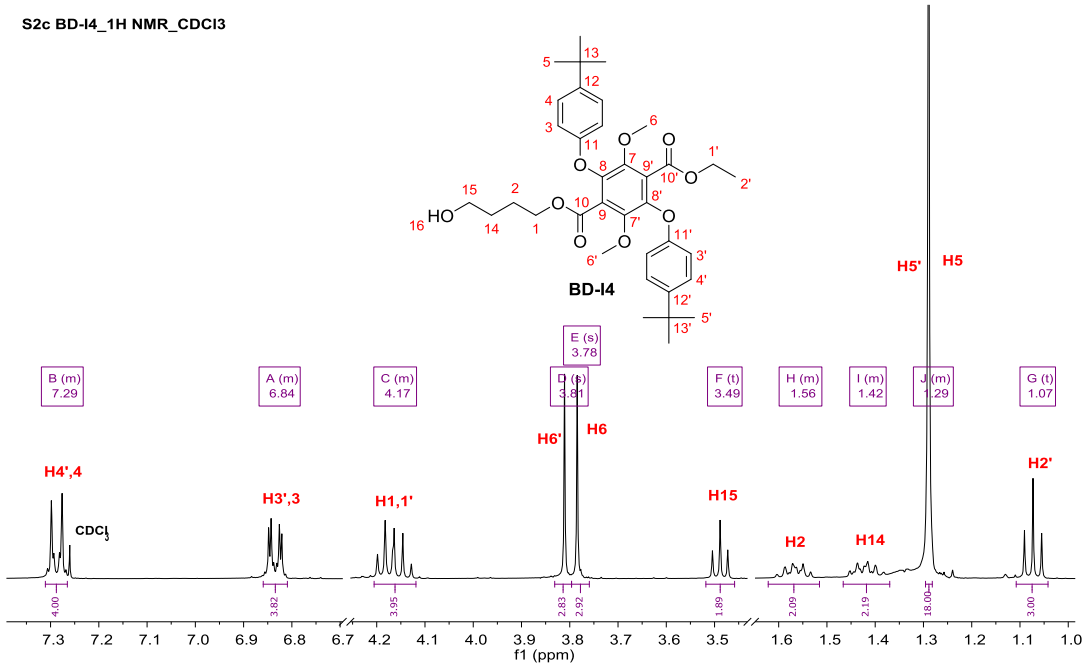

^{1}H NMR (400 MHz, Chloroform - *d*) δ 7.31 – 7.27 (m, 4H, H4, H4'), 6.86 – 6.81 (m, 4H, H3', H3), 4.21 – 4.12 (m, 4H, H1, H1'), 3.81 (s, 3H, H6'), 3.78 (s, 3H, H6), 3.49 (t, *J* = 6.3 Hz, 2H, H15), 1.62 – 1.52 (m, 2H, H2), 1.47 – 1.37 (m, 2H, H14), 1.30 – 1.28 (m, 18H, H5', H5), 1.07 (t, *J* = 7.1 Hz, 3H, H2').

Figure 3: *^{1}H NMR spectrum (400 MHz, $CDCl_3$) of* **BD-I4**.

The asymmetry in **BD-I4** is apparent in its ^{1}H NMR spectrum in Figure 3 as there are two separate singlets corresponding to its methoxy groups at 3.81 ppm (H6') and 3.78 ppm (H6) instead of one. A few of its other peaks such as H4,4' (7.29

ppm), H3,3’ (6.84 ppm), H1,1’ (4.17 ppm) and H5,5’ (1.29 ppm) were also found to overlap. An easily recognisable triplet at 1.07 ppm belonged to the H2’ of the CH_3 unit on the unreacted arm, whilst peaks attributed to the CH_2 protons on the newly attached butyl chain were seen as a triplet at 3.49 ppm (H15) as well as at 1.56 ppm (H2) and 1.42 ppm (H14) as multiplets.

The ^{13}C NMR spectrum of **BD-I4-BD** in Figure 3 (SI) was very straightforward, unlike **BD-I4**’s in Figure 4 which has two of each peaks in addition to some overlapped ones. With careful analysis of its COSY, HSQC and HMBC NMR spectra, all of its carbon peaks were assigned. The two carbonyl carbons are seen at 164.1 ppm (C10) and 163.9 ppm (C10’) with C10 located very similar to that of **BD-I4-BD** and C10’ located very similar to that of **I4**. The HMBC NMR spectrum of **BD-I4** in Figure 4 (SI) also showed correlations between the H1 protons with C10 carbon and H1’ protons with C10’ carbon.

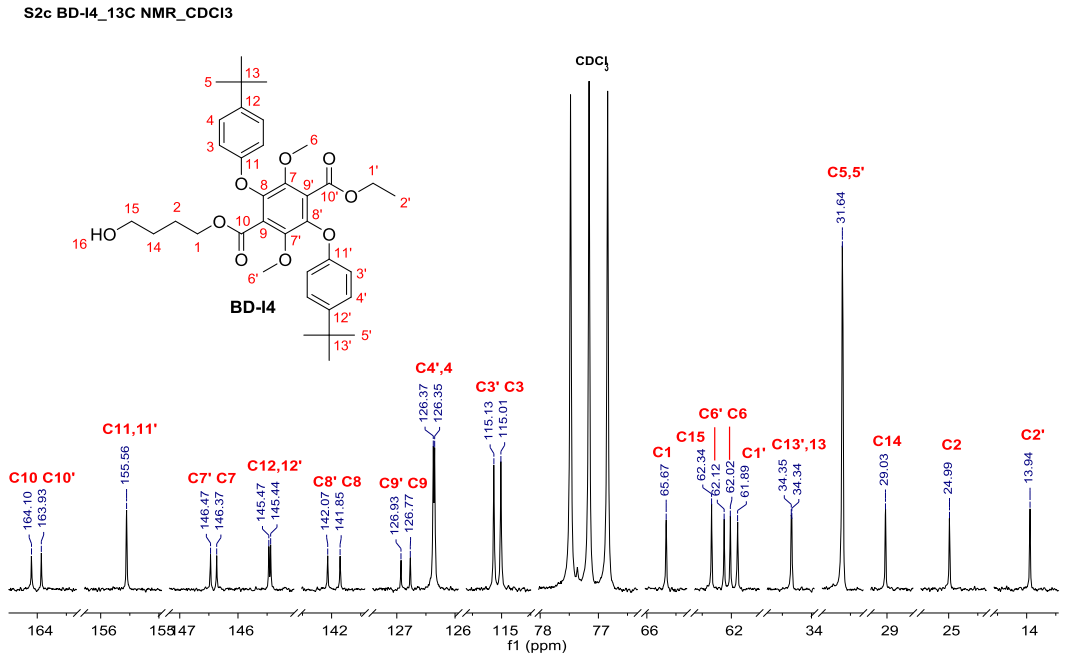

^{13}C NMR (101 MHz, $CDCl_3$) δ 164.10 (C10), 163.93 (C10'), 155.56 (C11, C11'), 146.47 (C7'), 146.37 (C7), 145.47, 145.44 (C12, C12'), 142.07 (C8'), 141.85 (C8), 126.93 (C9'), 126.77 (C9), 126.37, 126.35 (C4', C4), 115.13 (C3'), 115.01 (C3), 65.67 (C1), 62.34 (C15), 62.12 (C6'), 62.02 (C6), 61.89 (C1'), 34.35, 34.34 (C13', C13), 31.64 (C5, C5'), 29.03 (C14), 24.99 (C2), 13.94 (C2').

Figure 4: *^{13}C NMR spectrum (101 MHz, $CDCl_3$) of* **BD-I4**.

The positive nanoESI of **BD-I4-BD** (Figure 9 – SI) showed the presence of $[M+Na]^+$ species at m/z = 689.3285 and $[M+NH_4]^+$ species at m/z = 684.3737 (in DCM/MeOH + NH_4OAc). The positive nanoESI of **BD-I4** (Figure 10 – SI), on the other hand, showed the presence of $[M+H]^+$ species at m/z = 623.3206 (in

DCM/MeOH + NH_4OAc). All of the mass spectra matched their corresponding theoretical isotope model within a mass error of 2 ppm.

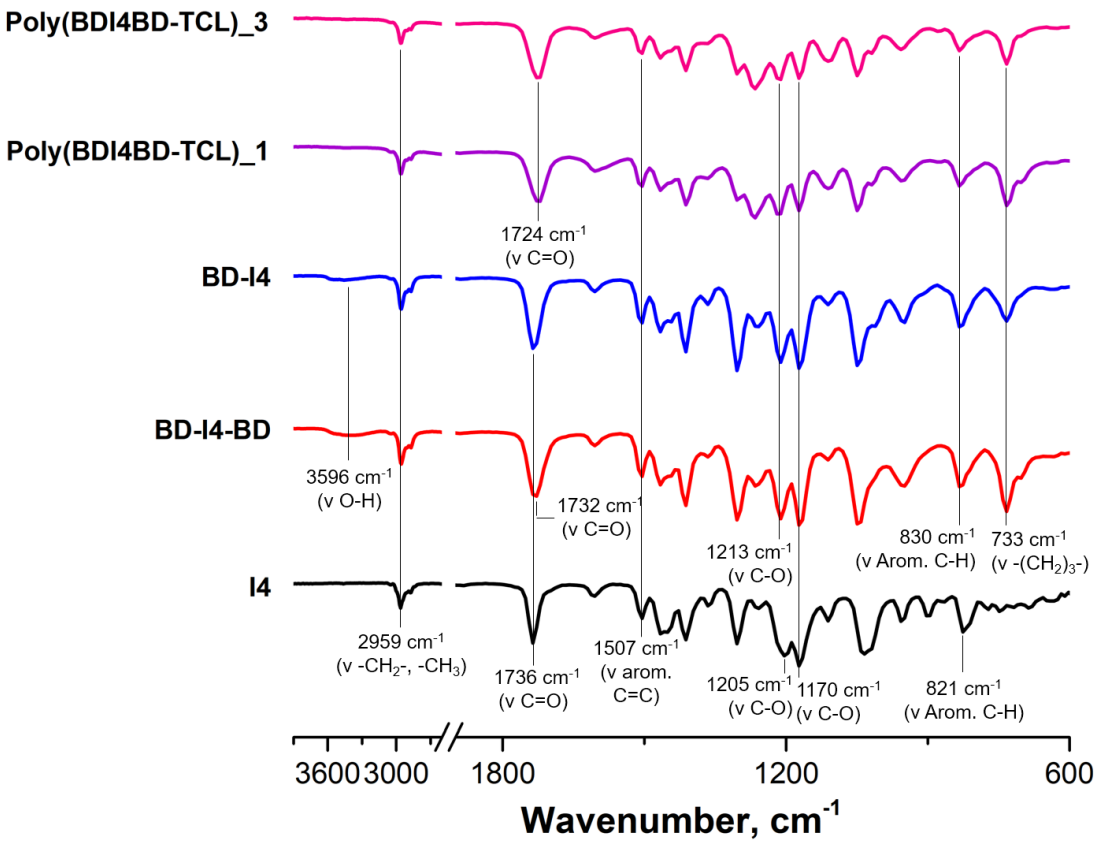

Figure 5: *FT-IR spectra of* **I4**, **BD-I4-BD**, **BD-I4**, **Poly(BDI4BD-TCL)_1** *and* **Poly(BDI4BD-TCL)_3**.

The appearance of a new peak at 3596 cm^{-1} in the FT-IR spectrum of **BD-I4-BD** and **BD-I4** in Figure 5 corresponding to the O-H stretching vibration of an alkyl alcohol, once again substantiated the successful synthesis of pre-polymers. Interestingly, both compounds could be differentiated from each other by comparing the intensity of the O-H stretching vibration. **BD-I4-BD** with two terminal hydroxyl groups has a more intense O-H stretching vibration than **BD-I4** with only one terminal hydroxyl group. The characteristic C=O stretching vibration of an aromatic ester was also seen slightly shifted in **BD-I4-BD** (1732 cm^{-1}) but remained unchanged for the asymmetric counterpart, **BD-I4** (1736 cm^{-1}) when compared to **I4**.

3.3 Synthesis of Pre-polymer, BD-CM1-BD

CM1 was synthesised via cyclisation of **I3** and **TetraEGdiOTs** with the use of K_2CO_3 as a base and KPF_6 as a templating agent as shown in Scheme 1. The synthetic procedure involved and its characterisation were reported in Chapter 5. With the synthesis of pre-polymer **BD-I4-BD** being successful, a similar reaction procedure was employed for the synthesis of pre-polymer **BD-CM1-BD** via transesterification[3] of **CM1** crystals and **BD** in the presence of TNBT as catalyst. The crude material was then purified via column chromatography to yield **BD-CM1-BD** and its asymmetrical sibling **BD-CM1**. The compounds were characterised by 2D NMR spectroscopy, FT-IR and mass spectrometry.

Similar to what has been mentioned regarding **BD-I4-BD** and **BD-I4** in Section 3.2, the difference in symmetry between the two new compounds were apparent in the NMR spectra of **BD-CM1-BD** and **BD-CM1** making them distinguishable from one another.

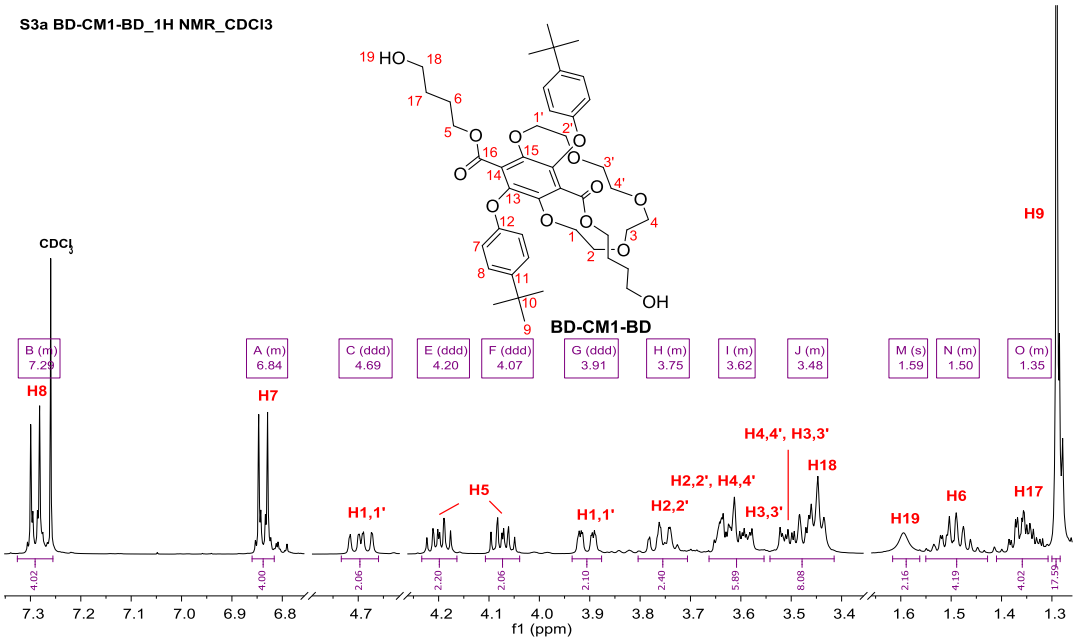

^{1}H NMR (500 MHz, Chloroform - *d*) δ 7.33 – 7.26 (m, 4H, H8), 6.86 – 6.82 (m, 4H, H7), 4.69 (ddd, *J* = 13.0, 8.9, 1.3 Hz, 2H, H1, H1'), 4.20 (ddd, *J* = 10.9, 6.8, 5.9 Hz, 2H, H5), 4.07 (ddd, *J* = 10.9, 6.7, 5.9 Hz, 2H, H5), 3.91 (ddd, *J* = 13.0, 3.6, 1.5 Hz, 2H, H1, H1'), 3.80 – 3.71 (m, 2H, H2, H2'), 3.66 – 3.55 (m, 6H, H2, H2', H4, H4', H3, H3'), 3.54 – 3.41 (m, 8H, H4, H4', H3, H3', H18), 1.59 (s, 2H, H19), 1.55 – 1.43 (m, 4H, H6), 1.41 – 1.31 (m, 4H, H17), 1.29 (s, 18H, H9).

Figure 6: *^{1}H NMR spectrum (500 MHz, $CDCl_3$) of* **BD-CM1-BD***.*

From the ^{1}H NMR spectrum of **BD-CM1-BD** in Figure 6, peaks attributed to the CH_2 protons on the newly attached butyl chains were seen as two sets of mirroring multiplets (at 4.20 and 4.07 ppm – H5), an overlapped multiplet at 3.48 ppm (H18) as well as multiplets at 1.50 ppm (H6) and 1.35 ppm (H17). The two

protons from the terminal OH groups (H19) could also be seen as a broad peak at 1.59 ppm. The diastereotropic nature of the OCH_2 protons of the crown ether characteristic of **CM1** in its ^1H NMR spectrum (Chapter 5, Figure 1) was unaltered by transesterification and was observed in **BD-CM1-BD** as prominent multiplet signals around 3.93-3.42 ppm and 4.69 ppm.

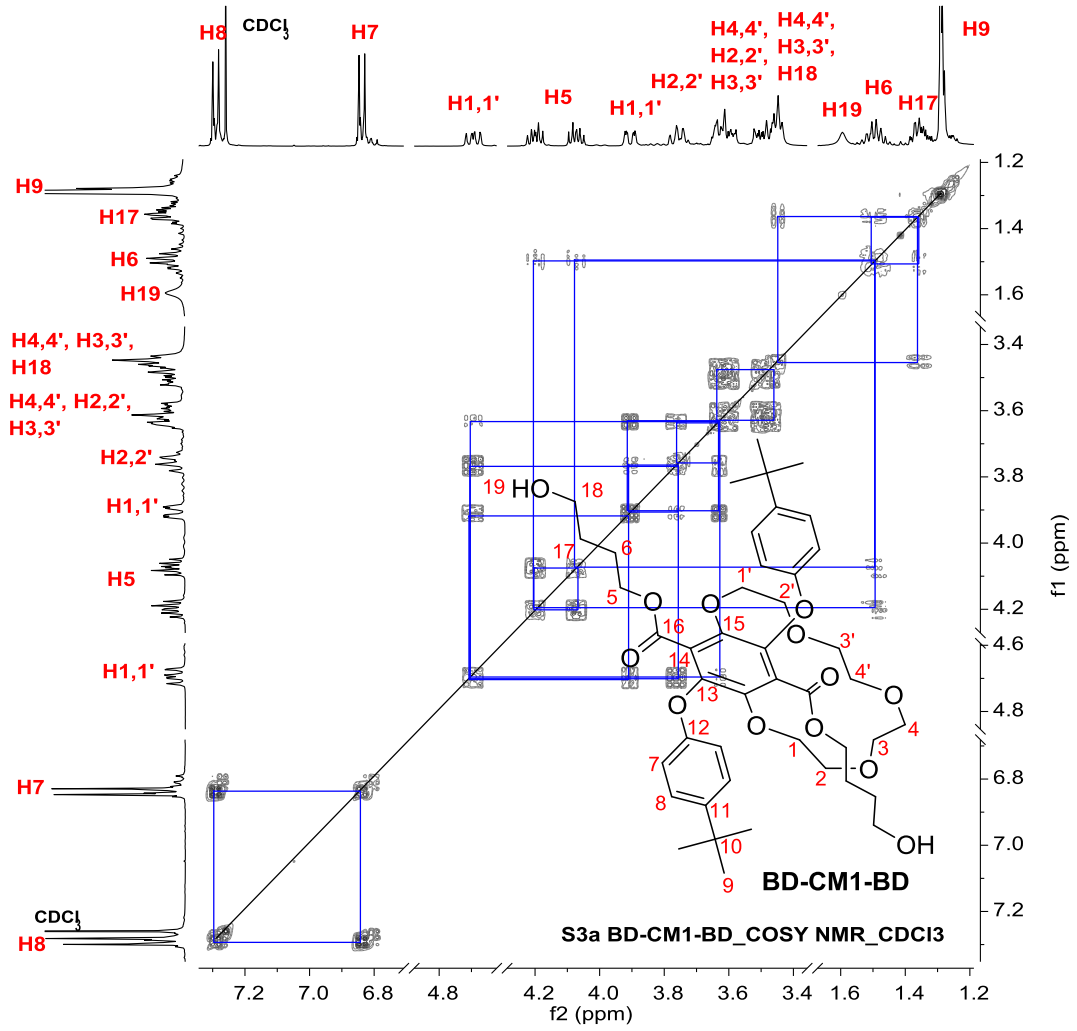

Figure 7: *COSY NMR spectrum (500 MHz, $CDCl_3$) of* **BD-CM1-BD**.

Interestingly, just like **CM1**, **BD-CM1-BD** with its ethyl ester groups substituted by butyl chains and terminal alcohol groups, also exhibited two sets of complex mirroring multiplets (H5) that were correlated to the H6 protons in its COSY NMR spectrum in Figure 7. This can be attributed to slow interconverting conformers of **BD-CM1-BD** which imparted inequivalence to the CH_2 protons on the butyl chains. Very similar conformations to that of **CM1** in Figure 3 (Chapter 5) was believed to have caused such inequivalency.

Undoubtedly the ^{1}H NMR spectrum of asymmetrical **BD-CM1** (Figure 8) appeared to be much more complicated than its symmetrical counterpart with two sets of peaks each in addition to overlapping ones. The presence of diasterotropic OCH_2 protons of the crown ether as well as inequivalent CH_2 protons on the butyl chain and ethyl ester group made the assignment of peaks more challenging.

From the complex spectrum, an easily recognisable triplet at 0.99 ppm belonged to the H6' of the CH_3 unit on the unreacted arm, whilst peaks attributed to the CH_2 protons on the newly attached butyl chain were seen as two sets of overlapped mirroring multiplets (at 4.19 and 4.07 ppm – H5,5'), an overlapped multiplet at 3.48 ppm (H18) as well as multiplets at 1.50 ppm (H6) and 1.36 ppm (H17).

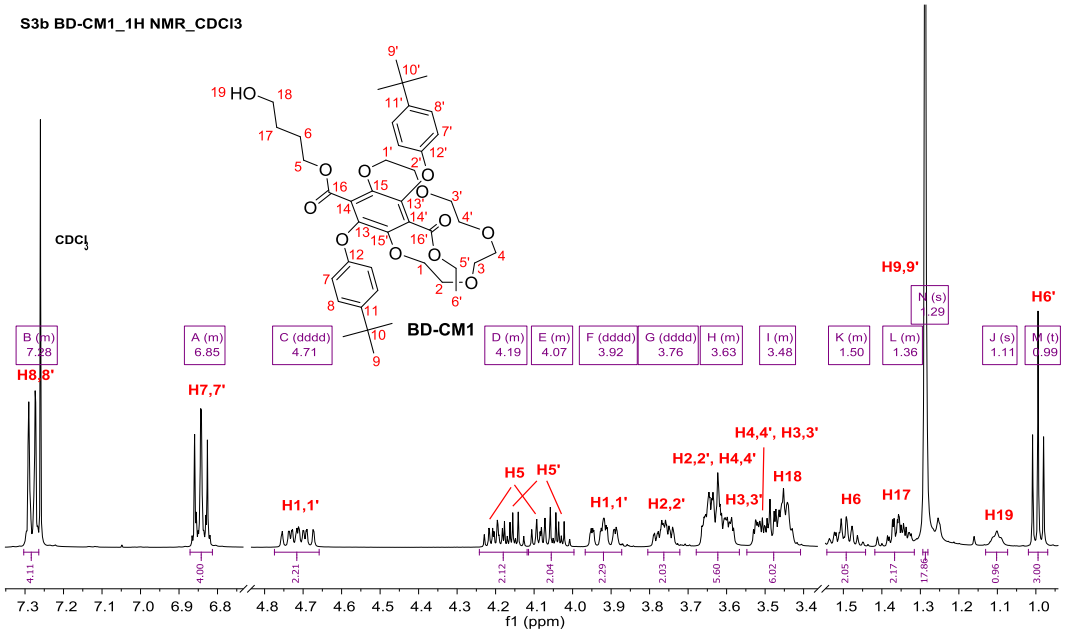

^{1}H NMR (500 MHz, Chloroform - *d*) δ 7.30 – 7.26 (m, 4H, H8, H8'), 6.87 – 6.81 (m, 4H, H7, H7'), 4.71 (dddd, *J* = 18.8, 13.0, 9.0, 1.3 Hz, 2H, H1, H1'), 4.24 – 4.12 (m, 2H, H5, H5'), 4.11 – 4.00 (m, 2H, H5, H5'), 3.92 (dddd,*J* = 17.5, 13.0, 3.5, 1.5 Hz, 2H, H1, H1'), 3.76 (dddd, *J* = 10.5, 8.8, 4.8, 1.4 Hz, 2H, H2, H2'), 3.68 – 3.57 (m, 6H, H2, H2', H4, H4', H3, H3'), 3.55 – 3.41 (m, 6H, H4, H4', H3, H3', H18), 1.54 – 1.44 (m, 2H, H6), 1.42 – 1.32 (m, 2H, H17), 1.29 (s, 18H, H9, H9'), 1.11 (s, 1H, H19), 0.99 (t, *J* = 7.1 Hz, 3H, H6').

Figure 8: *^{1}H NMR spectrum (500 MHz, $CDCl_3$) of* **BD-CM1**.

The ^{13}C NMR spectrum of **BD-CM1** in Figure 6 (SI) was as complex as its ^{1}H NMR spectrum, however, with careful analysis of its COSY, HSQC and HMBC NMR spectra, all of its carbon peaks were assigned. The two carbonyl carbons were seen at 164.6 ppm (C16) and 164.4 ppm (C16') and were correlated with their respective H5 and H5' protons in the COSY NMR spectrum (Figure 6 – SI).

The positive nanoESI of **BD-CM1-BD** (Figure 11 – SI) showed the presence of $[M+NH_4]^+$ species at m/z = 814.4367 (in DCM/MeOH + NH_4OAc) while the

positive nanoESI of **BD-CM1** (Figure 12 – SI) showed the presence of $[M+ NH_4]^+$ species at m/z = 770.4103 (in DCM/MeOH + NH_4OAc). Both of the mass spectra matched their corresponding theoretical isotope model within a mass error of 1 ppm.

The successful synthesis of pre-polymers was once again substantiated by the appearance of a new peak at 3337 cm^{-1} in the FT-IR spectrum of **BD-CM1-BD** and **BD-CM1** in Figure 9, corresponding to the O-H stretching vibration of an alkyl alcohol. By comparison, **BD-CM1-BD** with two terminal hydroxyl groups has a more intense O-H stretching vibration than **BD-CM1** with only one terminal hydroxyl group. The characteristic C=O stretching vibration of an aromatic ester was also seen slightly shifted in **BD-CM1-BD** (1733 cm^{-1}) but remained unchanged for the asymmetric counterpart, **BD-CM1** (1737 cm^{-1}) when compared to **CM1**.

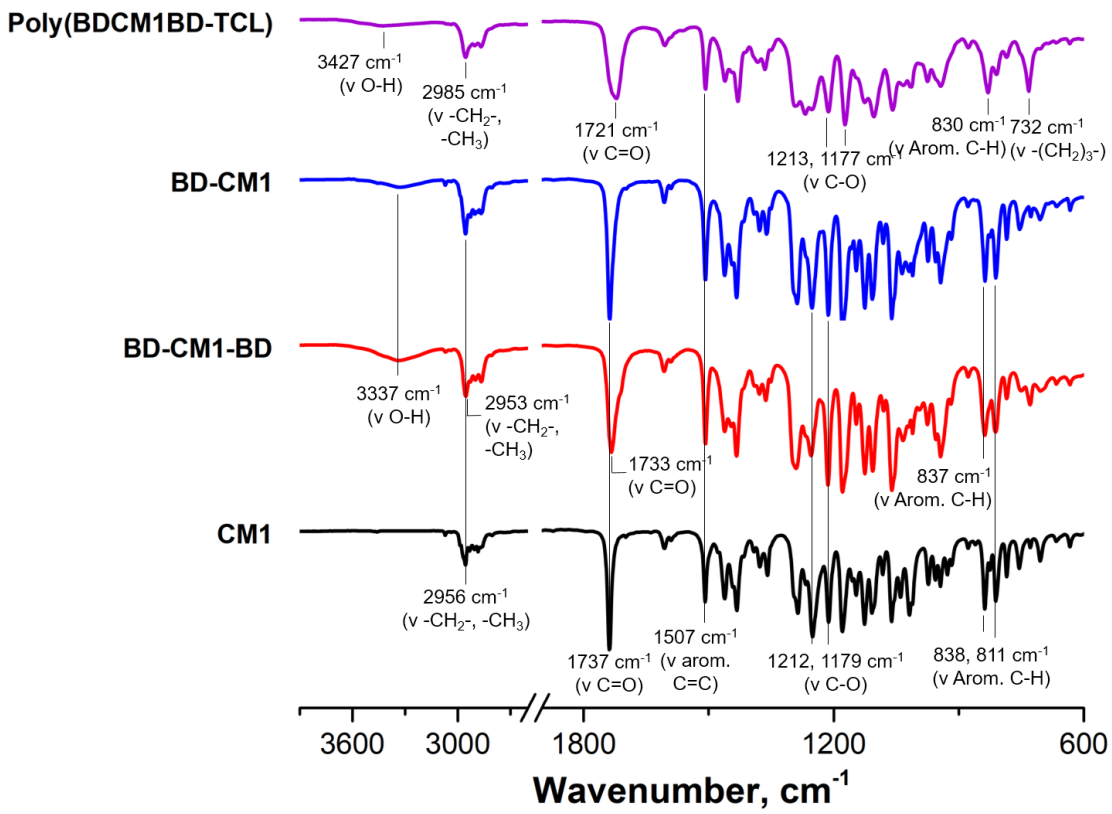

Figure 9: *FT-IR spectra of* **CM1**, **BD-CM1-BD**, **BD-CM1** *and* **Poly(BDCM1BD-TCL)**.

3.4 Synthesis of Poly(EGI3EG-TCL)

Copolymer, **Poly(EGI3EG-TCL)** was synthesised via nucleophilic addition-elimination reaction of pre-polymer, **EG-I3-EG** and **TCL** as shown in Scheme 2. In this polymerisation, **EG-I3-EG** was used in slight excess so that the end groups would be –OH capped. The appearance of broad peaks in the ^{1}H NMR spectrum of **Poly(EGI3EG-TCL)** shown in Figure 10 was the first sign of a successful synthesis of oligomer/polymer because of the overlapping proton signals from its repeating units. The end group proton signals (appeared as small peaks) and the repeating unit proton signals (appeared as larger peaks) were assigned by colour, as follows.

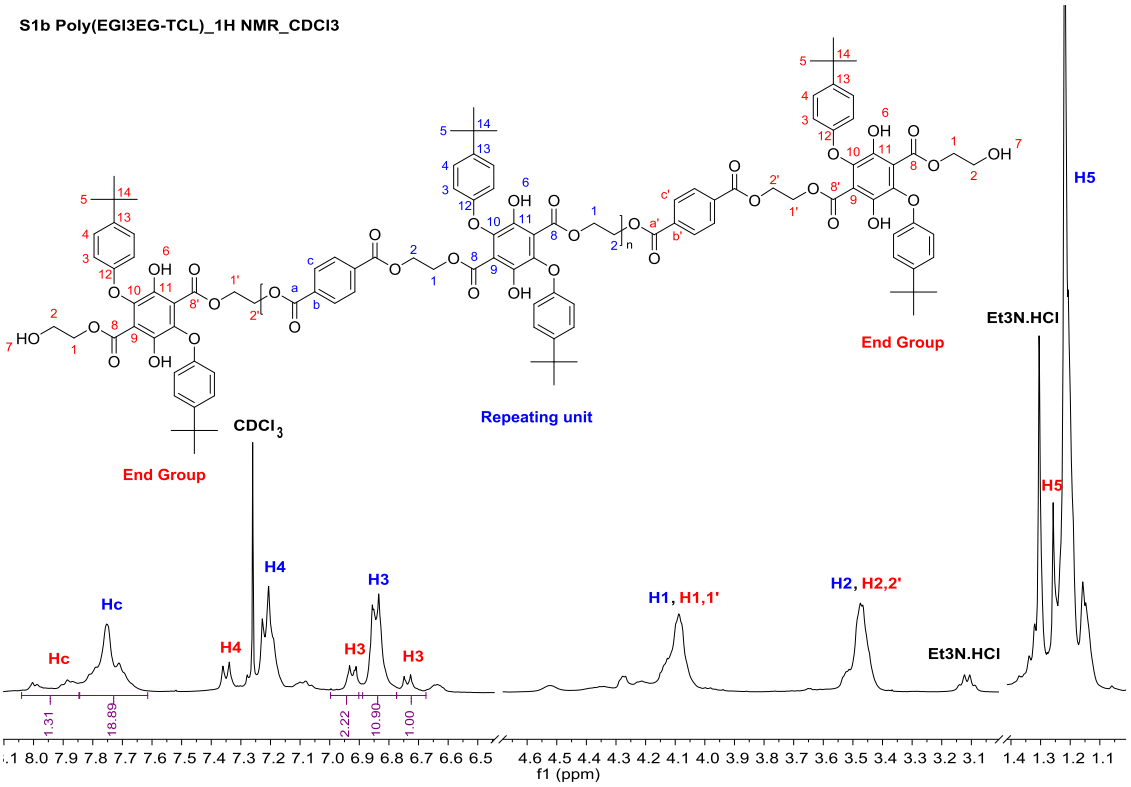

Figure 10: *^{1}H NMR spectrum (400 MHz, $CDCl_3$) of* **Poly(EGI3EG-TCL)**.

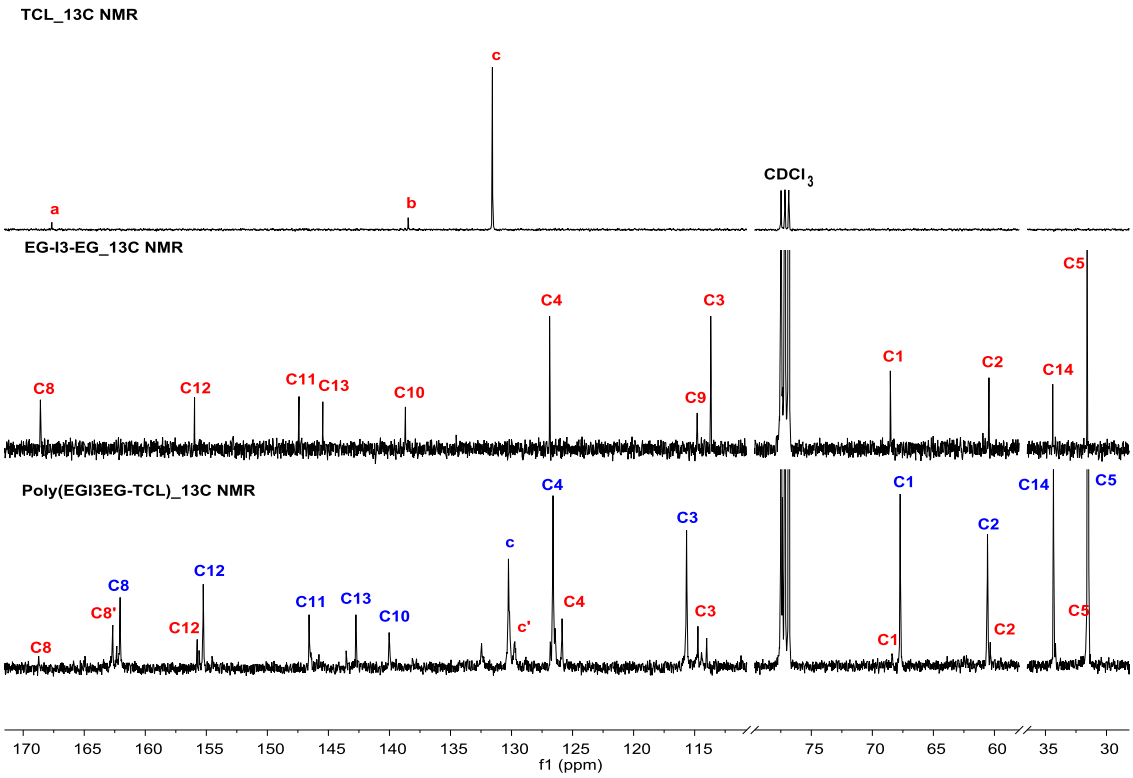

Figure 11: *Comparison of ^{13}C NMR spectra (400 MHz, $CDCl_3$) of* **TCL**, **EG-I3-EG** *and* **Poly(EGI3EG-TCL)**.

By comparing the ^{13}C NMR spectrum of **Poly(EGI3EG-TCL**) with that of its monomers (Figure 11), the stronger intensity carbon peaks attributed to the repeating unit of the polymer were assigned (in **blue**) whereas the weaker intensity carbon peaks of the end groups were assigned (in **red**). The labelled carbon peaks were then used to locate their corresponding protons from the HSQC NMR spectrum of **Poly(EGI3EG-TCL)** in Figure 12. The proton assignments were double-checked with the COSY NMR spectrum in Figure 13. By concurrently working back and forth its ^{1}H, ^{13}C, HSQC and COSY NMR spectra, most of the peaks in the ^{1}H and ^{13}C NMR spectra of **Poly(EGI3EG-TCL)** could be identified.

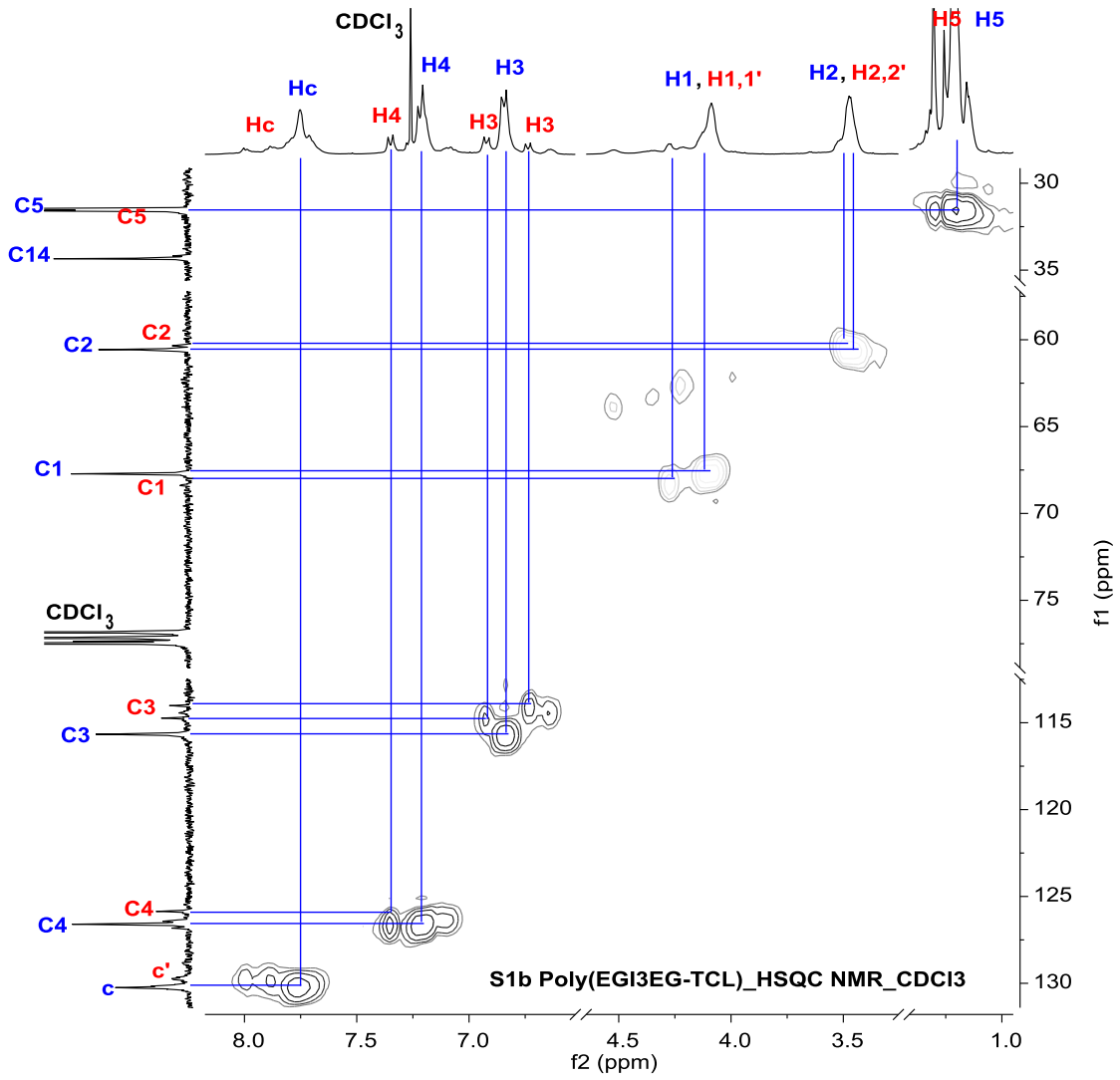

Figure 12: *HSQC NMR spectrum (400 MHz, $CDCl_3$) of* **Poly(EGI3EG-TCL)**.

The two carbon peaks (115.7 and 126.6 ppm) in the ^{13}C NMR of **Poly(EGI3EG-TCL)** (Figure 11) will be used as examples in this case to demonstrate how they were assigned. Since the peaks were in range with that of the **C3** carbon (113.6 ppm) and **C4** carbon (126.9 ppm) of **EG-I3-EG**, the peaks can be labelled as **C3** and **C4** of the repeating unit of **Poly(EGI3EG-TCL)**, respectively. From Figure 12, **C3** corresponded directly with the proton peak at 6.84 ppm whereas **C4** corresponded to the proton peak at 7.21 ppm. Hence, the corresponding proton peaks were labelled as **H3** and **H4**, respectively. The correlation between both **H3** and **H4** peaks, as reflected in the COSY NMR spectrum (Figure 13), further substantiated the assignments. The assignment process was then repeated until all of the proton and carbon peaks were properly assigned.

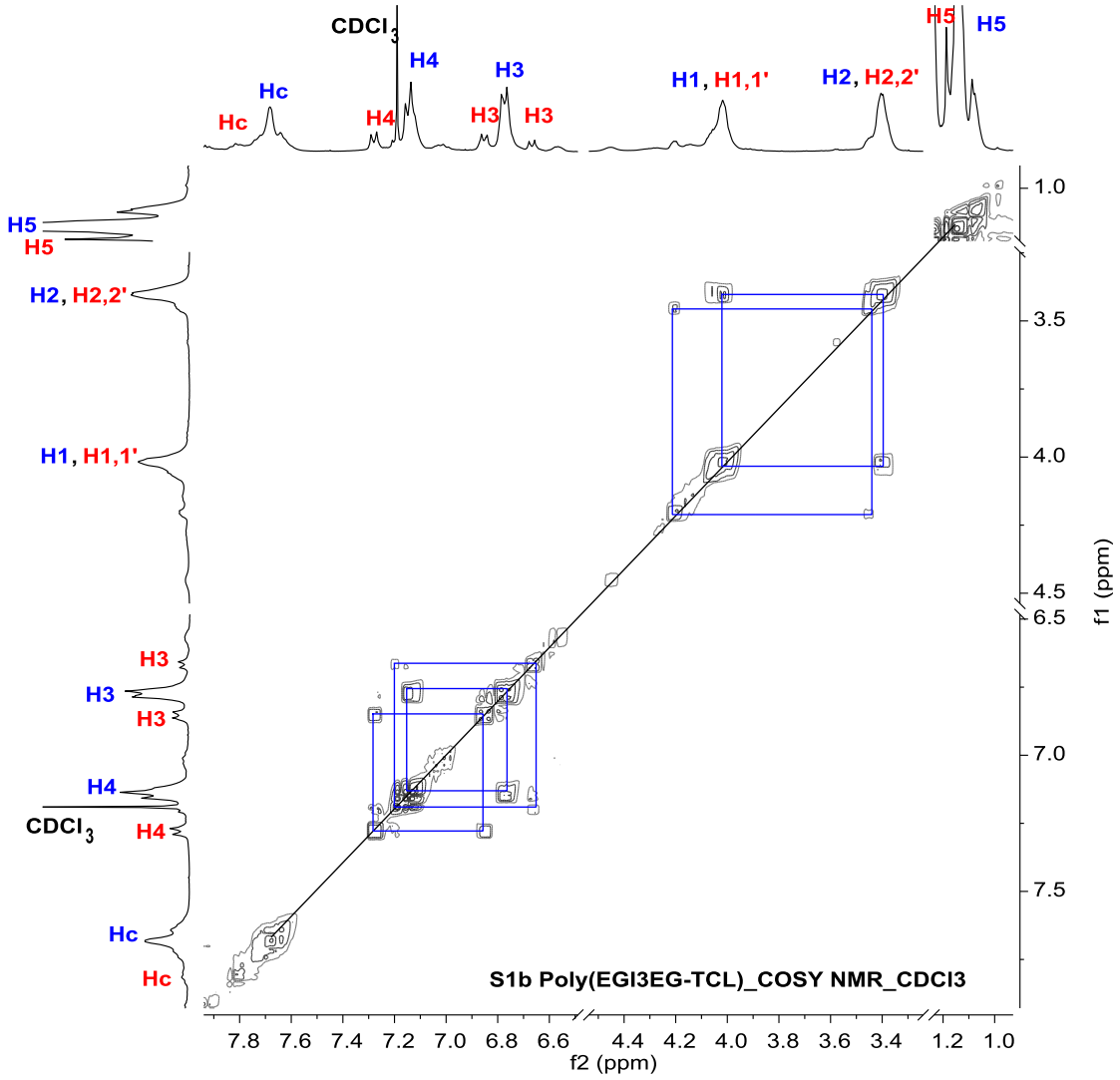

Figure 13: *COSY NMR spectrum (400 MHz, $CDCl_3$) of* **Poly(EGI3EG-TCL)**.

DOSY NMR spectroscopy was employed for the determination of the diffusion coefficient, D, and the identification of proton peaks of a polymer from a mixture of compounds. The former was later used to estimate the molecular weight (M_w) of **Poly(EGI3EG-TCL)**.

There were two ambiguous peaks (at 1.31 and 3.11 ppm) in the ^{1}H NMR spectrum of **Poly(EGI3EG-TCL)** (Figure 10). From the 2D DOSY NMR spectrum, the two peaks were found to have higher D values than the proton peaks of the **Poly(EGI3EG-TCL)**. Since the D value is inversely proportional to the hydrodynamic radius of a compound, the D value difference meant that the two peaks belonged to a different and much smaller sized compound (later identified as triethylamine hydrochloride, $Et_3N.HCl$). Therefore, to avoid confusion, they were omitted from the HSQC (Figure 12) and COSY NMR spectra (Figure 13).

The number of repeating monomer units, n can be calculated from its ^{1}H NMR spectrum by dividing the quotient of repeating unit protons with the quotient of end group protons whilst the number average molecular weight, M_n of a polymer can be calculated by the sum of formula weight, FW of the end groups and repeating units. In the case of **Poly(EGI3EG-TCL)**, the two values were calculated as follows:

$$\mathbf{FW} = \underbrace{HO(O_8C_{32}H_{36})}_{565.62}-\underbrace{(C_{40}H_{40}O_{12})_n}_{(712.72)_n}-\underbrace{(C_{40}H_{40}O_{12})OH}_{729.73}$$

$$\text{No. of repeating monomer units, } \mathbf{n} = \frac{Quotient_{\text{repeating unit } protons}}{Quotient_{end\ group\ protons}}$$

$$= \frac{\left(\frac{Integral_{H3}+Integral_{Hc}}{n_{protons\ integrated}}\right)}{\left(\frac{Integral_{H3}+Integral_{Hc}}{n_{protons\ integrated}}\right)}$$

$$= \frac{\left(\frac{10.90+18.89}{4+4}\right)}{\left(\frac{2.22+1.00+1.31}{8+4}\right)}$$

$$= 9.89 \approx 10$$

$$\text{Molecular Weight, } \boldsymbol{M_n} = FW_{end\ group} + FW_{repeating\ unit,n}$$

$$= (565.62 + 729.73) + (712.72 \times 10)$$

$$= 8423$$

According to literature[4–6]the weight average molecular weight, M_w of polymers can be estimated from its D value using the linear correlation between the logarithm of diffusion coefficient (log D) and the molecular weight (log M_w). Thus, by using the D value (9.06 x 10^{-11} m^2s^{-1}) obtained from the 2D DOSY NMR spectrum of **Poly(EGI3EG-TCL)** and the equation of PS calibration curve from the paper by Grubbs *et al.*[4], the M_w of **Poly(EGI3EG-TCL)** was calculated as follows:

$$\log D = -0.537 \log M_w - 7.697$$

$$\log M_w = \frac{\log D + 7.697}{-0.537}$$

$$\log M_w = \frac{\log 9.06 \times 10^{-11} + 7.697}{-0.537}$$

$$M_w = 23360$$

From Table 1, the calculated M_w of **Poly(EGI3EG-TCL)** (23360 $gmol^{-1}$) was found to be relatively close to the M_w value obtained from the actual GPC experiment (25047 $gmol^{-1}$). In contrast, the calculated M_n (8423 $gmol^{-1}$) from the ^1H NMR spectrum appeared to be much lower than the M_n value from GPC (12806 $gmol^{-1}$).

Polymer	^1H and DOSY NMR				GPC[d]		
	M_n [a] $gmol^{-1}$	M_w [b] $gmol^{-1}$	PDI[c]	D m^2s^{-1}	M_n $gmol^{-1}$	M_w $gmol^{-1}$	PDI
Poly(EGI3EG-TCL)	8423	23360	2.77	9.06×10^{-11}	12806	25047	1.96
Poly(BDI4BD-TCL)	7839	10670	1.36	1.38×10^{-10}	1809	3471	1.92

[a] Number average molecular weight (M_n) was calculated from the ^1H NMR spectrum; [b] Weight average molecular weight (M_w) was calculated from diffusion coefficient, D obtained from the 2D DOSY NMR spectrum together with the equation of PS calibration curve by Grubbs *et al*. log D = -0.537 log M_w – 7.697 (R^2 = 0.9991); [c] PDI = M_w/M_n; [d] Monodispersed PS standard as the calibrant, THF/Toluene as the eluent.

Table 1: *Number average molecular weight (M_n), weight average molecular weight (M_w), and polydispersity index (PDI) of* **Poly(EGI3EG-TCL)** *and* **Poly(BDI4BD-TCL)**.

From the FT-IR spectrum of **Poly(EGI3EG-TCL)** in Figure 13 (SI), a shift from 1676 cm^{-1} (in **EG-I3-EG**) to 1742 cm^{-1} from the peak corresponding to the characteristic C=O stretching vibration of an aromatic ester once again substantiated the successful synthesis of copolymer.

Apart from structural characterisation, the glass transition temperature, T_g of the **Poly(EGI3EG-TCL)** was determined from the second heating curve in its DSC thermograms and was found to be 91 ^oC. This justified its brittleness at room temperature.

3.5 Synthesis of Poly(BDI4BD-TCL)

Copolymer, **Poly(BDI4BD-TCL)** was synthesised via a nucleophilic addition-elimination reaction of pre-polymer, **BD-I4-BD** and **TCL** as shown in Scheme 2. Similar to the synthesis of **Poly(EGI3EG-TCL)**, **BD-I4-BD** was used in slight excess in order to obtain a polymer with –OH chain ends. During the purification process, two samples were isolated: **Poly(BDI4BD-TCL)_1** (28 mg) and **Poly(BDI4BD-TCL)_3** (263 mg), both in the form of an off-white, opaque and brittle polymer. However, **Poly(BDI4BD-TCL)_1** was later found to be a mixture of higher molecular weight polymer and monomer via GPC and DOSY NMR spectroscopy. Therefore, this section on **Poly(BDI4BD-TCL)** will only focus on the synthesis and characterisation of **Poly(BDI4BD-TCL)_3**.

The ^{1}H NMR spectrum of **Poly(BDI4BD-TCL)** appeared slightly broadened – a tell-tale sign of a/an polymer/oligomer. A similar method of assigning NMR peaks was used as mentioned in Section 3.4. For easier comparison, the end group proton signals were assigned in **red** whilst the proton signals of the repeating units were assigned in **blue**.

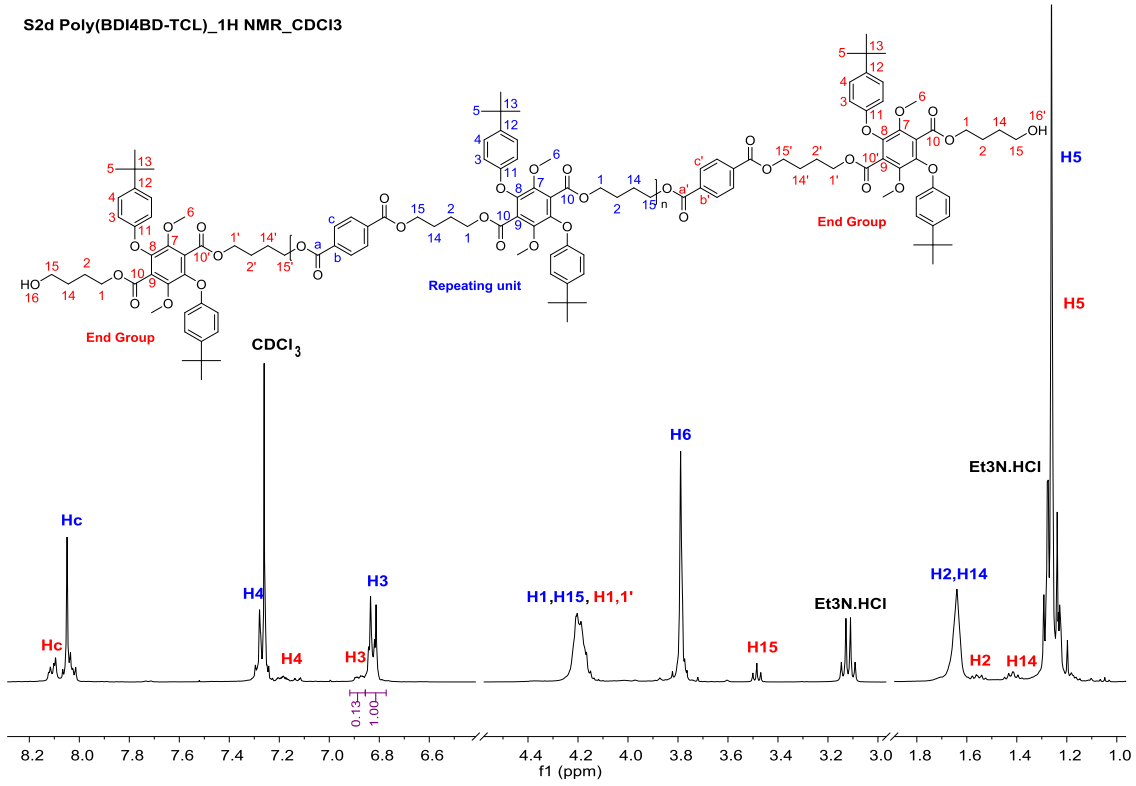

Figure 14: *^{1}H NMR spectrum (400 MHz, $CDCl_3$) of* **Poly(BDI4BD-TCL)**.

From Figure 14, each of the aromatic protons (**H3**, **H4** and **Hc**) in the repeating unit of **Poly(BDI4BD-TCL)** were seen with an accompanying end group proton peak nearby which correlated with one another in the COSY NMR spectrum (Figure 16). In contrast, the aliphatic protons (**H14** and **H15**) appeared to be overlapped with **H1** and **H2**, respectively. Their end group signals (**H14** and **H15**) were observed slightly further apart and were seen distinctively separated from its neighboring protons **H1** and **H2**. The $Et_3N.HCl$ peaks (at 1.28 and 3.12 ppm) also have a higher D value than the rest of the proton peaks from the 2D DOSY NMR spectrum of **Poly(BDI4BD-TCL)**. However, due to the presence of polymer proton peaks between the two $Et_3N.HCl$ peaks, they could not be omitted from the COSY (Figure 16), HSQC (Figure 17) and HMBC (Figure 18) NMR spectra.

The ^{13}C NMR spectrum of **Poly(BDI4BD-TCL)** was more complex in comparison to its monomers due to overlapping signals at 25.1 ppm (**C2**, **C14**, **C2**), 64.9 ppm (**C1**, **C15**, **C1,1'**) and 129.5 ppm (**c**, **c**). Fortunately, with the use of COSY, HSQC and HMBC NMR spectra, the peaks could be assigned.

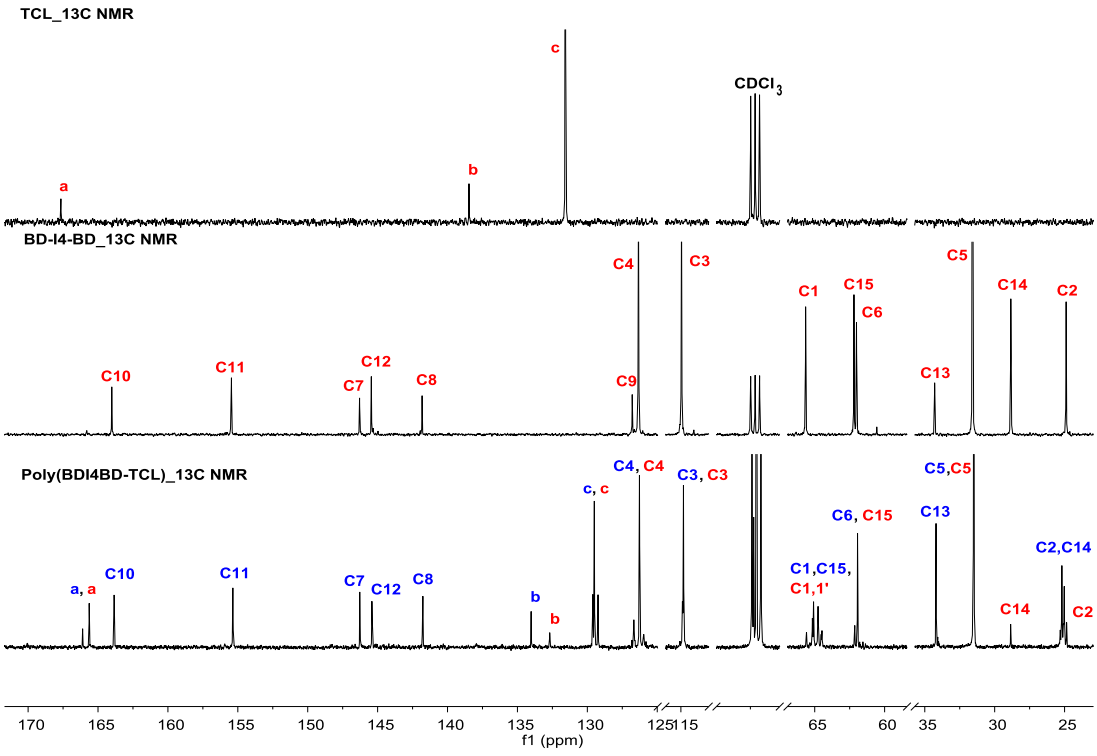

Figure 15: *Comparison of ^{13}C NMR spectra (400 MHz, $CDCl_3$) of* **TCL**, **BD-I4-BD** *and* **Poly(BDI4BD-TCL)**.

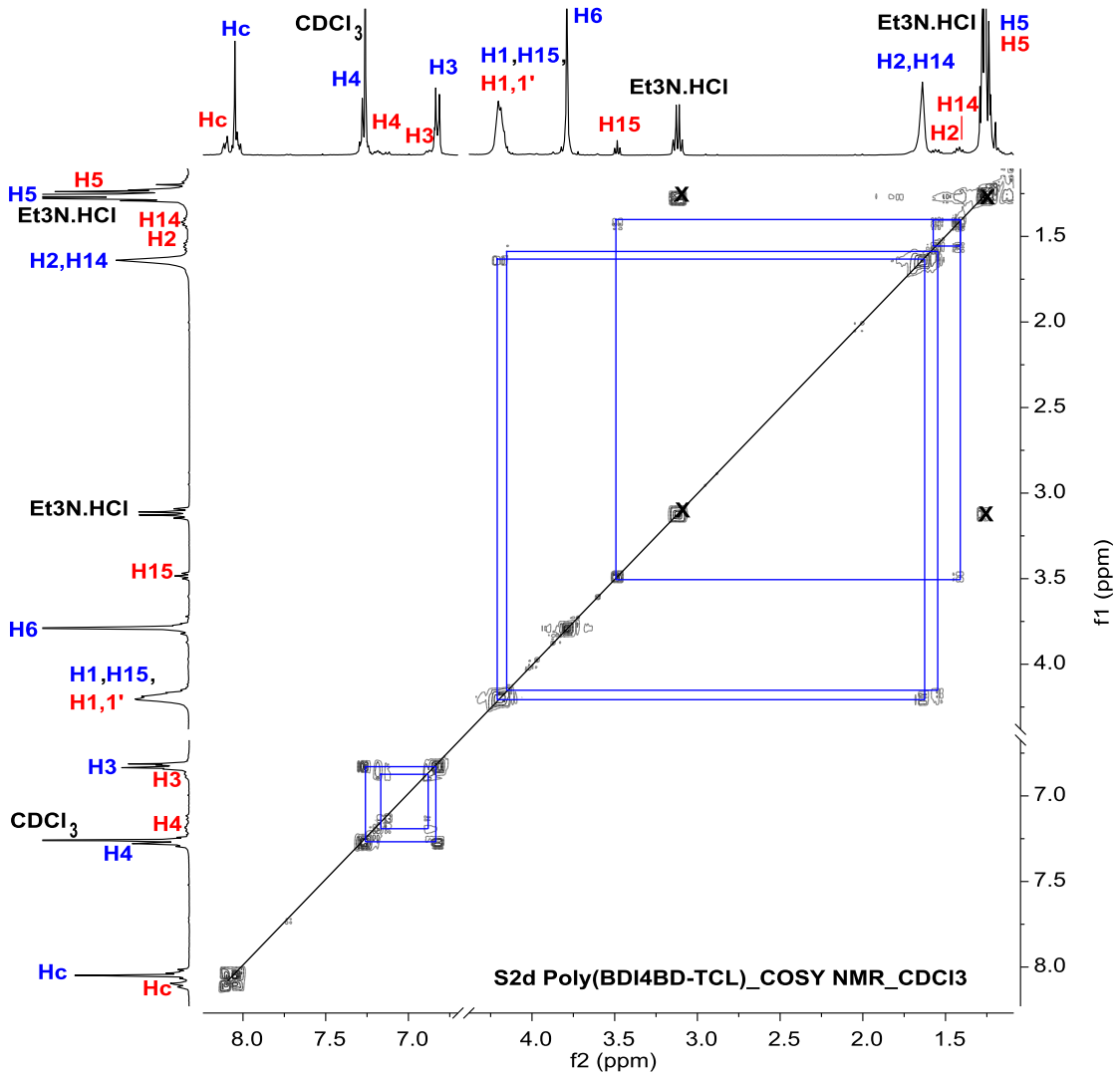

Figure 16: *COSY NMR spectrum (400 MHz, $CDCl_3$) of* **Poly(BDI4BD-TCL)**.

From the COSY NMR spectrum of **Poly(BDI4BD-TCL)** (Figure 16), correlations were observed between **H1** and **H2** protons, **H14** and **H15**, **H2** and **H14** as well as **H14** and **H15**. The correlation between **H1**, **H15** with **C2**, **C14** and **a** as well as between **H2**, **H14** with **C2**, **C14**, **C1** and **C15** observed in the HMBC NMR spectrum (Figure 18) further consolidated the assignments of proton peaks (at 1.64 and 4.20 ppm).

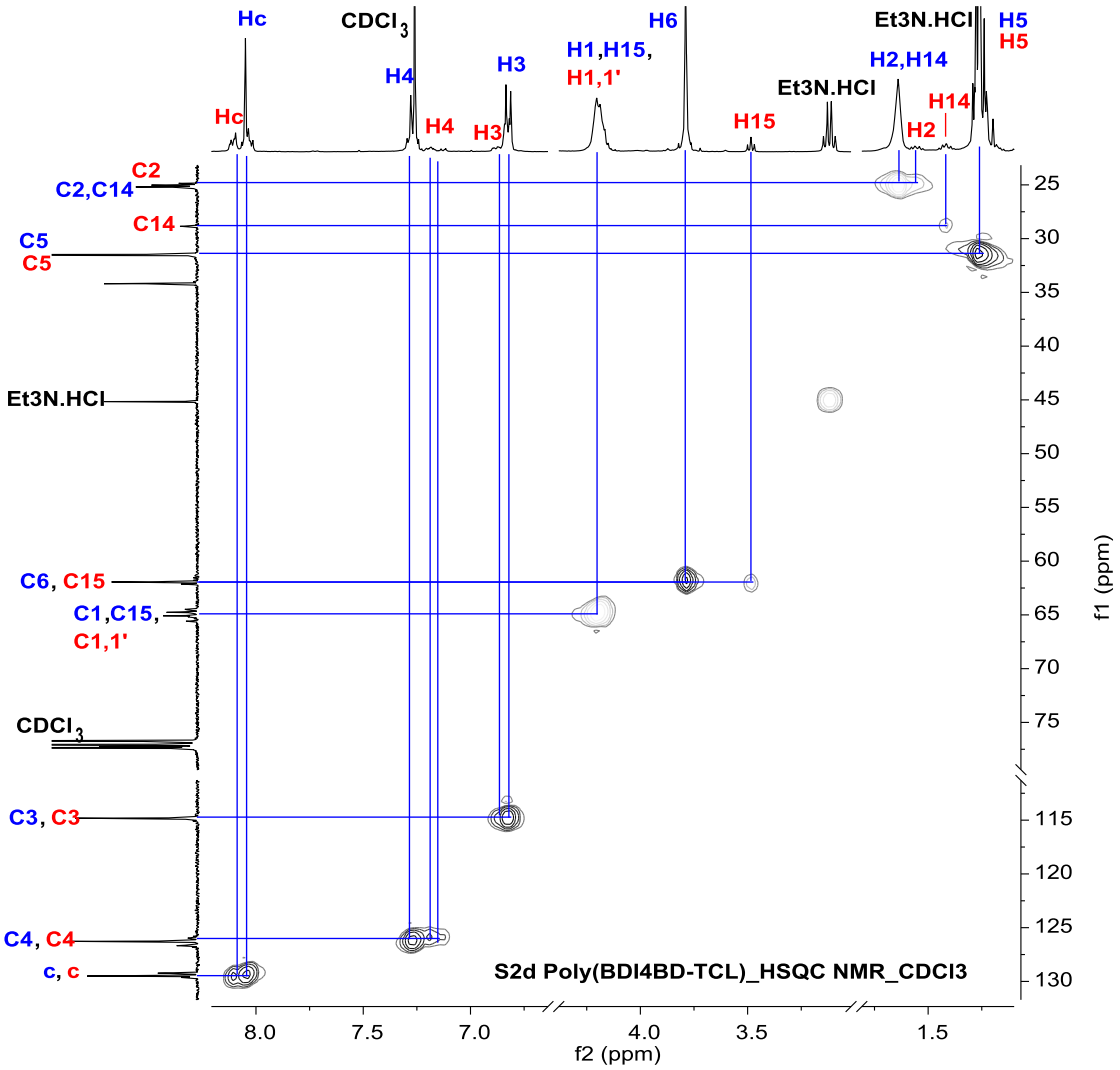

Figure 17: *HSQC NMR spectrum (400 MHz, $CDCl_3$) of* **Poly(BDI4BD-TCL)**.

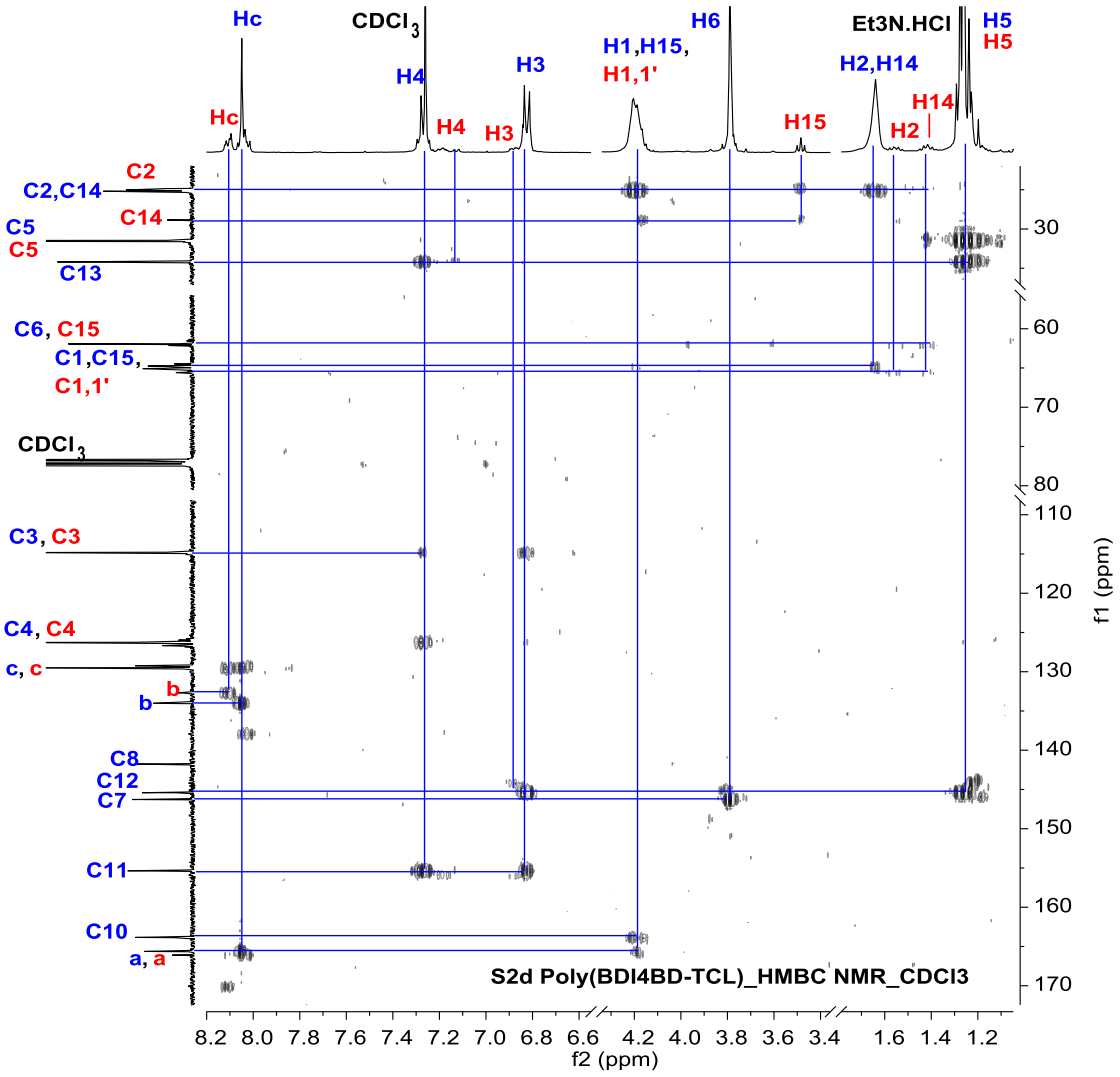

Figure 18: *HMBC NMR spectrum (400 MHz, $CDCl_3$) of* **Poly(BDI4BD-TCL)**.

The number of repeating monomer units, n, and the number average molecular weight, M_n of **Poly(BDI4BD-TCL)** were calculated as follows:

$$\text{FW} = \underbrace{HO(O_8C_{38}H_{48})}_{649.77}-\underbrace{(C_{46}H_{52}O_{12})_n}_{(796.88)_n}-\underbrace{(C_{46}H_{52}O_{12})OH}_{813.88}$$

$$\text{No. of repeating monomer units, } \mathbf{n} = \frac{Quotient_{\text{repeating unit } protons}}{Quotient_{end\ group\ protons}}$$

$$= \frac{\left(\frac{Integral_{H3}}{n_{protons\ integrated}}\right)}{\left(\frac{Integral_{H3}}{n_{protons\ integrated}}\right)}$$

$$= \frac{\left(\frac{1.00}{4}\right)}{\left(\frac{0.13}{4}\right)}$$

$$= 7.69 \approx 8$$

$$\text{Molecular Weight, } \boldsymbol{M_n} = FW_{end\ group} + FW_{repeating\ unit,n}$$

$$= (649.77 + 813.88) + (796.88 \times 8)$$

$$= 7839$$

The weight average molecular weight, M_w of **Poly(BDI4BD-TCL)** was estimated using the D value of 1.38 x 10^{-10} m^2s^{-1} from the 2D DOSY NMR spectrum and the following equation:

$$\log D = -0.537 \log M_w - 7.697$$

$$\log M_w = \frac{\log D + 7.697}{-0.537}$$

$$\log M_w = \frac{\log 1.38 \times 10^{-10} + 7.697}{-0.537}$$

$$M_w = 10670$$

From Table 1, the calculated M_n (7839 $gmol^{-1}$) of **Poly(BDI4BD-TCL)** by ^1H NMR spectrum was found to be four times larger than the M_n value obtained from the actual GPC experiment (1809 $gmol^{-1}$), while the calculated M_w (10670 $gmol^{-1}$) from the diffusion coefficient value was three-fold larger than the M_n value from GPC (3471 $gmol^{-1}$). This may be due to underestimation of GPC because it operates with the assumption that the polymer introduced in the system behaves

like that of PS in THF/toluene. The copolymer in this case could have had a very different hydrodynamic volume and behaviour in THF/toluene.

The polydispersity index, PDI of **Poly(BDI4BD-TCL)** obtained from NMR and GPC is around 2, slightly lower than the PDI value of **Poly(EGI3EG-TCL)** (around 3). This meant that the former polymer was a little bit more monodispersed than the latter.

The FT-IR spectrum of **Poly(BDI4BD-TCL)** in Figure 5 showed a shift in the peak corresponding to the characteristic C=O stretching vibration of an aromatic ester from 1732 cm^{-1} (in **BD-I4-BD**) to 1724 cm^{-1}. This once again corroborated the successful synthesis of a copolymer.

The glass transition temperature, T_g of the **Poly(BDI4BD-TCL)** was acquired from the second heating curve in its DSC thermograms and was found to be at 48 ^oC which was significantly lower than that of **Poly(EGI3EG-TCL)** (91 ^oC). This may be due to its longer aliphatic chain (butylene spacer instead of ethylene spacer) and a smaller number of repeating unit (n = 8). **Poly(BDI4BD-TCL)** appeared brittle at room temperature because its T_g value is higher than room temperature.

Both **Poly(BDI4BD-TCL)** and **Poly(EGI3EG-TCL)** exhibited solid-state fluorescence as shown in Figure 19b, with **Poly(BDI4BD-TCL)** glowing blue whereas **Poly(EGI3EG-TCL)** glowed green when viewed under a 312 nm UV lamp.

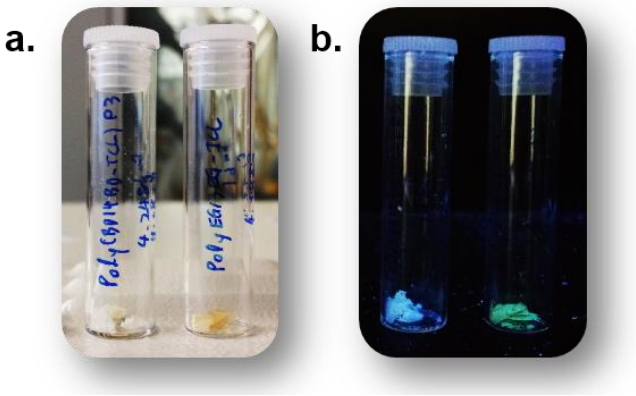

Figure 19: *Side-by-side comparison of* **Poly(BDI4BD-TCL)** *(left) and* **Poly(EGI3EG-TCL)** *(right) in* ***a)*** *normal light conditions and* ***b)*** *under 312 nm UV irradiation.*

3.6 Synthesis of Poly(BDCM1BD-TCL)

Copolymer, **Poly(BDCM1BD-TCL)** was synthesised via a nucleophilic addition-elimination reaction of pre-polymer, **BD-CM1-BD** and **TCL** as shown in Scheme 2. A slight excess of **BD-CM1-BD** compared to **TCL** was used to obtain an –OH terminated copolymer. The reaction yielded 96 mg of an opaque off-white polymer. Unfortunately, due time limitation and the lack of product, further purification and various polymer characterisation/analysis were put on hold.

From Figure 20, the peaks observed in the ^{1}H NMR spectrum of crude **Poly(BDCM1BD-TCL)** appeared slightly broadened – characteristic of a polymer/oligomer. Similar to the previous two copolymers in Section 3.4 and 3.5, two peaks around (1.3 and 3 ppm) attributed to $Et_3N.HCl$ were present. With the use of coloured circles, areas corresponding to different parts of the repeating unit of **Poly(BDCM1BD-TCL)** could be identified. The peak around 8 ppm labelled with a blue circle is from the benzene ring of **TCL**, the nine peaks labelled with red circles belong to protons from the butylene spacers and the 4-*tert*-butylphenyl units, while the remaining five peaks labelled with pink circles correspond to the CH_2 protons of the crown ether ring. Although most of the peaks observed in the ^{1}H NMR spectrum could be assigned to parts of the chemical structure of **Poly(BDCM1BD-TCL)**, the lack of small proton signals around the main proton peaks suggested that this compound might only have a few repeating units – thereby rendering the end group proton signals indistinguishable from that of the repeating units.

A shift in peak corresponding to the characteristic C=O stretching vibration of an aromatic ester from 1733 cm^{-1} (in **BD-CM1-BD**) to 1721 cm^{-1} was observed in the FT-IR spectrum of **Poly(BDCM1BD-TCL)** (Figure 9). This implied successful synthesis of possibly an oligomer.

In order to proceed with the characterisation of the product, 2D DOSY NMR experiments needed to be carried out to check if all of the peaks belonged to a single compound or if a mixture was present. If the sample contained only one major compound, then the peaks should be properly assigned with the help of its COSY, HSQC and HMBC NMR spectra. However, if the sample contained more than one compound, then it would require additional purification which could be

problematic with the little amount of compound left. At this stage, no conclusive statements can be made regarding the synthesis of **Poly(BDCM1BD-TCL)**.

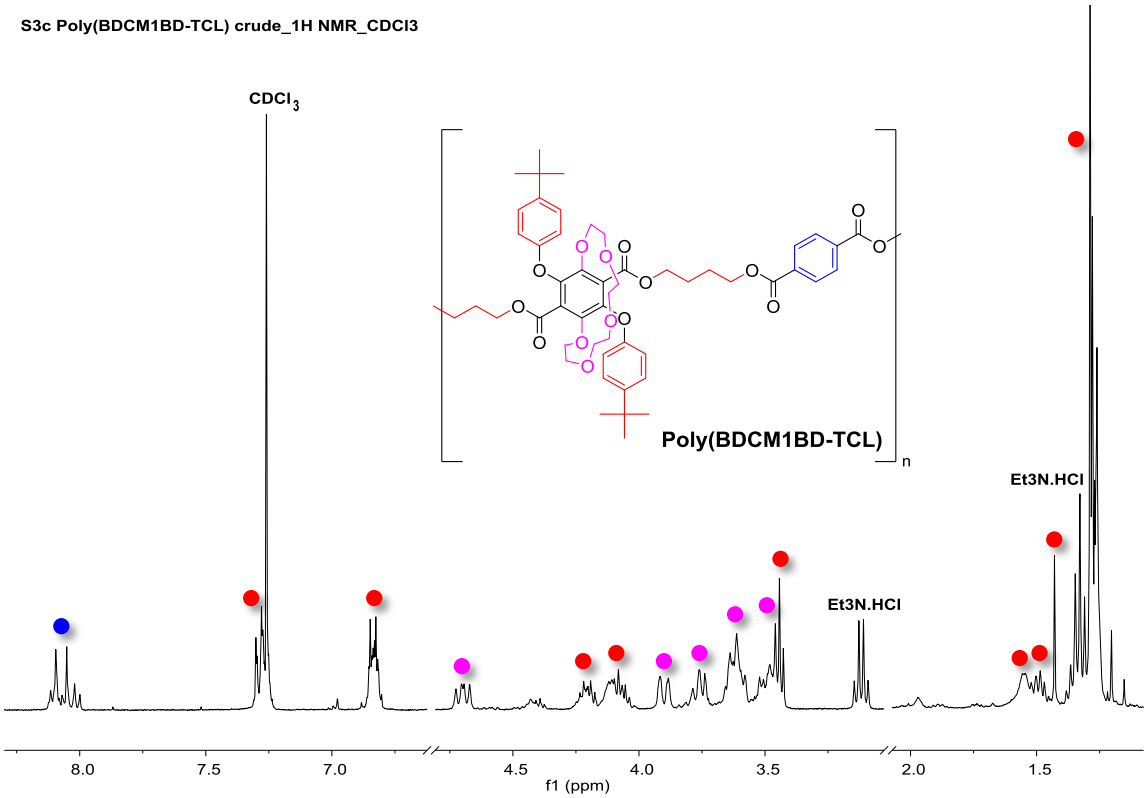

Figure 20: *1H NMR spectrum (400 MHz, CDCl3) of* **Poly(BDCM1BD-TCL)**.

4. Conclusions

In this chapter, the successful synthesis and characterisation of intermediate (**I4**), pre-polymers (**EG-I3-EG**, **BD-I4-BD**, **BD-CM1-BD**), their corresponding asymmetrical counterparts (**BD-I4** and **BD-CM1**) and copolymers (**Poly(EGI3EG-TCL)**, **Poly(BDI4BD-TCL)** and **Poly(BDCM1BD-TCL)**) were discussed. The intermediate and pre-polymers (both symmetrical and asymmetrical) were characterised via the use of NMR spectroscopy, FT-IR spectroscopy, mass spectrometry and crystal XRD (whenever possible). Beside basic structural analysis of the copolymers by NMR and FT-IR spectroscopy, the number average and weight average molecular weights (M_n and M_w) were determined by two methods (NMR and GPC). There were relatively huge discrepancies between the values obtained from both methods. The T_g of **Poly(BDI4BD-TCL)** (48 ^oC) was found to be lower than that of **Poly(EGI3EG-TCL)** (91 ^oC) due the use of longer butylene spacer between repeating terephthalate cores, however, the copolymers were both brittle at room temperature (since T_g > room temperature).

Due to time limitations, further purification and characterisation of **Poly(BDCM1BD-TCL)** were not carried out. Initial inspection of the ^{1}H NMR spectrum of the crude showed possibility of it being an oligomer with a low number of repeating units. At this point, no conclusive statements can be made regarding the polymer until its 2D DOSY NMR spectrum is recorded. Overall, the polymerisation yielded low molecular weight polyesters. Therefore – for future work, more controlled polymerisation/ modification should be attempted. Instead of synthesising a copolymer via nucleophilic addition-elimination reaction of pre-polymer, **BD-CM1-BD** and **TCL**, the asymmetrical pre-polymer, **BD-CM1** should be modified onto a known molecular weight polymer backbone. This way the amount of monomer introduced can be better estimated, the resulting polymer could be easily characterised and the concept of crown-aligned polymer could be tested.

Appendix. Supplementary Information, SI

Supplementary information, SI related to this chapter can be found at the end of this thesis.

References

1 V. B. Gupta and Z. Bashir, in *Handbook of Thermoplastic Polyesters*, Wiley-VCH Verlag GmbH & Co. KGaA, Weinheim, FRG, 2005, pp. 317–361.

2 J. Gong, X. J. Lou, W. Da Li, X. K. Jing, H. B. Chen, J. B. Zeng, X. L. Wang and Y. Z. Wang, *J. Polym. Sci. Part A Polym. Chem.*, 2010, **48**, 2828–2837.

3 J. Hsu and K. Y. Choi, *J. Appl. Polym. Sci.*, 1987, **33**, 329–351.

4 W. Li, H. Chung, C. Daeffler, J. A. Johnson and R. H. Grubbs, *Macromolecules*, 2012, **45**, 9595–9603.

5 J. G. Rosenboom, J. De Roo, G. Storti and M. Morbidelli, *Macromol. Chem. Phys.*, 2017, **218**, 1600436.

6 K. Gu, J. Onorato, S. S. Xiao, C. K. Luscombe and Y. L. Loo, *Chem. Mater.*, 2018, **30**, 570–576.

Chapter 7

Conclusion and Future Work

1. Conclusion

The followings are summaries of each chapter:

Chapter 2

1. Two series of pyrene-based **PECH** polymers namely **AP** and **YC Series** have been successfully synthesised and characterised.
2. Chemical modification of pyrene moieties onto **PECH** should only be done via the use of carboxylate anion as a nucleophile.
3. Both series of polymers encountered partial solubility issues which may be attributed to the intra and intermolecular π-π interactions of pyrene in close proximity leading to “pseudo-crosslinking”.
4. As a result, a new series of polymer based on anthracene needed to be synthesised to test out the concept of dual properties (liquid crystallinity and fluorescence) in a single polymer.

Chapter 3

1. Two types of azides (**TetraEGdiN$_3$** and **AC-N$_3$**) were synthesised and characterised as starting materials for the CuAAC reaction with **uPPCOOMe** from Chapter 2.
2. Among several CuAAC reaction conditions attempted, only one appeared to be successful in the synthesis of **Pyr2COOMe**.
3. However, when the same reaction conditions were used in the synthesis of **Pyr3COOMe**, the ‘click’ was unsuccessful.
4. The incorporation of tetraethylene glycol chains to **uPPCOOMe** to form **Pyr2COOMe** did lengthen the π-π stacking distance by 5-18 Å which could potentially alleviate the issue of “pseudo-crosslinking” mentioned in Chapter 2.
5. The crown-like cavity of **Pyr2COOMe** did interact with $NaPF_6$ in CD_3CN leading to a change in chemical shifts in its ^1H NMR spectrum.

Chapter 4

1. Six anthracene-bearing **PECH** polymers (**PA Series**) were synthesised and characterised along with two other **TAP** containing **PA polymers** (**URV Series**).
2. Interestingly, **PA polymers** exhibited “vampire-like” properties: changes from sol to gel upon contact with sunlight/365 nm UV irradiation.
3. The organogelation was found to be irreversible as various attempts were made to reverse the process.
4. The irreversible organogelation phenomenon can be attributed to the intra- and intermolecular photodimerisation of anthracene moieties within the polymer leading to the formation of crosslinking points/polymer chain entanglements.
5. With the incorporation of **TAP**, organogelation was prevented in **URV polymers**. This enabled **URV membranes** to be fabricated via immersion precipitation followed by thermal treatment.
6. The surface morphologies of **URV membranes** were studied. Unfortunately, only changes in local organisation were observed instead of a change in orientation.

Chapter 5

1. Successful synthesis and characterisation of crown ether, **CM1** and dimer **CM1a**.
2. The coincidental resemblance of **CM1**’s crystal structure and bluish fluorescence (in $CHCl_3$) of a real life jellyfish has made it an interesting molecule to study.
3. The ^1H NMR of **CM1** appeared to be more complex than its dimer, **CM1a** as it contains diastereotropic crown ether chain protons and inequivalent CH_2 protons on its ester groups.
4. Computational modelling studies were carried out on **CM1** with various alkali metal ions.
5. Apart from K^+, none other alkali metal hexafluorophosphate salts showed interactions with the cavity of **CM1**. The interactions were observed as a change in chemical shifts in its ^1H NMR spectrum.
6. **CM1**’s weak interaction with H^+: log K_a = 2.2 M^{-1} and ΔG = -12.6 kJ/mol.

Chapter 6

1. Intermediate **I4**, pre-polymers (**EG-I3-EG**, **BD-I4-BD** and **BD-CM1-BD**) and their asymmetrical counterparts (**BD-I4** and **BD-CM1**) were synthesised and characterised.
2. Copolymers **Poly(EGI3EG-TCL)**, **Poly(BDI4BD-TCL)** and **Poly (BDCM1BD-TCL)** were synthesised and characterised.
3. The number average and weight average molecular weights (M_n and M_w) of the polymers were determined by two methods (NMR and GPC).
4. The T_g of **Poly(BDCM1BD-TCL)** was 48 ^oC, which was lower than that of **Poly(EGI3EG-TCL)** (91 ^oC) due to the use of longer butylene spacer between repeating terephthalate cores.
5. All three polymers turned out to have low molecular weights and low repeating units, ranging from between 2-10.
6. Due to time limitations, further purification and characterisation of **Poly(BDCM1BD-TCL)** were put on hold.

2. Future Work

Chapter 2

1. Further analysis should be carried out to check the reversibility of the "pseudo-crosslinks" between pyrene moieties in **PA** and **YC polymers** and whether crosslinks could be reformed on demand.

Chapter 3

1. Titration experiments with $NaPF_6$ in CD_3CN should be carried out on **Pyr2COOMe** for the determination of binding constant.
2. The synthesis of **Pyr3COOMe** should be re-attempted using cation-coordinated **AC-N_3** instead of uncoordinated ones.
3. **Pyr2COOMe** could be chemically modified onto **PECH** polymers or directly polymerised.

Chapter 4

1. Chemical modification of **PECH** and **P(ECH-co-EO)** with different **TAP** / **9-ACAK** ratios (preferably more **TAP** than **9-ACAK** moieties).
2. Look for possible relationship between **TAP** / **9-ACAK** ratios and the liquid crystallinity of the resulting polymers.
3. Attempt various thermal treatment conditions to find the optimal condition for the formation of homeotropic orientation.
4. Further analysis on the irreversible organogelation of **PA polymers**. Find out whether its gel fluorescence can be “switched off” in the presence of a trigger or if there is anything that would reverse the organogelation process.
5. Carry out further characterisations on the organogels.

Chapter 5

1. Re-attempt crystallisation of **CM1** with various cations.
2. Carry out further cation/proton binding studies using NMR, UV-Vis or fluorescence spectroscopy.
3. Synthesis of crown ether terephthalate with a larger cavity and compare it to **CM1**.
4. Attempt crystallisation and binding studies of **CM1a** with larger molecules as guests to its cavity, e.g. Paraquat.

Chapter 6

1. Attempt more controlled polymerisation/modification of symmetrical pre-polymer **BD-CM1-BD** and asymmetrical pre-polymer **BD-CM1**.
2. Repeat synthesis of **Poly(BDCM1BD-TCL)** to obtain larger quantities, then proceed to purification and characterisation.
3. Instead of synthesising a copolymer via nucleophilic addition-elimination reaction of pre-polymer, **BD-CM1** should be modified onto a known molecular weight polymer backbone.

Chapter 2 Supplementary Information, SI

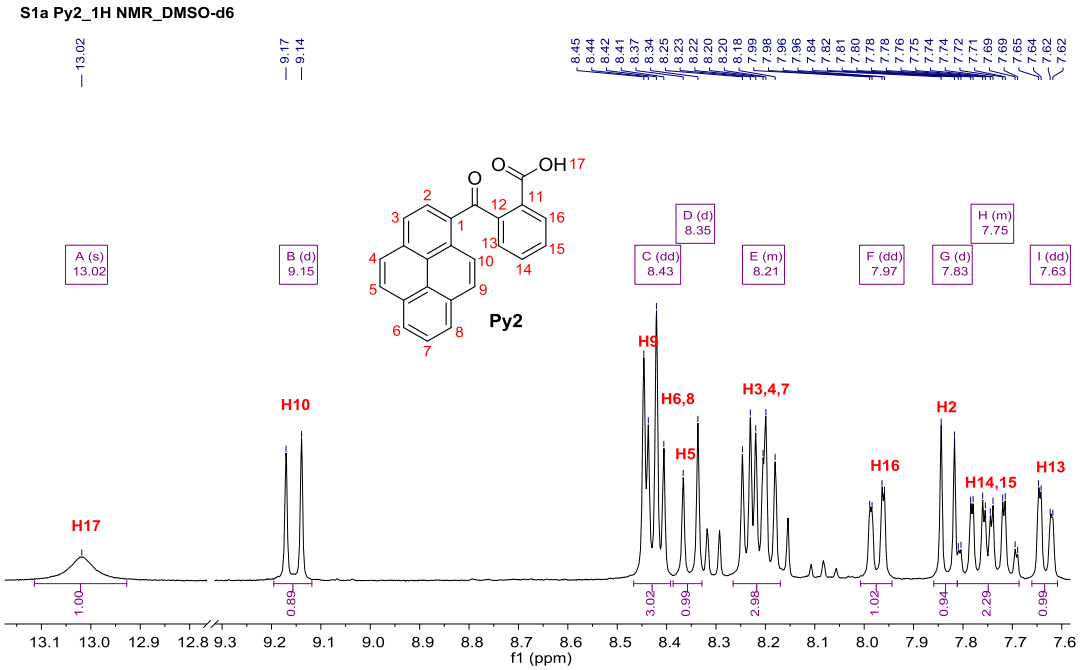

^{1}H NMR (300 MHz, DMSO- d_6) δ 13.02 (s, 1H, H17), 9.15 (d, *J* = 9.4 Hz, 1H, H10), 8.43 (dd, *J* = 8.6, 3.6 Hz, 3H, H9, H6, H8), 8.35 (d, *J* = 9.0 Hz, 1H, H5), 8.27 – 8.17 (m, 3H, H3, H4, H7), 7.97 (dd, *J* = 7.5, 1.5 Hz, 1H, H16), 7.83 (d, *J* = 8.1 Hz, 1H, H2), 7.81 – 7.69 (m, 2H, H14, H15), 7.63 (dd, *J* = 7.1, 1.6 Hz, 1H, H13).

Figure 1: *^{1}H NMR spectrum (300 MHz, DMSO-d_6) of* **Py2**.

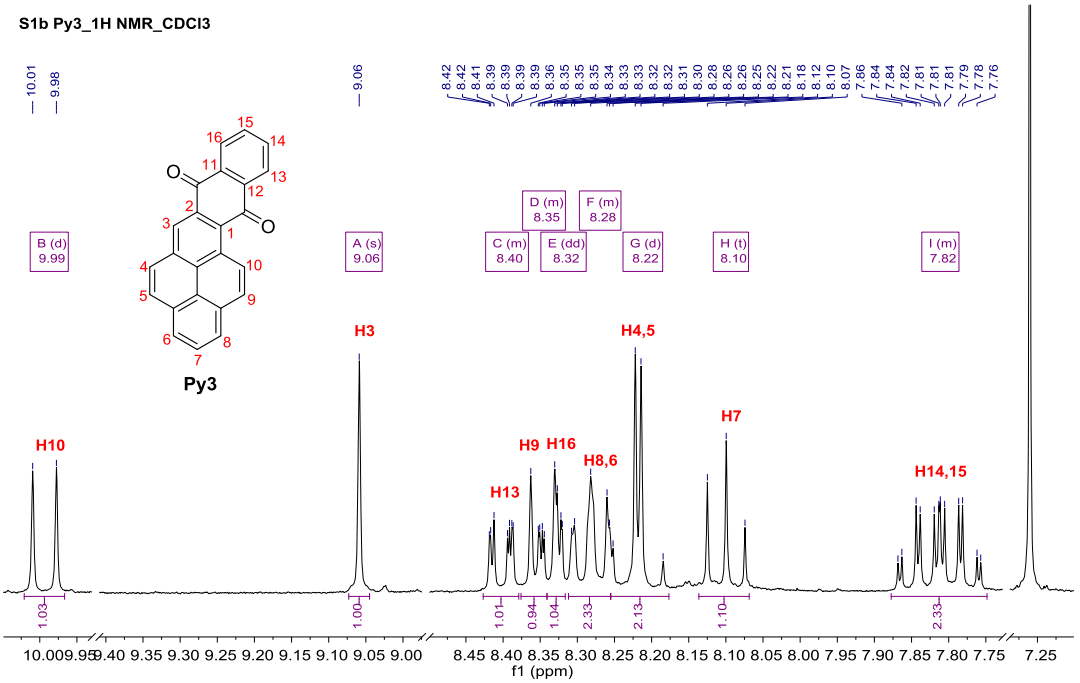

^{1}H NMR (300 MHz, Chloroform-*d*) δ 9.99 (d, *J* = 9.6 Hz, 1H, H10), 9.06 (s, 1H, H3), 8.43 – 8.38 (m, 1H, H13), 8.38 – 8.34 (m, 1H, H9), 8.32 (dd, *J* = 2.3, 0.8 Hz, 1H, H16), 8.31 – 8.26 (m, 2H, H8, H6), 8.22 (d, *J* = 2.3 Hz, 2H, H4, H5), 8.10 (t, *J* = 7.6 Hz, 1H, H7), 7.88 – 7.75 (m, 2H, H14, H15).

Figure 2: *^{1}H NMR spectrum (300 MHz, $CDCl_3$) of* **Py3**.

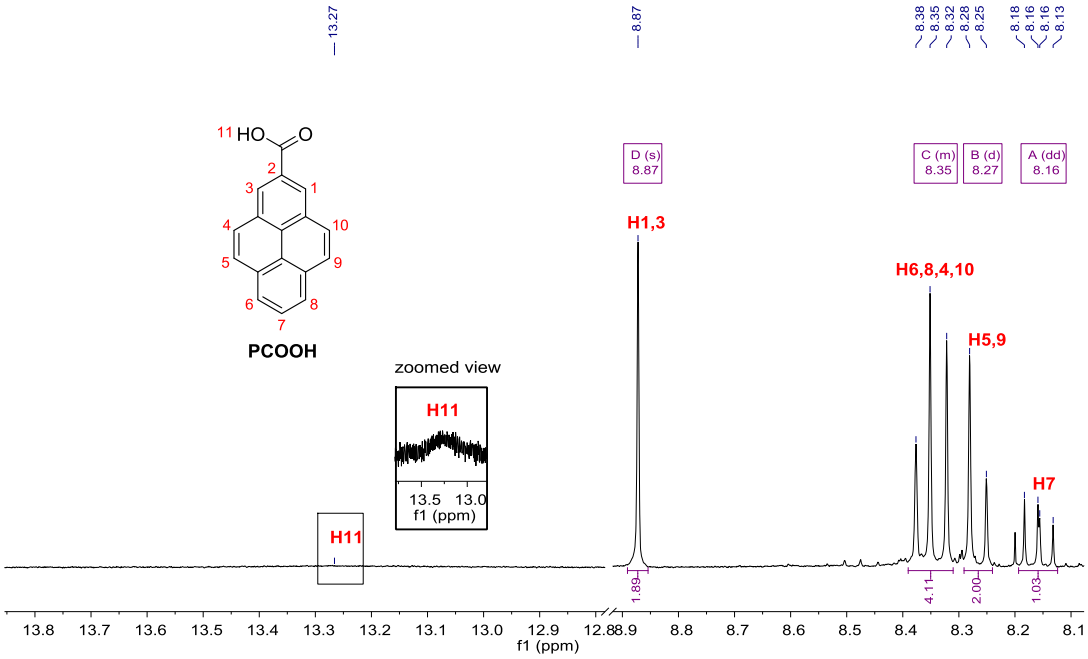

^{1}H NMR (300 MHz, DMSO- d_6) δ 13.27 (br s, H11), 8.87 (s, 2H, H1, H3), 8.39 – 8.31 (m, 4H, H6, H8, H4, H10), 8.27 (d, J = 9.0 Hz, 2H, H5, H9), 8.16 (dd,J = 8.2, 7.2 Hz, 1H, H7).

Figure 3: *^{1}H NMR spectrum (300 MHz, DMSO-d_6) of* **PCOOH**.

S1d PCOOK_1H NMR_DMSO-d6

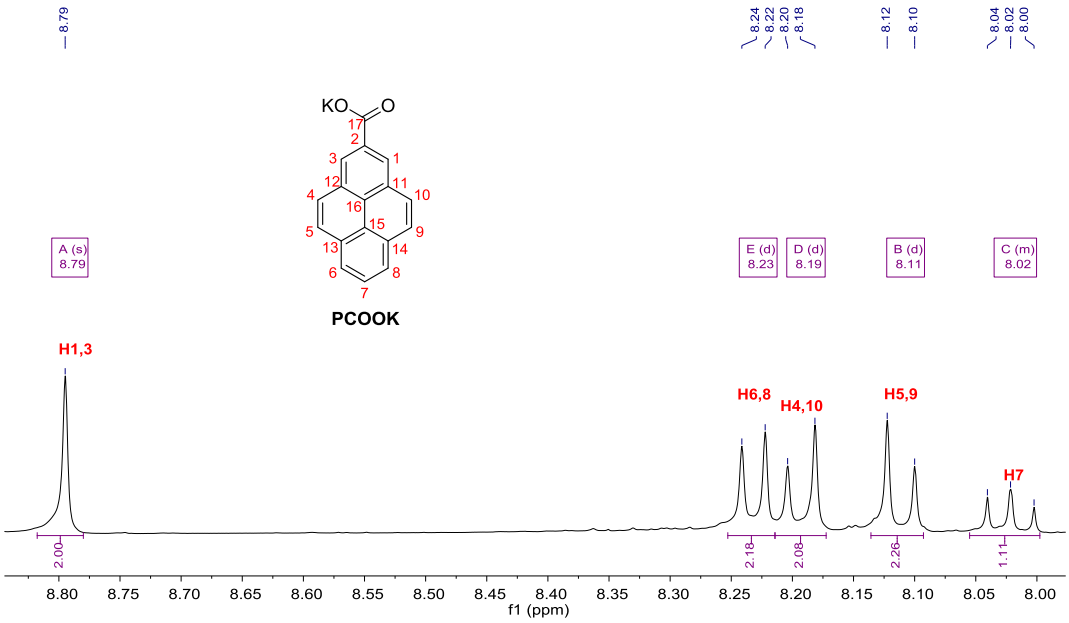

^{1}H NMR (400 MHz, DMSO- d_6) δ 8.79 (s, 2H, H1, H3), 8.23 (d, J = 7.6 Hz, 2H, H6, H8), 8.19 (d, J = 8.9 Hz, 2H, H4, H10), 8.11 (d, J = 9.0 Hz, 2H, H5, H9), 8.06 – 8.00 (m, 1H, H7).

S1d PCOOK_13C NMR_DMSO-d6

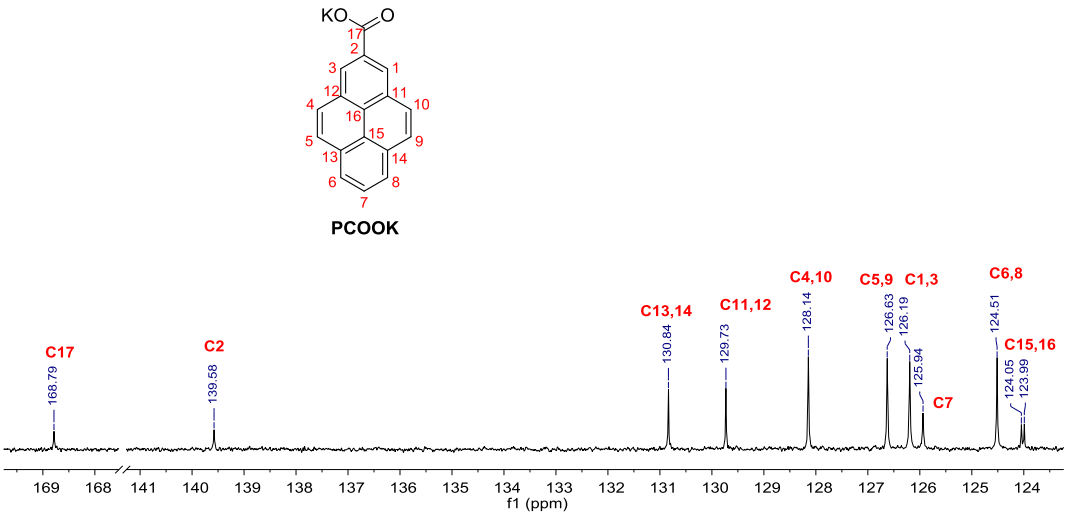

^{13}C NMR (101 MHz, DMSO- d_6) δ 168.79 (C17), 139.58 (C2), 130.84 (C13,C14), 129.73 (C11,C12), 128.14 (C4,C10), 126.63 (C5,C9), 126.19 (C1,C3), 125.94 (C7), 124.51 (C6,C8), 124.05, 123.99 (C15,C16).

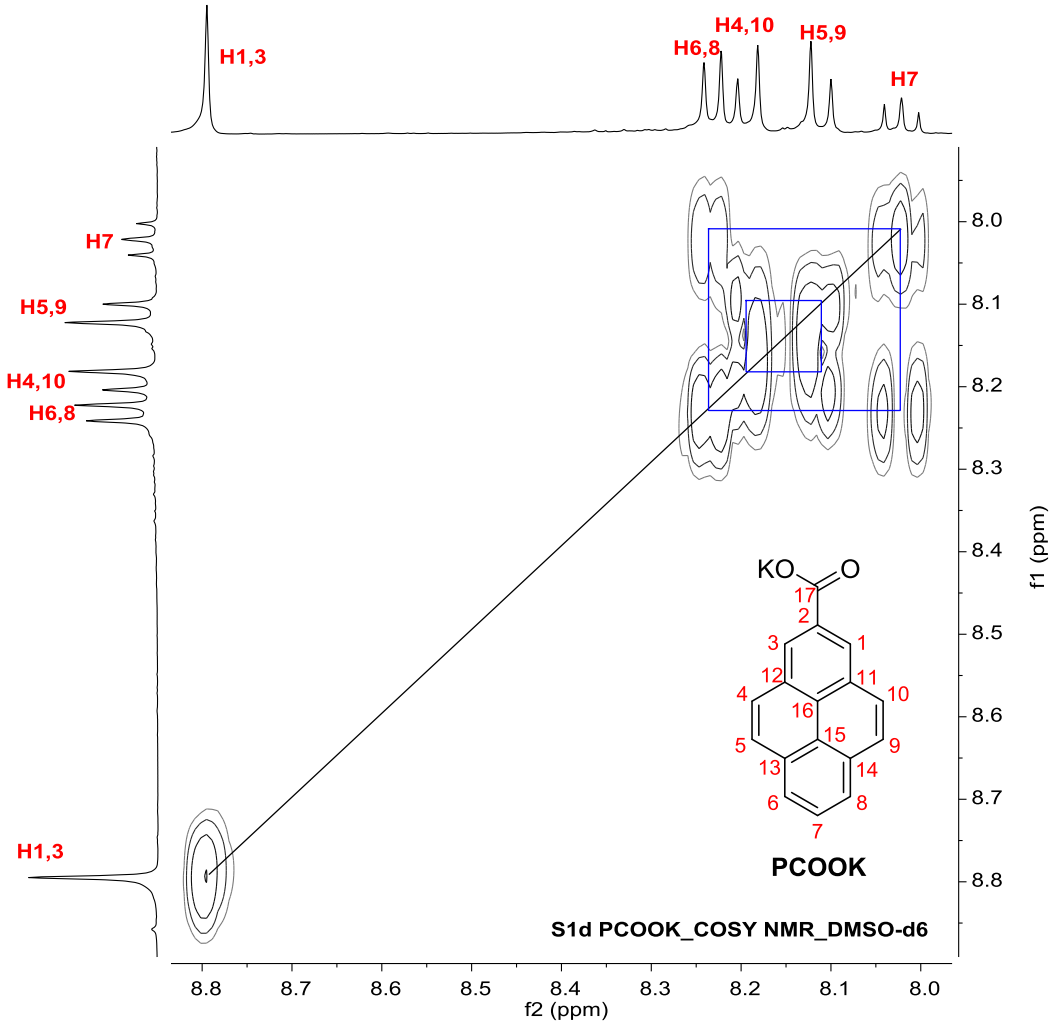
H1,3
H6,8
H4,10
H5,9
H7
H7
H5,9
H4,10
H6,8
H1,3
KO
O
17
2
3
1
12
11
4
10
16
5
15
9
13
14
6
8
7
PCOOK
S1d PCOOK_COSY NMR_DMSO-d6
8.8
8.7
8.6
8.5
8.4
8.3
8.2
8.1
8.0
f2 (ppm)
8.0
8.1
8.2
8.3
8.4
8.5
8.6
8.7
8.8
f1 (ppm)

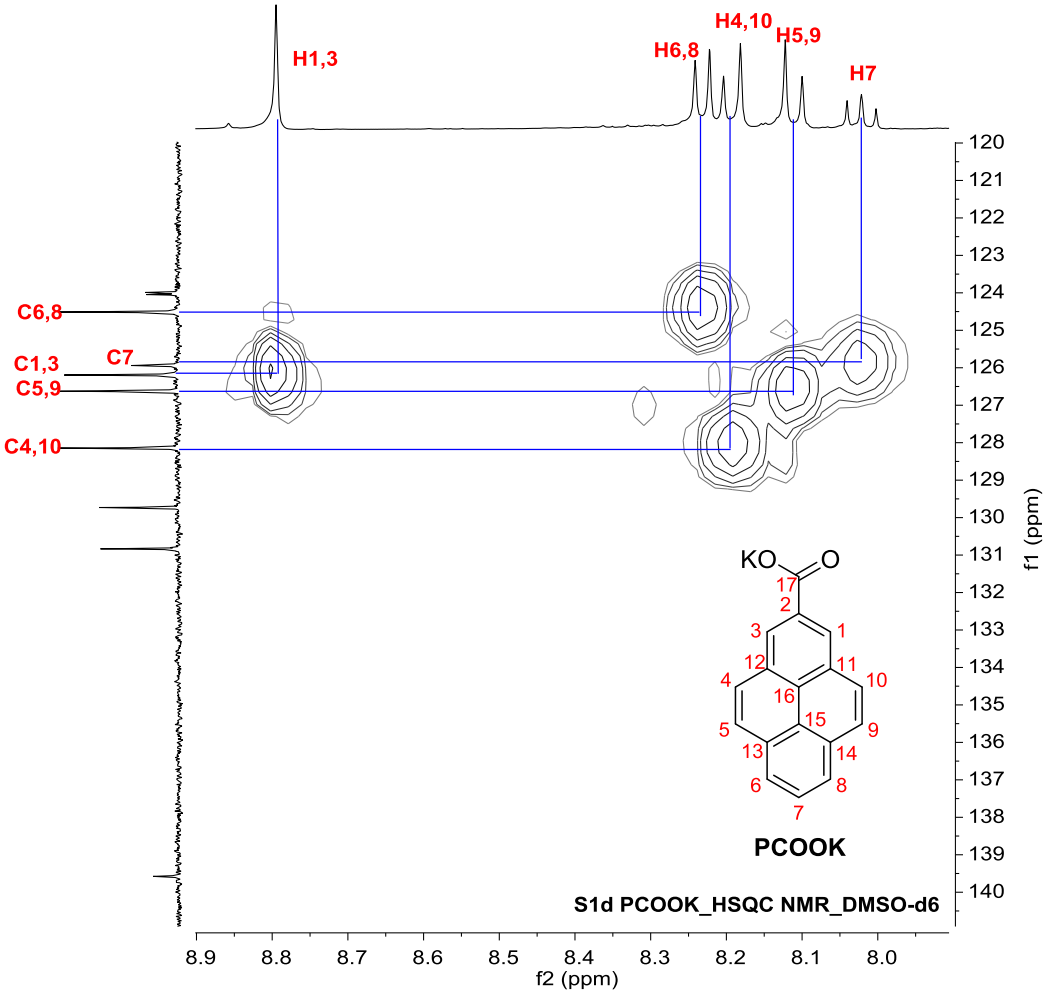
H1,3
H6,8
H4,10
H5,9
H7
C6,8
C1,3
C7
C5,9
C4,10
KO
O
PCOOK
S1d PCOOK_HSQC NMR_DMSO-d6
f2 (ppm)
f1 (ppm)

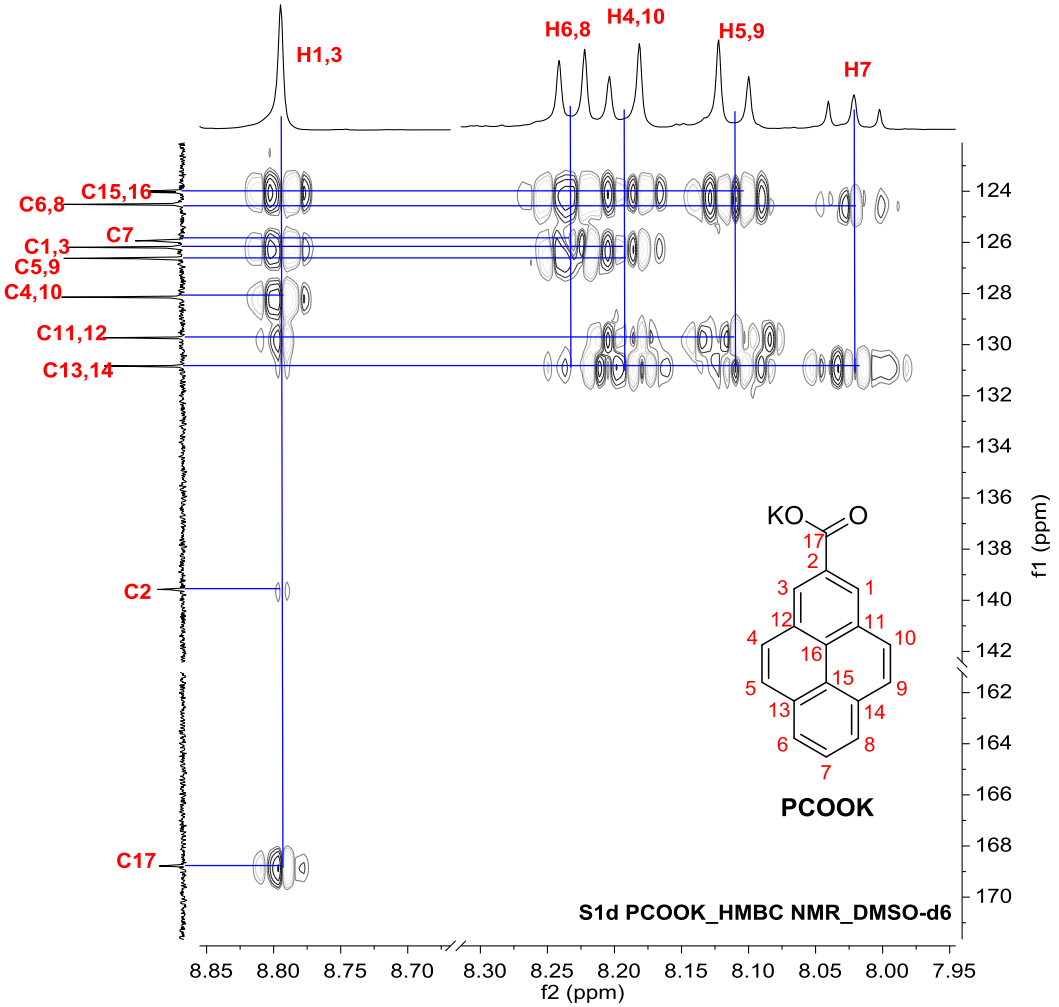

Figure 4: *^{1}H, ^{13}C, COSY, HSQC, HMBC NMR spectra (400 MHz, DMSO-d_6) of* **PCOOK**.

S2d uPPCOOMe_1H NMR_CDCl3

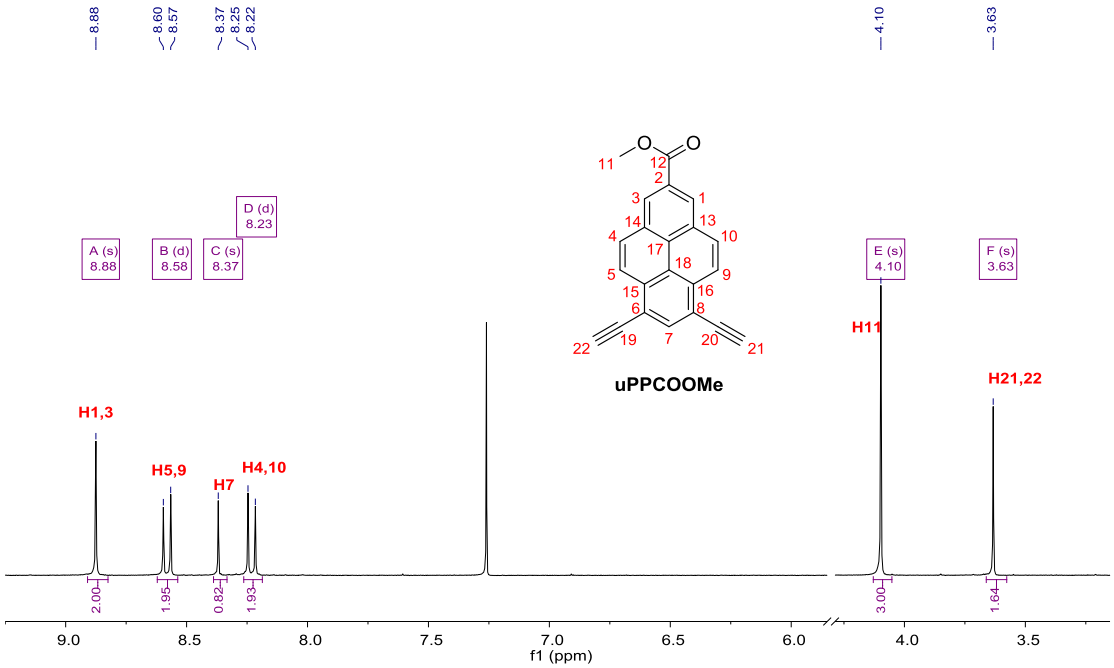

^{1}H NMR (300 MHz, Chloroform- *d*) δ 8.88 (s, 2H, H1, H3), 8.58 (d, *J* = 9.1 Hz, 2H, H5, H9), 8.37 (s, 1H, H7), 8.23 (d, *J* = 9.1 Hz, 2H, H4, H10), 4.10 (s, 3H, H11), 3.63 (s, 2H, H21, H22).

S2d uPPCOOMe_13C NMR_CDCl3

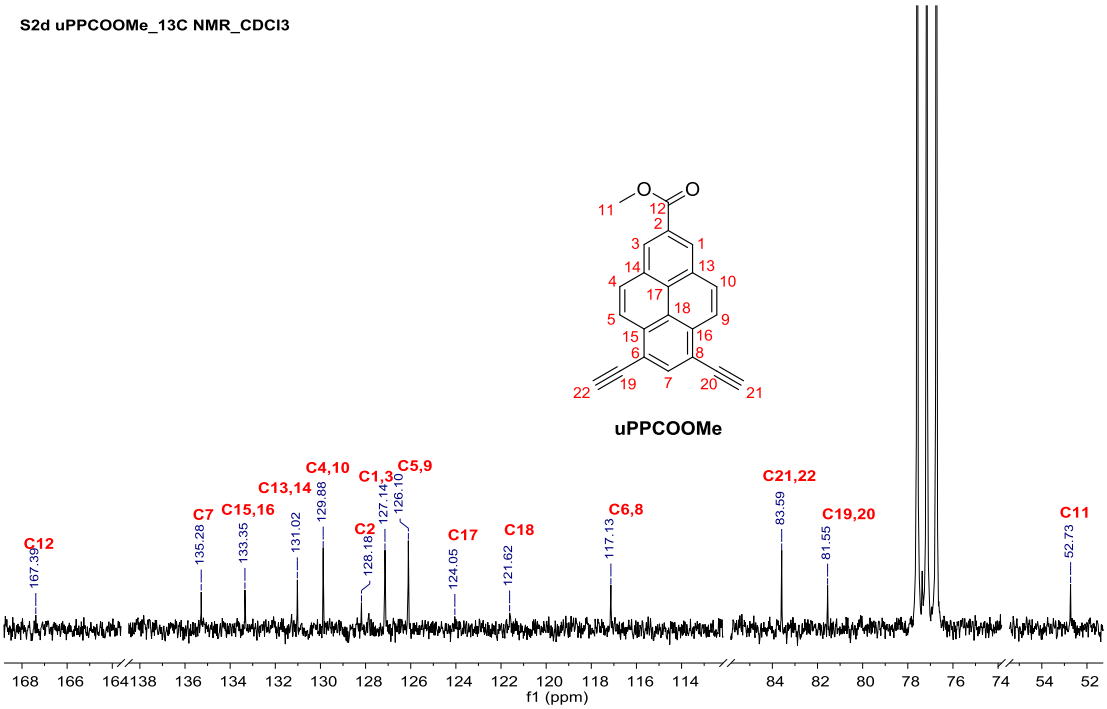

^{13}C NMR (75 MHz, Chloroform- *d*) δ 167.39 (C12), 135.28 (C7), 133.35 (C15,C16), 131.02 (C13,C14), 129.88 (C4,C10), 128.18 (C2), 127.14 (C1, C3), 126.10 (C5,C9), 124.05 (C17), 121.62 (C18), 117.13 (C6,C8), 83.59 (C21,C22), 81.55 (C19,C20), 52.73 (C11).

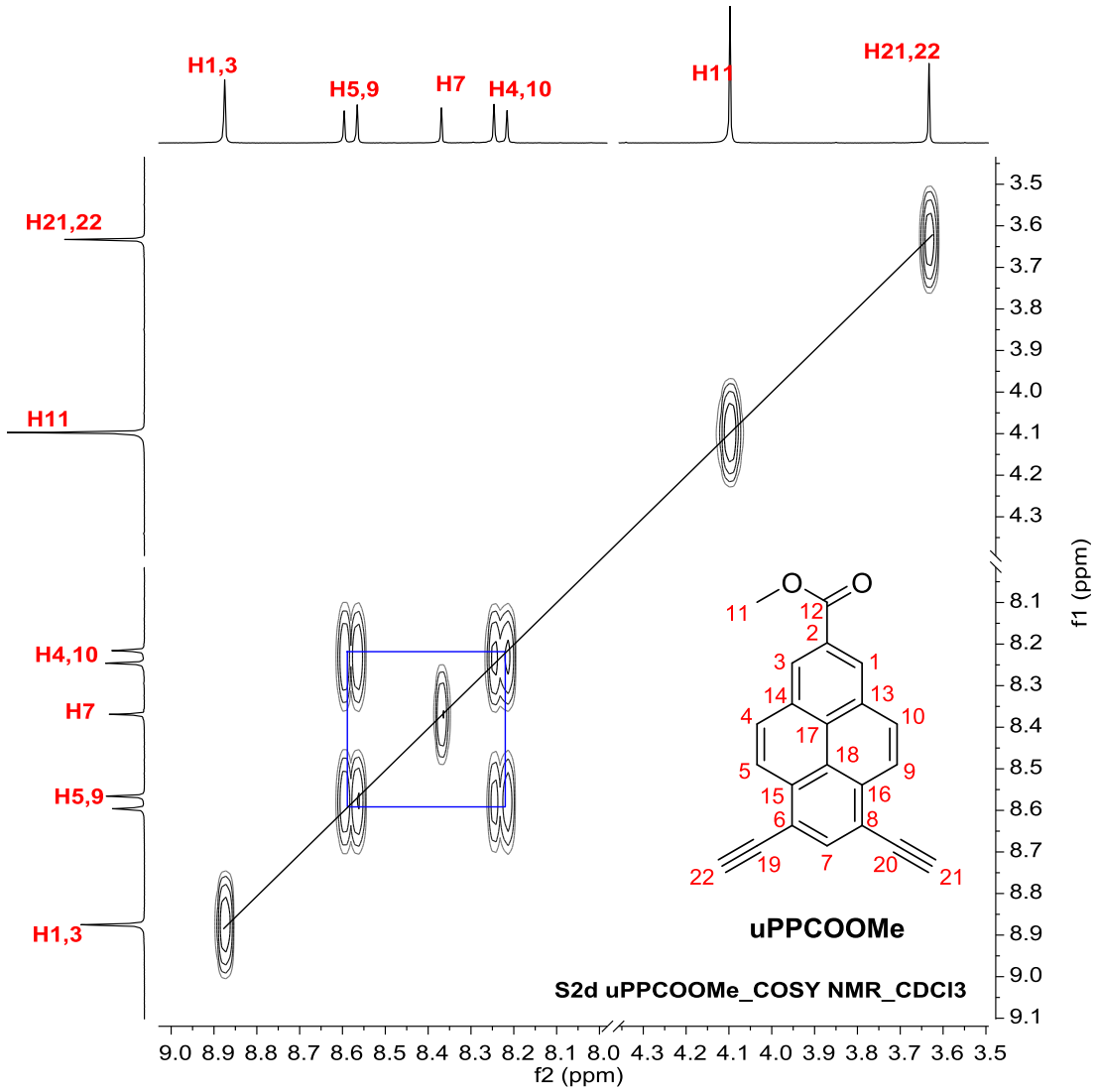
H1,3
H5,9
H7
H4,10
H11
H21,22
H21,22
H11
H4,10
H7
H5,9
H1,3
f1 (ppm)
f2 (ppm)
uPPCOOMe
S2d uPPCOOMe_COSY NMR_CDCl3

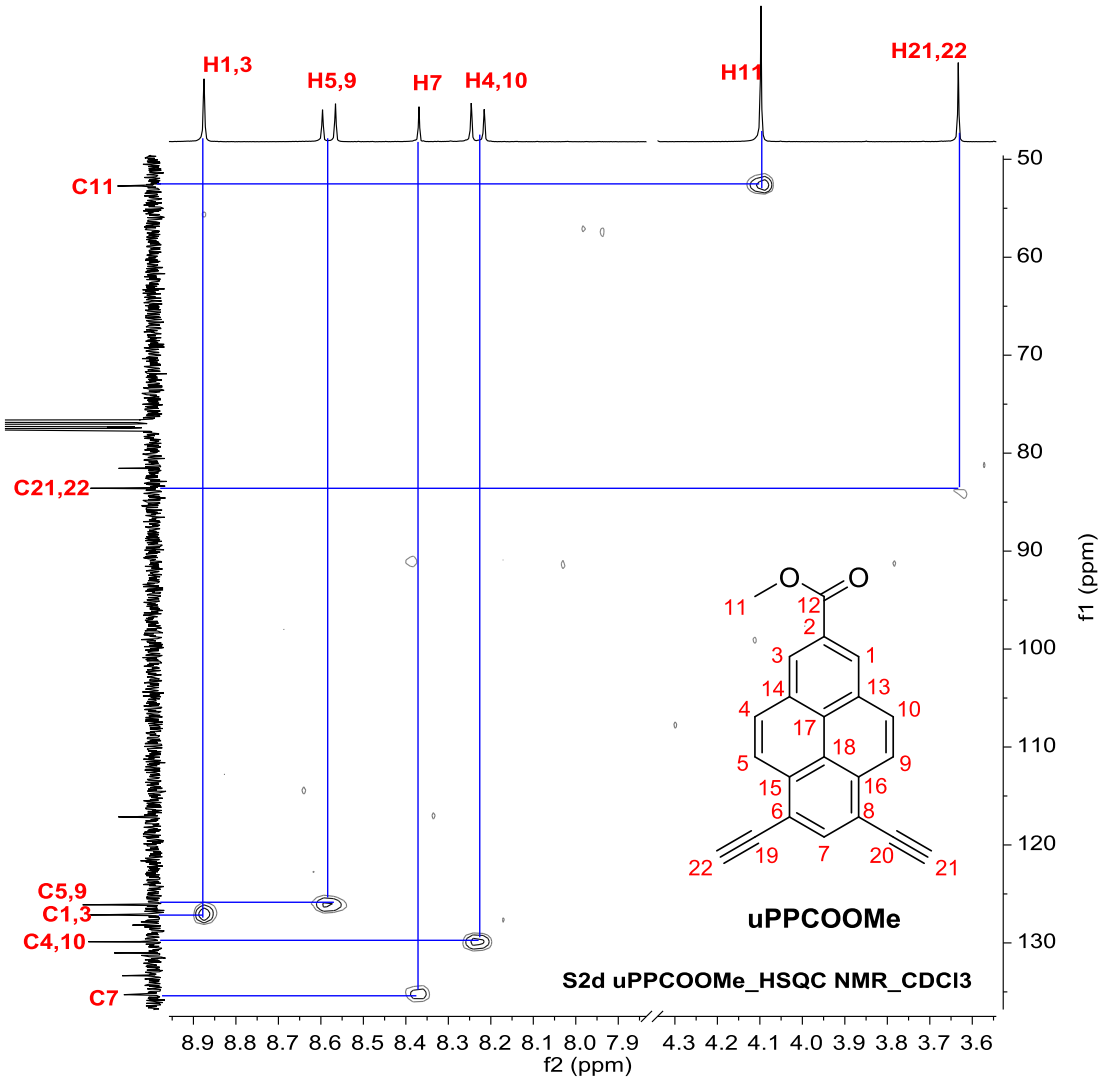
H1,3
H5,9
H7
H4,10
H11
H21,22
C11
C21,22
C5,9
C1,3
C4,10
C7
f1 (ppm)
f2 (ppm)
uPPCOOMe
S2d uPPCOOMe_HSQC NMR_CDCl3

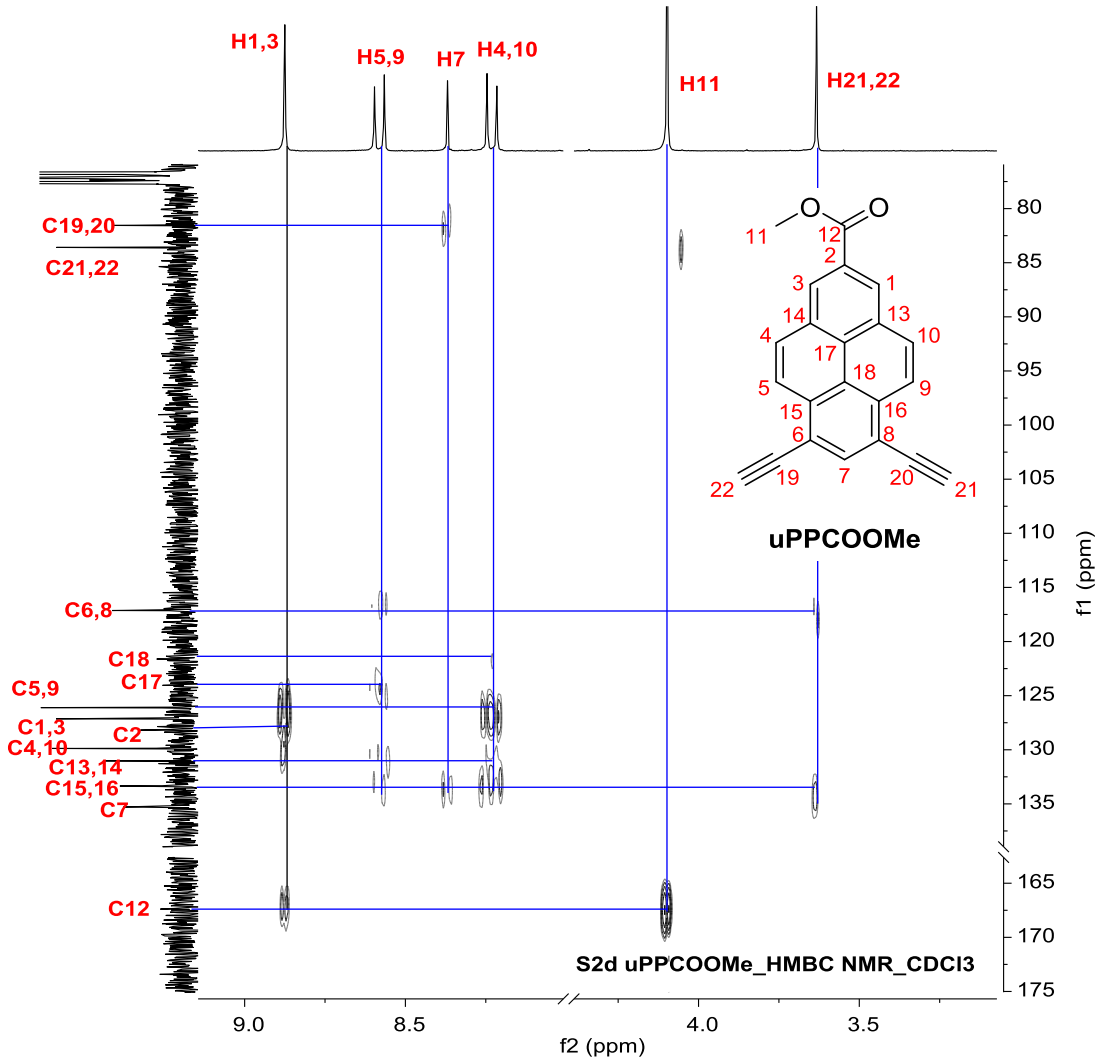

Figure 5: *^{1}H, ^{13}C, COSY, HSQC, HMBC NMR spectra (300 MHz, $CDCl_3$) of* **uPPCOOMe**.

S2e uPPCOOK_1H NMR_DMSO-d6

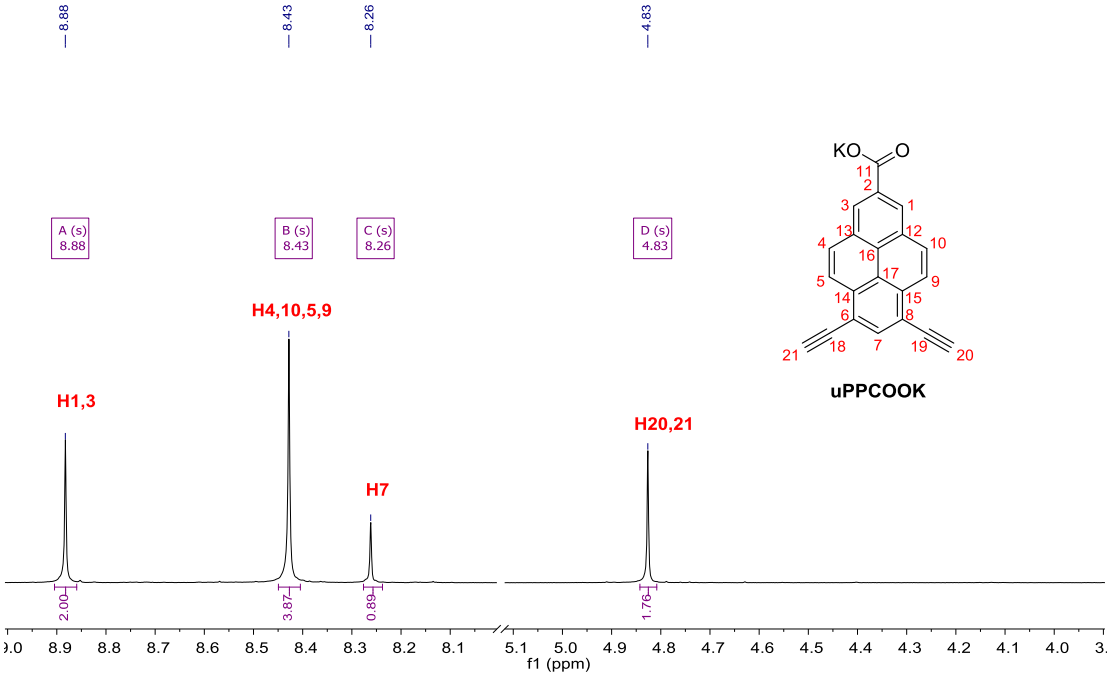

^{1}H NMR (300 MHz, DMSO- d_6) δ 8.88 (s, 2H, H1, H3), 8.43 (s, 4H, H4, H10, H5, H9), 8.26 (s, 1H, H7), 4.83 (s, 2H, H20, H21).

S2e uPPCOOK_13C NMR_DMSO-d6

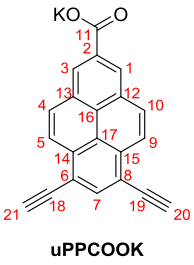

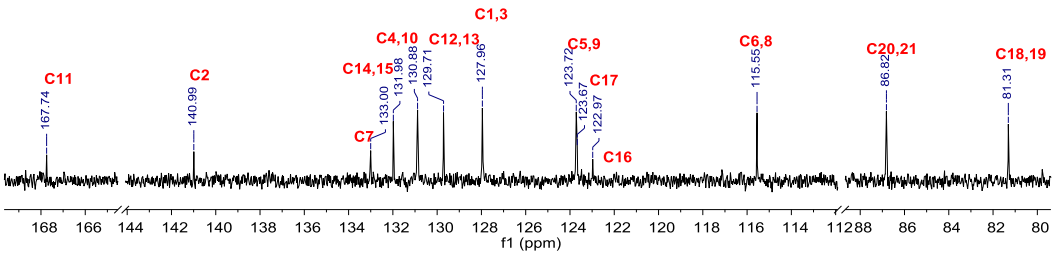

^{13}C NMR (75 MHz, DMSO- d_6) δ 167.74 (C11), 140.99 (C2), 133.00 (C7), 131.98 (C14,C15), 130.88 (C4,C10), 129.71 (C12,C13), 127.96 (C1,C3), 123.72 (C5,C9), 123.67 (C17), 122.97 (C16), 115.55 (C6,C8), 86.82 (C20,C21), 81.31 (C18,C19).

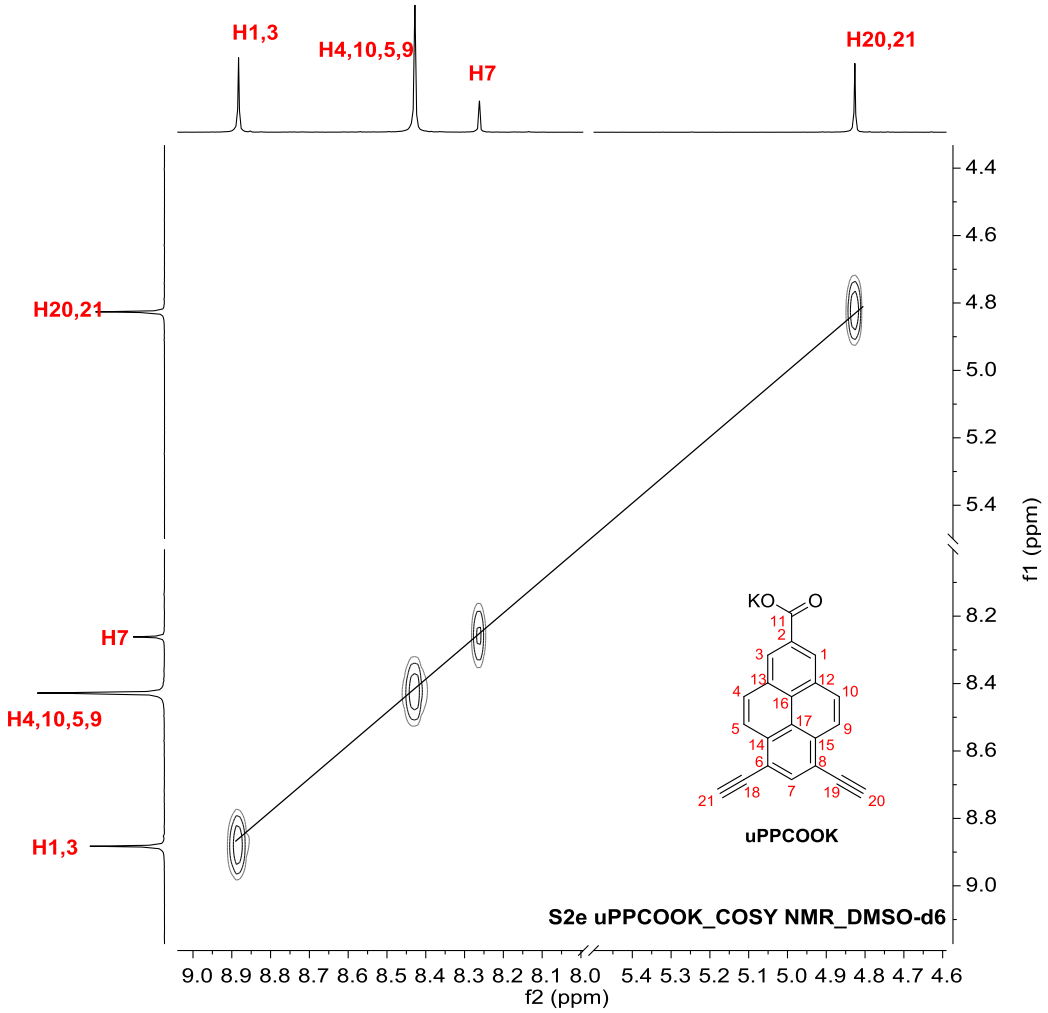
H1,3
H4,10,5,9
H7
H20,21
H20,21
H7
H4,10,5,9
H1,3
f1 (ppm)
f2 (ppm)
uPPCOOK
S2e uPPCOOK_COSY NMR_DMSO-d6

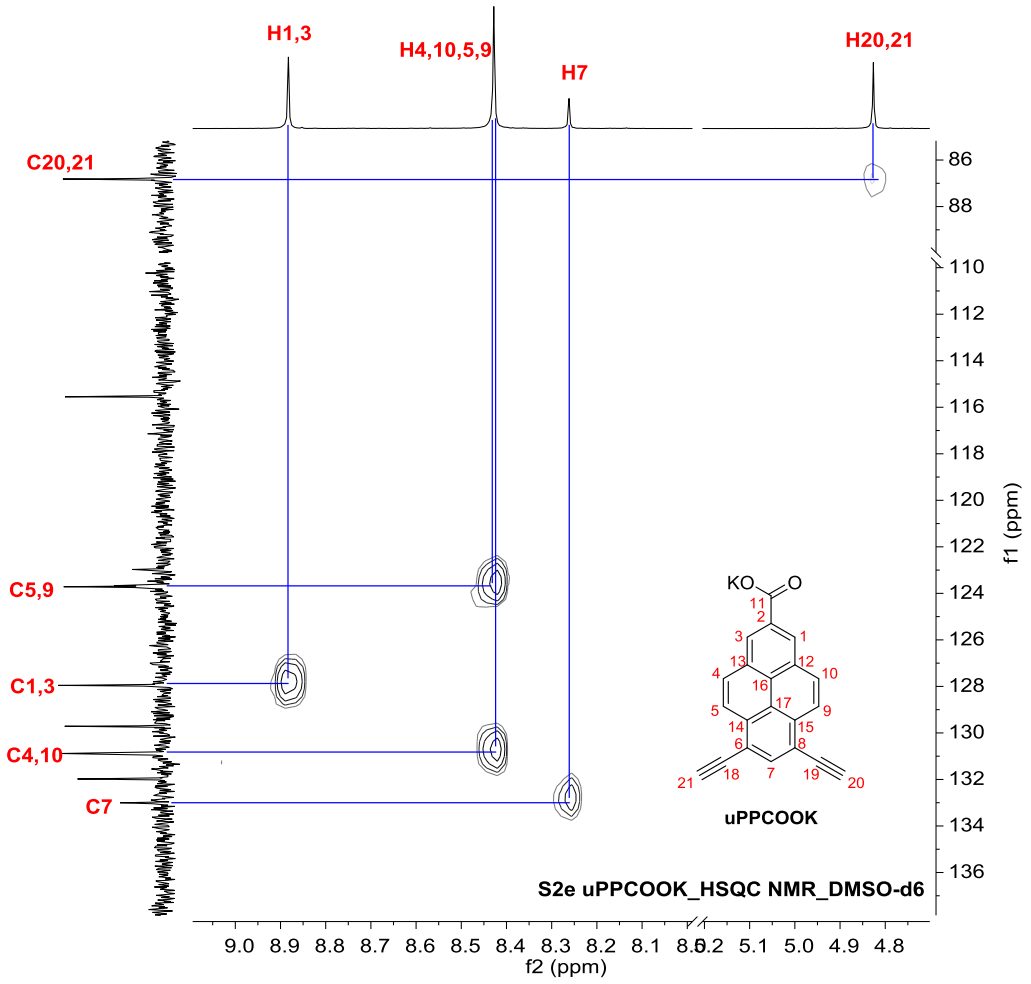
H1,3
H4,10,5,9
H7
H20,21
C20,21
C5,9
C1,3
C4,10
C7
KO
O
uPPCOOK
S2e uPPCOOK_HSQC NMR_DMSO-d6
f1 (ppm)
f2 (ppm)

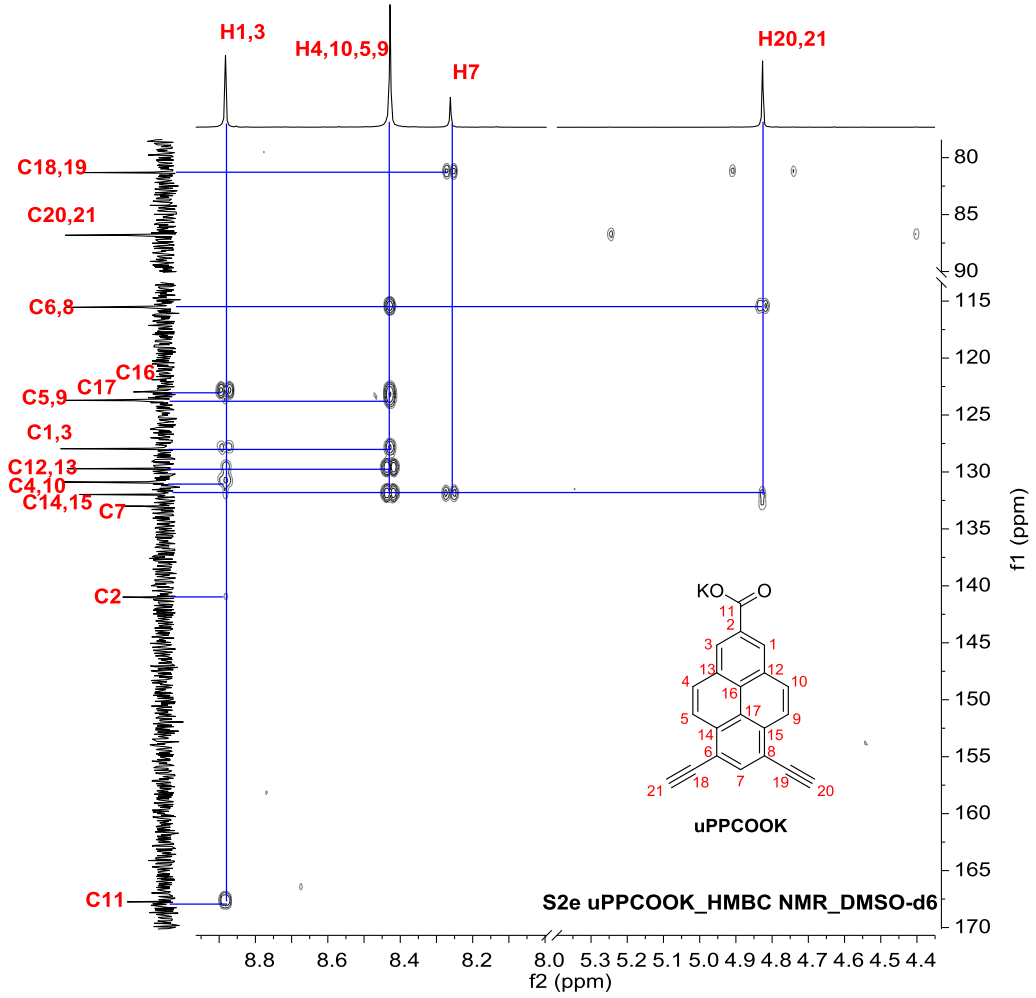

Figure 6: *^{1}H, ^{13}C, COSY, HSQC, HMBC NMR spectra (300 MHz, DMSO-d_6) of* **uPPCOOK**.

S7 AP1_1H NMR_TCE-d2

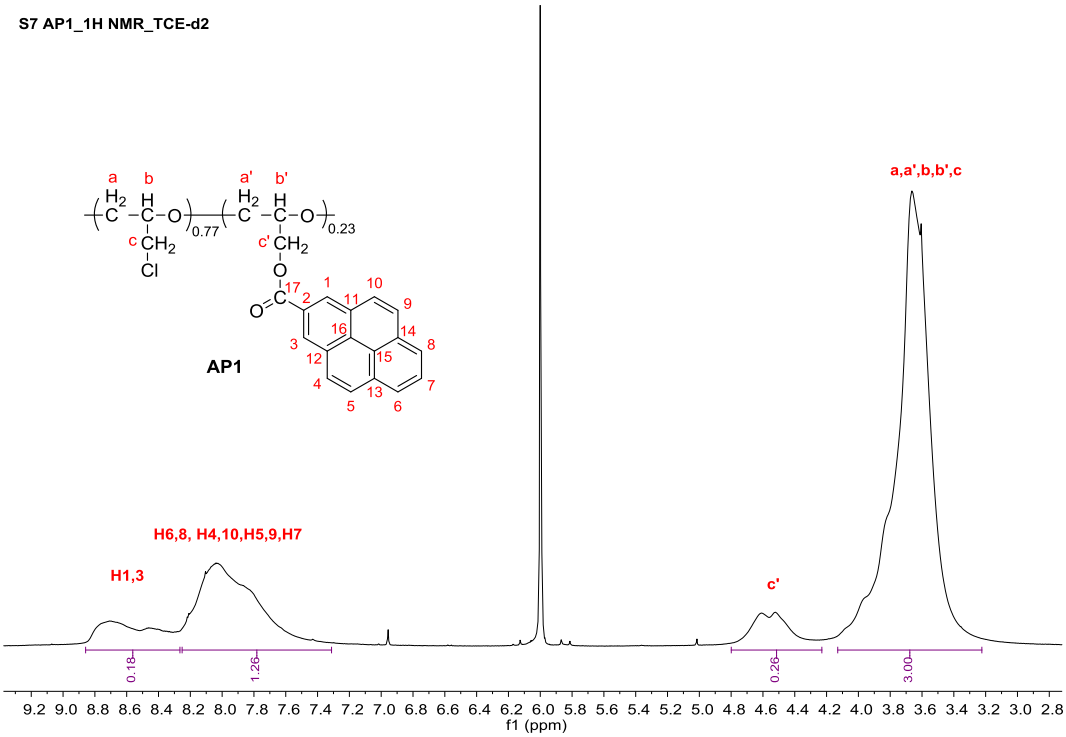

S8 YC2_13C NMR_TCE-d2

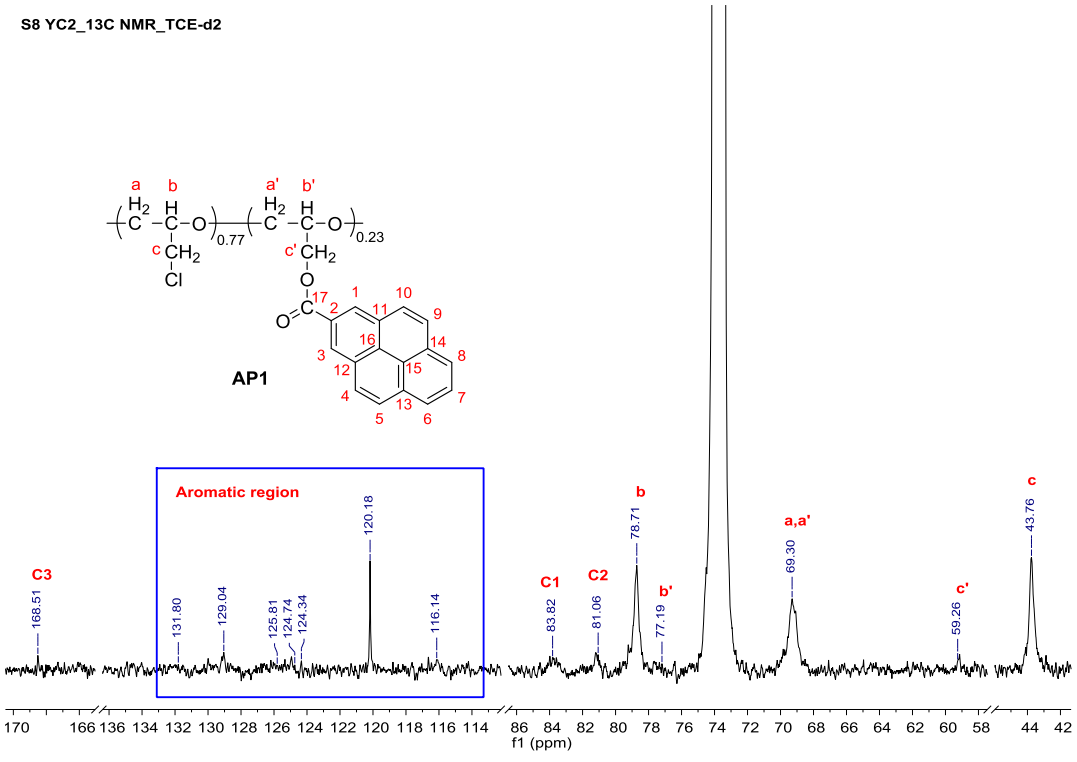

^{1}H NMR		**^{13}C NMR**	
Signal (ppm)	**Assignment**	**Signal (ppm)**	**Assignment**
8.86-8.50	H1,3	166.64	C17
8.50-7.32	H6,8, H4,10, H5,9, H7	131.29-130.56	C11,12, C13,14
4.80-4.23	c’	128.10-125.42	C1,3, C4,10, C5,9, C6,8, C7, C2
4.14-3.22	a,a’,b,b’,c	123.73	C15,16
		78.71	b
		77.55	b’
		69.89-69.06	a,a’
		64.30	c’
		43.76	c

Table 1: *^{1}H and ^{13}C NMR data of* **AP1** *and their corresponding assignments.*

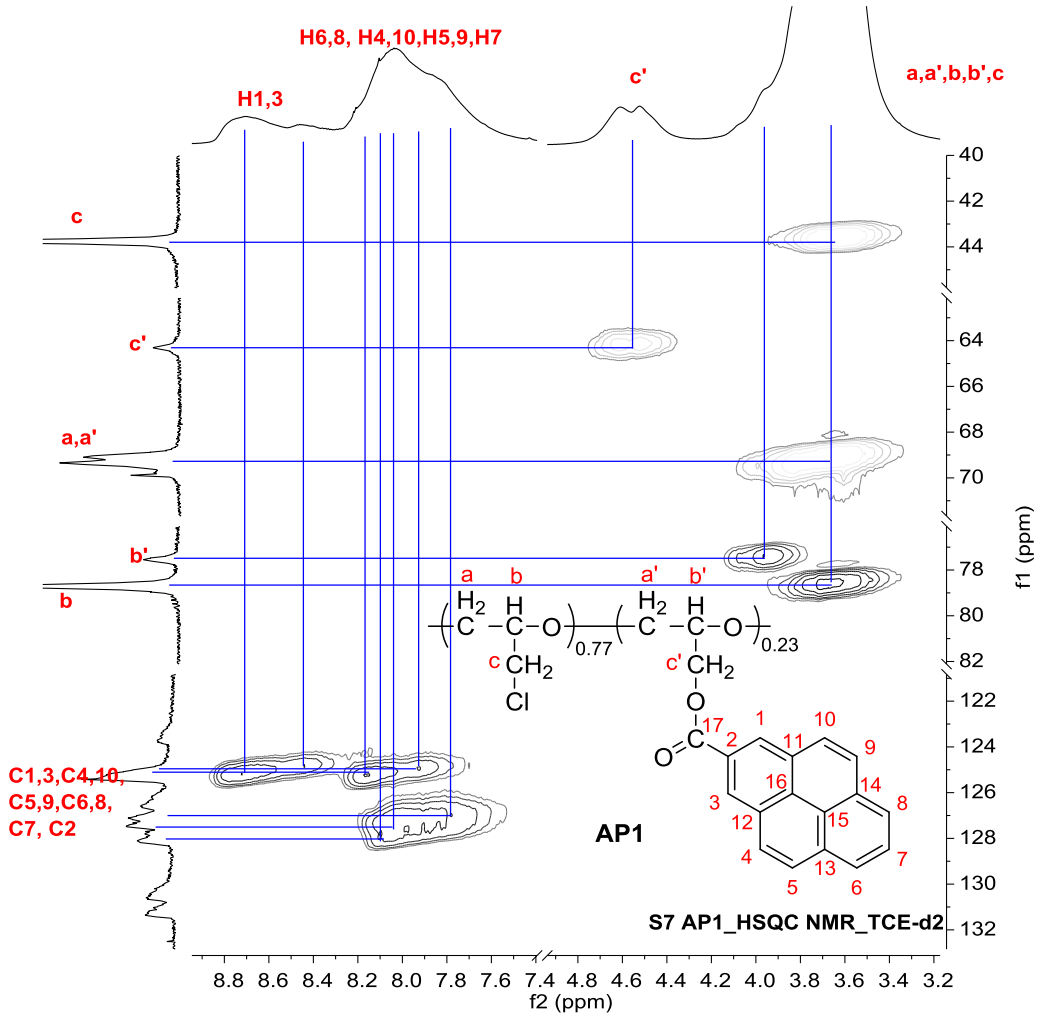
H6,8, H4,10,H5,9,H7
H1,3
c'
a,a',b,b',c
c
c'
a,a'
b'
b
C1,3,C4,10,
C5,9,C6,8,
C7, C2
a
b
a'
b'
c
c'
0.77
0.23
AP1
S7 AP1_HSQC NMR_TCE-d2
f1 (ppm)
f2 (ppm)

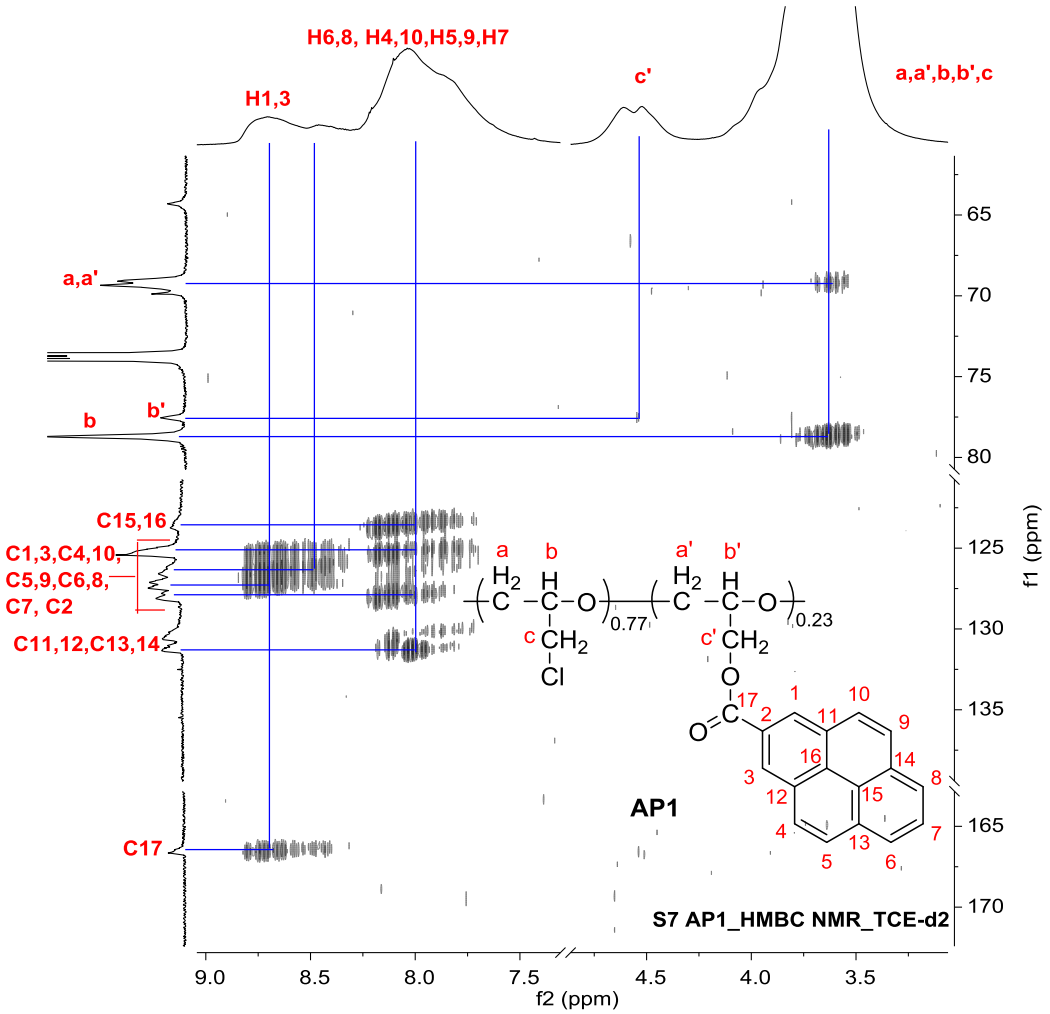

Figure 7: *^{1}H, ^{13}C, HSQC, HMBC NMR spectra (700 MHz, TCE-d_2) of* **AP1**.

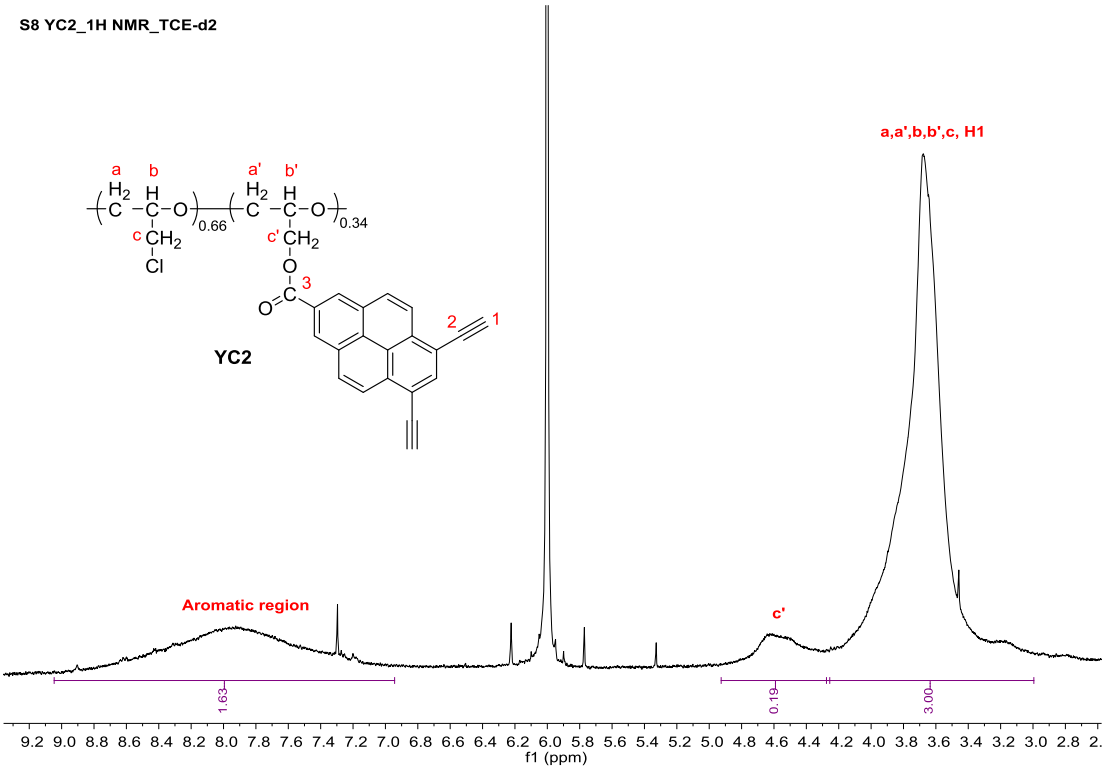

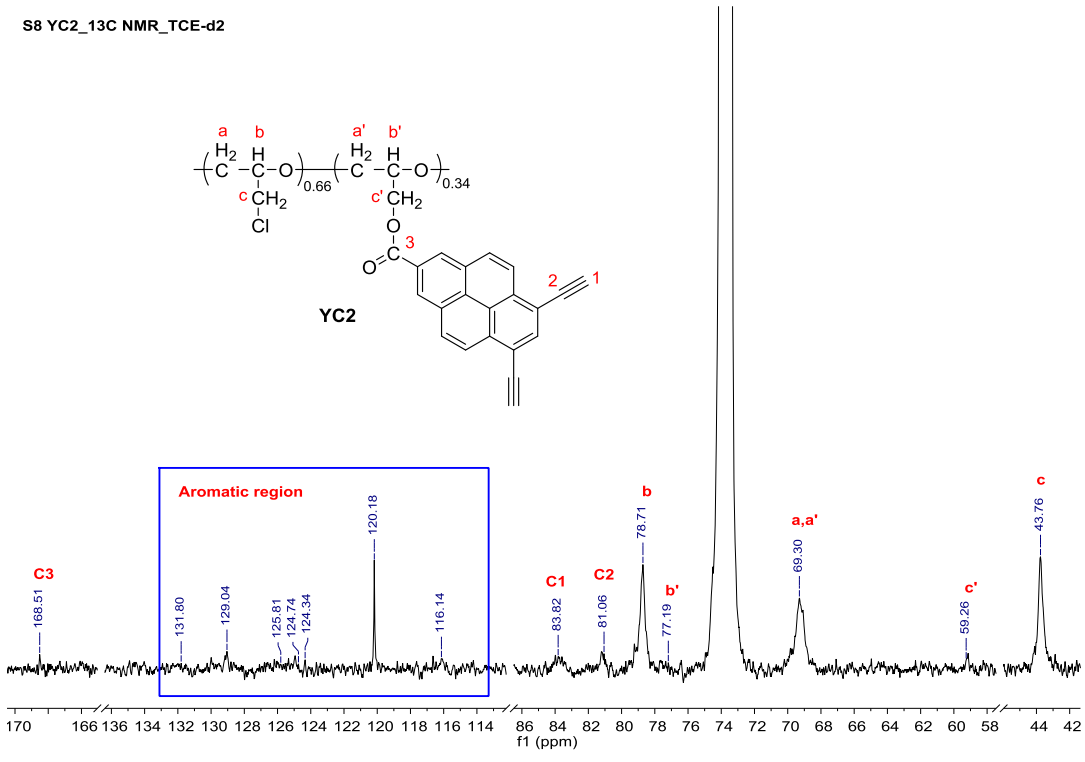

Figure 8: *^{1}H and ^{13}C NMR spectra (400 MHz, TCE-d_2) of* **YC2**.

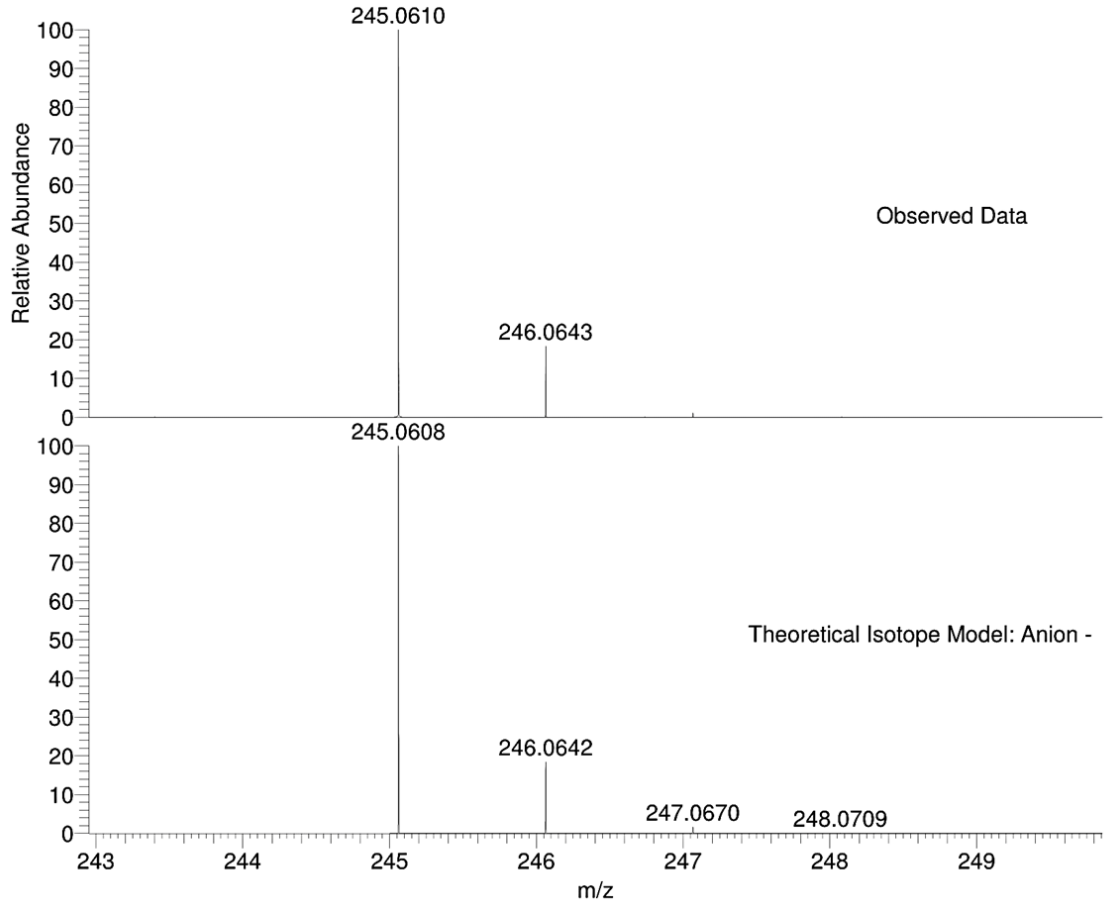

Figure 9: *Mass spectra of* **PCOOK** *showing its* $[M-K]^-$ *ion.*

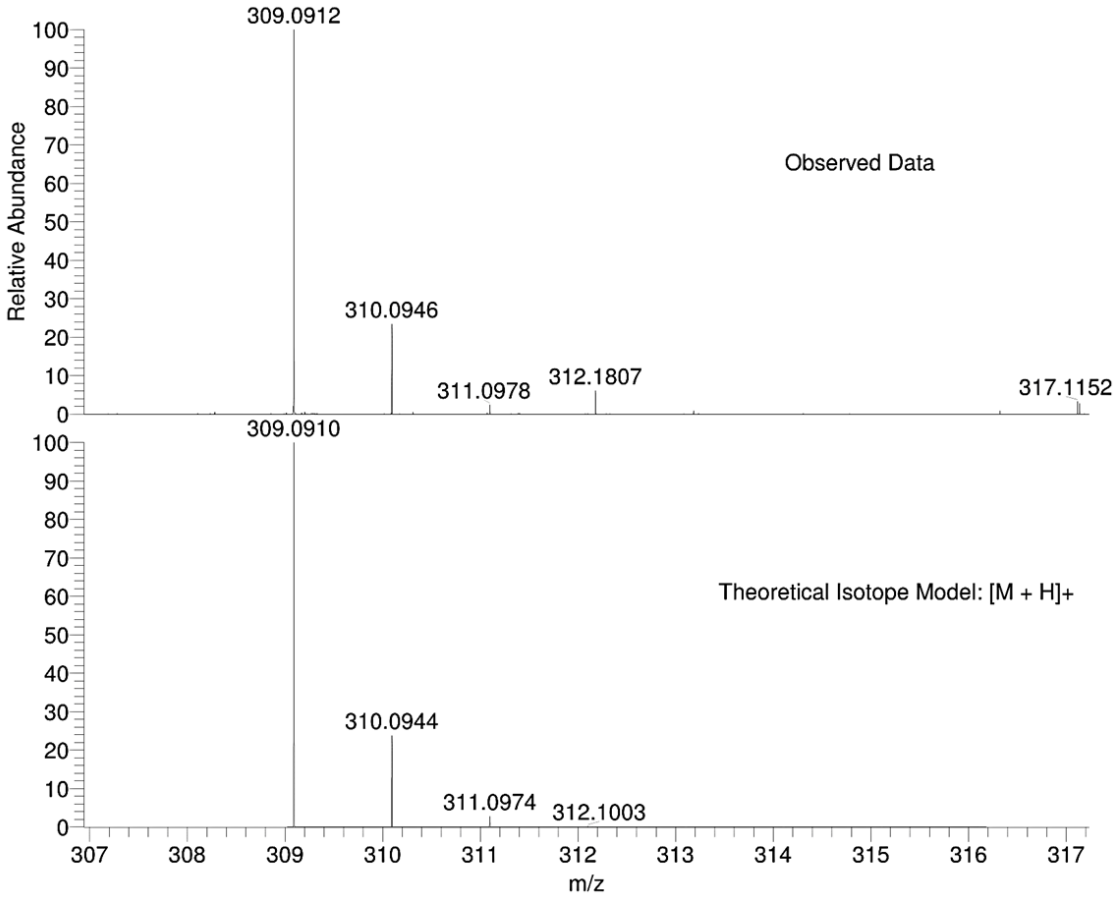

Figure 10: *Mass spectra of* **uPPCOOMe** *showing its* $[M+H]^+$ *ion.*

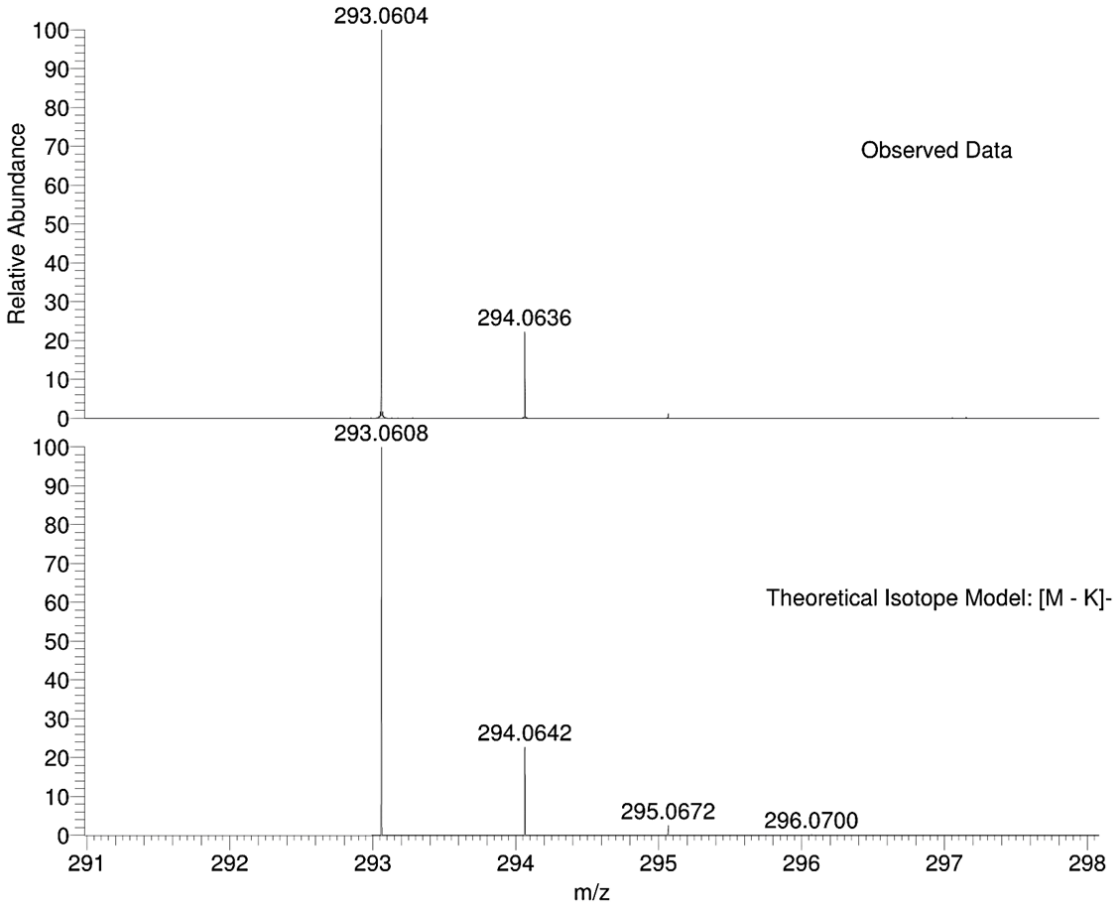

Figure 11: *Mass spectra of* **uPPCOOK** *showing its [M-K]- ion.*

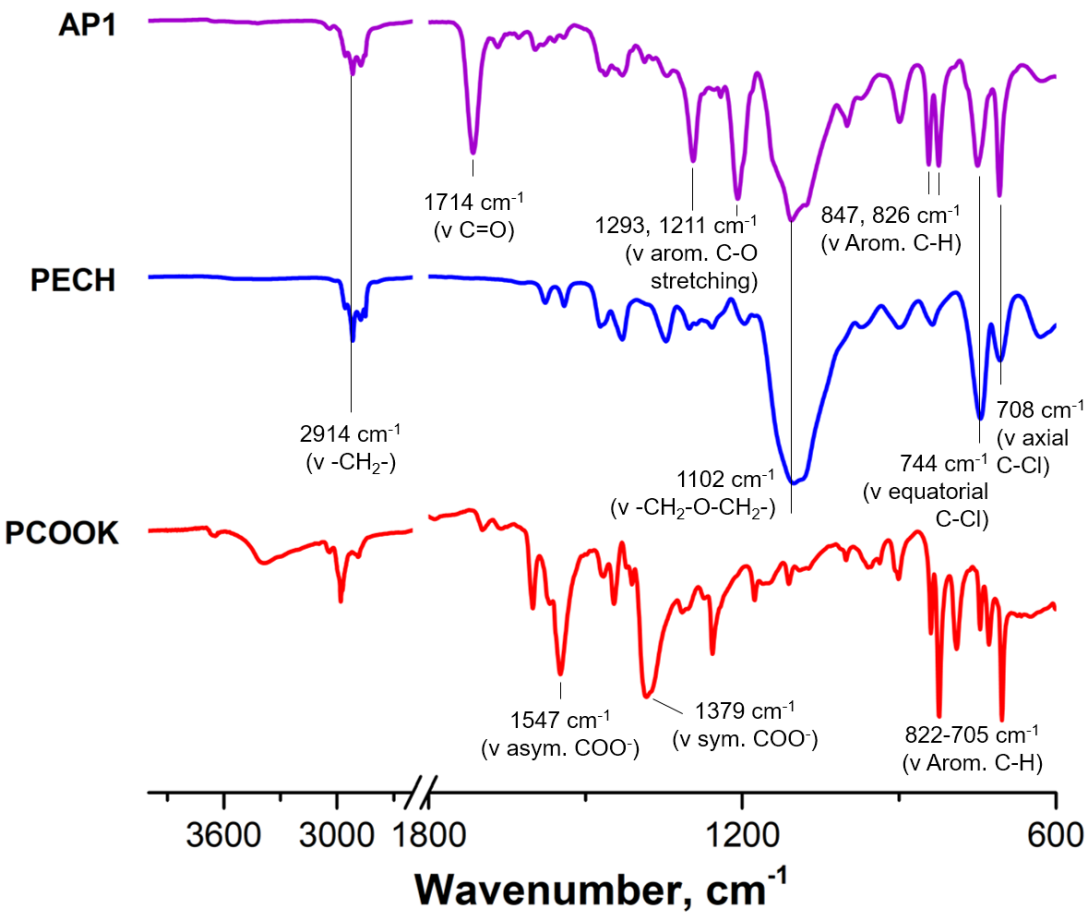

Figure 12: *FT-IR spectra of* **PCOOK**, **PECH** *and* **AP1**.

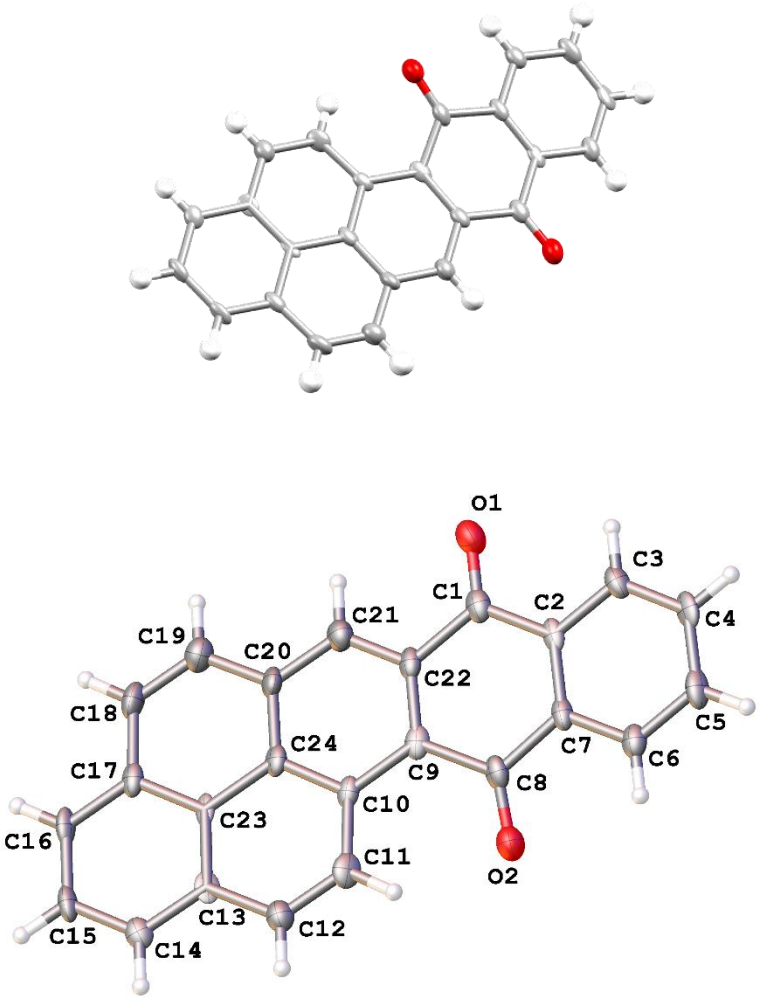

Figure 13: *X-ray crystal structure of* **Py2**.

Py3	
Empirical formula	$C_{24}H_{12}O_2$
Formula weight	332.34
Temperature/K	100.0(2)
Crystal system	monoclinic
Space group	Pc
a/Å	7.997(3)
b/Å	3.7978(14)
c/Å	24.492(9)
α/°	90
β/°	99.032(5)
γ/°	90
Volume/Å^3	734.6(5)
Z	2
ρ_{calc}g/cm^3	1.502
μ/mm^{-1}	0.089
F(000)	344.0
Crystal size/mm^3	0.15 × 0.03 × 0.02
Radiation	Synchrotron (λ = 0.6889)
2Θ range for data collection/°	3.264 to 49.034
Index ranges	-9 ≤ h ≤ 9, -4 ≤ k ≤ 4, -29 ≤ l ≤ 29
Reflections collected	4227
Independent reflections	2417 [R_{int} = 0.0597, R_{sigma} = 0.1332]
Data/restraints/parameters	2417/251/235
Goodness-of-fit on F^2	1.057
Final R indexes [I>=2σ (I)]	R_1 = 0.0780, wR_2 = 0.1857
Final R indexes [all data]	R_1 = 0.1213, wR_2 = 0.2054
Largest diff. peak/hole / e Å^{-3}	0.39/-0.31
Flack parameter	-1.8(10)

Table 2: *Crystal data and structure refinement for* ***Py3****.*

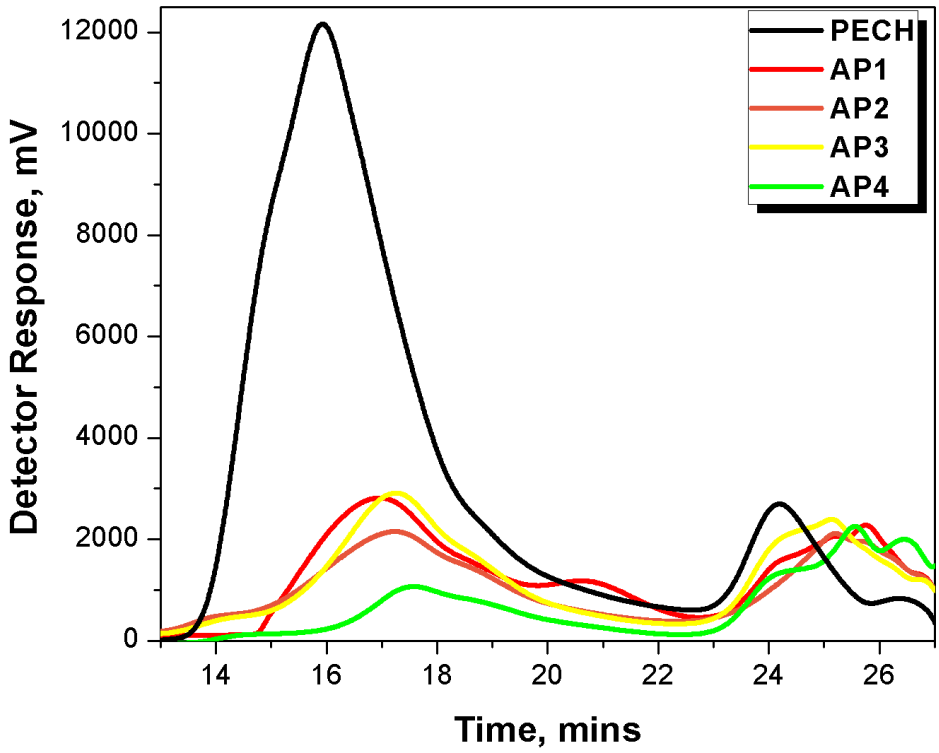

Figure 14: *GPC molecular weight distribution curves of* **AP Series***.*

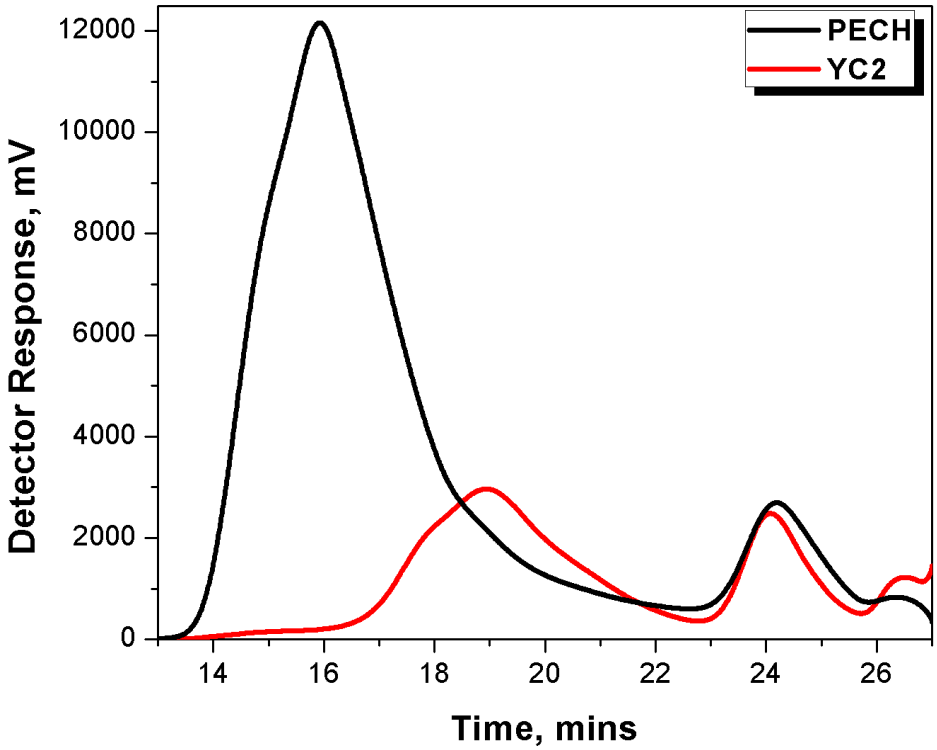

Figure 15: *GPC molecular weight distribution curves of* **YC Series***.*

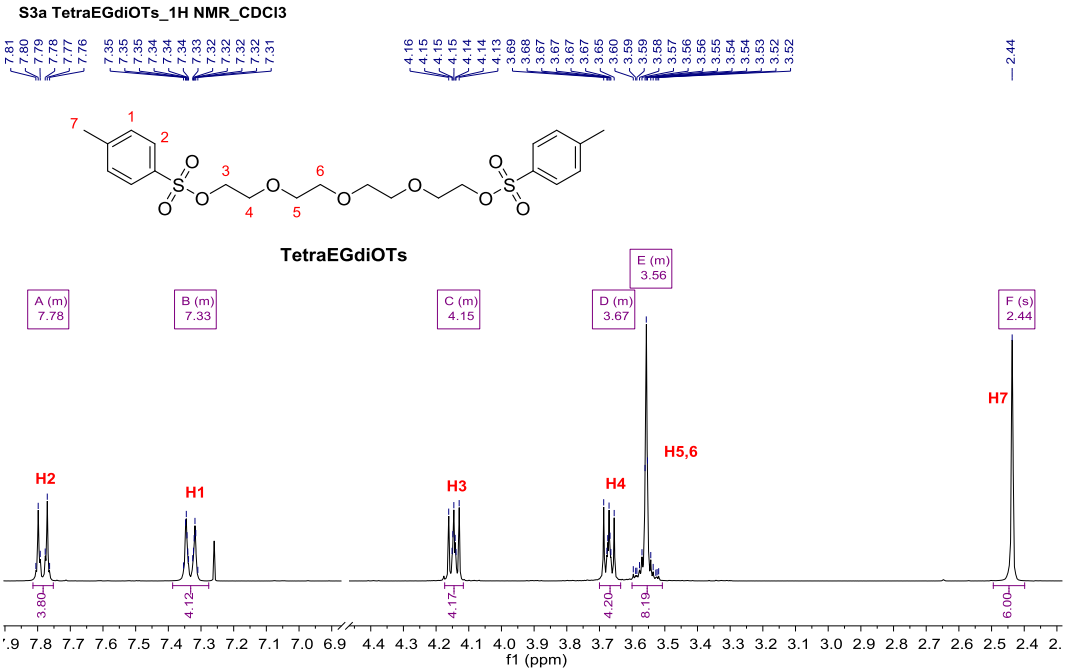

^{1}H NMR (300 MHz, Chloroform-*d*) δ 7.81 – 7.75 (m, 4H, H2), 7.39 – 7.28 (m, 4H, H1), 4.17 – 4.12 (m, 4H, H3), 3.70 – 3.64 (m, 4H, H4), 3.60 – 3.51 8H, H5, H6), 2.44 (s, 6H, H7).

Figure 1: *^{1}H NMR spectrum (300 MHz, $CDCl_3$) of* **TetraEGdiOTs**.

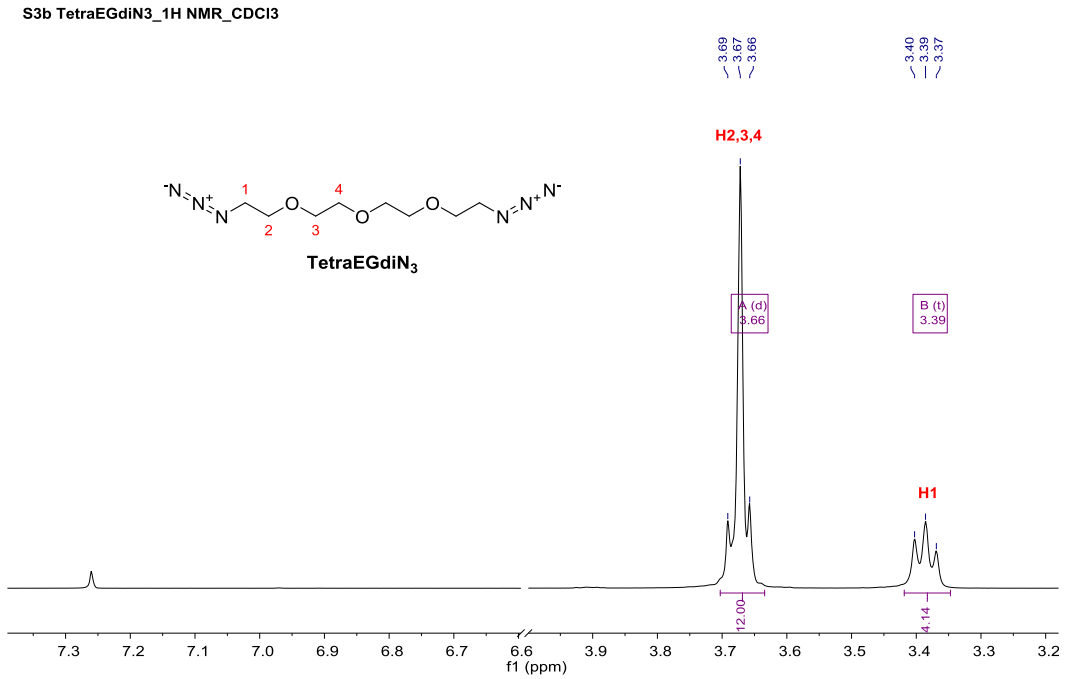

^{1}H NMR (300 MHz, Chloroform-*d*) δ 3.66 (d,*J* = 4.4 Hz, 12H, H2, H3, H4), 3.39 (t,*J* = 5.0 Hz, 4H, H1).

Figure 2: *^{1}H NMR spectrum (300 MHz, $CDCl_3$) of* **TetraEGdiN$_3$**.

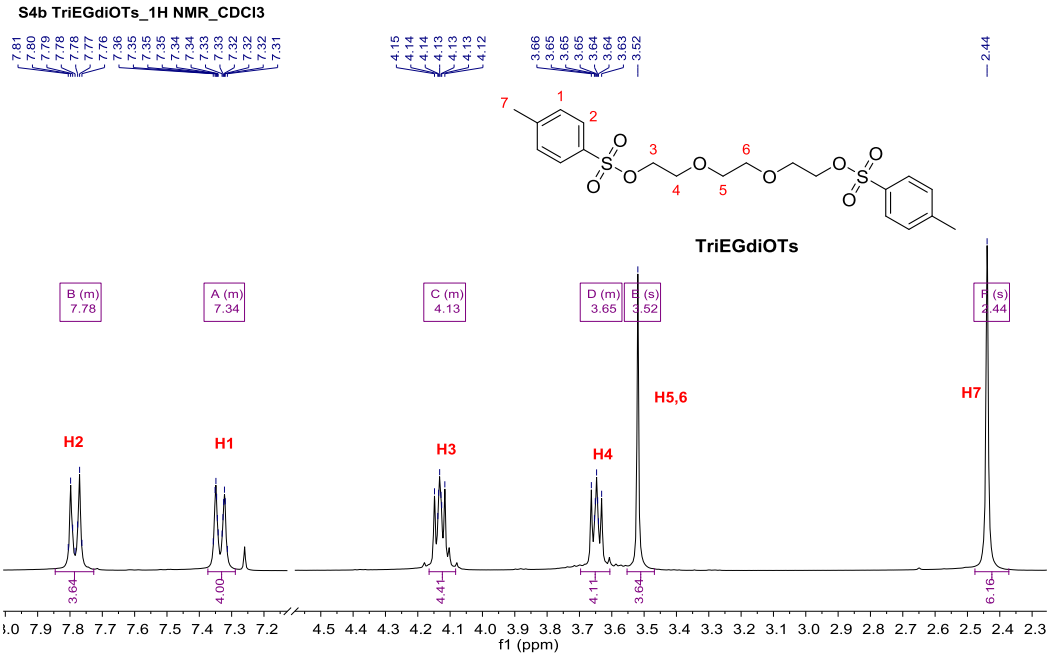

^{1}H NMR (300 MHz, Chloroform-*d*) δ 7.85 – 7.73 (m, 4H, H2), 7.37 – 7.29 (m, 4H, H1), 4.16 – 4.08 (m, 4H, H3), 3.70 – 3.61 (m, 4H, H4), 3.52 (s, 4H, H5, H6), 2.44 (s, 6H, H7).

Figure 3: *^{1}H NMR spectrum (300 MHz, $CDCl_3$) of* **TriEGdiOTs**.

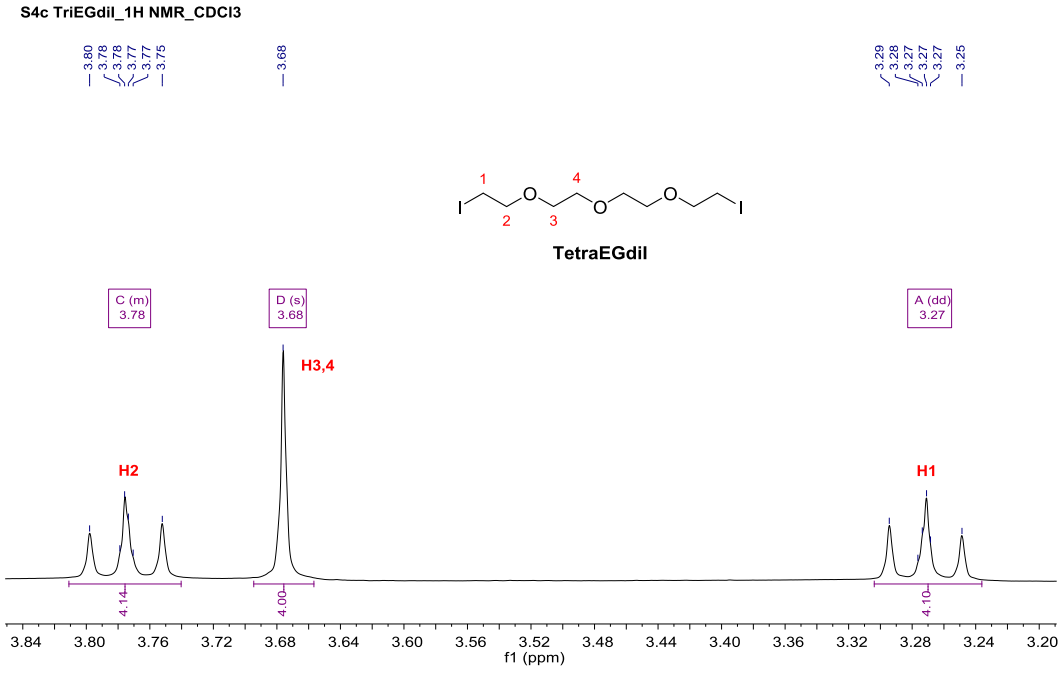

^{1}H NMR (300 MHz, Chloroform-*d*) δ 3.81 – 3.74 (m, 4H), 3.68 (s, 4H), 3.27 (dd, *J* = 7.3, 6.5 Hz, 4H).

Figure 4: *^{1}H NMR spectrum (300 MHz, $CDCl_3$) of* **TriEGdiI**.

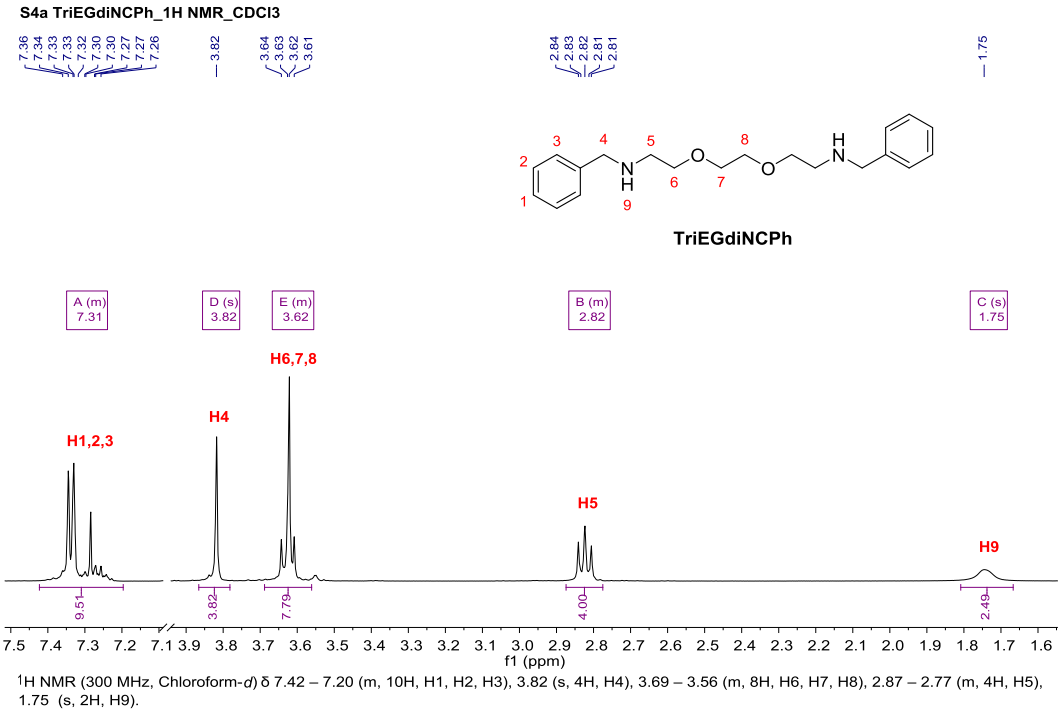

^{1}H NMR (300 MHz, Chloroform-*d*) δ 7.42 – 7.20 (m, 10H, H1, H2, H3), 3.82 (s, 4H, H4), 3.69 – 3.56 (m, 8H, H6, H7, H8), 2.87 – 2.77 (m, 4H, H5), 1.75 (s, 2H, H9).

Figure 5: *^{1}H NMR spectrum (300 MHz, $CDCl_3$) of* **TriEGdiNCPh**.

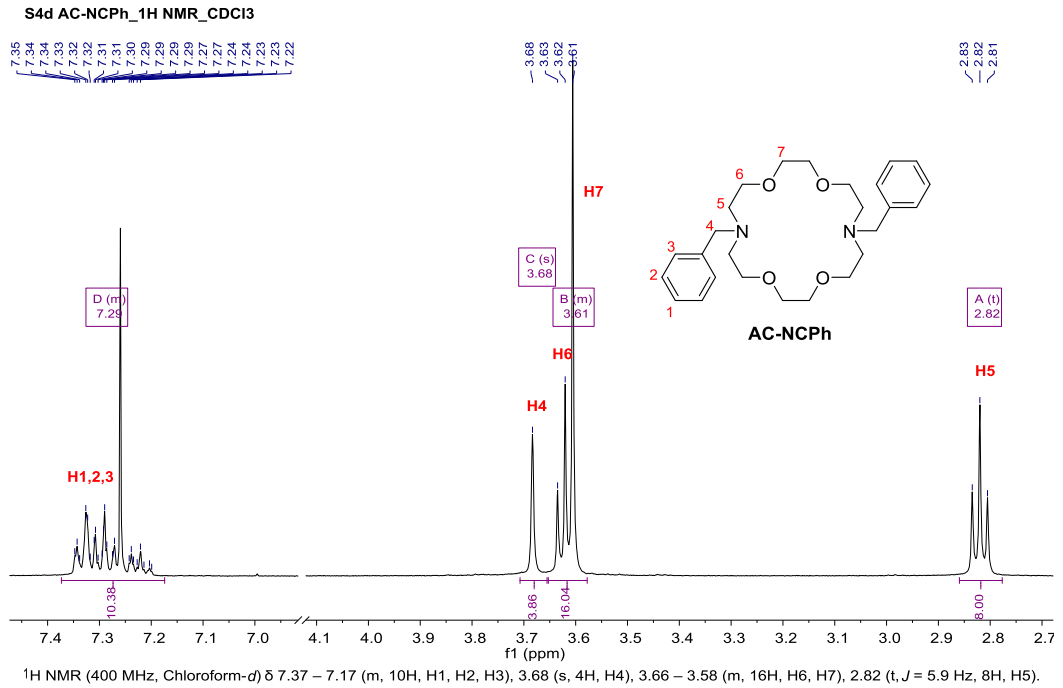

^{1}H NMR (400 MHz, Chloroform-*d*) δ 7.37 – 7.17 (m, 10H, H1, H2, H3), 3.68 (s, 4H, H4), 3.66 – 3.58 (m, 16H, H6, H7), 2.82 (t, *J* = 5.9 Hz, 8H, H5).

Figure 6: *^{1}H NMR spectrum (400 MHz, $CDCl_3$) of* **AC-NCPh**.

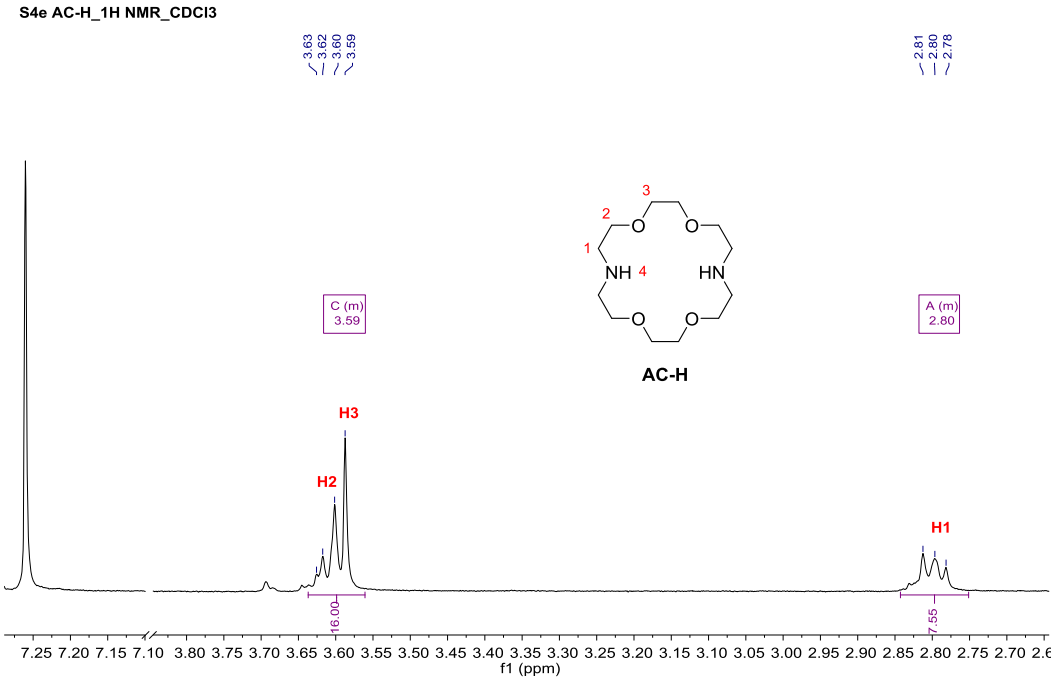

^{1}H NMR (300 MHz, Chloroform-*d*) δ 3.64 – 3.56 (m, 16H, H2, H3), 2.84 – 2.75 (m, 8H, H1).

Figure 7: *^{1}H NMR spectrum (300 MHz, $CDCl_3$) of* **AC-H**.

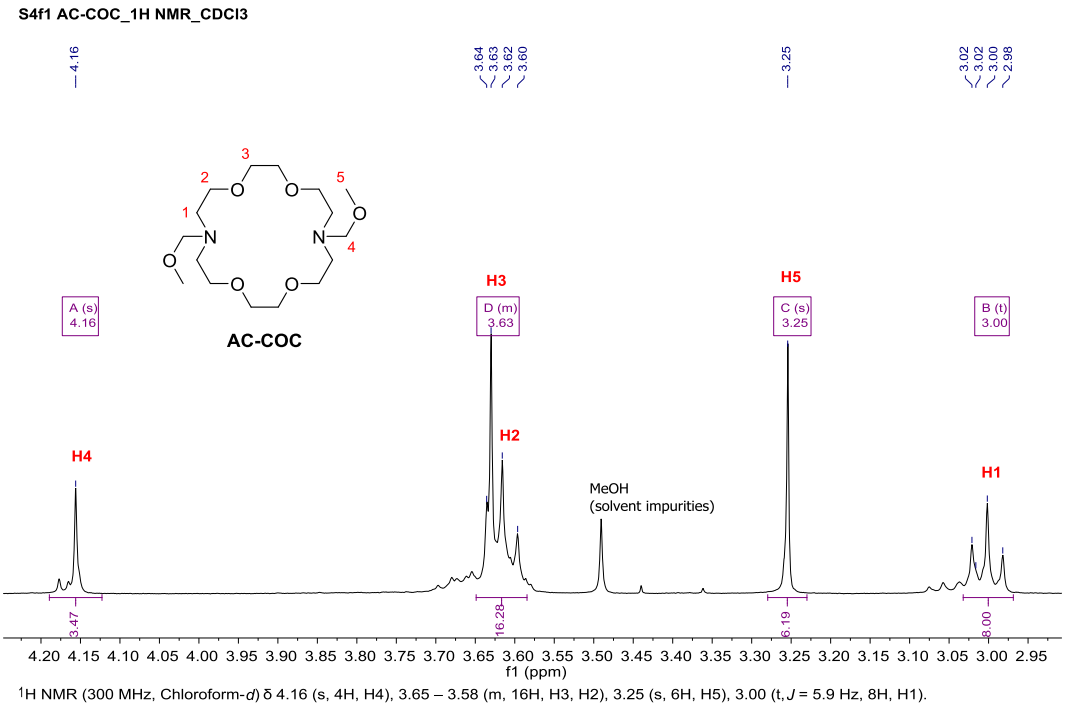

^{1}H NMR (300 MHz, Chloroform-*d*) δ 4.16 (s, 4H, H4), 3.65 – 3.58 (m, 16H, H3, H2), 3.25 (s, 6H, H5), 3.00 (t, *J* = 5.9 Hz, 8H, H1).

Figure 8: *^{1}H NMR spectrum (300 MHz, $CDCl_3$) of* **AC-COC**.

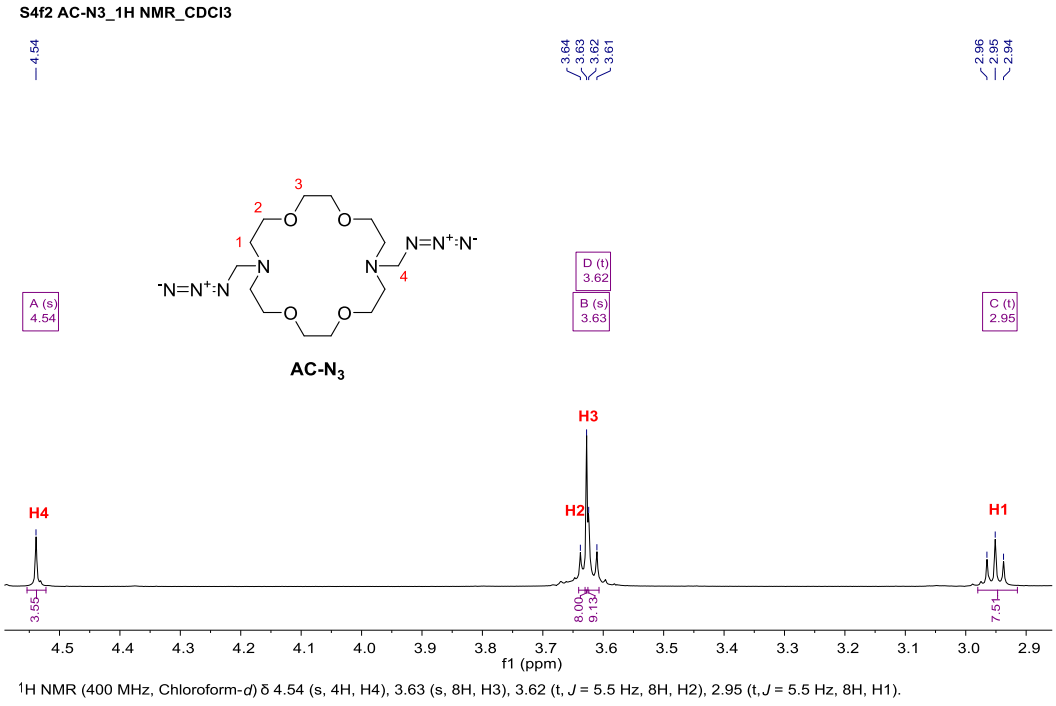

^{1}H NMR (400 MHz, Chloroform-*d*) δ 4.54 (s, 4H, H4), 3.63 (s, 8H, H3), 3.62 (t, *J* = 5.5 Hz, 8H, H2), 2.95 (t, *J* = 5.5 Hz, 8H, H1).

Figure 9: *^{1}H NMR spectrum (400 MHz, $CDCl_3$) of* **AC-N_3**.

S3c Pyr2COOMe_1H NMR_CDCl3

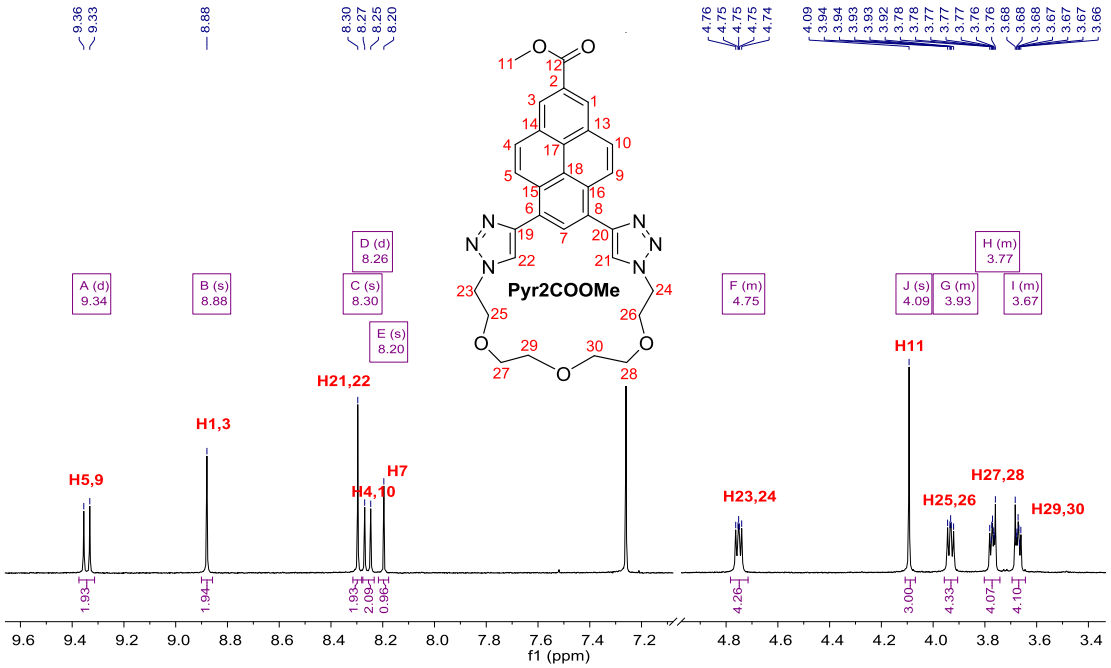

^{1}H NMR (400 MHz, Chloroform- *d*) δ 9.34 (d, *J* = 9.3 Hz, 2H, H5, H9), 8.88 (s, 2H, H1, H3), 8.30 (s, 2H, H21, H22), 8.26 (d, *J* = 9.3 Hz, 2H, H4, H10), 8.20 (s, 1H, H7), 4.78 – 4.72 (m, 4H, H23, H24), 4.09 (s, 3H, H11), 3.96 – 3.91 (m, 4H, H25, H26), 3.80 – 3.74 (m, 4H, H27, H28), 3.69 – 3.64 (m, 4H, H29, H30).

S3c Pyr2COOMe_13C NMR_CDCl3

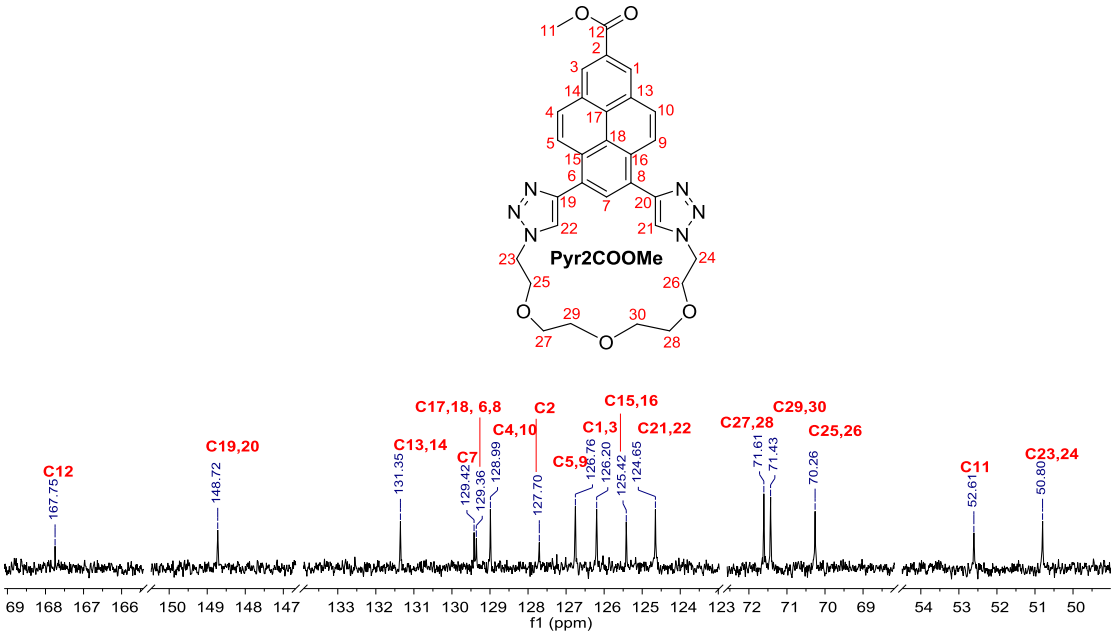

^{13}C NMR (101 MHz, Chloroform- *d*) δ 167.75 (C12), 148.72 (C19,C20), 131.35 (C13,C14), 129.42 (C7), 129.36 (C17,C18,C6,C8), 128.99 (C4,C10) 127.70 (C2), 126.76 (C5,C9), 126.20 (C1,C3), 125.42 (C15,C16), 124.65 (C21,C22), 71.61 (C27,C28), 71.43 (C29,C30), 70.26 (C25,C26), 52.61 (C11), 50.80 (C23,24).

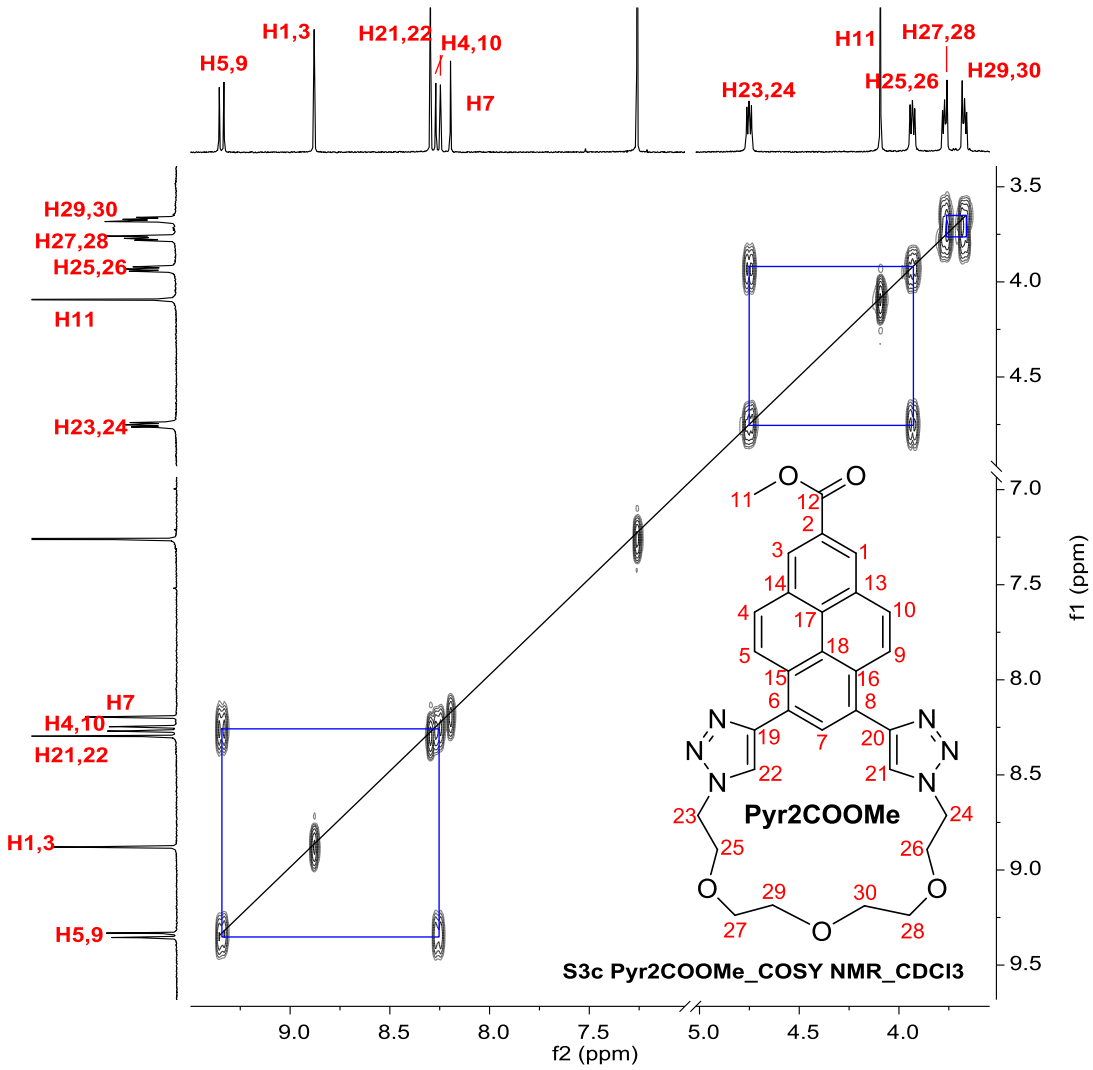
H5,9
H1,3
H21,22
H4,10
H7
H23,24
H11
H27,28
H25,26
H29,30
H29,30
H27,28
H25,26
H11
H23,24
H7
H4,10
H21,22
H1,3
H5,9
Pyr2COOMe
S3c Pyr2COOMe_COSY NMR_CDCl3
f2 (ppm)
f1 (ppm)

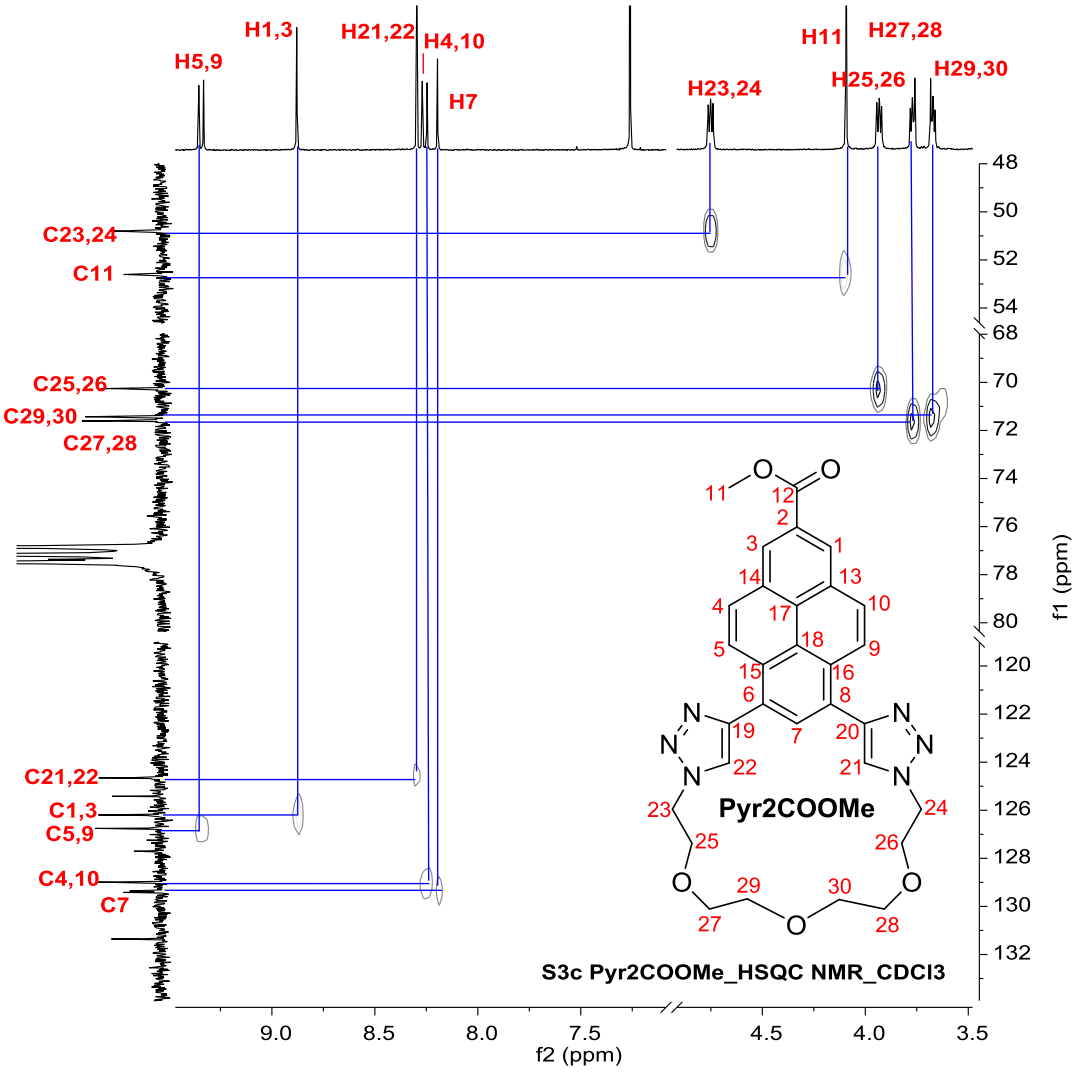
H1,3
H21,22
H4,10
H5,9
H7
H23,24
H11
H27,28
H25,26
H29,30
C23,24
C11
C25,26
C29,30
C27,28
C21,22
C1,3
C5,9
C4,10
C7
Pyr2COOMe
S3c Pyr2COOMe_HSQC NMR_CDCl3
f2 (ppm)
f1 (ppm)

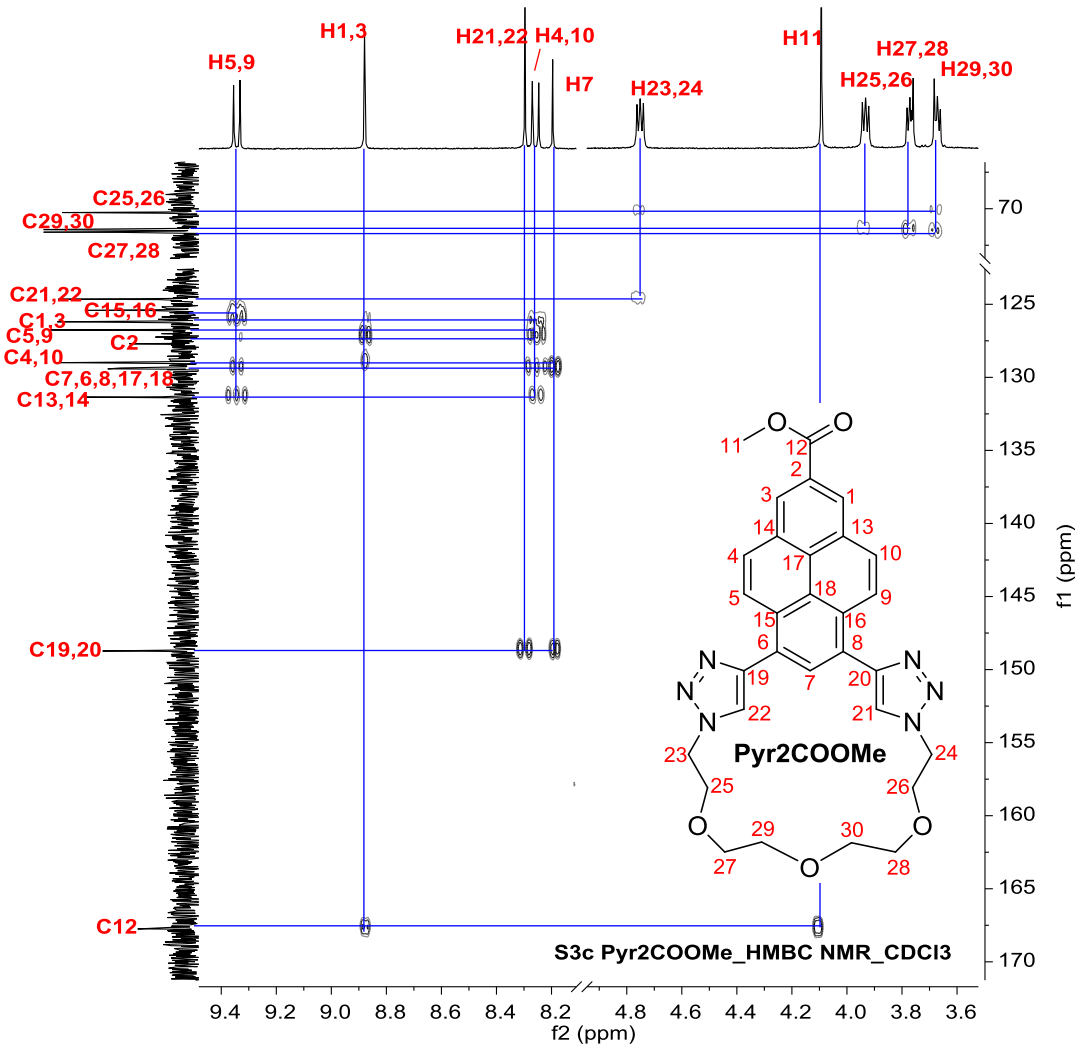

Figure 10: *^{1}H, ^{13}C, COSY, HSQC, HMBC NMR spectra (400 MHz, $CDCl_3$) of* **Pyr2COOMe**.

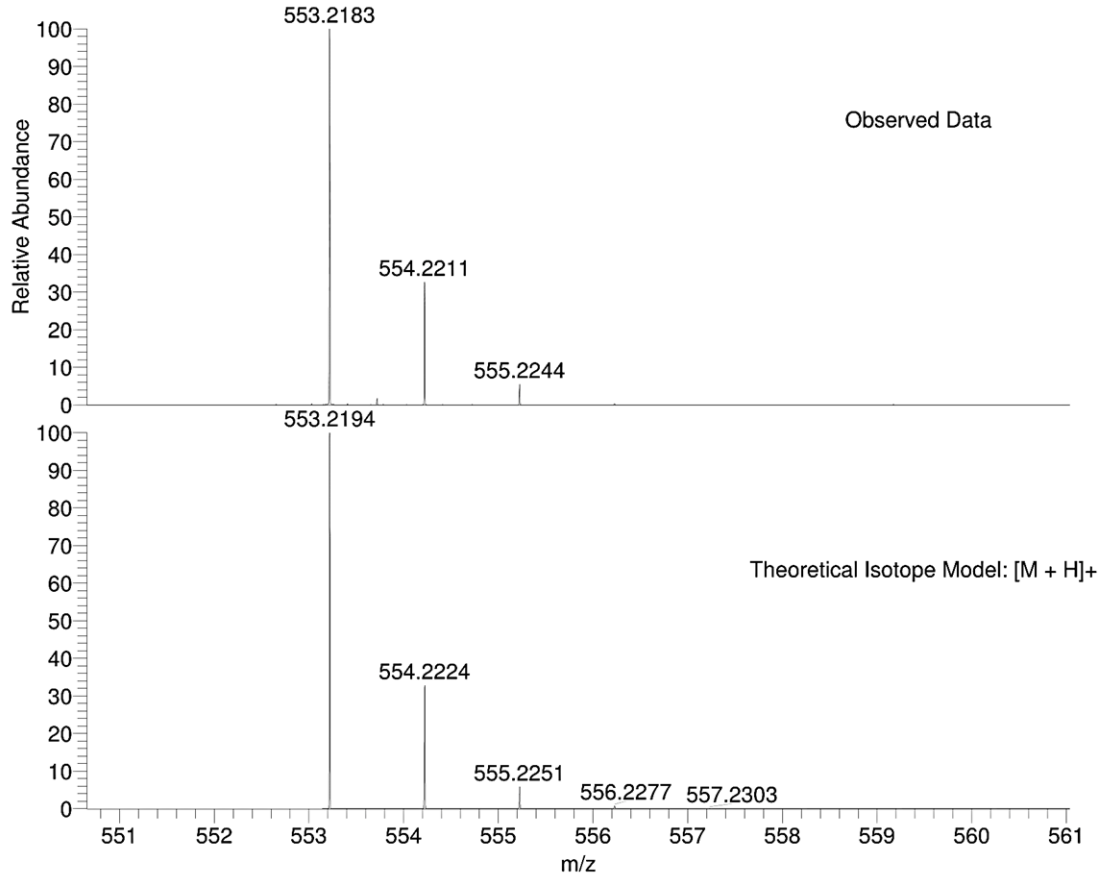

Figure 11: *Mass spectra of* **Pyr2COOMe** *showing its* $[M+H]^+$ *ion.*

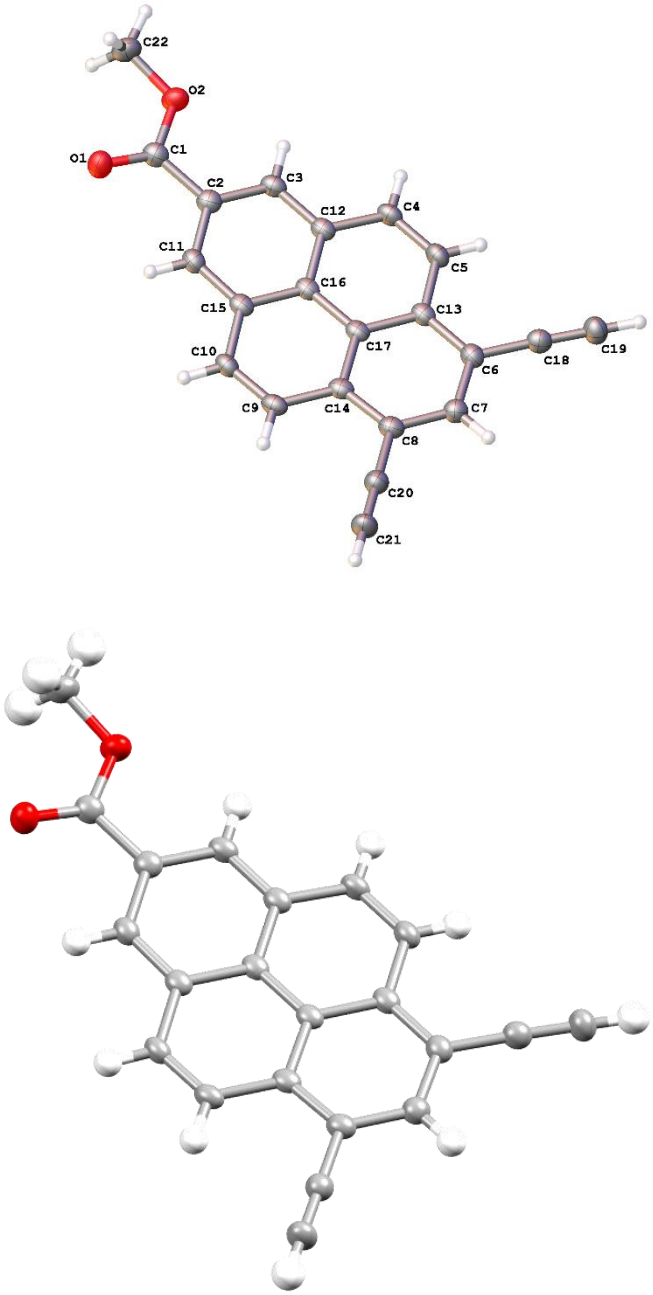

Figure 12: *X-ray crystal structure of* **uPPCOOMe**.

uPPCOOMe	
Empirical formula	$C_{22}H_{12}O_2$
Formula weight	308.32
Temperature/K	150.0(2)
Crystal system	monoclinic
Space group	$P2_1/n$
a/Å	14.6505(3)
b/Å	3.80657(8)
c/Å	26.0697(5)
α/°	90
β/°	96.3269(18)
γ/°	90
Volume/Å^3	1445.01(5)
Z	4
ρ_{calc}g/cm^3	1.417
μ/mm^{-1}	0.718
F(000)	640.0
Crystal size/mm^3	0.3 × 0.14 × 0.04
Radiation	CuKα (λ = 1.54184)
2Θ range for data collection/°	6.628 to 134.146
Index ranges	-17 ≤ h ≤ 16, -4 ≤ k ≤ 4, -31 ≤ l ≤ 30
Reflections collected	18887
Independent reflections	2590 [R_{int} = 0.0595, R_{sigma} = 0.0275]
Data/restraints/parameters	2590/0/218
Goodness-of-fit on F^2	1.032
Final R indexes [I>=2σ (I)]	R_1 = 0.0387, wR_2 = 0.1009
Final R indexes [all data]	R_1 = 0.0465, wR_2 = 0.1097
Largest diff. peak/hole / e Å^{-3}	0.16/-0.19

Table 1: *Crystal data and structure refinement for* ***uPPCOOMe****.*

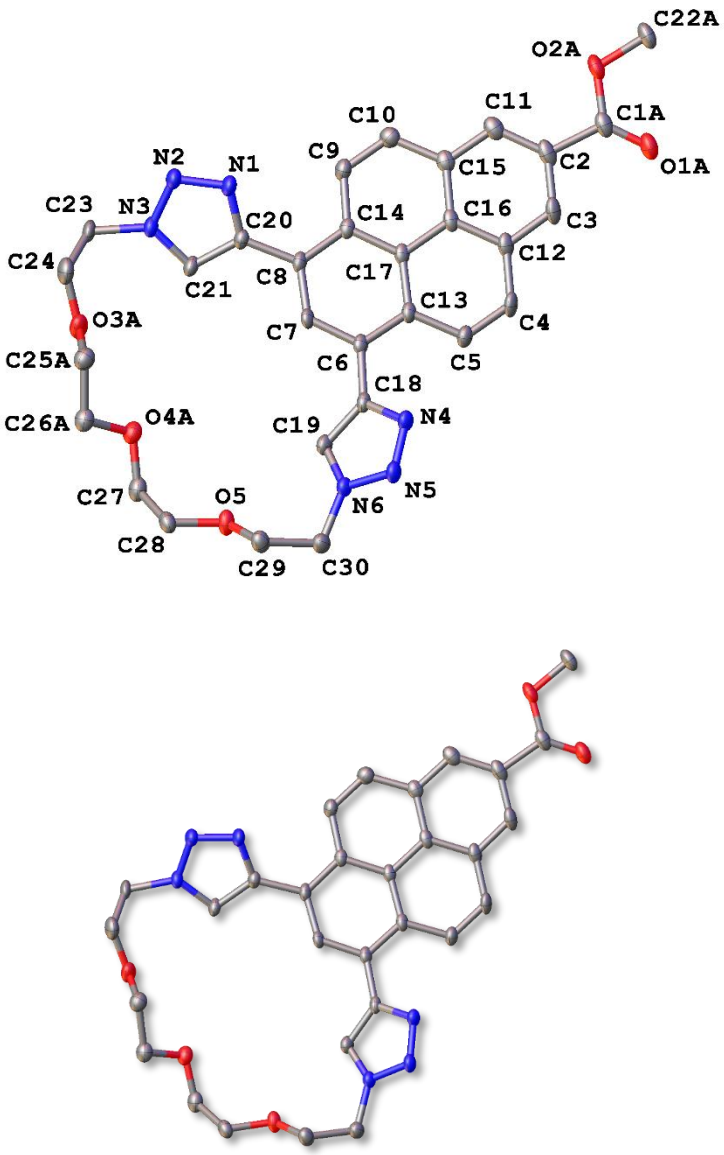

Figure 13: *X-ray crystal structure of* ***Pyr2COOMe****.*

Pyr2COOMe	
Empirical formula	$C_{30}H_{28}N_6O_5$
Formula weight	552.58
Temperature/K	100.0(2)
Crystal system	triclinic
Space group	P-1
a/Å	11.6813(6)
b/Å	12.7799(7)
c/Å	18.1483(10)
α/°	87.8220(10)
β/°	87.4860(10)
γ/°	73.4550(10)
Volume/Å^3	2593.7(2)
Z	4
ρ_{calc}g/cm^3	1.415
μ/mm^{-1}	0.099
F(000)	1160.0
Crystal size/mm^3	0.13 × 0.125 × 0.01
Radiation	MoKα (λ = 0.71073)
2Θ range for data collection/°	2.246 to 50.7
Index ranges	-14 ≤ h ≤ 14, -15 ≤ k ≤ 15, -21 ≤ l ≤ 21
Reflections collected	26783
Independent reflections	9409 [R_{int} = 0.0449, R_{sigma} = 0.0589]
Data/restraints/parameters	9409/859/799
Goodness-of-fit on F^2	1.041
Final R indexes [I>=2σ (I)]	R_1 = 0.0597, wR_2 = 0.1634
Final R indexes [all data]	R_1 = 0.0663, wR_2 = 0.1698
Largest diff. peak/hole / e Å^{-3}	0.88/-0.34

Table 2: *Crystal data and structure refinement for* ***Pyr2COOMe****.*

Chapter 4 Supplementary Information, SI

S5 9-ACAK_1H NMR_DMSO-d6

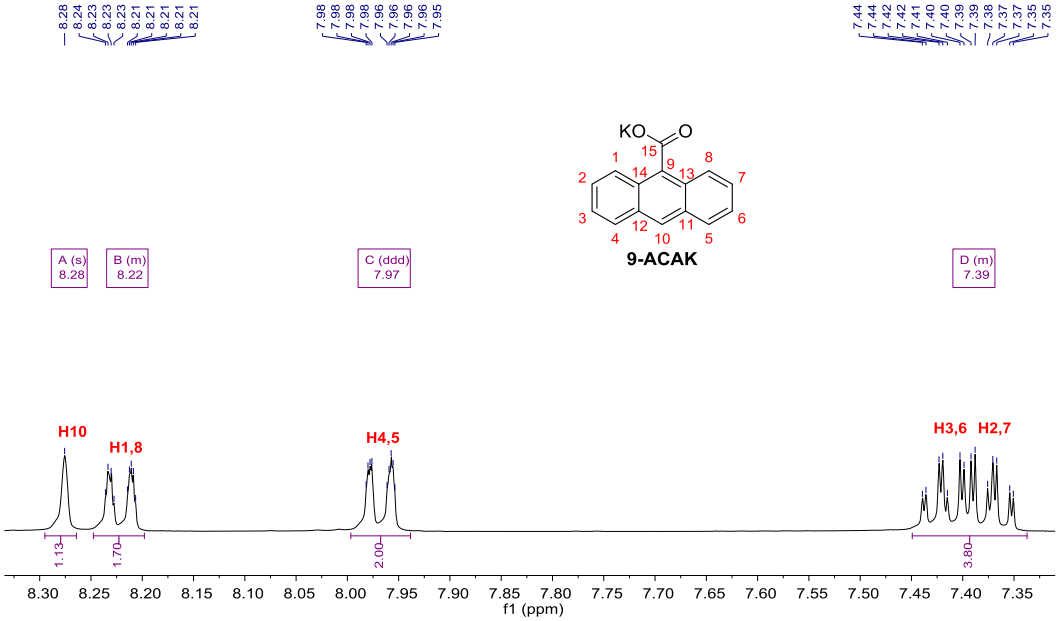

^{1}H NMR (400 MHz, DMSO- d_6) δ 8.28 (s, 1H, H10), 8.25 – 8.20 (m, 2H, H1, H8), 7.97 (ddd, J = 8.2, 1.5, 0.7 Hz, 2H, H4, H5), 7.45 – 7.34 (m, 4H, H3, H6, H2, H7).

S5 9-ACAK_13C NMR_DMSO-d6

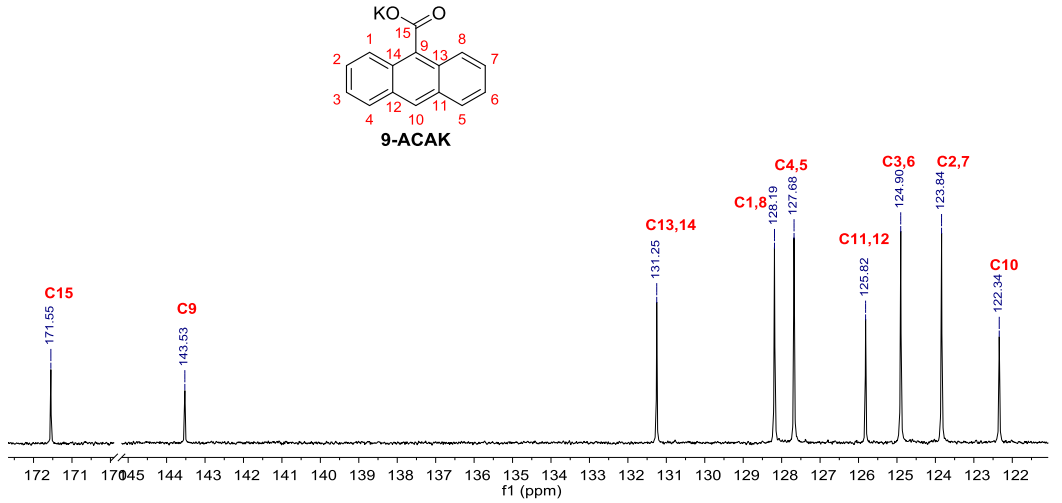

^{13}C NMR (101 MHz, DMSO-d_6) δ 171.55 (C15), 143.53 (C9), 131.25 (C13,C14), 128.19 (C1,C8), 127.68 (C4,C5), 125.82 (C11,C12), 124.90 (C3, C6), 123.84 (C2,C7), 122.34 (C10).

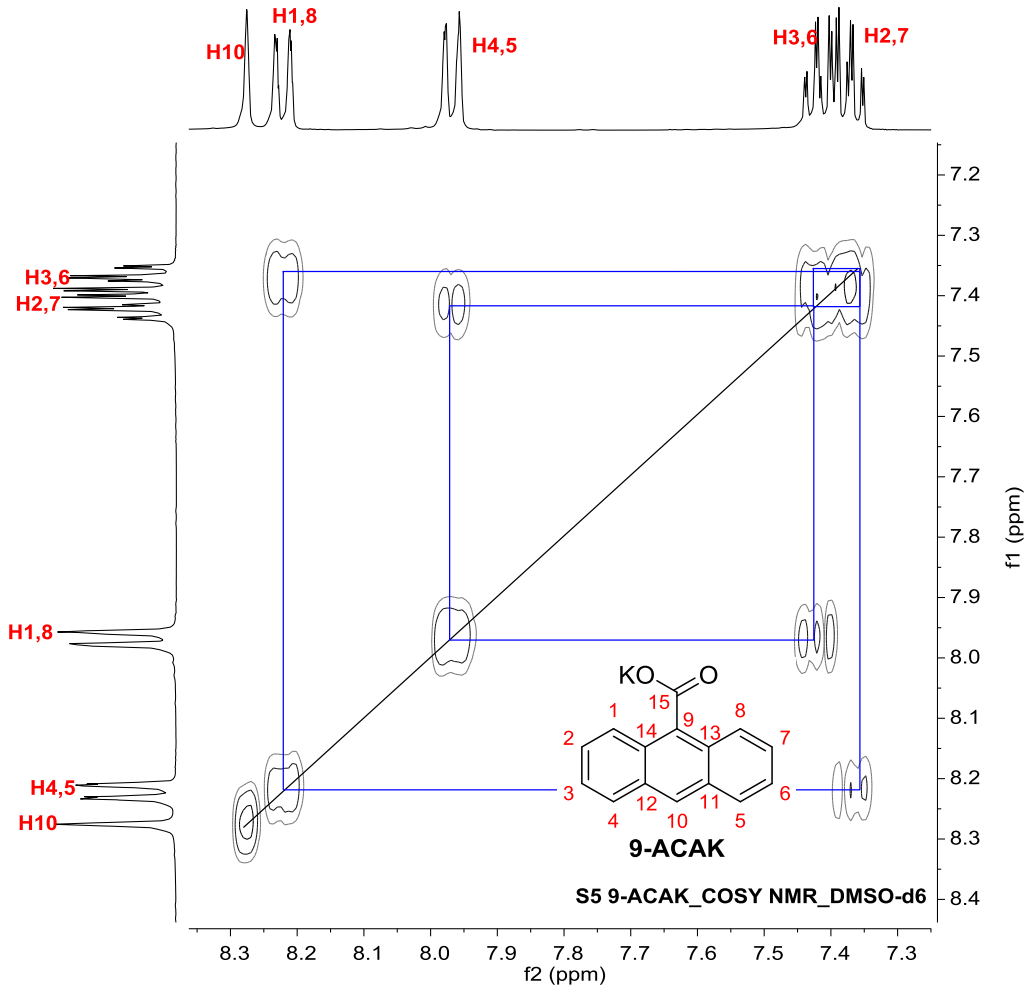
H1,8
H10
H4,5
H3,6
H2,7
H3,6
H2,7
H1,8
H4,5
H10
KO
O
1
15
8
2
14
9
13
7
3
12
11
6
4
10
5
9-ACAK
S5 9-ACAK_COSY NMR_DMSO-d6
f1 (ppm)
f2 (ppm)
8.3
8.2
8.1
8.0
7.9
7.8
7.7
7.6
7.5
7.4
7.3
7.2
7.3
7.4
7.5
7.6
7.7
7.8
7.9
8.0
8.1
8.2
8.3
8.4

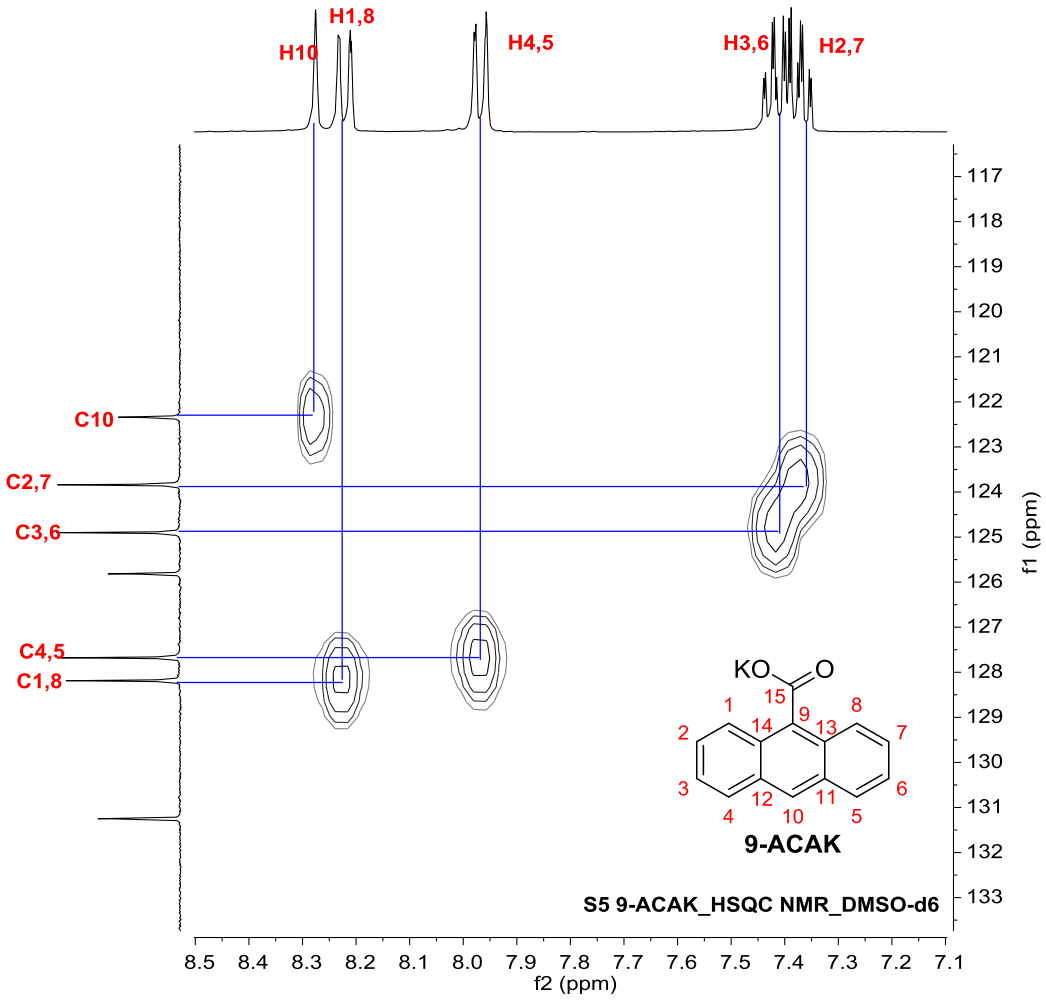
H1,8
H10
H4,5
H3,6
H2,7
C10
C2,7
C3,6
C4,5
C1,8
KO
O
1
15
8
9
14
13
2
7
3
6
12
11
4
10
5
9-ACAK
S5 9-ACAK_HSQC NMR_DMSO-d6
f1 (ppm)
f2 (ppm)
117
118
119
120
121
122
123
124
125
126
127
128
129
130
131
132
133
8.5
8.4
8.3
8.2
8.1
8.0
7.9
7.8
7.7
7.6
7.5
7.4
7.3
7.2
7.1

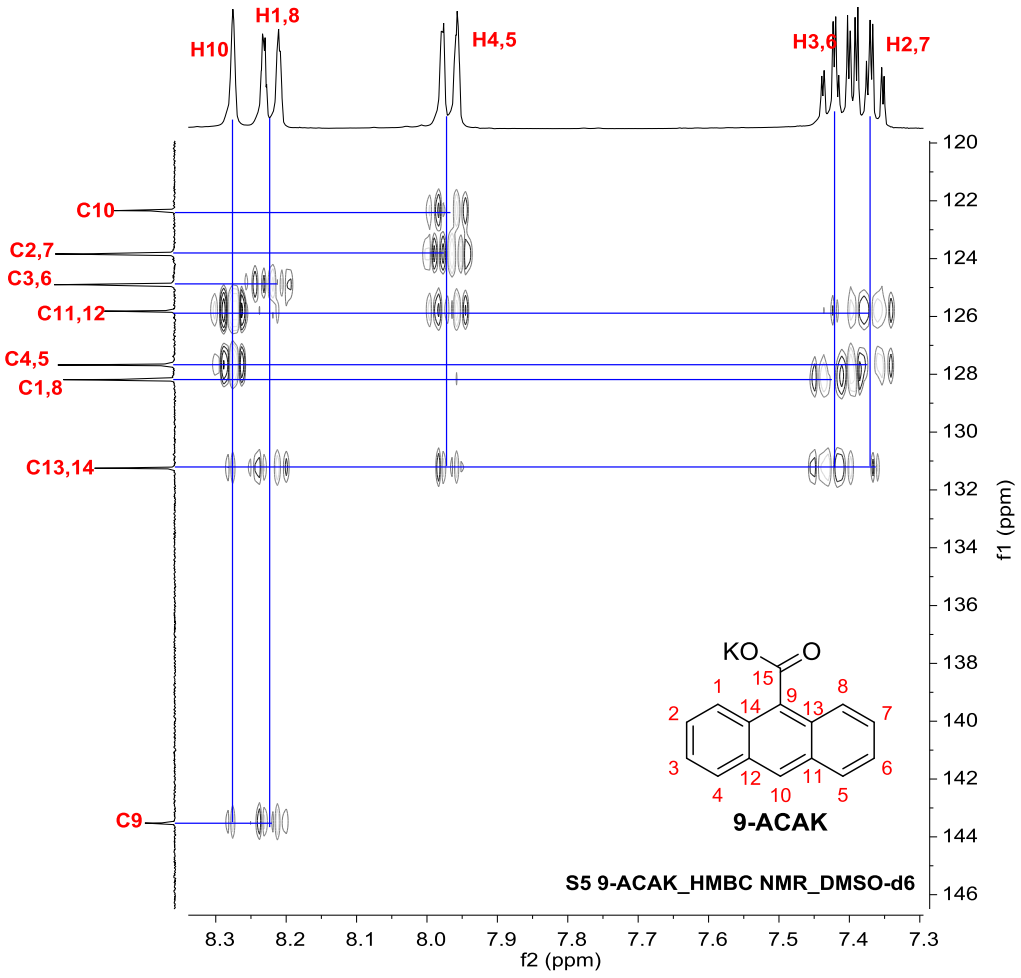

Figure 1: *^{1}H, ^{13}C, COSY, HSQC, HMBC NMR spectra (400 MHz, DMSO-d_6) of* **9-ACAK**.

S9 PA6_1H NMR_TCE-d2

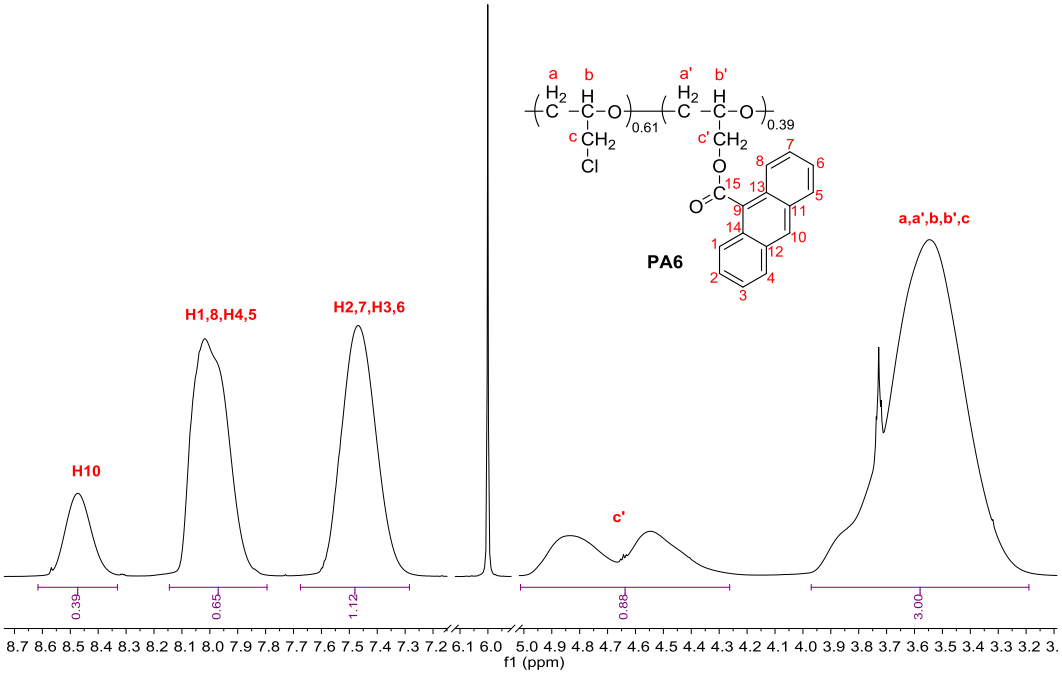

S9 PA6_13C NMR_TCE-d2

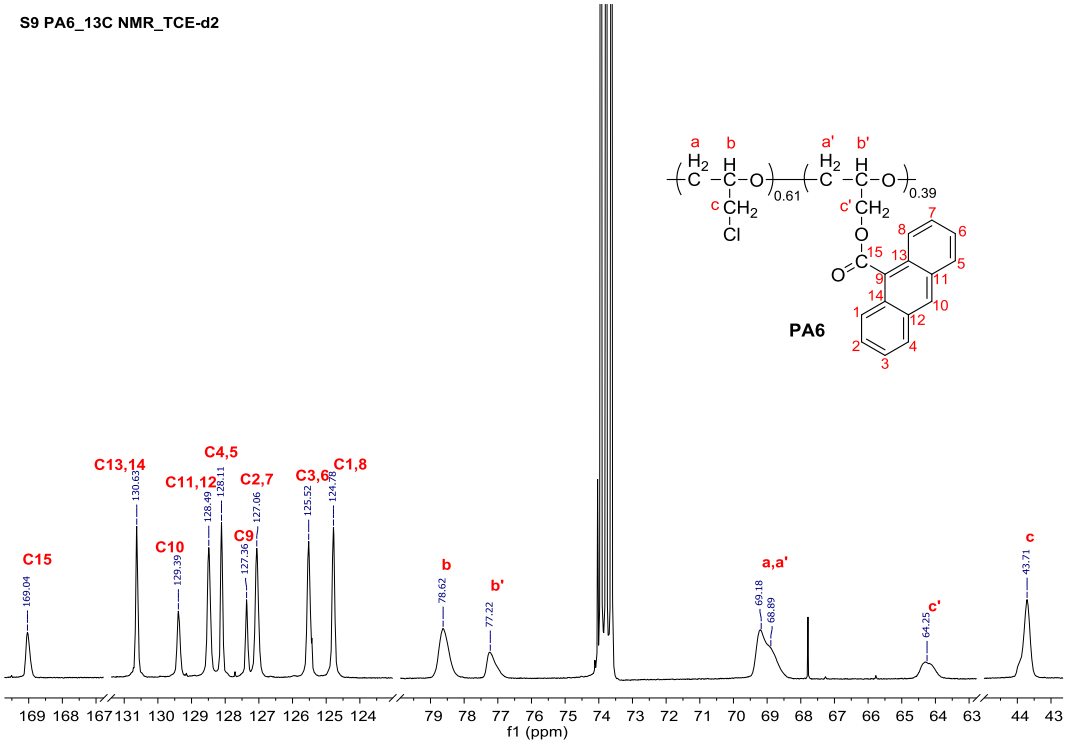

^{1}H NMR	PA6	^{13}C NMR	
Signal (ppm)	**Assignment**	**Signal (ppm)**	**Assignment**
8.58-8.32	H10	169.04	C15
8.14-7.79	H1,8, H4,5	130.63	C13,14
7.62-7.28	H2,7, H3,6	129.39	C10
5.01-4.26	c’	128.49	C11,12
3.97-3.19	a,a’,b,b’,c	128.11	C4,5
		127.36	C9
		127.06	C2,7
		125.52	C3,6
		124.78	C1,8
		78.62	b
		77.22	b’
		69.18-68.89	a,a’
		64.25	c’
		43.71	c

Table 1: *^{1}H and ^{13}C NMR data of* **PA6** *and their corresponding assignments.*

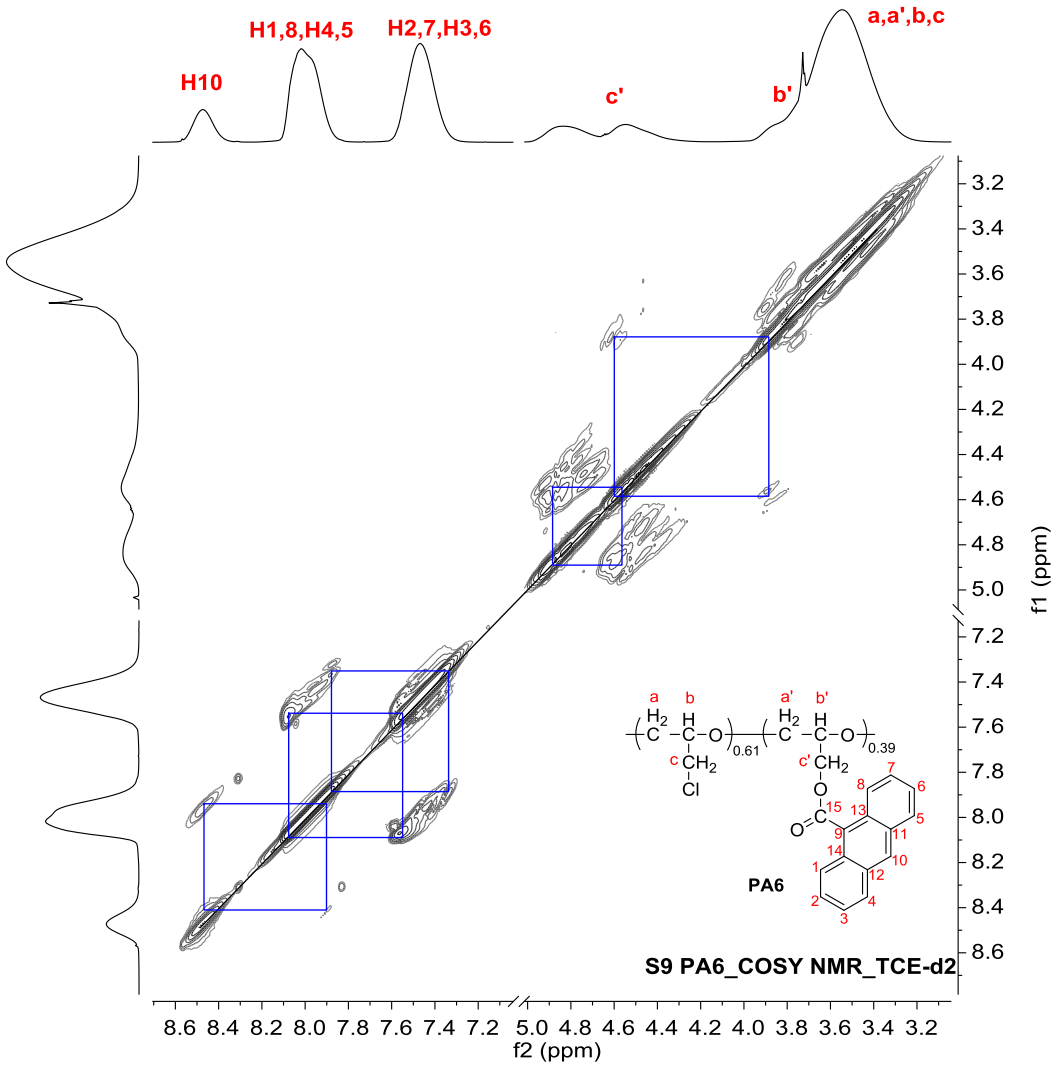
H10
H1,8,H4,5
H2,7,H3,6
c'
b'
a,a',b,c
f1 (ppm)
f2 (ppm)
PA6
S9 PA6_COSY NMR_TCE-d2

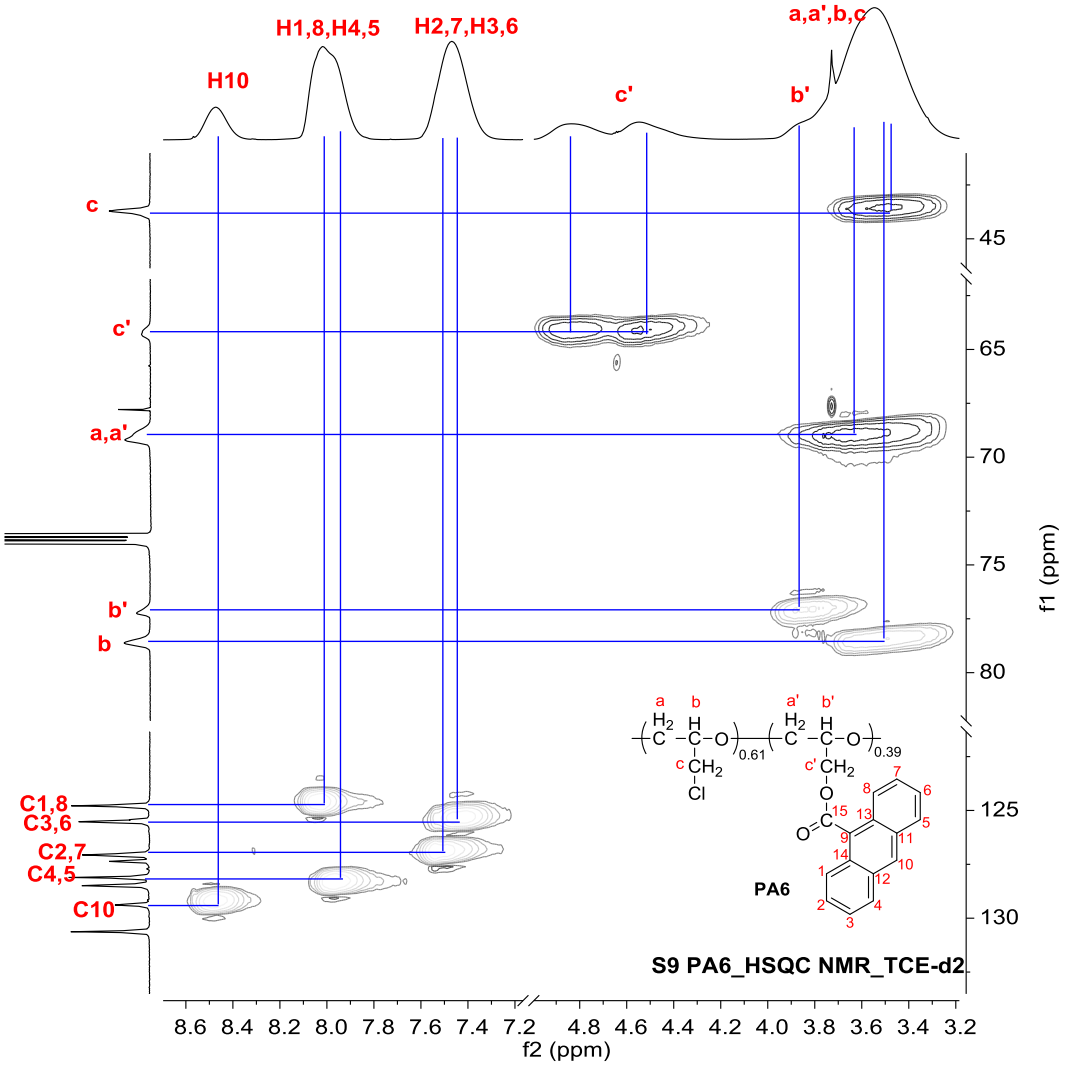
H1,8,H4,5
H2,7,H3,6
a,a',b,c
H10
c'
b'
c
c'
a,a'
b'
b
C1,8
C3,6
C2,7
C4,5
C10
PA6
S9 PA6_HSQC NMR_TCE-d2
f1 (ppm)
f2 (ppm)

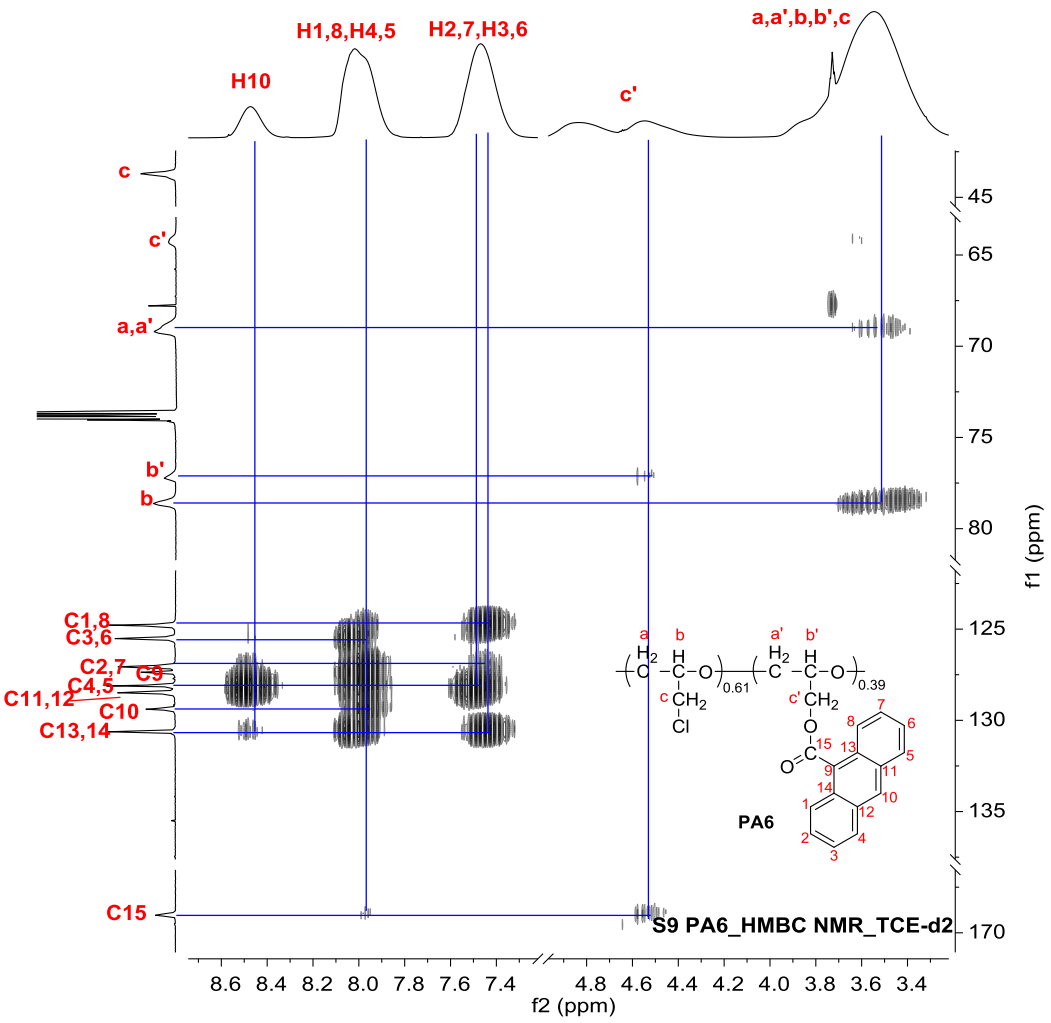

Figure 2: *^{1}H, ^{13}C, COSY, HSQC, HMBC NMR spectra (700 MHz, TCE-d_2) of* **PA6**.

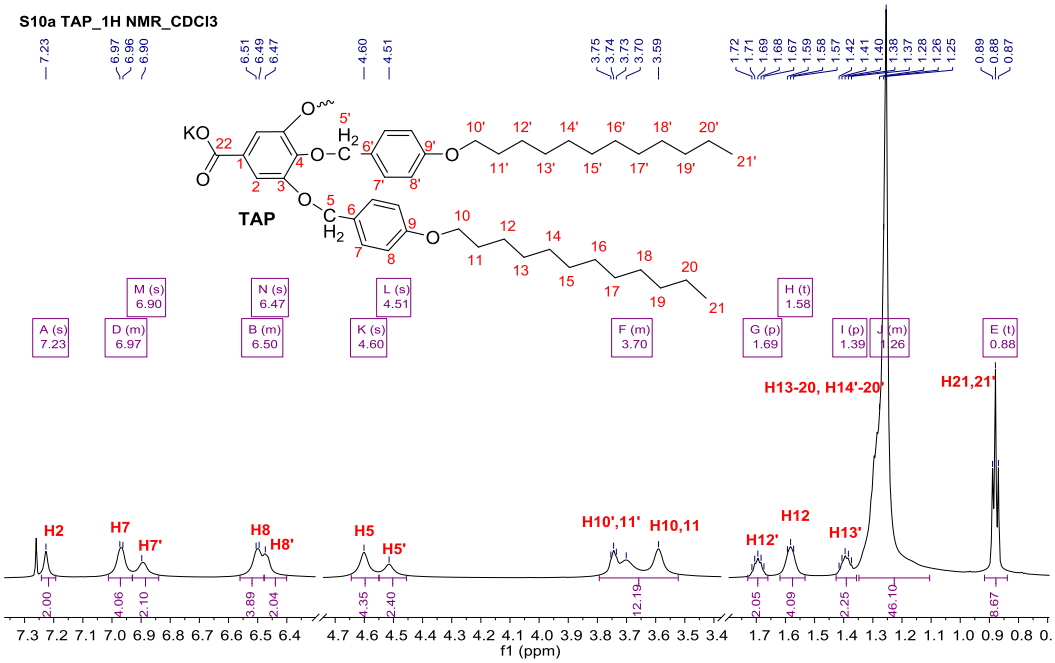

^{1}H NMR (700 MHz, Chloroform-*d*) δ 7.23 (s, 2H, H2), 7.01 – 6.93 (m, 4H, H7), 6.90 (s, 2H, H7'), 6.56 – 6.48 (m, 4H, H8), 6.47 (s, 2H,H8'), 4.60 (s, 4H, H5), 4.51 (s, 2H, H5'), 3.79 – 3.52 (m, 12H, H10', H11', H10, H11), 1.69 (p, *J* = 6.9 Hz, 2H, H12'), 1.58 (t, *J* = 7.4 Hz, 4H, H12), 1.39 (p, *J* = 7.2 Hz, 2H, H13'), 1.35 – 1.11 (m, 46H, H13-H20, H14'-H20'), 0.88 (t, *J* = 7.0 Hz, 9H, H21, H21').

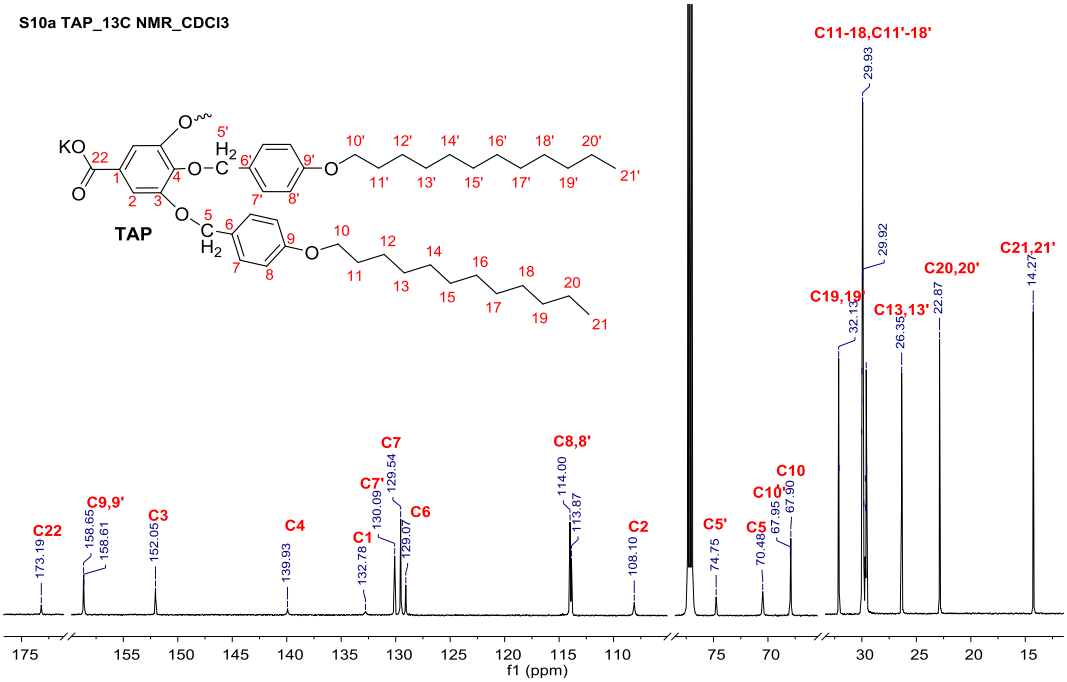

^{13}C NMR (176 MHz, Chloroform-*d*) δ 173.19 (C22), 158.65, 158.61 (C9,C9'), 152.05 (C3), 139.93 (C4), 132.78 (C1), 130.09 (C7'), 129.54 (C7), 129.07 (C6), 114.00, 113.87 (C8,C8'), 108.10 (C2), 74.75 (C5'), 70.48 (C5), 67.95 (C10'), 67.90 (C10), 32.13 (C19,C19'), 32.10, 30.02, 29.98, 29.93, 29.92, 29.87, 29.82, 29.68, 29.66, 29.60, 29.55 (C11-C18,C11'-C18'), 26.35 (C13,C13'), 22.87 (C20,C20'), 14.27 (C21,C21').

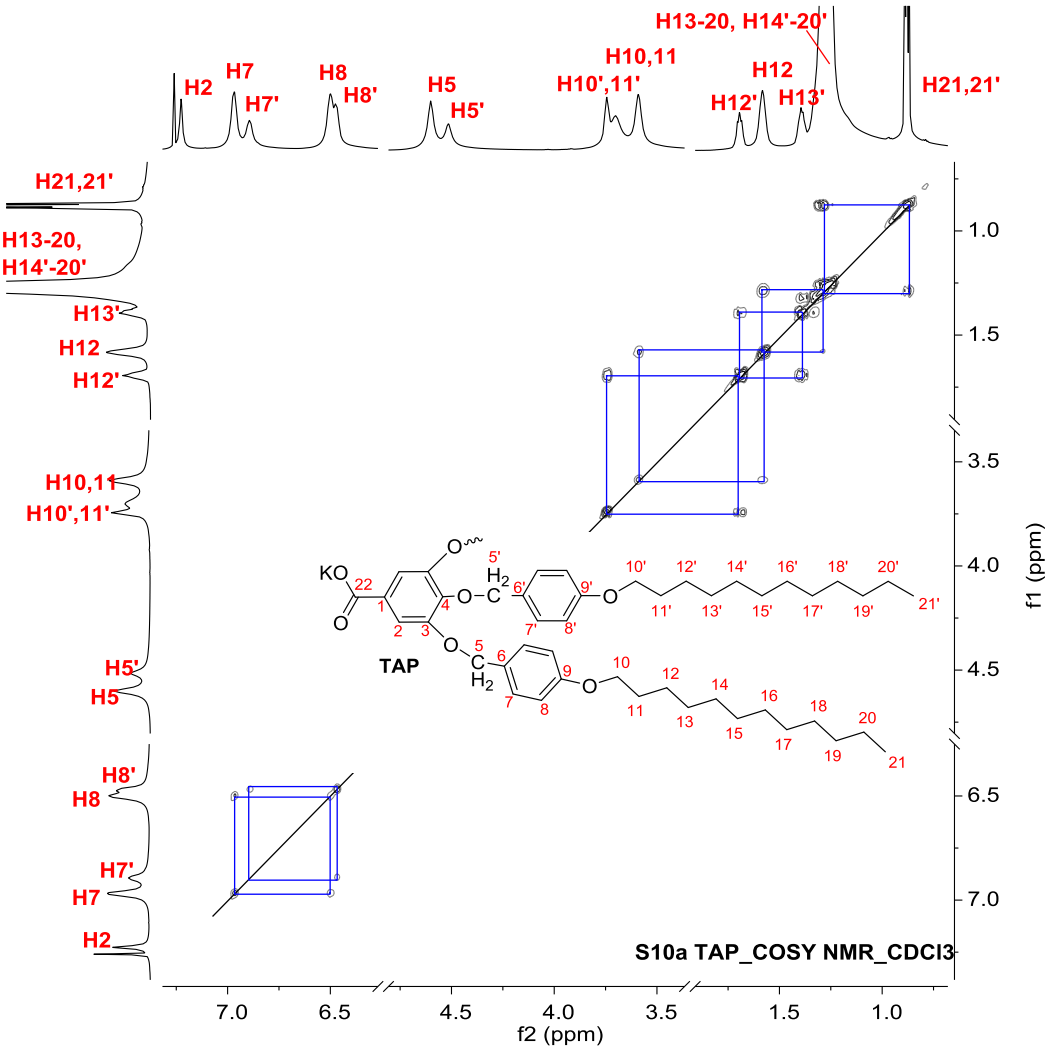
H13-20, H14'-20'
H2
H7
H7'
H8
H8'
H5
H5'
H10,11
H10',11'
H12
H12'
H13'
H21,21'
H13-20,
H14'-20'
H13'
H12
H12'
H10,11
H10',11'
H5'
H5
H8'
H8
H7'
H7
H2
TAP
S10a TAP_COSY NMR_CDCl3
f1 (ppm)
f2 (ppm)
1.0
1.5
3.5
4.0
4.5
6.5
7.0

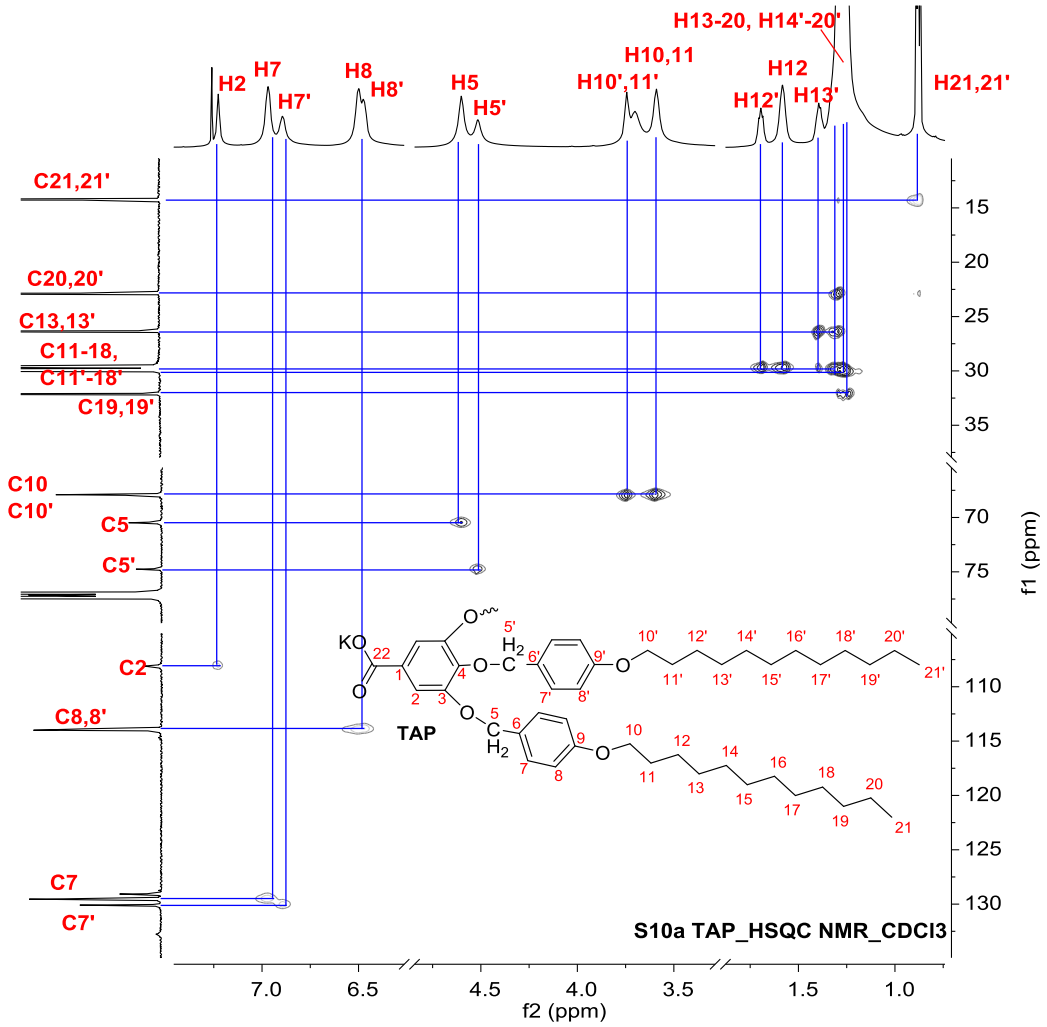
H13-20, H14'-20'
H2
H7
H7'
H8
H8'
H5
H5'
H10,11
H10',11'
H12
H12'
H13'
H21,21'
C21,21'
C20,20'
C13,13'
C11-18,
C11'-18'
C19,19'
C10
C10'
C5
C5'
C2
C8,8'
C7
C7'
TAP
S10a TAP_HSQC NMR_CDCl3
f2 (ppm)
f1 (ppm)

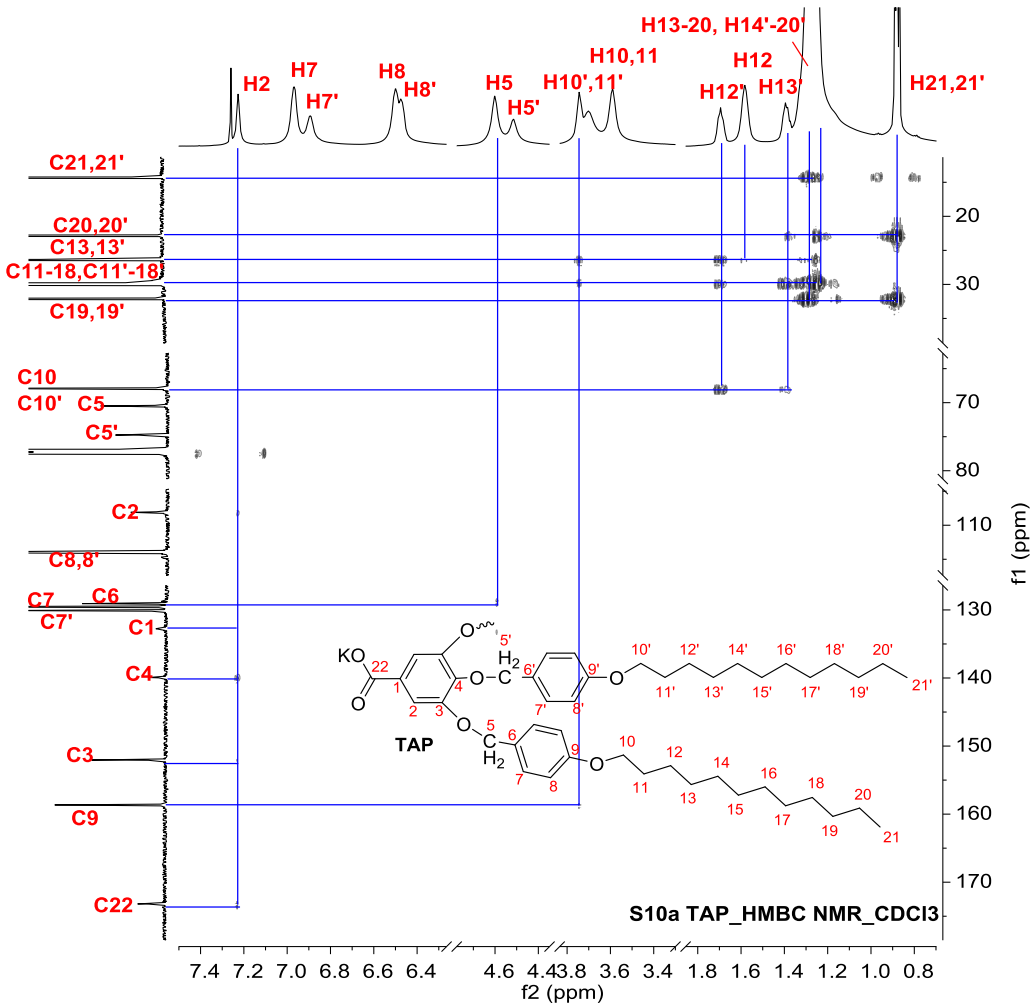

Figure 3: *^{1}H, ^{13}C, COSY, HSQC, HMBC NMR spectra (700 MHz, $CDCl_3$) of* **TAP**.

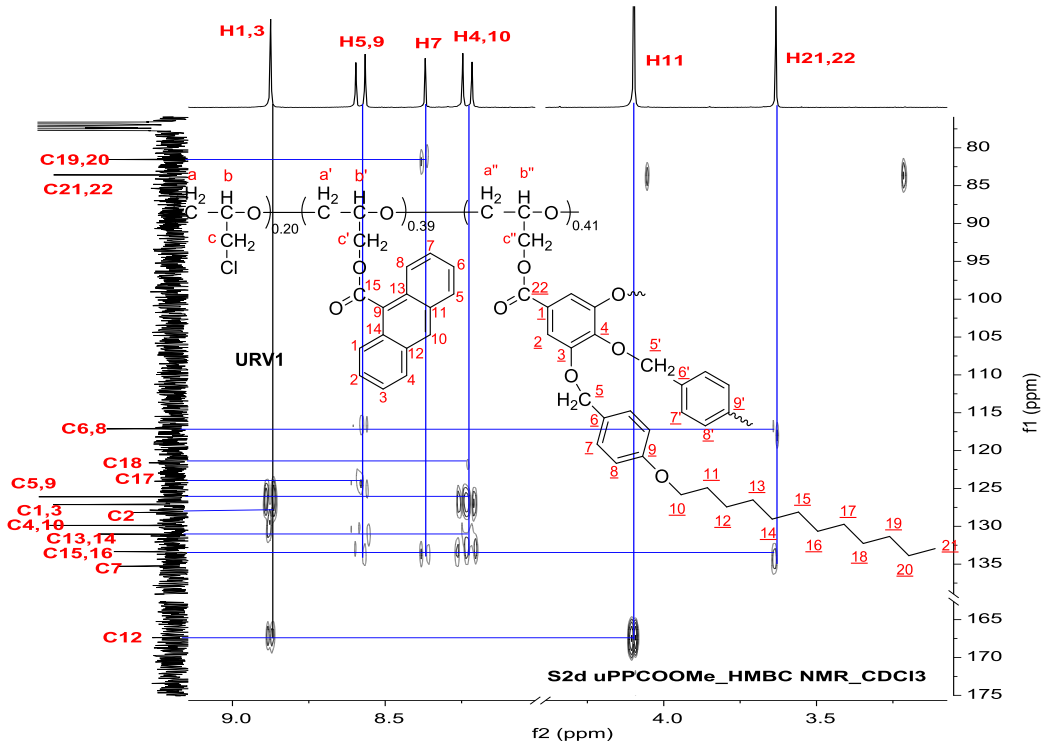
H1,3
H5,9
H7
H4,10
H11
H21,22
C19,20
C21,22
C6,8
C18
C17
C5,9
C1,3
C2
C4,10
C13,14
C15,16
C7
C12
URV1
S2d uPPCOOMe_HMBC NMR_CDCl3
f2 (ppm)
f1 (ppm)

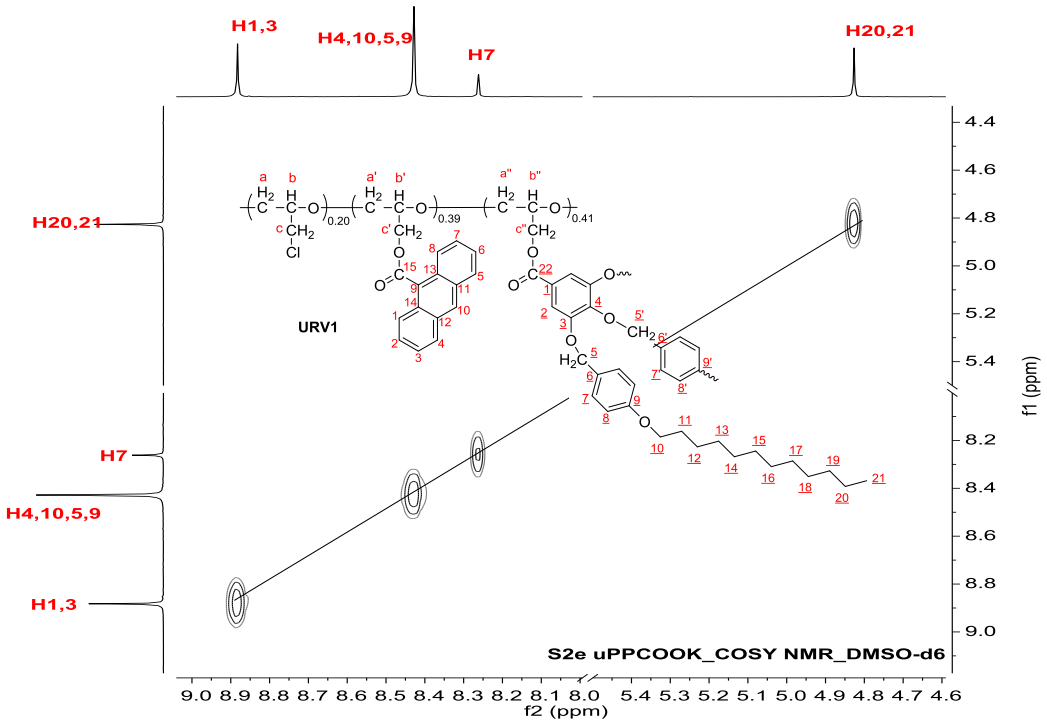
H1,3
H4,10,5,9
H7
H20,21
H20,21
H7
H4,10,5,9
H1,3
URV1
S2e uPPCOOK_COSY NMR_DMSO-d6
f2 (ppm)
f1 (ppm)

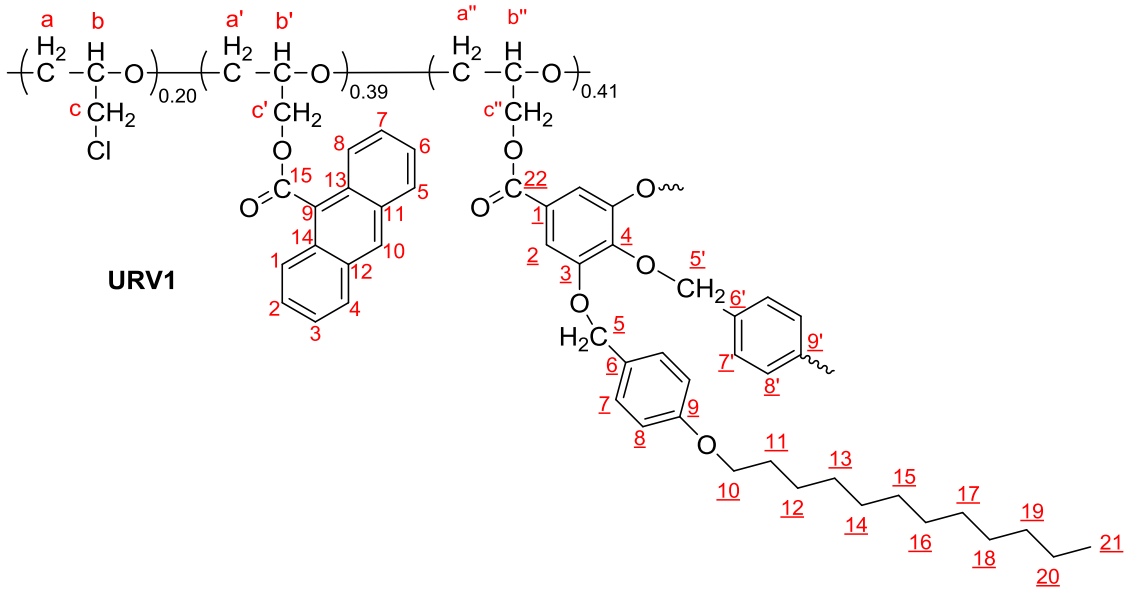

URV1

^{1}H NMR	URV1	^{13}C NMR	
Signal (ppm)	**Assignment**	**Signal (ppm)**	**Assignment**
8.45-8.19	H10	168.92	C15
8.09-7.90	H1,8	165.61	C22
7.90-7.70	H4,5	158.72	C9,9’
7.48-7.06	H2,7, H3,6, H2, H7,7’	152.37	C3
6.91-6.60	H8,8’	142.16	C4
5.00-4.62	H5,5’	130.55	C13,14
4.62-4.02	c’,c’’, H10’, H11’	129.98	C7’
3.97-3.76	H10, H11	129.25-129.19	C10, C7
3.76-3.19	a,a’,a’’,b,b’,b’’,c	128.41	C11,12
1.83-1.64	H12,12’	128.09	C4,5
1.46-1.36	H13’	127.36	C9
1.36-1.16	H13-20, H14’-20’	126.96	C2,7
0.93-0.84	H21,21’	125.44-125.40	C3,6
		124.78	C1,8
		114.16-113.91	C8,8’
		108.41	C2
		78.43	b
		77.20	b’,b’’
		74.62	C5’
		70.58	C5
		68.88	a,a’,a’’
		67.83	C10,10’
		63.91	c’
		43.54	c
		31.84	C19,19’
		29.59-29.19	C11-18, C11’-18’
		25.97	C13,13’
		22.65	C20,20’
		14.16	C21,21’

Table 2: *^{1}H and ^{13}C NMR data of* **URV1** *and their corresponding assignments.*

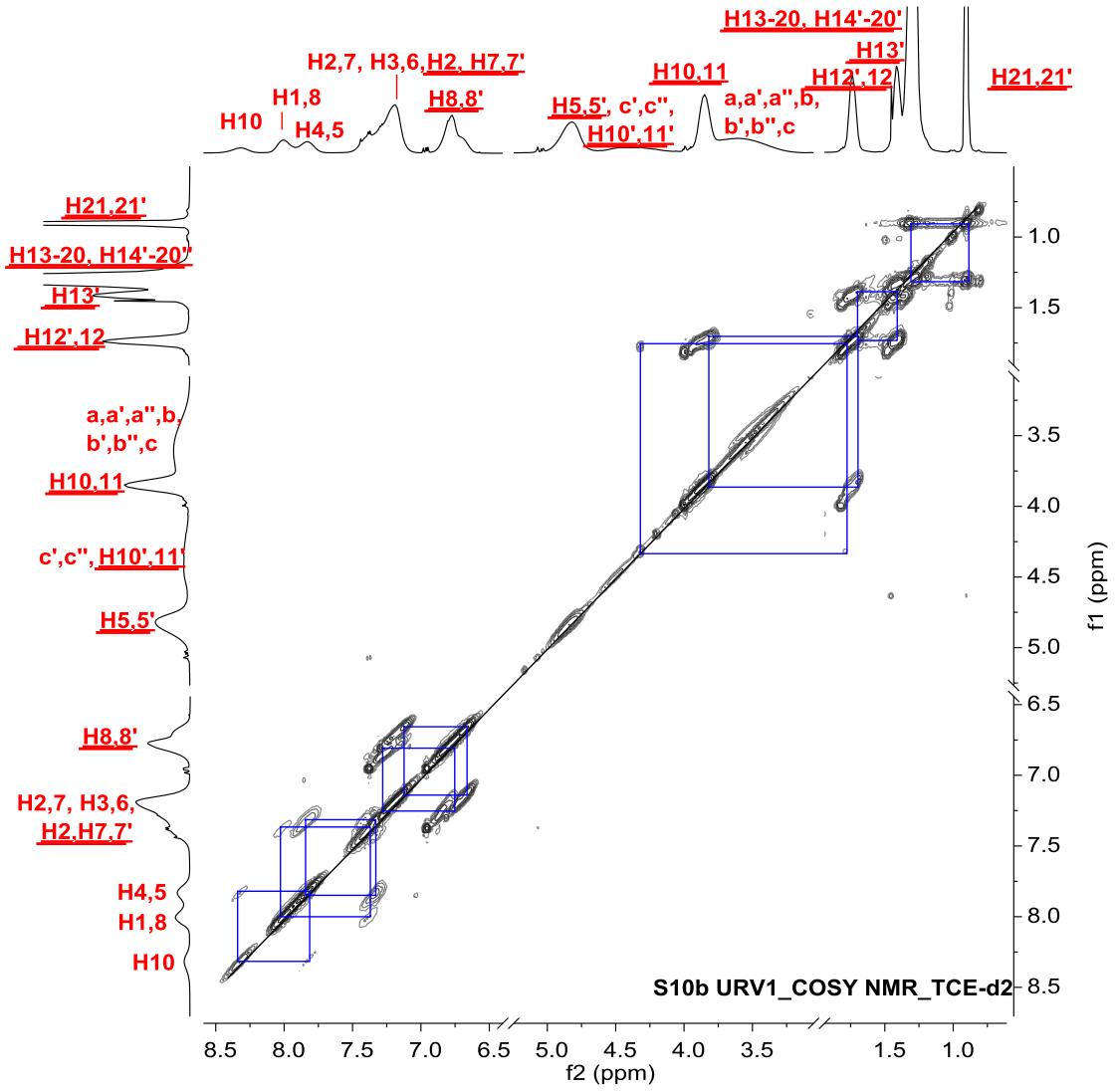
H13-20, H14'-20'
H13'
H12',12
H21,21'
H2,7, H3,6,H2, H7,7'
H10,11
H1,8
H8,8'
H10
H4,5
H5,5', c',c'',
H10',11'
a,a',a'',b,
b',b'',c
H21,21'
H13-20, H14'-20''
H13'
H12',12
a,a',a'',b,
b',b'',c
H10,11
c',c'', H10',11'
H5,5'
H8,8'
H2,7, H3,6,
H2,H7,7'
H4,5
H1,8
H10
S10b URV1_COSY NMR_TCE-d2
f2 (ppm)
f1 (ppm)

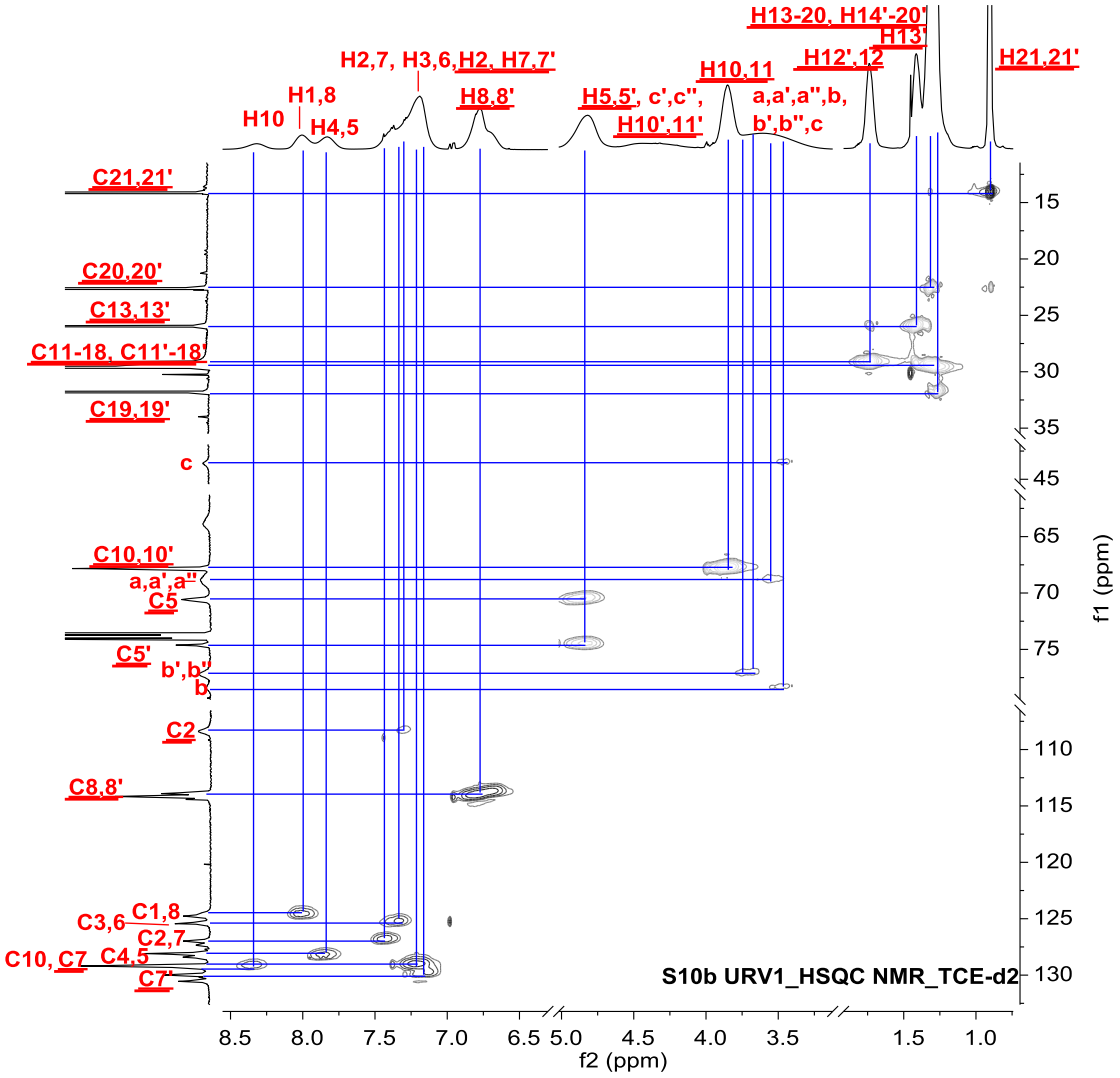
H13-20, H14'-20'
H13'
H12',12
H21,21'
H2,7, H3,6,H2, H7,7'
H10,11
H1,8
H10
H4,5
H8,8'
H5,5', c',c'',
H10',11'
a,a',a'',b,
b',b'',c
C21,21'
C20,20'
C13,13'
C11-18, C11'-18'
C19,19'
c
C10,10'
a,a',a''
C5
C5'
b',b''
b
C2
C8,8'
C3,6
C1,8
C2,7
C10, C7
C4,5
C7'
S10b URV1_HSQC NMR_TCE-d2
f2 (ppm)
f1 (ppm)

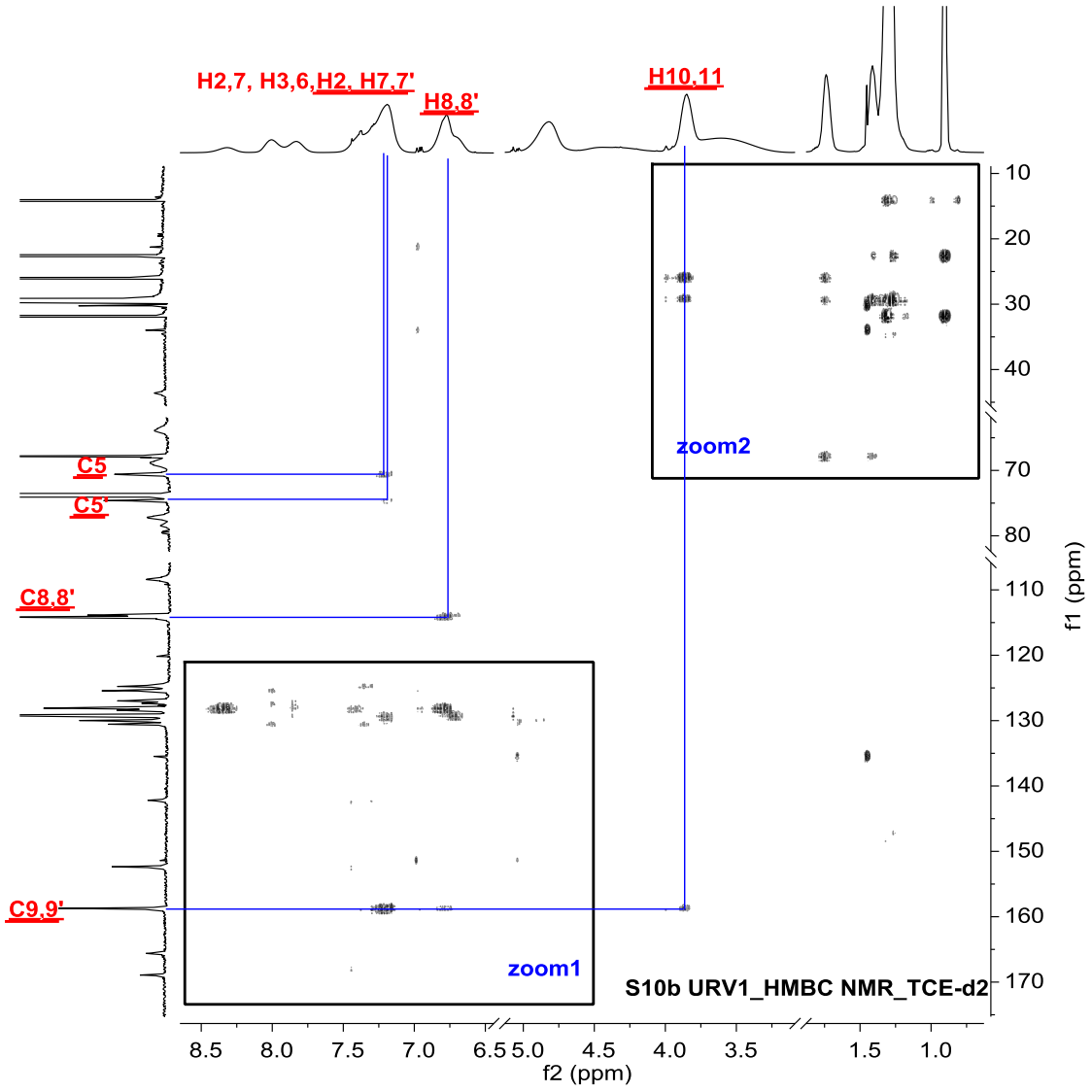
H2,7, H3,6,H2, H7,7'
H8,8'
H10,11
C5
C5'
C8,8'
C9,9'
zoom1
zoom2
S10b URV1_HMBC NMR_TCE-d2
f2 (ppm)
f1 (ppm)

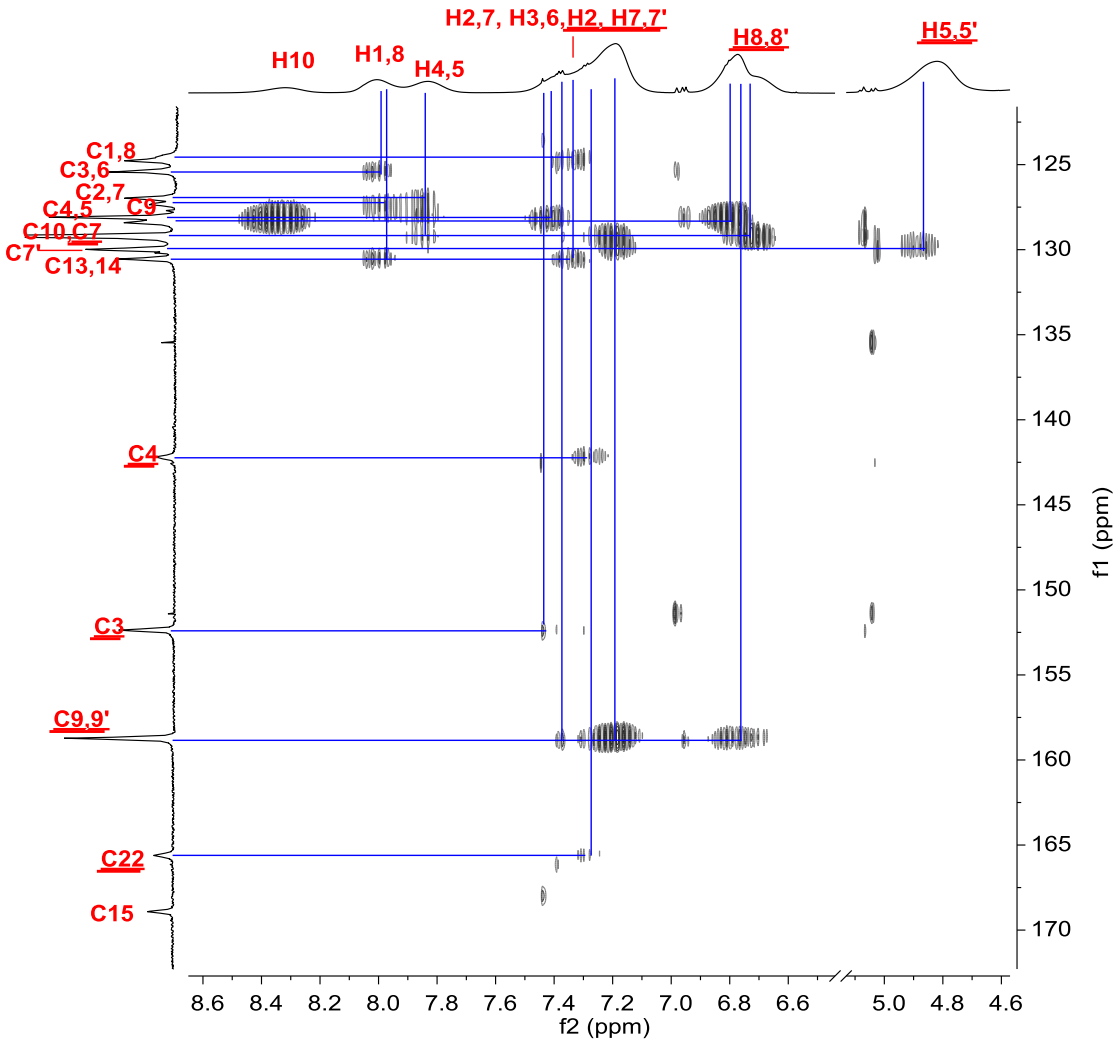
H10
H1,8
H4,5
H2,7, H3,6,H2, H7,7'
H8,8'
H5,5'
C1,8
C3,6
C2,7
C4,5
C9
C10,C7
C7'
C13,14
C4
C3
C9,9'
C22
C15
8.6
8.4
8.2
8.0
7.8
7.6
7.4
7.2
7.0
6.8
6.6
5.0
4.8
4.6
f2 (ppm)
125
130
135
140
145
150
155
160
165
170
f1 (ppm)

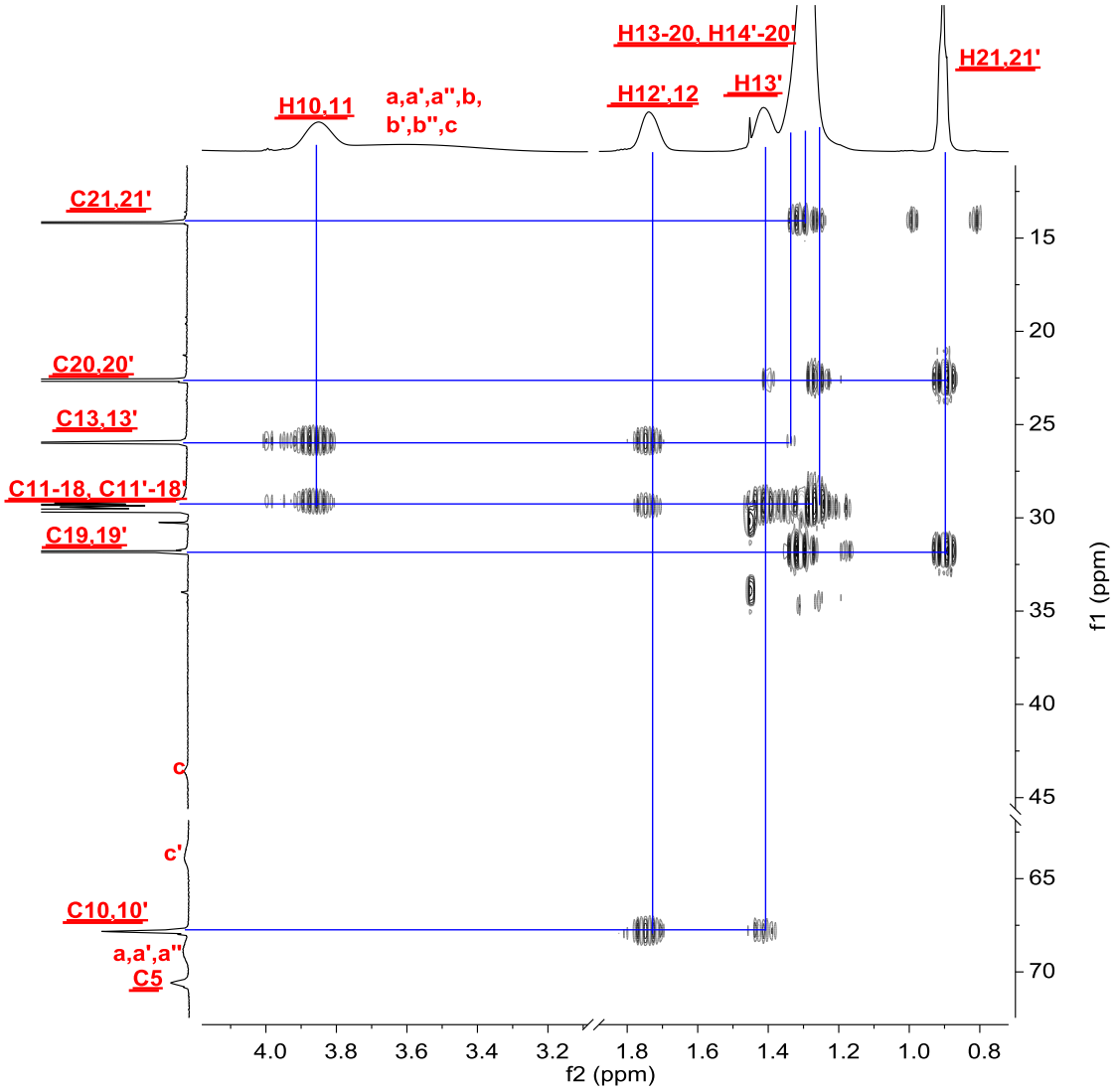

Figure 4: *^{1}H, ^{13}C, COSY, HSQC, HMBC NMR spectra (700 MHz, TCE-d_2) of* **URV1**.

S5a di-9ACAK_1H NMR_D2O

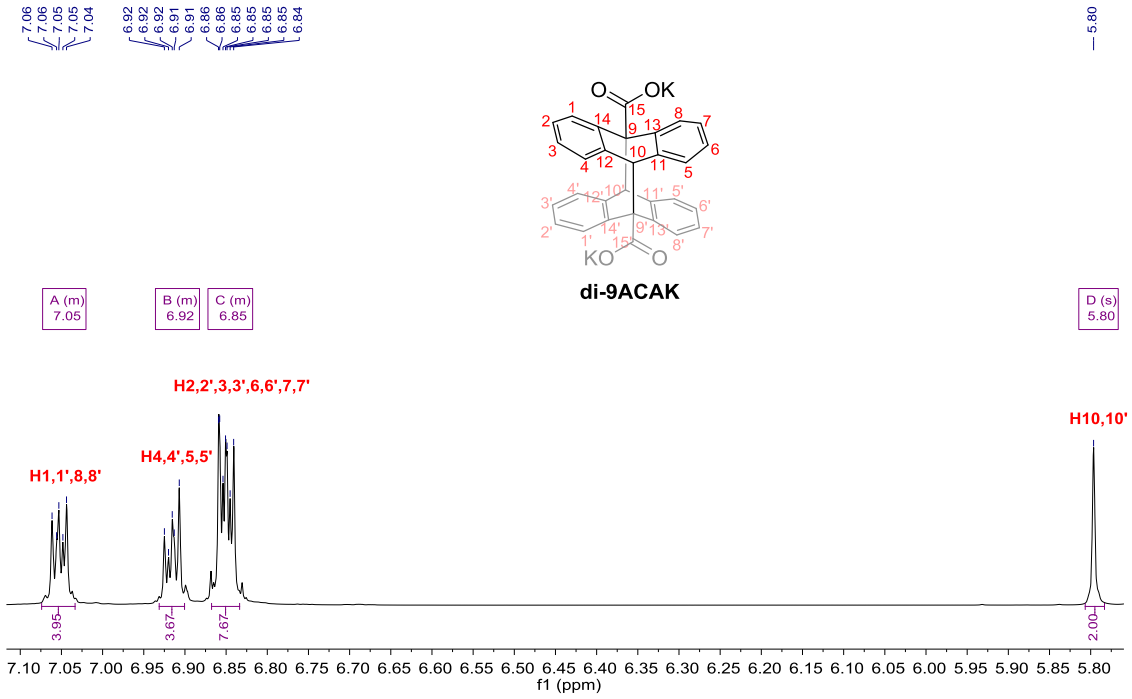

^{1}H NMR (500 MHz, Deuterium Oxide) δ 7.07 – 7.03 (m, 4H, H1, H1', H8, H8'), 6.93 – 6.90 (m, 4H, H4, H4', H5, H5'), 6.87 – 6.83 (m, 8H, H2, H2', H3, H3', H6, H6', H7, H7'), 5.80 (s, 2H, H10, H10').

S1d PCOOK_13C NMR_DMSO-d6

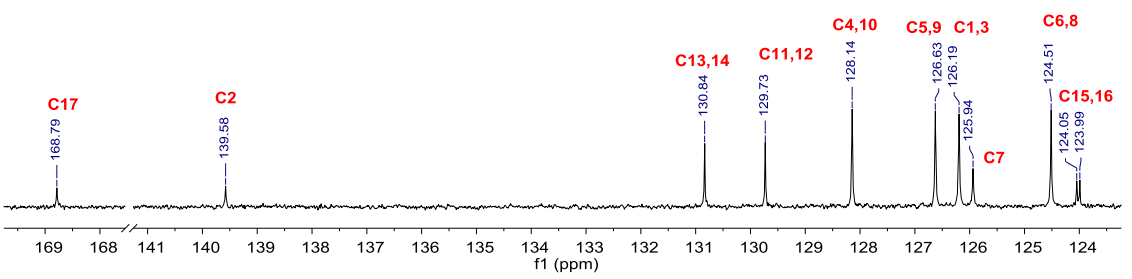

^{13}C NMR (101 MHz, DMSO- d_6) δ 168.79 (C17), 139.58 (C2), 130.84 (C13,C14), 129.73 (C11,C12), 128.14 (C4,C10), 126.63 (C5,C9), 126.19 (C1,C3), 125.94 (C7), 124.51 (C6,C8), 124.05, 123.99 (C15,C16).

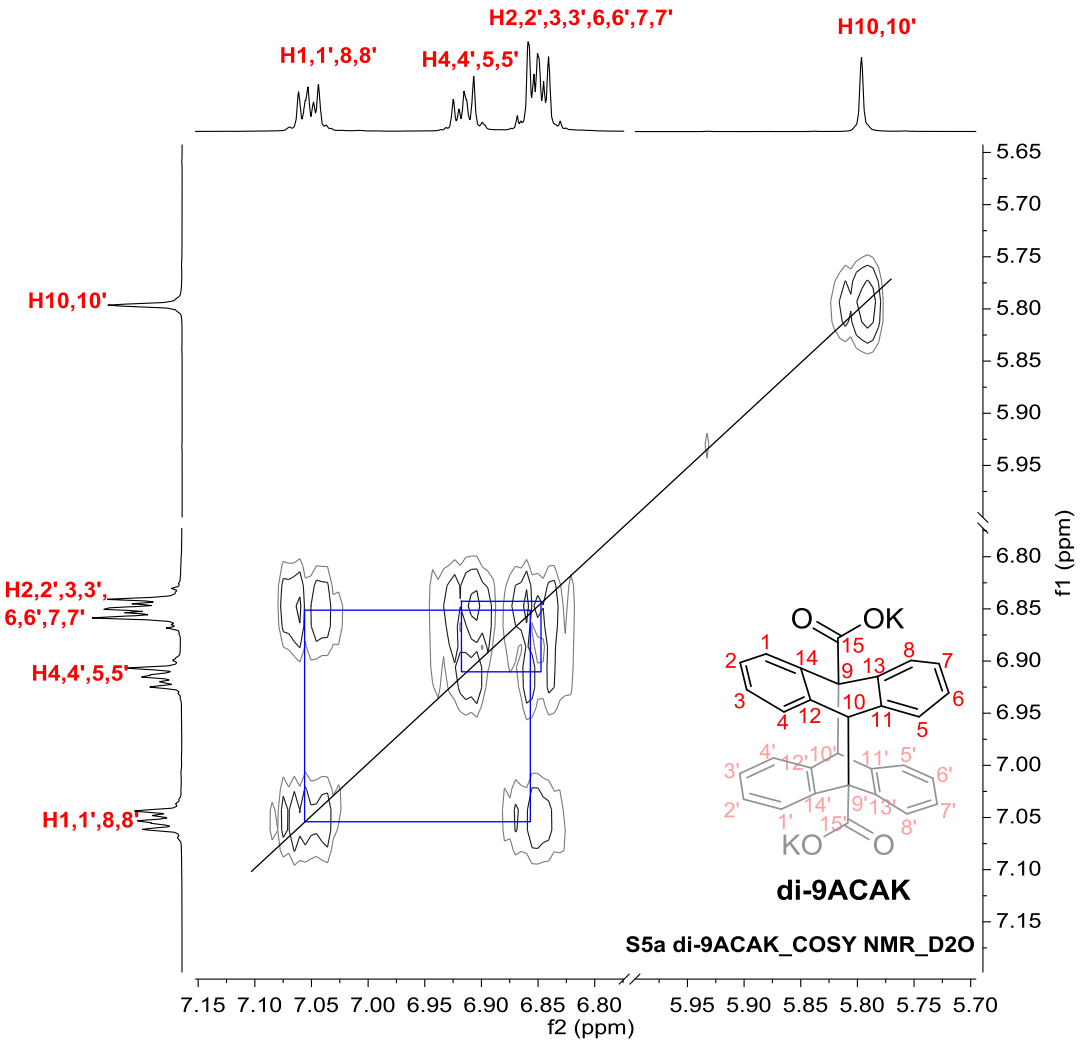
H2,2',3,3',6,6',7,7'
H10,10'
H1,1',8,8'
H4,4',5,5'
H10,10'
H2,2',3,3',
6,6',7,7'
H4,4',5,5'
H1,1',8,8
O
OK
KO
O
di-9ACAK
S5a di-9ACAK_COSY NMR_D2O
f1 (ppm)
f2 (ppm)
5.65
5.70
5.75
5.80
5.85
5.90
5.95
6.80
6.85
6.90
6.95
7.00
7.05
7.10
7.15
7.15 7.10 7.05 7.00 6.95 6.90 6.85 6.80
5.95 5.90 5.85 5.80 5.75 5.70

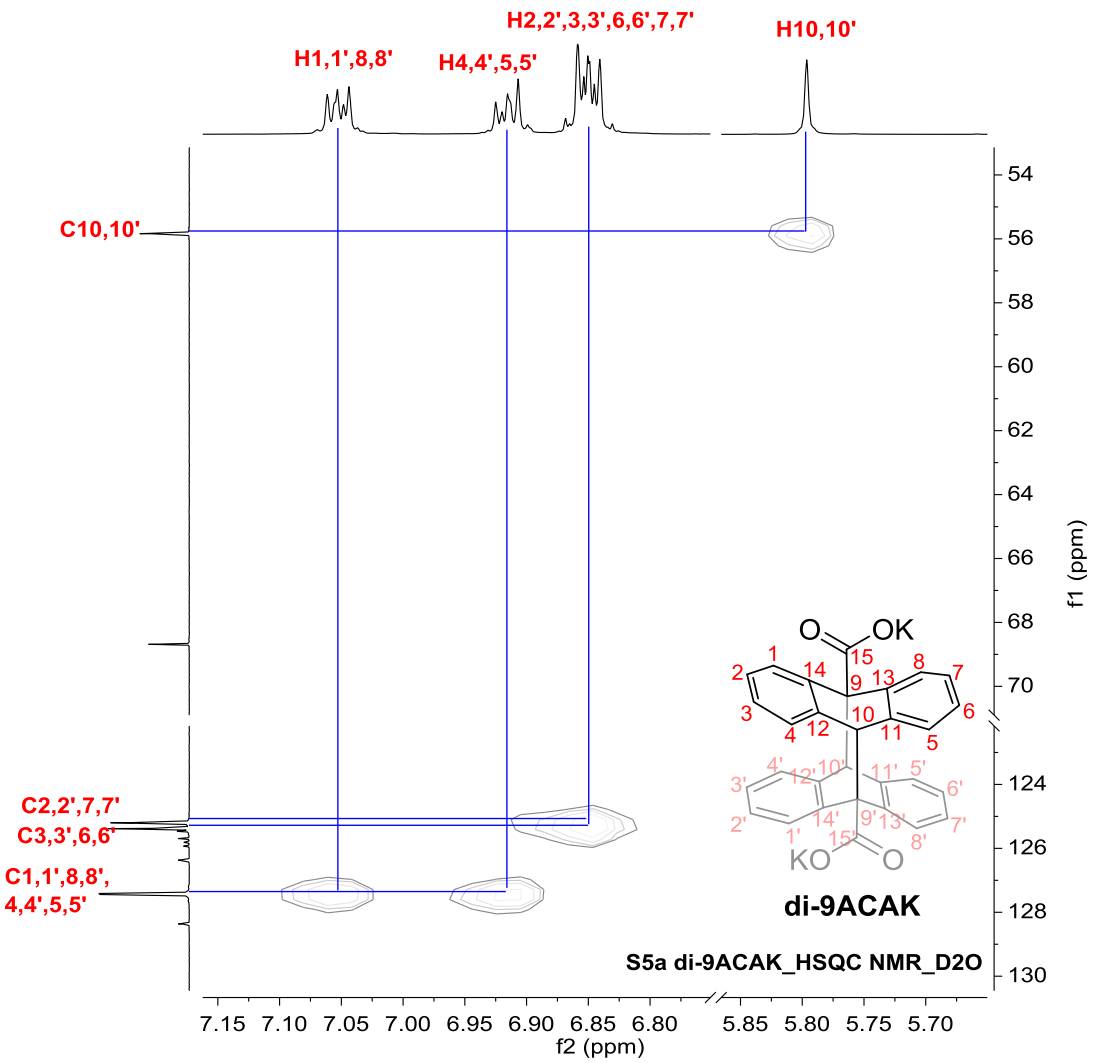
H1,1',8,8'
H4,4',5,5'
H2,2',3,3',6,6',7,7'
H10,10'
C10,10'
C2,2',7,7'
C3,3',6,6'
C1,1',8,8',
4,4',5,5'
f1 (ppm)
f2 (ppm)
di-9ACAK
S5a di-9ACAK_HSQC NMR_D2O

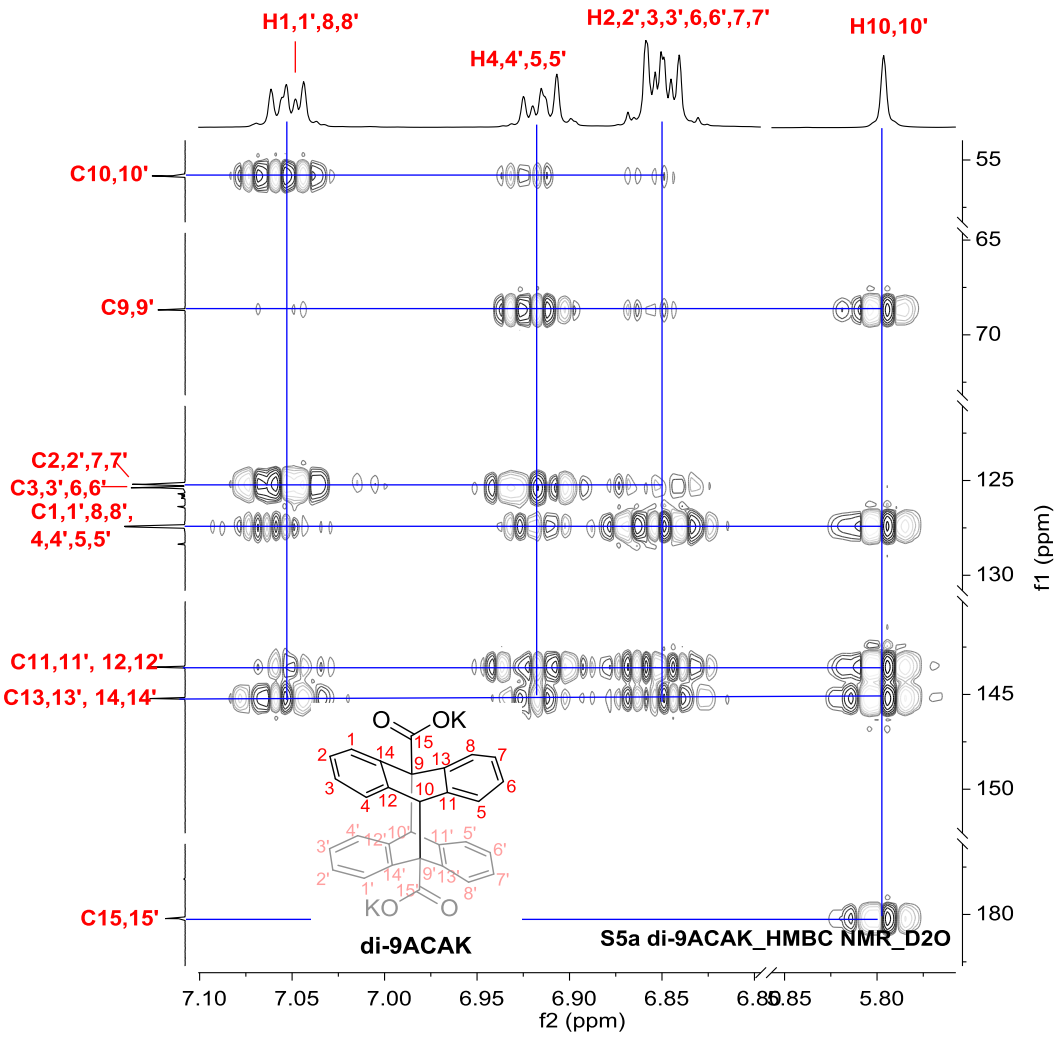

Figure 5: *^{1}H, ^{13}C, COSY, HSQC, HMBC NMR spectra (500 MHz, D_2O) of di-***9ACAK**.

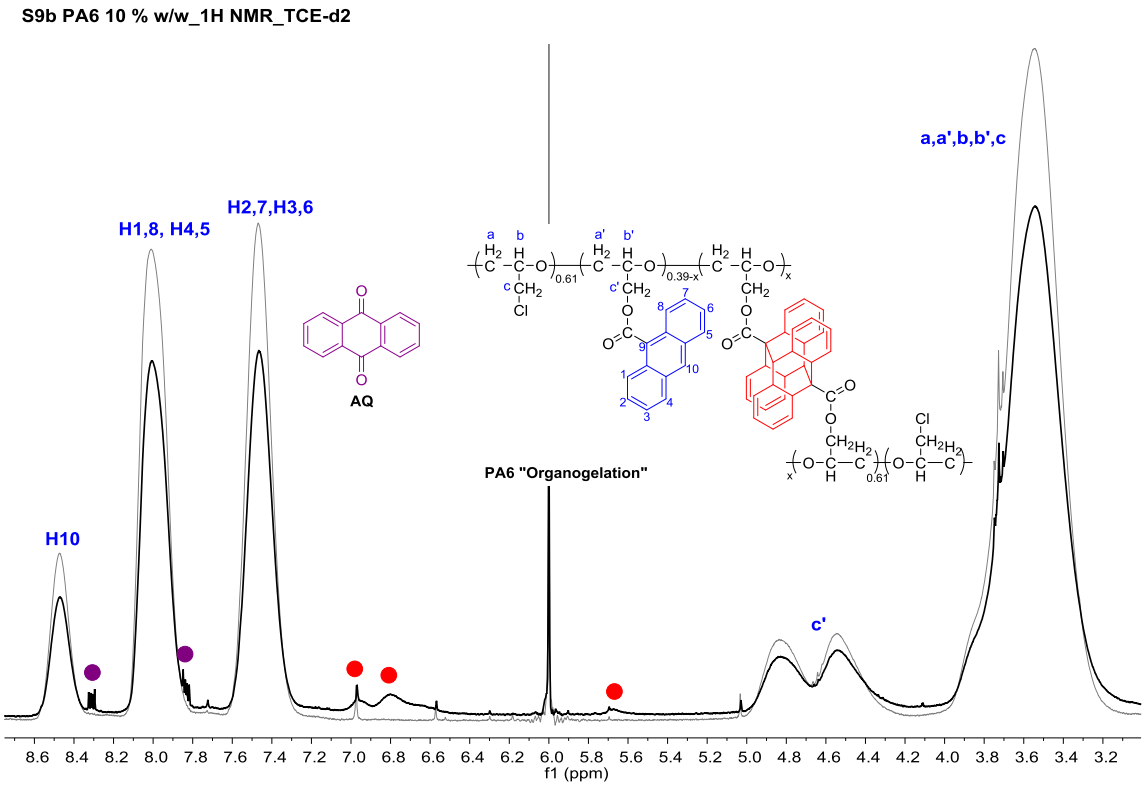

Figure 6: *^{1}H NMR spectra (300 MHz, TCE-d_2) of* **PA6** *(before and* ***after****).*

Solvents	PA6 solubility (√ – soluble, X – insoluble, N – nonsolvent)
Acetone	X
Chloroform	√
Dibutyl ether	X
Diethyl ether	X
Diisopropyl ether	X
Dimethyl sulfoxide	X
1,4-dioxane	√
Ethanol	N
Ethyl acetate	X
Methanol	N
1,1,2,2-tetrachloroethane	√
Tetrahydrofuran	√
Toluene	X
Water	N

Table 3: **PA6** *solubility testing in various solvents.*

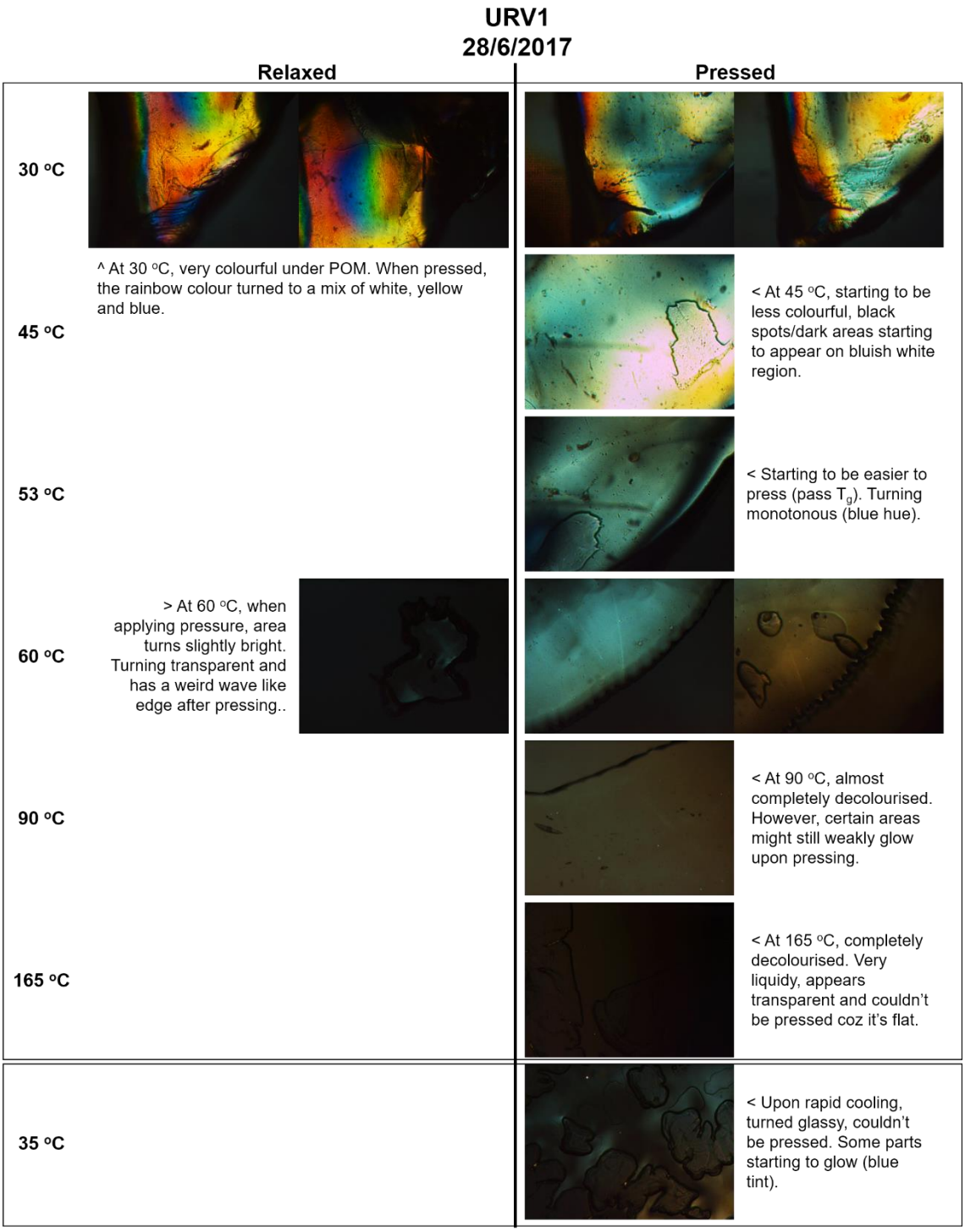

Figure 7: *POM observations of* **URV1***.*

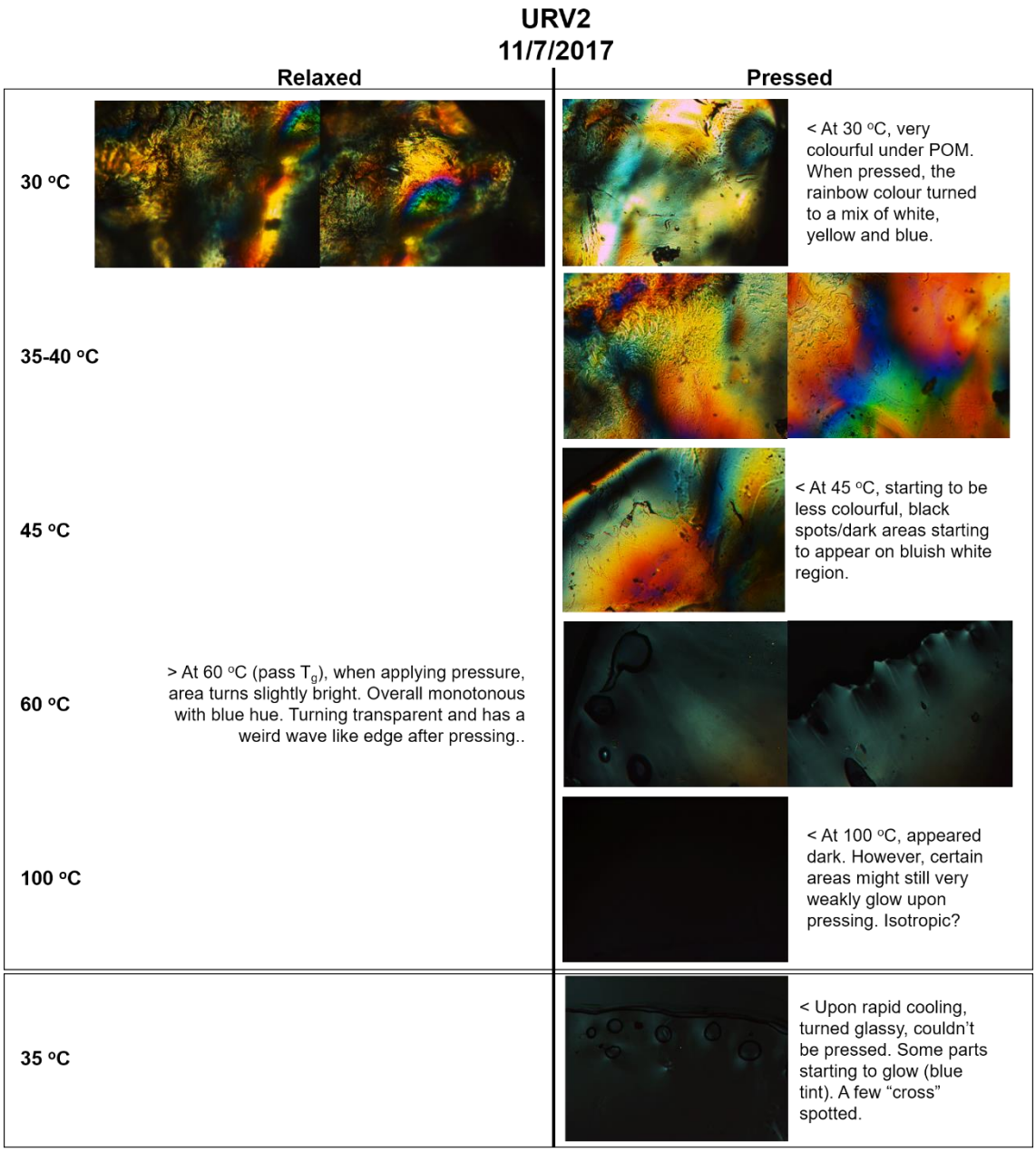

Figure 8: *POM observations of* **URV2***.*

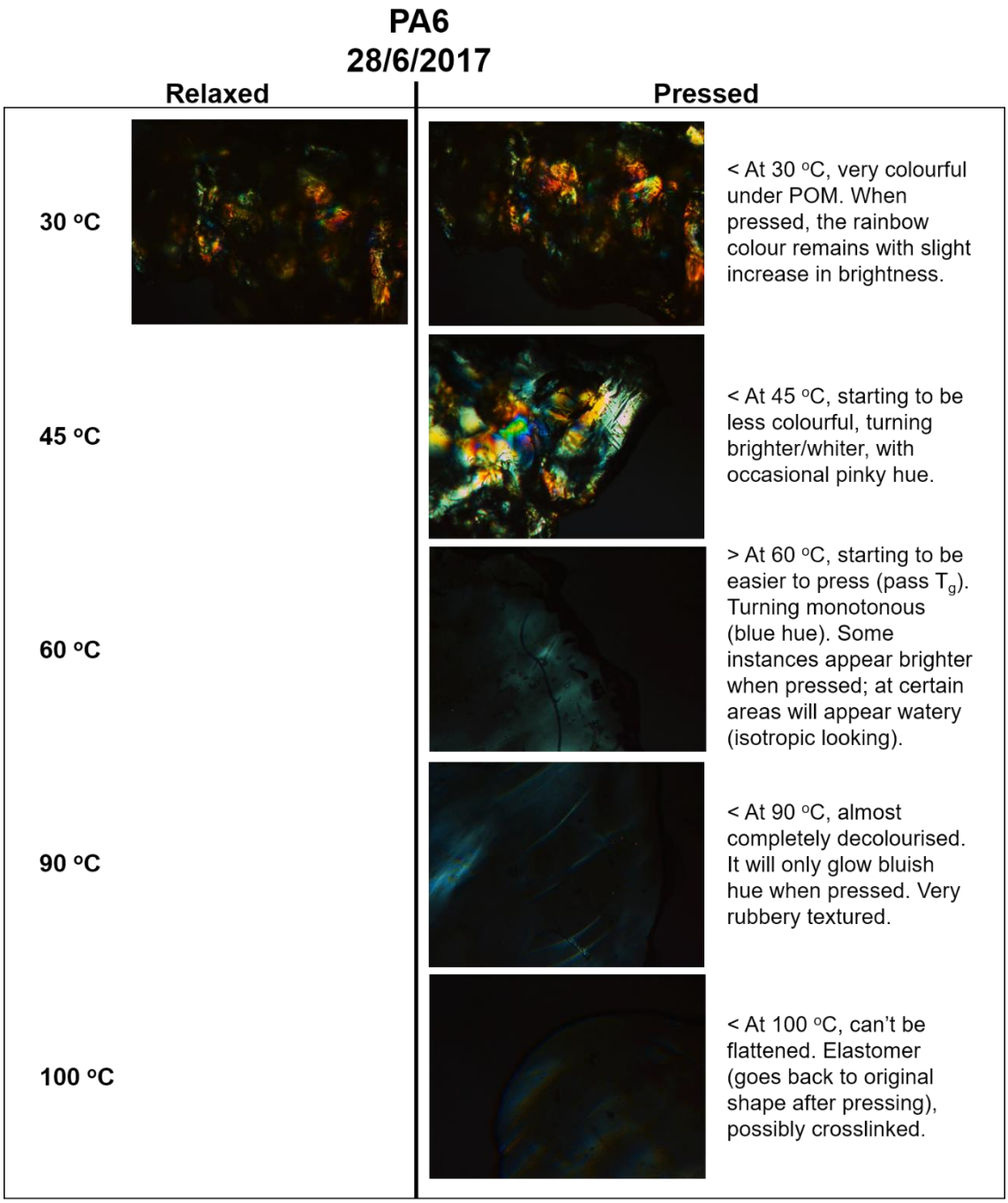

Figure 9: *POM observations of* **PA6***.*

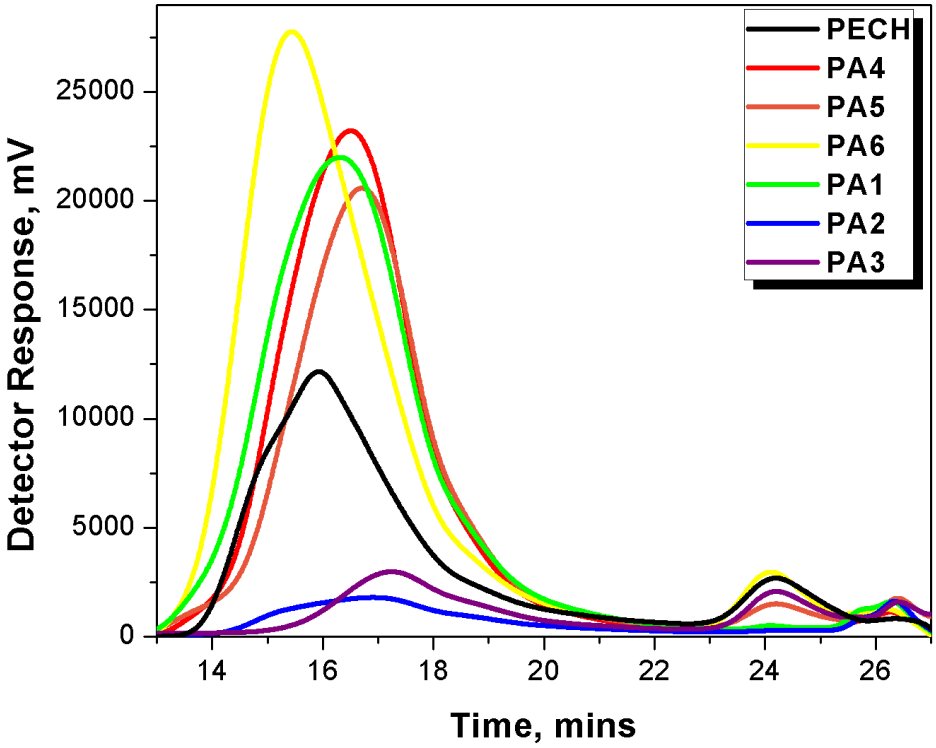

Figure 10: *GPC molecular weight distribution curves of* **PA Series**.

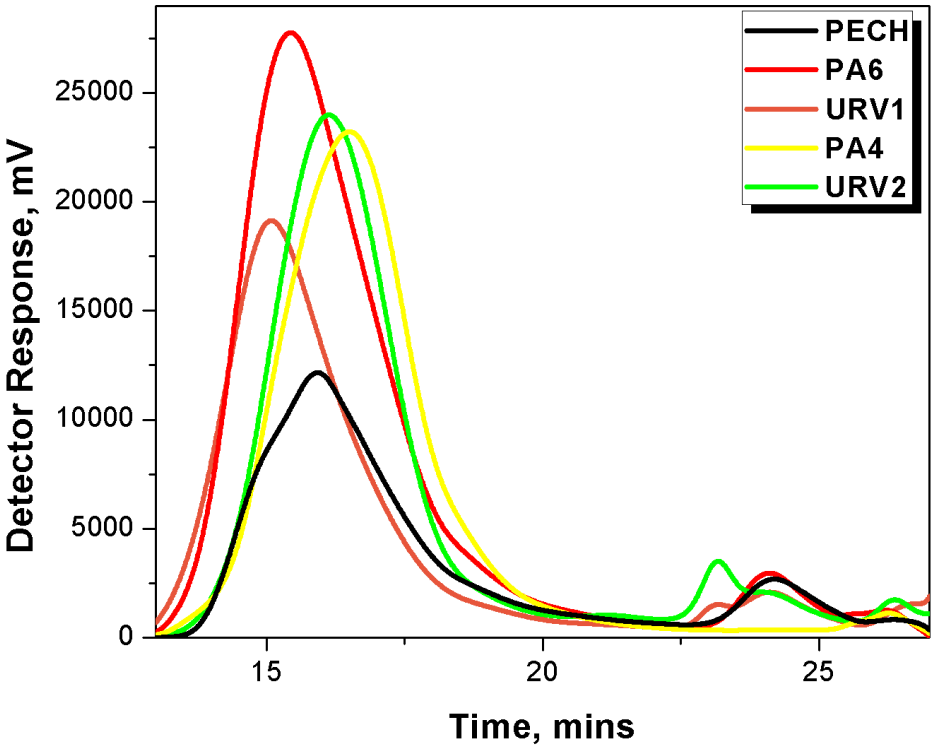

Figure 11: *GPC molecular weight distribution curves of* **URV Series**.

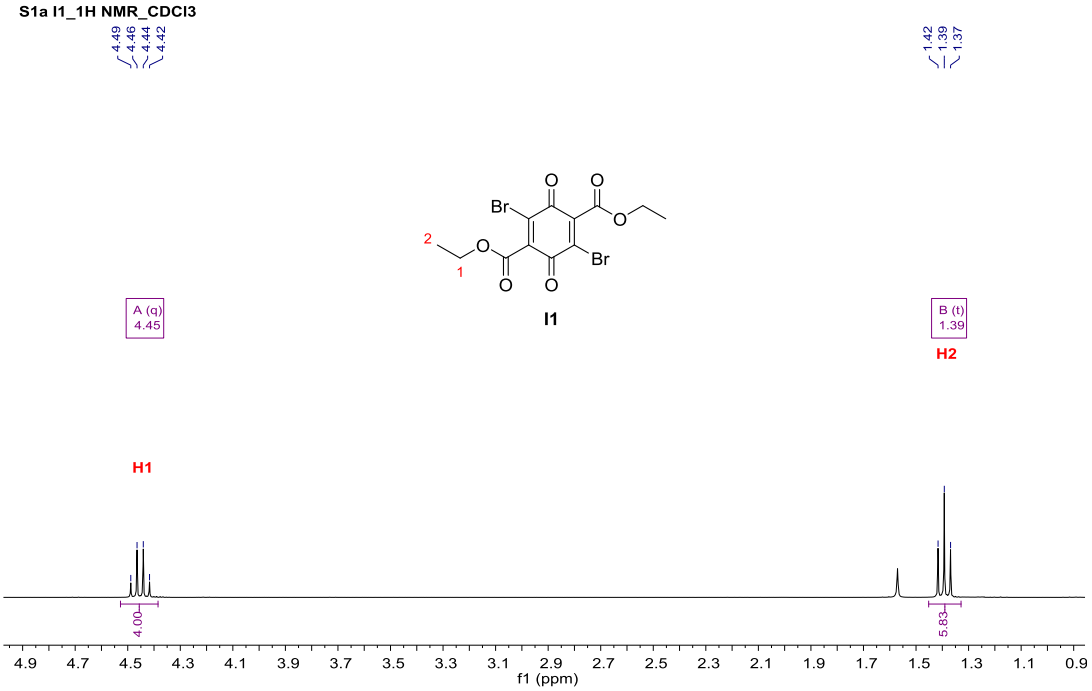

^{1}H NMR (300 MHz, Chloroform - *d*) δ 4.45 (q, *J* = 7.1 Hz, 4H, H1), 1.39 (t, *J* = 7.1 Hz, 6H, H2).

Figure 1: *^{1}H NMR spectrum (300 MHz, $CDCl_3$) of* **I1**.

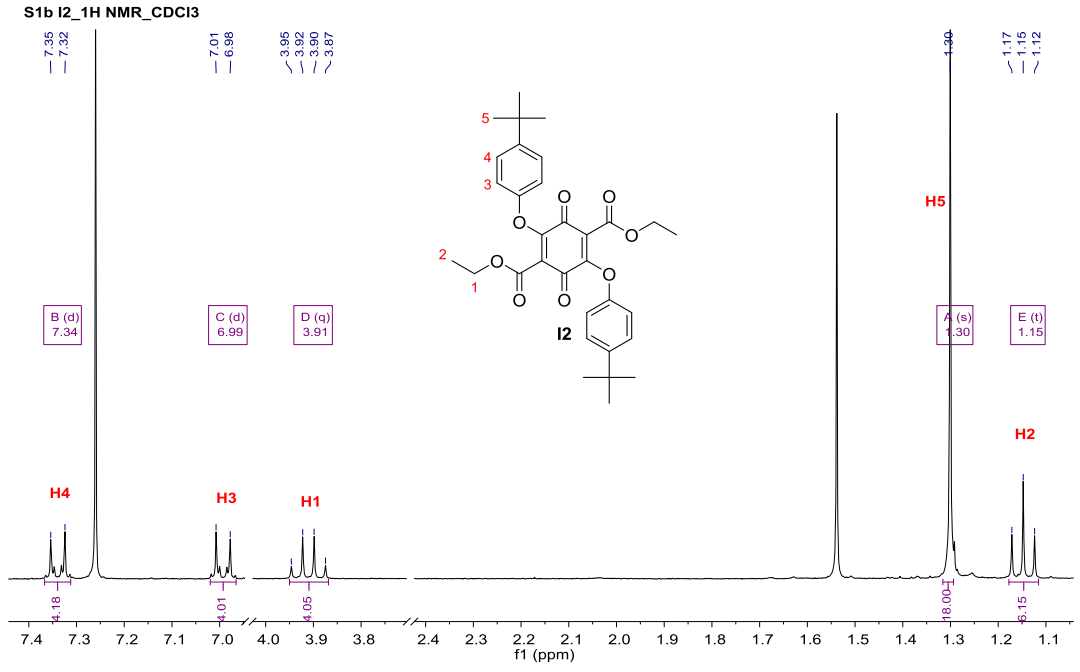

^{1}H NMR (300 MHz, Chloroform -*d*) δ 7.34 (d, *J* = 8.9 Hz, 4H, H4), 6.99 (d, *J* = 8.9 Hz, 4H, H3), 3.91 (q, *J* = 7.2 Hz, 4H, H1), 1.30 (s, 18H, H5), 1.15 (t, *J* = 7.2 Hz, 6H, H2).

Figure 2: *^{1}H NMR spectrum (300 MHz, $CDCl_3$) of* **I2**.

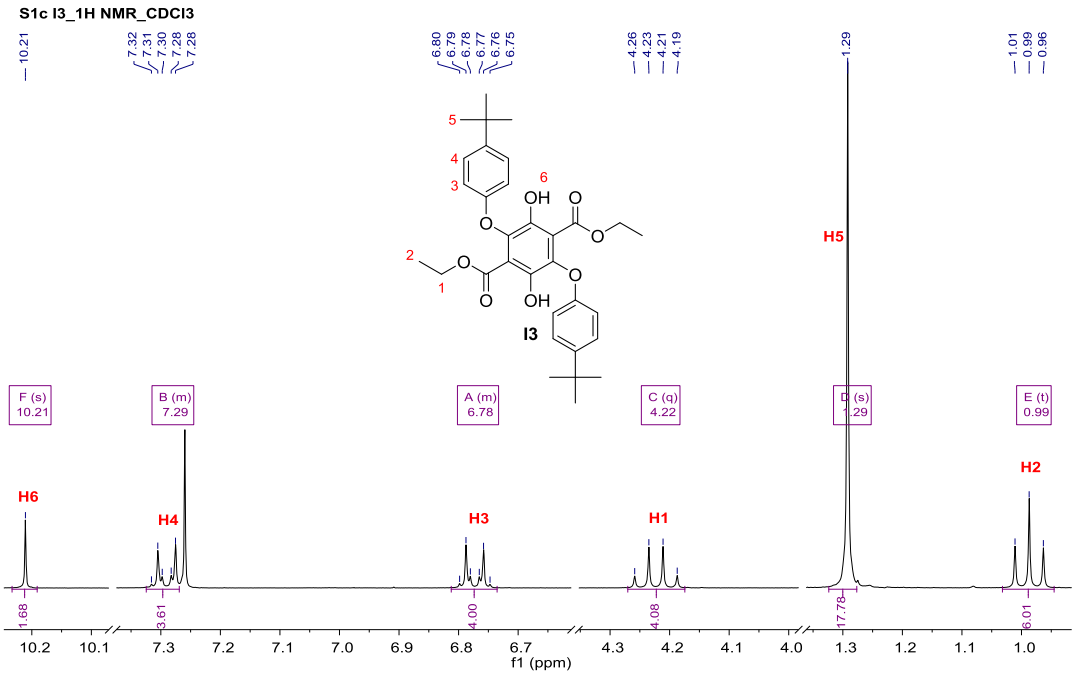

^{1}H NMR (300 MHz, Chloroform - *d*) δ 10.21 (s, 2H, H6), 7.32 – 7.27 (m, 4H, H4), 6.81 – 6.74 (m, 4H, H3), 4.22 (q, *J* = 7.1 Hz, 4H, H1), 1.29 (s, 18H, H5), 0.99 (t, *J* = 7.1 Hz, 6H, H2).

Figure 3: *^{1}H NMR spectrum (300 MHz, $CDCl_3$) of* **I3**.

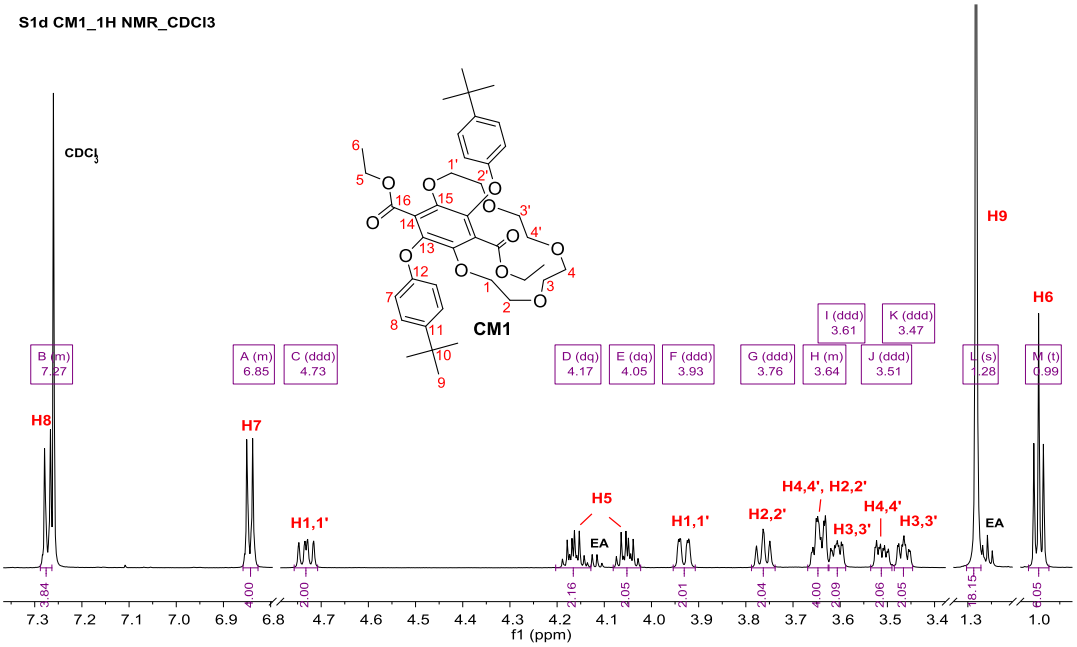

^{1}H NMR (700 MHz, Chloroform - *d*) δ 7.29 – 7.26 (m, 4H, H8), 6.86 – 6.83 (m, 4H, H7), 4.73 (ddd, *J* = 13.0, 9.0, 1.3 Hz, 2H, H1, H1'), 4.17 (dq, *J* = 10.9, 7.1 Hz, 2H, H5), 4.05 (dq, *J* = 10.9, 7.1 Hz, 2H, H5), 3.93 (ddd, *J* = 13.1, 3.5, 1.5 Hz, 2H, H1, H1'), 3.76 (ddd, *J* = 10.7, 9.1, 1.5 Hz, 2H, H2, H2'), 3.67 – 3.63 (m, 4H, H4, H4', H2, H2'), 3.61 (ddd, *J* = 10.0, 5.7, 2.2 Hz, 2H, H3, H3'), 3.51 (ddd, *J* = 11.8, 5.8, 2.2 Hz, 2H, H4, H4'), 3.47 (ddd, *J* = 9.3, 6.7, 2.2 Hz, 2H, H3, H3'), 1.28 (s, 18H, H9), 0.99 (t,*J* = 7.1 Hz, 6H, H6).

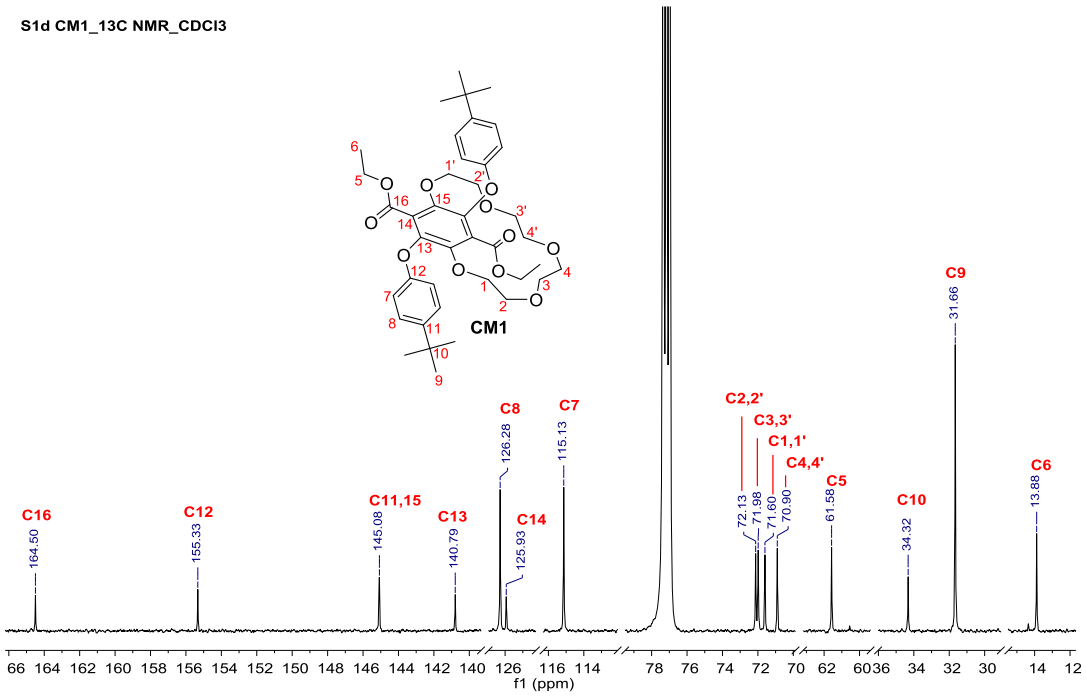

^{13}C NMR (176 MHz, $CDCl_3$) δ 164.50 (C16), 155.33 (C12), 145.08 (C11,C15), 140.79 (C13), 126.28 (C8), 125.93 (C14), 115.13 (C7), 72.13 (C2,C2'), 71.98 (C3,C3'), 71.60 (C1,C1'), 70.90 (C4,C4'), 61.58 (C5), 34.32 (C10), 31.66 (C9), 13.88 (C6).

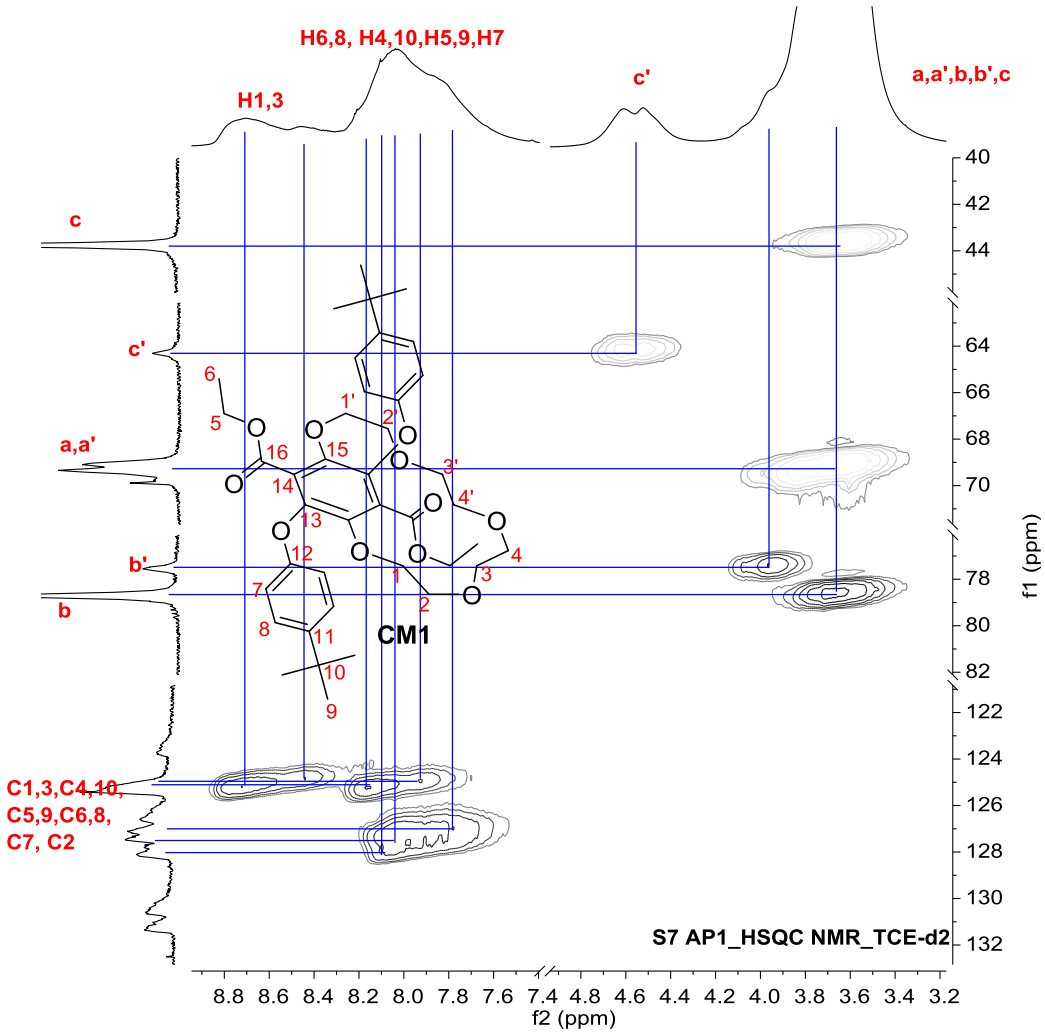
H6,8, H4,10,H5,9,H7
H1,3
c'
a,a',b,b',c
c
c'
a,a'
b'
b
C1,3,C4,10,
C5,9,C6,8,
C7, C2
CM1
S7 AP1_HSQC NMR_TCE-d2
f2 (ppm)
f1 (ppm)

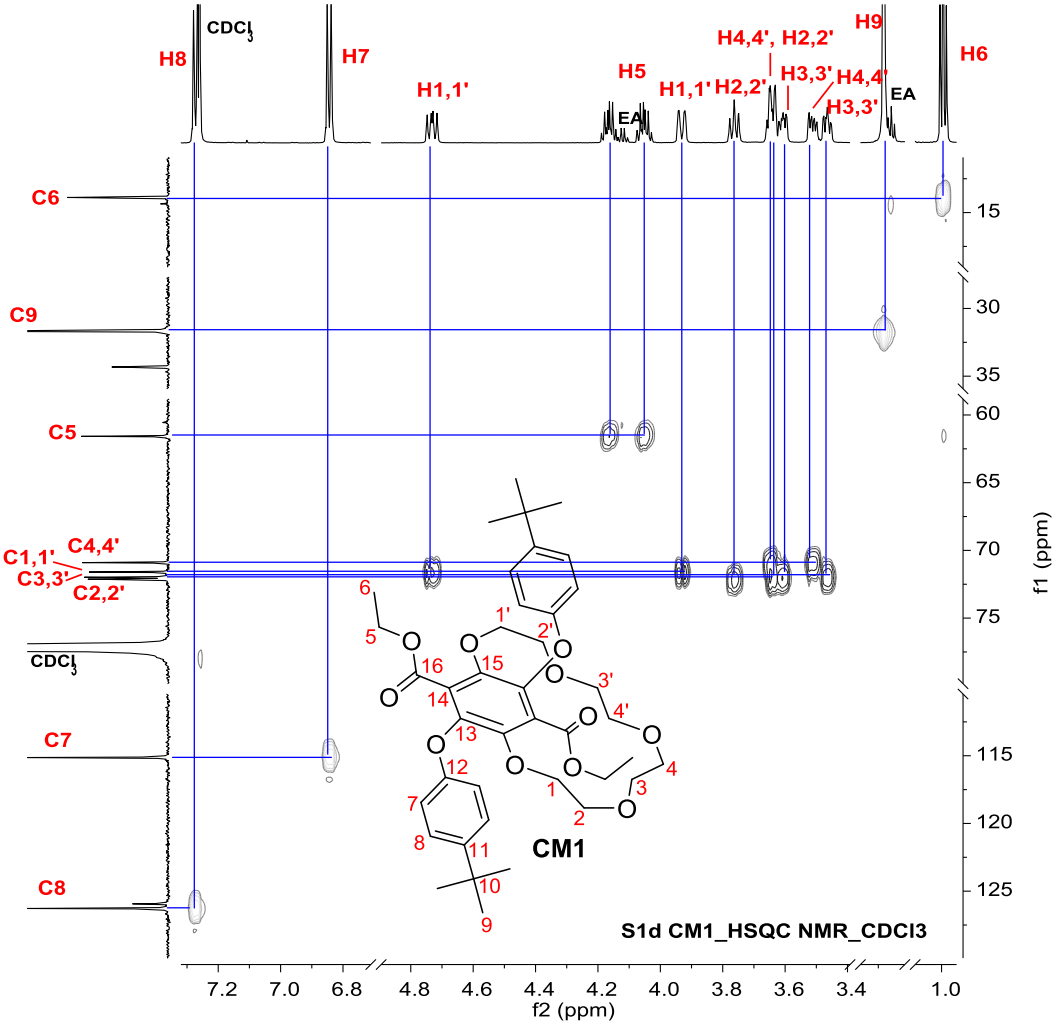
H8
CDCl3
H7
H1,1'
H5
EA
H1,1'
H2,2'
H4,4', H2,2'
H3,3'
H9
H4,4'
H3,3'
EA
H6
C6
C9
C5
C1,1'
C4,4'
C3,3'
C2,2'
CDCl3
C7
C8
CM1
S1d CM1_HSQC NMR_CDCl3
f2 (ppm)
f1 (ppm)

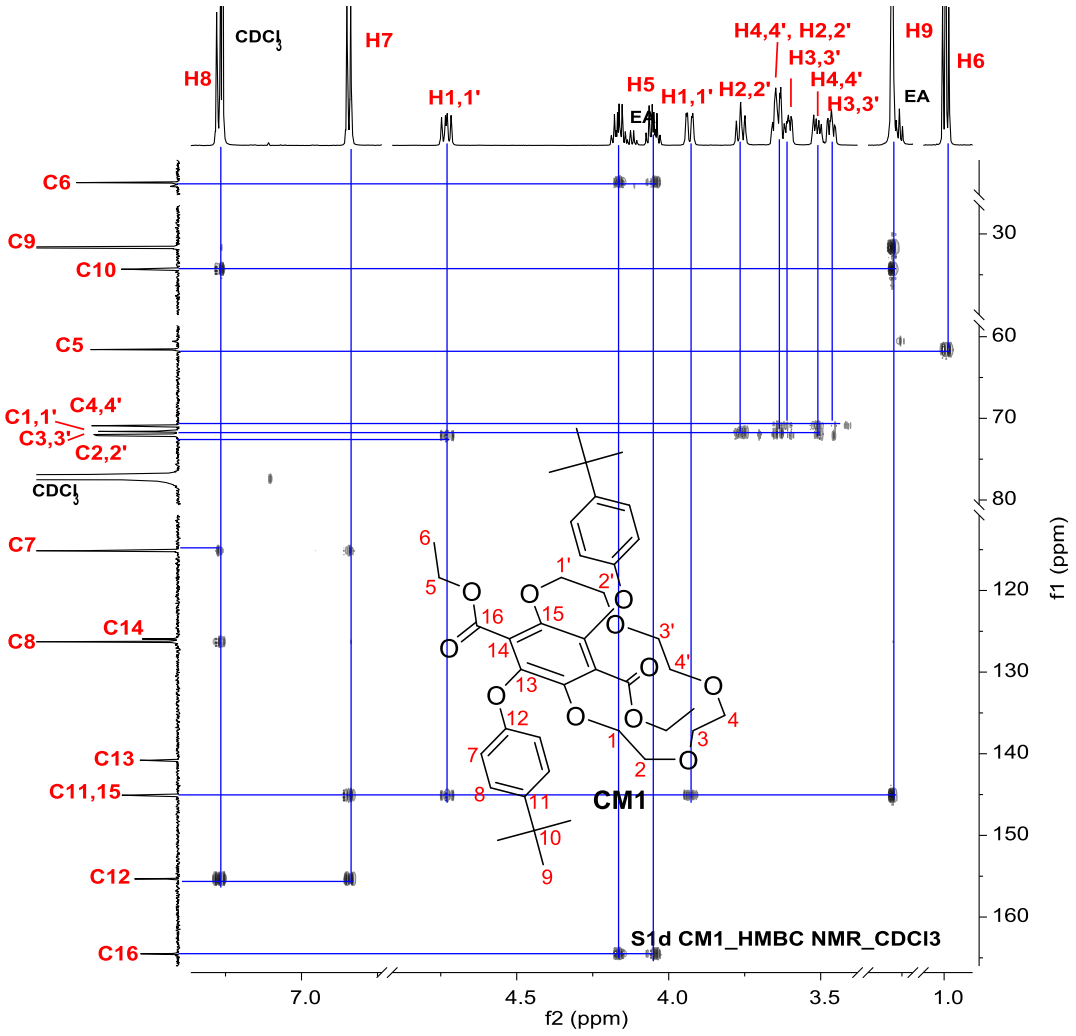

Figure 4: *^{1}H, ^{13}C, COSY, HSQC, HMBC NMR spectra (700 MHz, $CDCl_3$) of* **CM1**.

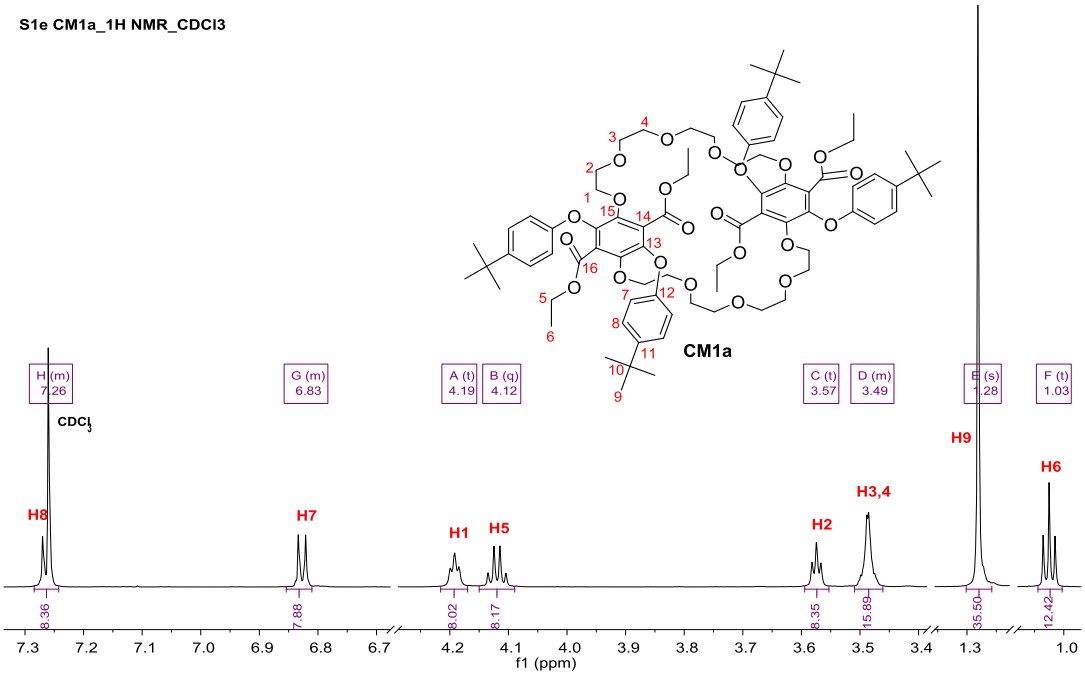

^{1}H NMR (700 MHz, Chloroform - *d*) δ 7.28 – 7.24 (m, 8H, H8), 6.85 – 6.81 (m, 8H, H7), 4.19 (t, *J* = 5.4 Hz, 8H, H1), 4.12 (q,*J* = 7.1 Hz, 8H, H5), 3.57 (t, *J* = 5.3 Hz, 8H, H2), 3.51 – 3.46 (m, 16H, H3, H4), 1.28 (s, 36H, H9), 1.03 (t, *J* = 7.1 Hz, 12H, H6).

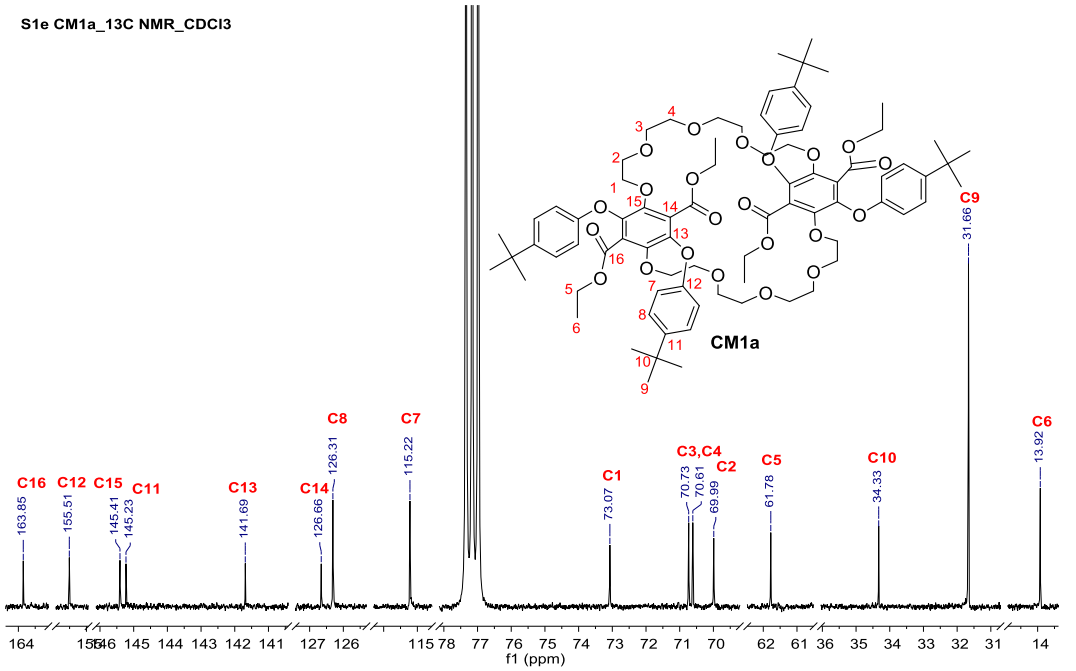

^{13}C NMR (176 MHz, $CDCl_3$) δ 163.85 (C16), 155.51 (C12), 145.41 (C15), 145.23 (C11), 141.69 (C13), 126.66 (C14), 126.31 (C8), 115.22 (C7), 73.07 (C1), 70.73, 70.61 (C3,C4), 69.99 (C2), 61.78 (C5), 34.33 (C10), 31.66 (C9), 13.92 (C6).

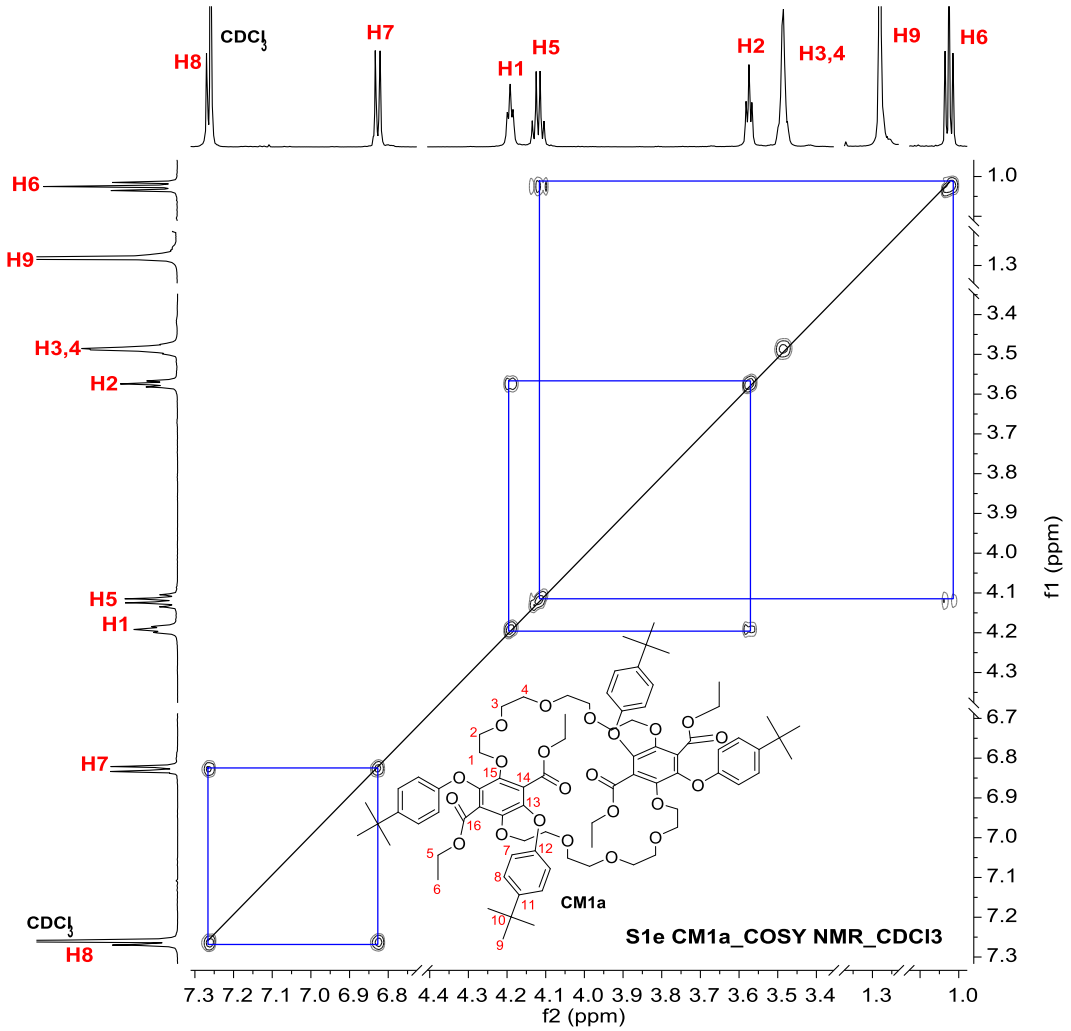
H8
CDCl3
H7
H1
H5
H2
H3,4
H9
H6
H6
H9
H3,4
H2
H5
H1
H7
CDCl3
H8
1.0
1.3
3.4
3.5
3.6
3.7
3.8
3.9
4.0
4.1
4.2
4.3
6.7
6.8
6.9
7.0
7.1
7.2
7.3
f1 (ppm)
7.3 7.2 7.1 7.0 6.9 6.8 4.4 4.3 4.2 4.1 4.0 3.9 3.8 3.7 3.6 3.5 3.4 1.3 1.0
f2 (ppm)
CM1a
S1e CM1a_COSY NMR_CDCl3

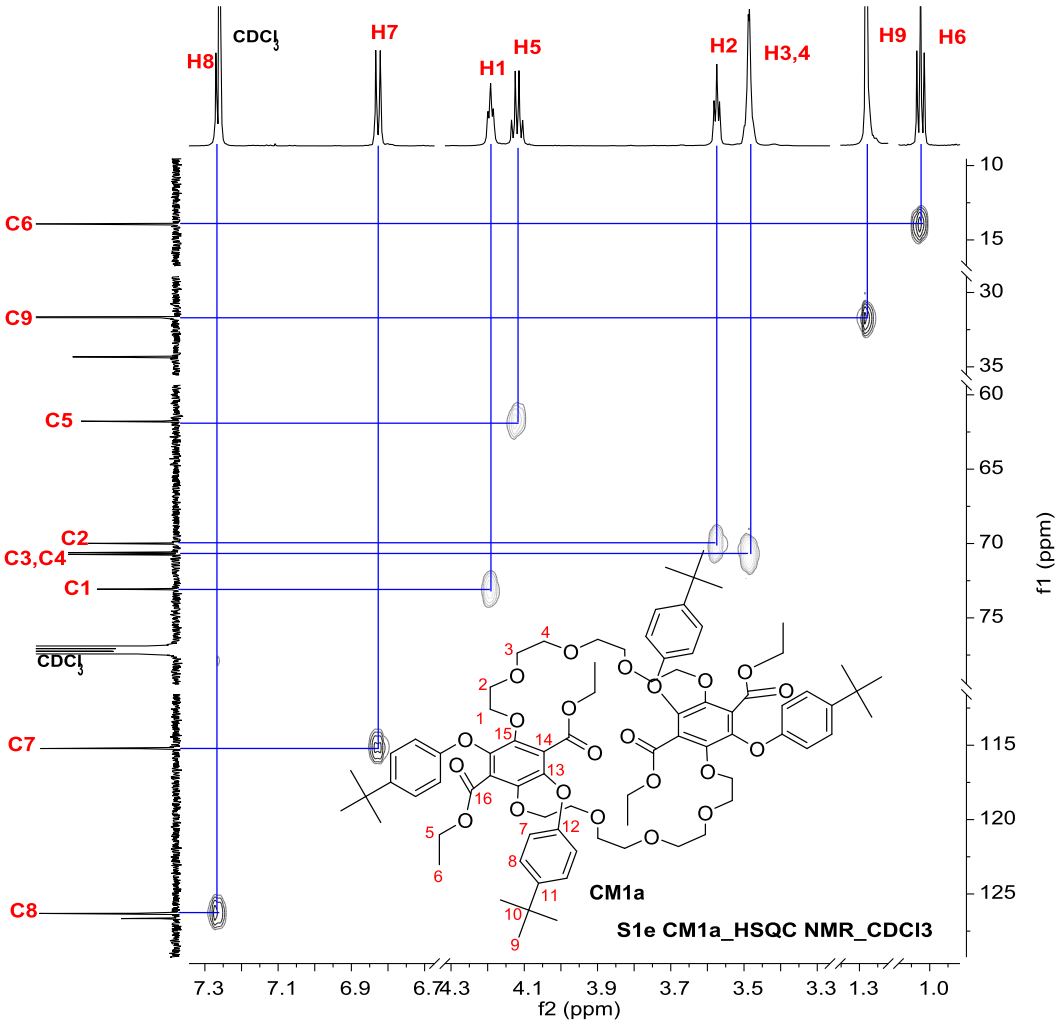
H8
CDCl3
H7
H1
H5
H2
H3,4
H9
H6
C6
C9
C5
C2
C3,C4
C1
CDCl3
C7
C8
CM1a
S1e CM1a_HSQC NMR_CDCl3
f2 (ppm)
f1 (ppm)

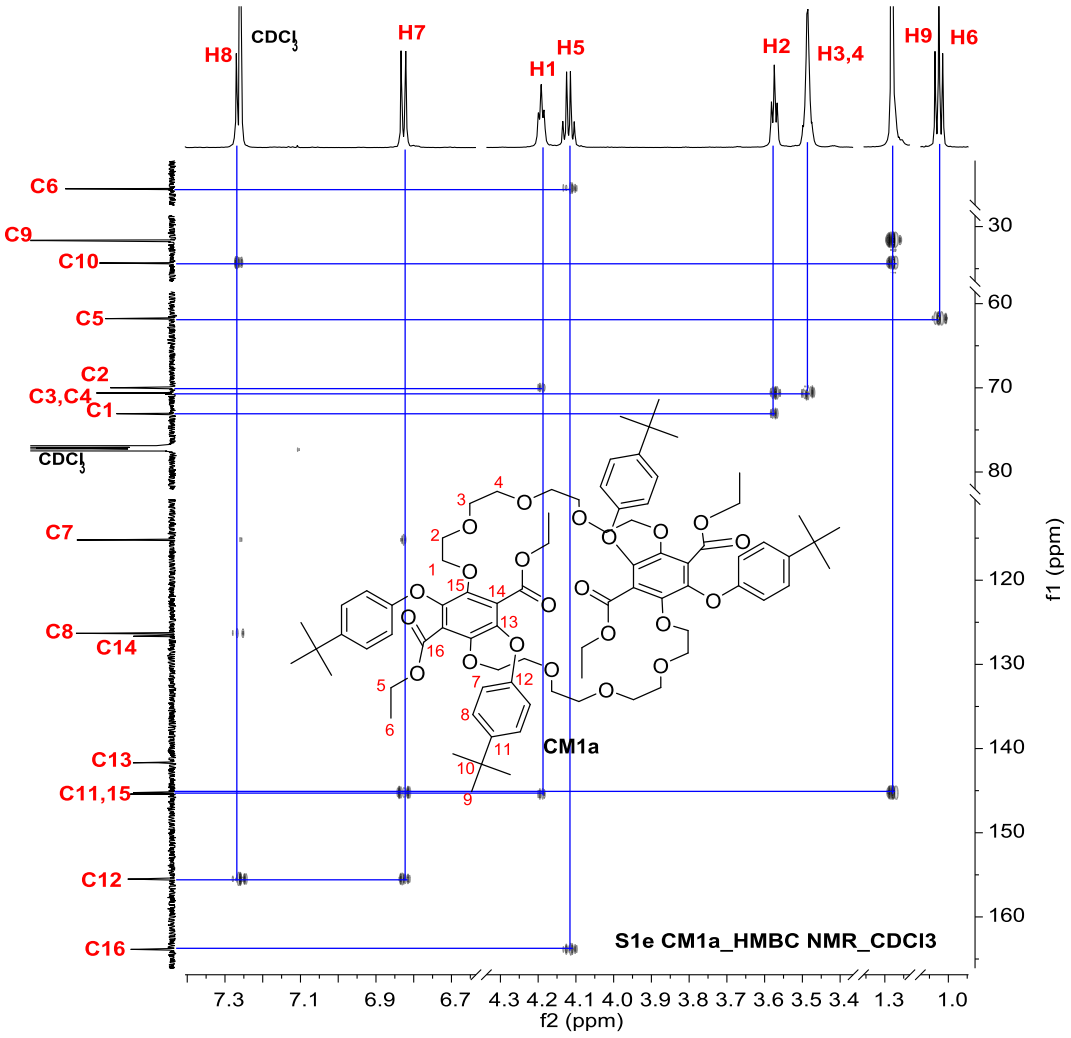

Figure 5: *^{1}H, ^{13}C, COSY, HSQC, HMBC NMR spectra (700 MHz, $CDCl_3$) of* **CM1a**.

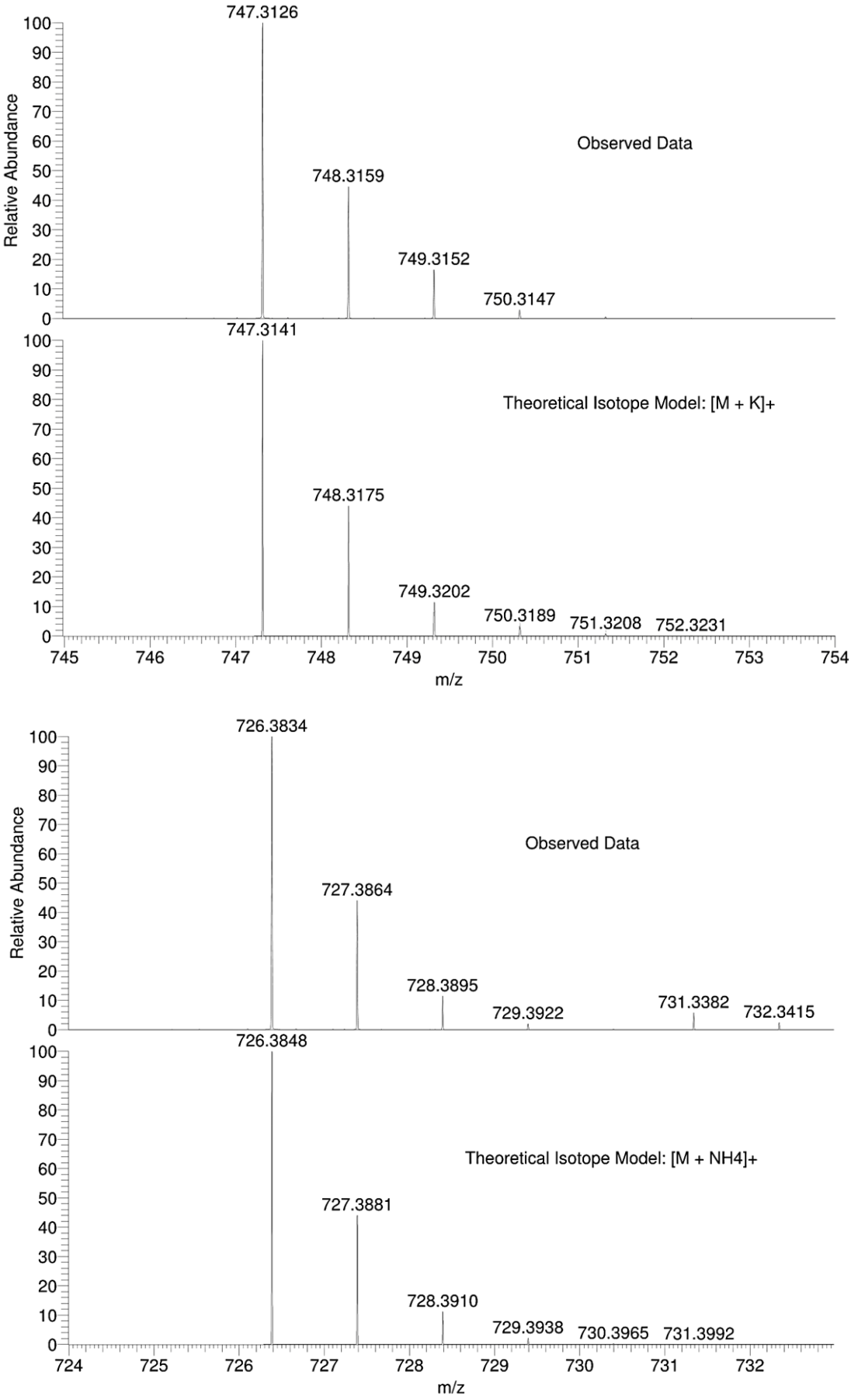

Figure 6: *Mass spectra of* **CM1** *showing its* $[M+K]^+$ *and* $[M+NH_4]^+$ *ions.*

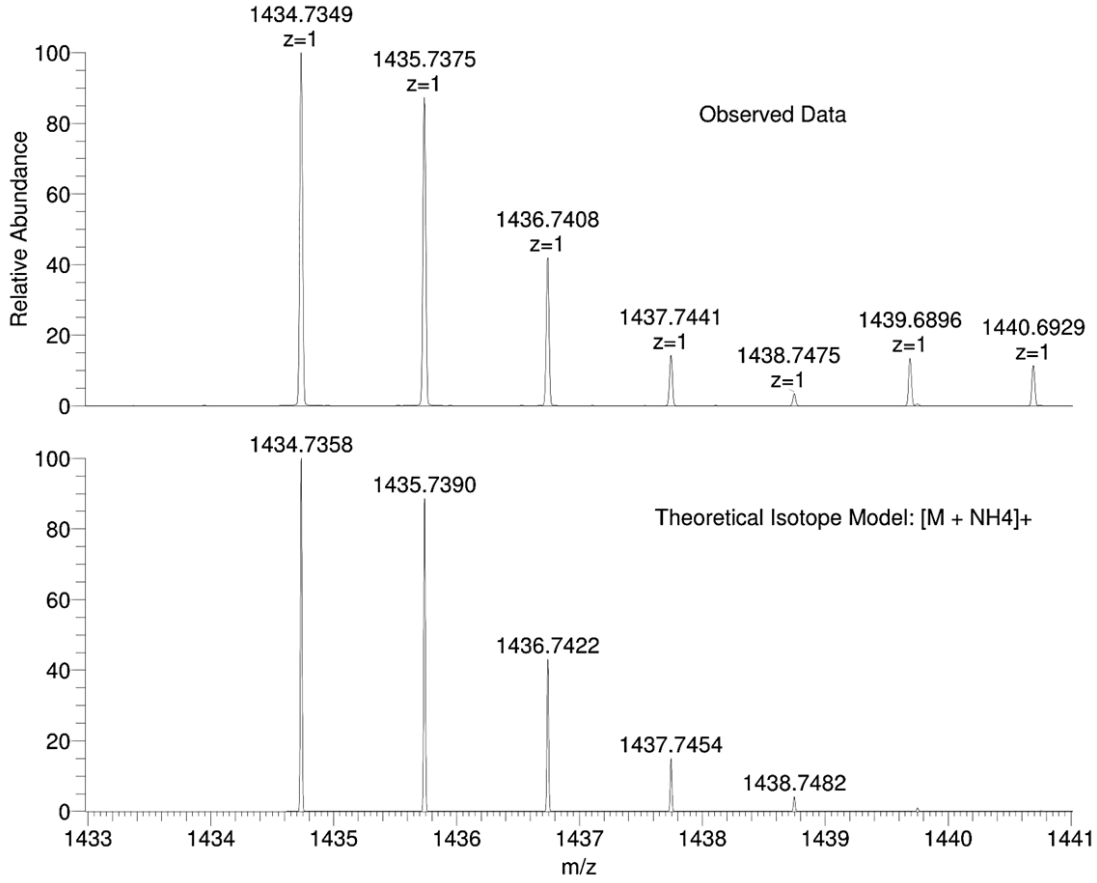

Figure 7: *Mass spectra of* **CM1a** *showing its* $[M+NH_4]^+$ *ion.*

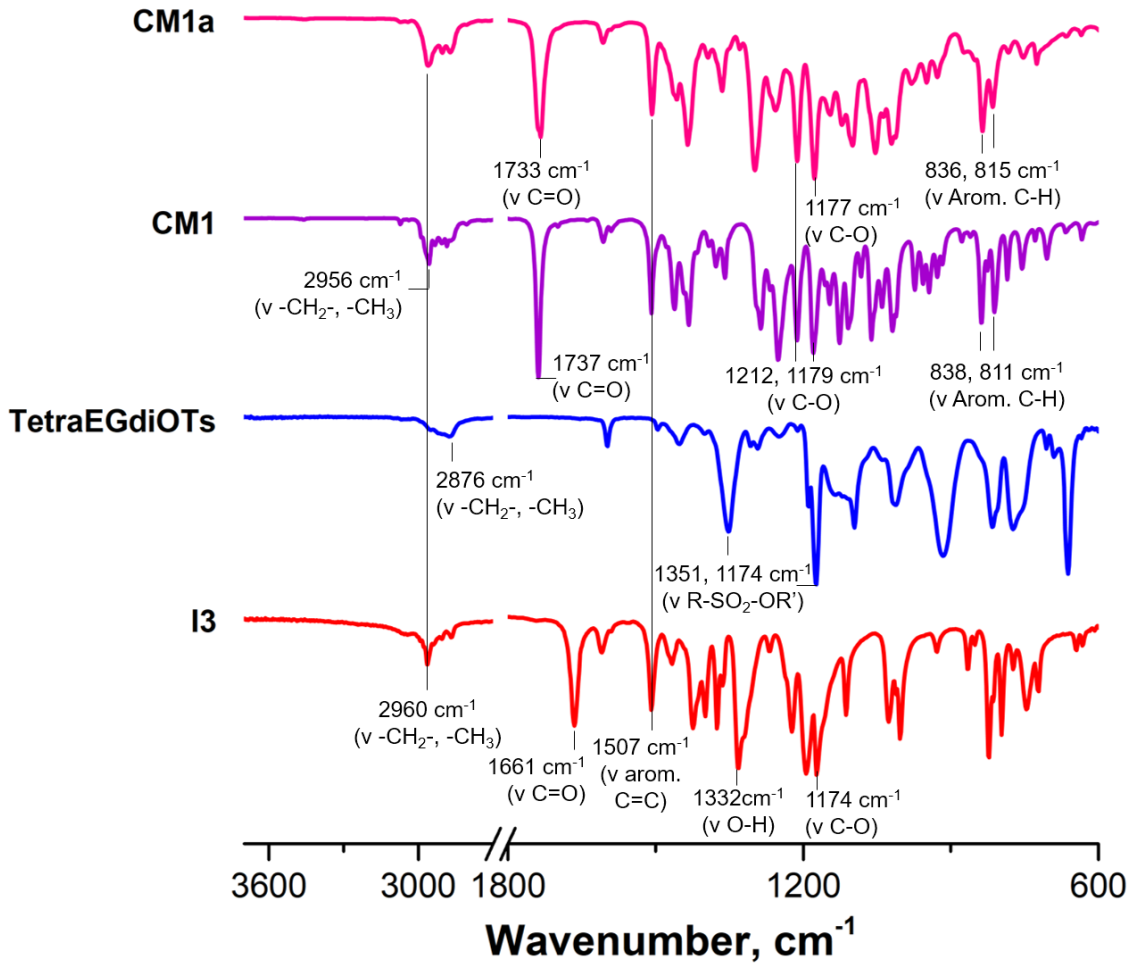

Figure 8: *FT-IR spectra of* **I3**, **TetraEGdiOTs**, **CM1** *and* **CM1a**.

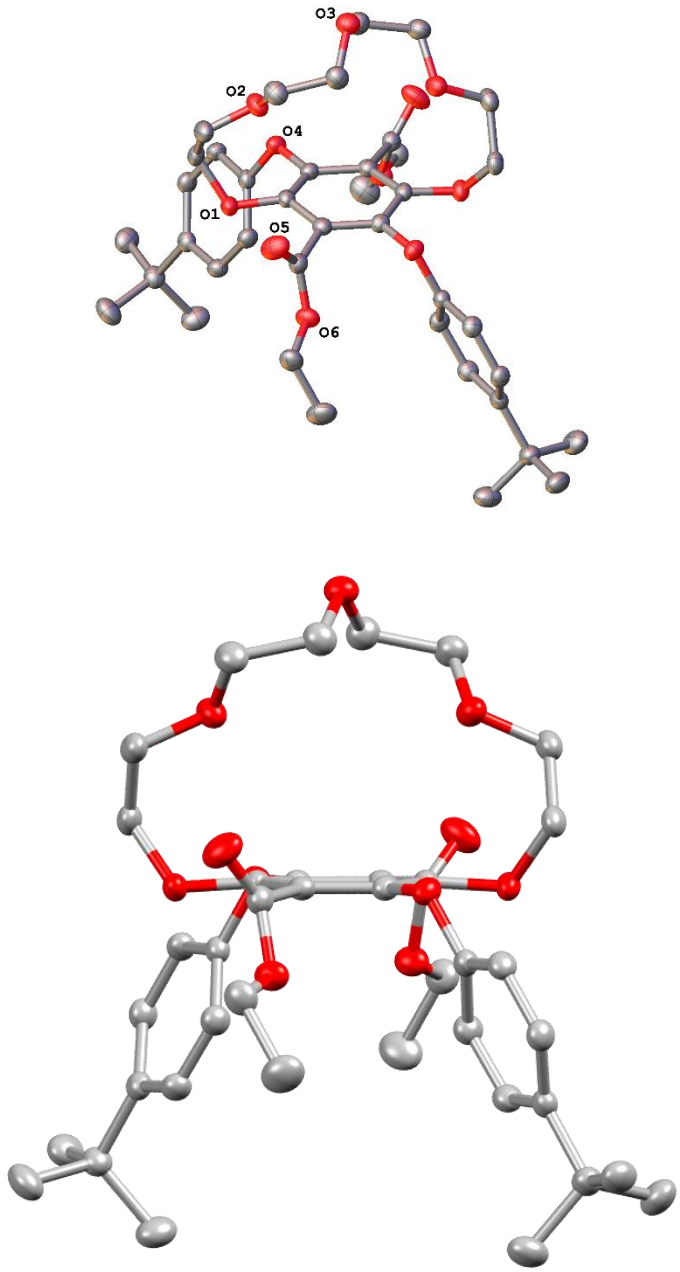

Figure 9: *X-ray crystal structure of* **CM1**.

CM1	
Empirical formula	$C_{40}H_{52}O_{11}$
Formula weight	708.81
Temperature/K	150.0(2)
Crystal system	orthorhombic
Space group	Pbcn
a/Å	17.16525(17)
b/Å	8.82601(8)
c/Å	24.8213(3)
α/°	90
β/°	90
γ/°	90
Volume/Å^3	3760.45(6)
Z	4
ρ_{calc}g/cm^3	1.252
μ/mm^{-1}	0.742
F(000)	1520.0
Crystal size/mm^3	0.34 × 0.15 × 0.09
Radiation	CuKα (λ = 1.54184)
2Θ range for data collection/°	7.122 to 133.792
Index ranges	-20 ≤ h ≤ 20, -10 ≤ k ≤ 10, -27 ≤ l ≤ 29
Reflections collected	49871
Independent reflections	3355 [R_{int} = 0.0466, R_{sigma} = 0.0159]
Data/restraints/parameters	3355/0/235
Goodness-of-fit on F^2	1.032
Final R indexes [I>=2σ (I)]	R_1 = 0.0329, wR_2 = 0.0822
Final R indexes [all data]	R_1 = 0.0401, wR_2 = 0.0879
Largest diff. peak/hole / e Å^{-3}	0.16/-0.21

Table 1: *Crystal data and structure refinement for* **CM1***.*

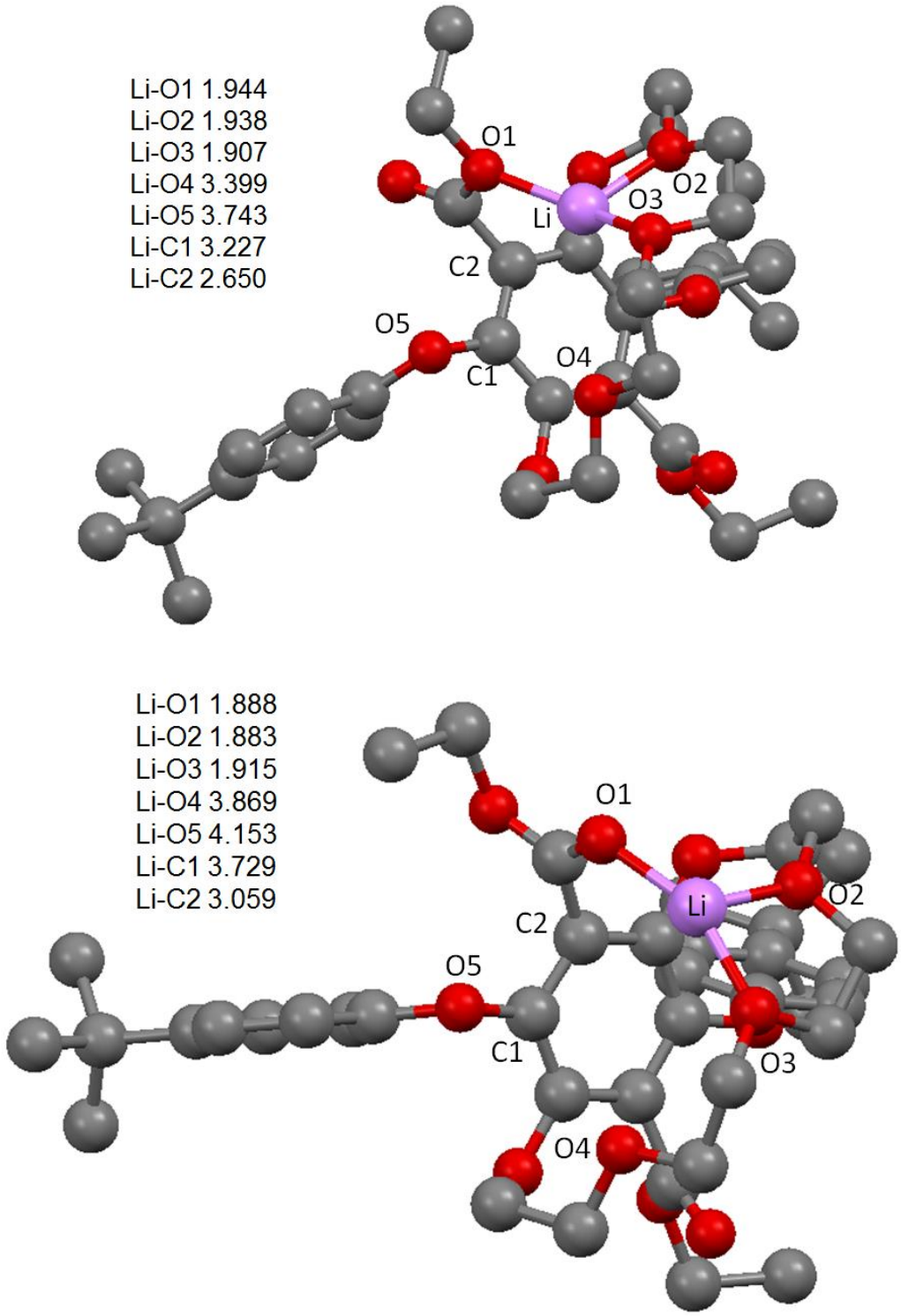

Figure 10: *Gaussian calculated energy-minimised gas phase structures for a Li^+ adduct of* **CM1** *using B3LYP and a 6-311G basis set. Distances shown as the insert are in Å and hydrogens are omitted for clarity.*

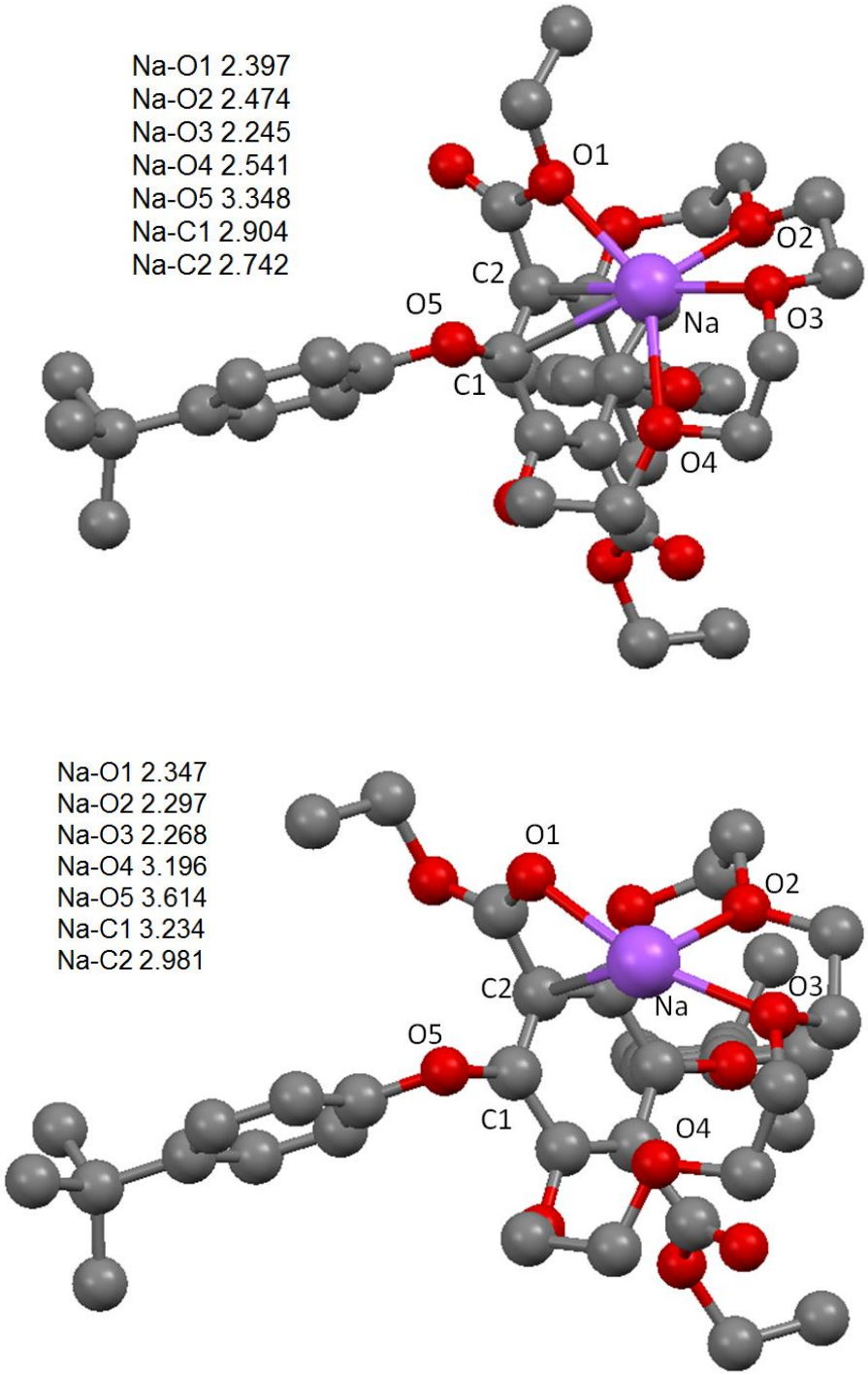

Figure 11: *Gaussian calculated energy-minimised gas phase structures for a Na^+ adduct of* **CM1** *using B3LYP and a 6-311G basis set. Distances shown as the insert are in Å and hydrogens are omitted for clarity.*

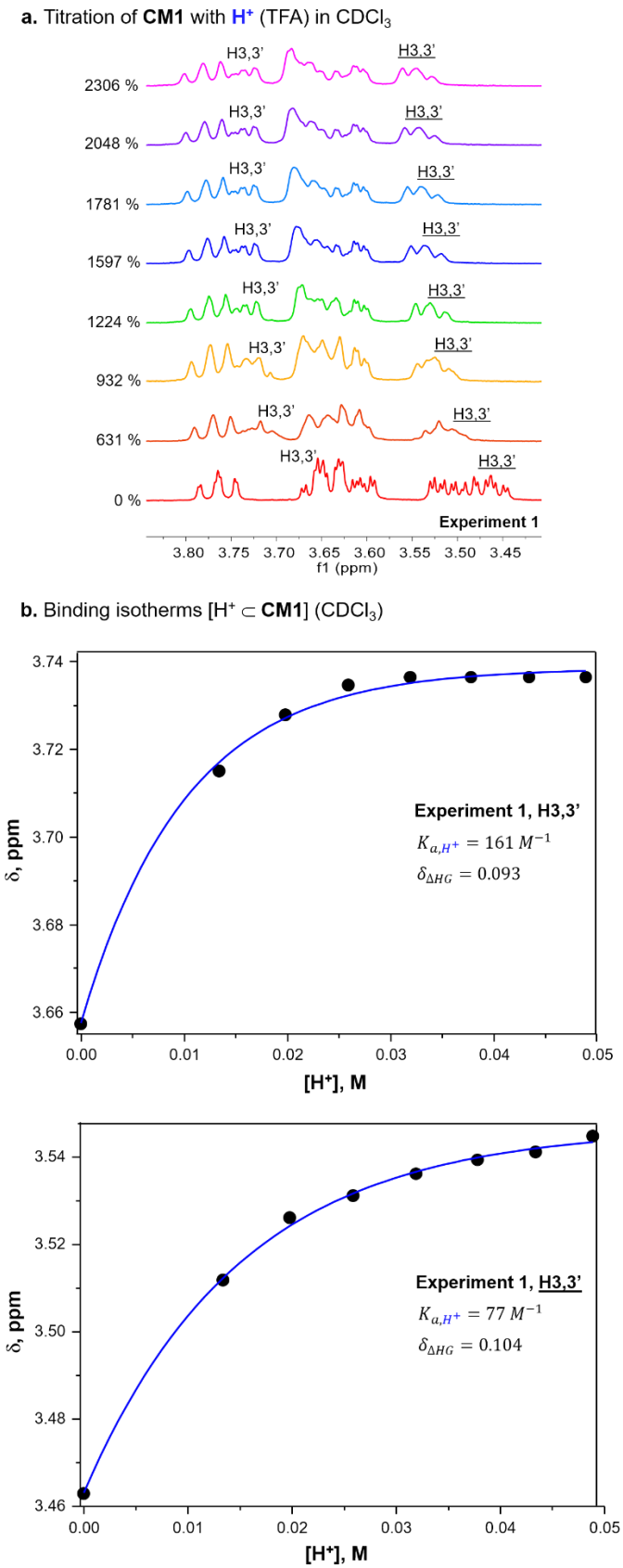

Figure 12: a) *Partial ^{1}H NMR (500 MHz, 298 K, $CDCl_3$) stack plot of* **CM1** *(2 mM) titration with TFA from 0 to 2306 mol % and* ***b)*** *Non-linear fit of binding isotherms [$H^+ \subset$* **CM1***].*

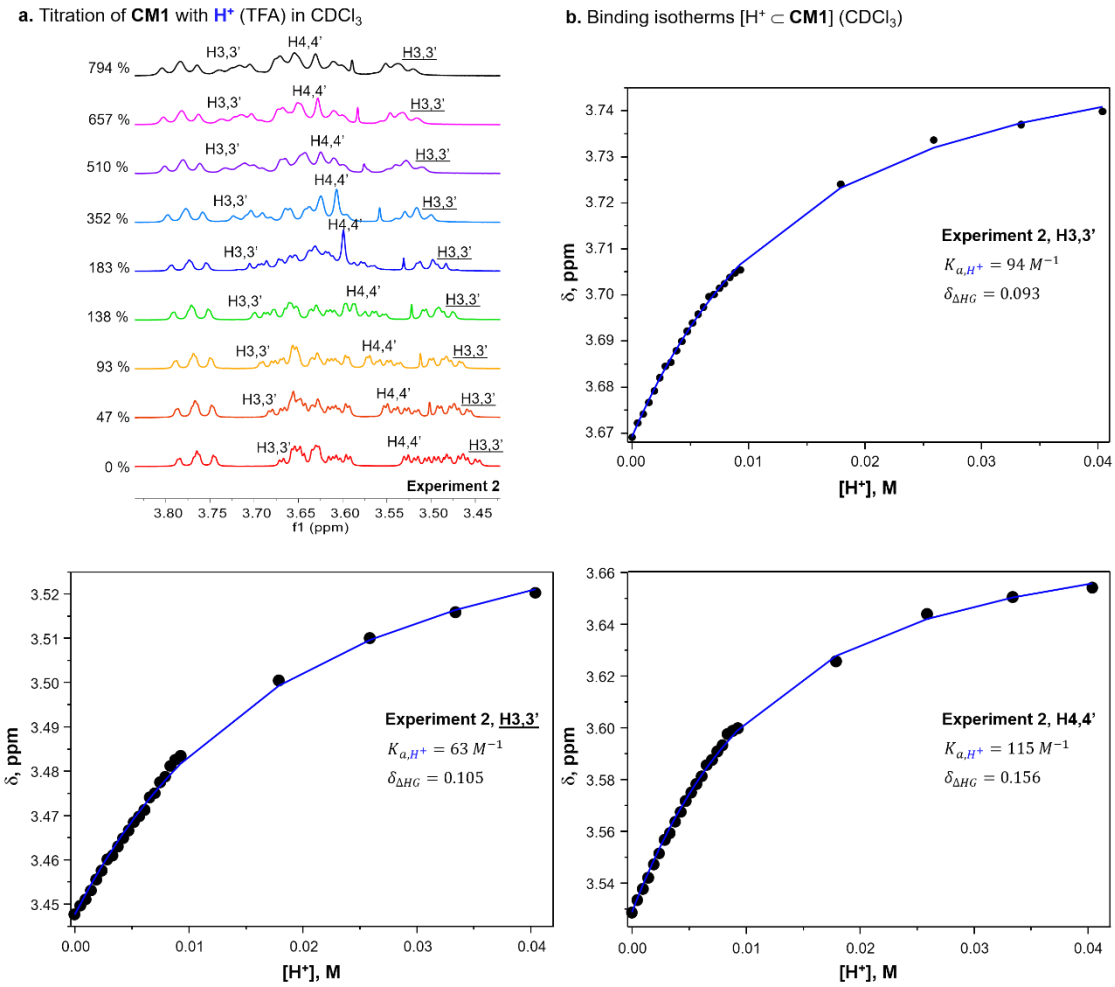

Figure 13: a) *Partial ^{1}H NMR (500 MHz, 298 K, $CDCl_3$) stack plot of* **CM1** *(5 mM) titration with TFA from 0 to 794 mol % and* ***b)*** *Non-linear fit of binding isotherms [$H^+ \subset$* **CM1***].*

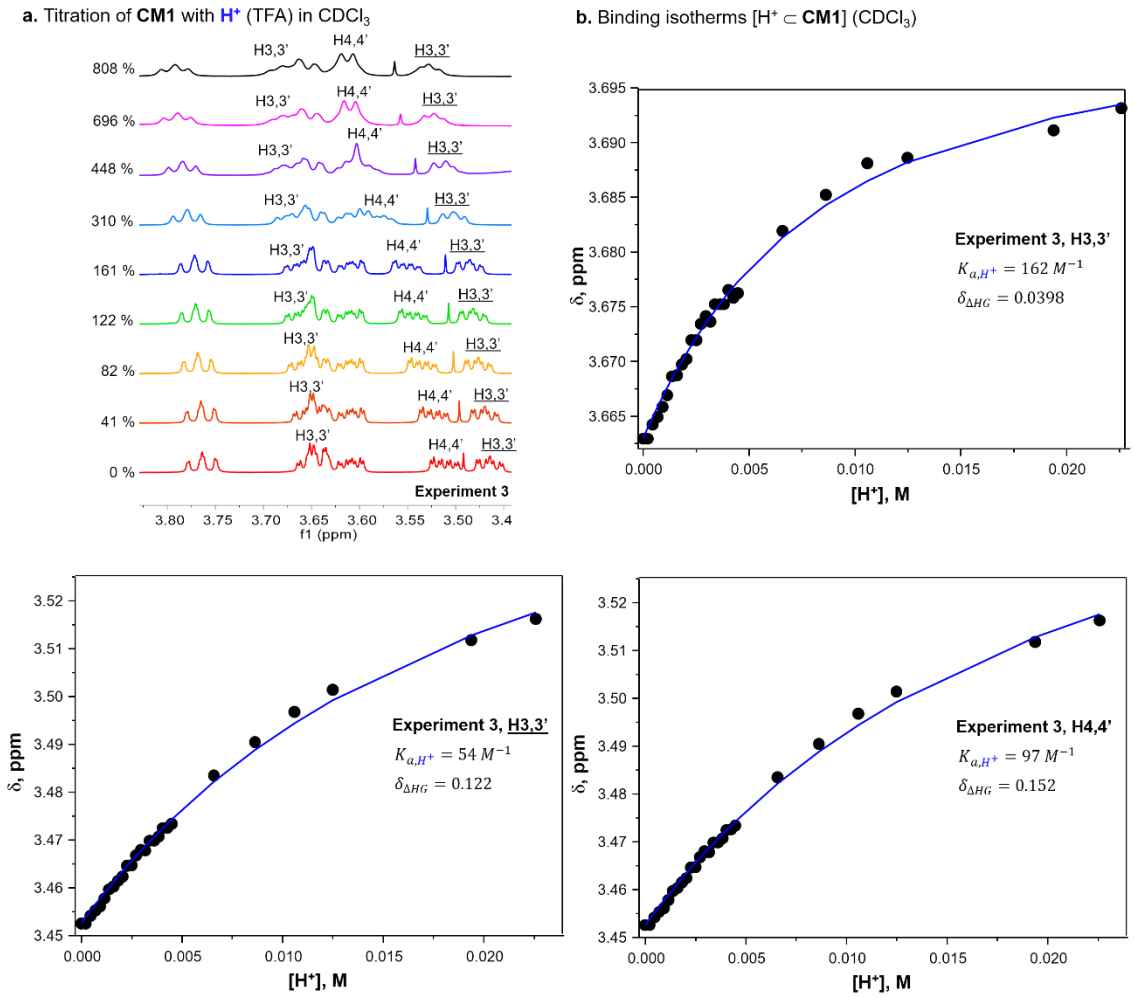

Figure 14: a) *Partial ^{1}H NMR (700 MHz, 298 K, $CDCl_3$) stack plot of* **CM1** *(3 mM) titration with TFA from 0 to 808 mol % and* ***b)*** *Non-linear fit of binding isotherms [$H^+ \subset$* **CM1***].*

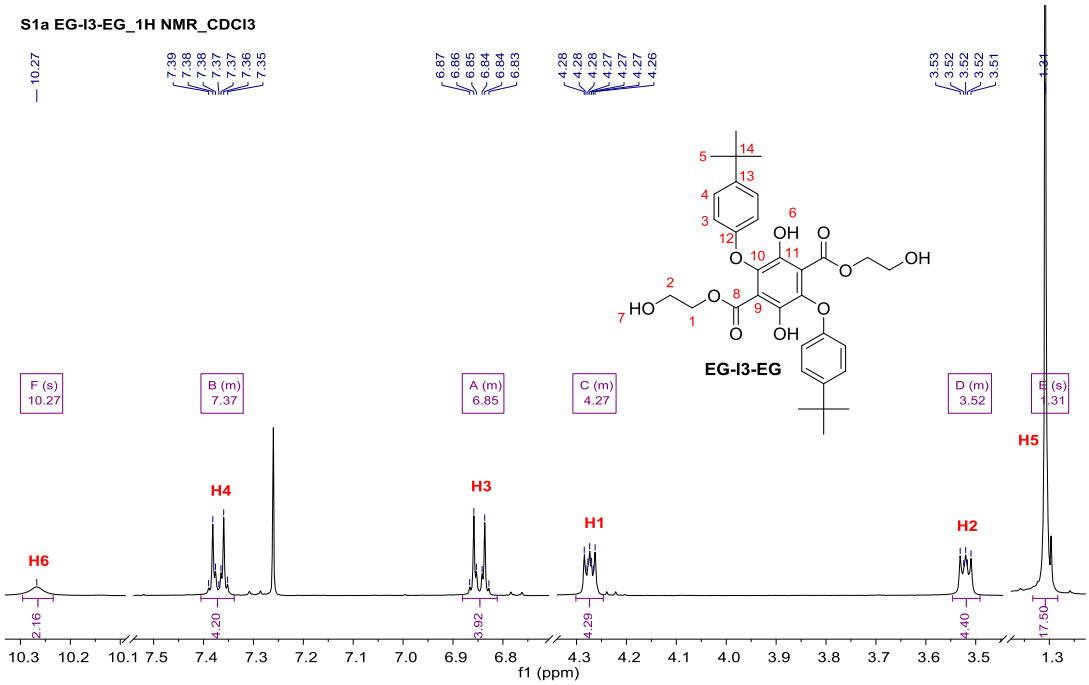

^{1}H NMR (400 MHz, Chloroform - *d*) δ 10.27 (s, 2H, H6), 7.41 – 7.34 (m, 4H, H4), 6.88 – 6.81 (m, 4H, H3), 4.30 – 4.25 (m, 4H, H1), 3.55 – 3.49 (m, 4H, H2), 1.31 (s, 18H, H5).

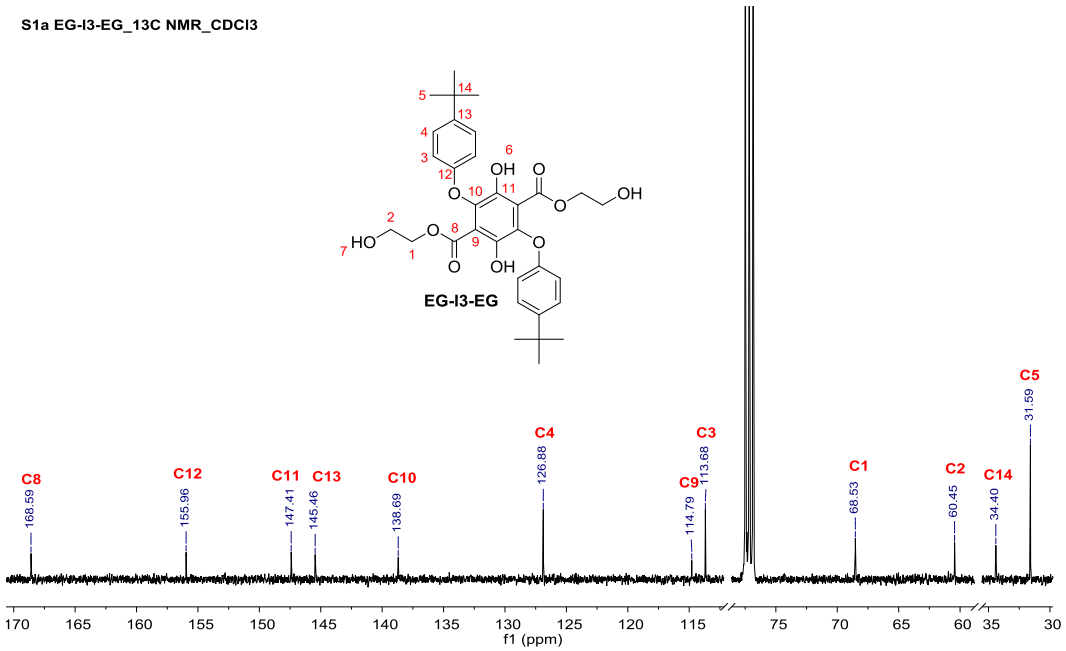

^{13}C NMR (101 MHz, $CDCl_3$) δ 168.59 (C8), 155.96 (C12), 147.41 (C11), 145.46 (C13), 138.69 (C10), 126.88 (C4), 114.79 (C9), 113.68 (C3), 68.53 (C1), 60.45 (C2), 34.40 (C14), 31.59 (C5).

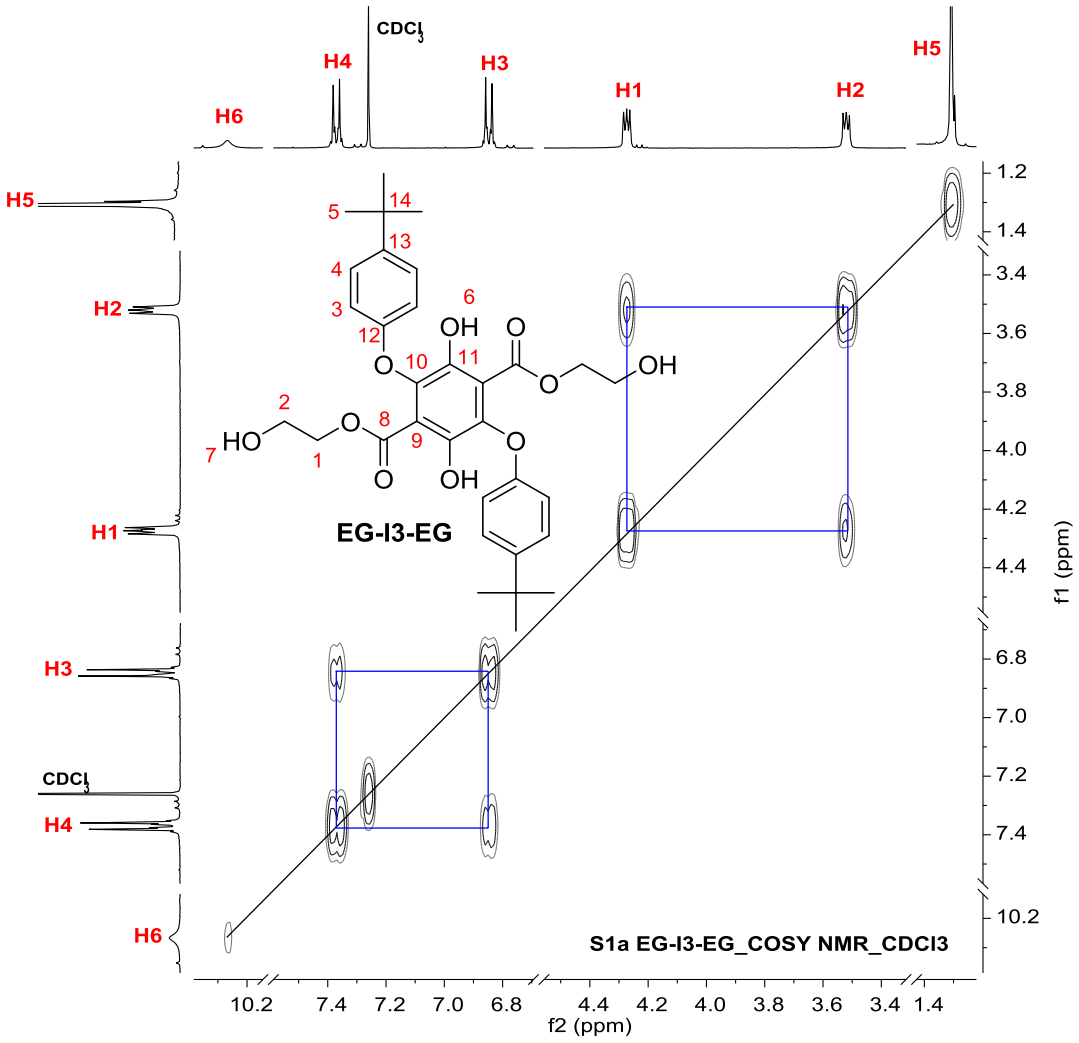
CDCl3
H4
H3
H1
H2
H5
H6
EG-I3-EG
S1a EG-I3-EG_COSY NMR_CDCl3
f2 (ppm)
f1 (ppm)

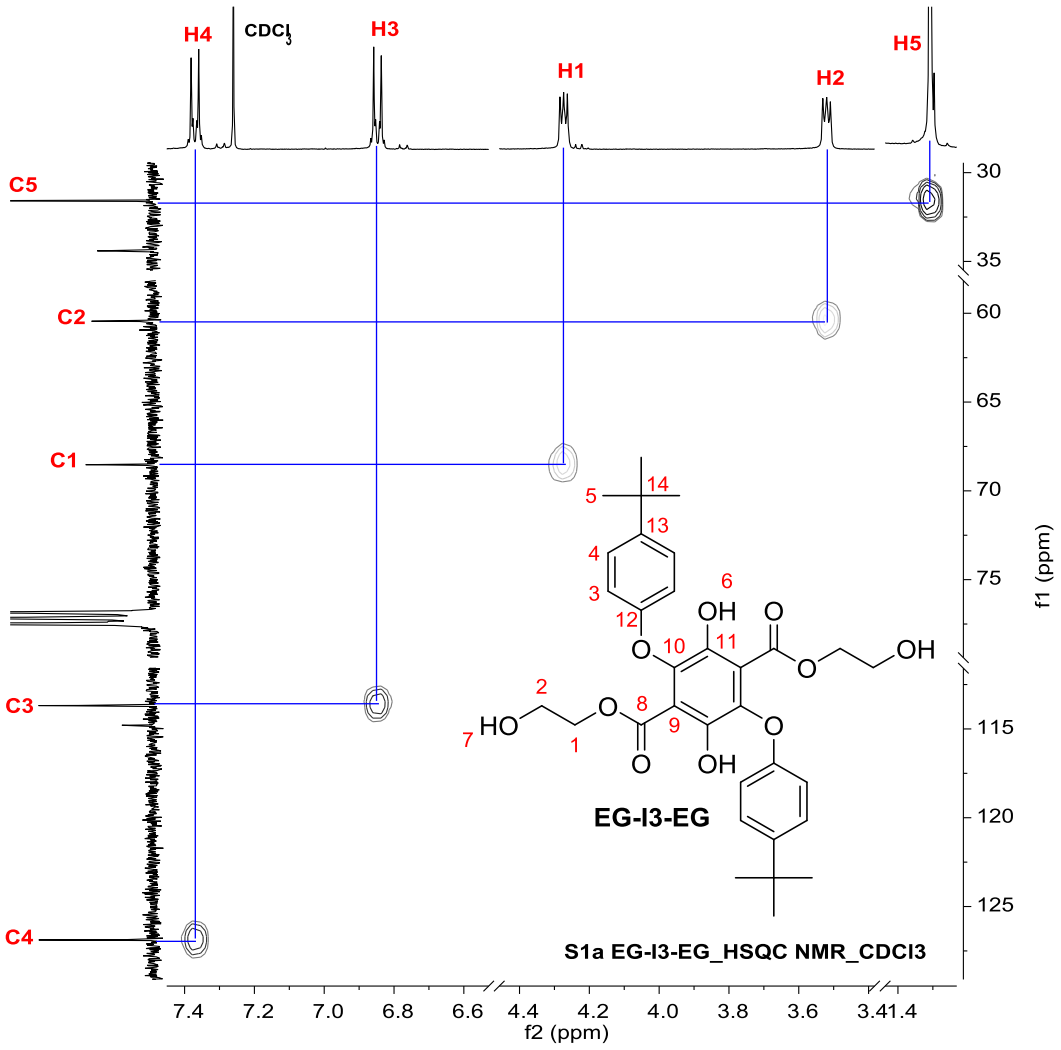
H4
CDCl3
H3
H1
H2
H5
C5
C2
C1
C3
C4
30
35
60
65
70
75
115
120
125
f1 (ppm)
7.4
7.2
7.0
6.8
6.6
4.4
4.2
4.0
3.8
3.6
3.41.4
f2 (ppm)
EG-I3-EG
S1a EG-I3-EG_HSQC NMR_CDCl3

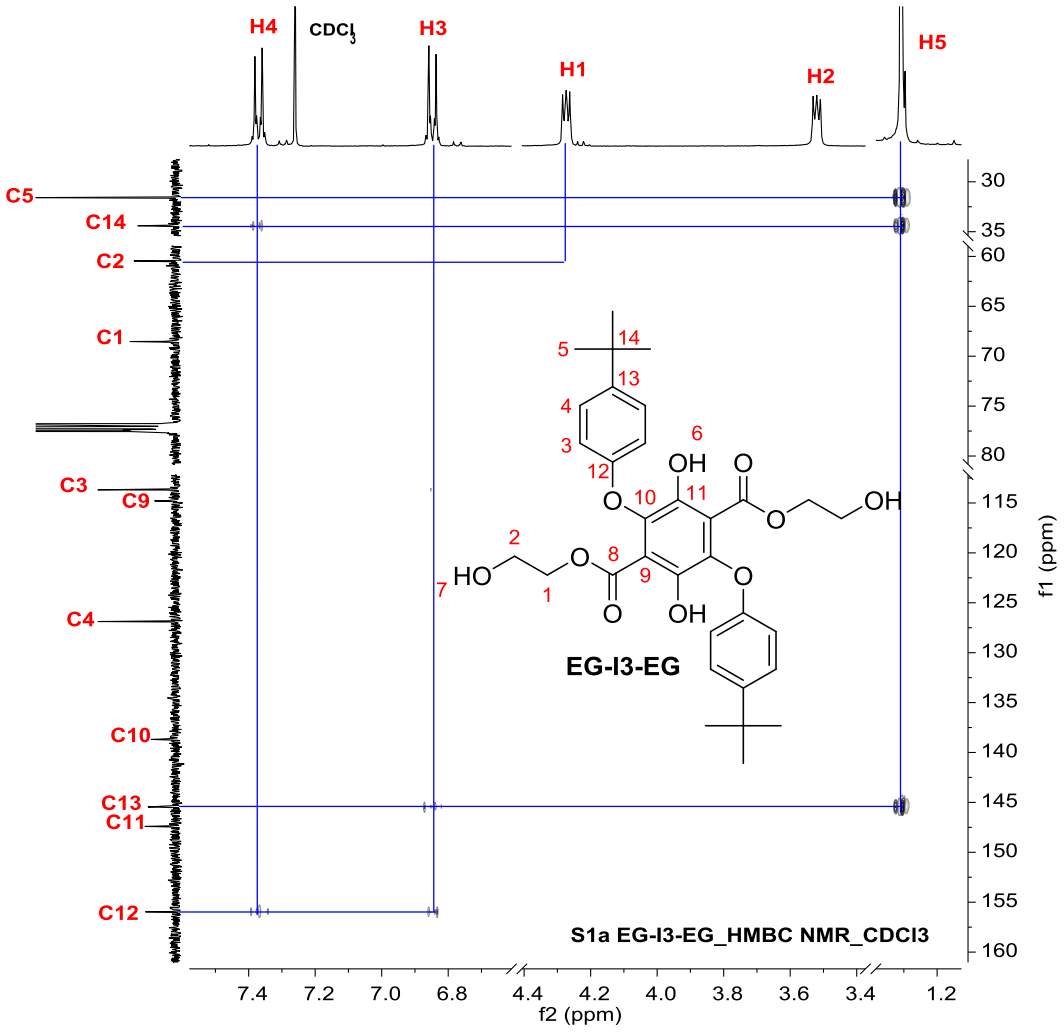

Figure 1: *^{1}H, ^{13}C, COSY, HSQC, HMBC NMR spectra (400 MHz, $CDCl_3$) of* **EG-I3-EG**.

S2a I4_1H NMR_CDCl3

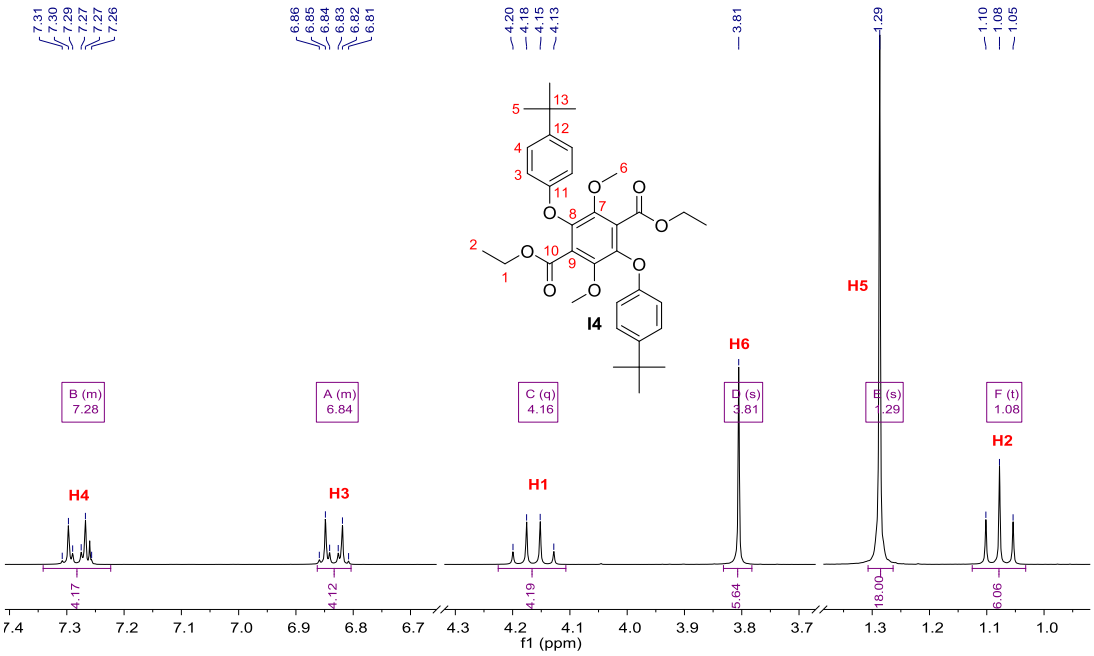

^{1}H NMR (300 MHz, Chloroform - *d*) δ 7.34 – 7.22 (m, 4H, H4), 6.86 – 6.80 (m, 4H, H3), 4.16 (q, *J* = 7.1 Hz, 4H, H1), 3.81 (s, 6H, H6), 1.29 (s, 18H, H5), 1.08 (t, *J* = 7.1 Hz, 6H, H2).

S2a I4_13C NMR_CDCl3

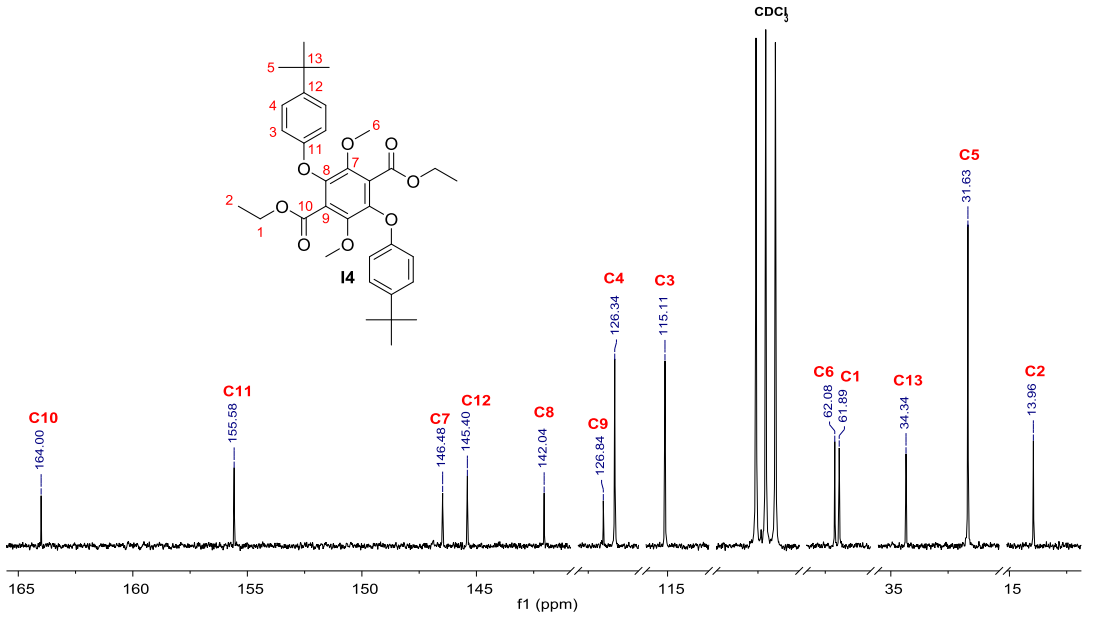

^{13}C NMR (75 MHz, $CDCl_3$) δ 164.00 (C10), 155.58 (C11), 146.48 (C7), 145.40 (C12), 142.04 (C8), 126.84 (C9), 126.34 (C4), 115.11 (C3), 62.08 (C6) 61.89 (C1), 34.34 (C13), 31.63 (C5), 13.96 (C2).

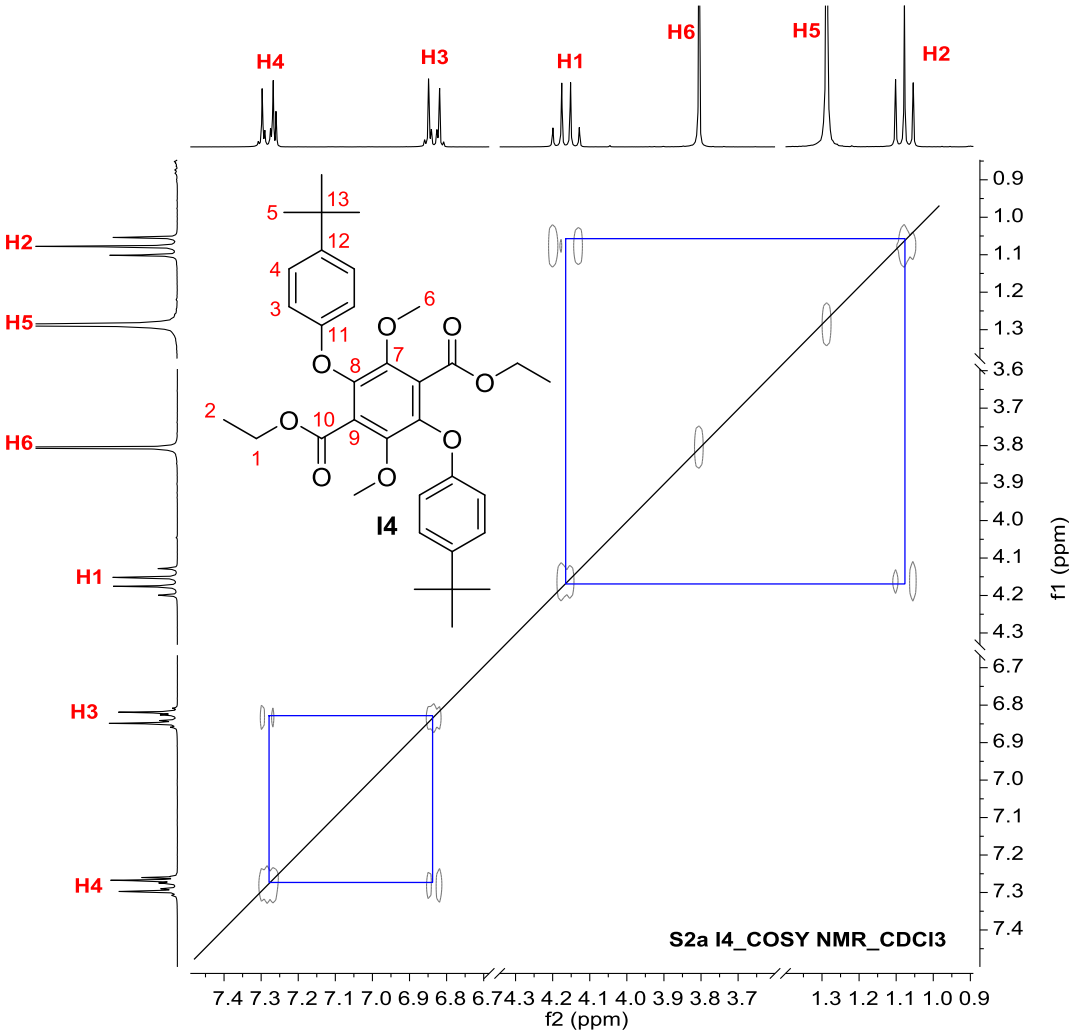
H4
H3
H1
H6
H5
H2
H2
H5
H6
H1
H3
H4
13
5
12
4
3
11
6
O
O
7
O
8
O
2
10
9
1
O
O
O
I4
S2a I4_COSY NMR_CDCl3
0.9
1.0
1.1
1.2
1.3
3.6
3.7
3.8
3.9
4.0
4.1
4.2
4.3
6.7
6.8
6.9
7.0
7.1
7.2
7.3
7.4
f1 (ppm)
7.4 7.3 7.2 7.1 7.0 6.9 6.8 6.7
4.3 4.2 4.1 4.0 3.9 3.8 3.7
1.3 1.2 1.1 1.0 0.9
f2 (ppm)

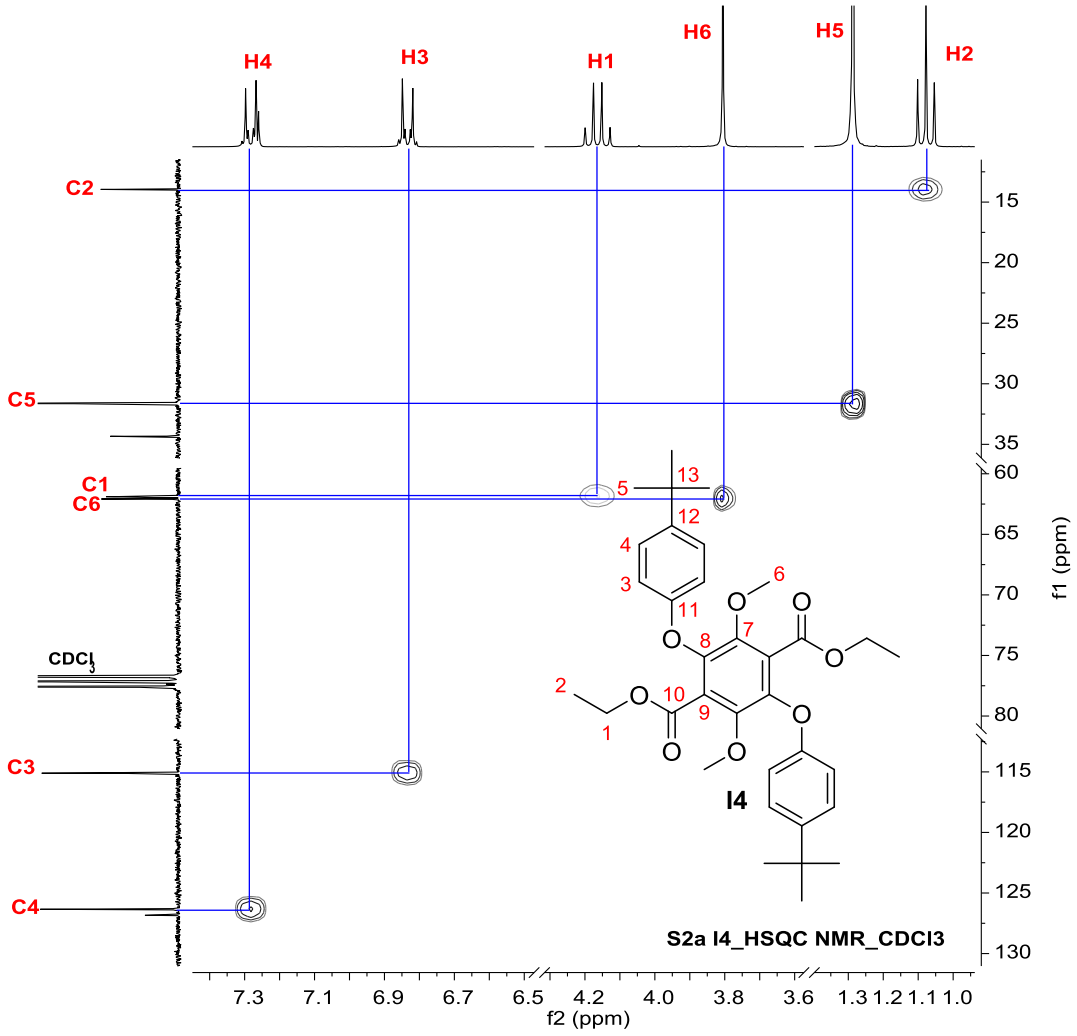
H4
H3
H1
H6
H5
H2
C2
C5
C1
C6
CDCl3
C3
C4
I4
S2a I4_HSQC NMR_CDCl3
f2 (ppm)
f1 (ppm)

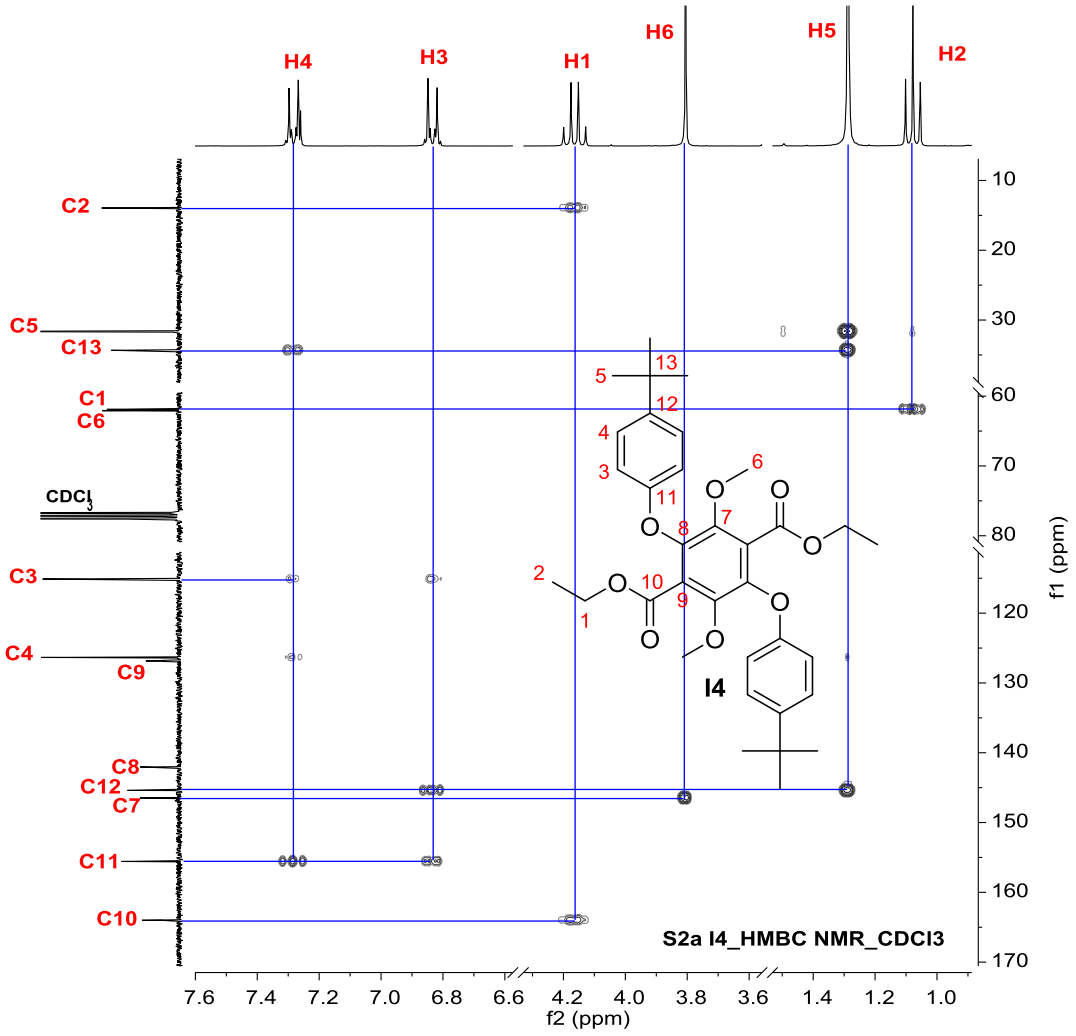

Figure 2: *^{1}H, ^{13}C, COSY, HSQC, HMBC NMR spectra (300 MHz, $CDCl_3$) of* **I4**.

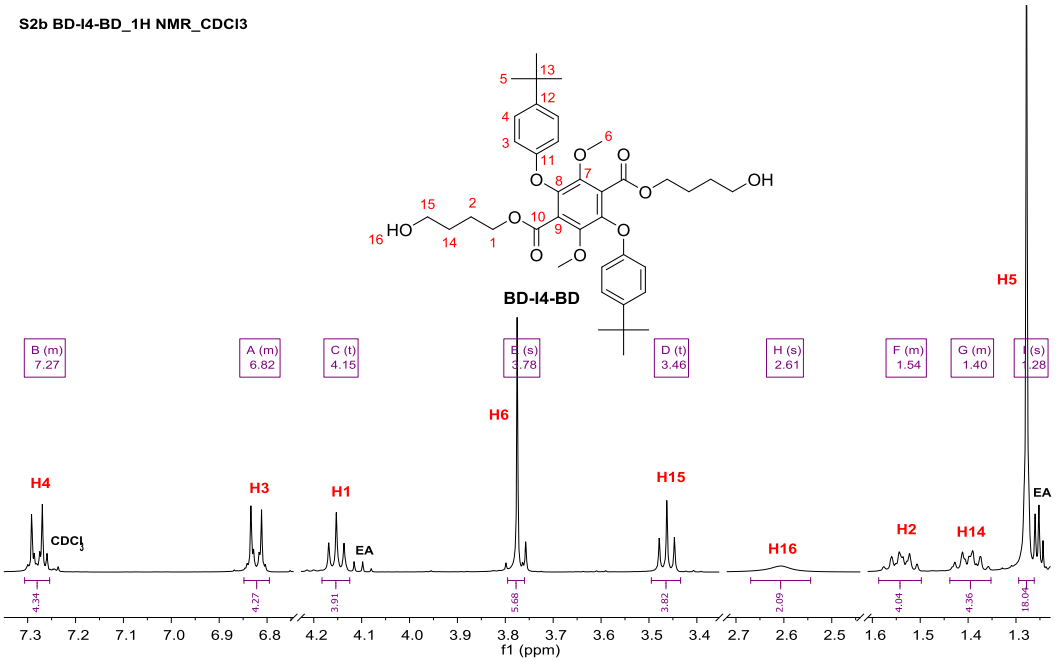

^{1}H NMR (400 MHz, Chloroform - *d*) δ 7.31 – 7.25 (m, 4H, H4), 6.85 – 6.80 (m, 4H, H3), 4.15 (t, *J* = 6.4 Hz, 4H, H1), 3.78 (s, 6H, H6), 3.46 (t, *J* = 6.3 Hz, 4H, H15), 2.61 (s, 2H, H16), 1.59 – 1.50 (m, 4H, H2), 1.44 – 1.35 (m, 4H, H14), 1.28 (s, 18H, H5).

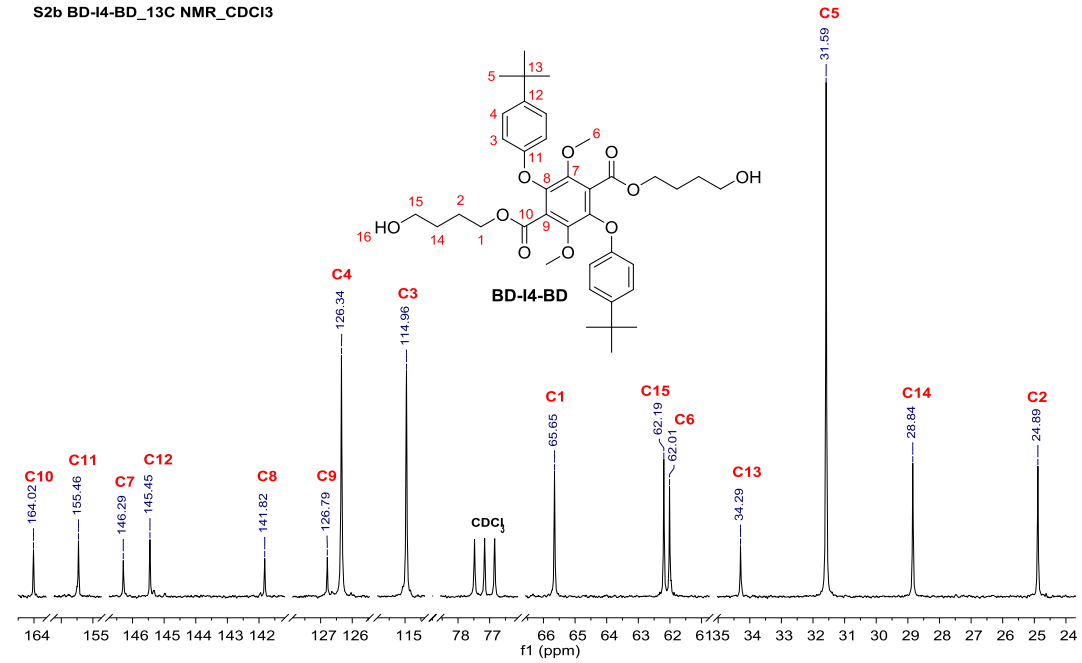

^{13}C NMR (101 MHz, $CDCl_3$) δ 164.02 (C10), 155.46 (C11), 146.29 (C7), 145.45 (C12), 141.82 (C8), 126.79 (C9), 126.34 (C4), 114.96 (C3), 65.65 (C1), 62.19 (C15), 62.01 (C6), 34.29 (C13), 31.59 (C5), 28.84 (C14), 24.89 (C2).

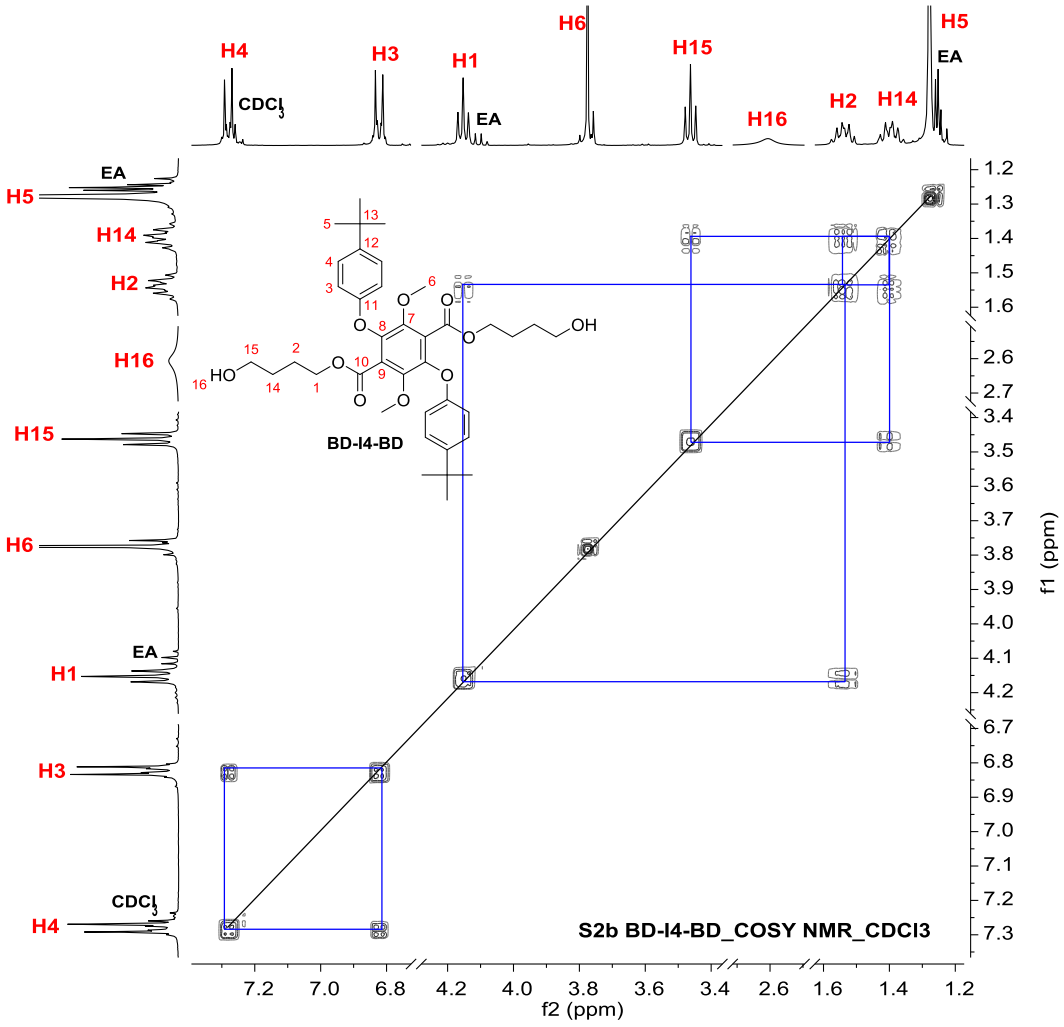
H4
CDCl3
H3
H1
EA
H6
H15
H16
H2
H14
H5
EA
EA
H5
H14
H2
H16
H15
H6
EA
H1
H3
CDCl3
H4
BD-I4-BD
S2b BD-I4-BD_COSY NMR_CDCl3
f2 (ppm)
f1 (ppm)

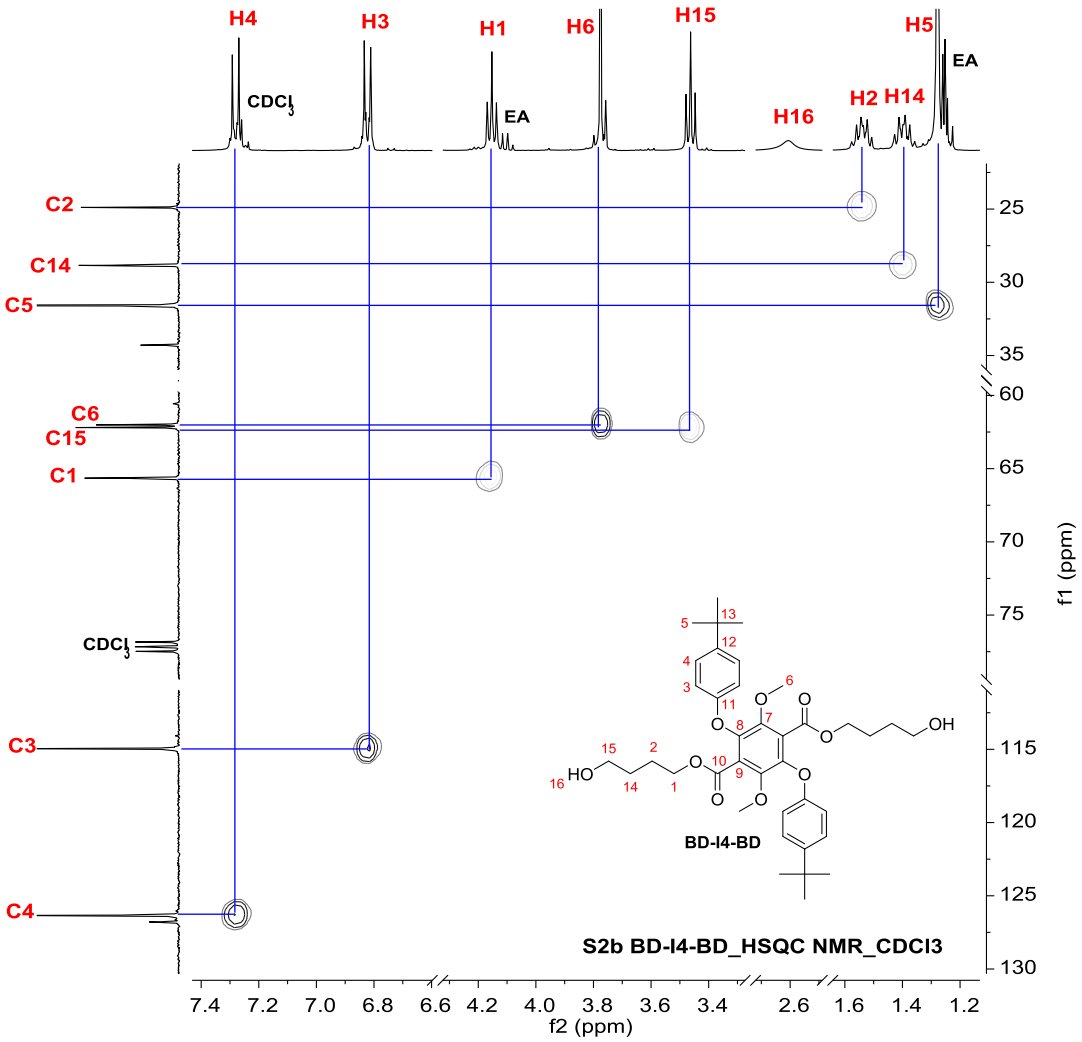
H4
H3
H1
H6
H15
H5
EA
CDCl3
EA
H16
H2 H14
C2
C14
C5
C6
C15
C1
CDCl3
C3
C4
BD-I4-BD
S2b BD-I4-BD_HSQC NMR_CDCl3
f1 (ppm)
f2 (ppm)

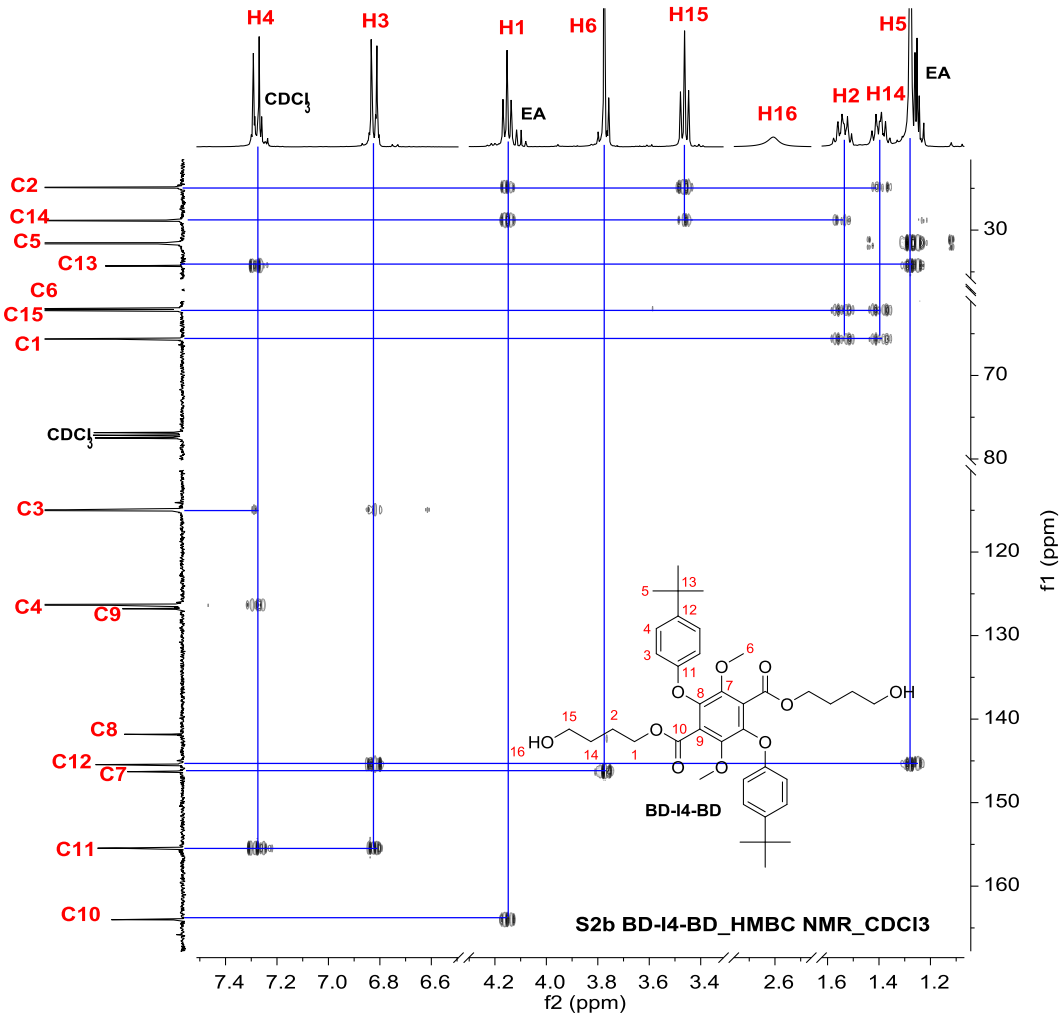

Figure 3: *^{1}H, ^{13}C, COSY, HSQC, HMBC NMR spectra (400 MHz, $CDCl_3$) of* **BD-I4-BD**.

S2c BD-I4_1H NMR_CDCl3

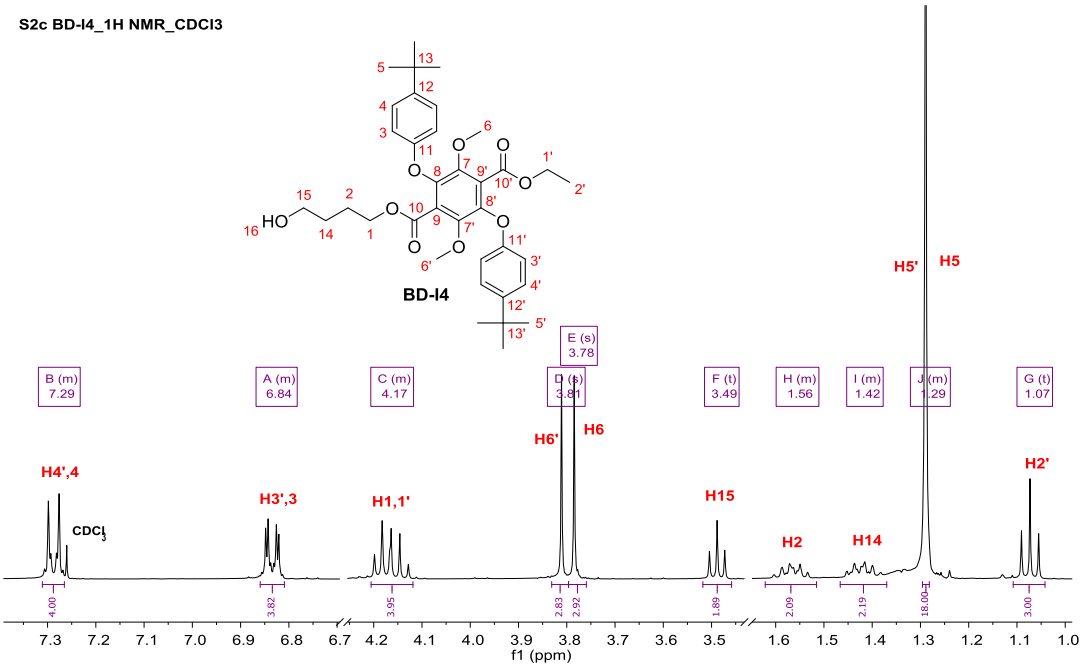

^{1}H NMR (400 MHz, Chloroform - *d*) δ 7.31 – 7.27 (m, 4H, H4, H4'), 6.86 – 6.81 (m, 4H, H3', H3), 4.21 – 4.12 (m, 4H, H1, H1'), 3.81 (s, 3H, H6'), 3.78 (s, 3H, H6), 3.49 (t, *J* = 6.3 Hz, 2H, H15), 1.62 – 1.52 (m, 2H, H2), 1.47 – 1.37 (m, 2H, H14), 1.30 – 1.28 (m, 18H, H5', H5), 1.07 (t, *J* = 7.1 Hz, 3H, H2').

S2c BD-I4_13C NMR_CDCl3

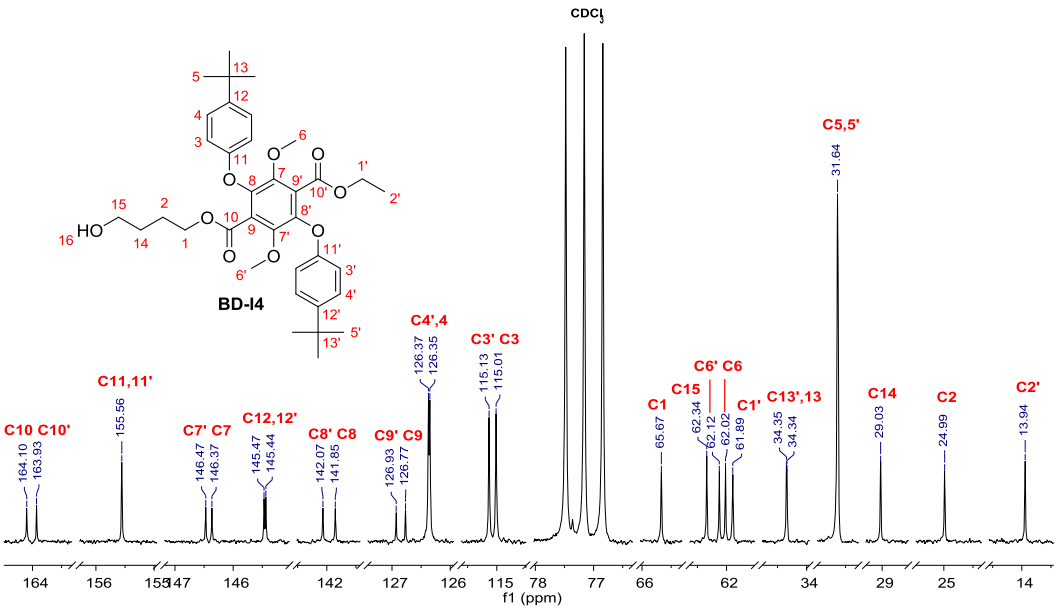

^{13}C NMR (101 MHz, $CDCl_3$) δ 164.10 (C10), 163.93 (C10'), 155.56 (C11, C11'), 146.47 (C7'), 146.37 (C7), 145.47, 145.44 (C12, C12'), 142.07 (C8'), 141.85 (C8), 126.93 (C9'), 126.77 (C9), 126.37, 126.35 (C4', C4), 115.13 (C3'), 115.01 (C3), 65.67 (C1), 62.34 (C15), 62.12 (C6'), 62.02 (C6), 61.89 (C1'), 34.35, 34.34 (C13', C13), 31.64 (C5, C5'), 29.03 (C14), 24.99 (C2), 13.94 (C2').

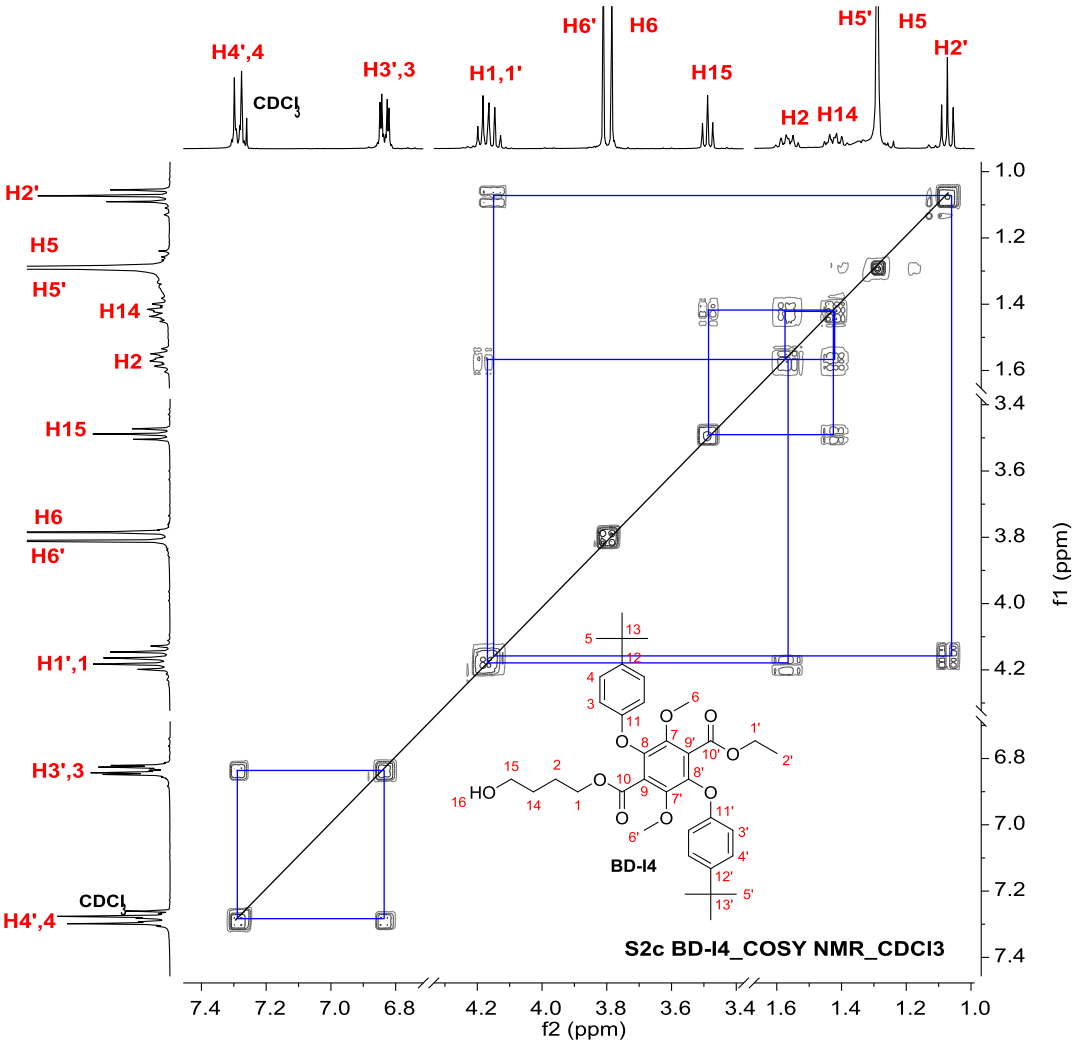
H4',4
CDCl3
H3',3
H1,1'
H6'
H6
H15
H2
H14
H5'
H5
H2'
H2'
H5
H5'
H14
H2
H15
H6
H6'
H1',1
H3',3
CDCl3
H4',4
BD-I4
S2c BD-I4_COSY NMR_CDCl3
f2 (ppm)
f1 (ppm)
7.4
7.2
7.0
6.8
4.2
4.0
3.8
3.6
3.4
1.6
1.4
1.2
1.0

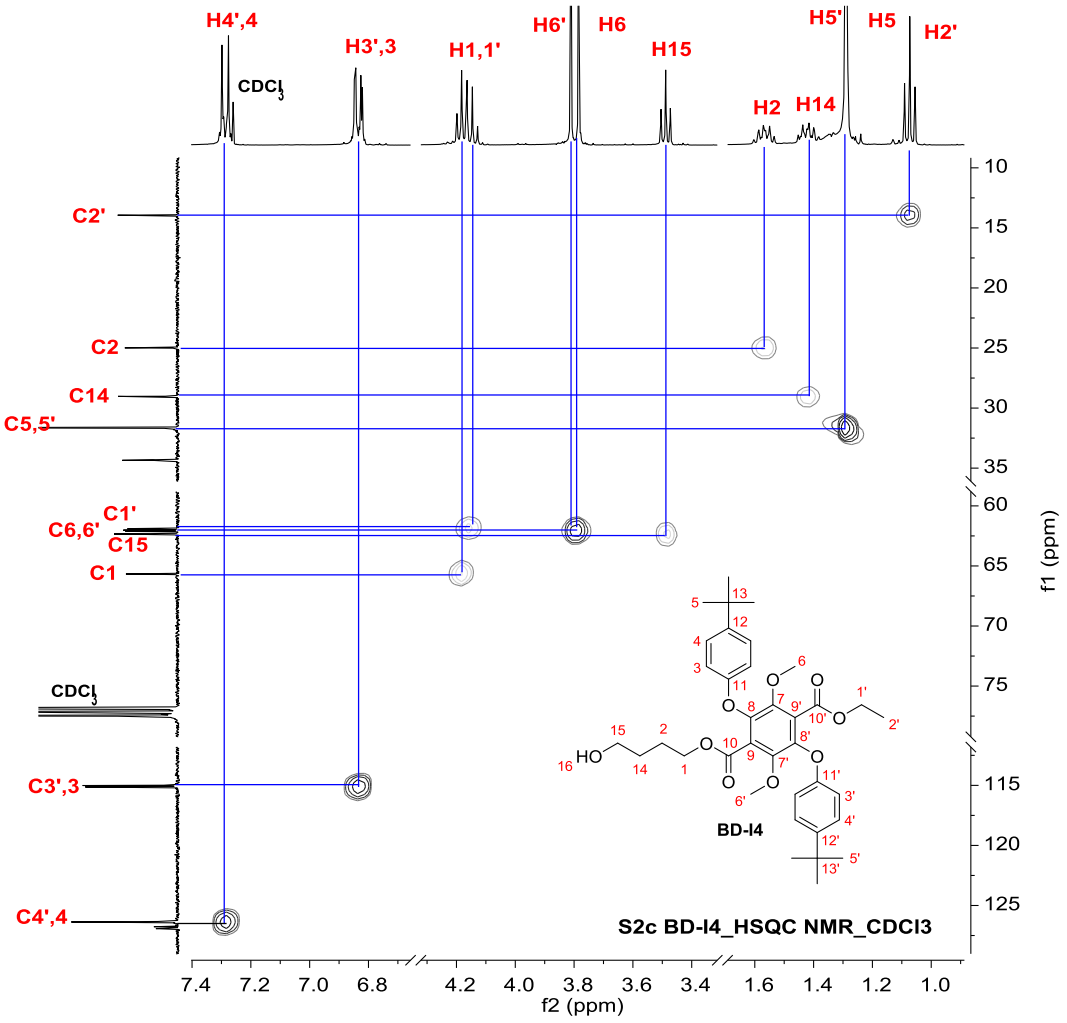
H4',4
H3',3
H1,1'
H6'
H6
H15
H5'
H5
H2'
H2
H14
CDCl3
C2'
C2
C14
C5,5'
C1'
C6,6'
C15
C1
CDCl3
C3',3
C4',4
BD-I4
S2c BD-I4_HSQC NMR_CDCl3
f1 (ppm)
f2 (ppm)

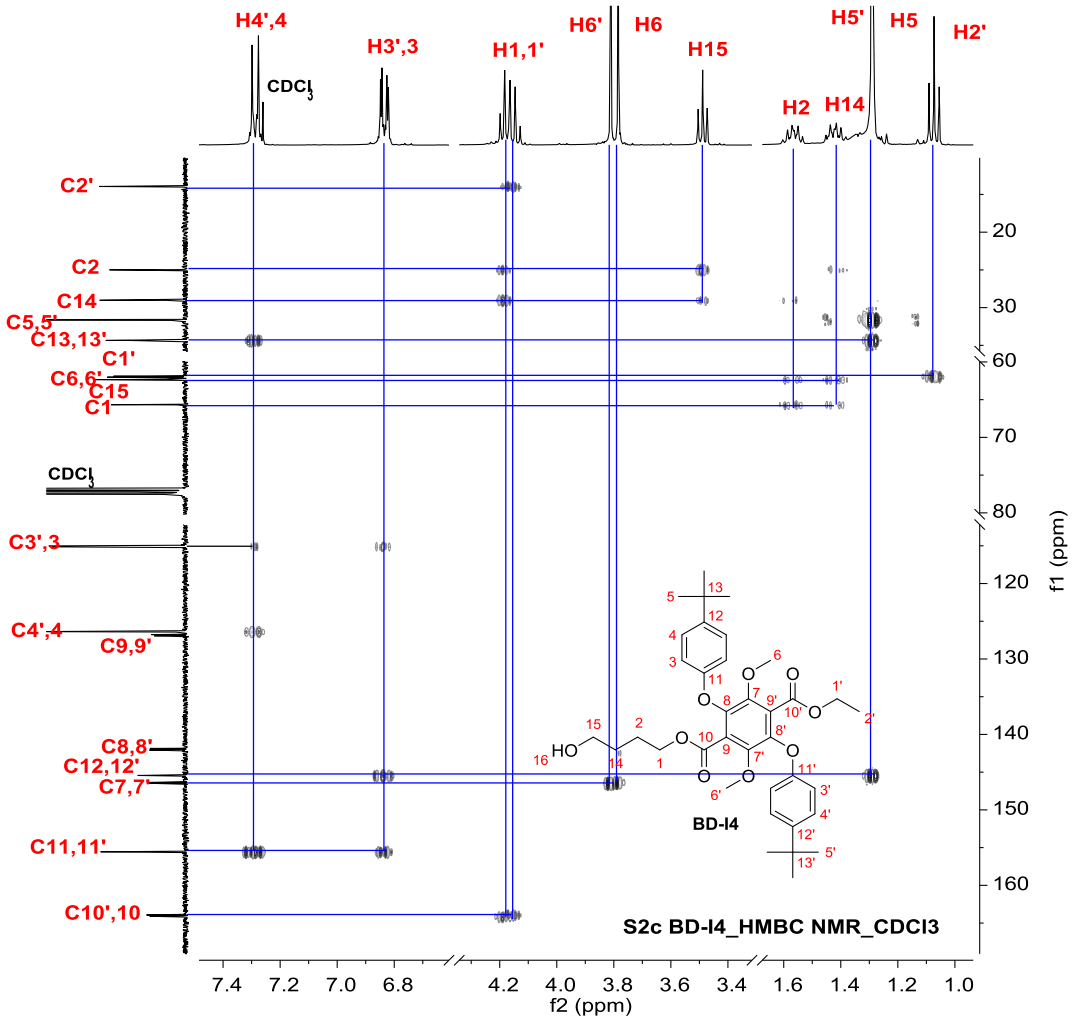

Figure 4: *^{1}H, ^{13}C, COSY, HSQC, HMBC NMR spectra (400 MHz, $CDCl_3$) of* **BD-I4**.

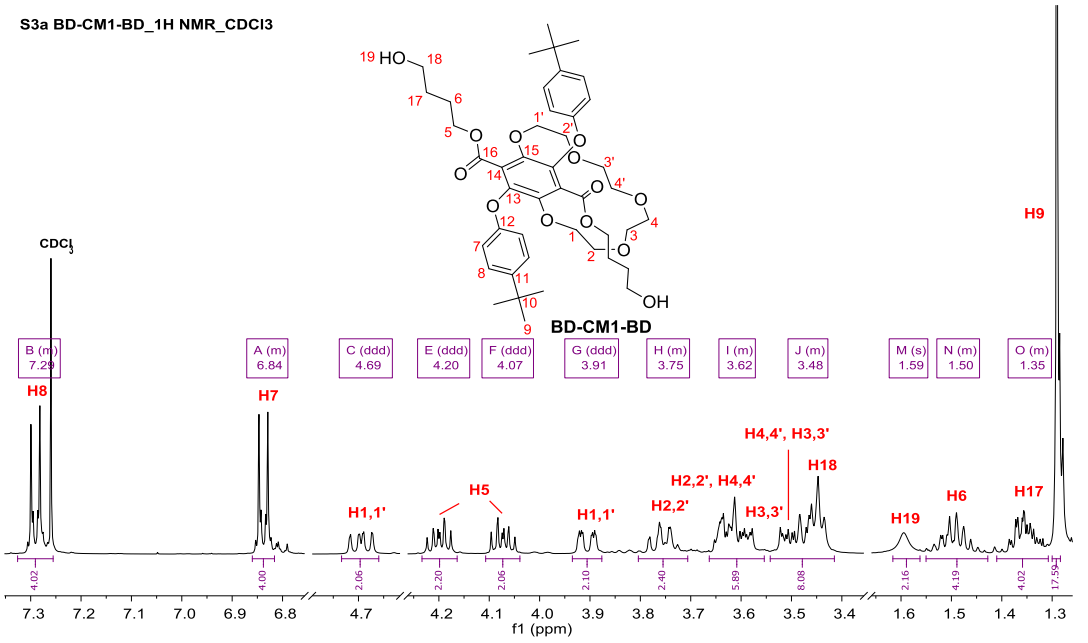

^{1}H NMR (500 MHz, Chloroform - *d*) δ 7.33 – 7.26 (m, 4H, H8), 6.86 – 6.82 (m, 4H, H7), 4.69 (ddd, *J* = 13.0, 8.9, 1.3 Hz, 2H, H1, H1'), 4.20 (ddd, *J* = 10.9, 6.8, 5.9 Hz, 2H, H5), 4.07 (ddd, *J* = 10.9, 6.7, 5.9 Hz, 2H, H5), 3.91 (ddd, *J* = 13.0, 3.6, 1.5 Hz, 2H, H1, H1'), 3.80 – 3.71 (m, 2H, H2, H2'), 3.66 – 3.55 (m, 6H, H2, H2', H4, H4', H3, H3'), 3.54 – 3.41 (m, 8H, H4, H4', H3, H3', H18), 1.59 (s, 2H, H19), 1.55 – 1.43 (m, 4H, H6), 1.41 – 1.31 (m, 4H, H17), 1.29 (s, 18H, H9).

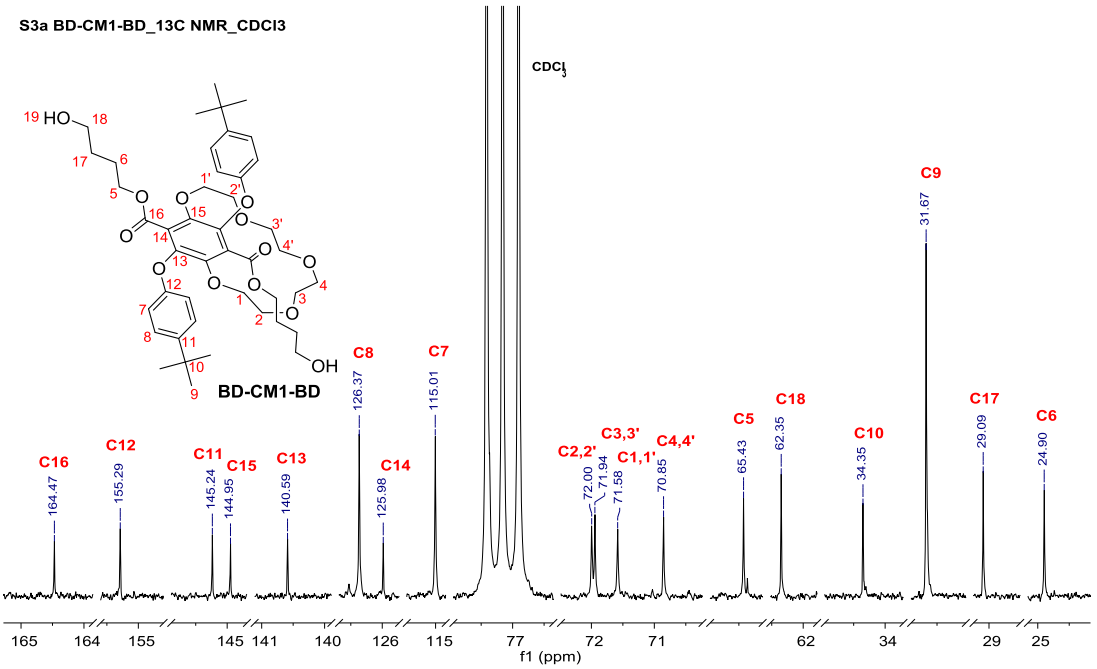

^{13}C NMR (126 MHz, $CDCl_3$) δ 164.47 (C16), 155.29 (C12), 145.24 (C11), 144.95 (C15), 140.59 (C13), 126.37 (C8), 125.98 (C14), 115.01 (C7), 72.00 (C2, C2'), 71.94 (C3, C3'), 71.58 (C1, C1'), 70.85 (C4, C4'), 65.43 (C5), 62.35 (C18), 34.35 (C10), 31.67 (C9), 29.09 (C17), 24.90 (C6).

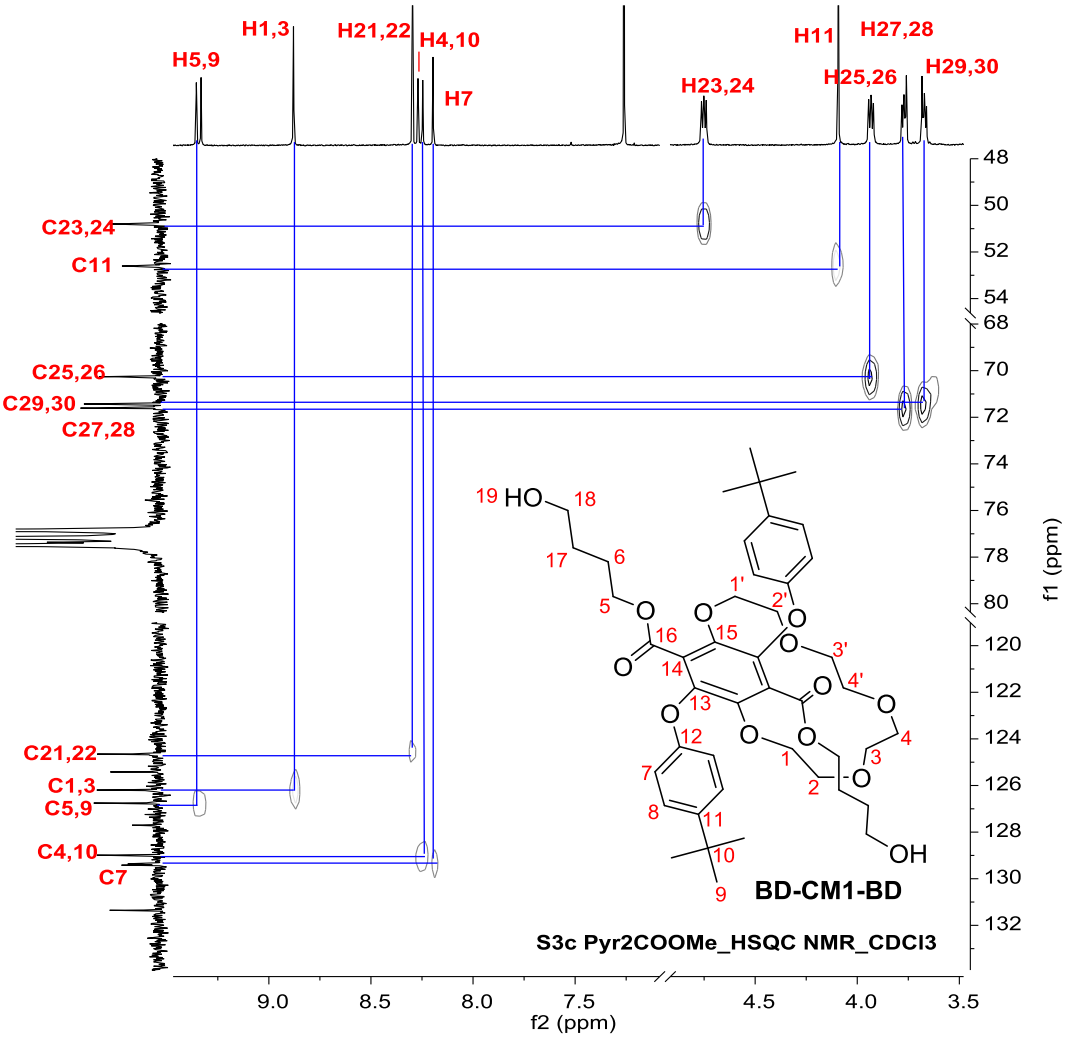
H1,3
H21,22
H4,10
H5,9
H7
H23,24
H11
H27,28
H25,26
H29,30
C23,24
C11
C25,26
C29,30
C27,28
C21,22
C1,3
C5,9
C4,10
C7
19 HO
18
17
6
5
16
15
14
13
12
7
8
11
10
9
1'
2'
3'
4'
1
2
3
4
OH
BD-CM1-BD
S3c Pyr2COOMe_HSQC NMR_CDCl3
f2 (ppm)
f1 (ppm)

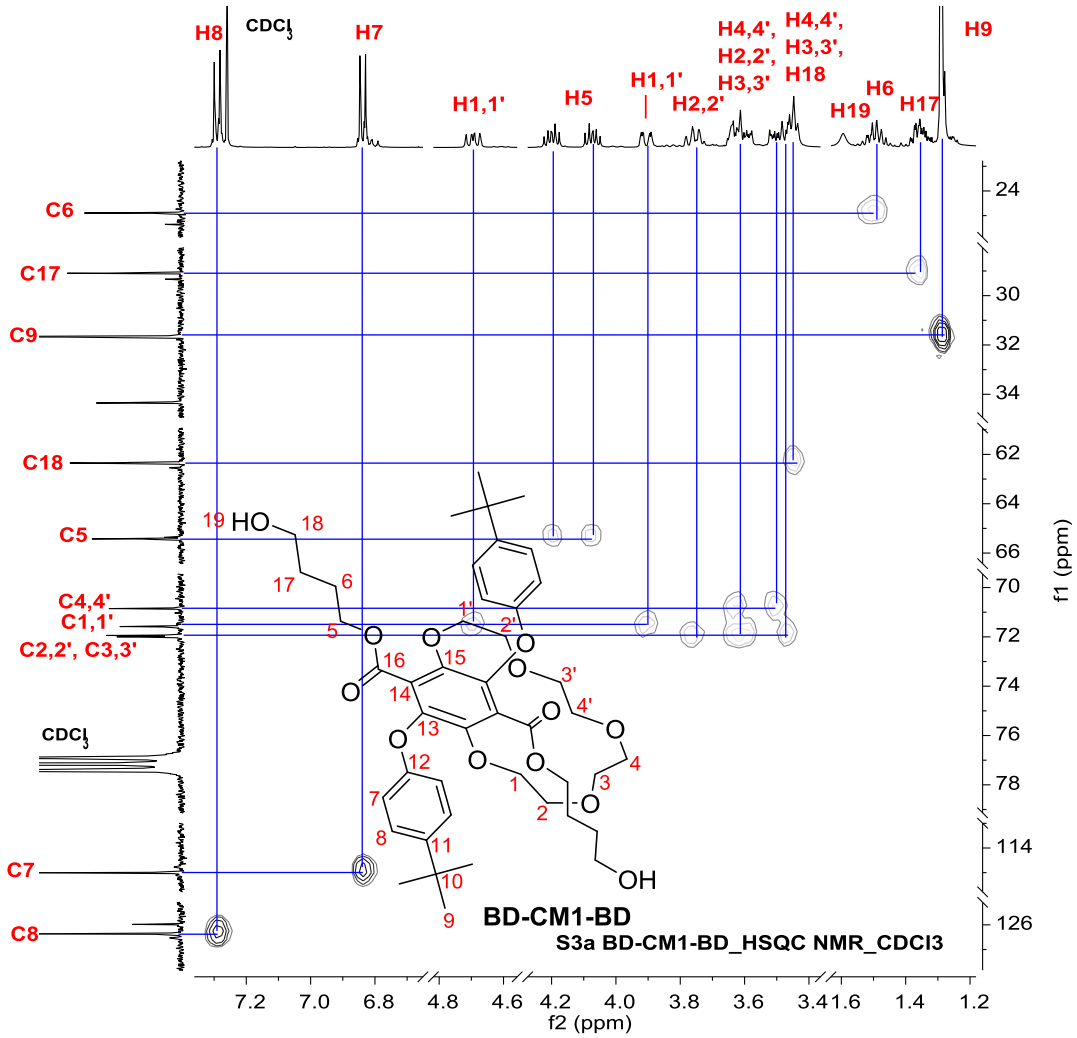
H8
CDCl3
H7
H1,1'
H5
H1,1'
H2,2'
H4,4',
H2,2',
H3,3'
H4,4',
H3,3',
H18
H19
H6
H17
H9
C6
C17
C9
C18
C5
C4,4'
C1,1'
C2,2', C3,3'
CDCl3
C7
C8
19 HO
18
17
6
5
1'
2'
16
15
14
13
12
7
8
11
10
9
3'
4'
4
3
2
1
OH
BD-CM1-BD
S3a BD-CM1-BD_HSQC NMR_CDCl3
f2 (ppm)
f1 (ppm)

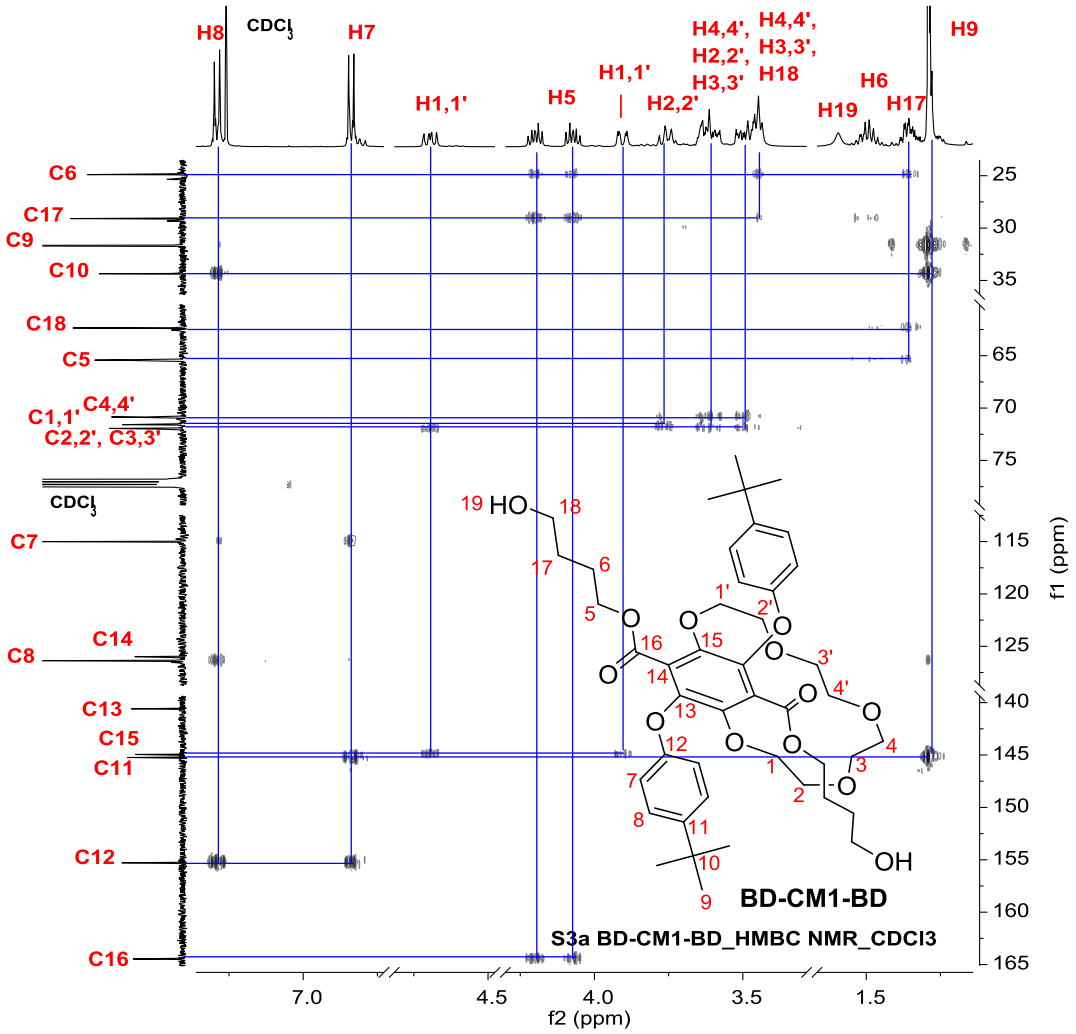

Figure 5: *^{1}H, ^{13}C, COSY, HSQC, HMBC NMR spectra (500 MHz, $CDCl_3$) of* **BD-CM1-BD**.

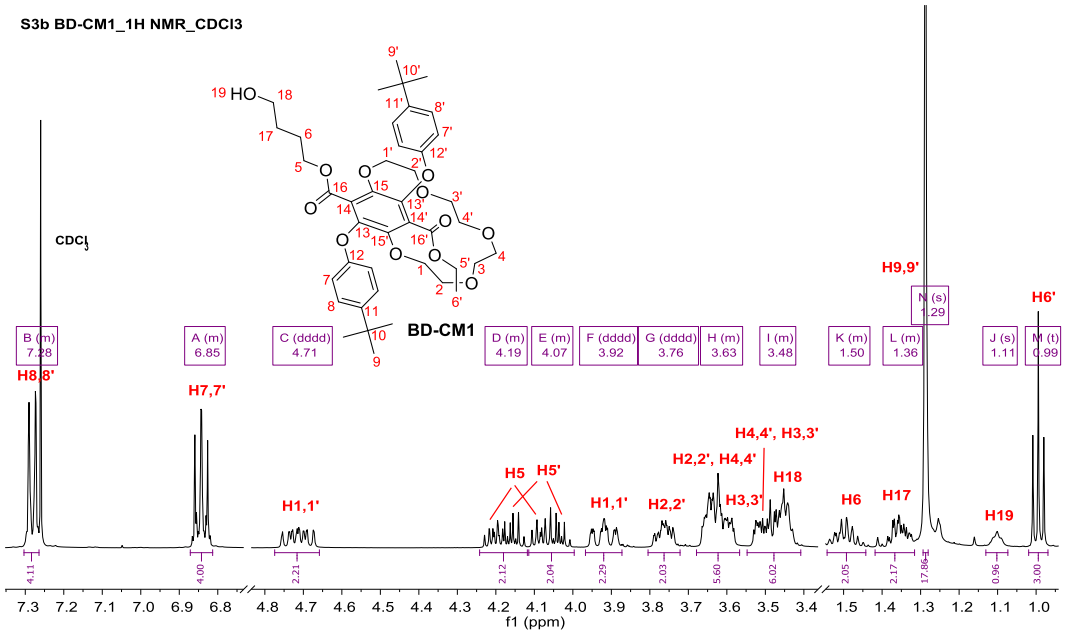

^{1}H NMR (500 MHz, Chloroform - *d*) δ 7.30 – 7.26 (m, 4H, H8, H8'), 6.87 – 6.81 (m, 4H, H7, H7'), 4.71 (dddd, *J* = 18.8, 13.0, 9.0, 1.3 Hz, 2H, H1, H1'), 4.24 – 4.12 (m, 2H, H5, H5'), 4.11 – 4.00 (m, 2H, H5, H5'), 3.92 (dddd,*J* = 17.5, 13.0, 3.5, 1.5 Hz, 2H, H1, H1'), 3.76 (dddd, *J* = 10.5, 8.8, 4.8, 1.4 Hz, 2H, H2, H2'), 3.68 – 3.57 (m, 6H, H2, H2', H4, H4', H3, H3'), 3.55 – 3.41 (m, 6H, H4, H4', H3, H3', H18), 1.54 – 1.44 (m, 2H, H6), 1.42 – 1.32 (m, 2H, H17), 1.29 (s, 18H, H9, H9'), 1.11 (s, 1H, H19), 0.99 (t, *J* = 7.1 Hz, 3H, H6').

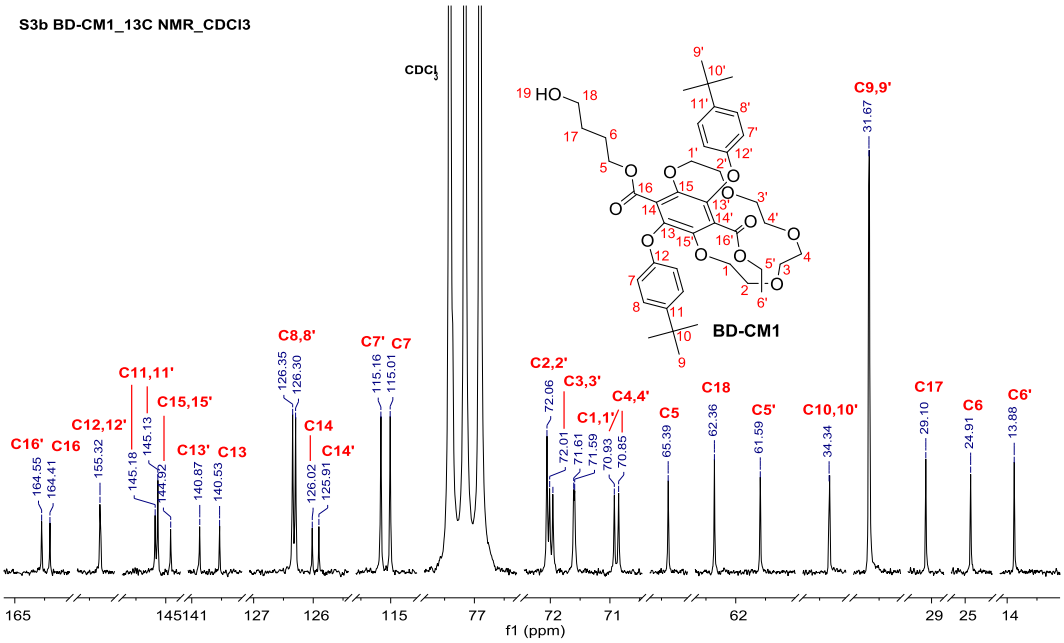

^{13}C NMR (126 MHz, $CDCl_3$) δ 164.55 (C16'), 164.41 (C16), 155.32 (C12, C12'), 145.18, 145.13 (C11, C11'), 144.92 (C15, C15'), 140.87 (C13'), 140.53 (C13), 126.35, 126.30 (C8, C8'), 126.02 (C14), 125.91 (C14'), 115.16 (C7'), 115.01 (C7), 72.06 (C2, C2'), 72.01 (C3, C3'), 71.61, 71.59 (C1, C1'), 70.93, 70.85 (C4, C4'), 65.39 (C5), 62.36 (C18), 61.59 (C5'), 34.34 (C10, C10'), 31.67 (C9, C9'), 29.10 (C17), 24.91 (C6), 13.88 (C6').

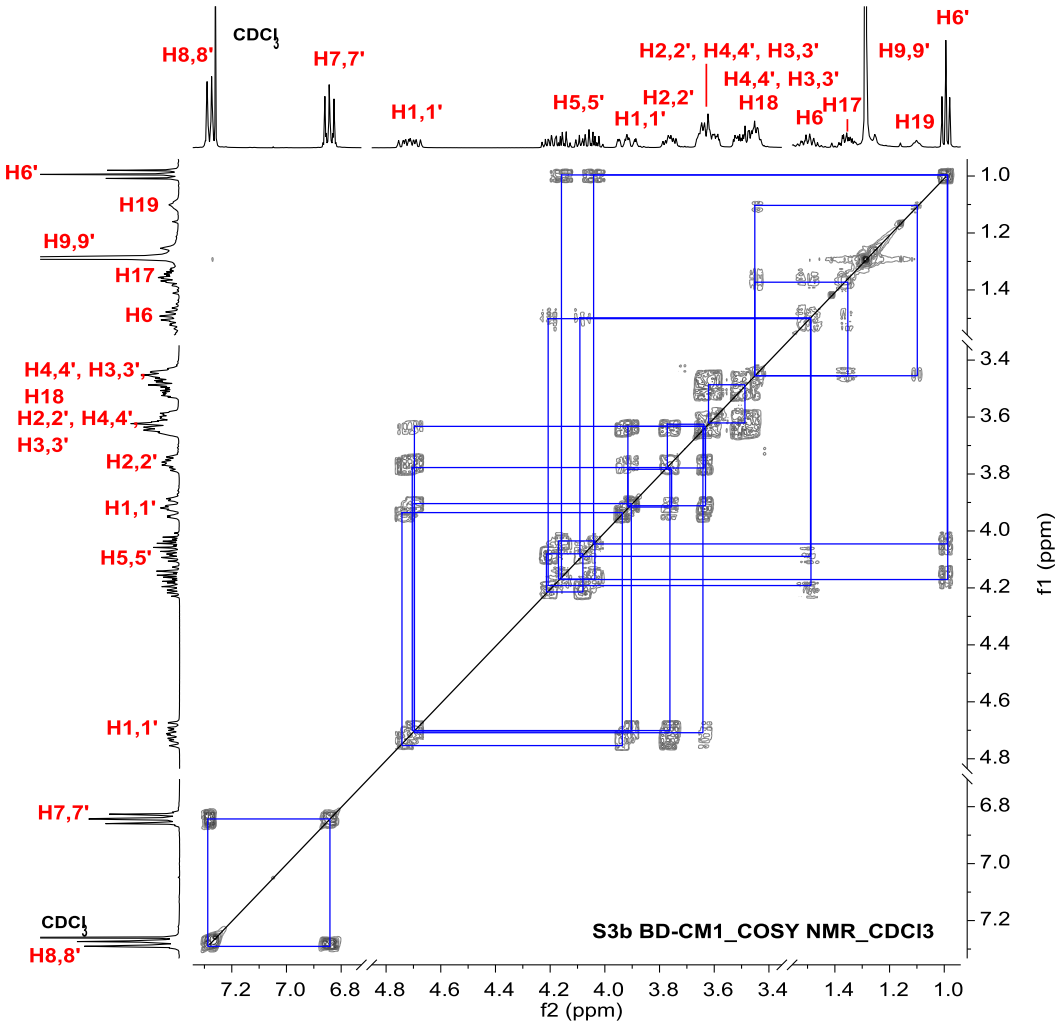
H8,8'
CDCl3
H7,7'
H1,1'
H5,5'
H2,2', H4,4', H3,3'
H1,1'
H2,2'
H4,4', H3,3'
H18
H6
H17
H9,9'
H6'
H19
H6'
H19
H9,9'
H17
H6
H4,4', H3,3'
H18
H2,2', H4,4',
H3,3'
H2,2'
H1,1'
H5,5'
H1,1'
H7,7'
CDCl3
H8,8'
S3b BD-CM1_COSY NMR_CDCl3
f1 (ppm)
f2 (ppm)

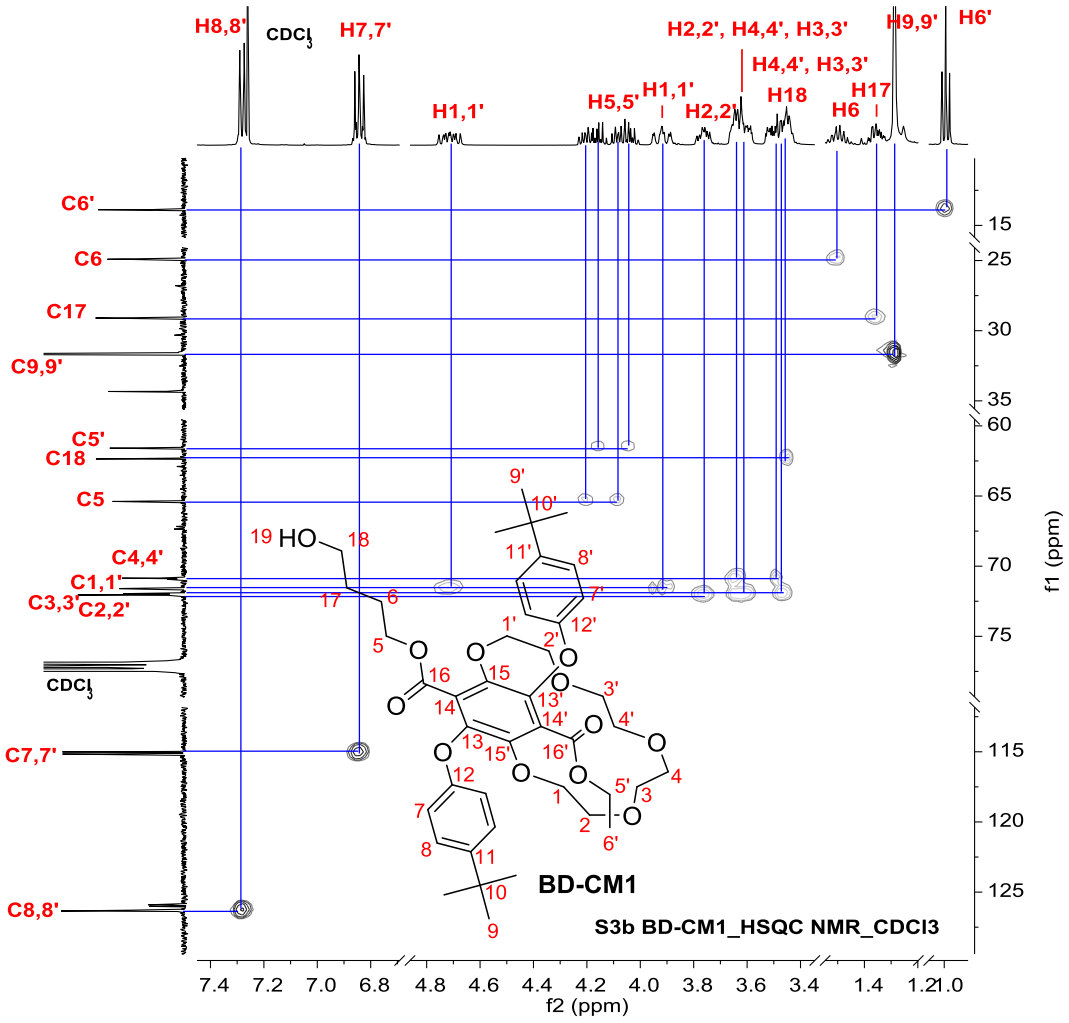
H8,8'
CDCl3
H7,7'
H1,1'
H5,5'
H1,1'
H2,2'
H2,2', H4,4', H3,3'
H4,4', H3,3'
H18
H6
H17
H9,9'
H6'
C6'
C6
C17
C9,9'
C5'
C18
C5
C4,4'
C1,1'
C3,3'
C2,2'
CDCl3
C7,7'
C8,8'
BD-CM1
S3b BD-CM1_HSQC NMR_CDCl3
f2 (ppm)
f1 (ppm)

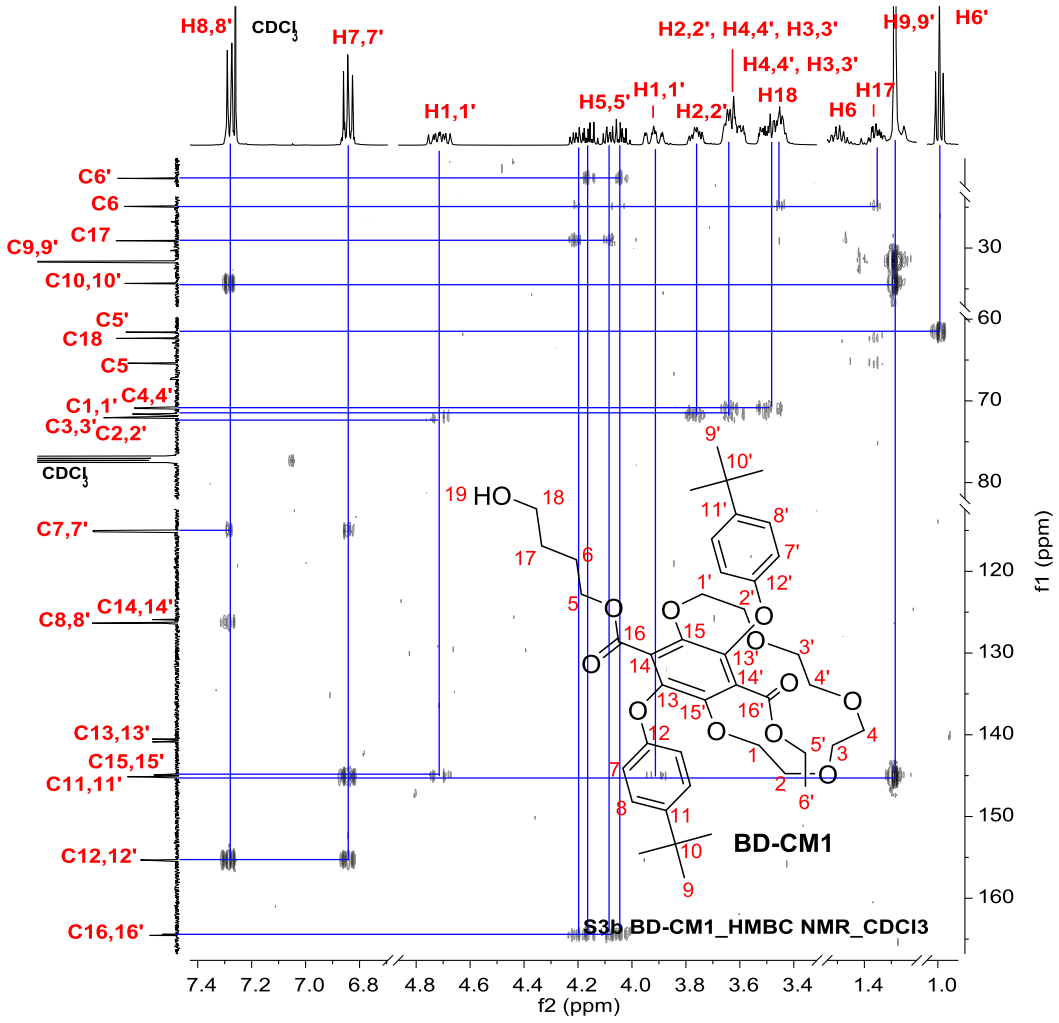

Figure 6: *^{1}H, ^{13}C, COSY, HSQC, HMBC NMR spectra (500 MHz, $CDCl_3$) of* **BD-CM1**.

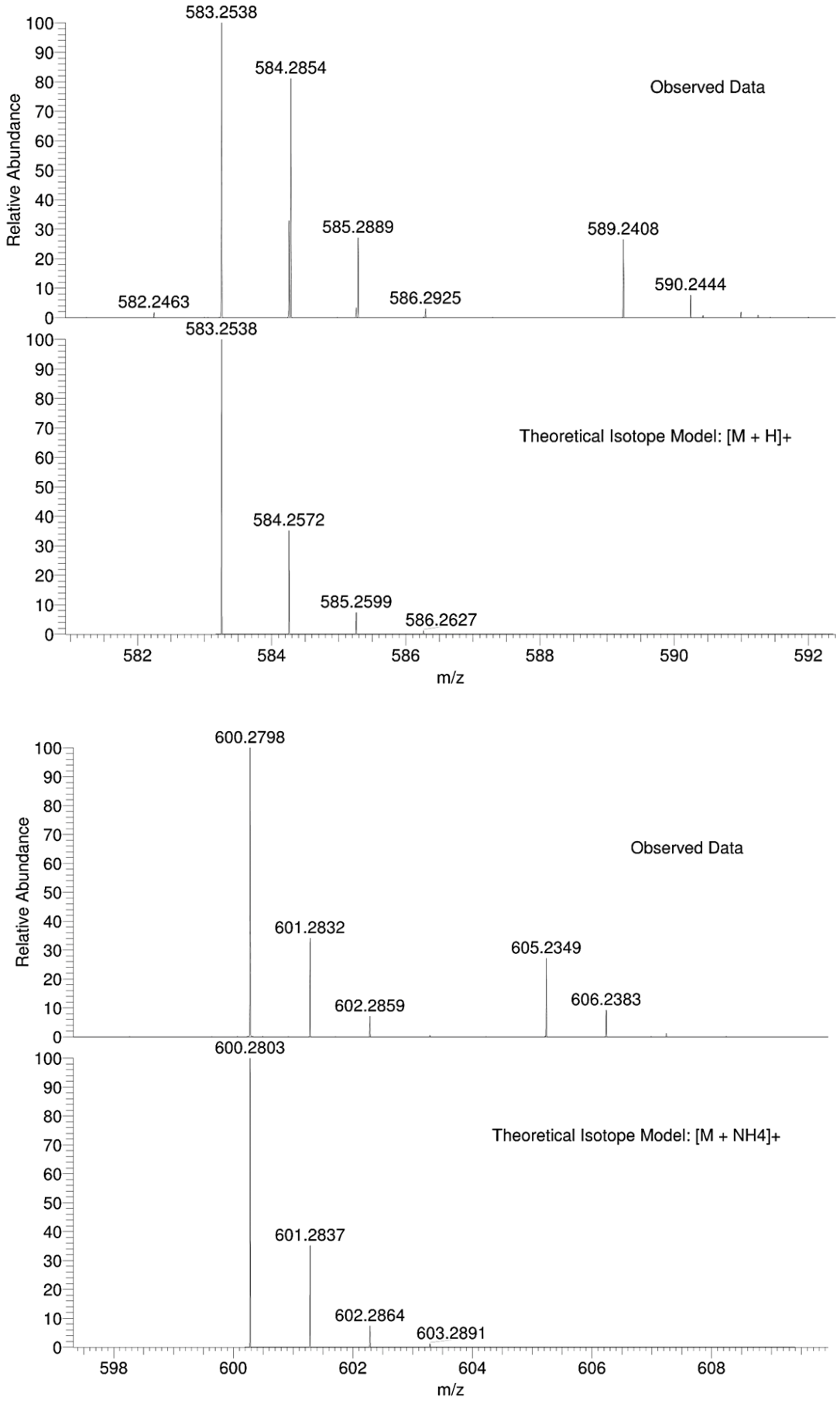

Figure 7: *Mass spectra of* **EG-I3-EG** *showing its* $[M+H]^+$ *and* $[M+NH_4]^+$ *ions.*

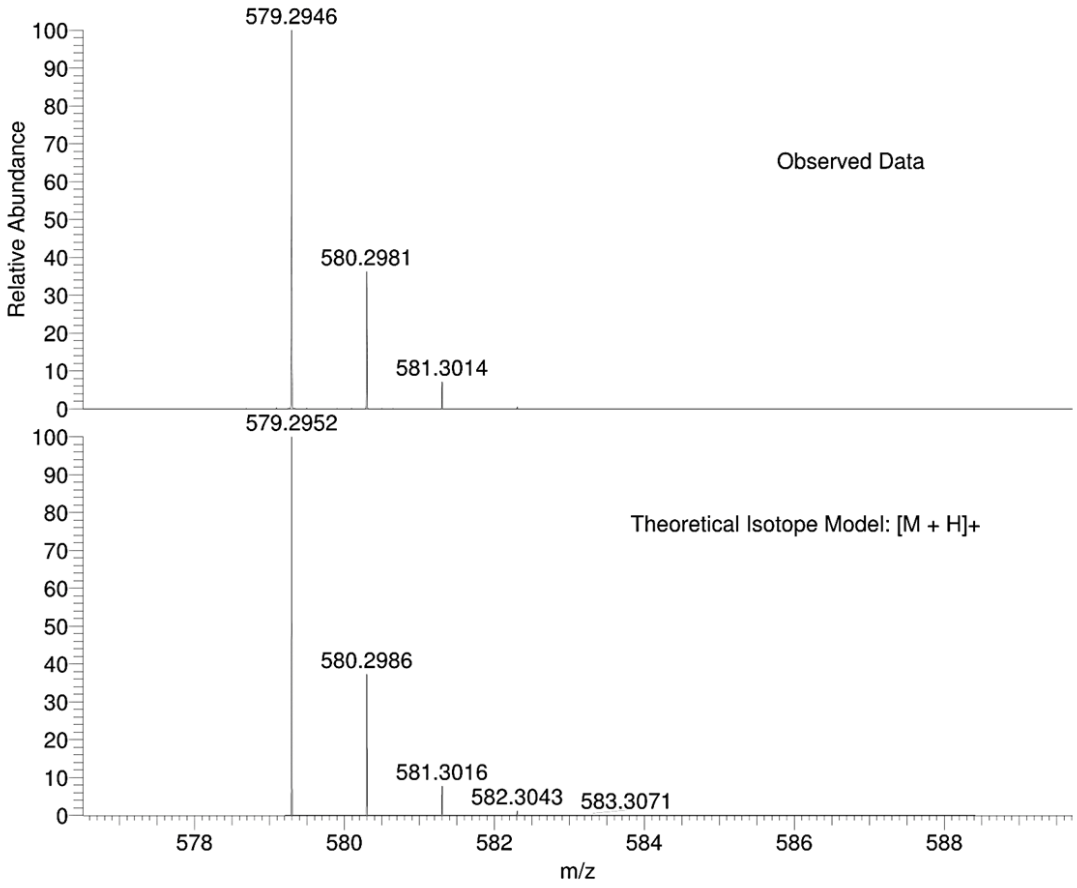

Figure 8: *Mass spectra of* **I4** *showing its* $[M+H]^+$ *ion.*

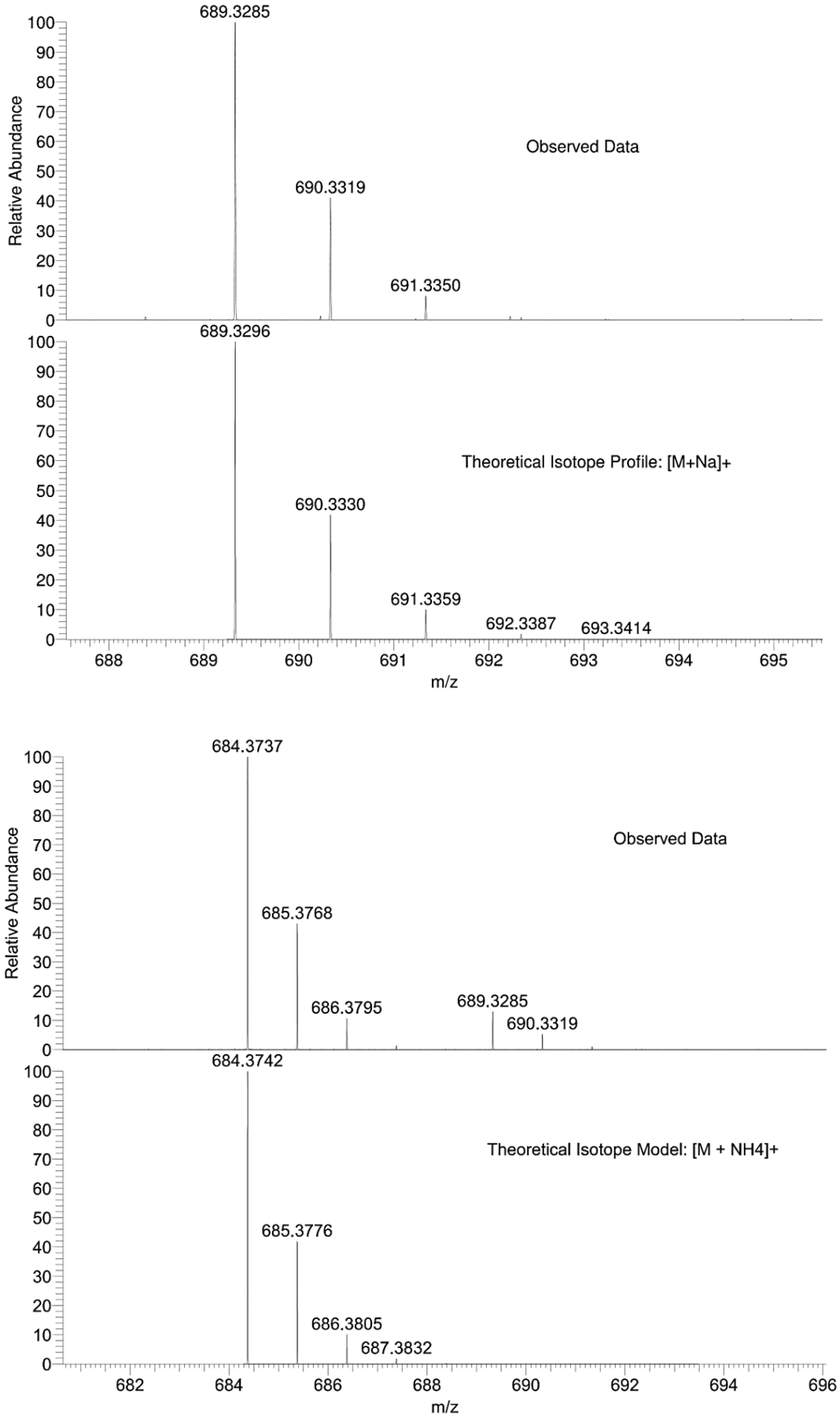

Figure 9: *Mass spectra of* **BD-I4-BD** *showing its* $[M+Na]^+$ *and* $[M+NH_4]^+$ *ions.*

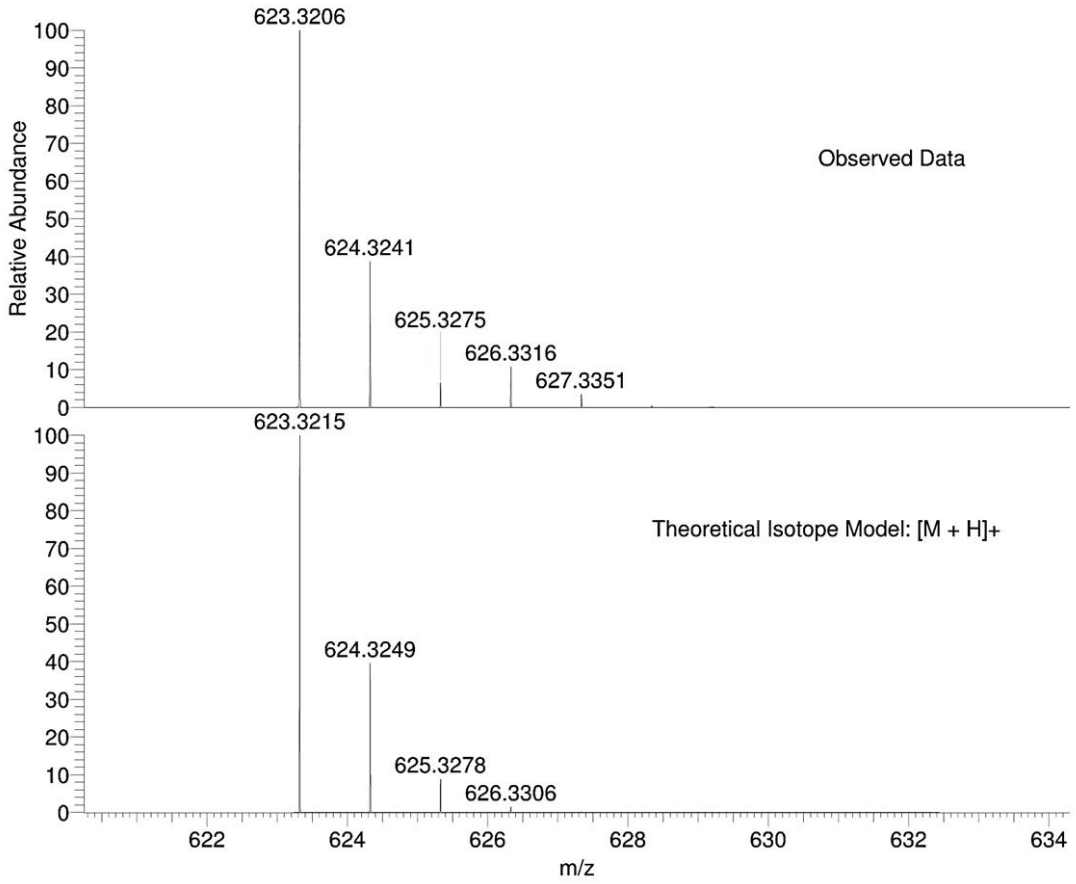

Figure 10: *Mass spectra of* **BD-I4** *showing its* $[M+H]^+$ *ion.*

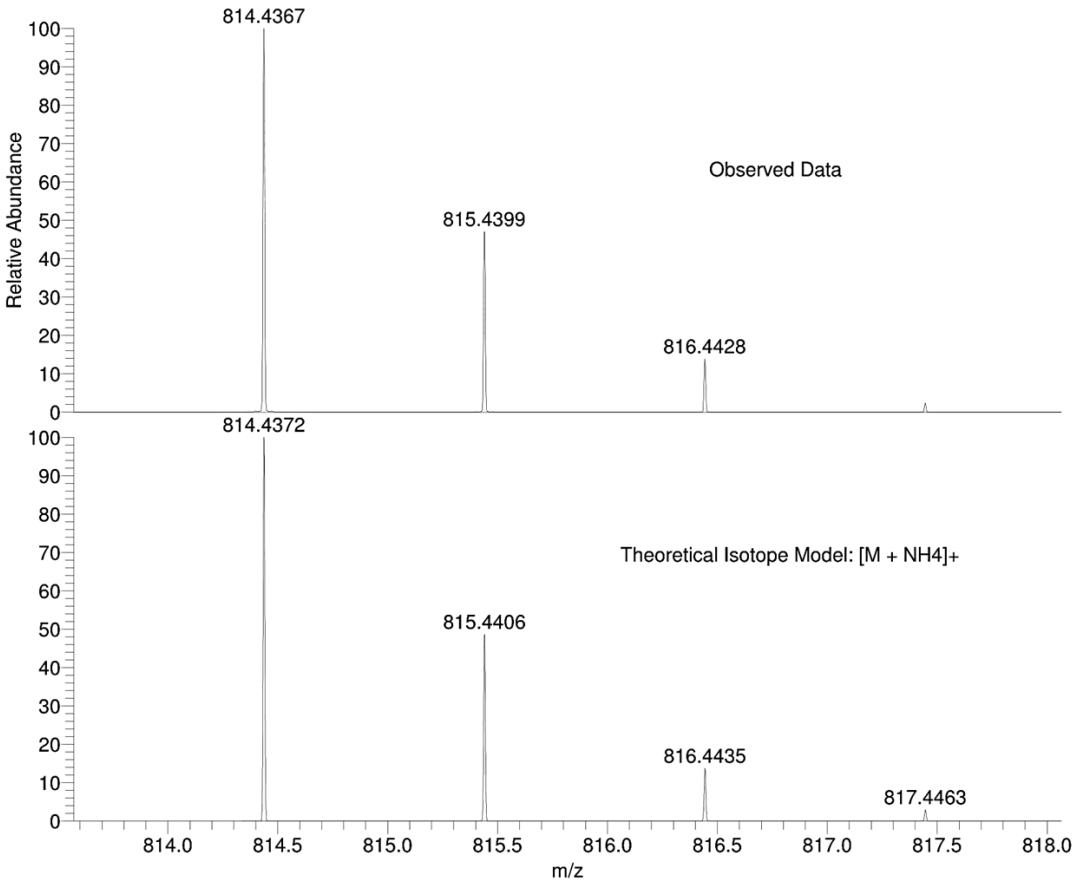

Figure 11: *Mass spectra of* **BD-CM1-BD** *showing its* $[M+NH_4]^+$ *ion.*

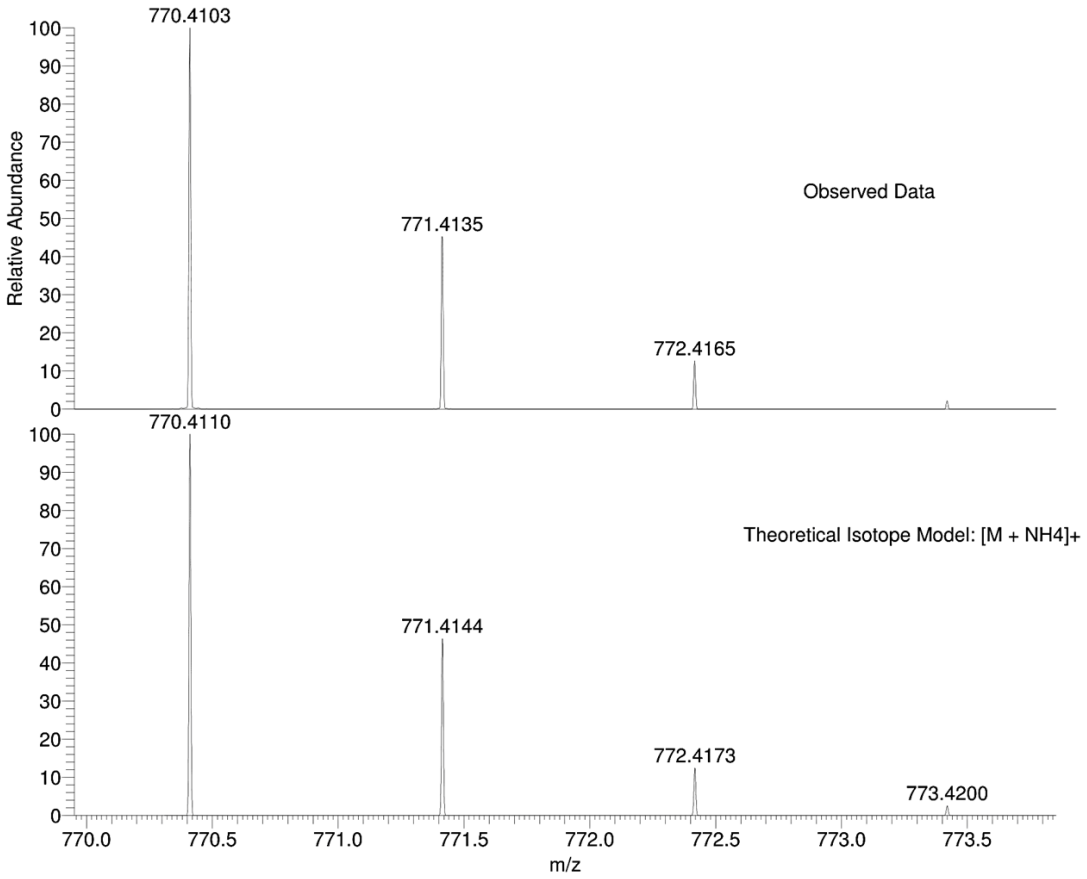

Figure 12: *Mass spectra of* **BD-CM1** *showing its* $[M+NH_4]^+$ *ion.*

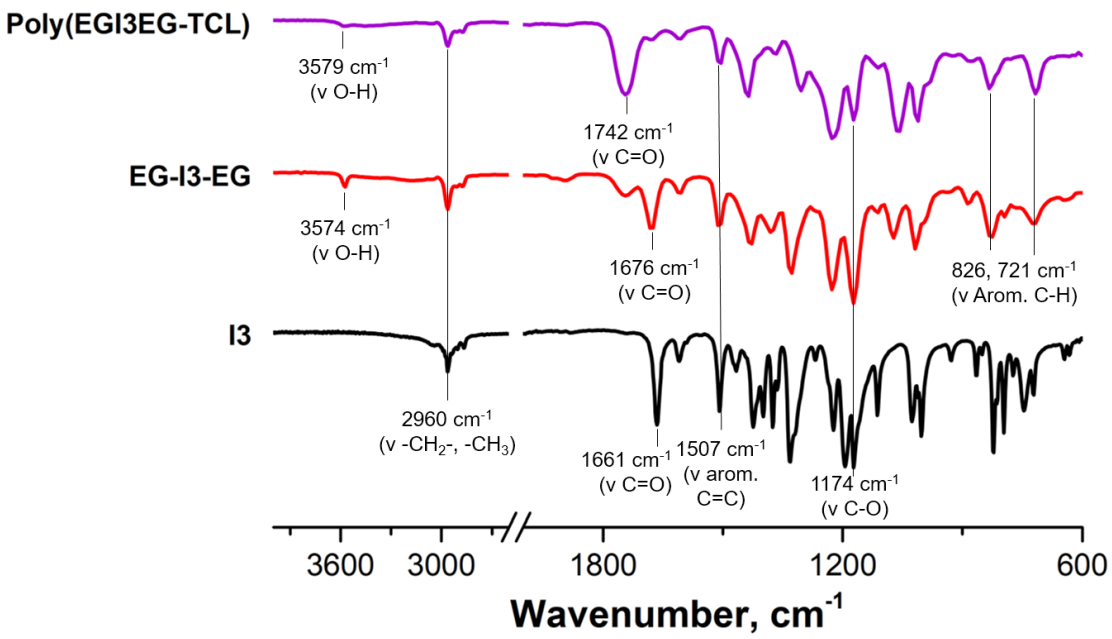

Figure 13: *FT-IR spectra of* **I3**, **EG-I3-EG** *and* **Poly(EGI3EG-TCL)**.

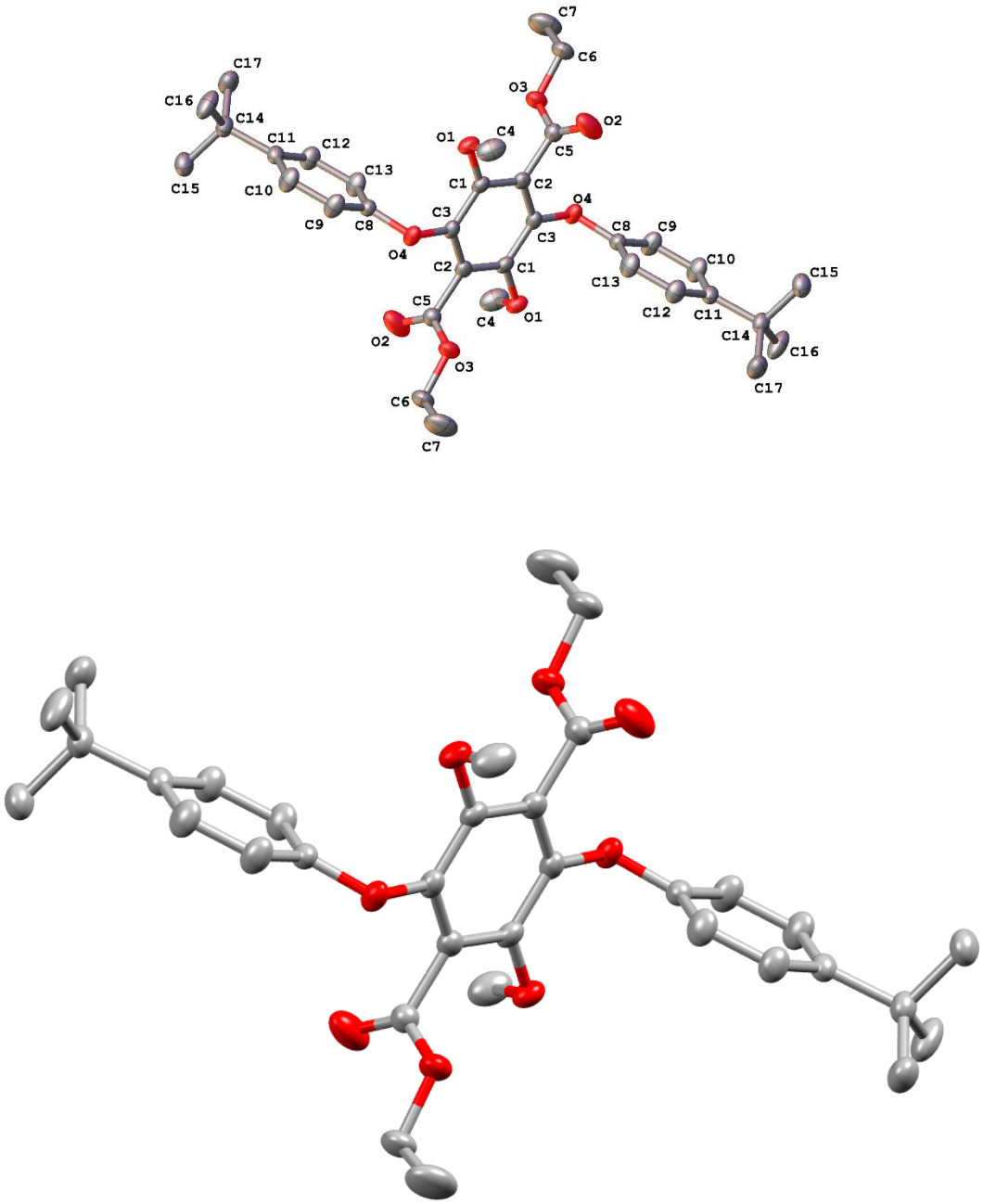

Figure 14: *X-ray crystal structure of* ***I4****.*

I4	
Empirical formula	$C_{34}H_{42}O_8$
Formula weight	578.67
Temperature/K	150.0(2)
Crystal system	monoclinic
Space group	$P2_1/c$
a/Å	5.9780(3)
b/Å	10.5544(4)
c/Å	25.1034(10)
α/°	90
β/°	92.057(4)
γ/°	90
Volume/Å^3	1582.85(13)
Z	2
ρ_{calc}g/cm^3	1.214
μ/mm^{-1}	0.697
F(000)	620.0
Crystal size/mm^3	0.18 × 0.14 × 0.12
Radiation	CuKα (λ = 1.54184)
2Θ range for data collection/°	7.048 to 133.792
Index ranges	-7 ≤ h ≤ 6, -11 ≤ k ≤ 12, -29 ≤ l ≤ 24
Reflections collected	14110
Independent reflections	2806 [R_{int} = 0.0384, R_{sigma} = 0.0259]
Data/restraints/parameters	2806/0/195
Goodness-of-fit on F^2	1.052
Final R indexes [I>=2σ (I)]	R_1 = 0.0392, wR_2 = 0.0958
Final R indexes [all data]	R_1 = 0.0487, wR_2 = 0.1039
Largest diff. peak/hole / e Å^{-3}	0.29/-0.25

Table 1: *Crystal data and structure refinement for* **I4***.*

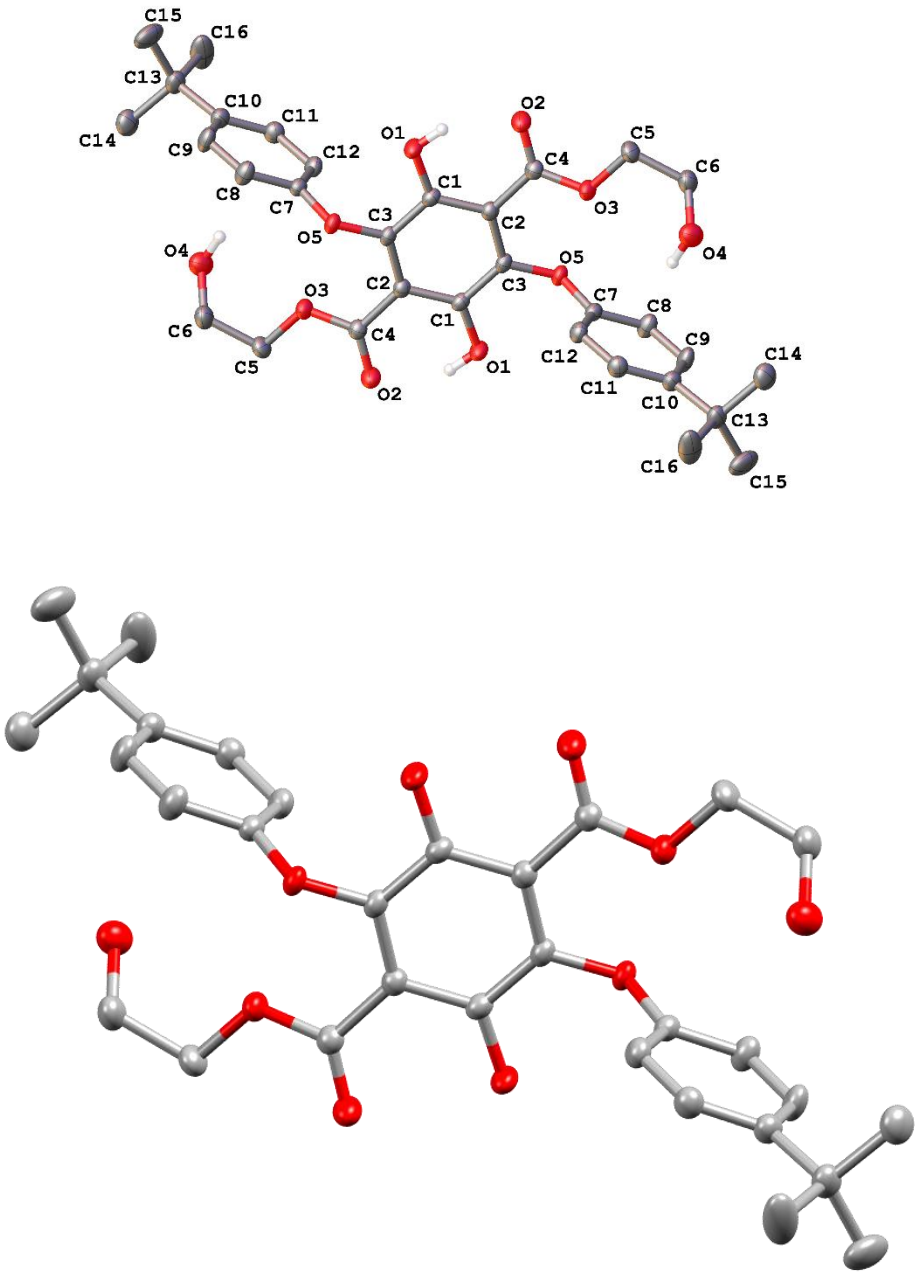

Figure 15: *X-ray crystal structure of* **EG-I3-EG**.

EG-I3-EG	
Empirical formula	$C_{34}H_{40}Cl_6O_{10}$
Formula weight	821.36
Temperature/K	150.0(2)
Crystal system	triclinic
Space group	P-1
a/Å	6.1698(2)
b/Å	8.7425(3)
c/Å	18.2846(4)
α/°	79.864(2)
β/°	83.699(2)
γ/°	80.021(3)
Volume/Å^3	952.98(5)
Z	1
ρ_{calc}g/cm^3	1.431
μ/mm^{-1}	4.571
F(000)	426.0
Crystal size/mm^3	0.34 × 0.08 × 0.06
Radiation	CuKα (λ = 1.54184)
2Θ range for data collection/°	9.862 to 133.572
Index ranges	-7 ≤ h ≤ 7, -10 ≤ k ≤ 10, -21 ≤ l ≤ 21
Reflections collected	32589
Independent reflections	3384 [R_{int} = 0.0339, R_{sigma} = 0.0141]
Data/restraints/parameters	3384/21/262
Goodness-of-fit on F^2	1.028
Final R indexes [I>=2σ (I)]	R_1 = 0.0295, wR_2 = 0.0756
Final R indexes [all data]	R_1 = 0.0346, wR_2 = 0.0790
Largest diff. peak/hole / e Å^{-3}	0.23/-0.21

Table 2: *Crystal data and structure refinement for* **EG-I3-EG**.

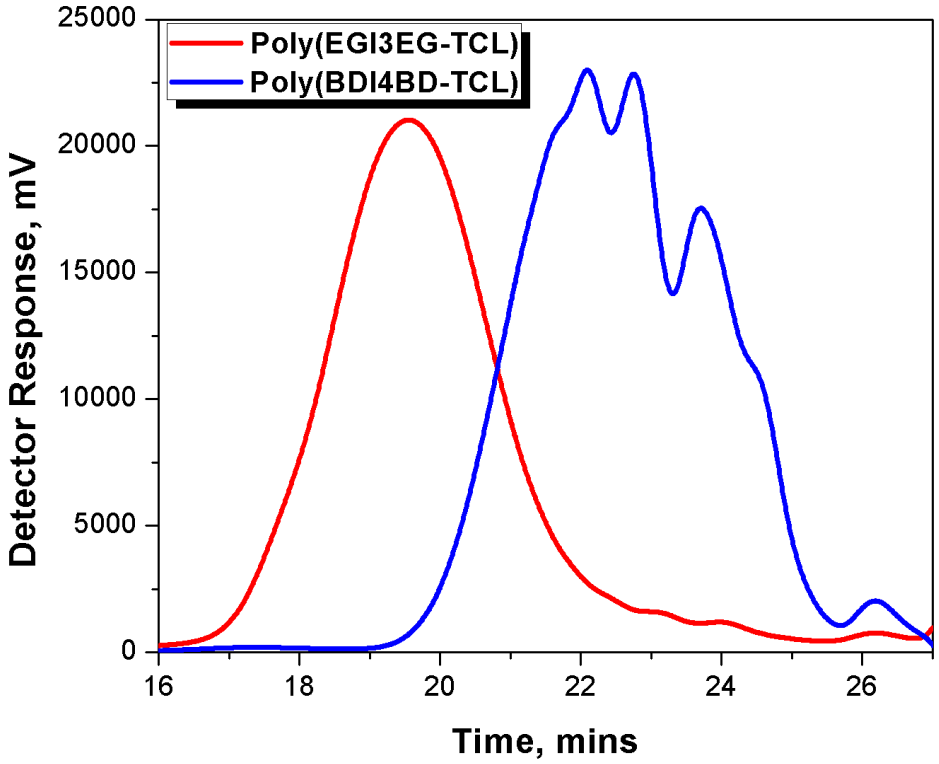

Figure 16: *GPC molecular weight distribution curves of* **Poly(EGI3EG-TCL)** *and* **Poly(BDI4BD-TCL)**.